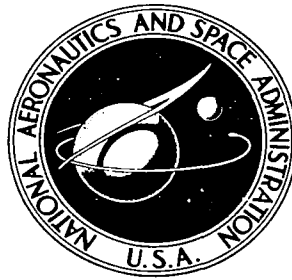
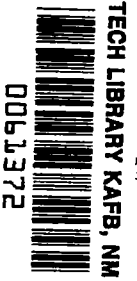


**NASA CONTRACTOR
REPORT**



NASA CR-2



NASA CR-2763

LOAN COPY: RETURN TO
AFWL TECHNICAL LIBRARY
KIRTLAND AFB, N. M.

**SKYLAB S-193 RADAR ALTIMETER
EXPERIMENT ANALYSES AND RESULTS**

G. S. Brown, editor

Prepared by
APPLIED SCIENCE ASSOCIATES, INC.
Apex, N. C. 27502
for Wallops Flight Center

NATIONAL AERONAUTICS AND SPACE ADMINISTRATION • WASHINGTON, D. C. • FEBRUARY 1977

FOREWORD

This report was prepared for the National Aeronautics and Space Administration, Wallops Flight Center by Applied Science Associates, Inc., under Contract No. NAS6-2520 (Task 3.10). Mr. J. T. McGoogan of NASA/WFC acted as technical monitor/coordinator of the subject task.

The report contains contributions from a number of authors; each chapter of the report is identified as to the individual responsible for its content. The affiliation of these authors is summarized below.

Applied Science Associates, Inc.

105 East Chatham

Apex, N. C. 27502

Dr. G. S. Brown

Mr. W. J. Curry

Dr. G. S. Hayne

Dr. L. S. Miller

Directorate of Applied Science

National Aeronautics and Space Administration

Wallops Flight Center

Wallops Island, VA 23337

Mr. C. L. Parsons

Dr. E. J. Walsh

Dr. E. L. Hofmeister of the General Electric Company, Utica, New York, provided valuable assistance on the design details of the S-193 radar altimeter.



TABLE OF CONTENTS

	<u>Page</u>
FOREWORD	ii
ABSTRACT	iii
<u>CHAPTER</u>	
1 INTRODUCTION AND SUMMARY OF RESULTS	1
References.	4
2 ALTITUDE DATA FILTERING CONSIDERATIONS.	6
1.0 Introduction and Summary of Results.	6
2.0 Discussion of Altitude Filtering Procedures.	11
3.0 Derivation of the Linear Minimum Variance Altitude Filter.	15
References	24
3 POINTING ANGLE ESTIMATION VIA WAVEFORM ANALYSIS	25
1.0 Background	25
2.0 Analysis	25
3.0 Discussion of Results.	39
References	46
Appendix	47
4 POINTING ANGLE ESTIMATION VIA TRACKER BANDWIDTH ANALYSIS.	50
1.0 Introduction	50
2.0 Effect of Pointing Angle on Skylab Tracking Loop Bandwidth.	53
3.0 Effect of Pointing Angle on Altitude Tracking Jitter	55
References	60
Appendix	61
5 AN OBSERVATIONAL STUDY OF σ° VARIATIONS IN THE VICINITY OF THE GULF STREAM.	63
1.0 Introduction	63
2.0 Skylab 2 EREP Pass 9 Analysis.	66
3.0 Skylab 3 EREP Pass 17 Analysis	79
4.0 Theoretical Expectations	84
References	91

TABLE OF CONTENTS (Cont'd.)

CHAPTER	<u>Page</u>
6 ANALYSIS OF A TROPICAL METEOROLOGICAL DISTURBANCE USING RECEIVED POWER AND WAVEFORM DATA.	92
1.0 Introduction	92
2.0 The Radar Equation	92
2.1 Calculation of the Sensitivity of P_r to Atmospheric Attenuation	94
3.0 The Skylab Altimeter Data Set.	102
4.0 Concluding Remarks	109
References	112
7 HIGH SEA STATE MEASUREMENTS OF σ° FOR NEAR NORMAL INCIDENCE . .	114
1.0 Introduction	114
2.0 Available Sea Surface Data	114
3.0 σ° Variation Over Selected Areas	115
3.1 Average σ° Variation with Surface Conditions.	128
4.0 Summary.	135
References	136
8 MEASUREMENTS OF σ° AS A FUNCTION OF INCIDENCE ANGLE	137
1.0 Introduction	137
2.0 Analysis	139
References	152
9 AN EXAMINATION OF NEAR NORMAL INCIDENCE BACKSCATTERING FROM THE GREAT SALT LAKE DESERT AREA OF UTAH	153
1.0 Introduction	153
1.1 Classification of Extended Target Scattering Surfaces.	154
1.2 Backscattering Cross Section (σ°) Behavior for Various Scales of Roughness	158
2.0 Measurement Results From The Great Salt Lake Desert Area .	164
2.1 Return Waveform Statistical Characteristics and Their Implications.	168
2.2 Other Consequences of This Type of Scattering	176

TABLE OF CONTENTS (Cont'd.)

CHAPTER	<u>Page</u>
2.2.1 Comments on Previous Analyses.	176
2.2.2 Agreement of Model and Low Noise Altitude Data.	179
2.2.3 Transitions in the Waveform Data as a Function of Surface Conditions.	182
3.0 Correlation Of The Model With Laser Profilometer Surface Measurements	190
4.0 Conclusions.	193
References	195
10 PULSE-TO-PULSE CORRELATION MEASUREMENTS	197
1.0 Background	197
2.0 Comparison of Measurements and Theory.	202
2.1 The Effect of Pointing Direction.	207
References	221
Appendix	234
11 THE EFFECT OF TRACKING LOOP JITTER ON FIRST AND SECOND ORDER WAVEFORM STATISTICS	237
1.0 Introduction	237
2.0 Jitter-Free Analysis	237
3.0 Analysis Including Jitter.	245
References	250
12 CORRELATION OF WAVEFORM DERIVED SEA STATE ESTIMATES AND GROUND TRUTH.	253
1.0 Introduction	253
2.0 Waveform Data Processing Operations.	258
3.0 Time Realignment Uncertainty	259
References	267
Appendix A	268
Appendix B	318
Appendix C	322

TABLE OF CONTENTS (Cont'd.)

CHAPTER	<u>Page</u>
13 SYSTEM RELATED OBSERVATIONS	327
1.0 Introduction	327
2.0 r-Factor Verification Using Waveform Data.	327
3.0 Mode III Bandwidth Switching Malfunction	331
4.0 100 ns/10 MHz Intrapulse Autocorrelation Function.	335
5.0 100 ns/10 MHz Sampled Waveform Considerations.	338
6.0 Estimated Average IF Single Pulse Signal-To-Noise Ratio	363
7.0 Data Problems.	370
References	375

CHAPTER 1

Introduction and Summary of Results

by

G. S. Brown

This report is the last of a quartet of reports sponsored by Wallops Flight Center and concerned with the Skylab S-193 radar altimeter experiment. In the first report of this series [1], orbit-subtracted altitude measurements were compared to existing geoid models and bottom topography, and an error budget for the altitude measurement process was discussed. The second report [2] comprised a compilation of inferred values for the ocean surface backscattering cross section per unit area (σ^0) and presented altimeter derived estimates of very near nadir pointing angles. The third report [3] detailed the statistical characteristics of the altimeter/orbit derived altitude residuals including such important results as the variance and stationarity of the residuals. These efforts were, therefore, primarily concerned with compiling corrected measurement results for future analysis and interpretation.

A number of other publications have dealt with the more obvious results and applications of the S-193 radar altimeter data, [4] - [16]. This report presents results which are more along the lines of the original S-193 radar altimeter experiment. Specifically, it is directed toward previously unpublished material on the following; (1) instrument performance relative to theoretical expectations, (2) in depth analyses of the applications of the radar derived data, (3) implications of new results from the data relative to models of the rough surface backscattering process, and (4) identification of system anomalies or malfunctions. Results relative to all operating modes (except Nadir Align) are discussed. Other than the very important fact that the Nadir Align Mode appeared to function properly, not much additional information could be obtained from this mode.

The organization of the report is such that the chapters may be directly related to a given operating mode of the altimeter. Chapters 2, 3 and 4 present material relative to Mode I (Waveform and Altimetry); Chapters 5 through 9 relate to Mode II (Radar Backscattering Cross Section); Chapter 10 discusses the results of the Mode III measurements (Interpulse Correlation);

Chapters 11 and 12 present results from Mode V (Short Pulse and Pulse Compression); finally, Chapter 13 discusses system related observations and malfunctions.

Chapter 2 discusses the very important topic of optimum filtering of the altitude residual data to recover the geoid; it is shown that even optimum filters such as the Wiener-Hopf type require additional damping in order to prevent oscillatory behavior in the output data. Chapter 3 addresses the problem of pointing angle estimation using average waveform data; it is shown that a 1500-pulse average return waveform is sufficient to provide a pointing angle estimate which has a one-sigma statistical precision of ± 0.04 degrees. Chapter 4 considers the pointing angle estimation problem using tracker bandwidth data; the technique is shown to be complementary to the waveform approach since it is most accurate for a pointing error of greater than 0.9 degrees. Chapter 5 presents experimental and theoretical results on the identification of major current boundaries by observation of the backscattered power; the results are most encouraging but clearly indicate the need for more detailed surface truth information. Chapter 6 reviews the effect of meteorological conditions upon the attenuation of the backscattered power and presents experimental data to demonstrate the remote sensing capability of the altimeter in the Intertropical Convergence Zone (ITCZ). Chapter 7 reviews the measurement of σ° for near normal incidence during high waveheight and large windspeed conditions in the North Atlantic and concludes that there is a definite saturation effect resulting in a minimum value for σ° of about 8 dB. Chapter 8 discusses some of the difficulties associated with interpreting the off-nadir measurements of σ° and reviews two particular data sets; both data sets imply a rather low sea-state, however, there is also a marked difference in the two results. Chapter 9 examines the backscattered signal characteristics over the Great Salt Lake Desert area of Utah and concludes that this data set does not represent specular reflection but rather is a special case of random scattering where the mean square surface slope is extremely small. Chapter 10 presents the results of the pulse-to-pulse correlation experiment (Mode III) and concludes that the decorrelation times are in very good agreement with theoretical predictions based upon the Van Cittert-Zernike theorem of quasi-monochromatic optics; furthermore, it is demonstrated that the measurement of the pulse-to-pulse correlation is a significant indicator of direction

of pointing error. Chapter 11 examines the effect of tracking loop jitter on the first and second moments of the waveform as recorded by the tracking loop positioned Sample and Hold gates; it is shown that the effect upon the short pulse return is significant and should be corrected and a simplified means of correcting the data is presented. Chapter 12 discusses the estimation of surface waveheight from the shape of the leading edge of the average short pulse return and examines the error residual after time realignment and special filtering; high sea state measurements obtained in the North Atlantic are shown to adequately predict the surface waveheight to within the error bounds of the estimation process. Chapter 13 details measurements and results relating to system performance or malfunction, model verification, and data correction or problems. One of the most striking results of this chapter is the very large signal-to-noise ratio margin during the SL-2 and SL-3 missions. Furthermore, analyses of waveform data provide results which corroborate the technique used to correct received power data for waveform dependent AGC effects, and, therefore, effectively decrease prior estimates [2] of the error bounds on the measurement of σ^0 .

In view of the results obtained from the Skylab S-193 radar altimeter as presented here and elsewhere, the altimeter experiment was probably the most successful of all the Earth Resources Experiment Package (EREP) sensors. This statement reflects not only the fact that all of the basic objectives and goals of the experiment were either fulfilled or exceeded but that a number of other important results were obtained. Among these were the ability to estimate pointing angle magnitude and direction from the radar data, the future capabilities gained from the processing of radar data, and the insight as to how next-generation radar altimeters might be better designed. All of these factors, for example, have had a direct effect upon the subsequent GEOS-III dedicated radar altimeter and are also influencing the design of the SEASAT-A altimeter.

The Skylab radar altimeter experiment has clearly demonstrated that altimetry from space can be of significant benefit to mankind in his quest for knowledge about the earth and its oceans.

REFERENCES

1. McGoogan, J. T., C. D. Leitao, and W. T. Wells, "Summary of Skylab S-193 Altimeter Altitude Results," NASA TM X-69355, Wallops Flight Center, Wallops Island, VA., February, 1975.
2. Brown, G. S., "Reduced Backscattering Cross Section (σ^0) Data From The Skylab S-193 Radar Altimeter," NASA CR-141401, Applied Science Associates, Inc., Apex, N. C., October, 1975.
3. Hatch, W. E., "Noise Characteristics of the Skylab S-193 Altimeter Altitude Measurements," NASA CR-141403, Business and Technological Systems, Inc., Seabrook, MD., November, 1975.
4. McGoogan, J. T., "Precision Satellite Altimetry," IEEE INTERCON Record, New York, May, 1974.
5. McGoogan, J. T., L. S. Miller, G. S. Brown and G. S. Hayne, "The S-193 Radar Altimeter Experiment," Proc. of IEEE, vol. 62, pp. 793-803, June, 1974.
6. McGoogan, J. T., C. D. Leitao, W. T. Wells and L. S. Miller, "Skylab S-193 Altimeter Experiment Performance, Results, and Applications," International Symposium On Marine Geodesy, Columbus, Ohio, June, 1974.
7. Smith, A. G., "Microwave/Optical/Infrared Image Processing For Ocean Current Recognition," NASA CR-137468, Applied Science Associates, Inc., Apex, N. C. July, 1974.
8. Leitao, C. D. and J. T. McGoogan, "Skylab Radar Altimeter: Short Wavelength Perturbations Detected in Ocean Surface Profiles," Science, vol. 186, September, 1974.
9. Brown, G. S., "A Closed Form Relation For The Average Return Waveform From A Near-Nadir Pointed, Short Pulse, Satellite Based Radar Altimeter," USNC/URSI-IEEE Joint Meeting, Boulder, Colorado, October, 1974.
10. McGoogan, J. T., C. D. Leitao, W. T. Wells, L. S. Miller, and G. S. Brown, "Skylab Altimeter Applications and Scientific Results," AIAA/AGU Conf. on Scientific Experiments of Skylab, Huntsville, Alabama, October, 1974.

REFERENCES (Cont'd.)

11. Parsons, C. L., "Some Observations of Ocean Backscattering Using S-193 Radar Altimeter Data," AGU Meeting, San Francisco, California, December, 1974.
12. Shapiro, A. and B. S. Yaplee, "Anomalous Radar Backscattering From Terrain at High Altitudes," Proc. of IEEE, vol. 63, pg. 717, April, 1975.
13. Brown, G. S., "Near-Nadir Measurements of σ^0 For The Ocean Surface From The Skylab Radar Altimeter," Joint USNC/URSI-IEEE Meeting, Urbana, Illinois, June, 1975.
14. McGoogan, J. T., "Satellite Altimetry Applications," IEEE Trans. On Microwave Theory & Techn., Vol. MTT-23, pp. 970-978, December, 1975.
15. Parsons, C. L., "Total Attenuation Measurements of the ITCZ by Satellite Altimeter," Bulletin of the American Meteorological Society, September, 1976 (to be published).
16. Brown, G. S., "The Average Impulse Response Of A Rough Surface and Its Applications," IEEE Trans. on Antennas and Propagation, January, 1977 (to be published).

CHAPTER 2

Altitude Data Filtering Considerations

by

L. S. Miller

1.0 Introduction and Summary of Results

This chapter discusses the general problem of processing altitude data and the importance of geoidal power spectral density (PSD) information in the design of optimal procedures. Smoothed altitude data are first presented using a number of different filtering procedures to demonstrate the sensitivity of derived geoid information and the importance of filter transient response. The design of a linear time-invariant filter based on the Wiener-Hopf theory and measured PSD information is obtained. This filter is then evaluated from the standpoint of its transient behavior and the results it produces. Overall results of this work are as follows: 1) some of the filtering procedures used were found to produce considerable distortion in the geoidal data; 2) the Wiener-Hopf result provides a readily implemented analytical basis for altitude filter design, however, modifications of the theoretical results are needed to suppress under-damped characteristics; 3) in future studies, the derivation and evaluation of geoid estimators should be undertaken with emphasis on characterization of the spatial variability of geoidal PSD information.

Figures 1 through 4 show filtered altitude data for SL-4 EREP Pass 87; the time span of the data is about 50 sec. from 20 HR 14 MIN 55 SEC to 20 HR 15 MIN 45 SEC *. Figure 1 shows results obtained using a low pass polynomial; based on comparisons with unfiltered data, this filter is considered to be the best ad hoc procedure of those considered. Figure 2 shows a low pass Butterworth filter with a time constant of approximately 1 sec; the result is seen to be oscillatory with a frequency determined by the specific filter. Figure 3 also shows a Butterworth filter response for which the time constant was about 10 times the previous Butterworth filter. A comparison of Figures 1 and 3 shows this filter to produce major distortions in the trend line or geoidal estimate - the response is markedly sluggish. Figure 4 shows filtered

*These results were computed by C. Leitao of Wallops Flight Center.

SEA SURFACE HEIGHT (METERS)

SL-4, EREP PASS 87

START \approx 20 HR. 14 MIN. 55 SEC.

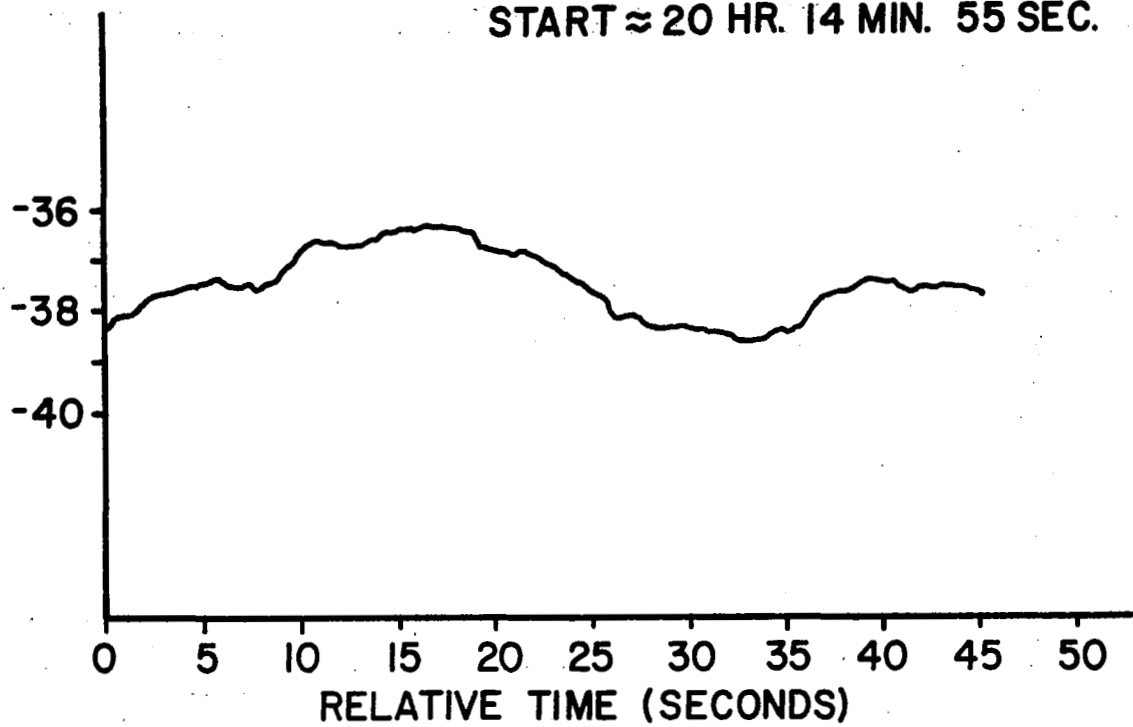


Figure 1. Low pass polynomial filter results.

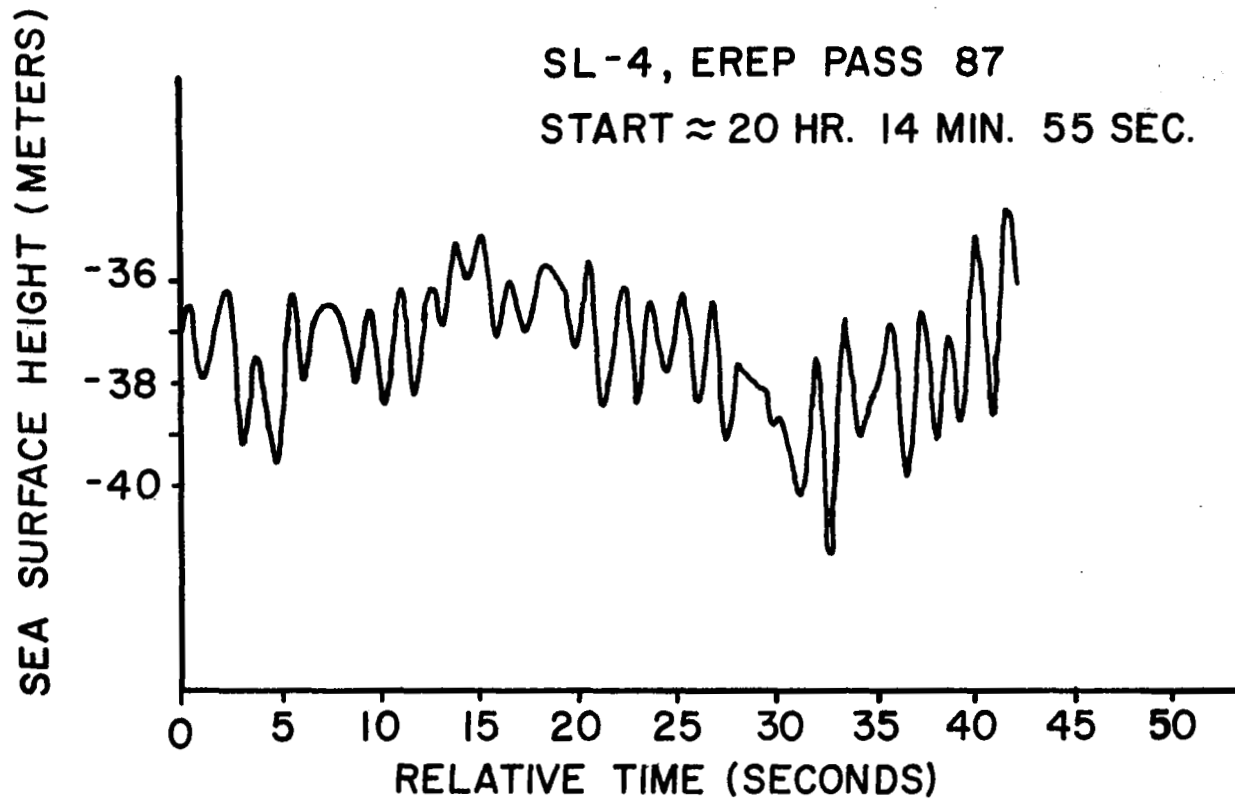


Figure 2. Low pass Butterworth filter (time constant \approx 1 sec.) results.

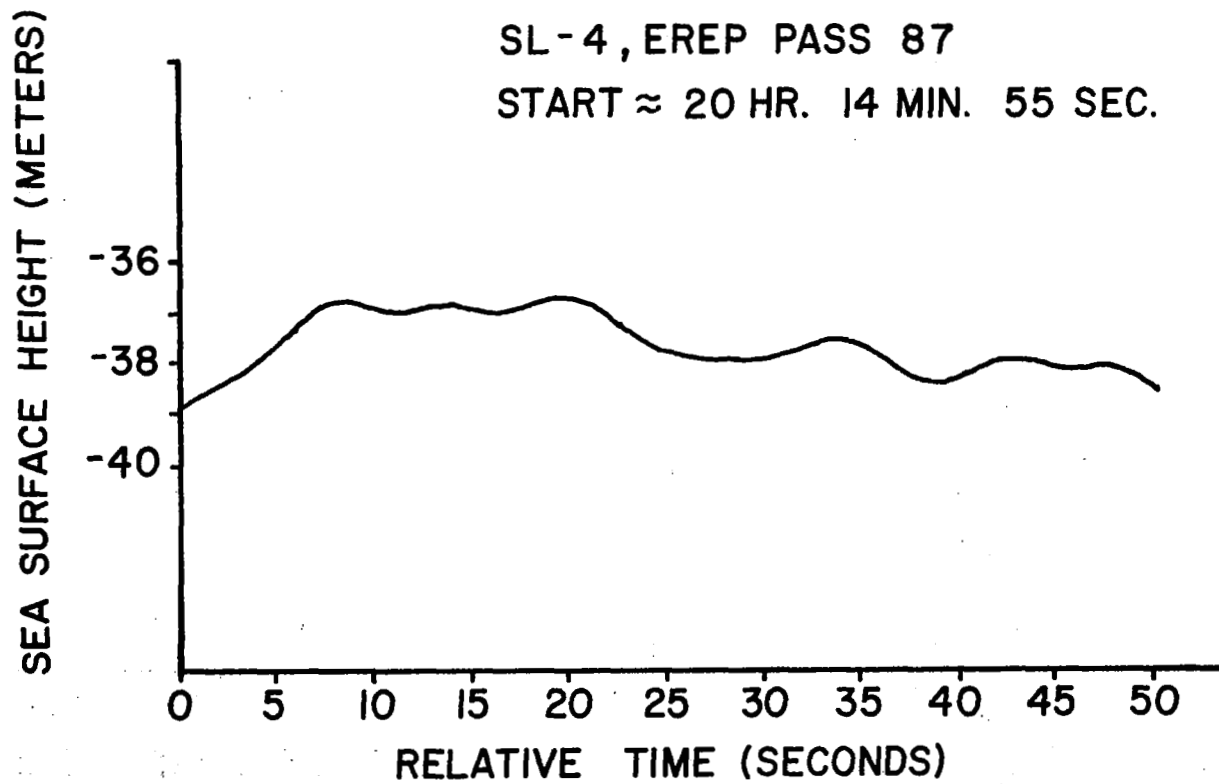


Figure 3. Low pass Butterworth filter (time constant \approx 10 sec.) results.

SEA SURFACE HEIGHT (METERS)

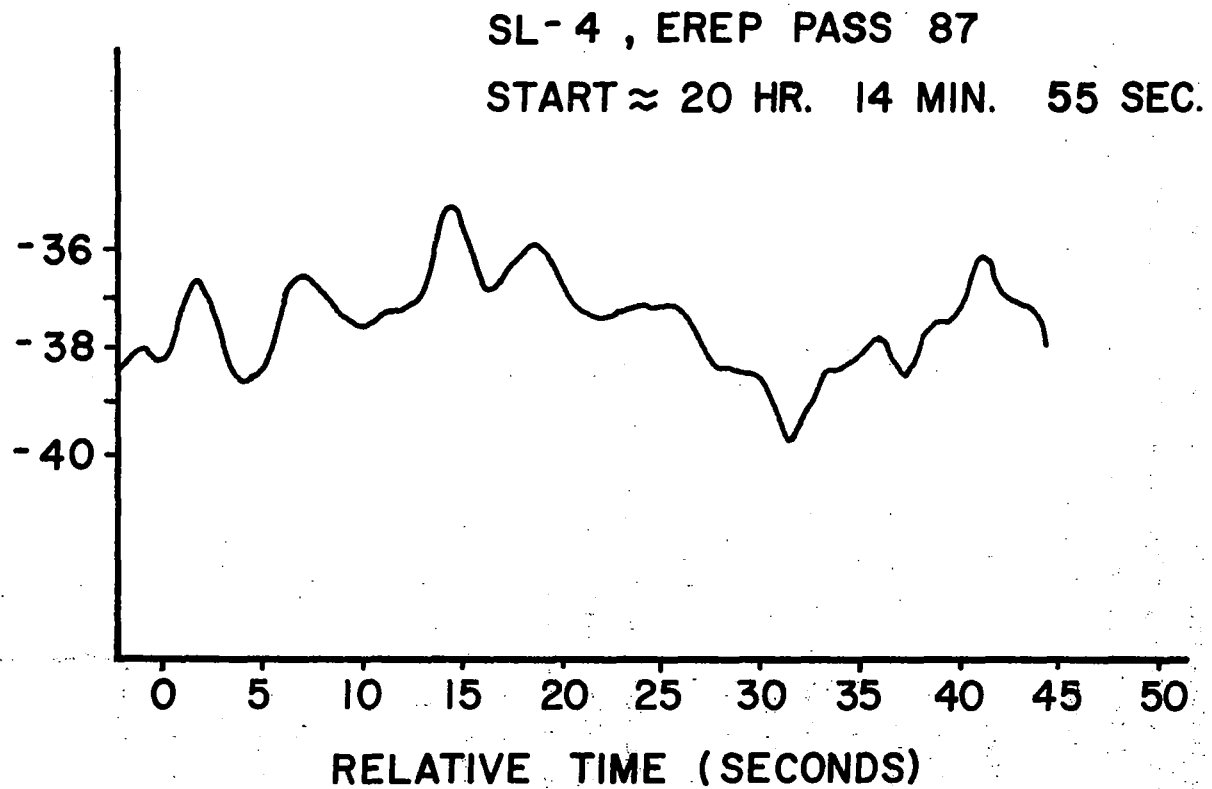


Figure 4. Wiener filter results for an altitude noise level of 0.4 meters.

data using a Wiener filter for an assumed altitude noise level in the raw data of 0.4 meters. The details of this filter are given in Section 3. Figure 4 indicates that this filter results in an oscillatory response akin to the Butterworth filter. Figures 5 and 6 present filtered altitude data* using a critically damped form of the Wiener filter derived in Section 3; Figure 5 is for an rms noise level of 0.4 meters and Figure 6 for 0.8 meters. The response of this filter is seen to be similar to the polynomial filter.

2.0 Discussion of Altitude Filtering Procedures

This section discusses the general problem of processing the altitude data and the importance of the geoidal power spectral density (PSD) information. The design of the time-invariant filtering procedure is derived based on the Wiener-Hopf theory and on an observed geoidal PSD. This filter is then examined and, in accordance with the literature on Wiener filter theory [1], found to be under damped. A modified form of the Wiener filter is then developed and evaluated in Section 3.

The altimeter data processing problem is somewhat circular. In order to optimally process altimeter data some a priori statistical description of the surface undulation such as its power spectrum or autocorrelation is needed; however, the altimeter data itself represents a considerable advance in knowledge of the earth's geoid. There is general agreement that a single description of the geoidal spectrum will not be adequate because of its spatial variability. That is, any processing technique must be based on a valid PSD estimate for the local region under investigation. Rigorous data processing studies will require a twofold approach: one in which geodetic estimation is the objective and one in which surface statistical characterization will be needed. This type of processing is shown in block diagram form in Figure 7.

Using a state-variable representation (c.f. [2] - [3]) for the observations y and x for the quantity to be estimated

*The starting time for Figures 5 and 6 is 2.5 seconds earlier than the starting time for the previous figures.

SEA SURFACE HEIGHT (METERS)

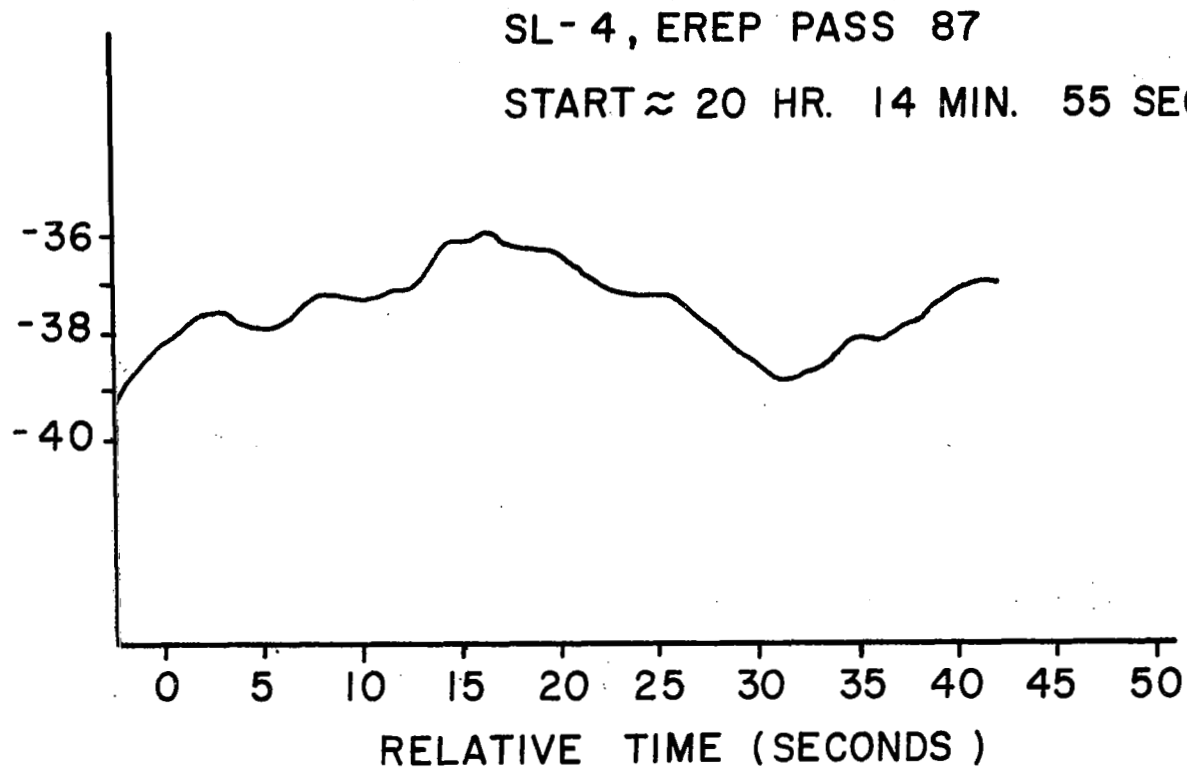


Figure 5. Filter results using a critically damped form of the Wiener filter and an altitude noise level of 0.4 meters.

SEA SURFACE HEIGHT (METERS)

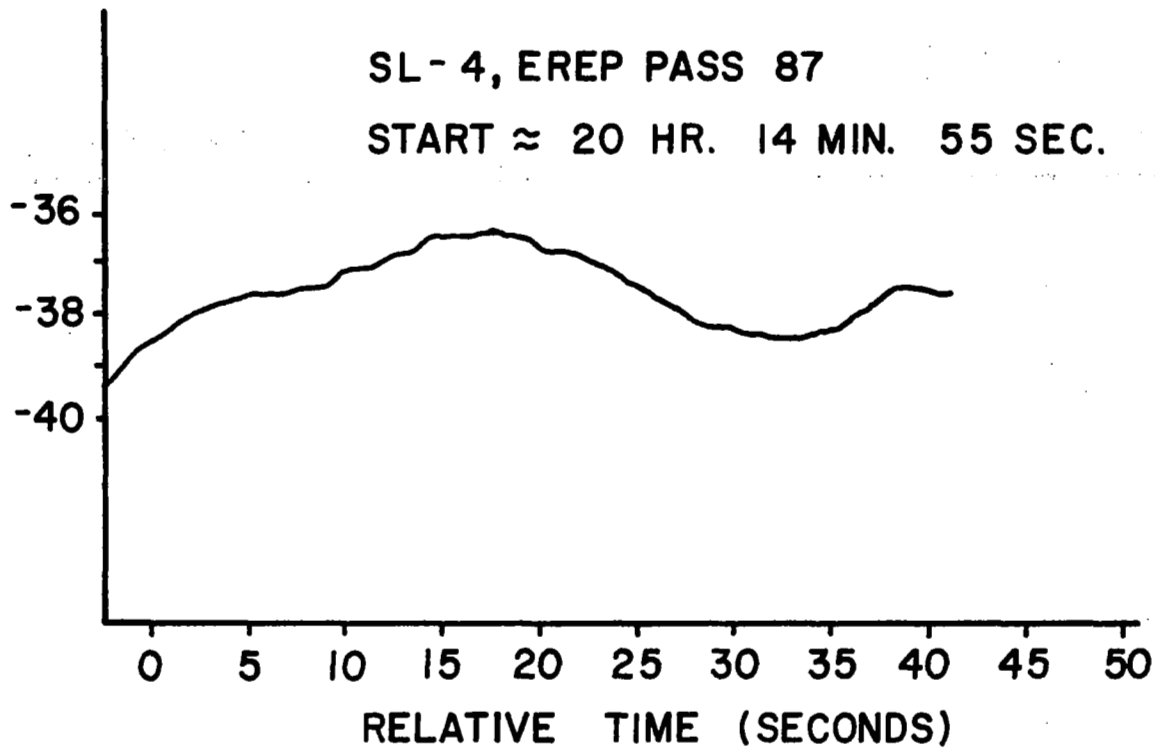


Figure 6. Filter results using a critically damped form of the Wiener filter and an altitude noise level of 0.8 meters.

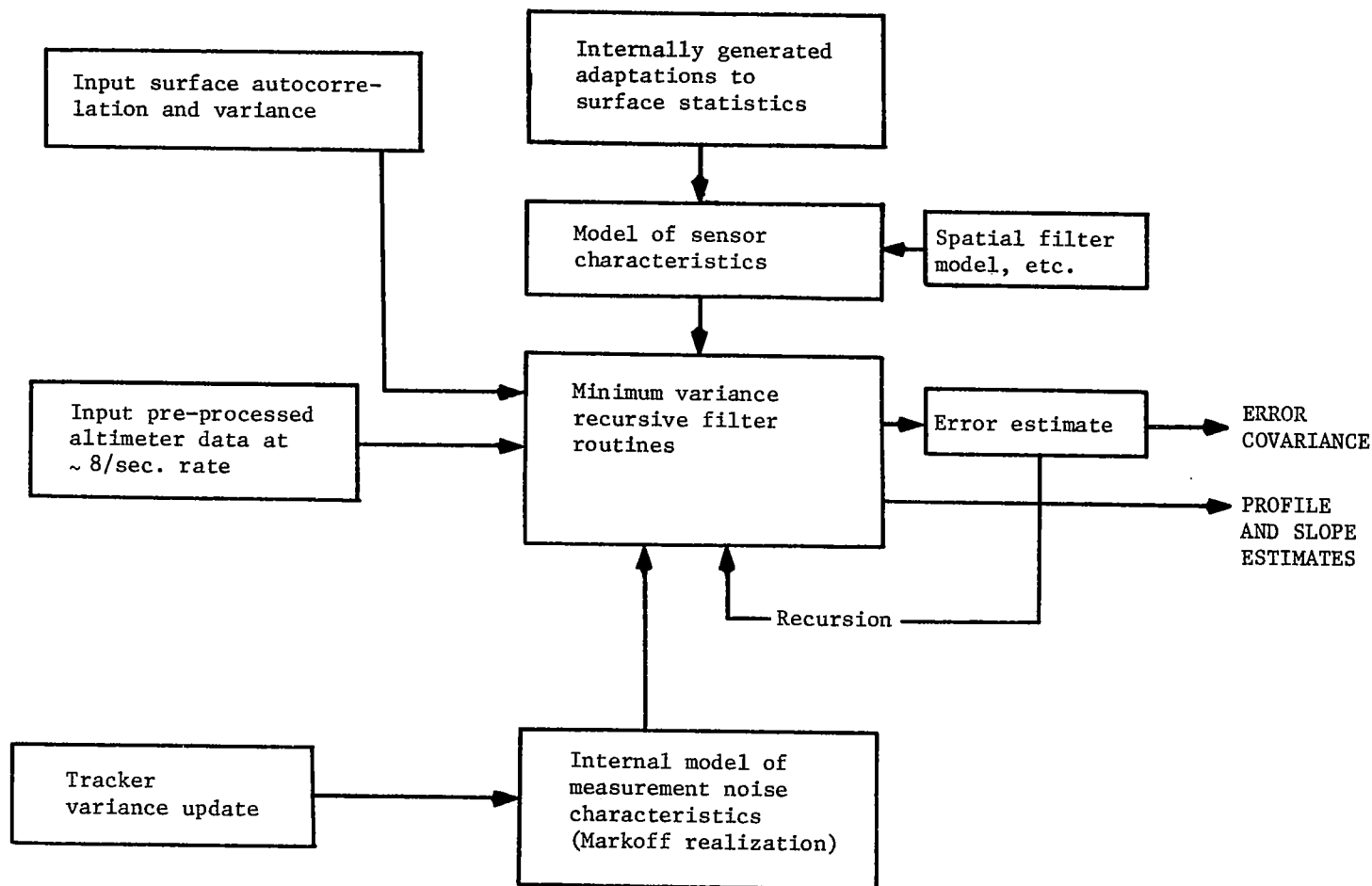


Figure 7. Conceptual diagram of geoidal data processing operations.

$$x_{n+1} = A_n x_n + u_n$$

$$y_n = Cx_n + v_n$$

where A_n is the transition matrix, C is the observation constraint matrix, and u_n and v_n the random terms; use of the TASC model [10] for the auto-correlation function or power spectral density, i.e.

$$R_{gg}(t) = \sigma_g^2 \left(1 + \alpha t + \frac{\alpha^2 t^2}{3} \right) \exp(-\alpha t^2)$$

$$S_{gg}(\omega) = \frac{16\sigma_g^2 \alpha^5}{3(\omega^2 + \alpha^2)^3},$$

is seen to lead to a third order Markoff process. If this description is coupled with a sixth order spatial filter process [7], the matrix dimensionality is seen to be quite large. In addition the matrix set may also require partitioning because the altimeter noise term v_n contains several components, one of which may be highly correlated, i.e. the ϵ_{Q1} term discussed in [5].

In the minimum variance stationary statistics work discussed below, the results indicate that the spatial filter effect is of minor importance in geoid undulation estimation using S-193 data. For the geoid PSD and instrument random errors examined, the cutoff wavelength of the derived filter is considerably longer than the wavelength range for which spatial filter effects are significant. For geoid slope estimation, spatial filter effects may be substantial. It should also be noted that the Kaula PSD asymptote [6] does not decay rapidly enough to provide a bounded form for the slope PSD.

The objective of the above discussion is to indicate the scope and a priori information needed to develop a recursive form of geoid estimation. Ultimately, recursive techniques should be compared with the simpler technique given below to determine if the complexity of recursive methods is justified.

3.0 Derivation of the Linear Minimum Variance Altitude Filter

This section gives the design of a linear, minimum variance filter

based on the Wiener-Hopf formulation for the case of stationary statistical processes. For reasons given above, the spatial filter effect is not included in the derivation.

References [7] and [8] present a form for the geoidal PSD, $S(\omega)$, which was based on computed values from SL-2, EREP Pass 4. In equation form the density is

$$S(\omega) = \frac{71.66(6.554 \times 10^{-4})}{\omega^4 + 0.0512\omega^2 + 6.554 \times 10^{-4}} \quad (1)$$

As discussed in [7] and [8], the transfer function of the Wiener-Hopf filter is given by

$$H_o(\omega) = \frac{S(\omega)}{S(\omega) + N(\omega)} \quad (2)$$

where $N(\omega)$ is the spectral density of the measurement noise, which is assumed to be an additive process. Denoting the altimeter tracking noise as σ_h , the noise density is approximated by the following;

$$N(\omega) \approx \frac{\sigma_h^2}{2\pi\beta_n} \text{ meters}^2/\text{radian} \quad (3)$$

where the noise bandwidth, β_n , for the altimeter is 3.3 Hz. Substituting (1) and (3) into (2), the optimal transfer function is found to be

$$H_o(\omega) = \frac{0.97439}{\omega^4 + 0.0512\omega^2 + 0.97505} \quad \left| \begin{array}{l} \sigma_h = 1 \text{ m.} \end{array} \right. \quad (4a)$$

$$H_o(\omega) = \frac{3.893}{\omega^4 + 0.0512\omega^2 + 3.8939} \quad \left| \begin{array}{l} \sigma_h = .5 \text{ m.} \end{array} \right. \quad (4b)$$

The impulse response function of the filter may be found by Fourier transforming $H_o(\omega)$; it is

$$h(\tau) = \left\{ \cos[.4809|\tau|] + 1.48 \sin[.4809|\tau|] \right\} \exp(-.711|\tau|) \Big|_{\sigma_h = 1 \text{ m}} \quad (5a)$$

$$h(\tau) = \left\{ \cos[.9868|\tau|] + 1.013 \sin[.9868|\tau|] \right\} \exp(-.9997|\tau|) \Big|_{\sigma_h = .5 \text{ m}} \quad (5b)$$

For subsequent use, the impulse response of a critically damped filter will also be needed. The standard form for a second order transfer function is

$$[H(j\omega)]^{-1} = -\omega^2 + j 2\zeta a\omega + a^2 \quad (6)$$

and since $S(\omega) = H(j\omega)^* H(j\omega)$,

$$[S(\omega)]^{-1} = \omega^4 + (4\zeta^2 - 2)a^2 \omega^2 + a^4 \quad (7)$$

which is the general form of the PSD for a second order shaping filter realization with damping coefficient ζ . Substitution of numerical values from (4a), i.e. $\sigma_h = 1 \text{ m}$, shows the damping coefficient for the Wiener filter to be $\zeta \approx .72$. It should be noted that the damping coefficient is dependent upon the variance of the noise process. The critically damped ($\zeta=1$) equivalent of (4a) is

$$H_C(\omega) = \frac{0.97439}{\omega^4 + 1.9748\omega^2 + 0.97505} \quad (8)$$

For the more general case, (1) can be rewritten, with obvious definition of coefficients, as

$$S(\omega) = \frac{S_o a^4}{\omega^4 + b \omega^2 + a^4} \quad (9)$$

and the equivalent Wiener filter transfer function is given by

$$H_o(\omega) = \frac{S_o a^4 / N_o}{\omega^4 + b\omega^2 + \left(1 + \frac{S_o}{N_o}\right) a^4}$$

where $N_o = \sigma_h^2 / (2\pi\beta_n)$. For critical damping ($\zeta=1$),

$$b = 2a^2 \sqrt{1 + S_o / N_o} ,$$

and the transfer function reduces to the following form;

$$H_C(\omega) = \frac{a^4 S_o \frac{2\pi\beta_n}{\sigma_h^2}}{\omega^4 + 2a^2 \omega^2 \sqrt{\frac{S_o 2\pi\beta_n}{\sigma_h^2} + 1} + a^4 \left(\frac{S_o 2\pi\beta_n}{\sigma_h^2} + 1 \right)} \quad (10)$$

while the corresponding impulse response is

$$h_c(t) = \left\{ 1 + a \left(\frac{S_o 2\pi\beta_n}{\sigma_h^2} + 1 \right)^{\frac{1}{4}} |\tau| \right\} \exp \left[-a \left(\frac{S_o 2\pi\beta_n}{\sigma_h^2} + 1 \right)^{\frac{1}{4}} |\tau| \right]$$

Since $\frac{S_o 2\pi\beta_n}{\sigma_h^2} \gg 1$ to a good approximation and $a = .16002$, $S_o = 71.66$, $\beta_n = 3.3$

$$h_c(t) \approx \left(1 + \frac{0.993}{\sqrt{\sigma_h}} |\tau| \right) \exp \left[- \frac{0.993}{\sqrt{\sigma_h}} |\tau| \right] \quad (11)$$

Computer programs have been written which generate weighting coefficients for the Wiener filter from (5) and the modified Wiener filter from (11). Using (11) as an example, the continuous-time form was first converted into a discrete time form. With the S-193 data products, eight altitude values are available per frame (a frame period is 1.04 seconds). Assuming equal spacing of period T for the altitude values, the weighting sequence is

$$w(n) = e^{-\left(\frac{0.12412(n-48)}{\sqrt{\sigma_h}} \right)} \left\{ 1 + \frac{0.12412(n-48)}{\sqrt{\sigma_h}} \right\} \quad n \geq 0$$

This expression was evaluated for $n=0$ to $n=96$ (equivalent to approximately 12 seconds). The resulting 97 values were then normalized such that,*

$$\sum_0^{96} w(n) = 1$$

to ensure that the filter operation would not cause a constant offset in the output data. Figures 8 and 9 show the resulting weighting coefficients for the two filter types. Note that the reduced damping effect in the Wiener filter is evident in the oscillatory nature of the time response.

As a parenthetic remark, in a strict sense the S-193 sampled altitude data is not uniformly spaced. In each frame the altitude data is recorded as shown in Figure 10; therefore, the data span per frame is as shown in Figure 11. The values which are uniformly weighted over samples $A_1 \dots A_8$ will have a mid point coincident with A_4 . That is, the averaged altitude value should be associated with the time of occurrence of A_4 .

As mentioned previously, the minimum variance Wiener procedure is a statistical method that does not assess time-series distortion. Quoting from [1]; " Systems designed to minimize root-mean-square error often exhibit large overshoots and a long settling time. This oscillatory response is a direct result of the heavy weighting that this criterion places on large errors ... the minimum resulting from this technique is quite broad ... an appreciably wide variation of characteristics is permitted without a serious change in the index of performance."

The insensitivity of error in the estimate to filter characteristics may be quantified as follows. The mean square error can be shown to be [9] given by

*For the discrete Fourier transform $X_m = \sum_{n=0}^N x_n \left(e^{j 2\pi/N} \right)^{mn}$; for the zero frequency term to be unity $X_0 = \sum x_n = 1$.

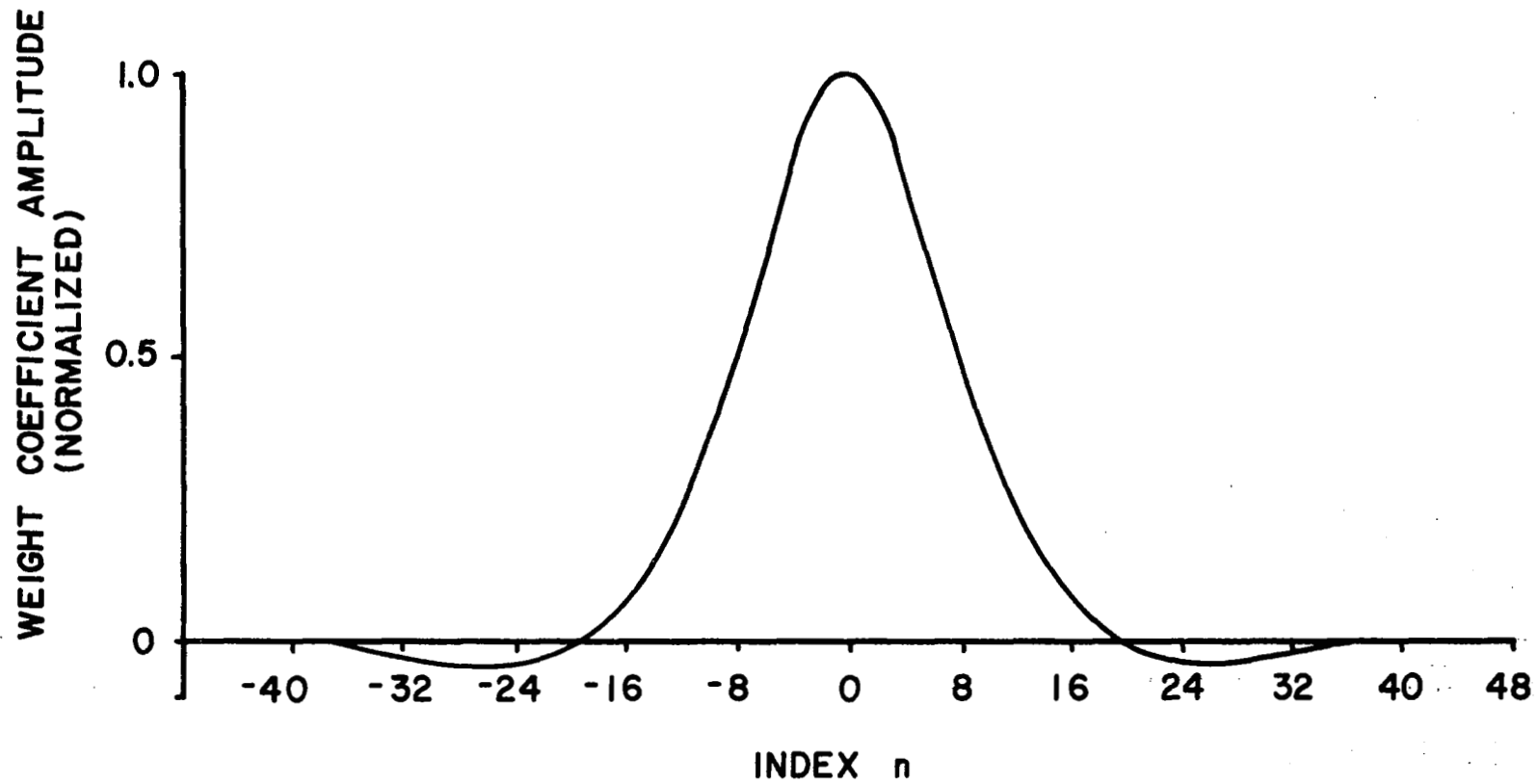
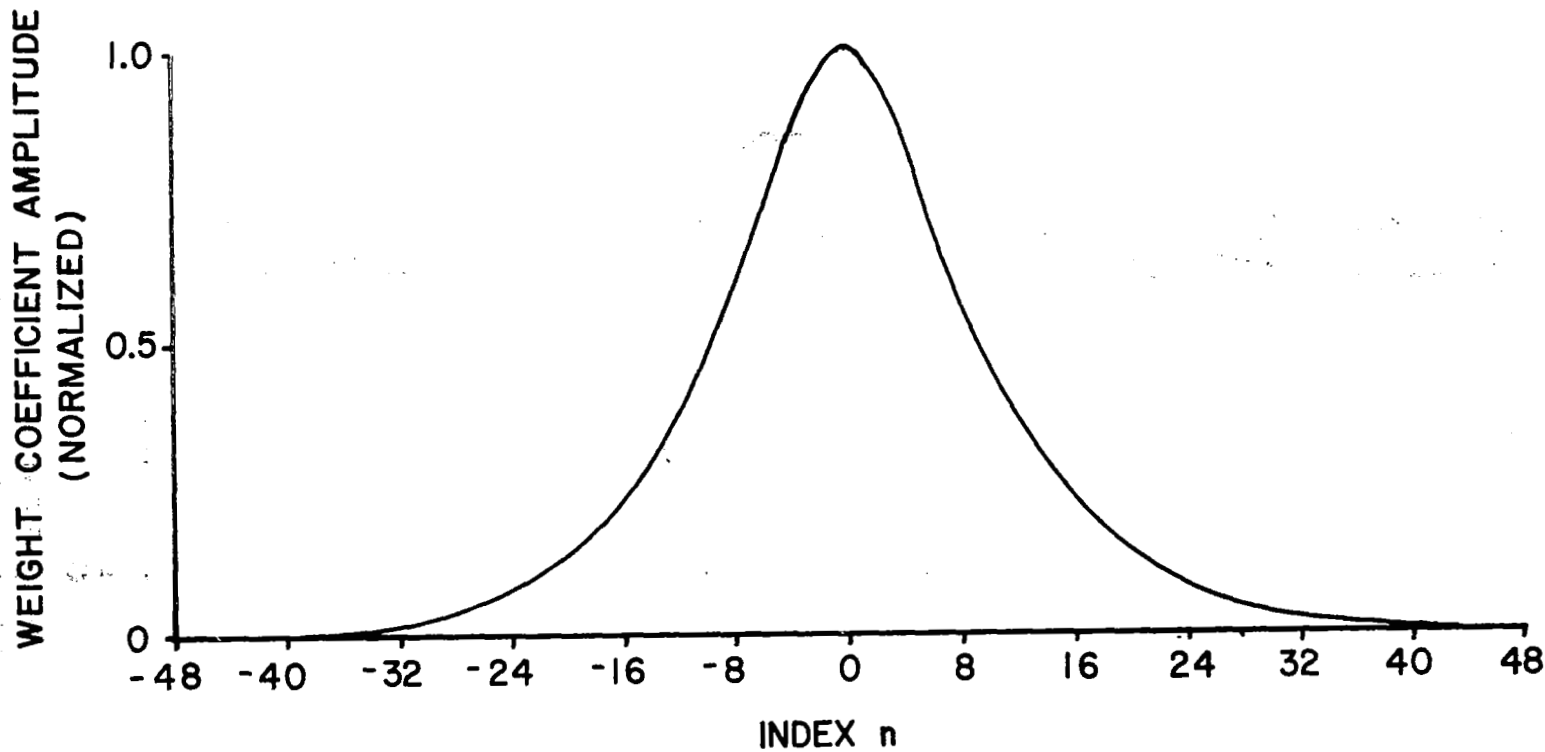


Figure 8. Normalized weighting coefficient's amplitude envelope as a function of the index for the optimum Wiener filter ($\sigma_h = 1.0$ meter).



-21-

Figure 9. Normalized weighting coefficient's amplitude envelope as a function of the index for the modified Wiener filter ($\sigma_h = 1.0$ meter).

$A_i = i^{\text{th}}$ ALTITUDE OUTPUT

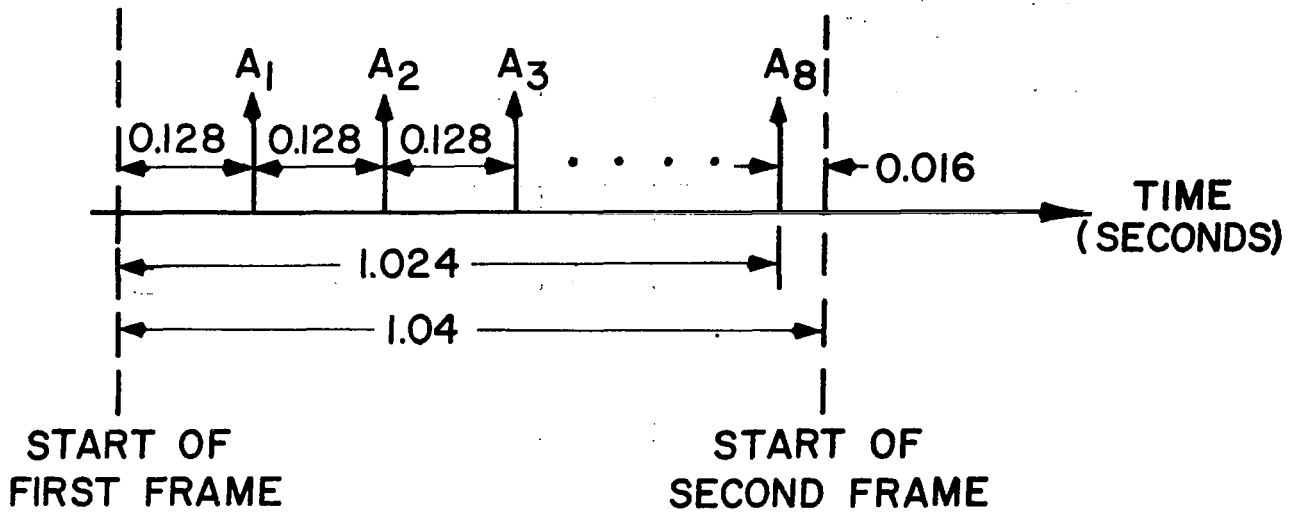


Figure 10. Altitude data per frame (1.04 secs.) output.

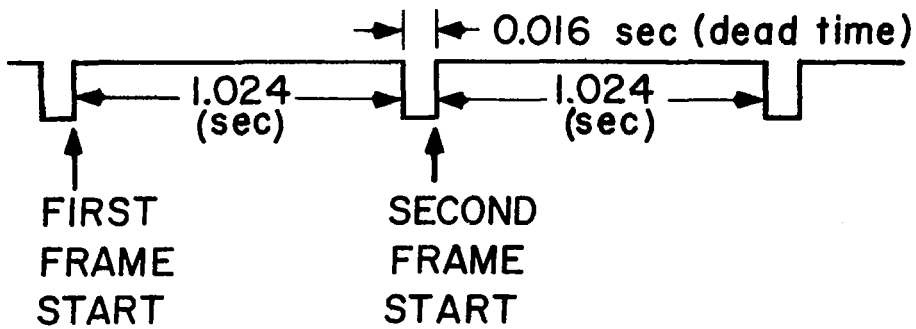


Figure 11. Data span timing.

$$\text{M.S.E.} = \frac{1}{2\pi} \int_{-\infty}^{\infty} S(\omega) d\omega - \frac{1}{2\pi} \int_{-\infty}^{\infty} [S(\omega) + N(\omega)] |H(j\omega)|^2 d\omega$$

This equation has been numerically evaluated using

$$H(j\omega) = \frac{a^4}{\omega^4 + (4\zeta^2 - 2)a^2\omega^2 + a^4}$$

and for maintaining the bandwidth constant as the damping coefficient was varied. The equivalent noise bandwidth defined by

$$\frac{1}{2\pi} \int_{-\infty}^{\infty} |H(j\omega)|^2 d\omega$$

was held constant by changing the "a" term. The resulting error sensitivity is shown in Table I. For the geoidal PSD used, Table I shows the rms error for the critically damped filter to be about 1.5 times the error of the optimum filter.

TABLE I
Error Sensitivity Versus Damping Coefficient: ξ
For $\sigma_h = 1$ meter

DAMPING FACTOR ζ	rms error (meters)
.716 (optimal value)	.22
.86	.27
1.0 (critically damped)	.33
1.414	.40

In summary, these results show the importance of proper filter design and evaluation; some of the above discussed ad hoc filters can introduce characteristics which would amount to major alterations in the ensuing

geoidal data. The modified Wiener filter has been subjected to considerable evaluation and is considered to be a reliable procedure. Adaptive or recursive filters may provide some improvement in geoid estimation, and thus broaden the basis of analytical design of geoidal data processors. Additional work in the area of geoidal PSD characterization is a prerequisite for such filter design.

REFERENCES

1. Shinnars, S. M., Control System Design, John Wiley & Sons, Inc., N. Y., 1964.
2. Liebelt, P. B., An Introduction to Optimal Estimation, Addison-Wesley Co., Reading, Mass., 1967.
3. Miller, L. S., "Third Quarterly Progress Report - GEOS-III Investigation" Contract No. NAS6-2621, Applied Science Associates, Inc., Apex, N. C., Jan. 1976.
4. Jazwinski, A. H., Stochastic Processes and Filter Theory, Academic Press, New York, 1970.
5. Hofmeister, E., et al., "Design Error Analysis of the GEOS-C Radar Altimeter," General Electric Co., Utica, N. Y., May, 1975.
6. Brown, R. D. and S. Vincent, "Power Spectra of Geoid Undulations," paper presented at the AGU Meeting, San Francisco, Dec., 1972.
7. Miller, L. S. and G. S. Brown, "Engineering Studies Related to the GEOS-C Altimeter," NASA CR-137462, Applied Science Associates, Inc., Apex, N. C., May, 1974.
8. McGoogan, J. T., C. D. Leitao, W. T. Wells and L. S. Miller, "Skylab Altimeter Experiment Performance, Results and Applications," AGU International Symp. on Marine Geodesy, Columbus, Ohio, June, 1974.
9. Davenport, W. and W. Root, Random Signals and Noise, McGraw-Hill, 1958.
10. Cohen, C and B. Zondek, "Accuracy of Deflection of the Vertical Derived from Satellite Altimetry," Naval Weapons Laboratory Tech. Report TR-2626, Dahlgren, Va., Oct., 1971.

CHAPTER 3

Pointing Angle Estimation Via Waveform Analysis

by

G. S. Brown

1.0 Background

For modes in which the 100 ns pulse was transmitted, the average return power waveform exhibited a significant decay or droop in the trailing edge portion of the return. This decay was due to the very narrow beam-width antenna employed with the S-193 radar altimeter. When the antenna was pointed away from nadir, the shape of the average return changed. More specifically, a pointing error relative to nadir gave rise to the following waveform effects; the rise time portion of the return increased, and the decay rate of the trailing edge of the return decreased. For relatively small pointing errors, say less than 0.8° , the change in the rise time portion of the return was much less apparent than the change in the trailing edge of the return as shown in Figure 1.

The variation of the trailing edge of the return with pointing angle indicated that the average return waveform data could be used to estimate the pointing angle of the S-193 antenna relative to nadir. A preliminary analysis of the error involved in estimating the pointing angle via the average waveform approach [1] indicated that a minimum error on the order of $\pm 0.05^\circ$ might be possible. Since the data reduction for σ° , altitude, and surface roughness required extremely good estimates of pointing error, i.e. $\leq \pm 0.1^\circ$, and since the spacecraft attitude control system could not approach this accuracy, the waveform technique was used to estimate the altimeter antenna pointing angle with respect to nadir. For this reason it is essential that estimates of the errors involved in the technique are obtained. The purpose of this chapter, therefore, is to discuss the waveform approach to attitude estimation with particular emphasis upon the errors involved in the technique as applied to the Skylab S-193 system.

2.0 Analysis

Probably the most crucial parameter in the waveform technique is an accurate measure of the radar antenna pattern. Although this measurement

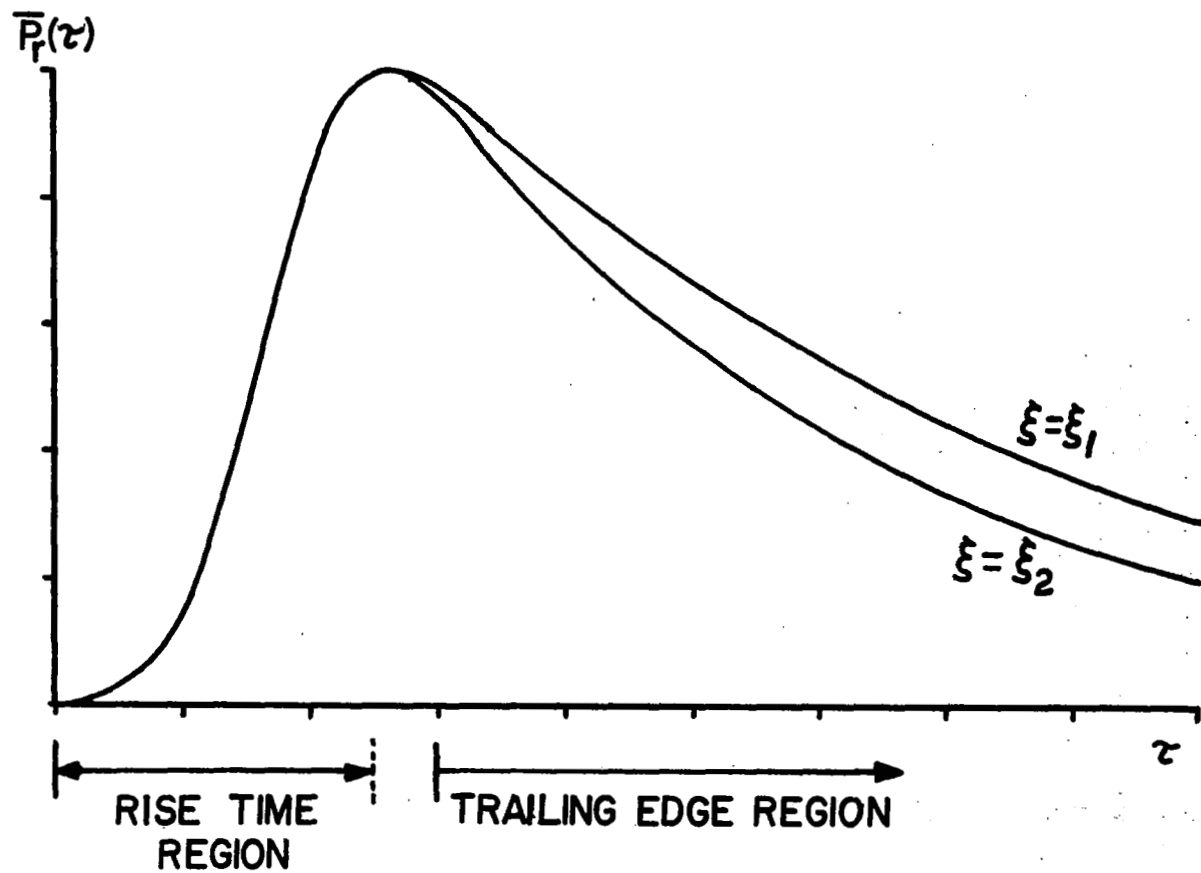


Figure 1. Typical shape of the average return power as a function of delay time for the S-193 100 ns/100 MHz configuration.

should be easily accomplished, such was not the case for the S-193 antenna. That is, for the patterns taken on the flight unit antenna, there was some concern that receiver saturation effects distorted the patterns. Sometime after launch, the protoflight antenna was modified to simulate the flight unit as closely as possible and patterns were taken for this antenna [2]. A comparison between the two sets of pattern measurements showed surprisingly good agreement within about 10 dB of the beam maximum. The second set of patterns confirmed the fact that there was a significant pattern asymmetry in the azimuthal coordinate. Sample waveform calculations also showed that this asymmetry would have to be incorporated into the mathematical model for the average return waveform. Having accomplished this analysis [3], it was found that the same average return waveform (after normalization) could be generated by distinctly different pointing angles in the along-track and cross-track directions. The only data reduction effort affected by this directional dependence was the σ^0 computation [3]; waveform and altitude corrections were dependent only upon the shape of the average return and not upon whether the pointing error was in the pitch or roll direction. The numerical error estimates presented here are only valid for pointing errors in the pitch direction*, however, the analysis is perfectly general and can be applied to any direction of pointing error.

The first estimates of pointing angle were obtained by comparing the measured average waveform with templates obtained by computing the expected average return for a range of pointing angles. This method was satisfactory for acquiring quick estimates, but it did suffer two major drawbacks in regard to accuracy. In understanding these, one must realize that the average return waveform was not acquired by 24 separate Sample and Hold (S&H) gates operating on each individual return. Rather, there were only eight distinct S&H gates which functioned in three different but contiguous array positions.** In the first array position, the gates generally were sampling noise ahead of the return. In the second array position the gates generally sampled the

*For no yaw, this spacecraft referenced coordinate corresponds to the along-track direction.

**These three array positions were designated as sub-sub modes 0, 1 and 2 (S²M 0,1&2) for the 100 ns/10 MHz data.

leading edge and peak of the average return while in the third array position the gates sampled the trailing edge of the return. Thus, for any one return only eight sampled values were available and their location on the average return depended upon the location of the array at the time of sampling. Since pulse-to-pulse decorrelation was assured by the low prf (250 pulses per second), this design was a reasonable approach to reducing peak power drain on the spacecraft batteries. This approach did give rise to two previously noted problems. The first, and most significant, was the fact that the attitude of the Skylab spacecraft was often changing during data acquisition. For long averaging intervals, this meant that the average waveform data acquired by the three contiguous array positions might correspond to three different pointing angles. Thus, it would be very difficult to align these three data sets and generate one estimate of the pointing angle, and, even if it could be done, it was not always clear how the estimate was actually related to the true range of pointing angles. A second problem occurred when the number of returns per array position was relatively small, say less than 200. For these cases it was sometimes noted that the averaged sampled values in each array position did not align in amplitude. In particular, it was found that the averaged samples from S^2M1 and 2 did not form a smooth curve as predicted by the theoretical average return waveform, but seemed to be displaced in amplitude relative to each other. This condition was a result of a rapidly varying AGC which could not properly normalize the return (as measured by the S&H gates) in such a short time. Although the cause was known, it made the task of estimating the pointing angle more difficult because of the discontinuity.

These two problems clearly indicated that the template approach to attitude determination was far from optimum. In devising an alternate technique, we have heavily weighted the considerations presented above rather than attempting to minimize the error due to the statistical fluctuation of the return. An approach was selected which is somewhat akin to the attitude estimation technique used for the GEOS-III radar altimeter [4]. Figure 2 illustrates the general position of the S&H gates on the average return for all three sub-sub modes or array positions. The greatest variation in the waveform as a function of pointing angle will occur in $S^2M 2$ or the trailing edge portion of the return. If we limit the estimation

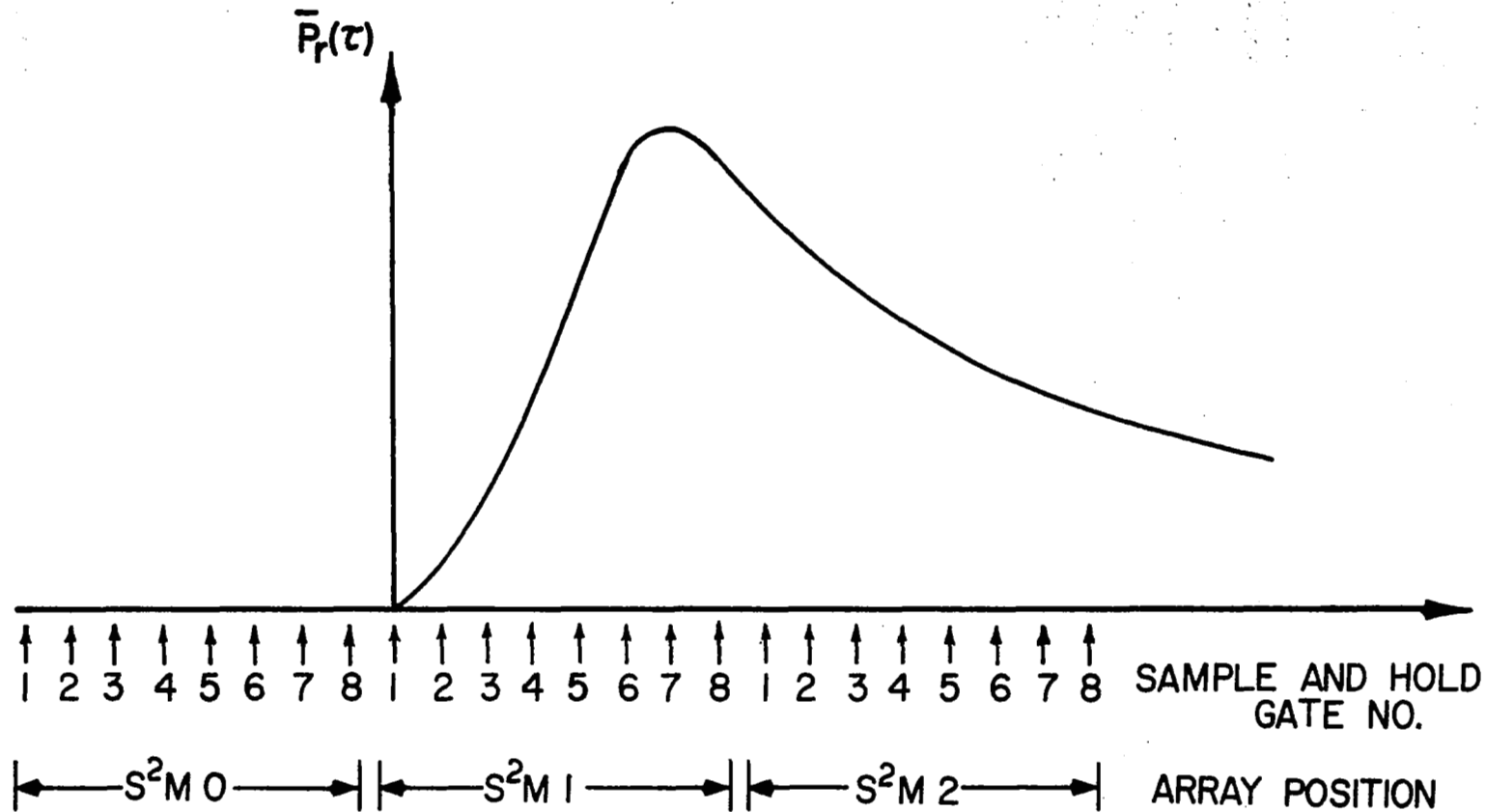


Figure 2. Approximate location of the Sample and Hold gates on the average return waveform.

technique to only the S&H data in $S^2M 2$ we can avoid the problem of data discontinuities resulting from inadequate AGC normalization. Normalization can still be a problem unless we properly use the S&H data in $S^2M 2$; this suggests some form of ratio estimator. That is, if we divide the sum of S&H gates 5 thru 8 by the sum of S&H gates 1 thru 4 we obtain an estimator function which is independent of how the S&H values are normalized in $S^2M 2$. This is important since the AGC normalization can be shown to be a function of pointing angle*. Thus, by rationing sums of S&H values in $S^2M 2$ we avoid the problem of AGC normalization and also reduce the effects of attitude variation during data acquisition. Furthermore, this approach will also provide an easily computed recipe for determining pointing errors and is relatively insensitive to small changes in the positioning of the S&H gates due to jitter and waveform induced tracker bias.

For this analysis, we will ignore receiver thermal noise effects since, during SL-2 and SL-3, it exceeded 20 dB for those cases where we could use the waveform technique. Let $x_i(\tau_j)$ and $y_i(\tau_j)$ be the IF in-phase and quadrature voltage components of the i^{th} return at a relative delay time τ_j . In the 100 ns/10 MHz modes, the video filter has a bandwidth which is more than ten times as large as the one-sided IF bandwidth. Thus, the video output is given by the following;

$$v_i(\tau_j) = K[x_i^2(\tau_j) + y_i^2(\tau_j)]$$

where K is a constant determined by the peak of the average return power and the radar receiver gains and losses. It should be noted that under the assumptions of linear incoherent scattering theory, $x_i(\tau_j)$ and $y_i(\tau_j)$ are each zero mean, jointly Gaussian random variables whose variance is equal to one-half the average return power, $\bar{P}_r(\tau_j)$. Also, $x_i(\tau_j)$ and $y_i(\tau_j)$ are independent random variables. The m-pulse average values of the waveform obtained in $S^2M 2$ are given by $V_m(\tau_1)$, $V_m(\tau_2)$, ..., $V_m(\tau_8)$ where

*The peak averaging AGC will normalize the peak of the mean return to different values for different pointing angles because of the r-factor (see Chapter 13).

$$v_m(\tau_j) = \frac{1}{m} \sum_{i=1}^m v_i(\tau_j)$$

for $j = 1, 2, \dots, 8$. The estimator function, A_ξ , is defined by the ratio of the sum of the m -pulse averages obtained from the last four gates to the sum of the m -pulse averages obtained from the first four gates, i.e.

$$A_\xi = \frac{\sum_{j=5}^8 v_m(\tau_j)}{\sum_{j=1}^4 v_m(\tau_j)}$$

Let W_m and U_m be defined as follows;

$$W_m = \sum_{j=5}^8 v_m(\tau_j)$$

$$U_m = \sum_{j=1}^4 v_m(\tau_j)$$

Since W_m and U_m are random variables whose variance is very small (for large m), we are justified in using the approximate expression for the mean and variance of the ratio of two random variables [5]. That is, for the mean

$$\begin{aligned} \bar{A}_\xi &\approx \frac{\bar{W}_m}{\bar{U}_m} - \frac{1}{\bar{U}_m^2} E \left\{ (U_m - \bar{U}_m)(W_m - \bar{W}_m) \right\} \\ &+ \frac{2\bar{W}_m}{\bar{U}_m^3} \text{Var}(U_m) \end{aligned} \quad (1)$$

where the over-bar indicates the mean value and $E\{\cdot\}$ is the mean value operator. The variance of U_m is

$$\text{Var}(U_m) = E \left\{ \sum_{j=1}^4 \sum_{k=1}^4 v_m(\tau_j) v_m(\tau_k) \right\} - 4K^2 \left[\sum_{i=1}^4 \bar{P}_r(\tau_i) \right]^2$$

however, since $x_i(\tau_j)$ and $y_i(\tau_j)$ are Gaussian (see Appendix)

$$E \left\{ \sum_{j=1}^4 \sum_{k=1}^4 v_m(\tau_j) v_m(\tau_k) \right\} = 4K^2 \sum_{j=1}^4 \sum_{k=1}^4 \bar{P}_r(\tau_j) \bar{P}_r(\tau_k) + \frac{4K^2}{m} \sum_{j=1}^4 \sum_{k=1}^4 R_x^2(\tau_j, \tau_k)$$

where $R_x(\tau_j, \tau_k)$ is the intrapulse autocorrelation function of the IF signal, i.e.

$$R_x(\tau_j, \tau_k) = E \left\{ x_i(\tau_j) x_i(\tau_k) \right\}$$

By the same procedure, it can be shown that

$$E \left\{ (U_m - \bar{U}_m)(W_m - \bar{W}_m) \right\} = \frac{4K^2}{m} \sum_{j=1}^4 \sum_{k=5}^8 R_x^2(\tau_j, \tau_k)$$

Thus, the average value of the estimator function is given by

$$\bar{A}_\xi = \frac{\sum_{j=5}^8 \bar{P}_r(\tau_j)}{\sum_{i=1}^4 \bar{P}_r(\tau_i)} \left\{ 1 + \frac{1}{m} \frac{\sum_{j=1}^4 \sum_{k=1}^4 R_x^2(\tau_j, \tau_k)}{\left[\sum_{j=1}^4 \bar{P}_r(\tau_j) \right]^2} - \frac{1}{m} \frac{\sum_{j=1}^4 \sum_{k=5}^8 R_x^2(\tau_j, \tau_k)}{\left[\sum_{j=1}^4 \sum_{k=5}^8 \bar{P}_r(\tau_j) \bar{P}_r(\tau_k) \right]} \right\} \quad (2)$$

The approximate expression for the variance of the ratio of two random processes is given by [5] the following;

$$\text{Var}(A_{\xi}) \approx \frac{\text{Var}(W_m)}{\bar{U}_m^2} + \frac{\bar{W}_m^2}{\bar{U}_m^4} \text{Var}(U_m) - \frac{2\bar{W}_m}{\bar{U}_m^3} E \left\{ (U_m - \bar{U}_m)(W_m - \bar{W}_m) \right\}$$

Using the results presented in the Appendix for the joint first moment and the variances of U_m and W_m , the above expression reduces to the following form;

$$\text{Var}(A_{\xi}) = \frac{\bar{A}_{\xi}^2}{m} \left[\frac{\sum_{j=5}^8 \sum_{k=5}^8 R_x^2(\tau_j, \tau_k)}{\left[\sum_{j=5}^8 \bar{P}_r(\tau_j) \right]^2} + \frac{\sum_{j=1}^4 \sum_{k=1}^4 R_x^2(\tau_j, \tau_k)}{\left[\sum_{j=1}^4 \bar{P}_r(\tau_j) \right]^2} - 2 \frac{\sum_{j=1}^4 \sum_{k=5}^8 R^2(\tau_j, \tau_k)}{\left[\sum_{j=5}^8 \bar{P}_r(\tau_j) \right] \left[\sum_{k=1}^4 \bar{P}_r(\tau_k) \right]} \right] \quad (3)$$

We would like to show that the average value of the estimator function is equal to the ratio of the average values of W_m and U_m , i.e.

$$\bar{A}_{\xi} \approx \frac{\bar{W}_m}{\bar{U}_m} = \frac{\sum_{j=5}^8 \bar{P}_r(\tau_j)}{\sum_{j=1}^4 \bar{P}_r(\tau_j)} \quad (4)$$

If this could be done, we could compute the theoretical dependence of \bar{A}_{ξ} upon ξ and using this curve and measured values of $\bar{P}_r(\tau_j)$ conversely determine the pointing angle. We note, however, from equation (2) that there are

additional terms in the expression for \bar{A}_ξ which depend upon the number of pulses averaged (m) and their intrapulse autocorrelation functions. It can be shown that the autocorrelation function obeys the following inequality

$$R_x^2(\tau_j, \tau_k) \leq \bar{P}_r(\tau_j) \bar{P}_r(\tau_k) \quad ,$$

thus

$$\frac{\frac{1}{m} \sum_{j=1}^4 \sum_{k=1}^4 R_x^2(\tau_j, \tau_k)}{\left[\sum_{j=1}^4 \bar{P}_r(\tau_j) \right]^2} \leq \frac{1}{m}$$

and

$$\frac{\frac{1}{m} \sum_{j=1}^4 \sum_{k=5}^8 R_x^2(\tau_j, \tau_k)}{\sum_{j=1}^4 \sum_{k=5}^8 \bar{P}_r(\tau_j) \bar{P}_r(\tau_k)} \leq \frac{1}{m}$$

We therefore see that the terms dependent upon the autocorrelation functions in equation (2) introduce a correction which is inversely proportional to the number of pulses averaged. For $m=200$, the minimum number of pulses averaged, this correction is less than one percent and may be ignored. That is, equation (4) is a valid numerical approximation for our purposes.

The average return power may be analytically described as a convolution of the system point target response, the flat surface impulse response and the tracking loop time jitter density function. However, in the third array position ($S^2M 2$), this convolution is approximately equal to a constant times the flat surface impulse response. For a pointing error in the pitch direction only, it has previously been shown [3] that the expression for the average return power becomes

$$\bar{P}_r(\tau) \approx \hat{P}_r e^{-\frac{4c}{\gamma h} \tau (\cos 2\xi + \delta \cos \xi)} \sum_{m=0}^5 \frac{\Gamma(m+1/2)}{\sqrt{\pi} \Gamma(m+1)} \left(\frac{2a}{\beta}\right)^m I_{2m}(\beta) \quad (5)$$

where

$$a = \frac{4c\delta\tau}{\gamma h} \cos \xi$$

$$\beta = \frac{4}{\gamma} \left[\sin 2\xi + 2\delta \sin \xi \right] \sqrt{\frac{c\tau}{h}}$$

c is the speed of light, h is the nominal altitude (435.5 km), ξ is the pointing angle relative to nadir, and γ and δ are antenna pattern parameters ($\gamma = 7 \times 10^{-4}$, $\delta = 0.75$).*

Berger [6] has previously obtained a closed-form relation for the pre-detection intrapulse autocorrelation function which did not include the effects of off-nadir pointing. Ignoring sea-state effects, correcting some of his algebraic errors, and including pointing error we find the following approximate form which is valid in the trailing edge region of the return;

$$R_x(t, t+\tau) \approx e^{-\frac{\tau^2}{8\sigma_p^2}} \bar{P}_r(t - \tau/2) \quad (6)$$

where σ_p is the Gaussian width of the post detection point target response (29.25 ns). Inherent in (6) is the assumption that the video bandwidth is much larger than the IF bandwidth so that we can infer the autocorrelation properties of the IF output from the video output. Equation (6) is interesting in that it shows a distinct separability in the two primary contributors to the behavior of the nonstationary autocorrelation function. That is, the Gaussian factor is a consequence of the matched filter conditions resulting from the 100 ns pulsewidth and the 10 MHz (two-sided) IF bandwidth while $\bar{P}_r(t - \tau/2)$ arises due to the random nature of the scattering process. We note that this "decoupled" form of the pre-detection autocorrelation function is valid only in the trailing edge of the return.

*These values are valid only for missions SL-2 and SL-3.

It was previously noted that the ratio estimator was relatively insensitive to jitter and S&H positioning by the tracker. In the case of jitter this is easily seen since jitter has the greatest effect where the average waveform exhibits curvature. Since we are dealing with the trailing edge of the return, the curvature of the average return is relatively small over the effective extent of the jitter density function. The position of the S&H gates on the average return is determined by the tracking loop centroid tracking point, i.e. the point at which the tracking law is satisfied on the average return. Thus, as the pointing angle changes, resulting in a change in the shape of the average return waveform, the position of the S&H gates on the average return is also altered. For a pointing error of less than about 0.4° the change in position of the S&H gates on the average return is less than about 10 ns and may be ignored. However, for $\xi > 0.4^\circ$ the positioning of the S&H gates is a very sensitive function of pointing angle. Fortunately, the estimator function \bar{A}_ξ is, to a large degree, independent of the S&H position changes. To see this, we note that for $\xi \geq 0.4^\circ$ and τ large, say greater than 200 ns, the significant Bessel functions in (5) may be replaced by their asymptotic form, i.e.

$$I_{2m}(\beta) \sim \frac{e^\beta}{\sqrt{2\pi\beta}}$$

Thus,

$$\left(\frac{a}{\beta}\right)^m I_{2m}(\beta) \approx \frac{1}{\sqrt{2\pi}} \left(\frac{\delta \text{ctn} \xi}{1+\delta}\right)^m \left(\frac{c\tau}{h}\right)^{\frac{m-1}{2}} e^{\frac{8\sin\xi}{\gamma}(1+\delta)\sqrt{\frac{c\tau}{h}}} \quad (7)$$

where we have used the small angle approximation, i.e. $\sin 2\xi \approx 2\sin\xi$. The average return power in the trailing edge portion of the return is, using (7), given by (5)

$$\bar{P}_r(\tau_j) \approx \hat{P}_r e^{-\alpha_1 \tau_j + \alpha_2 \sqrt{\tau_j}} \sum_{m=0}^M \alpha_m [\tau_j]^{\frac{m-1}{2}} \quad (8)$$

where

$$\alpha_1 = \frac{4c}{\gamma h} (\cos 2\xi + \delta \cos \xi)$$

$$\alpha_2 = \frac{8(1+\delta)}{\gamma} \sin \xi \sqrt{\frac{c}{h}}$$

$$\alpha_m = \frac{\Gamma(m+1/2)}{\pi\sqrt{2} \Gamma(m+1)} \left[\frac{2\delta \cos \xi}{1+\delta} \right]^m \left(\frac{c}{h} \right)^{\frac{m-1}{2}}$$

and M is less than or equal to five. We now let

$$\tau_j = \tau_o + \left(\frac{2j-9}{2} \right) \Delta + \epsilon$$

where τ_o is delay time half-way between S&H gates 4 and 5 for no pointing error, j is equal to the S&H gate number, Δ is 25 ns, and ϵ is the change in the position of the array due to a pointing error ξ . From previous computations, $\tau_o \approx 287.5$ ns, $\epsilon_{MAX} \approx 60$ ns and, thus,

$$\sqrt{\tau_j} \approx \sqrt{\tau_o} \left[1 + \frac{\left(\frac{2j-9}{2} \right) \Delta}{2\tau_o} + \frac{\epsilon}{2\tau_o} \right]$$

and, similarly,

$$\tau_j^{\frac{m-1}{2}} \approx \tau_o^{\frac{m-1}{2}} \left[1 + \left(\frac{m-1}{2} \right) \frac{\left(\frac{2j-9}{2} \right) \Delta}{\tau_o} + \left(\frac{m-1}{2} \right) \frac{\epsilon}{\tau_o} \right]$$

Substitution of these results in equation (8) yields the following for the average return power at the jth S&H gate;

$$\begin{aligned} \bar{P}_r(\tau_j) \approx \hat{P}_r e^{-\alpha_1(\tau_o + \epsilon) + \alpha_1\left(\sqrt{\tau_o} + \frac{\epsilon}{2\sqrt{\tau_o}}\right)} \\ \exp \left[-\alpha_1 \left(\frac{2j-9}{2} \right) \Delta + \alpha_2 \frac{\left(\frac{2j-9}{2} \right) \Delta}{2\sqrt{\tau_o}} \right] \sum_{m=0}^M \alpha_m \tau_o^{\frac{m-1}{2}} \left[1 \right. \\ \left. + \left(\frac{m-1}{2} \right) \frac{\left(\frac{2j-9}{2} \right) \Delta}{\tau_o} + \left(\frac{m-1}{2} \right) \frac{\epsilon}{\tau_o} \right] \end{aligned} \quad (9)$$

The dominant terms in equation (9) are the exponentials; however, the exponents do not involve any products of the S&H index j and the attitude induced positioning error ϵ . Thus,

$$\bar{P}_r(\tau_j) \approx \hat{P}_r e^{-\alpha_1(\tau_0 + \epsilon) + \alpha_1\left(\sqrt{\tau_0} + \frac{\epsilon}{2\sqrt{\tau_0}}\right) - \alpha_1\left(\frac{2j-9}{2}\right)\Delta + \alpha_2\left(\frac{2j-9}{2}\right)\Delta} \cdot \sum_{m=0}^M \alpha_m \tau_0^{\frac{m-1}{2}}$$

and the average estimator function is given by

$$\bar{A}_\xi \approx \frac{\sum_{j=5}^8 \left[e^{\left(\frac{2j-9}{2}\right)\Delta \left(-\alpha_1 + \frac{\alpha_2}{2\sqrt{\tau_0}}\right)} \cdot \sum_{m=0}^M \alpha_m \tau_0^{\frac{m-1}{2}} \right]}{\sum_{j=1}^4 \left[e^{\frac{2j-9}{2}\Delta \left(-\alpha_1 + \frac{\alpha_2}{2\sqrt{\tau_0}}\right)} \sum_{m=0}^M \alpha_m \tau_0^{\frac{m-1}{2}} \right]} \quad (10)$$

Equation (10) clearly shows that the estimator function is independent of the shift in the tracker centroid point ϵ (at least to the order of approximation used here). It turns out that this is a rather important result because if the estimator had not been relatively independent of S&H position it would have been necessary to incorporate the dependence into the model for \bar{A}_ξ . Although this could have been easily done, there was no guarantee that the tracking gates would behave as modeled since there was no temperature calibration data available on the gates. Thus, the estimator function as given by equation (4) avoids the very important problems of tracker jitter, AGC response and settling time, and tracker induced position changes of the S&H gates relative to the average return. Relative to a full waveform template or least-squares fitting approach, i.e. using all of the average waveform data and not just that acquired in S^2M^2 , the estimator approach may be

more suitable to the practical problems inherent in the S-193 operation.

3.0 Discussion Of Results

The variation of the average estimator function with pointing angle was computed from equation (4) using the results in (5) for the average return waveform. The dependence is shown in Figure 3. The results are shown out to about 0.9° because for larger pointing errors, the tracker centroid changed very rapidly with angle and the analysis became inaccurate. The variance of the estimator was computed for various number of pulse averages, and, using the curve in Figure 3, this result was translated into a one-sigma standard deviation of the angle estimate. The error is shown in Figure 4 for 200, 500 and 1500 pulses comprising* the average waveform. Of particular interest is the obvious flattening of the curve about the minimum error point due to the linear dependence of the estimator function on the pointing error. Also, as the number of pulses increases the flat portion of the curve becomes broader in extent indicating a minimum variance estimate over a larger range of pointing angles. For a 1500-pulse average, the minimum one-sigma error is 0.04° which is comparable with the original minimum variance estimate [1].

It should be noted that this particular approach to pointing angle estimation does not guarantee a minimum variance estimate in the sense of a maximum likelihood estimate. Its primary advantage is two-fold in that it overcomes certain previously mentioned problems which are not associated with the statistical fluctuation of the target and it also provides an easy means for estimating the pointing angle. That is, using offset and saturation corrected S&H data from $S^2M 2$, \bar{A}_ξ is computed from equation (4) and the corresponding estimate of pointing angle is obtained from the curve in Figure 3. In comparing the results obtained by this approach with the estimates resulting from the template method [3], we find very good agreement. That is, where a discrepancy does exist, it generally falls within the one-sigma error tolerances presented in Figure 4. In certain cases, there is an obvious

*The return waveforms are accumulated at a rate of 100 per second thus 200, 500 and 1500 pulses correspond to 2, 5 and 15 seconds averaging time.

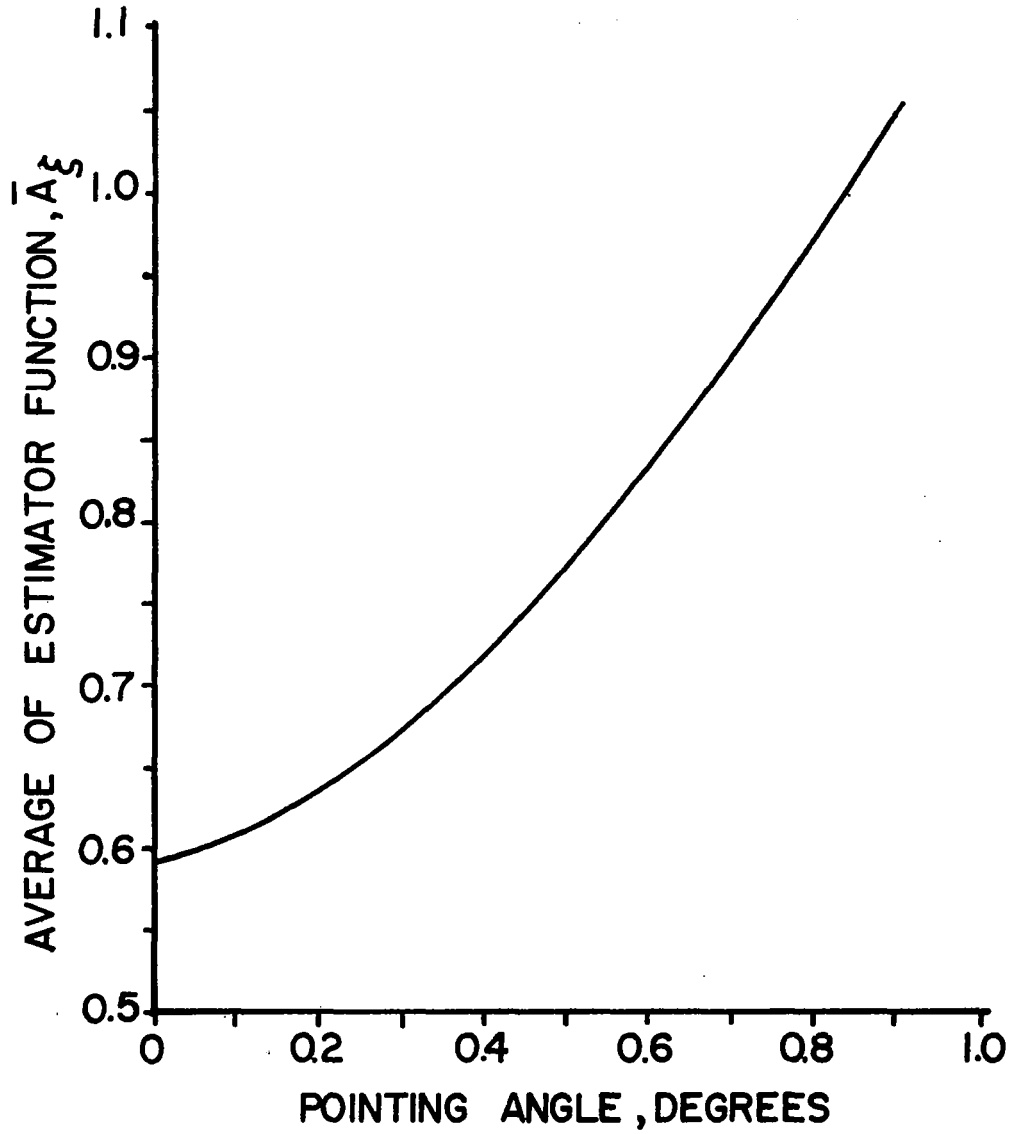


Figure 3. Dependence of the average attitude estimation function on pointing angle for missions SL-2 and SL-3.

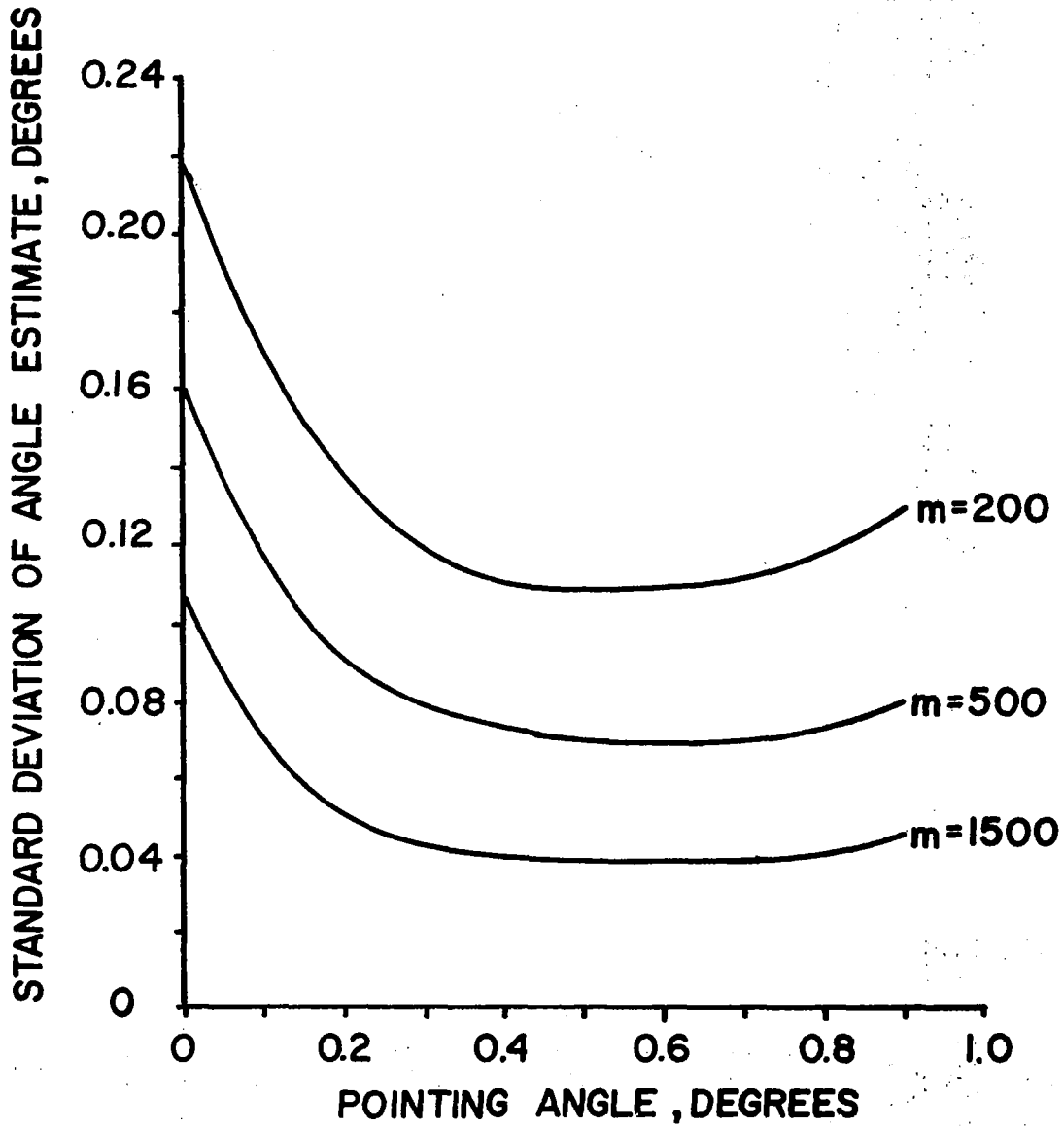


Figure 4. Standard deviation of the pointing angle estimate for typical pulse averages and missions SL-2 and SL-3.

attitude change during one or more of the three sub sub modes (S^2M). Whereas the template approach will produce some form of average pointing angle, it is not immediately clear how this relates to the actual variation in pointing angle during data acquisition. The estimator approach, on the other hand, will produce an estimate based only on the data in $S^2M 2$ and, thus, is more directly related to the behavior of the attitude control system at least during the last sub sub mode.

Figure 5 is an excellent example of inadequate normalization by the AGC and its affect on the average return waveform. The data points in $S^2M 1$ agree very well with the theoretical return for $\xi_p = 0.6^\circ$ considering the fact that jitter was ignored in the computation. Jitter would have the effect of decreasing the slope of the leading edge of the curve in Figure 5. The data points in $S^2M 2$ appear to be offset from the theoretical curve: multiplication by 0.885 realigns the data with the theoretical curve. Each of the data points shown in Figure 5 are based upon a 208 pulse average or about 2 seconds elapsed time. A measure of the variation in received power level may be obtained from a plot of how σ° changed over the same time interval such as shown in Figure 6 [3]. Whereas in $S^2M 0$ and 1 the variation in σ° is due to quantization, there is a distinct downward trend to the data in $S^2M 2$. Since the AGC time constant for a decreasing power level is on the order of 0.5 second and this figure is about one quarter of the averaging time, it is entirely likely that the AGC could not properly normalize the waveform data within the given averaging interval.

In the analysis presented in this chapter we have attributed the variation of the average return waveform in the trailing edge portion of the return entirely to antenna beamwidth and pointing angle effects. Under certain situations this assumption is false and can lead to erroneous estimates of the pointing angle. These situations are characterized by a very rapid decay of σ° with angle of incidence so that the variation of σ° in the trailing edge portion of the return must be accounted for. Such situations normally occur over surfaces having a relatively small rms roughness and a very large effective spatial correlation length. A more complete discussion of this topic is presented in the chapter on anomalous land scatter. Fortunately, it is nearly always possible to identify these occurrences since the return power is always much larger than for a typical rough surface. Under these

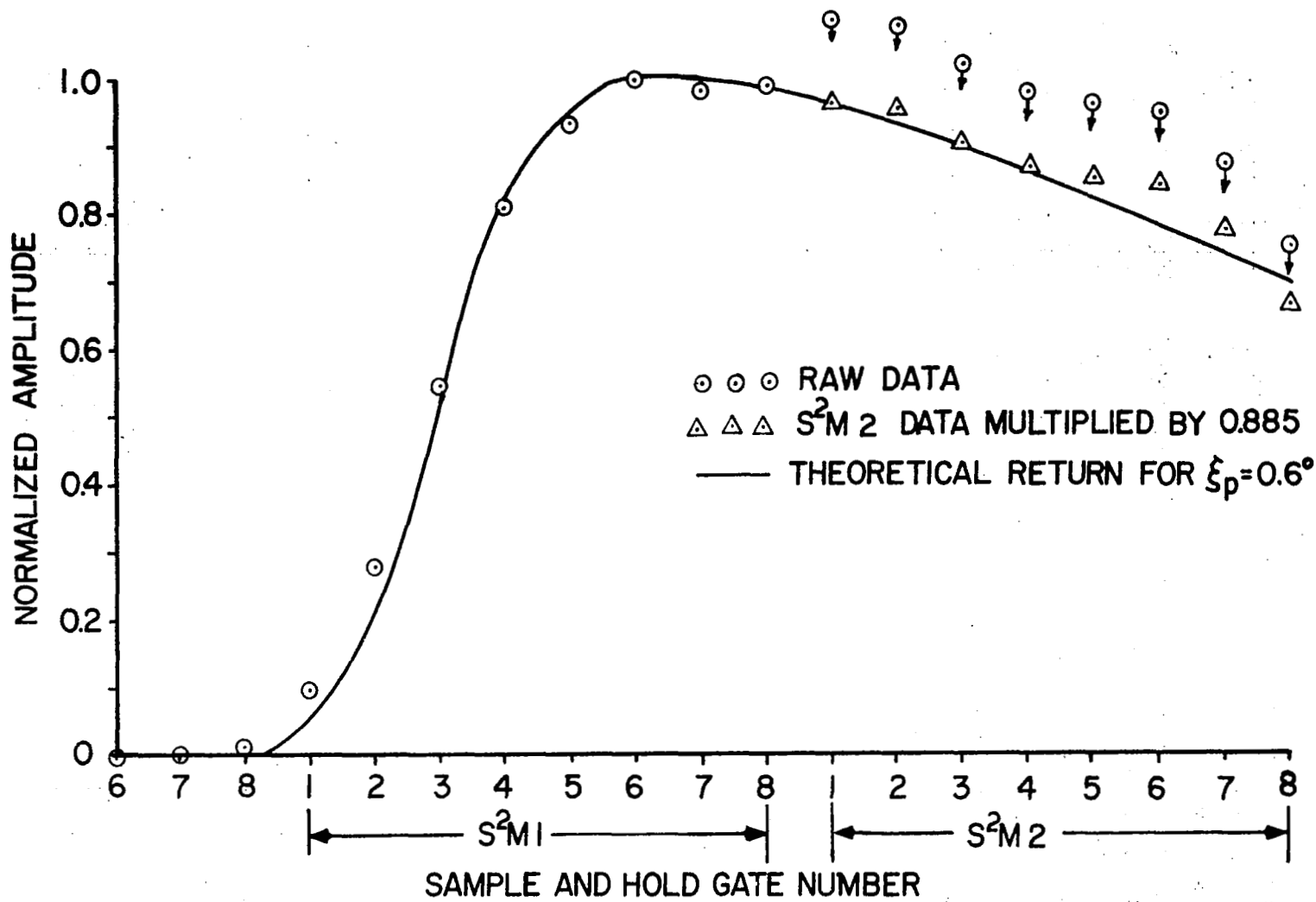


Figure 5. Corrected waveform data from SL-2, EREP Pass 9, second Mode II, Submode 6 showing the effect of inadequate AGC normalization in S²M 2.

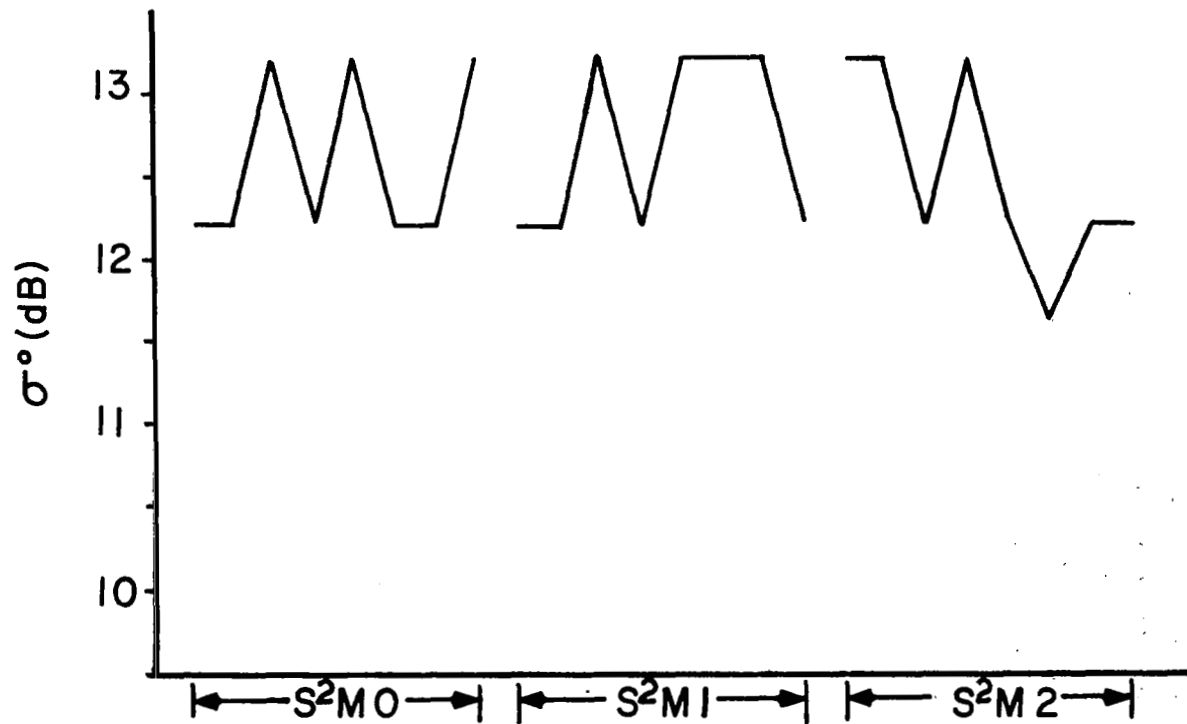


Figure 6. Variation of surface scattering cross section during acquisition of the waveform data shown in Figure 5.

circumstances, the attitude estimation technique fails. Only in one case was this particular phenomenon observed in the over-water Skylab data although it frequently appeared in the terrain scattering data.

In conclusion, we see that the waveform approach to attitude estimation is a very powerful tool which can be of significant benefit to the more general area of spacecraft attitude control. However, as illustrated in this chapter, it is essential that the estimation technique be properly designed to account for system behavior which is beyond the pure Rayleigh fluctuating nature of the return.

REFERENCES

1. Brown, G. S., "Estimating S-193 Radar Altimeter Antenna Pointing Angle From Average Waveform Data," Research Triangle Institute, Durham, N. C., 13 September, 1973 (Unpublished).
2. Lindberg, A. C., "Skylab S-193 Radiometer/Scatterometer/Altimeter Sensor Antenna Testing Results," Lockheed Electronics Company, Inc., Houston, Texas, Job Order No. 16-604, NASA Contract NAS9-12200, September, 1974.
3. Brown, G. S., "Reduced Backscattering Cross Section (σ^0) Data From The Skylab S-193 Radar Altimeter," NASA CR-141401, Applied Science Associates, Inc., Apex, N. C., October, 1975.
4. L. S. Miller & G. S. Brown, "Engineering Studies Related To The GEOS-C Radar Altimeter," NASA CR-137462, Applied Science Associates, Inc., Apex, N. C., May, 1974.
5. Papoulis, A., Probability, Random Variables, and Stochastic Processes, McGraw-Hill Book Co., New York, pg 212, 1965.
6. Berger, T., "Satellite Altimetry Using Ocean Backscatter," IEEE Trans. on Ant. & Propag., Vol. AP-20, pp 295-309, May 1972.

APPENDIX

The purpose of this Appendix is to derive some of the more complicated relationships required for the determination of the mean and variance of the estimator function, A_{ξ} . The first of the factors appears in equation (1), i.e. $E\left\{(U_m - \bar{U}_m)(W_m - \bar{W}_m)\right\}$. Expanding and taking the mean, we have

$$E\left\{(U_m - \bar{U}_m)(W_m - \bar{W}_m)\right\} = E\left\{U_m W_m\right\} - \bar{U}_m \bar{W}_m$$

But

$$E\left\{U_m W_m\right\} = E\left\{\sum_{j=5}^8 \sum_{k=1}^4 v_m(\tau_k) v_m(\tau_j)\right\}$$

or

$$\begin{aligned} E\left\{U_m W_m\right\} &= \frac{K^2}{m^2} E\left\{\sum_{j=5}^8 \sum_{k=1}^4 \left[\sum_{i=1}^m (x_i^2(\tau_k) + y_i^2(\tau_k))\right] \right. \\ &\quad \left. \cdot \left[\sum_{\ell=1}^m (x_{\ell}^2(\tau_j) + y_{\ell}^2(\tau_j))\right]\right\} \\ &= \frac{K^2}{m^2} E\left\{\sum_{j=5}^8 \sum_{k=1}^4 \sum_{i=1}^m \sum_{\ell=1}^m \left[x_i^2(\tau_k) x_{\ell}^2(\tau_j) + x_i^2(\tau_k) y_{\ell}^2(\tau_j) \right. \right. \\ &\quad \left. \left. + y_i^2(\tau_k) x_{\ell}^2(\tau_j) + y_i^2(\tau_k) y_{\ell}^2(\tau_j)\right]\right\} \end{aligned}$$

Taking the expectation operation inside the summations and realizing that since the x and y are each zero mean with joint Gaussian probability density functions, i.e.

$$\begin{aligned} E\{z_1 z_2 z_3 z_4\} &= E\{z_1 z_2\} E\{z_3 z_4\} + E\{z_1 z_3\} E\{z_2 z_4\} \\ &\quad + E\{z_1 z_4\} E\{z_2 z_3\} \quad , \end{aligned}$$

then

$$\begin{aligned}
 E\left\{U_m W_m\right\} &= \frac{K^2}{m} \sum_{j=5}^8 \sum_{k=1}^4 \sum_{i=1}^m \sum_{\ell=1}^m \left[E\left\{x_i^2(\tau_k)\right\} E\left\{x_\ell^2(\tau_j)\right\} \right. \\
 &+ 2E^2\left\{x_i(\tau_k)x_\ell(\tau_j)\right\} + E\left\{x_i^2(\tau_k)\right\} E\left\{y_\ell^2(\tau_j)\right\} \\
 &+ E\left\{y_i^2(\tau_k)\right\} E\left\{x_\ell^2(\tau_j)\right\} + E\left\{y_i^2(\tau_k)\right\} E\left\{y_\ell^2(\tau_j)\right\} \\
 &\left. + 2E^2\left\{y_i(\tau_k)y_\ell(\tau_j)\right\} \right]
 \end{aligned}$$

since the x and y processes are independent. Under the assumption of pulse-to-pulse independence,

$$2 \sum_{i=1}^m \sum_{\ell=1}^m E^2\left\{x_i(\tau_k)x_\ell(\tau_j)\right\} = 2m E^2\left\{x(\tau_k)x(\tau_j)\right\}$$

and similarly for the y(τ). Thus, we have

$$E\left\{U_m W_m\right\} = 4K^2 \sum_{j=5}^8 \sum_{k=1}^4 \left[\bar{P}_r(\tau_k)\bar{P}_r(\tau_j) + \frac{1}{m} R_x^2(\tau_k, \tau_j) \right]$$

where

$$R_x^2(\tau_k, \tau_j) = E^2\left\{x(\tau_k)x(\tau_j)\right\}$$

Subtracting the product of the means, we find for the joint first moment

$$E\left\{(U_m - \bar{U}_m)(W_m - \bar{W}_m)\right\} = \frac{4K^2}{m} \sum_{j=5}^8 \sum_{\ell=1}^4 R_x^2(\tau_j, \tau_\ell)$$

The reduction of the variances of U_m and W_m proceeds in exactly the same manner as above and, therefore, it is only necessary to present the results, i.e.

$$\text{Var}(U_m) = \frac{4K^2}{m} \sum_{j=1}^4 \sum_{k=1}^4 R_x^2(\tau_j, \tau_k)$$

$$\text{Var}(W_m) = \frac{4K^2}{m} \sum_{j=5}^8 \sum_{k=5}^8 R_x^2(\tau_j, \tau_k)$$

CHAPTER 4

Pointing Angle Estimation Via Tracker Bandwidth Analysis

by

L. S. Miller

1.0 Introduction and Summary of Results

This chapter discusses the effects of pointing angle on altitude tracker bias, tracker noise level and its bandwidth. As first noted by McGoogan, et al., [1], these dependencies can be, conversely, utilized to provide estimates of off-nadir angle, in addition to the estimates obtainable from the better-known waveform method. In fact, the two techniques are complementary, since the waveform method is most sensitive over a range of 0 - 0.9 degrees (see Chapter 3) and the tracking jitter technique is effective over a range of approximately .75 - 1.5 degrees. Because of the dependence of altitude data bias on pointing angle and the recurring problems with the Skylab attitude control systems [2], the technique discussed here provides a needed, albeit approximate, method for applying bias corrections to altitude data which might otherwise provide erroneous geodetic information. Because of the possibility of non-linear effects and the approximations contained in the tracker variance analyses, measurements should be made on the S-193 backup system to provide a more accurate relationship between tracker variance and off-nadir angle.

Figure 1 shows a graph of S-193 rms tracking jitter versus off-nadir angle based on both experimental data and computed values. The experimental values given in Figure 1 were obtained using the angle estimates given in [2] and the computed altitude data standard deviation given in [3], for those passes during SL-2 and SL-3 which were documented in both references. These values may be compared with the spectral analyses given by [3]. For small pointing angles the power spectral densities were found to be essentially flat out to 4 Hz (the Nyquist frequency for the S-193 altitude data rate). We show a 1.9 Hz 3 dB bandwidth, which, for the degree of spectral aliasing present, is considered to be within errors in the spectral computation. For large pointing angles ($>.9^\circ$) Hatch found altitude data noise bandwidths to be on the order of .2 - .26 Hz. Figure 2 shows a comparison of Hatch's power spectral density results with the present work; the agreement is considered to be quite close.

SL-4 data was excluded from this analysis since there was a significant reduction in signal-to-noise ratio (SNR) due to antenna damage*.

*The SL-4 SNR was estimated [2] to be about 25 dB less than during SL-2 and SL-3.

LEGEND

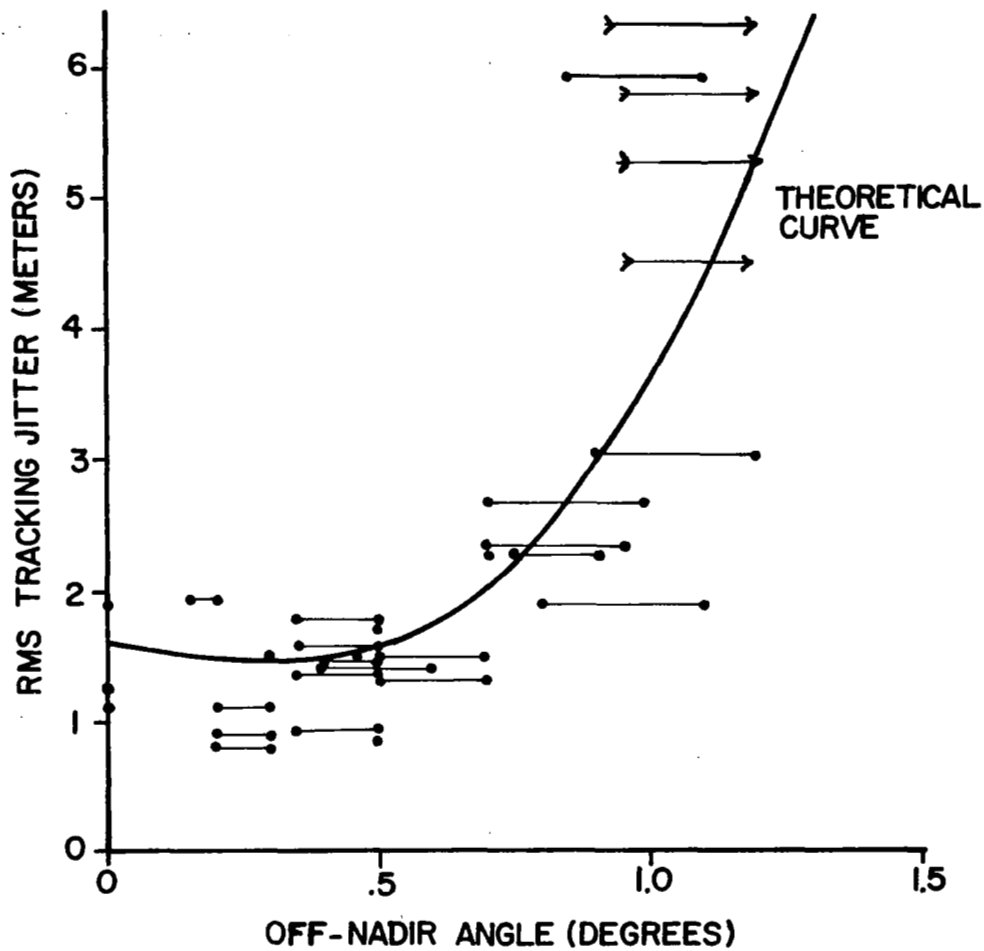
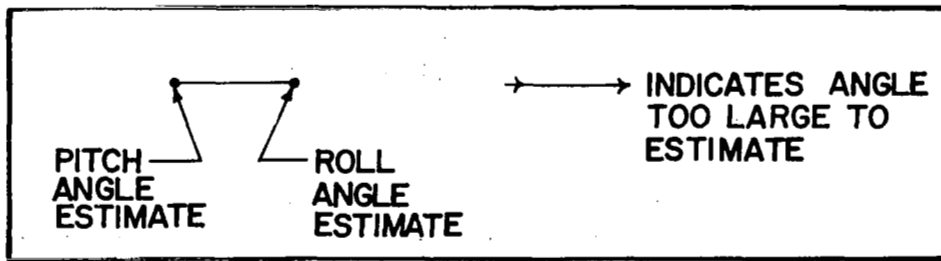


Figure 1. Comparison of measured and theoretical values of tracking jitter as a function of pointing angle.

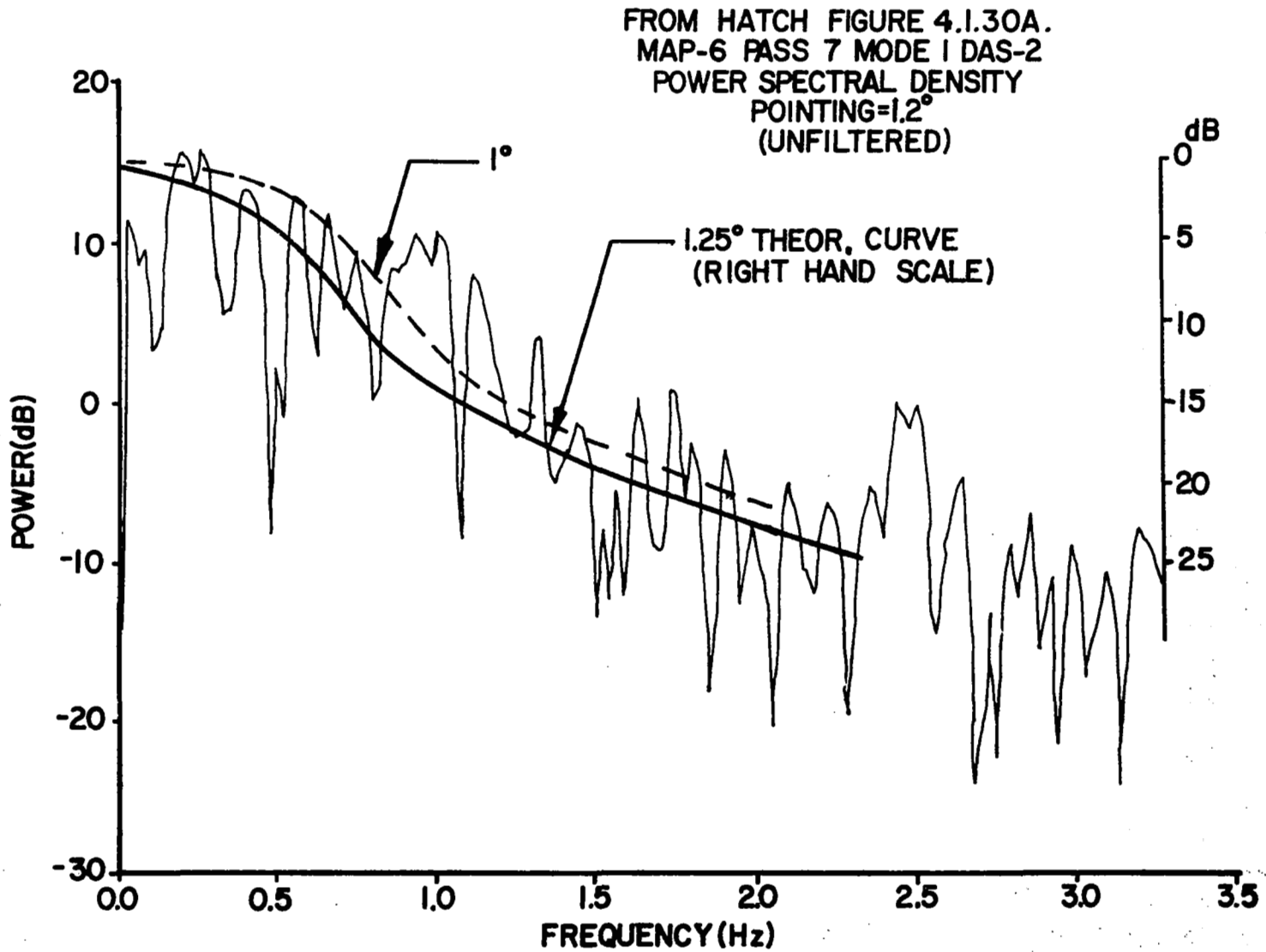


Figure 2. Comparison of experimental and theoretical altimeter residual spectra.

values shown in Figure 1 generally contain an upper and lower value; as discussed in [2] the upper value assumes a pointing error only in the roll coordinate and the lower value is for a pitch-only attitude error. The basis for the theoretical curve shown in Figure 1 will be discussed next. We begin by analyzing the change in tracker bandwidth versus off-nadir angle.

2.0 Effect of Pointing angle on Skylab Tracking Loop Bandwidth

The Skylab system is neither completely pulselength nor beamwidth limited and the received mean waveforms are highly dependent on pointing angle. This is true in regard to altitude tracker characteristics for both the 10 and 100 nanosecond modes since the video filter preceding the tracker* provides a bandwidth of ~5 MHz in both cases. Therefore, the mean waveforms as seen by the tracker will be essentially identical in the two modes.

The change in rise time and decay time of the mean waveforms with pointing angle effectively alters the slope of the time discriminator input-output characteristics; this effect is equivalent to a change in loop gain. As a result, the closed loop bandwidth is a function of pointing angle. This effect is clearly evident in experimental data (see Figure 3). Calculated values of bandwidth will be shown to be in a range of 2 Hz at 0° to 0.22 Hz at 1.5° pointing angle. The tracker should not function much beyond 1.5 degrees because the mean waveform slope is so small that the tracking law cannot be satisfied (the late-gate energy must be twice the early gate energy).

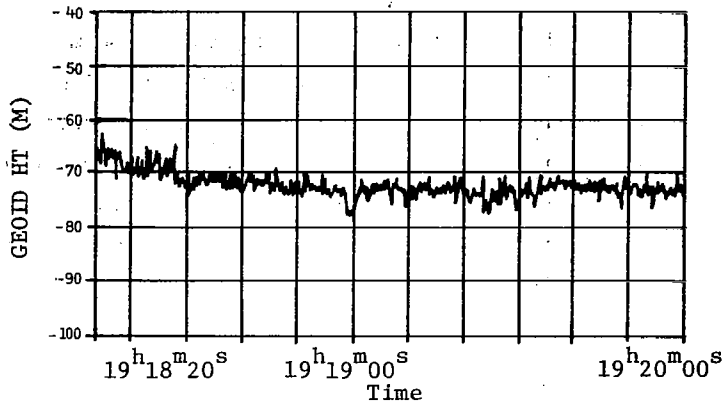
The continuous-time equivalent circuit of the tracking loop consists of a gain coefficient K_v followed by a lead-lag network and an integrator; the open-loop transfer function is

$$H_o(s) = \frac{K_v(t_2s+1)}{s(t_1s+1)}$$

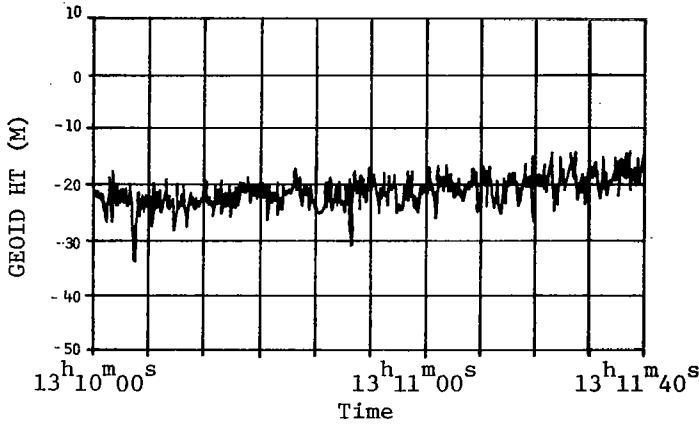
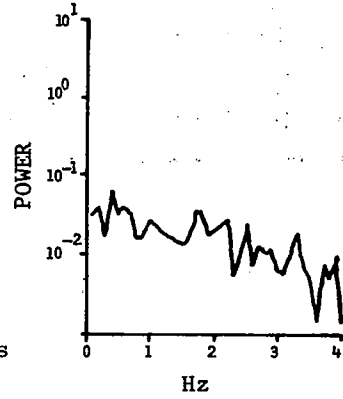
where (4) $t_1 = 8$, $t_2 = 0.25$, $K_v = 280$ and $s = j\omega$. The closed loop (magnitude-squared) transfer function (or power spectral density) is

$$|H_c(\omega)|^2 = \frac{K_v^2(.0625\omega^2 + 1)}{64\omega^4 + [(0.25K_v + 1)^2 - 16K_v]\omega^2 + K_v^2} \quad (1)$$

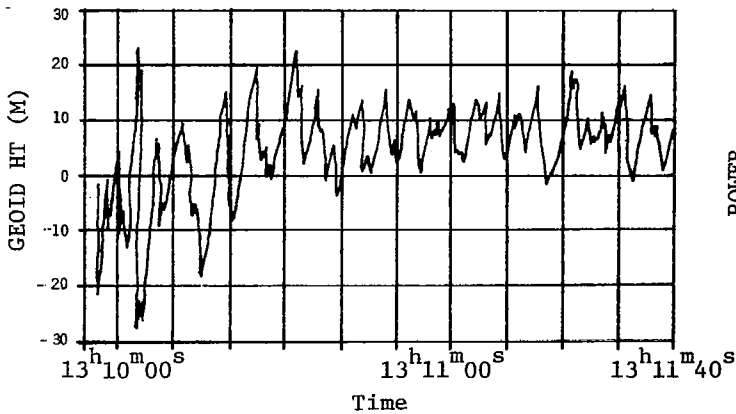
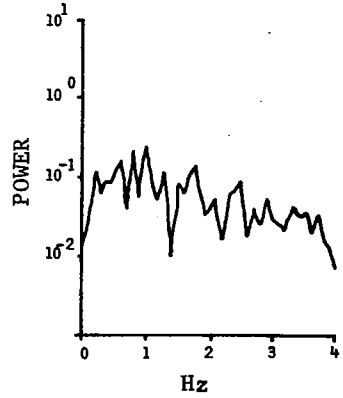
*This filter was in series with the tracker only.



SL-4 Pass 86 Pointing = 0.6°



SL-2 Pass 9 Pointing = 1.1°



SL-3 Pass 32 Pointing = 1.4°

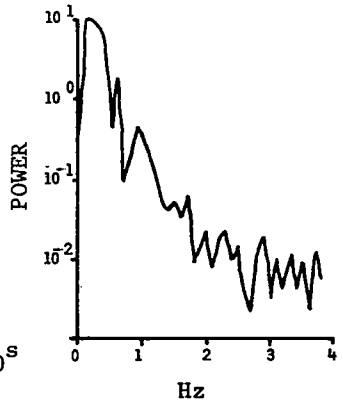


Figure 3. The effects of off-nadir pointing from Reference 1.

The change in closed loop bandwidth versus off-nadir angle has been computed as follows. The mean waveforms as a function of angle were first computed based on the closed form equation given in [2] (typical waveforms are shown in Figure 4). These (AGC normalized) waveforms were next numerically convolved with the altitude tracking gate configuration to produce time-discriminator curves, from which the slope of the control curve was extracted and used to scale the loop gain K_V . That is, the composite loop gain is defined as

$$K_V = K_O K_1$$

where K_O is the nominal (on-nadir) loop gain ($K_O = 280$) and K_1 is the slope of the time discriminator curve normalized to unity at nadir. The values so obtained are shown in Table I. Substitution of the values for K_1 given in Table I into (1) gives the loop bandwidth behavior shown in Figure 5. The Appendix gives tabulated values of magnitude of the loop transfer function versus pointing angle.

3.0 Effect of Pointing Angle on Altitude Tracking Jitter

As given in References 4 and 5, an approximate expression for the random tracking error for a split-gate tracker is

$$\sigma_\tau \approx \frac{T \sqrt{K_e^T(0;0)}}{\sqrt{N/\pi B_L}} \quad (2)$$

where T is the rise-time of the mean waveshape, N is the PRF, B_L is the 3dB closed loop bandwidth, and $K_e^T(0;0)$ is the normalized conditional covariance function of the equivalent additive noise for no error voltage out of the discriminator. Other details are given in the above cited references. For the type of receiver and tracker used in the S-193 system $K_e^T(0;0)$ is of the form

$$K_e^T(0;0) = A + B/\text{SNR} + C/\text{SNR}^2.$$

For the S-193 system Reference 4 gives values of $A = 7/6$, $B = 6$, and $C = 8$ and shows that σ_τ has essentially reached an asymptotic value of $K_e^T(0;0) \approx A$, for SNR values of $\geq 15\text{dB}$. Since we will only be concerned with SL-2 and SL-3 100 ns data, for which SNR values were typically 30dB, this asymptotic form will be used in the remainder of this section.

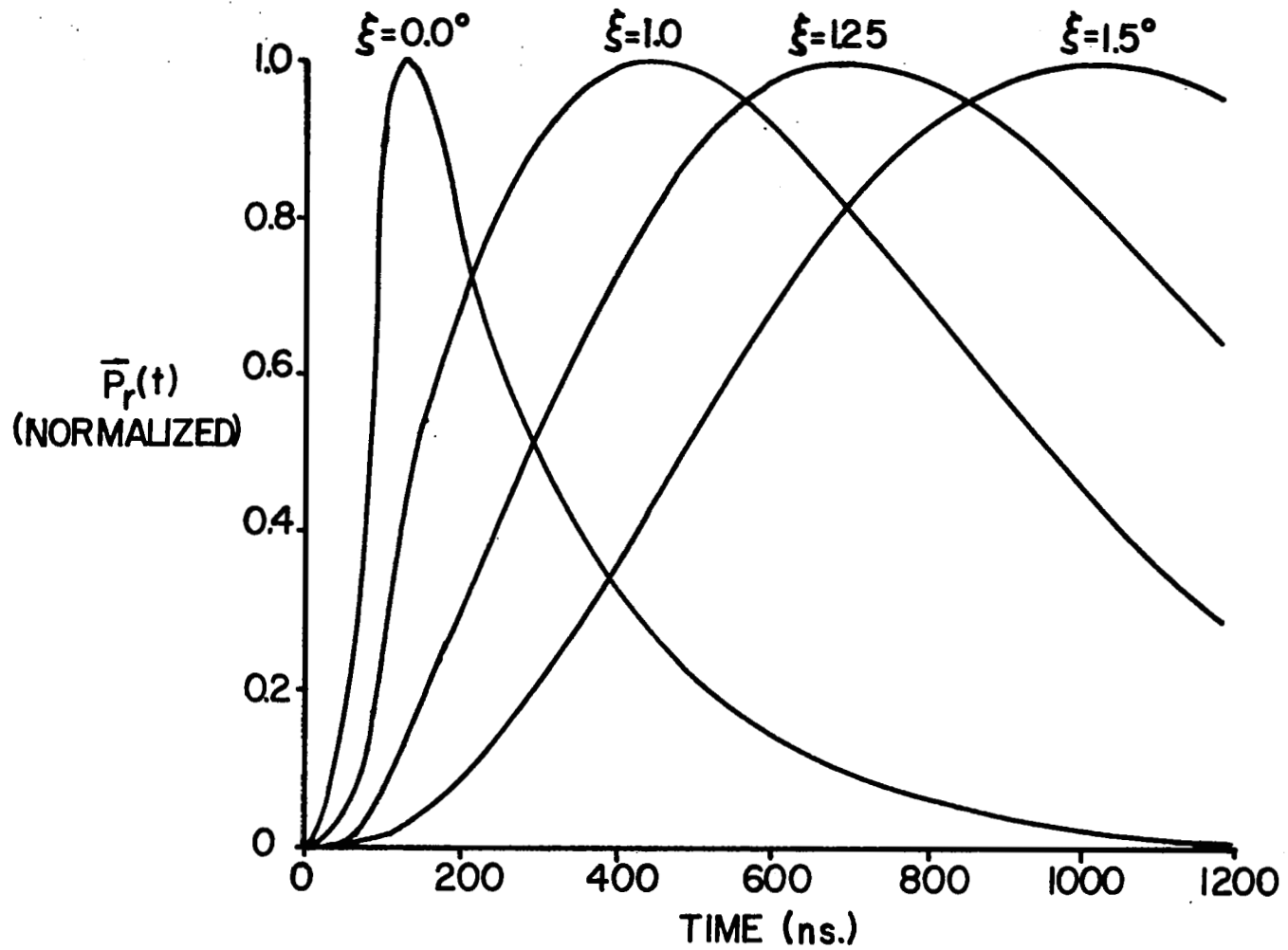


Figure 4. Mean return waveform as a function of delay time and pointing angle.

TABLE I

Time Discriminator Control Curve Slope As A Function of Pointing Angle

Off-Nadir Angle (degrees)	K_1	Increased time delay in tracking* point		Rise time at 10% - 90%
		(ns.)	(meters)	(ns.)
0	1	0	0	70
.5	.83	4	.6	70
1.0	.12	150	22.5	220
1.25	.11	220	33.0	410
1.5	.07	290	43.5	650

*Non-negative values correspond to an increase in measured altitude values as the off-nadir angle increases.

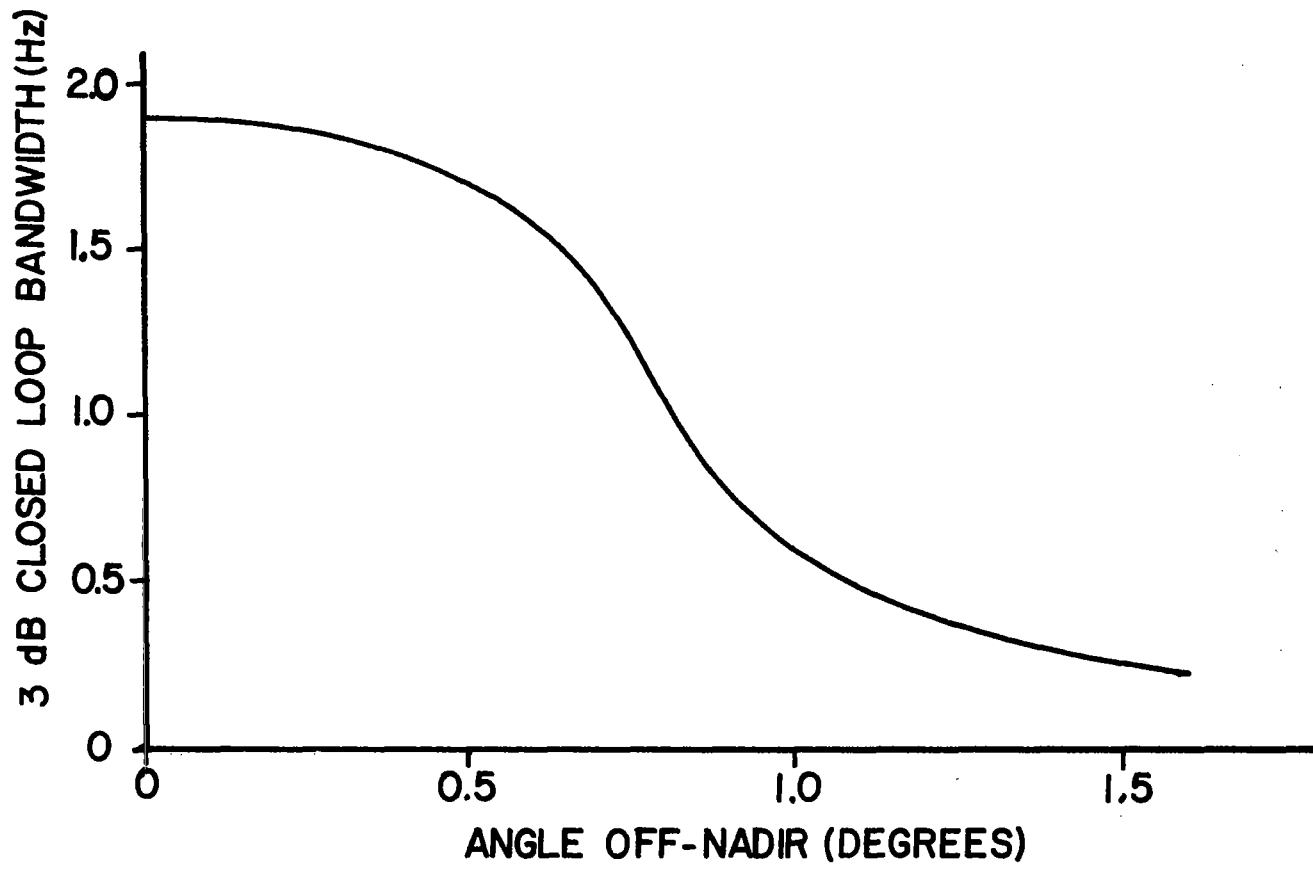


Figure 5. Tracker closed loop bandwidth as a function of pointing angle.

An estimate of σ_τ as a function of off-nadir angle can be made as follows. The T parameter is taken to be the off-nadir rise time of the mean waveform, B_L is the previously calculated closed loop bandwidth, and $K_e^T(0;0)$ is derived from the slope of the time discriminator curve (see Table I) and by numerical integration of the following;

$$K_e^T(0;0) = \frac{1}{(TK_1)^2} \int_{-\infty}^{\infty} \int_{-\infty}^{\infty} R^2(\alpha,\beta)r(\alpha)r(\beta)d\alpha d\beta,$$

where $R(\alpha,\beta)$ is the time varying autocorrelation function of the video waveform and $r(\cdot)$ is the tracking gate function. In these computations $R(\alpha,\beta)$ was obtained from the mean waveform rise-time and through use of the functional form given in Reference 6. The tracking gate function was assumed to correspond to rectangular gates, and the integration limits changed accordingly. Table II gives the results of these computations.

Table II

Tracking Jitter Versus Pointing Angle

Off-nadir Angle (degrees)	B_L (Hz)	$K_e^T(0;0)$	σ_τ (ns.)	σ_h (meters)
0	1.9	.97	10.7	1.6
.5	1.71	.97	10	1.5
1.0	.55	1.5	24	3.62
1.25	.45	1.6	38.7	5.8

REFERENCES

1. McGoogan, J. T., C. D. Leitao, and W. T. Wells, "Summary of Skylab S-193 Altimeter, Altitude Results," NASA TM X-69355, Wallops Flight Center, Wallops Island, Virginia, February, 1975.
2. Brown, G. S., "Reduced Backscattering Cross Section (σ^0) Data from the Skylab S-193 Radar Altimeter," NASA CR-141401, Applied Science Associates, Inc., Apex, North Carolina, October, 1975.
3. Hatch, W. E., "Noise Characteristics of the Skylab S-193 Altimeter Altitude Measurements," NASA CR-141403, Business and Technological Systems, Inc., Seabrook, Maryland, November, 1975.
4. Hofmeister, E. and B. Keeney, "Radar Altimeter Return Waveform Sampling Study," Final report on NASA Contract No. NAS-12-683, General Electric Co., Utica, New York, 1971.
5. Hofmeister, E. L., "Analysis and Measurement of the Performance of a Signal Tracking Loop for a Satellite Radar Altimeter when Excited by a Random Process," Ph.D. Dissertation, Syracuse Univ., December, 1973.
6. Godbey, T., E. Hofmeister, B. Keeney, and W. Kelly, "Radar Altimeter Study, Phase II," Final Report on NASA Contract No. NAS-12-683, General Electric Co., Utica, New York, 1971.

APPENDIX

This appendix contains tabulations of the magnitude of the tracking loop transfer function "H" versus frequency (Hz) for pointing angles of 0, .5, 1.0, 1.25, and 1.5 degrees.

Pointing Angle = 0°

FREQ = 0.00	H = 1.00
FREQ = 0.25	H = 1.06
FREQ = 0.50	H = 1.19
FREQ = 0.75	H = 1.24
FREQ = 1.00	H = 1.17
FREQ = 1.25	H = 1.03
FREQ = 1.50	H = 0.90
FREQ = 1.75	H = 0.79
FREQ = 2.00	H = 0.70
FREQ = 2.25	H = 0.62
FREQ = 2.50	H = 0.56
FREQ = 2.75	H = 0.51
FREQ = 3.00	H = 0.47
FREQ = 3.25	H = 0.43
FREQ = 3.50	H = 0.40
FREQ = 3.75	H = 0.37
FREQ = 4.00	H = 0.35
FREQ = 4.25	H = 0.33
FREQ = 4.50	H = 0.31
FREQ = 4.75	H = 0.30
FREQ = 5.00	H = 0.28
FREQ = 5.25	H = 0.27
FREQ = 5.50	H = 0.25
FREQ = 5.75	H = 0.24
FREQ = 6.00	H = 0.23
FREQ = 6.25	H = 0.23

*

Pointing Angle = .5°

FREQ = 0.00	H = 1.00
FREQ = 0.25	H = 1.08
FREQ = 0.50	H = 1.23
FREQ = 0.75	H = 1.27
FREQ = 1.00	H = 1.14
FREQ = 1.25	H = 0.96
FREQ = 1.50	H = 0.81
FREQ = 1.75	H = 0.69
FREQ = 2.00	H = 0.60
FREQ = 2.25	H = 0.53
FREQ = 2.50	H = 0.48
FREQ = 2.75	H = 0.43
FREQ = 3.00	H = 0.40
FREQ = 3.25	H = 0.36
FREQ = 3.50	H = 0.34
FREQ = 3.75	H = 0.31
FREQ = 4.00	H = 0.29
FREQ = 4.25	H = 0.28
FREQ = 4.50	H = 0.26
FREQ = 4.75	H = 0.25
FREQ = 5.00	H = 0.23
FREQ = 5.25	H = 0.22
FREQ = 5.50	H = 0.21
FREQ = 5.75	H = 0.20
FREQ = 6.00	H = 0.19
FREQ = 6.25	H = 0.19

*

Pointing Angle = 1°

FREQ = 0.00	H = 1.00
FREQ = 0.10	H = 1.10
FREQ = 0.20	H = 1.46
FREQ = 0.30	H = 2.01
FREQ = 0.40	H = 1.37
FREQ = 0.50	H = 0.79
FREQ = 0.60	H = 0.53
FREQ = 0.70	H = 0.39
FREQ = 0.80	H = 0.31
FREQ = 0.90	H = 0.26
FREQ = 1.00	H = 0.22
FREQ = 1.10	H = 0.19
FREQ = 1.20	H = 0.17
FREQ = 1.30	H = 0.15
FREQ = 1.40	H = 0.14
FREQ = 1.50	H = 0.13
FREQ = 1.60	H = 0.12
FREQ = 1.70	H = 0.11
FREQ = 1.80	H = 0.10
FREQ = 1.90	H = 0.10
FREQ = 2.00	H = 0.09

Pointing Angle = 1.25°

FREQ = 0.00	H = 1.00
FREQ = 0.10	H = 1.07
FREQ = 0.20	H = 1.25
FREQ = 0.30	H = 1.23
FREQ = 0.40	H = 0.87
FREQ = 0.50	H = 0.59
FREQ = 0.60	H = 0.43
FREQ = 0.70	H = 0.33
FREQ = 0.80	H = 0.27
FREQ = 0.90	H = 0.22
FREQ = 1.00	H = 0.19
FREQ = 1.10	H = 0.17
FREQ = 1.20	H = 0.15
FREQ = 1.30	H = 0.14
FREQ = 1.40	H = 0.12
FREQ = 1.50	H = 0.11
FREQ = 1.60	H = 0.11
FREQ = 1.70	H = 0.10
FREQ = 1.80	H = 0.09
FREQ = 1.90	H = 0.09
FREQ = 2.00	H = 0.08

Pointing Angle = 1.5°

FREQ = 0.00	H = 1.00
FREQ = 0.05	H = 0.99
FREQ = 0.10	H = 0.95
FREQ = 0.15	H = 0.87
FREQ = 0.20	H = 0.77
FREQ = 0.25	H = 0.65
FREQ = 0.30	H = 0.55
FREQ = 0.35	H = 0.46
FREQ = 0.40	H = 0.39
FREQ = 0.45	H = 0.33
FREQ = 0.50	H = 0.29
FREQ = 0.55	H = 0.25
FREQ = 0.60	H = 0.22
FREQ = 0.65	H = 0.20
FREQ = 0.70	H = 0.18
FREQ = 0.75	H = 0.16
FREQ = 0.80	H = 0.15
FREQ = 0.85	H = 0.14
FREQ = 0.90	H = 0.13
FREQ = 0.95	H = 0.12
FREQ = 1.00	H = 0.11
FREQ = 1.05	H = 0.11
FREQ = 1.10	H = 0.10

CHAPTER 5

An Observational Study of σ° Variations in the Vicinity of the Gulf Stream

by

C. L. Parsons

1.0 Introduction

The influence of wind shear and currents on the backscattering cross section per unit area, σ° , of the ocean's surface was investigated using return power measurements from two Skylab passes over the Atlantic Ocean near the east coast of the continental United States. The two groundtracks are shown in Figure 1. They were in close geographical proximity and were traversed during periods of fair weather; the effect of atmospheric attenuation on these measurements can therefore be discounted. Additionally, both measurement records include data taken over the Gulf Stream, the intense deep ocean current that roughly follows the edge of the continental shelf at these latitudes. The depth of the sea in the vicinity of the current and the strength of the flow eliminate the possible influence of the bottom topography on σ° in this region. Therefore, in a geographical sense, the two passes chosen are well-suited for the task of studying the influence of wind shear and current velocity on σ° .

The records* for the two passes are shown in Figure 2. It is seen that backscattering from the surface for the 9 August track was enhanced by nearly 6 dB over the background level while no increased return was found during the other. This intriguing difference was a second factor in the choice of these two records.

Each track will be discussed separately but the same investigation will be performed for each. The geography of each groundtrack will be described

*Editor's Note: The method employed by the S-193 altimeter to recover absolute received power was a preflight calibrated Automatic Gain Control (AGC). Because of the particular design of the AGC, it was waveform sensitive; this implied a change in the calibration as the waveform changed. In other than the 100 ns/10 MHz modes, it was not possible to recover the absolute received power and, therefore, σ° . For this reason, the plots in this and the next chapter show the relative variation in received power.

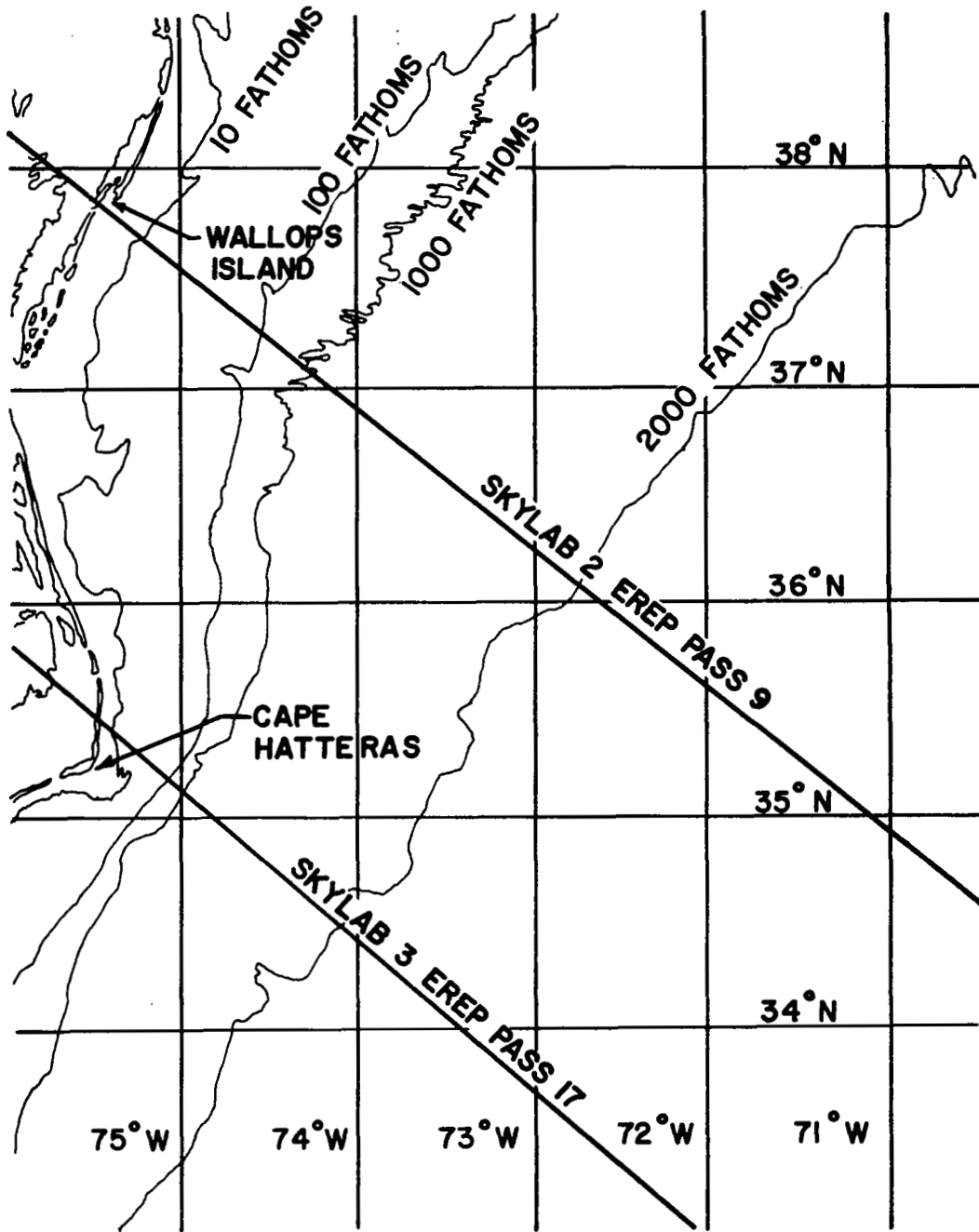


Figure 1. Ground tracks for SL-2 EREP Pass 9 and SL-3 Pass 17.

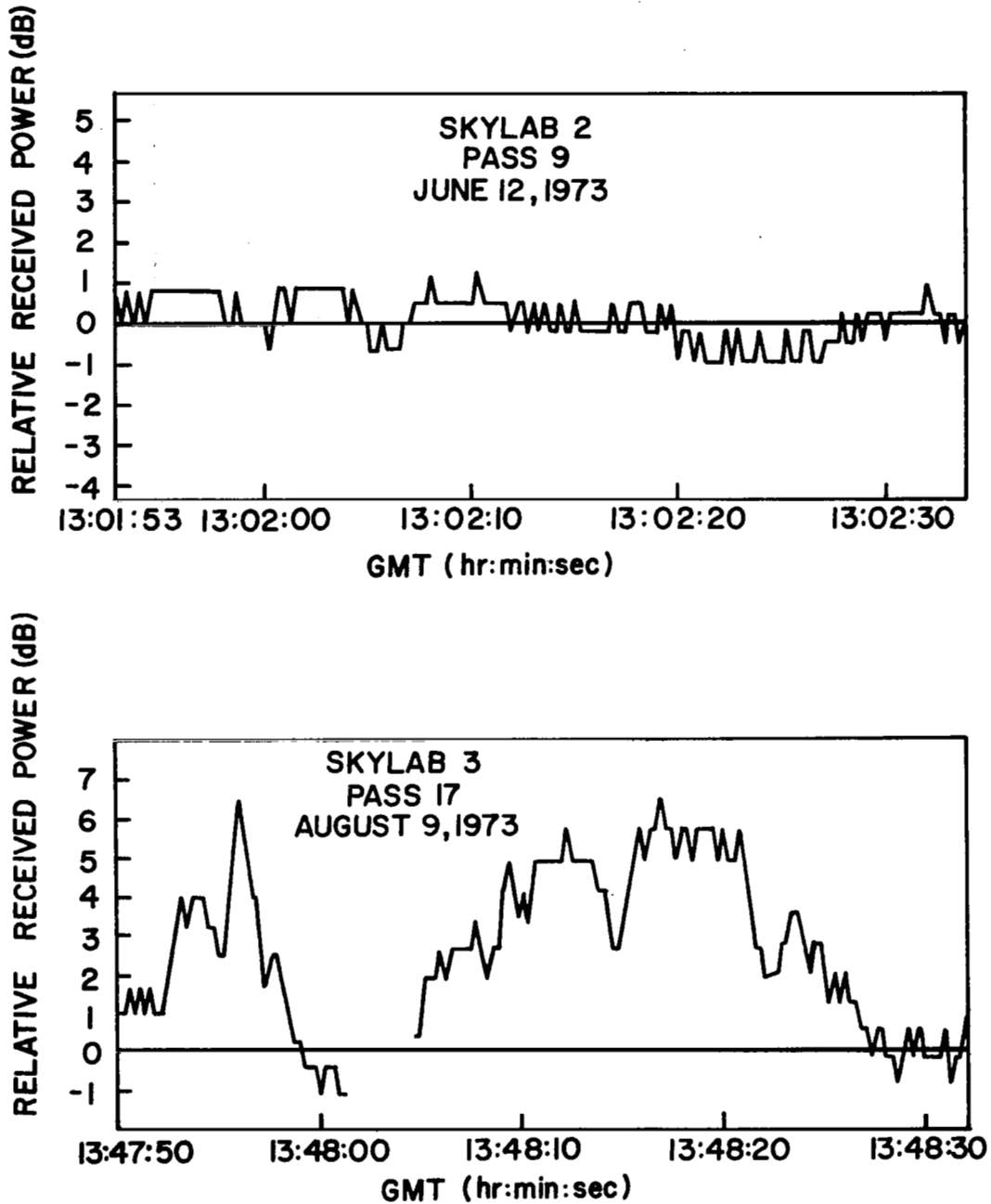


Figure 2. Relative received power records for SL-2 Pass 9 and SL-3 EREP Pass 17.

first. Then, in sequence, the synoptic meteorological conditions will be discussed, the Gulf Stream will be located as accurately as possible, and the wind, sea, and swell fields will be determined. Atmospheric and oceanographic in situ measurements by the heavy ship traffic in this portion of the ocean form the bulk of the data base necessary for the characterization of the latter. Any points or events of interest along the groundtrack will be related to the corresponding location on the received power record. In this way, the physical process exhibiting the greatest influence on surface backscattering will be isolated. After completing these analyses, conclusions will be drawn based upon the observations made in this study.

2.0 Skylab 2 EREP Pass 9 Analysis

Skylab 2 EREP Pass 9 passed directly over Wallops Island, Virginia, on June 12, 1973, at approximately 13 hr 01 m 30 sec. At an altitude of about 440 km, the S-190A multispectral camera aboard Skylab observed a scene 163 km square each time an exposure was taken. With a time delay between exposures of about 8 sec, the horizontal motion of the groundspot at a velocity of about 7.5 km sec^{-1} caused the camera to photograph completely a swath along the track of width 163 km. The boundaries of this swath are shown in Figure 3 for the case of Pass 9. The scene illuminated was uniform blue ocean crossed by a band of clouds of the type typically referred to as "popcorn cumulus." Malkus [1] modelled the effects of warm ocean eddies on the trade winds. It was found that the warm spots acted in a fashion similar to that exhibited by islands imbedded in tropical wind fields but to a lesser degree. For a warm spot of some elevated temperature and horizontal extent, horizontal convergence and accompanying updrafts were predicted. Isaacs [2] later reported that a circular mass of cumulus clouds about 60 miles in diameter and extending to an altitude of 7.5 km was observed directly above an excessively heated circular region of turbid water in the Gulf of Bengal. Because of the large temperature differential normally associated with the Gulf Stream, it is conjectured that the popcorn cumulus cloud band was caused by the "heated island" effect alluded to by Malkus and can be used to identify the approximate location of the Gulf Stream.

In addition to this means of finding the Gulf Stream, three other methods have been employed for the EREP Pass 9 analysis. A NOAA-2 thermal infrared

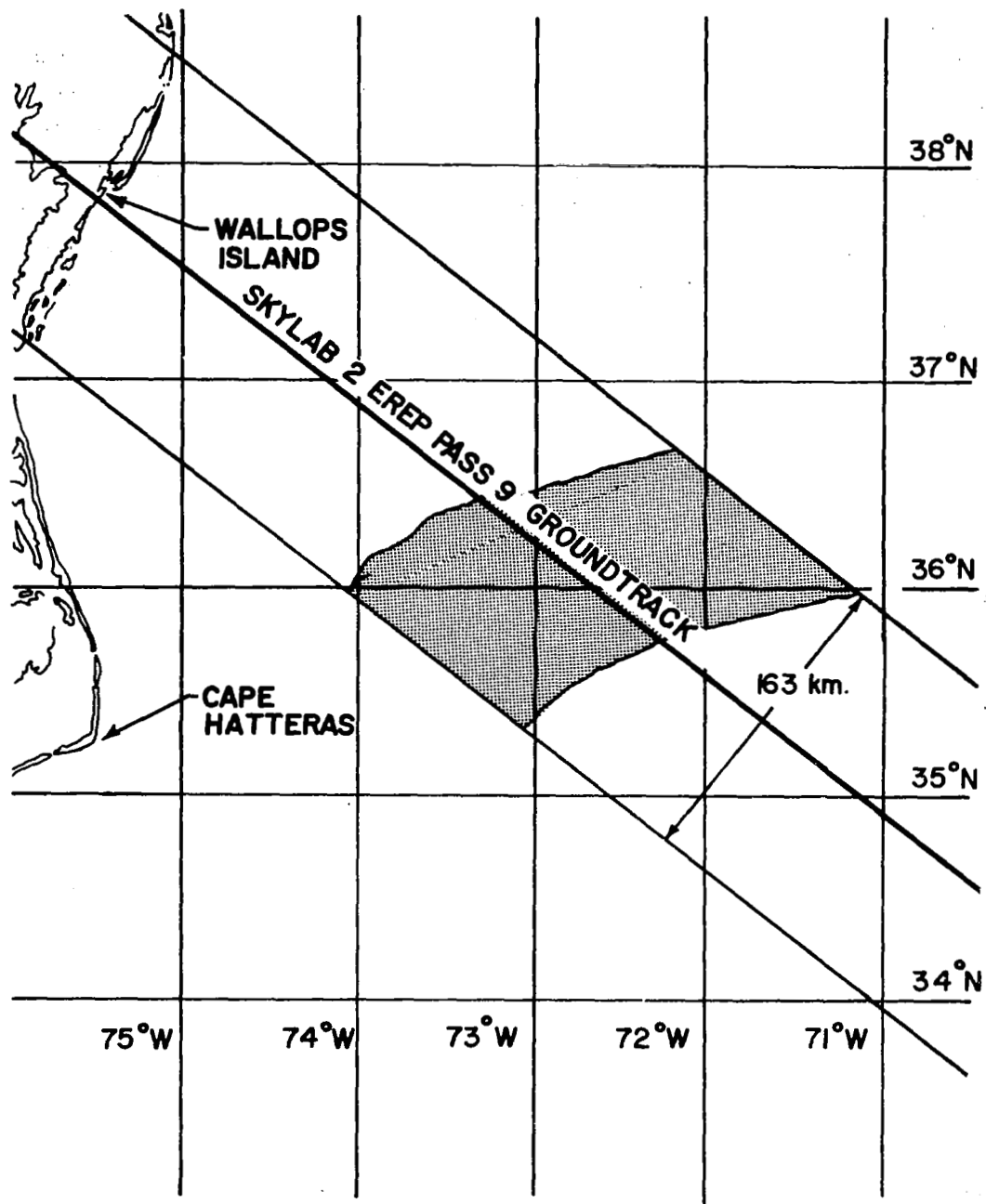


Figure 3. Visible cloud band location within the swath photographed by the S-190A camera during SL-2 EREP Pass 9.

Gulf Stream Analysis was available from the Environmental Sciences Group of the National Environmental Satellite Service for the area of interest. The Gulf Stream and slope water locations as identified from the imagery are found in Figure 4. Comparison with Figure 3 indicates that the cumulus band is nearly coincident with the Gulf Stream location determined from the NOAA-2 infrared data. Also in Figure 4 are the Gulf Stream western wall positions for early and late June as presented in the U. S. Naval Oceanographic Office publication, the Gulf Stream Monthly Summary [3]. To complete the figure, the mean position of the western wall as calculated by Khedouri and Gemmill [4] is shown. The various positions resulting from these sources will be compared in a later figure, but the agreement between the early June Naval Oceanographic Office position and the NOAA-2 satellite photography location is good.

Ship reports of wind and sea conditions were ordered from the archives of the Naval Weather Service Command, Asheville, North Carolina. The locations of all ships reporting data in the area of interest during the ten-day time period centered around June 12, 1973, were plotted. At each position, the reported sea surface temperature was recorded and an attempt was made to construct isotherms using these data. Figure 5 shows the 24°C and 26°C isotherms that resulted. The central axis of the Gulf Stream can be located by this method. However, the boundaries of the stream appear to be imprecisely determined. The spatial resolution obtained by using ten days of ship report data is still not high. For the ten days between June 7 and June 16, 202 separate weather and sea reports were available. Of these, 28 were from the Diamond Shoals Light Ship at 35.1°N and 75.3°W and 40 were reports by the Chesapeake Light Ship at 36.9°N and 75.7°W. These fixed stations are of little value to the effort of locating the western wall of the Gulf Stream. Therefore, only 134 reports were utilized. The average number per day is thus 13.4 in the geographical region bounded by the coast and 70.5°W and latitudes 35°N and 39°N. The density of the total number of reports in this area is too small for an accurate determination of the boundaries. The two fluctuations in the isotherms in Figure 5 near 36.5°N and 72°W may or may not be real. The times of the reports in the vicinity of these loops were checked to see if a movement of the Gulf Stream took place between the reports but such was not the case. Based upon this attempt, it was decided that ship

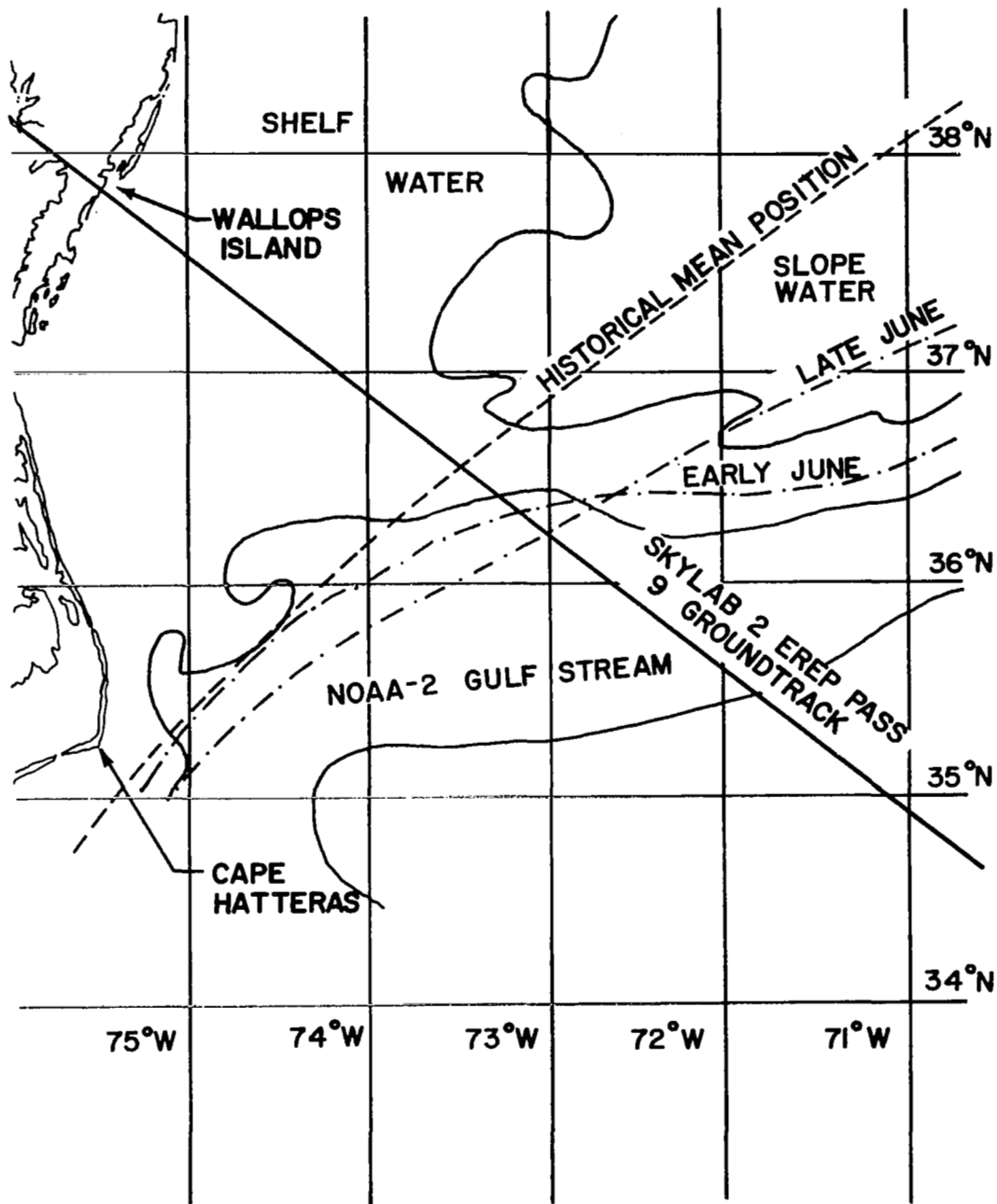


Figure 4. Location of the western wall of the Gulf Stream as determined by the U.S. Naval Oceanographic Office and the National Oceanographic and Atmospheric Administration. The historical mean position of the boundary for the month of June is also shown.

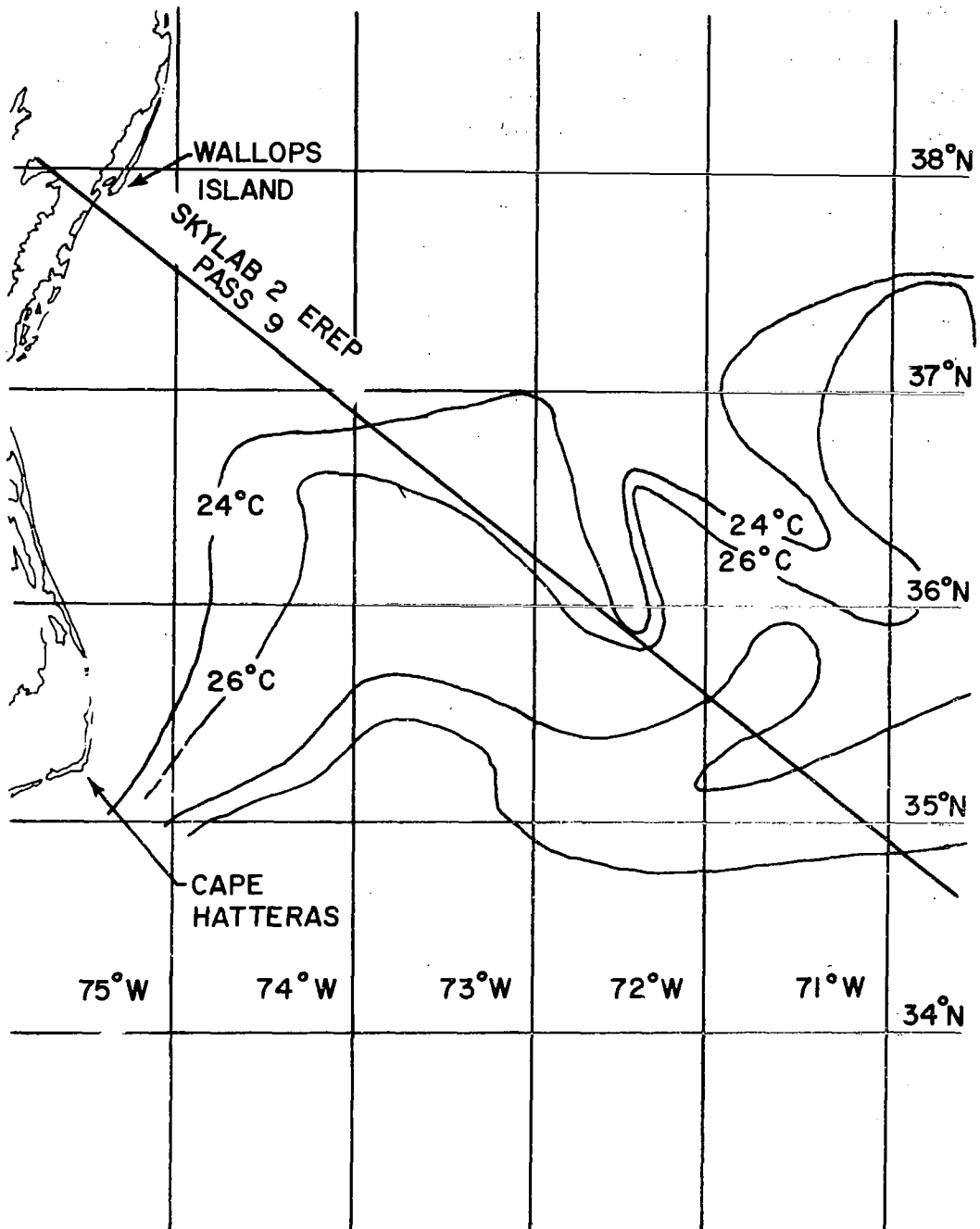


Figure 5. Location of the central core of the Gulf Stream using ship reports of surface temperature.

reports of sea surface temperature were not sufficient to accurately locate the current.

A request was made to the National Oceanographic Data Center (NODC) in Washington, D. C., for sounding data in the area near the date of the SKYLAB overpass. Twelve NODC station soundings, which were produced by Nansen cast type serial depth observations, were made between the 5th and 7th of June along a line between 32°N and 70.2°W and the location 35°N and 74.8°W. These are of little value in locating the Gulf Stream near the EREP Pass 9 ground-track. Eleven expendable bathythermograph (XBT) soundings were also available. Eight were made on June 22 and 23 by the Naval Oceanographic Office personnel aboard the RMS CUNARD AMBASSADOR traveling from Bermuda to New York. The data collected has been published in the Gulf Stream Monthly Summary [3] for June 1973 and by Gotthardt and Potocsky in the Journal of Physical Oceanography [5]. Again, the passage of the AMBASSADOR was too far from the groundtrack to pinpoint the location of the Gulf Stream. The reported 27°C temperature maximum in the core of the current, however, is in good agreement with the ship report data used to construct Figure 5.

Three other XBT soundings were produced on June 1 and 2 at the following locations:

37°10'N, 70°45'W
37°5'N, 72°3'W
37°2'N, 73°41'W

The latter sounding was taken in close proximity to the SKYLAB groundtrack on the 12th and is shown in Figure 6. Comparison of the surface temperature reported by a ship at 37.2°N and 73.5°W on June 12 with the 18°C shown in this figure indicates that the surface had warmed 4°C between the 2nd and the 12th. This is too great a change for the sounding data to be of value in this study. As was concluded for the case of the ship reports of sea surface temperature, temperature soundings were of little usefulness in this determination of Gulf Stream location.

The ocean has been seen to change its surface temperature distribution in time periods on the order of ten days. The surface winds and, in turn, the wind-driven sea will be much more variable than this. The ship reports of wind direction and speed and sea and swell are the primary data source

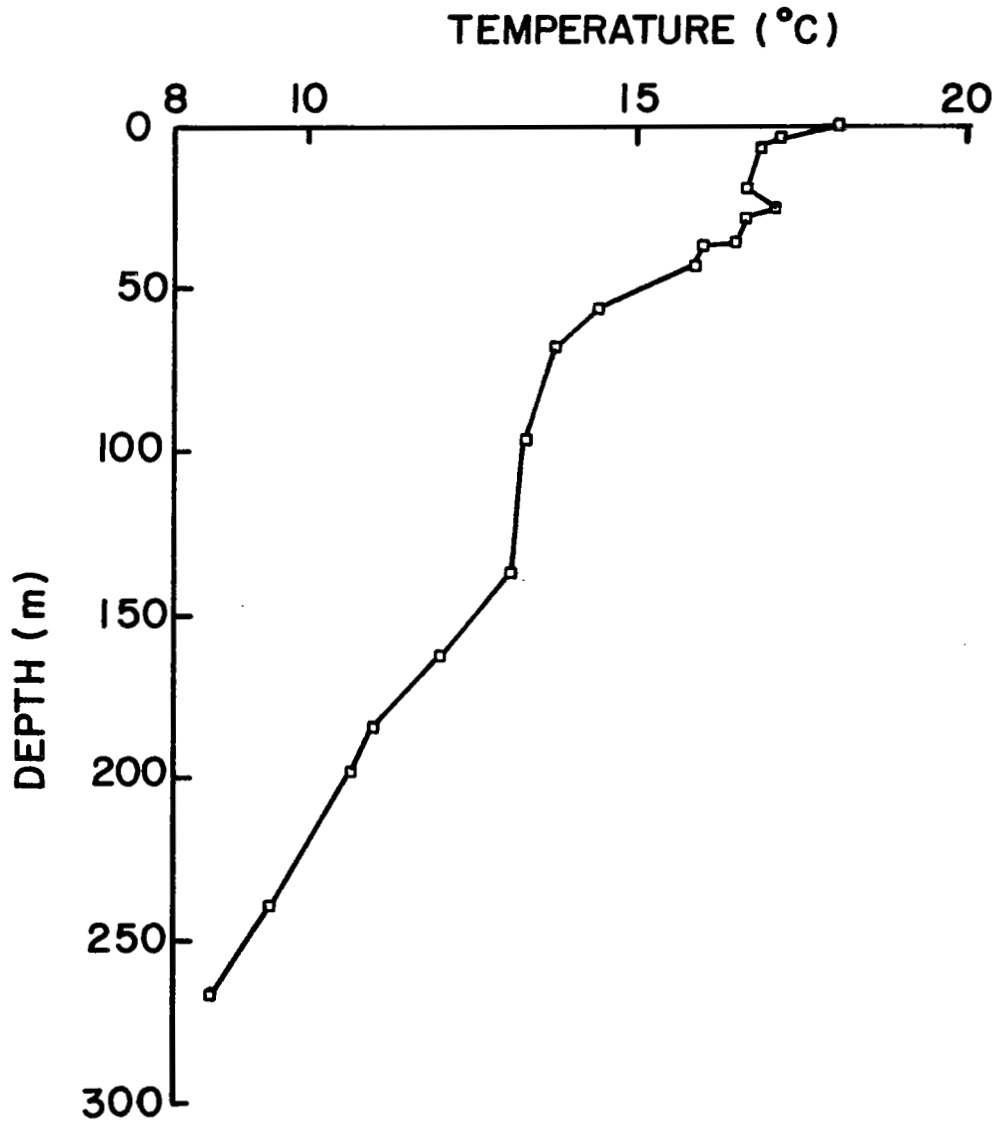


Figure 6. Temperature sounding produced by expendable bathythermograph located at 37°2'N, 73°43'W on 2 June, 1973.

for studying the geophysical conditions at the time of the overpass but a brief analysis of the synoptic situation both before and after the 12th is necessary to ascertain how many ship reports can be included in this portion of the study without losing data coherency. The monthly publication Weather-wise [6] was consulted for day-by-day maps of the synoptic weather conditions over the East Coast during June 1973. A description of these conditions and their influence on the weather in the area of the groundtrack follows. Ship reports of cloud cover, wind direction, and windspeed were used to corroborate the conditions deduced from the synoptic-scale maps.

June 7, 1973

A cold front was just nearing the Atlantic seaboard after a sluggish trip across the continental U. S. that consumed the entire first week of June. Winds in the ocean region extending from 35°N to 39°N and 70°W to the coast were from 5-15 knots in strength and oriented in general from the south. A high pressure system centered at about 32°N and 70°W with a core pressure of 1027.0 mb kept cloudiness at a minimum. Patches of flattened cumulus and dense cirrus were reported in the south of the region with clear skies in the north.

June 8, 1973

The rapidly dissipating front brought broken skies of altocumulus, stratocumulus, and cirrostratus into the northern portion of the area from 1200Z to 0000Z on the 9th. Winds were again from the south and light in the upper portions and near calm in the south. No wind shift accompanied the passing of the cold front and temperature and dew point deviations were negligible.

June 9, 1973

The center of high pressure was by now located at approximately 34°N and 58°W with a maximum pressure of 1029 mb. The winds shifted only slightly to blow from the south-southwest at 10-15 knots in general. The broken skies in the northern sector began to give way to scattered flattened cumuli, altostratus, and cirrus filaments. The southern portion of the area of interest also became cloud-covered with the same variety of clouds present.

June 10, 1973

The midatlantic seaboard was still under the influence of the high of central pressure 1025.0 mb now positioned near Bermuda. A report of three-tenths sky cover and the presence of cumulonimbi was received from a ship at 37.5°N and 74.6°W at 0000Z but otherwise clear skies were reported. Winds were again about 15 knots in intensity and from the southwest.

June 11, 1973

Local conditions remained unchanged from the 10th. Clear skies prevailed and the winds were light and variable from the southwest.

June 12, 1973

On the day of the SKYLAB overpass, a band of flattened cumulus was reported by ships in the lower one-third of the area. Winds were 10-15 knots in strength again blowing from the southwest in general and from the west in the region of the cloud band.

June 13, 1973

The advance of a cold air mass from the Northwest created a new low over Nova Scotia. A cold front associated with the cyclone began moving eastward and on the 13th was approaching the coast. In the region of interest, the day began with winds of 5-15 knots from the south and southwest. The wind direction and speed held during the course of the 13th as puffy cumulus and filaments of cirrus gave way to cumulus and altocumulus. No precipitation was reported but by the end of the day, stratus fractus was observed by a ship at 37.5°N and 74.5°W.

June 14, 1973

The low over Nova Scotia moved on out to sea pulling the cold front across the midatlantic coast between 0600 and 1200Z on the 14th. Wind direction changed from a southwest to a north-northwest orientation in the six hour period and maintained that direction of flow for the rest of the day. Only a few reports of 20 knot winds were received at 0000Z. The observations of stratus fractus continued through the 0600Z reporting period. Thereafter

puffy cumulus formations resumed their stations in the area of interest.

June 15, 1973

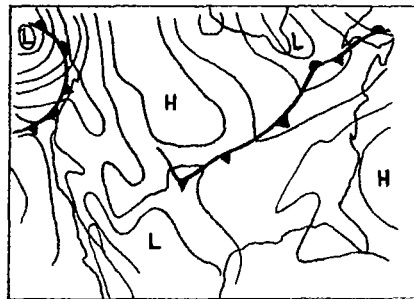
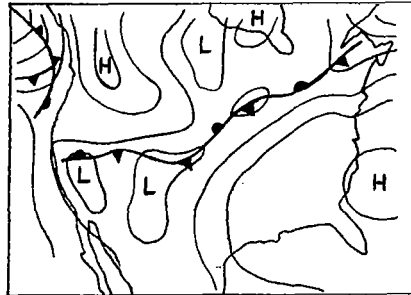
The aftermath of the cold front passage was characterized by northerly flow of 10-15 knot intensity with occasional reports of scattered clouds.

June 16, 1973

A high pressure system over Florida began to pump warmer air back into the region. The winds were restored to the southerly direction typical of this entire period of time. Scattered cloudiness prevailed with the usual puffy cumulus formations present across the southern half of the area.

The continental United States synoptic weather maps for the 11th and 12th of June are shown in Figure 7. It is readily apparent that there was little change in the weather in the area of the ground track. Indeed, a closer look at the ship reports of wind revealed that from the time of passage of the weak cold front late on the 8th through the time of the SKYLAB overpass, the wind field was very consistent. The reports for this entire period are charted in Figure 8. Included with the wind vectors are pressure, temperature, and dew point temperature readings. The winds are seen to have been blowing from the southwest at speeds ranging from 5 to 25 knots in magnitude. Because the earth-atmosphere system was so stable during this period, the ship reports of sea state and swell should also be coherent and comparable. The sea state and swell reports from the same 32 vessels whose wind, pressure, and temperature data are plotted in Figure 8 are tabulated in Table I. The significant wave height values ranged from one report of calm seas to one of 2.5 meter wave height with the preponderance of reports registering only one-half to one meter. The direction of propagation agrees with the wind field. The direction of swell was more variable but was again from the southwest predominantly. No trends of increasing or decreasing seas or swell and no shift in the dominant direction of propagation is evident from the data in Table I. Comparison of the location of the reporting ships with the NOAA-2 infrared photography revealed that there was no discernible effect of the Gulf Stream on significant wave height during the four-day period of June 9-12, 1973. The meager number of samples in the set of reporting stations raises some question about the validity of the following numbers,

JUNE 11, 1973



JUNE 12, 1973

Figure 7. Synoptic weather maps for the continental United States showing the stationary nature of the high pressure system located off of the east coast on 11 and 12 June, 1973.

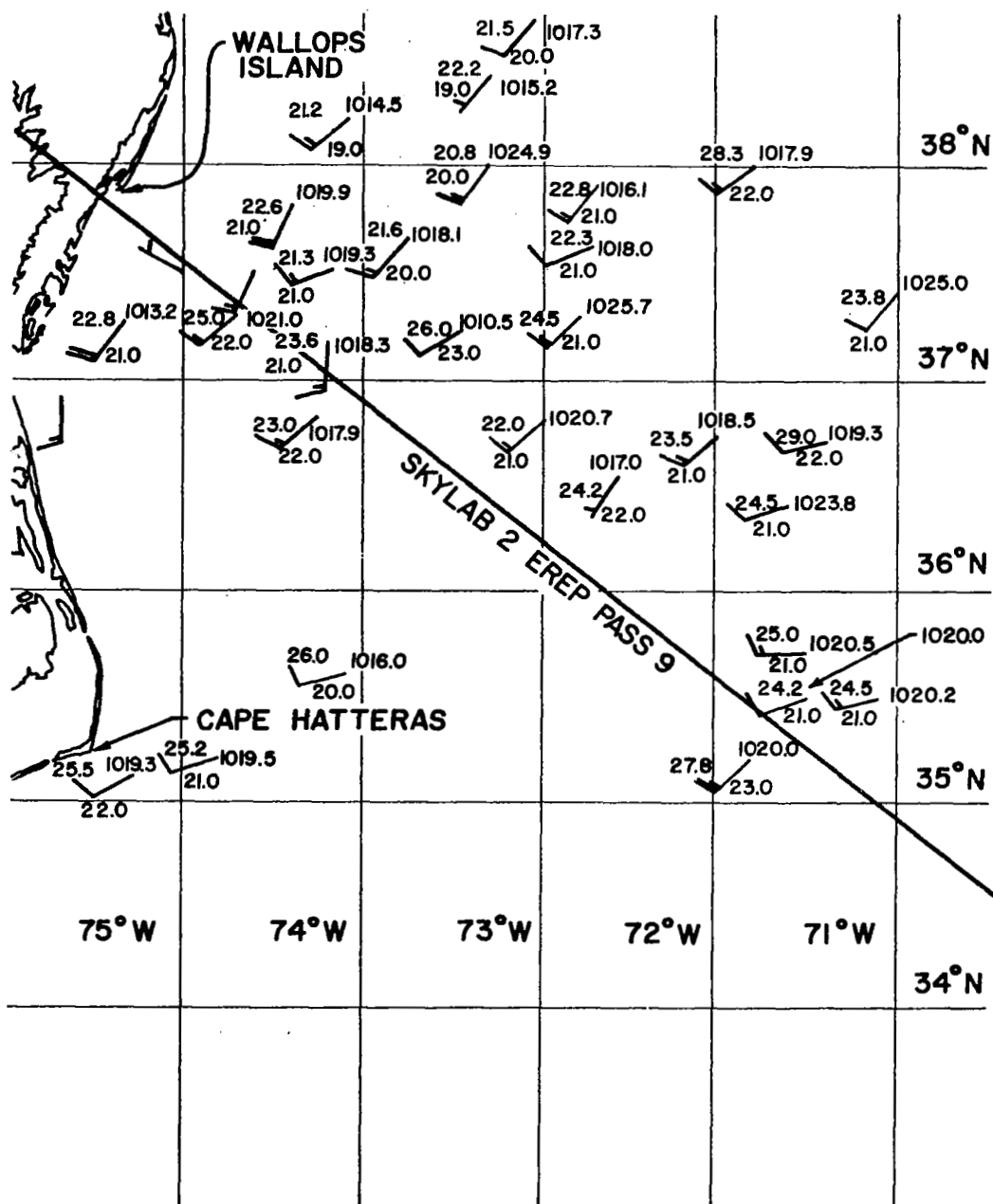


Figure 8. Ship reports of windspeed, direction, pressure, air temperature and sea temperature for the period 9-12 June, 1973.

TABLE I

Ship Reports of Sea State for June 9-12, 1973

DATE	TIME (GMT)	SWH (M)	PERIOD (SEC)	DIRECTION	SWELL HEIGHT (M)	PERIOD (SEC)	DIRECTION	LATITUDE (°N)	LONGITUDE (°W)
9	0000	—	—	—	1	<5	230	37.4	71.0
	1200	.5	<5	240	calm	—	—	35.5	71.5
	1200	.5	<5	220	—	—	180	37.3	72.8
	1200	1.5	<5	210	calm	—	—	38.0	73.3
	1800	.5	<5	220	calm	—	—	37.3	74.7
	1800	1.5	<5	200	1.5	8	250	37.0	74.4
10	0000	—	—	—	—	—	—	37.5	74.6
	0600	1.5	<5	230	calm	—	—	38.2	74.1
	1200	—	—	—	—	—	—	36.8	73.0
	1800	2	<5	230	3	<5	230	35.2	71.8
	1800	1	<5	250	calm	—	—	35.2	74.8
	1800	—	—	—	—	—	—	38.0	71.8
11	0000	.5	<5	220	1.5	<5	180	38.4	73.3
	0600	.5	<5	210	1.5	<5	180	36.5	72.6
	0600	—	—	—	—	—	—	37.5	75.0
	1200	1	<5	250	1	10	200	36.4	71.6
	1200	1.5	<5	240	1	6	190	36.8	74.3
	1200	—	—	—	.5	<5	250	37.6	72.8
	1200	1	<5	250	1	6	190	37.5	74.2
	1800	.5	<5	210	.5	11	200	38.6	73.1
12	0000	1	<5	260	1	12	240	35.6	74.1
	0000	.5	<5	210	1	<5	200	37.9	72.7
	0600	.5	<5	230	1	12	230	36.7	72.0
	0600	—	—	—	—	—	—	37.2	75.4
	1200	.5	<5	260	1	12	270	35.5	71.1
	1200	1	<5	270	1.5	—	210	35.7	71.5
	1200	calm	—	—	.5	11	230	35.1	75.3
	1200	1	<5	180	1.5	<5	130	36.9	75.7
	1200	1	<5	220	1.5	6	230	37.6	73.8
	1800	1	<5	250	1.5	<5	260	36.7	71.4
	1800	2.5	<5	220	2.5	6	220	37.2	73.5
	1800	.5	<5	180	.5	8	200	37.1	74.2

but the mean significant wave heights in the Sargasso Sea, the Gulf Stream, the shelf water, and the slope water regions were found to be 1.25, 1.2, .9, and 1.2 m respectively. The differences are not statistically significant.

The obvious finale of this investigation is to re-examine the received power record for Skylab 2 EREP Pass 9 in light of the in situ measurements that have been discussed. Figure 9 illustrates the agreement between the sea surface temperature isotherms, the NOAA-2 infrared photography, the S-190A imagery, and the U. S. Naval Oceanographic Office placements of the western wall of the Gulf Stream. The location in the photography and its match with the location of the popcorn cumulus cloud band in the S-190A imagery make the NOAA-2 position the most credible. The various western wall boundaries are also annotated in Figure 10, the EREP Pass 9 received power record. The variation in the signal strength in the figure is too small to be considered a significant manifestation of some surface geophysical process. The lack of influence of the Gulf Stream on the surface backscattering cross section as witnessed in the relative received power record, therefore, agrees with the calculation that significant wave height was unaltered in the presence of the current. A pass during which the received power record was modulated to a significant extent by some geophysical phenomenon will next be discussed.

3.0 Skylab 3 EREP Pass 17 Analysis

The groundtrack, the swath of observation of the S-190A cameras, and the area cloud cover for Skylab 3 EREP Pass 17 are all shown in Figure 11. Two features of the cloud cover warrant further comment. From the 34°N latitude parallel to the end of the track, the satellite passed over a bank of clouds that totally obscured the surface from view. A narrow band of puffy cumulus clouds oriented perpendicular to the groundtrack was crossed near the point 35°N 75°W. Figure 12 shows the position of the Gulf Stream as revealed in NOAA-2 imagery taken on August 27, 18 days after the overpass. Photography of the region was not available from NESS any closer in time to the date of passage due to the presence of clouds. The historical mean position of the western wall is also graphed. The agreement between the NOAA-2 location and the cumulus cloud band is again quite good. No effort was made

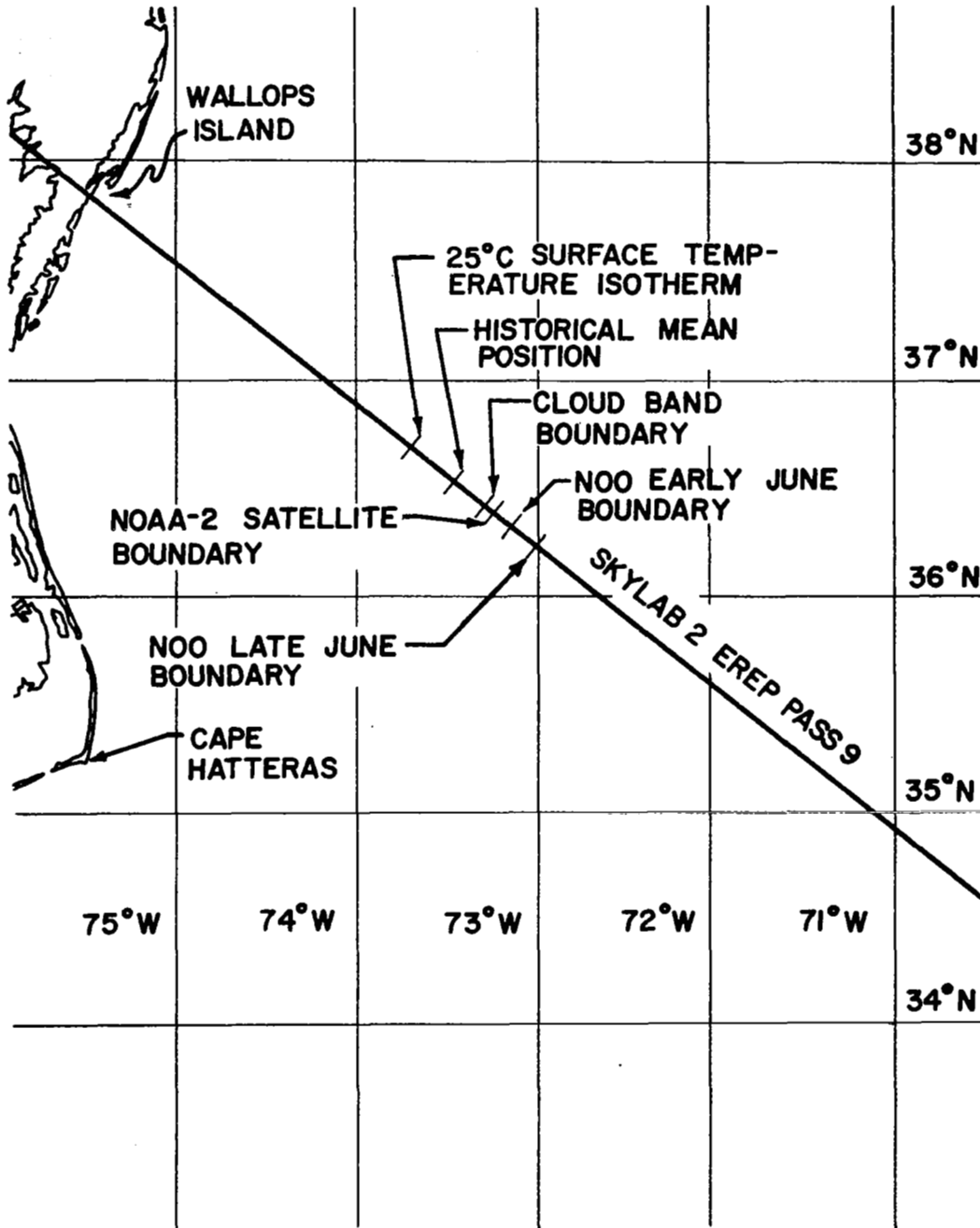


Figure 9. Summary of reported Gulf Stream western wall locations along the SL-2 EREP Pass 9 ground track.

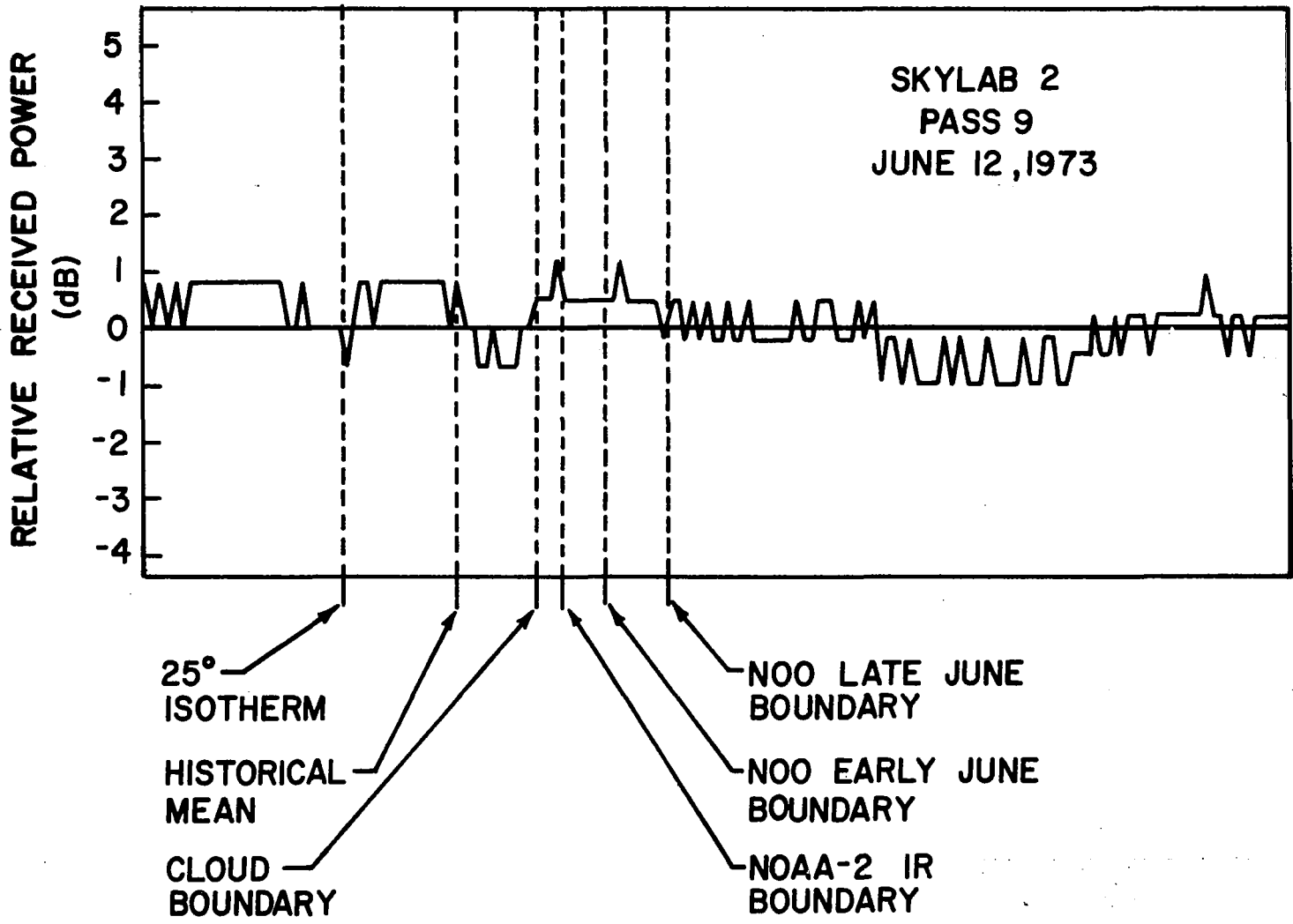


Figure 10. Correspondence of the reported Gulf Stream western wall locations with the SL-2 Pass 9 received power data.

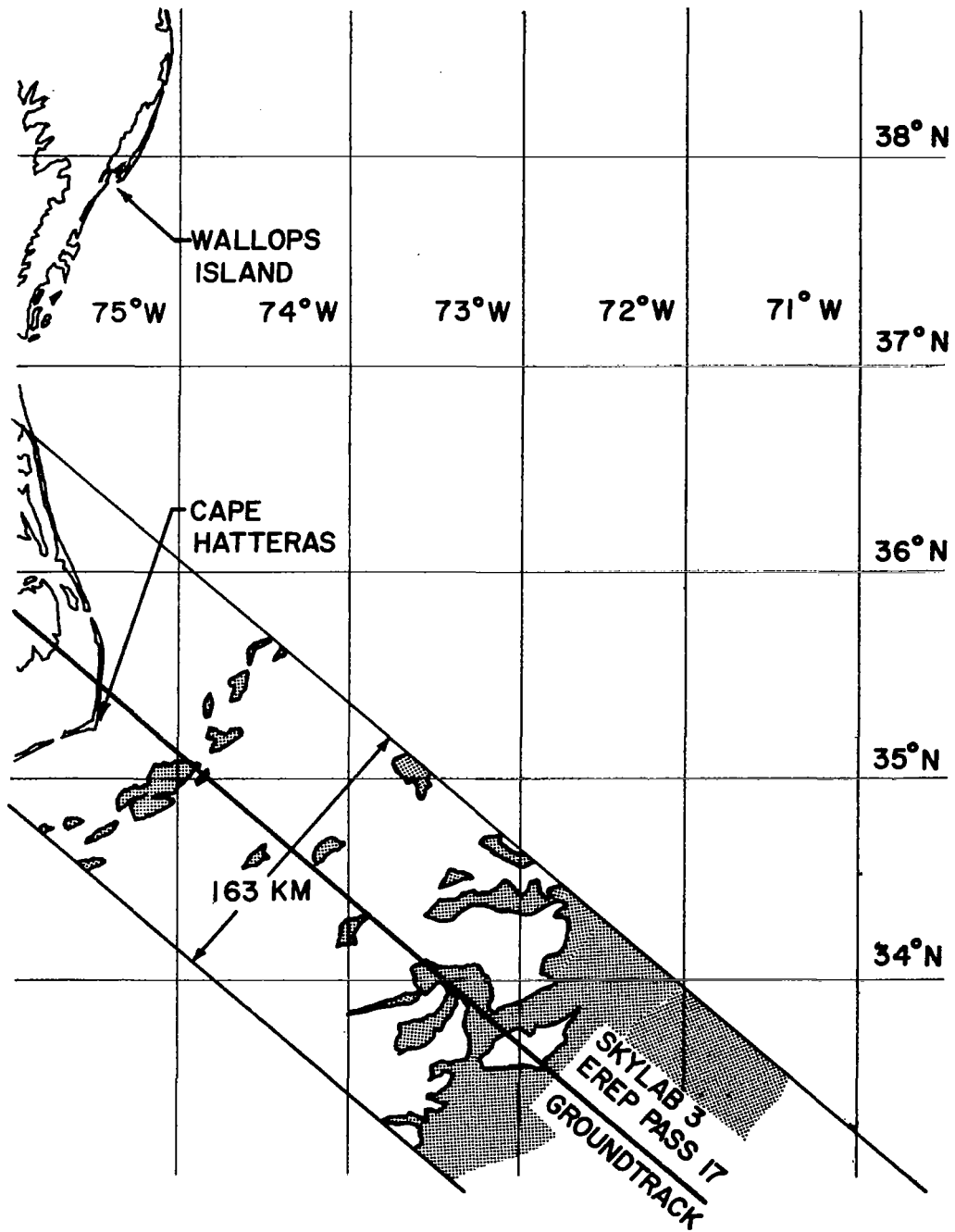


Figure 11. Visible cloud band location within the swath photographed by the S-190A camera during SL-3 EREP Pass 17.

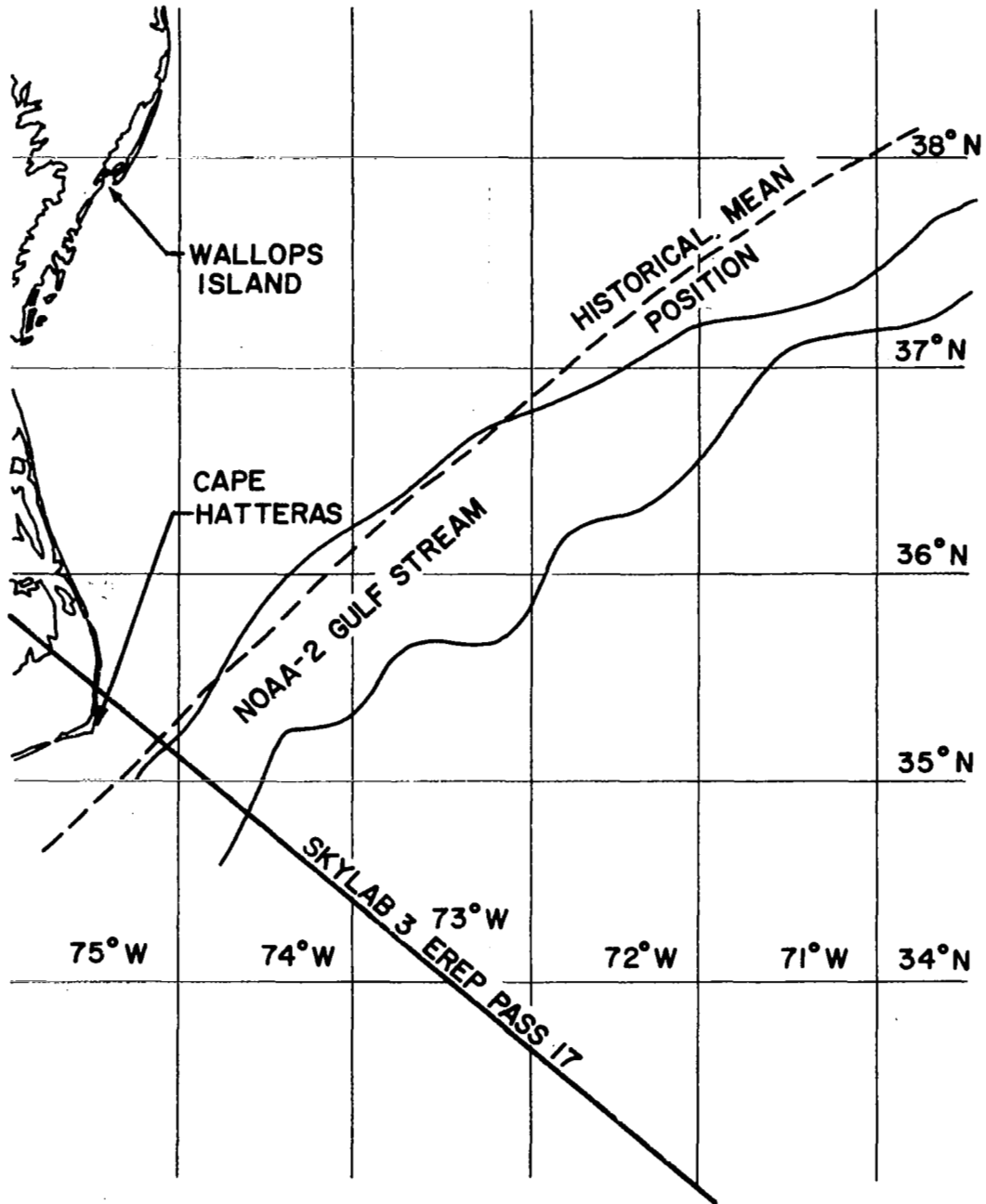


Figure 12. Location of the western wall of the Gulf Stream as determined from NOAA-2 infrared imagery. The historical mean position of the boundary for the month of August is also shown.

to locate the current boundary using sea surface temperature data because of the inadequacy of ship report data for the previous track analysis.

As before, the next activity was to evaluate the prevailing wind direction and speed and to determine the sea state and swell conditions. The ground-track of this arc was located in an area of the ocean less travelled by ships than the previously studied region slightly to the north. The more hazardous weather near Cape Hatteras and the large quantity of ship traffic to and from the naval facilities at Newport News, Virginia, are two reasons for this. Because the Gulf Stream flows so close to the coast near Cape Hatteras, the Diamond Shoals Lightship located at 35.1°N and 75.3°W was an excellent source of data for this groundtrack. Only one random ship report was received for the day in question from the area 34°N to 36°N and from 74°W to the coast. All reports for August 9, 1973, are tabulated in Table II, and the locations of the reporting stations in relationship to the Gulf Stream's position are plotted in Figure 13. For the Diamond Shoals and Chesapeake Lightships, only the reports closest in time to the 1348 GMT overpass are shown. There were no temperature soundings in this area according to the NODC. Therefore the wind vectors, pressure, and temperature measurements noted in this figure complete the data set available for the analysis of this track.

The position of the Gulf Stream as noted in Figure 13 is related to the S-193 radar altimeter received power plot in Figure 14. For this case, there is an obvious fluctuation in the signal strength that is larger than can be expected from either long or short-term instrumental effects. The Gulf Stream appears from this illustration to have been located in a region of low reflectivity sandwiched between surfaces of high backscattering.

4.0 Theoretical Expectations

Parsons and Brown [7] have computed the backscattering cross section per unit area that should be expected for the sea state resulting from an interacting current and wind-driven sea. If the current and wind are oriented in the same direction, then the effect of the current on the sea is to increase the wavelength of the dominant sea components and to decrease the significant wave height. On the other hand, if the two are oppositely directed, the current tends to chop up the sea, shorten the wavelength, and increase

TABLE II

Ship Report Data for August 9, 1973

TIME	SWH	PERIOD	DIRECTION	SWELL HEIGHT	PERIOD	DIRECTION	WINDSPEED	DIRECTION	LATITUDE	LONGITUDE
0000	1	<5	110	—	—	—	12	110	35.1	75.3
0000	.5	<5	90	.5	<5	90	10	90	36.9	75.7
0600	1.5	<5	170	—	—	—	12	170	35.1	75.3
0600	calm	—	—	.5	<5	90	calm	—	36.9	75.7
0600	—	—	—	—	—	—	2	320	36.9	75.5
1200	1	<5	290	1.5	<5	90	6	290	34.5	75.6
1200	calm	—	—	1.5	13	120	2	30	35.1	75.3
1200	calm	—	—	.5	<5	90	calm	—	36.9	75.7
1800	calm	—	—	.5	6	180	calm	—	35.1	75.3
1800	calm	—	—	.5	<5	90	calm	—	36.9	75.7

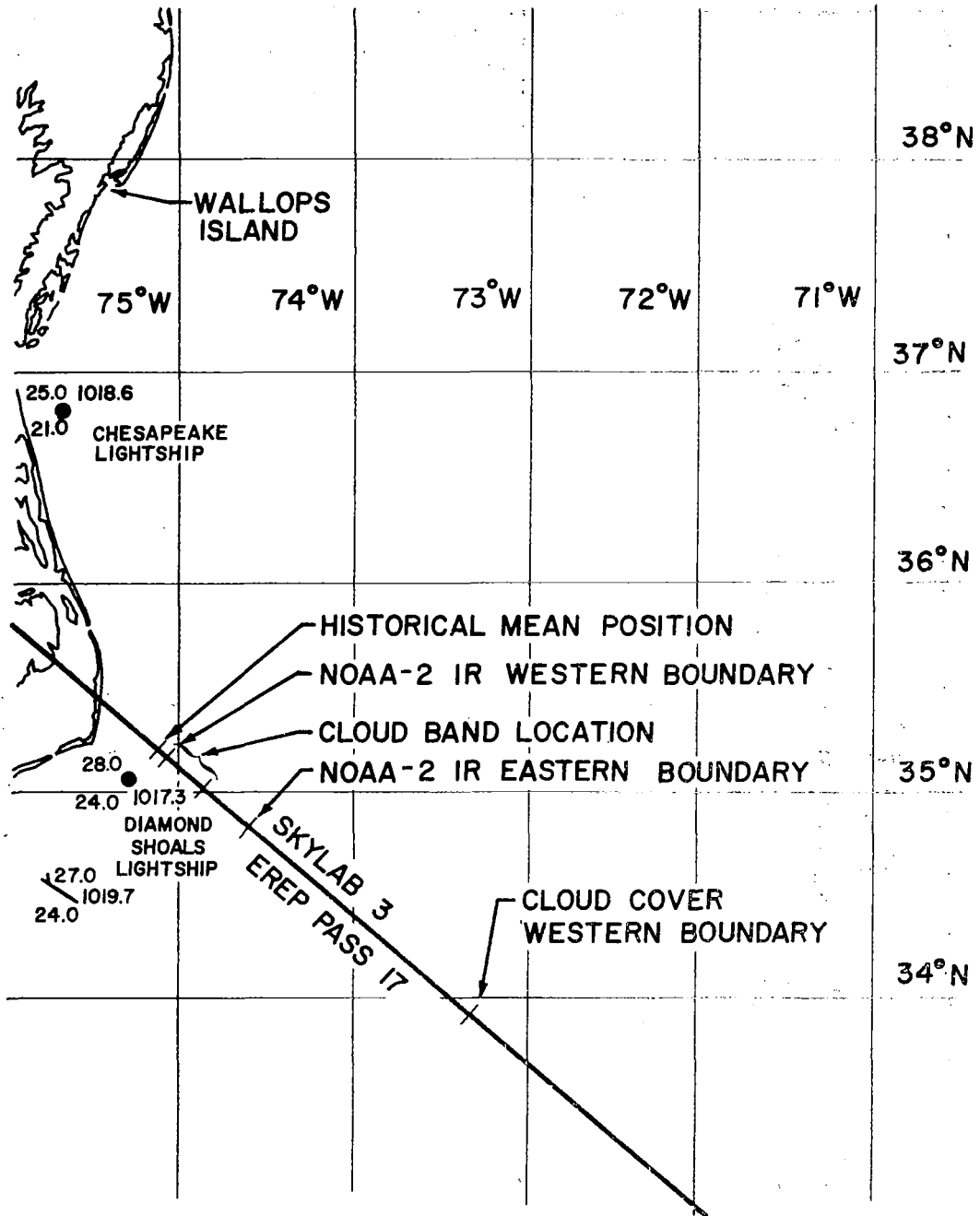


Figure 13. Summary of reported Gulf Stream western wall locations along the SL-3 EREP Pass 17 ground track.

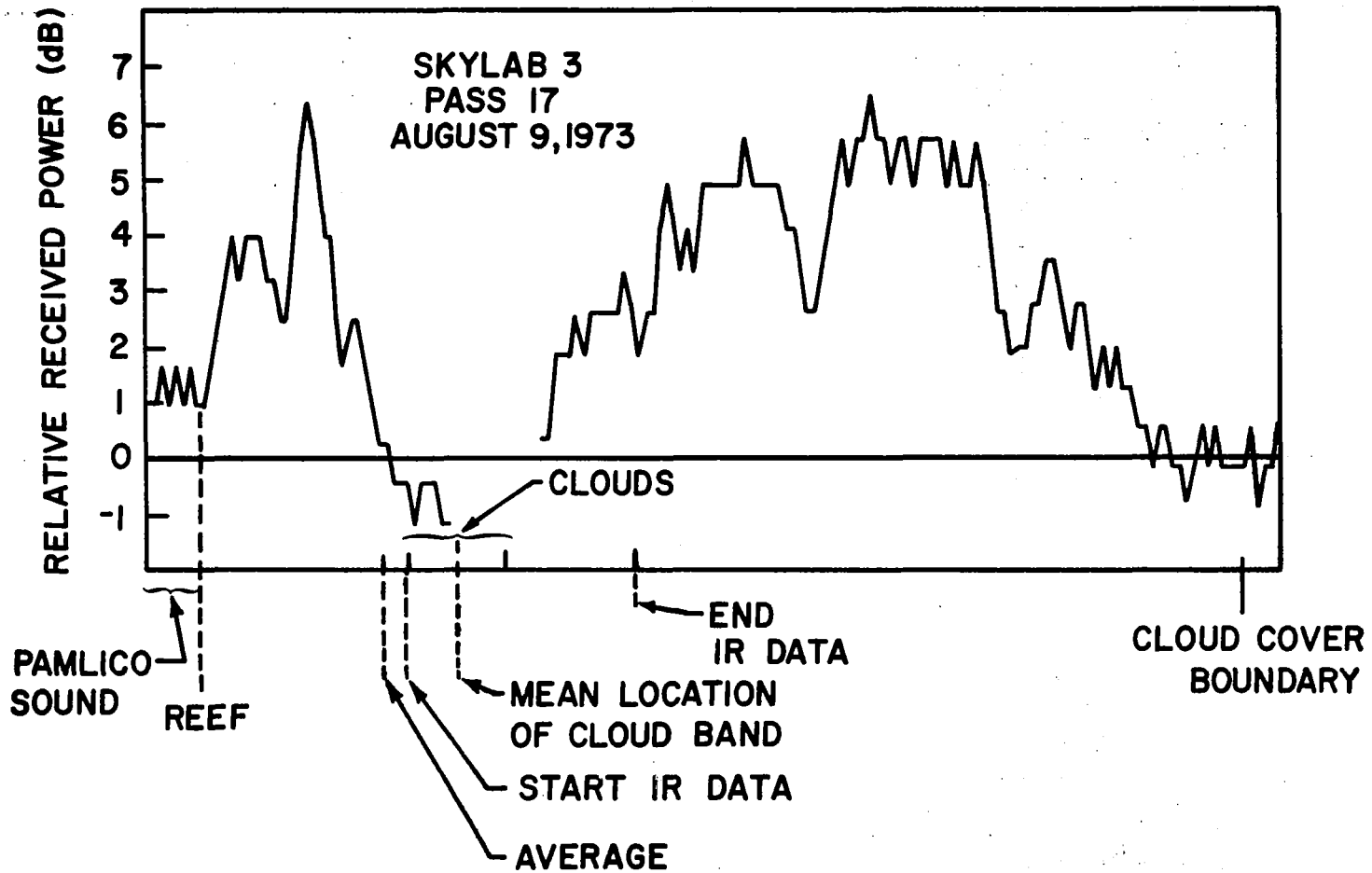


Figure 14. Correspondence of the reported Gulf Stream western wall locations with the SL-3 EREP Pass 17 received power.

the significant wave height. This is demonstrated in Figure 15 which is taken from Parsons and Brown [7]. With a component of the current's flow in the direction of the sea which is indicated on the chart by a positive current speed, the surface backscattering cross section per unit area, σ° , increases. A current flowing in opposition to the sea is identified by a negative current velocity and produces a decrease in σ° .

For the case of no current, the results in Figure 16 are obtained. The low wind speeds result in calm seas that nonlinearly increase σ° . The two areas of increased σ° above the background level on either side of the Gulf Stream during EREP Pass 17 are the result of the calm seas and winds reported by the Diamond Shoals and Chesapeake Lightships on August 9, 1973. They were limited in extent by the North Carolina coast on one side and the cloud bank on the other. The 1200 GMT report from Diamond Shoals, the closest report to the groundtrack in both time and space, and the estimated peak σ° value from Figure 14 are plotted as a single data point in Figure 16. The close agreement with theory is perhaps a matter of chance but the importance of the wind on σ° is demonstrated in this figure. Analyses of more tracks with surface reports is necessary to better determine the actual relationship.

In the region of the Gulf Stream, the value of σ° decreased to the background level or below. According to Table II, the winds were light or non-existent in the region but there was swell propagating in opposition to the current. At Diamond Shoals Lightship at 1200 GMT, there was 1.5 m of swell of wavelength 264 m arriving from 120°. The curves in Figure 15 are not appropriate for this case because they were derived assuming the sea state consists of waves distributed in frequency according to the Pierson-Moskowitz spectrum rather than the spectrum which characterizes swell. Nevertheless, Figure 15 amply illustrates the rapid falloff in σ° for a sea and current in opposition.

Theory predicts that over the Gulf Stream during EREP Pass 9, the altimeter should have received a signal enhanced by the increased backscattering from the surface. The wind field of 10 knots oriented in the direction of a 2 m sec^{-1} current should have raised σ° by 8.6 dB to 27.7 dB according to Figure 15. However, this was not observed. The reason that enhancement did not occur

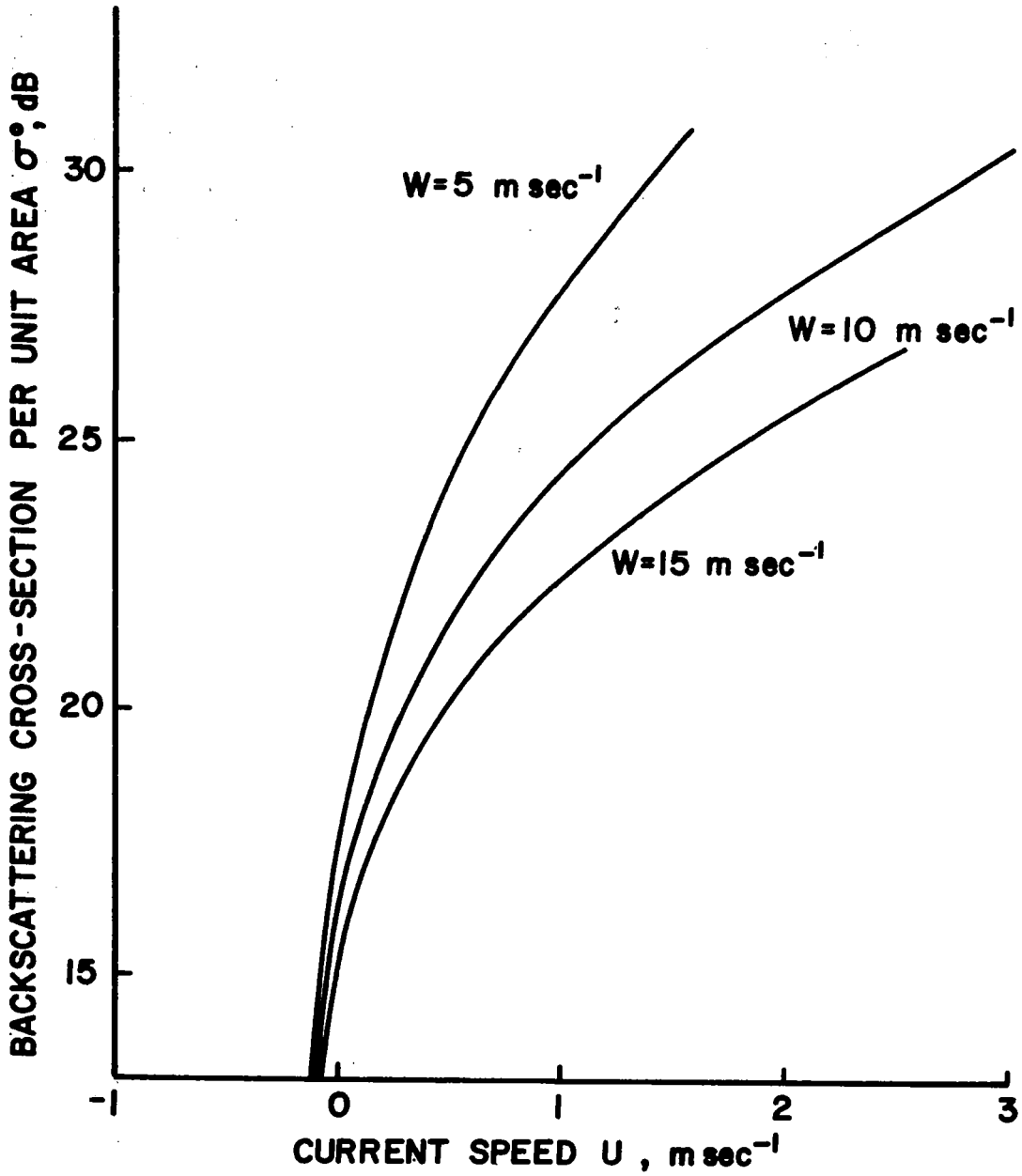


Figure 15. Variation of backscattering cross section per unit area σ° with current velocity as a function of wind speed. The wind field is assumed to be oriented in the direction of current flow.

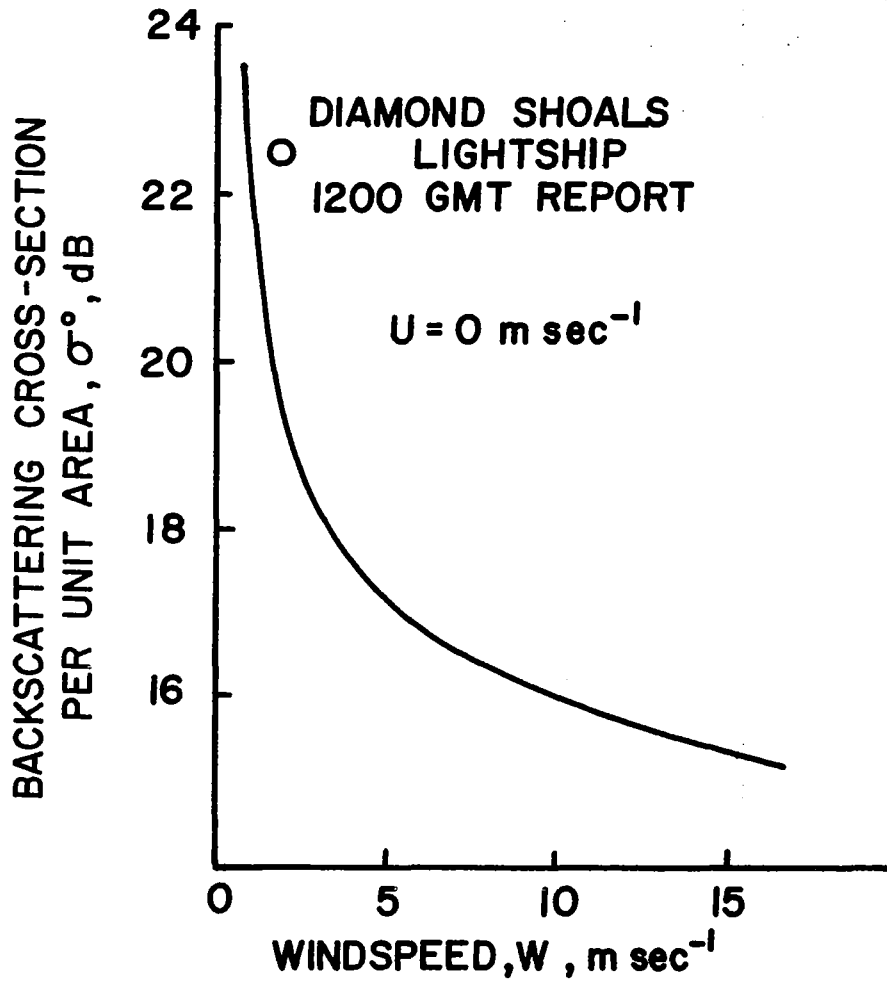


Figure 16. Variation of σ° with wind speed in the absence of current.

during EREP Pass 9 is not known at this time. More observational data is needed and more analysis must be performed before an answer can be found.

REFERENCES

1. Malkus, J. S., "Trade Cumulus Cloud Groups: Some Observations Suggesting a Mechanism of their Origin," Tellus, Volume 9, pp. 33-44, 1957.
2. Isaacs, J. D., "Note on an Association of Cumulus Clouds and Turbid Water," J. Geophys. Res., Volume 67, p. 2076, 1962.
3. Gulf Stream Monthly Summary, U. S. Naval Oceanographic Office, Washington, D. C., Volume 8, No. 6, June 1973.
4. Khedouri, E., and W. Gemmill, Statistical Summary of Gulf Stream and Slope Front Characteristics, NAVOCEANO Technical Note 6150-15-73, U. S. Naval Oceanographic Office, Washington, D. C., 1973.
5. Gotthardt, G. A., and G. J. Potocsky, "Life Cycle of a Gulf Stream Anticyclonic Eddy Observed from Several Oceanographic Platforms," J. Phys. Oceano., Volume 4, pp. 131-134, 1974.
6. Weatherwise, pp. 184-195, August, 1973.
7. Parsons, C. L., and G. S. Brown, "Remote Sensing of Ocean Currents Using Backscattering Cross Section Measurements by a Satellite," Journal of Geophysical Research, Submitted for Publication, 1976.

CHAPTER 6

Analysis of a Tropical Meteorological Disturbance Using Received Power and Waveform Data

by

C. L. Parsons

1.0 Introduction

Atmospheric attenuation can be defined as the reduction of the intensity of an electromagnetic wave by gases, clouds, and/or precipitation along its path through the atmosphere. Because these constituents are present in the troposphere much of the time (clouds and precipitation) or all of the time (water vapor and molecular oxygen), attenuation must be considered as one contributor to the signal levels that were detected in the S-193 receiver. In a recent paper by Ippolito [1], the effect of rain on a 15.3 GHz communications signal between the ATS-V satellite and the ground based receiver was substantiated. It was found that there was a high degree of correlation between the loss that the signal suffered under local precipitation conditions and the amount of rainfall that occurred as measured by surface rain gauges.

In this chapter, theoretical and experimental studies of the relative importance of many atmospheric attenuating substances will be used to derive numerical values for the sensitivity of the altimeter receiver to attenuation by gases, clouds, and precipitation. One example of actual attenuation during the SL-3 mission will be discussed in complete detail using waveform sampler data in addition to the AGC records. This was an extreme case where the received signal level decreased 6 dB in the Intertropical Convergence Zone (ITCZ). Finally, some comments concerning the potential of a down-looking active microwave radar as a meteorological sensor will be made.

2.0 The Radar Equation

The altimeter is time (or range) gated to sense the signal return from the earth's surface and the gating duration is sufficiently small that back-scattering from an intervening cloud layer will not be detected. Therefore, the general radar equation rather than the meteorological form is appropriate. The form for use in surface scattering is;

$$P_r = \left[\frac{NG_t P_t G^2 \lambda^2}{(4\pi)^3} \right] (\pi a^2) \sigma_o k_t r^{-4} \quad (1)$$

where P_r is the average received power, N is the pulse compression ratio, P_t is the peak transmitter power, G_t is the S-193 integrated receiver (TDA) gain, G is the antenna gain, λ is the wavelength, a is the radius of the footprint, σ_o is the surface radar cross section per unit area, k_t is an atmospheric transmission factor, and r is the satellite altitude.

The only term dependent on rainfall rate* and atmospheric attenuation in general is k_t , the transmission factor. In the absence of interfering weather, the AGC inferred measurement of received power, P_r , can be used to solve (1) for the surface backscattering cross section per unit area. Over a statistically uniform surface area such as the ocean, this value will not change appreciably and is therefore useful in evaluating (1) when precipitation is present. This technique is roughly analogous to the use of two radars operating at different frequencies, one of which is susceptible to atmospheric attenuation and the other which is not. This has been proposed by Eccles and Mueller [2], Cartmill [3], and Rogers and Wexler [4] among others as a method of computing the rainfall rate with ground based meteorological radars. From a satellite, however, it is not backscatter from the precipitation which is measured but backscatter from the earth's surface. Because of the unimportance of the former, empirical radar reflectivity - rainfall rate (Z-R) relationships are not needed and problems with the averaging of returns over range and backscattering volume and the deformation of echoes by non-planar targets are also avoided.

The attenuation factor which also is influential in conventional meteorological radar backscattering analyses is the term then that must accurately account for gaseous absorption and scattering and absorption by cloud droplets, raindrops, ice crystals, and hail. The estimates of attenuation made in this chapter will be based on the relative change in received power between attenuating and non-attenuating regions. Because the gaseous composition is not significantly affected by the presence of precipitation or clouds,

*The effect of the rainfall on the surface height spectrum and, consequently, σ_o is ignored.

there is no contribution from gaseous absorption in the measured signal strength change and therefore does not merit any further attention here.

If k_c and k_p are used to denote the attenuation coefficients for clouds and precipitation, respectively, in units of decibels per kilometer, and d_c and d_p are the one-way attenuation path lengths, the atmospheric transmission factor k can be expressed approximately as

$$k_t = \exp \left[-0.4606 (k_c d_c + k_p d_p) \right] \quad (2)$$

2.1 Calculations of the Sensitivity of P_r to Atmospheric Attenuation

Expressed in decibels of total attenuation, (2) becomes

$$k_a = 2(k_c d_c + k_p d_p) \quad (3)$$

In order to determine the sensitivity of the altimeter received power data to atmospheric attenuation, values for k_c and k_p typically used in conventional meteorological radar work will be used in (3) and the path lengths d_c and d_p required to produce one decibel changes in k_a will be computed.

By examining (3), it can be seen that the benefits of not having to average over backscattering volumes within a precipitating cell are offset by the lack of information at the satellite platform about the internal vertical structure of the cell. In particular, the vertical extents of the regions where rain, ice, and hail are present are unknown. The thickness of the cloud itself is not known without other on-board instrumentation.

Battan [5] expresses cloud droplet attenuation as

$$k_c = K_1 M \quad (4)$$

where K_1 is a specific attenuation coefficient dependent on cloud temperature and wavelength and M is the liquid water content in grams per cubic meter. Values of K_1 as computed by Gunn and East [6] are plotted in Figure 1. Table I lists typical values of maximum droplet radius, cloud droplet concentration, and liquid water content for different cloud types as reported by Mason [7].

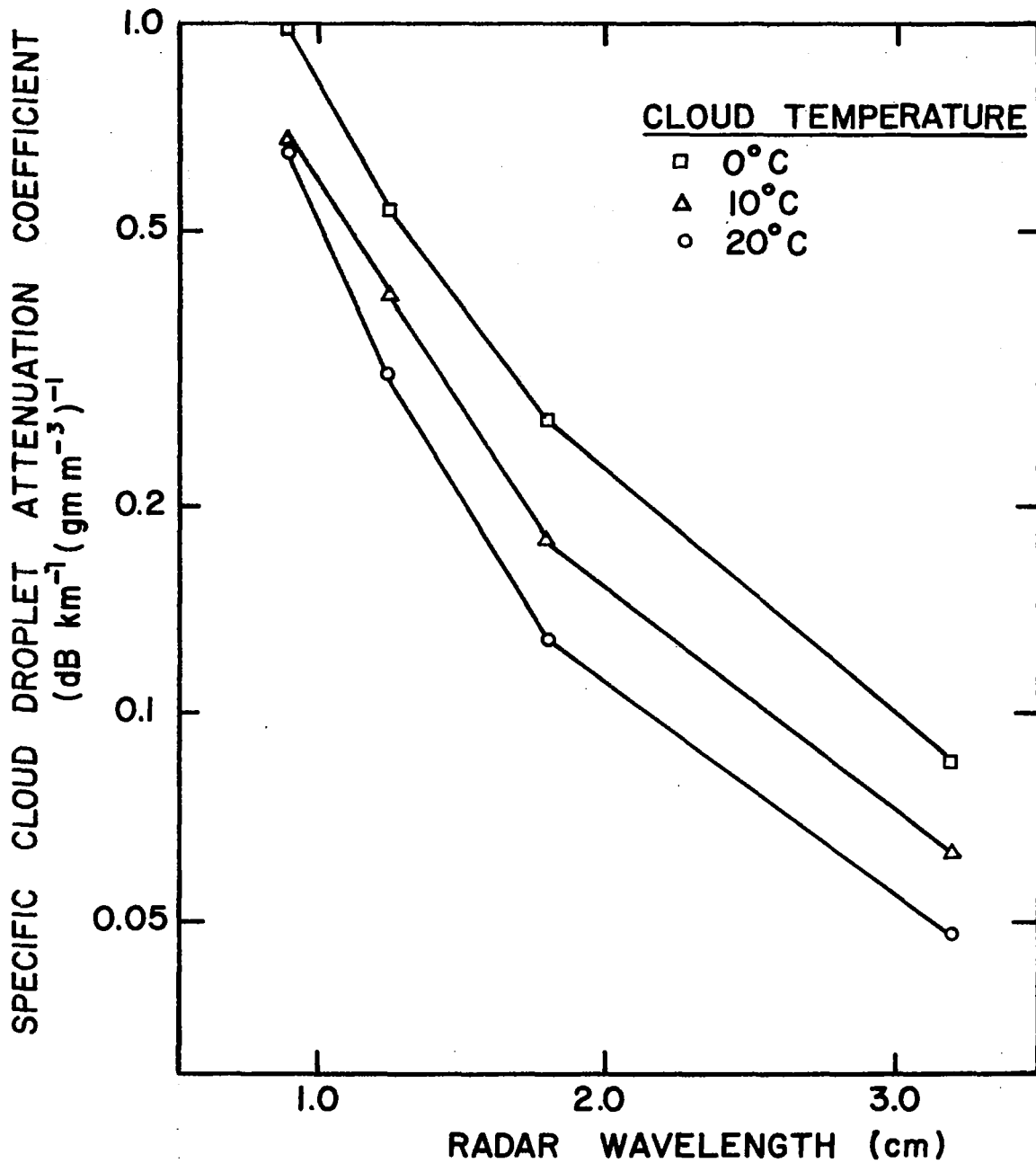


Figure 1. Cloud droplet attenuation coefficient per gm⁻³ as a function of wavelength. The variation with cloud temperature is indicated, from [6].

TABLE I

Characteristics of Cloud-Droplet Populations (after Mason [7])

Cloud Type	d_{\max} (10^{-6} m)	$N(\text{cm}^{-3})$	$M(\text{gm m}^{-3})$
Small Continental Cumulus (Australia)*	10	420	0.40
Small Continental Cumulus (England)*	30	210	0.45
Small Tradewind Cumulus (Hawaii)*	25	75	0.50
Cumulus Congestus	50	100	1.00
Cumulonimbus	100	100	2.00
Orographic Cloud (Hawaii)	35	45	0.30
Stratus (Hawaii)	45	24	0.35
Stratocumulus (Germany)	12	350	--

*Not more than 2 km deep

Figure 2 is a plot of a specific rainfall attenuation coefficient K_2 in $\text{db km}^{-1} (\text{min hr}^{-1})^{-1}$ versus wavelength using published values by Marshall and Palmer [8], Mueller and Jones [9], and Medhurst [10]. There is some dependence on rainfall rate as indicated. The close agreement between the various curves and the better resolution available with Medhurst's data made the latter study the choice for use in this paper. The variation of K_2 with rainfall rate R at a wavelength of 2.16 cm is plotted in Figure 3. If it is approximated by an expression of the form

$$K_2 = \alpha R^\beta \quad (5)$$

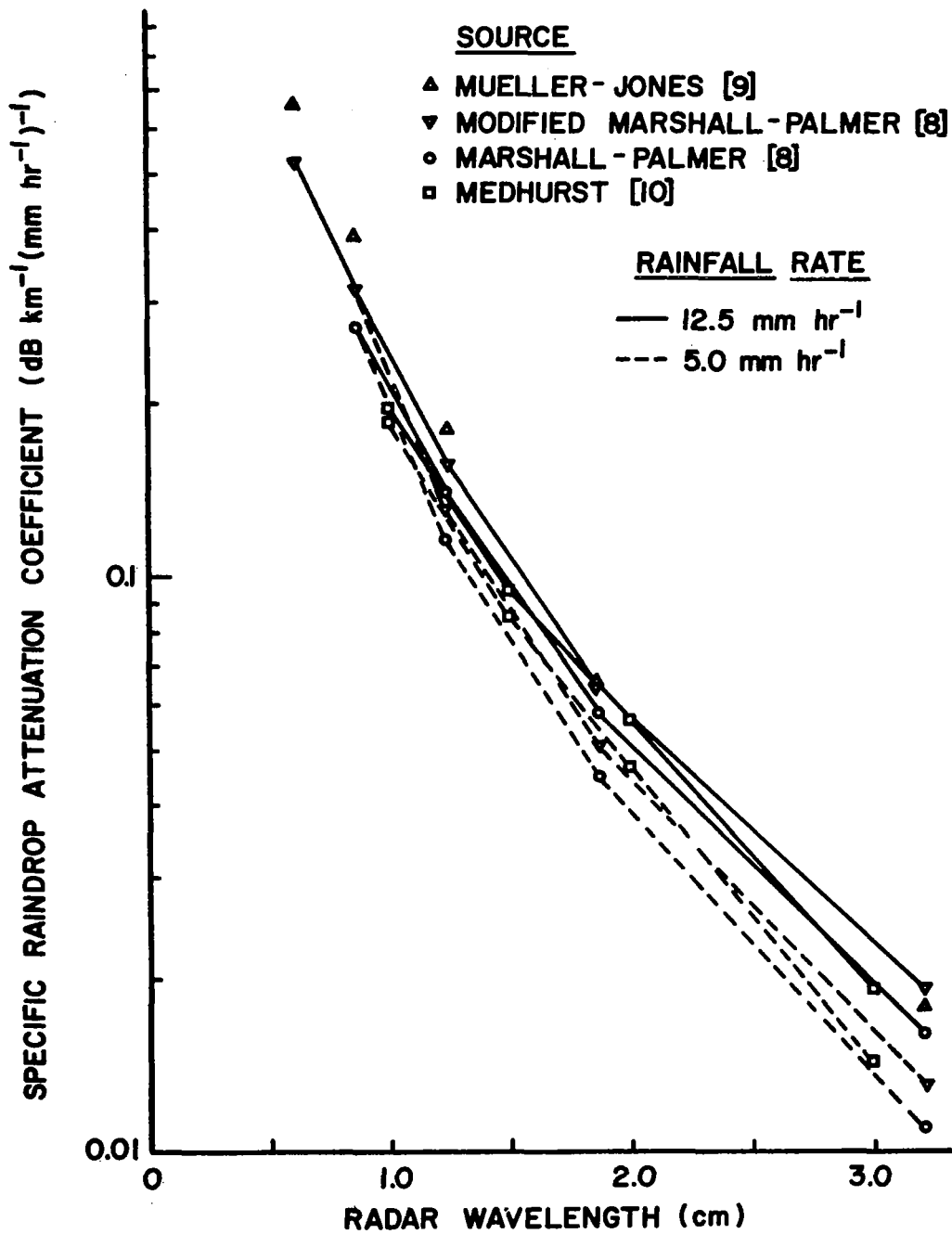


Figure 2. Raindrop attenuation coefficient per mm hr⁻¹ as a function of wavelength.

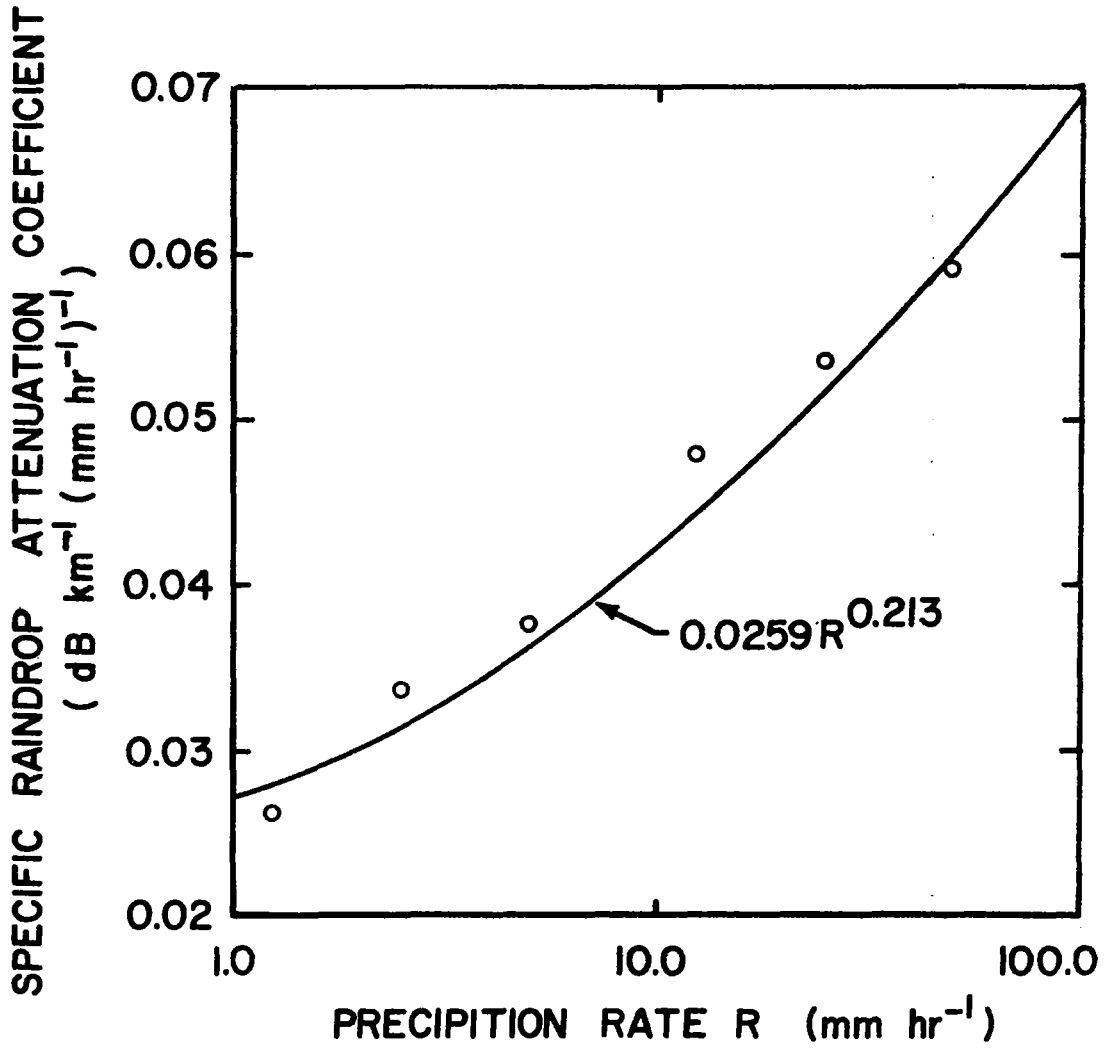


Figure 3. Raindrop attenuation coefficient for spherical, randomly distributed drops as a function of precipitation rate, from [10].

the constants α and β can be evaluated and are found to be 0.0259 and 0.213 respectively at a wavelength of 2.16 cm.

The description of attenuation by ice is even more difficult than for cloud droplets and rain. The great variability in shape and size of an individual ice crystal is compounded even further by the arbitrary orientations that are possible between the crystal and the direction of propagation of a radar pulse. Assuming spherical crystals and uniform rates of fall of 1.0 m sec^{-1} , Battan [5] calculated values of k_{\perp} for dry snow at 0°C . These results are tabulated in Table II.

TABLE II

Attenuation Coefficients in db km^{-1} for Low-Density
Snow at 0°C (after Battan [5])

<u>Wavelength (cm)</u>	<u>Precipitation Rate (mm hr^{-1})</u>		
	1	10	100
1.8	0.0046	0.344	33.5
3.2	0.001	0.040	3.41
10.0	0.00022	0.0026	0.057

Battan [11] also modeled the attenuation by spherical hail for various water shell thicknesses and maximum diameters. Table III lists the results.

TABLE III

Attenuation Coefficients in dB km^{-1} for Distributions of Spherical Hail (after Battan [11])

Maximum Diameter (cm)	Wavelength (cm)	Water Shell Thickness (cm)			
		Dry	0.01	0.05	0.10
0.97	3.21	0.12	0.91	1.68	1.50
1.93		1.21	3.01	3.72	3.49
2.89		1.66	3.46	4.03	3.79
0.97	5.5	0.015	0.19	0.56	0.94
1.93		0.18	0.79	2.48	2.30
2.89		0.37	1.12	2.82	2.60
0.97	10.0	0.002	0.051	0.058	0.08
1.93		0.017	0.15	0.34	0.89
2.89		0.034	0.19	0.60	1.18

Drawing upon the information contained in Tables I and II and Figures 1 and 3, the attenuation coefficients for various cloud types and precipitation types and intensities are tabulated below in Tables IV and V.

TABLE IV

Attenuation Coefficients k_p in dB km^{-1} for Various Precipitation Conditions

Precipitation Type	Precipitation Intensity (mm hr^{-1})		
	1	10	100
Rain	.0273	.0425	.07
Snow	.0026	.1600	-

TABLE V

Attenuation Coefficients k_c in dB km^{-1} for Various Cloud Types

Cloud Types	k_c (in dB km^{-1})
Cumulonimbus	0.270 @10°C
Stratus	0.047 @10°C
Small Continental Cumulus	0.040 @20°C

The impact of hail on attenuation has not been treated because of its rarity of occurrence, its small spatial extent, and the uncertainty with which its attenuation properties are known. However, it can be seen from Table III that its capability as an attenuator is high, especially at the shorter wavelengths. Obviously, if hail does happen to be present in the illumination cone of an altimeter, it will have a significant impact on the received signal strength. Note also in Table V that the values of k_c were computed using temperatures that were thought to best characterize the environment of the particular cloud type. The k_p and k_c values in Tables IV and V can be used in (3) to compute the cloud and precipitation cell thickness that are required to produce 1 dB changes in received power due to atmospheric attenuation. If it is assumed that there is no precipitation, then 1.85, 10.64, and 12.5 km thicknesses are needed respectively, for cumulonimbus, stratus and small continental cumulus cloud types. If the cloud attenuation is constant, then additional attenuations of 1 dB would be contributed by 18.31, 11.71, and 7.14 km thicknesses of precipitation cells exhibiting rainfall rates of 1, 10, and 100 mm hr^{-1} respectively, or by 3.13 km of 10 mm hr^{-1} snowfall. From this simplified sensitivity study, it can be seen that the cumulonimbus cloud, heavily laden as it is with liquid water droplets, should be expected to have the greatest effect on the altimeter received signal level and this was experimentally found to be the case.

3.0 The Skylab Altimeter Data Set

Without question, the strongest attenuation experienced by the altimeter during all three Skylab missions was sensed on 4 September 1973 during EREP Pass 25 of the SL-3 mission. As seen in the received power record in Figure 4, two cells were detected, one at approximately $14^{\text{h}}55^{\text{m}}45^{\text{s}}$ GMT and the other at $14^{\text{h}}56^{\text{m}}00^{\text{s}}$ GMT, near 8N, 27.5W. The altimeter was operating at that time in its pulse compression mode with an effective pulse width of 130 nsec.* At an altitude of 440 km, this resulted in a ground spot of radius 4.14 km. A measure of the received power was obtained every 0.26 sec. which coupled with an approximate satellite ground speed of 7.4 km sec^{-1} produced a spatial sample every 1.9 km.

Figure 5 is a sketch of a mosaic of S-190A Skylab camera photographs taken coincidentally with the altimeter's measurement of attenuation. This is the central core of cloud cover in the ITCZ for this day. The location of the two attenuation centers are also indicated in Figure 5 by the letters A and B. Immediately past both of these areas are dark regions thought to be shadows caused by cumulonimbus towers. For this latitude, date, and time of day, the southwest to northeast orientation of the groundtrack was such that shadows of an obstacle on the track would fall in this same manner. The sketch is used rather than the original photographs in order that these dark areas could be accentuated and made more visible.

The presence of cumulonimbi is confirmed if the sensitivity study in the preceding section is used to predict the thickness of the cloud or precipitation cell that would be needed to produce the 6 dB decrease actually seen in the received power records near cell B. The presence of the tropopause at a height of approximately 16 km places an upper limit on the thicknesses that are possible. Using Tables IV and V, the only reasonable single cause of the loss of signal strength would be a cumulonimbus tower reaching an altitude of 11 km. Of course, at the upper levels, the water content of the cloud would be present in the solid phase as well as the liquid. Fletcher

*Editors Note: The pulse compression network did not function properly until EREP Pass 39 of SL-3. Although the source of the problem was never identified, the data tended to indicate that the return was not being properly compressed. Prior to proper operation, the effective pulsewidth was probably close to 130 ns.

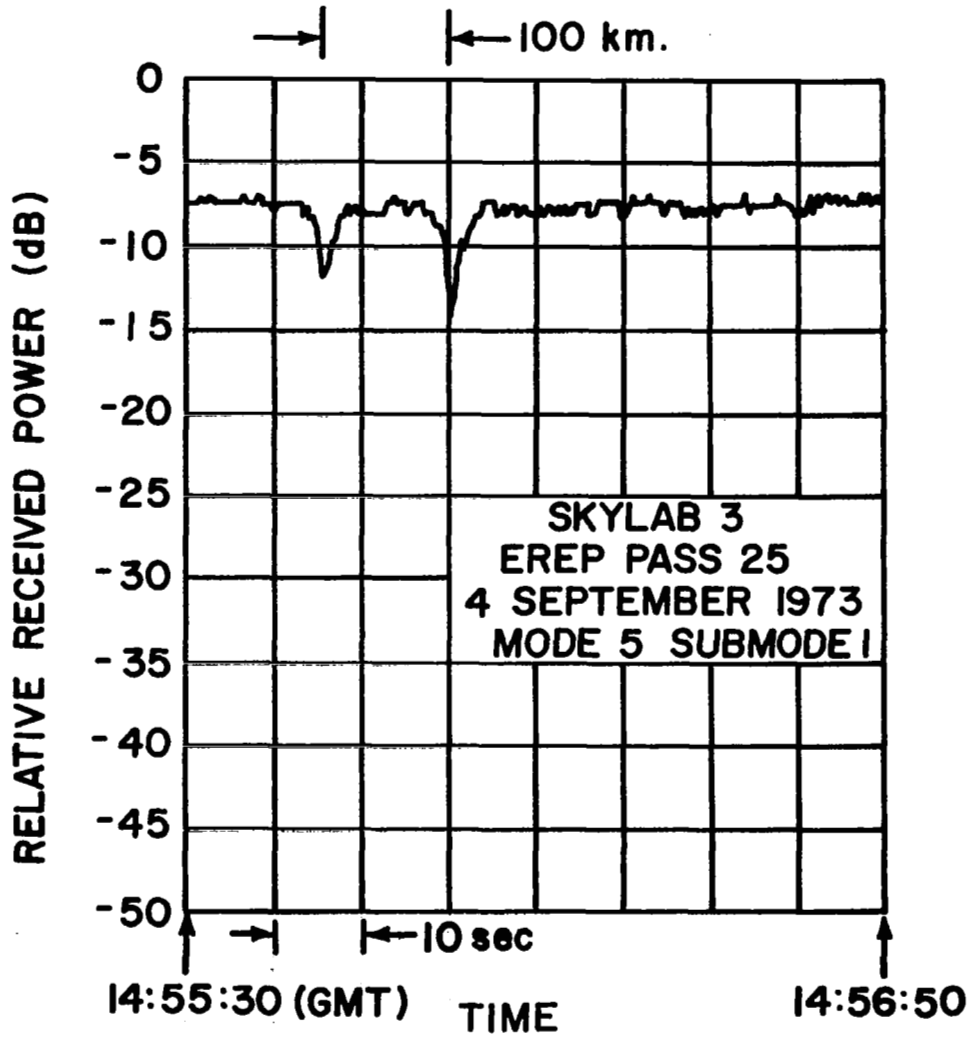


Figure 4. Skylab S-193 radar altimeter relative received power data measured on 4 September, 1973, during the SL-3 mission.

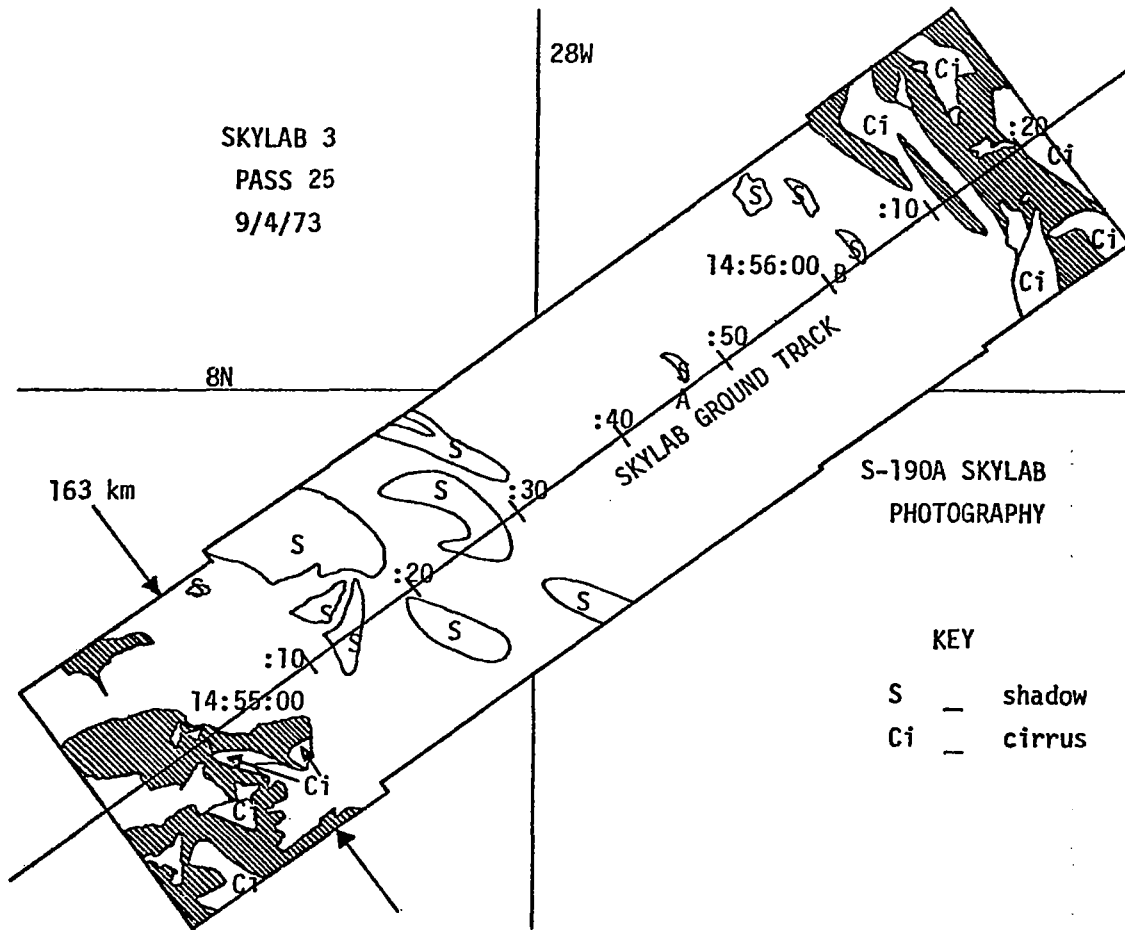


Figure 5. Mosaic of S-190A Skylab photographs taken coincidentally with the measurement of return power by the S-193 radar altimeter. Times are indicated and the location of the centers of the two attenuation cells are marked by the letters A and B. The shadows to the right of each disturbance are believed to be the result of the masking of the sun by tall cumulonimbus towers.

[12] states that water droplets within cumulus clouds seldom crystallize at altitudes below the -20°C isotherm because of the small concentrations of ice-forming nuclei at those levels. For a standard atmosphere (McClatchey, et al. [13]), this usually occurs at an altitude of about 8 km in the tropics. The cirrus development around the cells that can be seen in the S-190A imagery and the sensitivity study estimate of 11 km cumulonimbi are consistent with Mason [7] who reported that in the ITCZ, clouds may tower up to 15 km above the ground with anvil cirrus tops stretching in sheets hundreds of kilometers long. The additional presence of precipitation in any of the possible forms cannot be ruled out, of course, but it seems clear that the tropical cumulus towers were the major source of attenuation in the EREP Pass 25 data.

The Sample-and-Hold gate data for EREP Pass 25 were also studied. For purposes of clarity, the one second average voltage values measured and recorded from the eight gates are shown in two separate figures, with the records for gates 5 through 8 being presented in Figure 6 and those for 1 through 4 in Figure 7. The following observations can be made about the behavior of the Sample-and-Hold gates during the period of time when the AGC was responding to the attenuation.

- 1) All four average gate voltage records in Figure 6 were characterized by a sharp decrease in voltage level near Cell B.
- 2) Gates 5 through 8 did not experience a similar reduction near Cell A.
- 3) No diminution of signal strength is seen in the records in Figure 7 in the vicinity of either Cell A or Cell B.
- 4) An apparent correlation between the voltage records for gates 1-4 is observed near the time mark $14^{\text{h}}55^{\text{m}}54^{\text{s}}$, a location nearly equidistant between the two cells.

An alternate way of characterizing the behavior of the gates near Cell B is to reconstruct the shape of the return signal. Figure 8 shows the waveforms for time frames $14^{\text{h}}55^{\text{m}}57^{\text{s}}$, $14^{\text{h}}55^{\text{m}}58^{\text{s}}$, $14^{\text{h}}55^{\text{m}}59^{\text{s}}$, and $14^{\text{h}}56^{\text{m}}00^{\text{s}}$. There is a substantial dip in the plateau of the $14^{\text{h}}55^{\text{m}}59^{\text{s}}$ waveform. In Sample-and-Hole gate 6, the signal loss exceeds a 2σ excursion from the average waveform computed from the data for the entire EREP Pass 25. However, the 3σ limit is not reached. Observe, however, that the voltages for all four

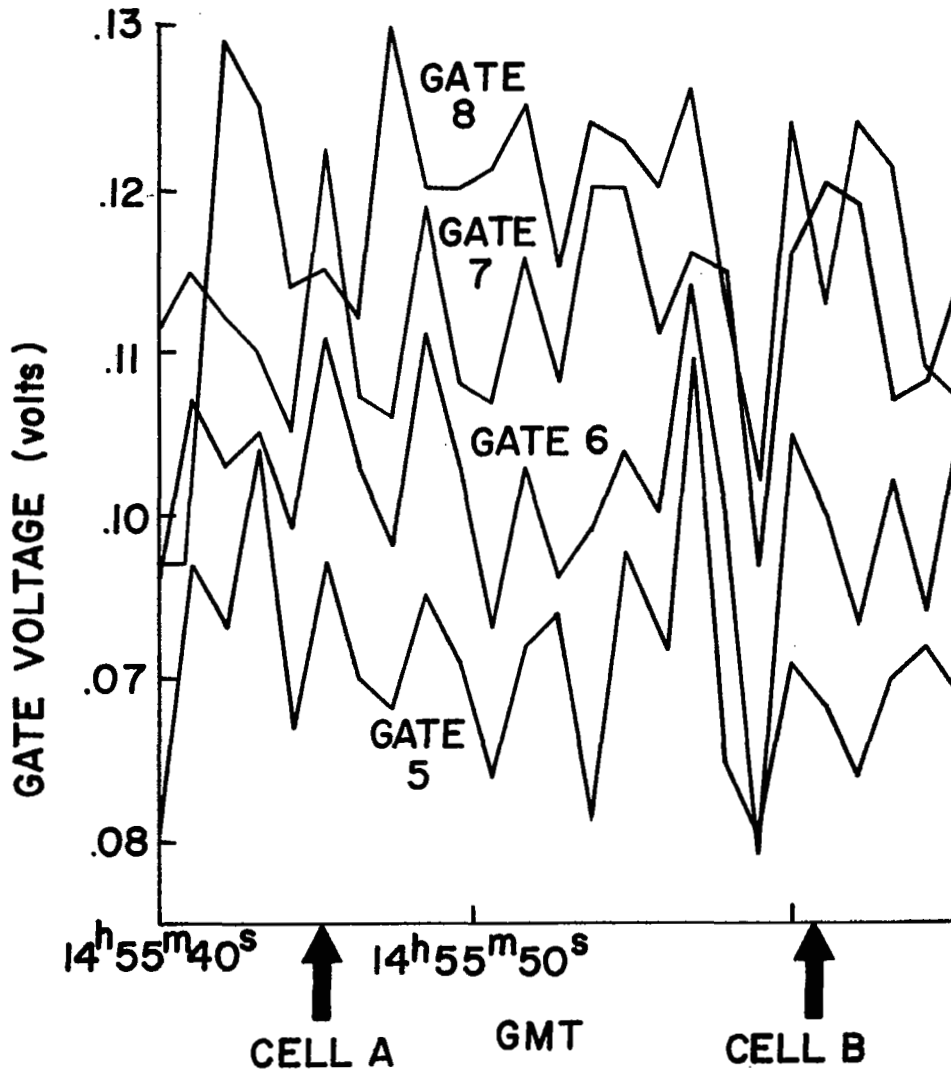


Figure 6. Sample and Hold gate voltages for gates 5 through 8 during the period of signal attenuation. The location of attenuation cells A and B are indicated.

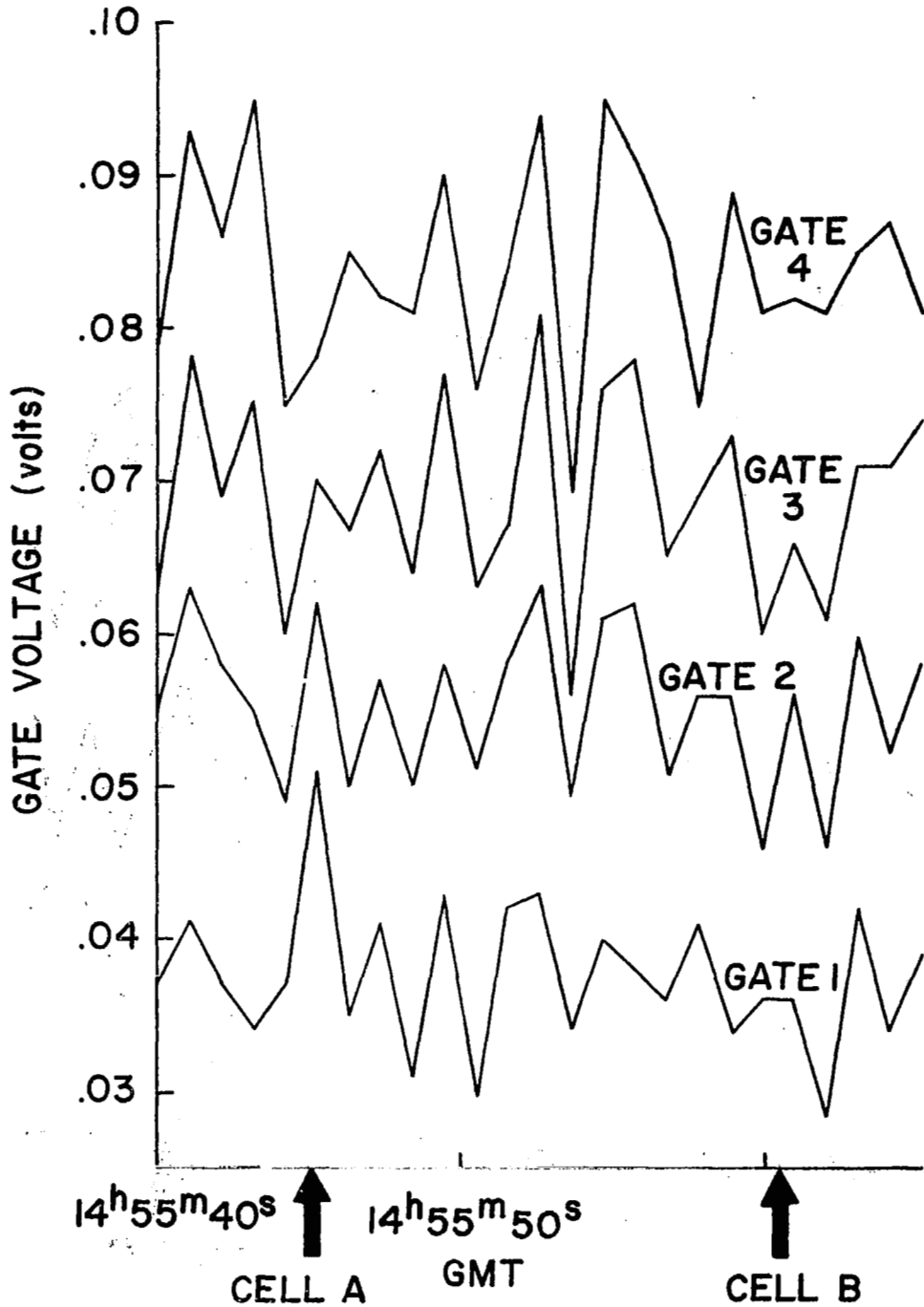


Figure 7. Sample and Hold gate voltages for gates 1 through 4 during the period of signal attenuation. The location of attenuation cells A and B are indicated.

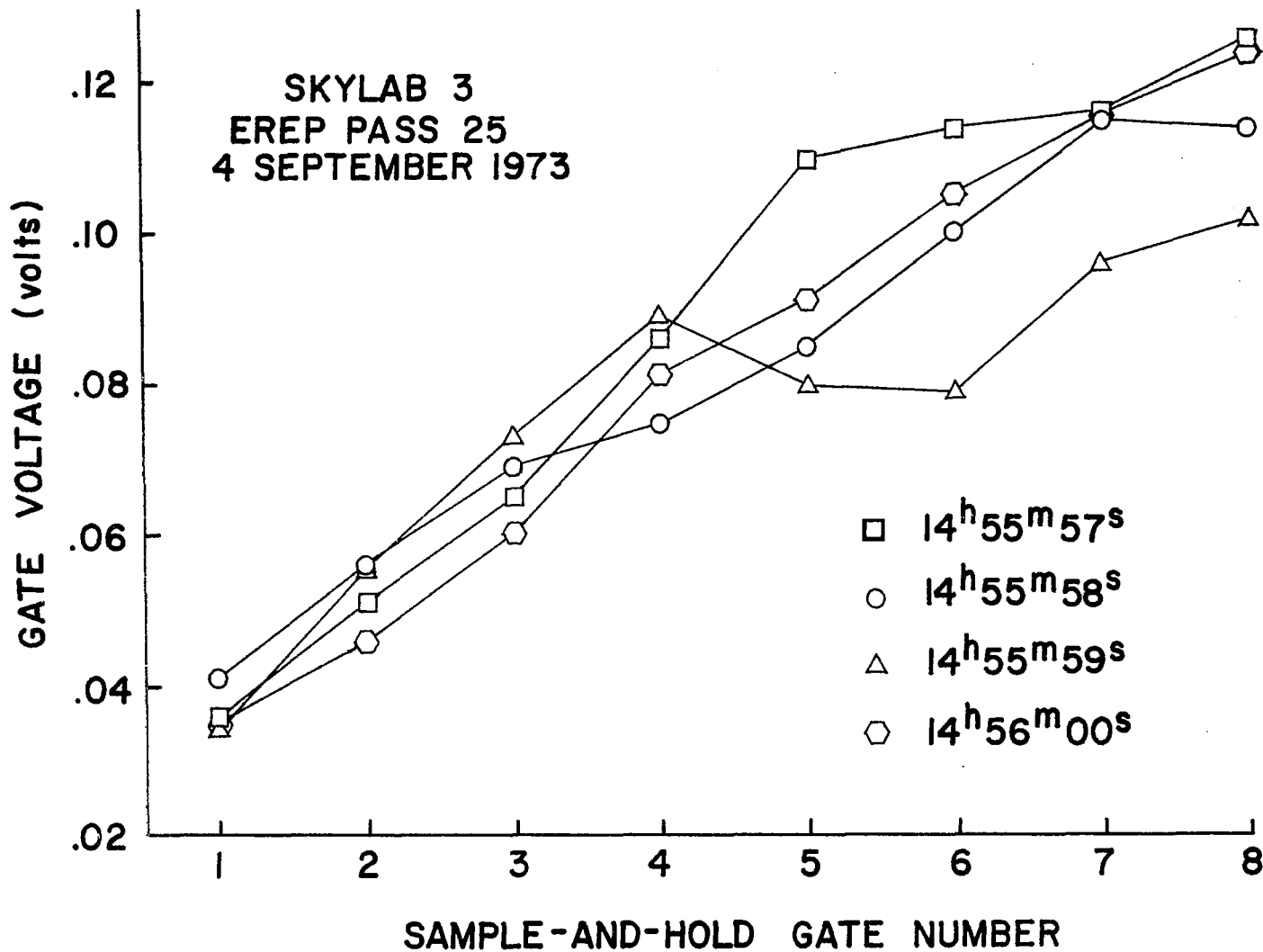


Figure 8. Average waveforms for data frames 14 hr 55 m 57 s, 14 hr 55 m 58 s, 14 hr 55 m 59 s, and 14 hr 56 m 00 s showing the decrease in the plateau voltage at time 14 hr 55 m 59 s.

gates 5-8 lie below the average waveform. If the average voltage-time record for all four is plotted as in Figure 9, then the attenuated level in frame 14^h55^m59^s does exceed the three sigma excursion limit. It is concluded that the signal attenuation was the result of an external influence and cannot be attributed to the random fluctuations of the measurement process. As seen in Figure 9, the close temporal proximity of this signal level drop to the return power measurement previously identified as the result of the attenuation of Cell B leads to the hypothesis that the onset of attenuation caused by Cell B was so abrupt that the AGC was not able to respond quickly enough, thereby allowing the voltages in gates 5-8 to decrease. Again referring to Figure 9, Cell A, in the context of this scenario, must have been weaker and/or more diffuse allowing the AGC to adjust appropriately without the attenuation affecting the gates at all.

A disconcerting aspect of these observations is the lack of attenuation in gates 1 through 4 near Cell B. No suitable explanation is known for this situation. However, it is possible that this is a manifestation of some surface or near surface condition unique to this situation. A lack of detailed knowledge of the characteristics of the altimeter during malfunctioning of the pulse compression system precludes further in depth analysis.

4.0 Concluding Remarks

The sensitivity study that was described in this chapter produced the conclusion that cumulonimbi are the most probable causes of strong attenuation of a satellite radar altimeter's signal, even more probable than intense rainfall. This result is dependent entirely on the validity of the attenuation coefficients and cloud liquid water content values used and although these values were drawn from reliable sources, there is much that is unknown about the physics of the ITCZ and precipitating clouds in general. For example, Simpson and Wiggert [14] comment that the distribution and structure of ice crystals at upper levels of the troposphere in the tropics are unknown. Fletcher [12] and Mason [7] both comment on the lack of reliable, accurate instrumentation to actually determine the highly variable liquid water content of a cloud. Medhurst's [10] treatment of rain is somewhat more acceptable, but the assumptions of vertical homogeneity and randomly spaced spherical single scattering drops are hypothesized by Medhurst as possible reasons for the discrepancy between predicted and measured rainfall rates. Even with

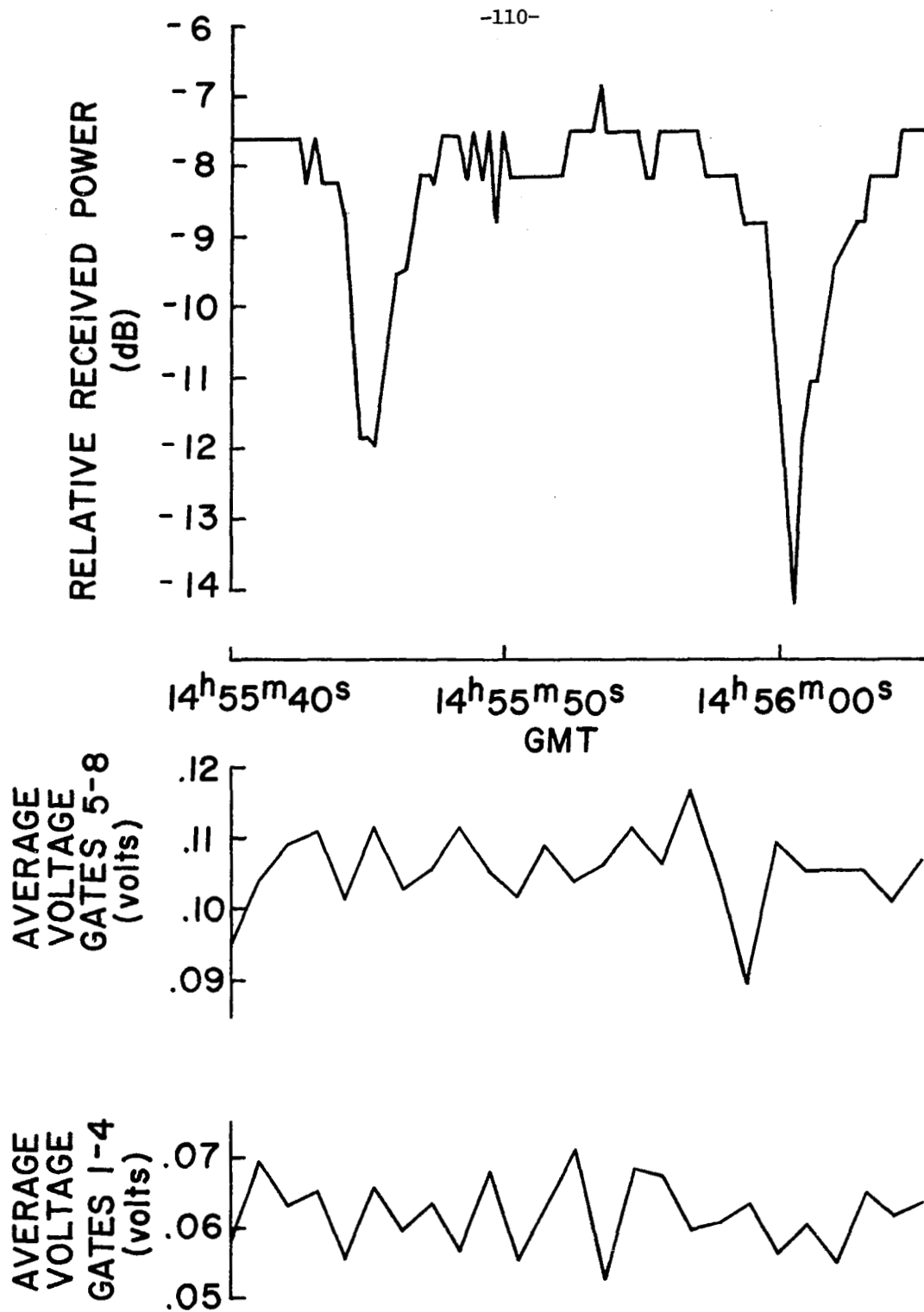


Figure 9. Comparison of the SL-3 EREP Pass 25 received power record with the voltage records generated by averaging the data from gates 1 through 4 and gates 5 through 8.

these considerations in mind, the presence of cumulonimbi at the locations of the 4.6 and 6 dB decreases in received signal strength as determined from the sensitivity study is supported by the presence of cirrus clouds in the S-190A imagery (signifying cloud heights greater than about 8 km) and by the two crescent shaped shadows that seem to be located at the appropriate spots to be caused by the billowing towers.

An interpretation was made of the relationship between the voltage records of the waveform samplers and the received signal level for EREP Pass 25 of the SL-3 mission. The absence or presence of a diminished Sample-and-Hold gate signal in the upper ramp and plateau gates near known regions of strong attenuation was shown to be undoubtedly a function of the abruptness of the regions and, therefore, of the AGC circuit's frequency response characteristic. The lack of a corresponding diminution of signal in the lower ramp and noise gates indicates that the ITCZ cloud cluster may have generated a wind field and/or precipitation pattern that altered the ocean's wave structure and thereby σ^0 that in essence compensated for the attenuation. The possible presence of wind shear at the boundary between the two attenuating cells was also seen in gates 2 through 4.

The true worth of the received power measurement and the waveform sampler records for geophysical work has yet to truly be recognized. In the past, they have been employed as necessary but subordinate systems in the radar altimeter. Hopefully, the information produced by these devices on aircraft and satellite altimeters in the future will be examined on its own merit as has been attempted here. It is felt that a significant contribution can be made to studies of the air-sea interaction by using the waveform samplers and the received power measurement to study the behavior of σ^0 in the presence of localized wind and precipitation conditions.

REFERENCES

1. Ippolito, L. J., "Effects of Precipitation on 15.3- and 31.65- GHz Earth-Space Transmissions with the ATS-V Satellite," Proc. IEEE, Vol. 59, pp. 189-205, 1971.
2. Eccles, P. J. and E. A. Mueller, "X-Band Attenuation and Liquid Water Content Estimation by a Dual-Wavelength Radar," J. Appl. Meteor., Vol. 10, pp.1252-1259, 1971.
3. Cartmill, R. H., "Rainfall Rate Measurement Using Two Radar Sets of Different Wavelengths: Theory", Proc. Tenth Wea. Radar Conf., Boston, Amer. Meteor. Soc., pp. 265-270, 1963.
4. Rogers, C. W. C. and R. Wexler, "Rainfall Determination from 0.86 and 1.82 cm Radar Measurements," Proc. Tenth Wea. Radar Conf., Boston, Amer. Meteor. Soc., pp. 260-265, 1963.
5. Battan, L. J., Radar Observation of the Atmosphere, Chicago, The University of Chicago Press, p. 324, 1973.
6. Gunn, K. L. S. and T. W. R. East, "The Microwave Properties of Precipitation Particles," Quart. J. Roy. Meteor. Soc., Vol. 80, pp. 522-545, 1954.
7. Mason, B. J., Clouds, Rain and Rainmaking, Cambridge, The Cambridge University Press, pg. 145, 1962.
8. Marshall, J. S. and W. M. K. Palmer, "The Distribution of Raindrops with Size," J. Meteor., Vol. 5, pp. 165-166, 1948.
9. Mueller, E. A. and D. M. A. Jones, "Drop Size Distributions in Florida," Proc. Eight Wea. Radar Conf., Boston, Amer. Meteor. Soc., pp. 299-305, 1960.
10. Medhurst, R. G., "Rainfall Attenuation of Centimeter Waves: Comparison of Theory and Measurement," IEEE Trans. Antennas and Propagation, Vol. AP-13, pp. 550-564, 1965.
11. Battan, L. J., "Radar Attenuation by Wet Ice Spheres," J. Appl. Meteor., Vol. 10, pp. 247-252, 1971.
12. Fletcher, N. H., The Physics of Rainclouds, Cambridge, The Cambridge University Press, pg. 386, 1962.

REFERENCES (Cont'd.)

13. McClatchey, F. A., R. W. Fenn, J. E. A. Selby, F. E. Volz, and J. S. Garing, "Optical Properties of the Atmosphere (Revised);" Env. Res. Papers (No. 354), AFCRL-71-0279, Vol. 98, 1971.
14. Simpson, J. and V. Wiggert, "1968 Florida Cumulus Seeding Experiment: Numerical Models Results," Mon. Wea. Rev., Vol. 99, pp. 87-118, 1971.

CHAPTER 7

High Sea State Measurements Of σ° For Near Normal Incidence

by

G. S. Brown.

W. J. Curry

1.0 Introduction

Microwave scattering from the ocean surface has recently received renewed interest because of the possibility of inferring surface behavior from the characteristics of the scattered energy. The most straightforward and easily measured characteristic is the peak of the average return power. This quantity is dependent upon the surface through the effective surface scattering cross section per unit scattering area, σ° .

Much effort has been directed toward theoretical investigations of rough surface scattering with the aim of determining what surface parameters influence the behavior of σ° . Unfortunately, some of these studies and the interpretation of the results have led to controversy and, consequently, greater confusion. In general, efforts have proceeded mainly along the lines of relating the variation of σ° to surface wind speed. The greatest interest appears to be concentrated on the variation of σ° with surface wind speed for an angle of incidence in the range of 30 to 60 degrees. However, the dependence of σ° upon surface conditions at near normal incidence, i.e. 0 degrees, is also important because of its impact on future radar altimeter design and the possibility that it may also be a means of sensing surface characteristics.

Measurements of σ° for near normal incidence have been made from stable platforms [1] and aircraft [2] under various ocean surface conditions. However, for both geometries there are definite problems in deconvolving σ° from the measured return power as a function of delay [3]. The Skylab S-193 radar altimeter provided the first opportunity to make high angular resolution measurements of σ° for near normal incidence. For various hardware and operational reasons, the reduction of Skylab data proved to be a monumental task; however, it was successfully completed and the σ° results have been reported [4]. This report represents an initial effort to correlate these measurements with known or estimated surface conditions during the presence of large surface wind speeds.

2.0 Available Sea Surface Data

As a part of their preliminary evaluation of the S-193 radar data, Wallops

Flight Center contracted with NOAA (Suitland, Md.) to provide hindcast surface data along selected portions of the spacecraft ground track. The selection process was dominated, primarily, by the desire to determine if the altimeter had responded to large waveheights as expected. Since surface roughness determination through average waveform distortion effects was of principle importance, the selected areas corresponded to regions where the 10 ns submode of Mode V was activated. Unfortunately, σ° could not be obtained from the short pulse data due to a lack of sufficient AGC calibration data. Thus, we were limited in this study to those areas where submode 0 (100 ns pulsewidth) was operated.

Fortunately, the limited surface data was most useful since it comprised unusually large waveheight and surface wind conditions. A short summary of the dates and general area for which we had both σ° and surface data is given in Table I. A typical format for the surface data provided by NOAA is shown in Figure 1. The solid straight line corresponds to the appropriate portion of the selected ground track. Along this line, significant waveheight ($H_{1/3}$) for both wind driven and swell components are given in 0.5 m. increments. Also indicated are the surface wind speed and direction and general descriptive weather conditions.

3.0 σ° Variation Over Selected Areas

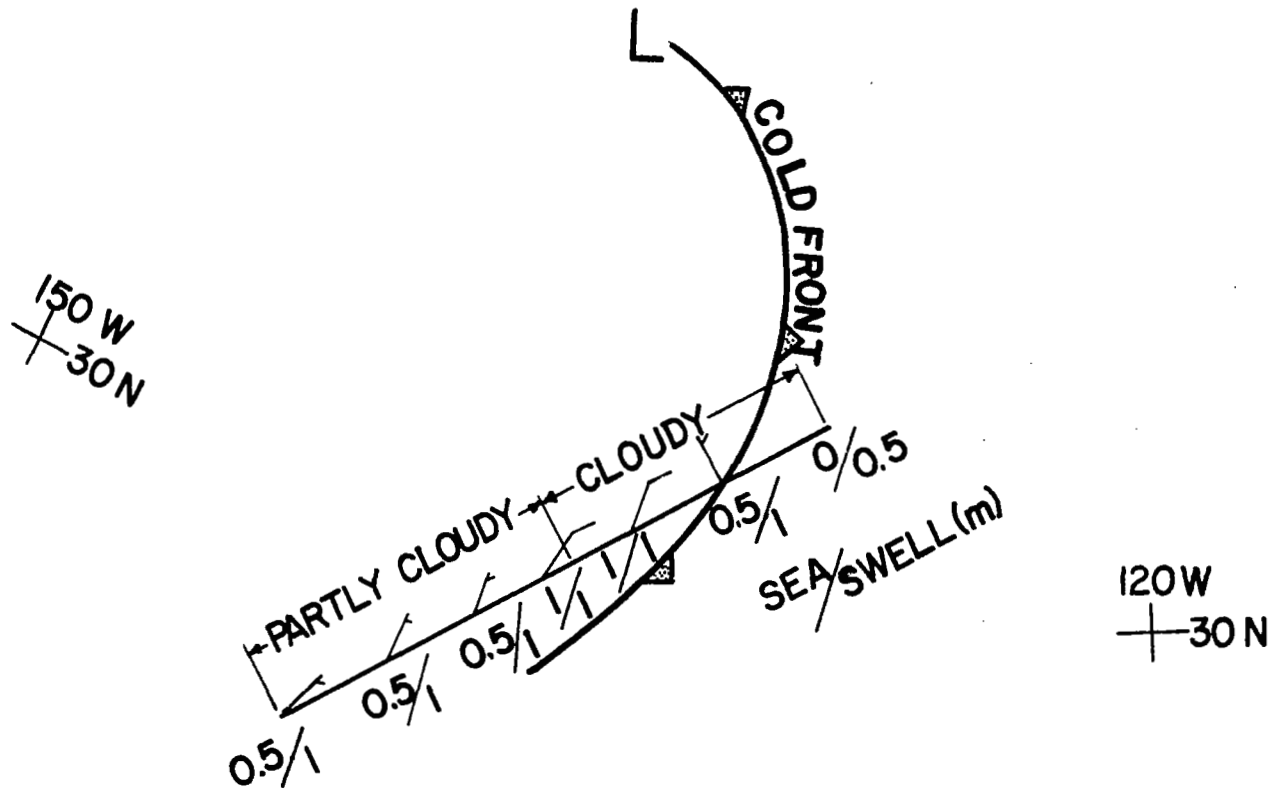
The basic data rate of the radar was one sample of average return power every 0.25 sec. The quantization imposed by the telemetry depended upon the received power, but for these data it was about 0.5 dB. In addition to other errors in the measurement of σ° , there was a basic uncertainty due to our lack of knowledge of the direction of pointing of the radar antenna [4]. Because of an asymmetrical antenna pattern, we could only estimate bounds on σ° . Fortunately, the bounds were rather close together so the pointing uncertainty was not considered to have a significant impact on the quality of the data.

Figures 2 through 11 show the behavior of σ° as a function of elapsed time (1 frame = 1.04 sec.) and distance along the ground track. In addition, we have also indicated the variation of significant waveheight and wind speed and direction as determined from the NOAA data. In submode 0 of Mode V, σ° data were obtained for a distance of about 100 km. This distance was relatively small in comparison to the granularity of the NOAA surface data. Thus, the 100 km distance comprised about one indicated change in surface conditions, at best. For this reason, we have chosen to plot the "raw" σ° data since the

TABLE I

A Short Summary of Dates and EREP Passes for
Which Both Surface Data and σ° Data Were Available

<u>DATE</u>	<u>DAY OF YEAR</u>	<u>EREP PASS</u>	<u>GENERAL AREA</u>
13 Sept., 1973	256	39	Azores
7 Jan., 1974	007	76	North Atlantic
8 Jan., 1974	008	78	North Atlantic
9 Jan., 1974	009	79	North Atlantic
12 Jan., 1974	012	82	North Atlantic (Off of Newfoundland)
14 Jan., 1974	014	83	North Atlantic
20 Jan., 1974	020	86	Mid Atlantic



1800 Z WED
SEP 12 1973

Figure 1. Typical NOAA hindcast data presentation for a selected ground track.

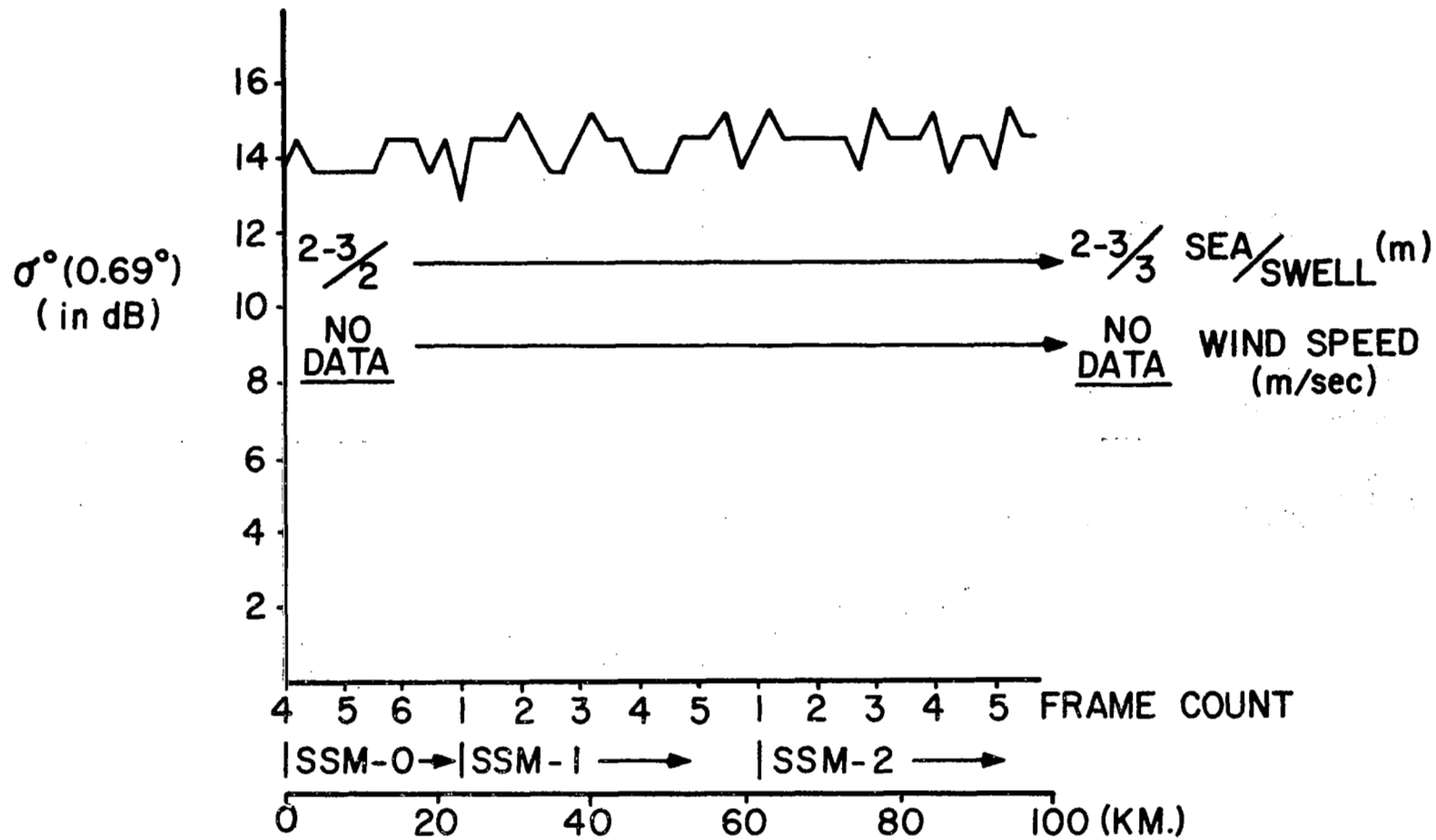


Figure 2. Measured σ^0 and corresponding surface conditions for SL-3 EREP Pass 39, Mode V (1 of 2), submode 0. (Add 0.4 dB for 0.9° pointing error in roll).

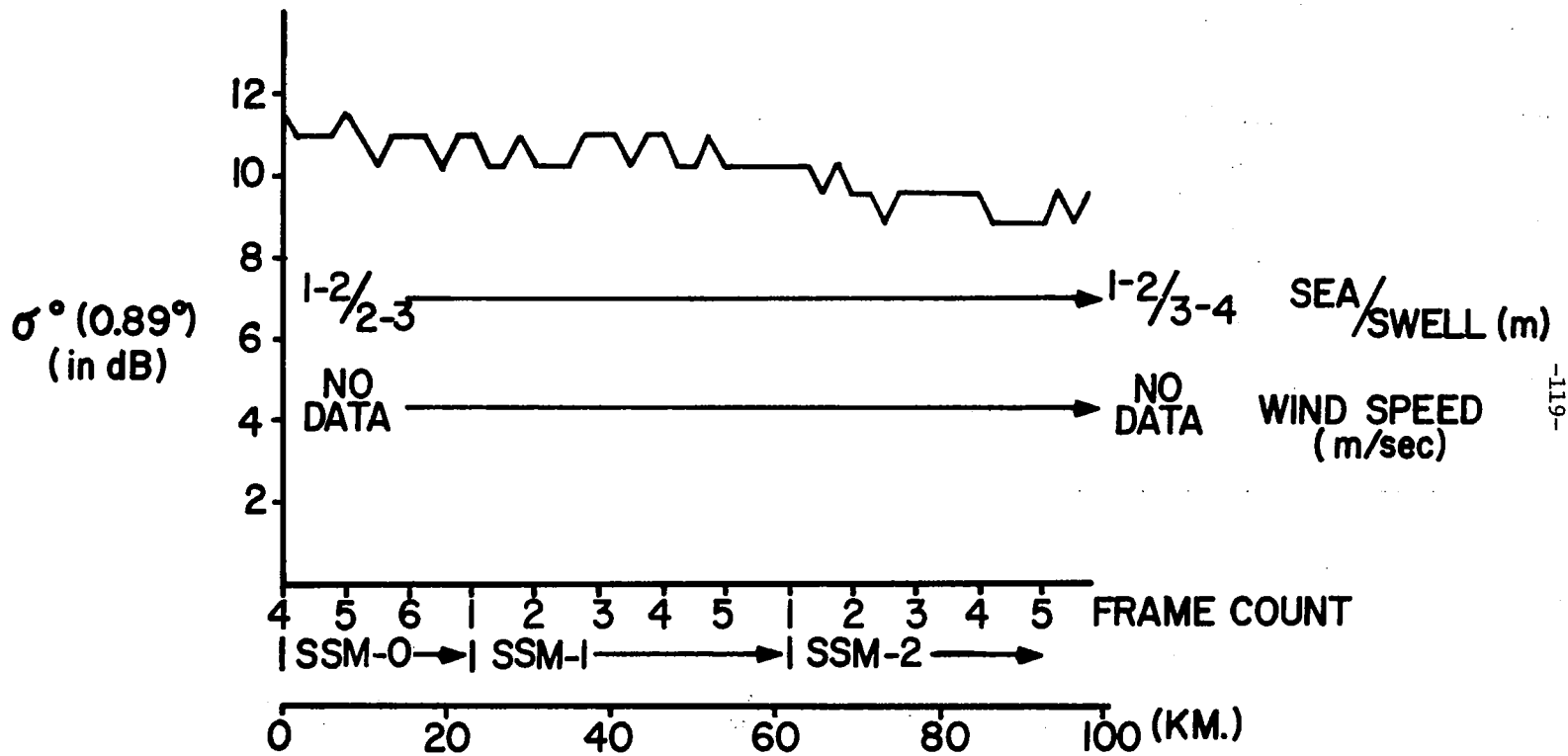


Figure 3. Measured σ^0 and corresponding surface conditions for SL-3 EREP Pass 39, Mode V (2 of 2). (Add 1.9 dB for 1.1° pointing error in roll).

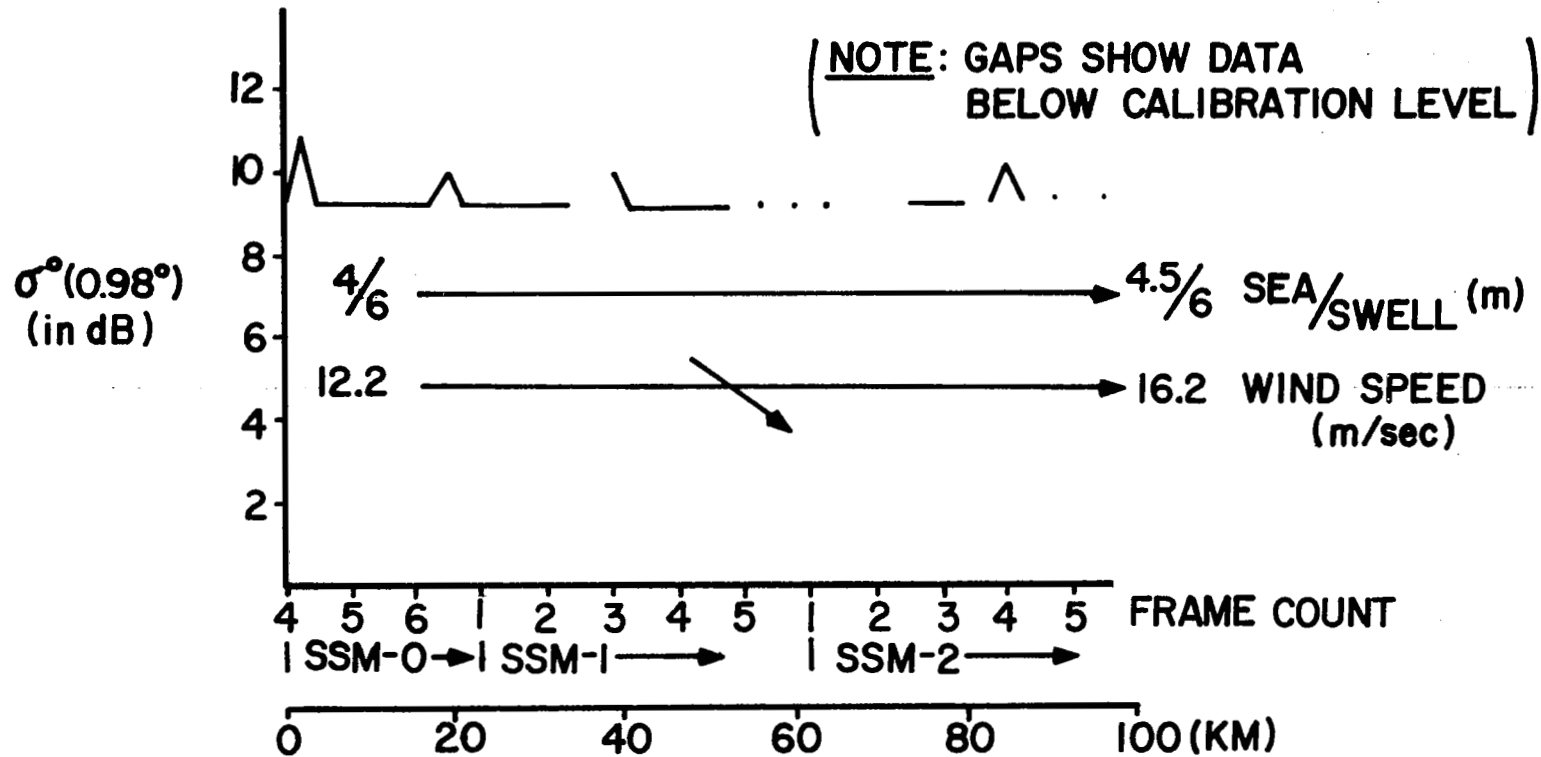


Figure 4. Measured σ^0 and corresponding surface conditions for SL-4 EREP Pass 76, Mode V (3 of 5), submode 0. (Add 0.3 dB for 1.05° pointing error in roll.)

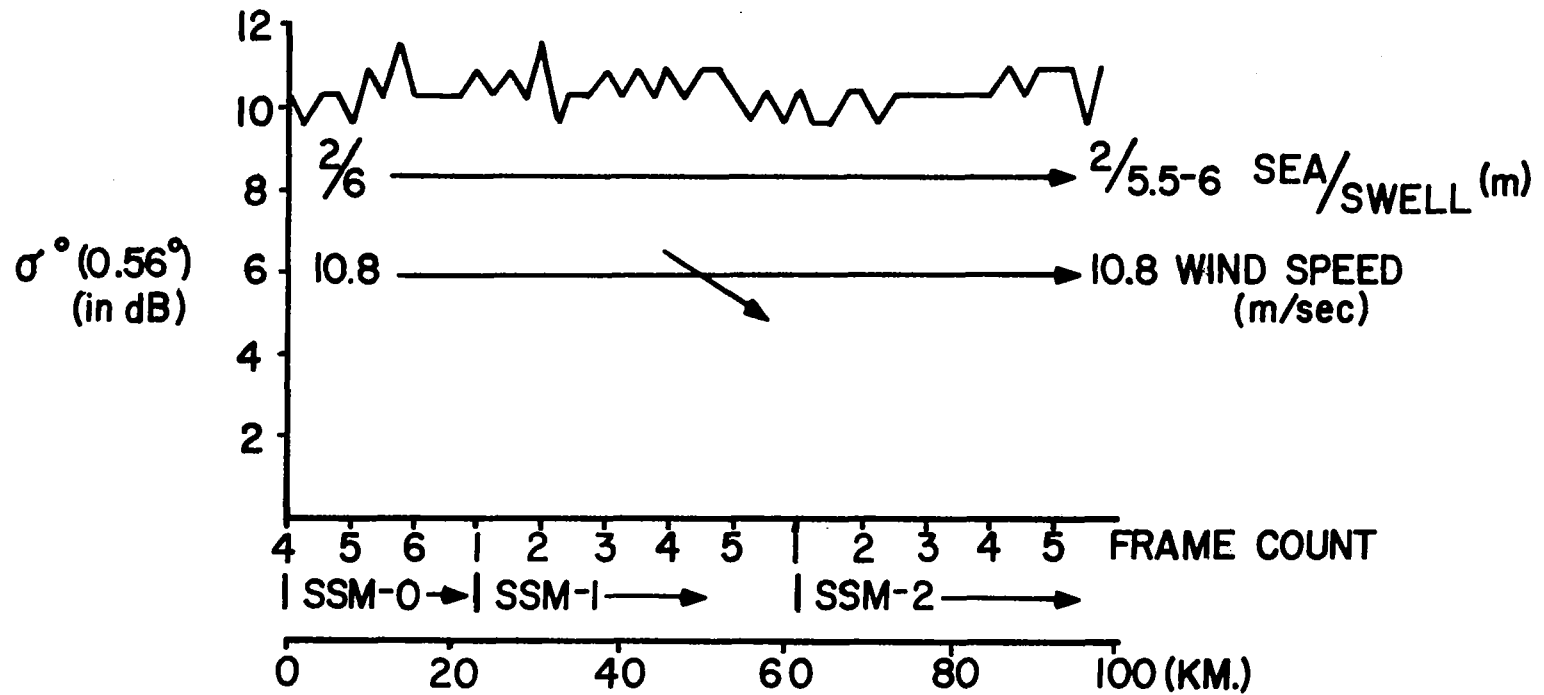


Figure 5. Measured σ^0 and corresponding surface conditions for SL-4 EREP Pass 78, Mode V (2 of 2), submode 0. (Add 0.1 dB for pointing error in roll.)

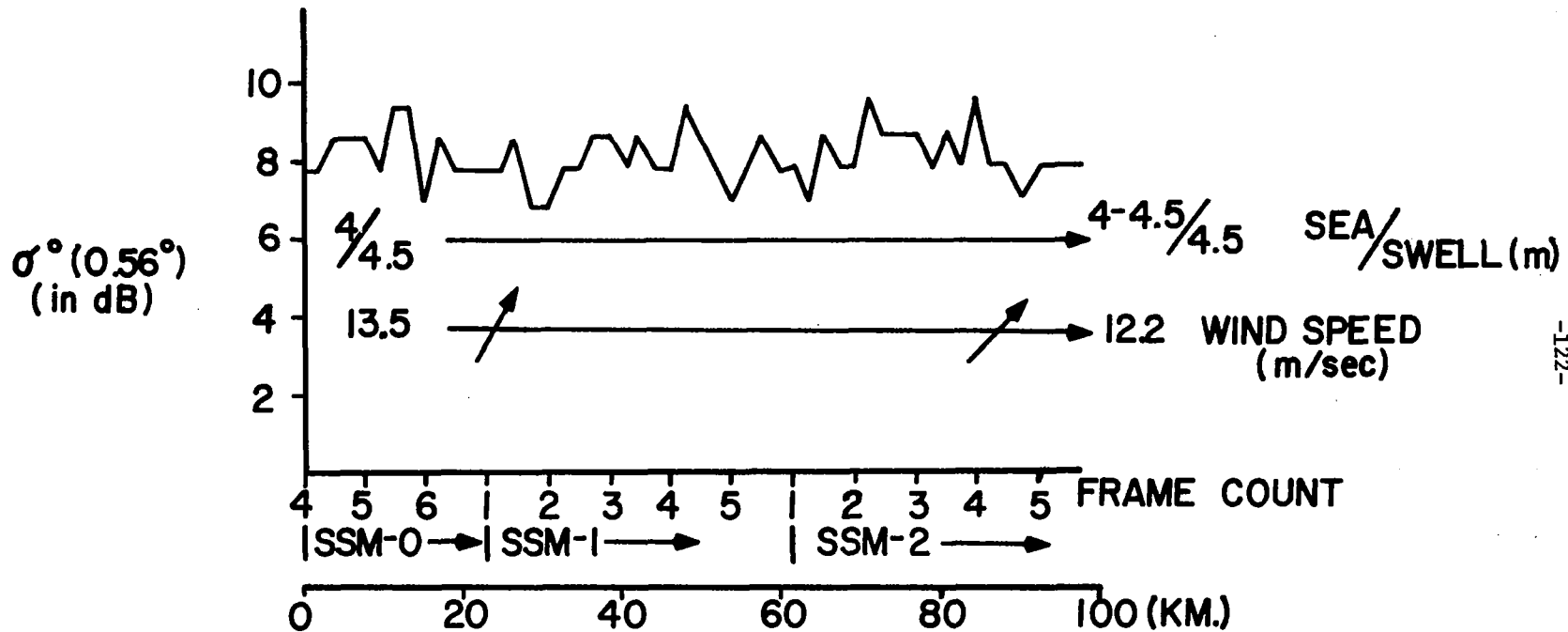
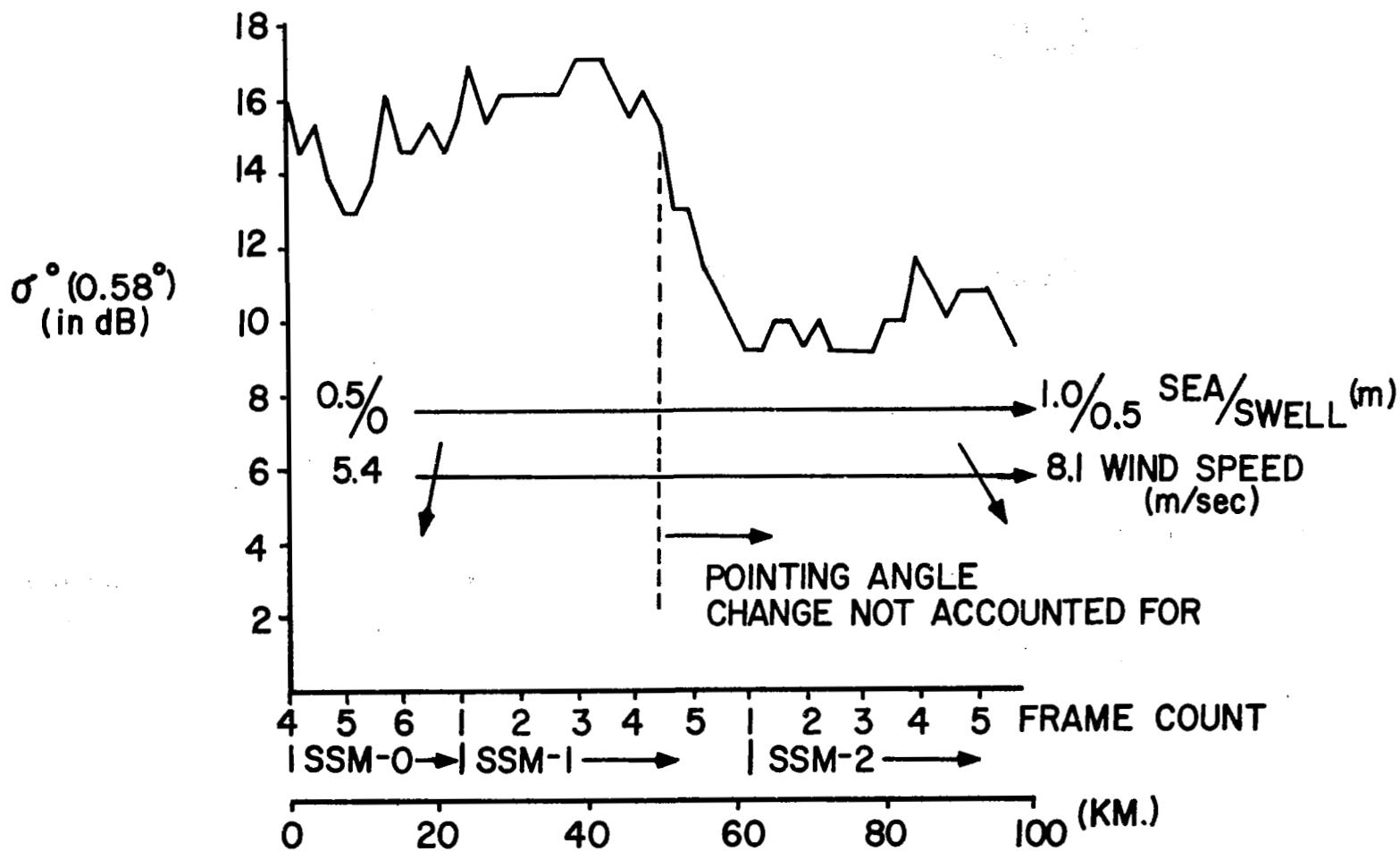


Figure 6. Measured σ^0 and corresponding surface conditions for SL-4 EREP Pass 79, Mode V (4 of 4), submode 0. (Add 0.1 dB for 0.45° pointing error in roll.)



-123-

Figure 7. Measured σ^0 and corresponding surface conditions for SL-4 EREP Pass 82, Mode V (1 of 4), submode 0. (Add 0.1 dB for 0.65° pointing error in roll.)

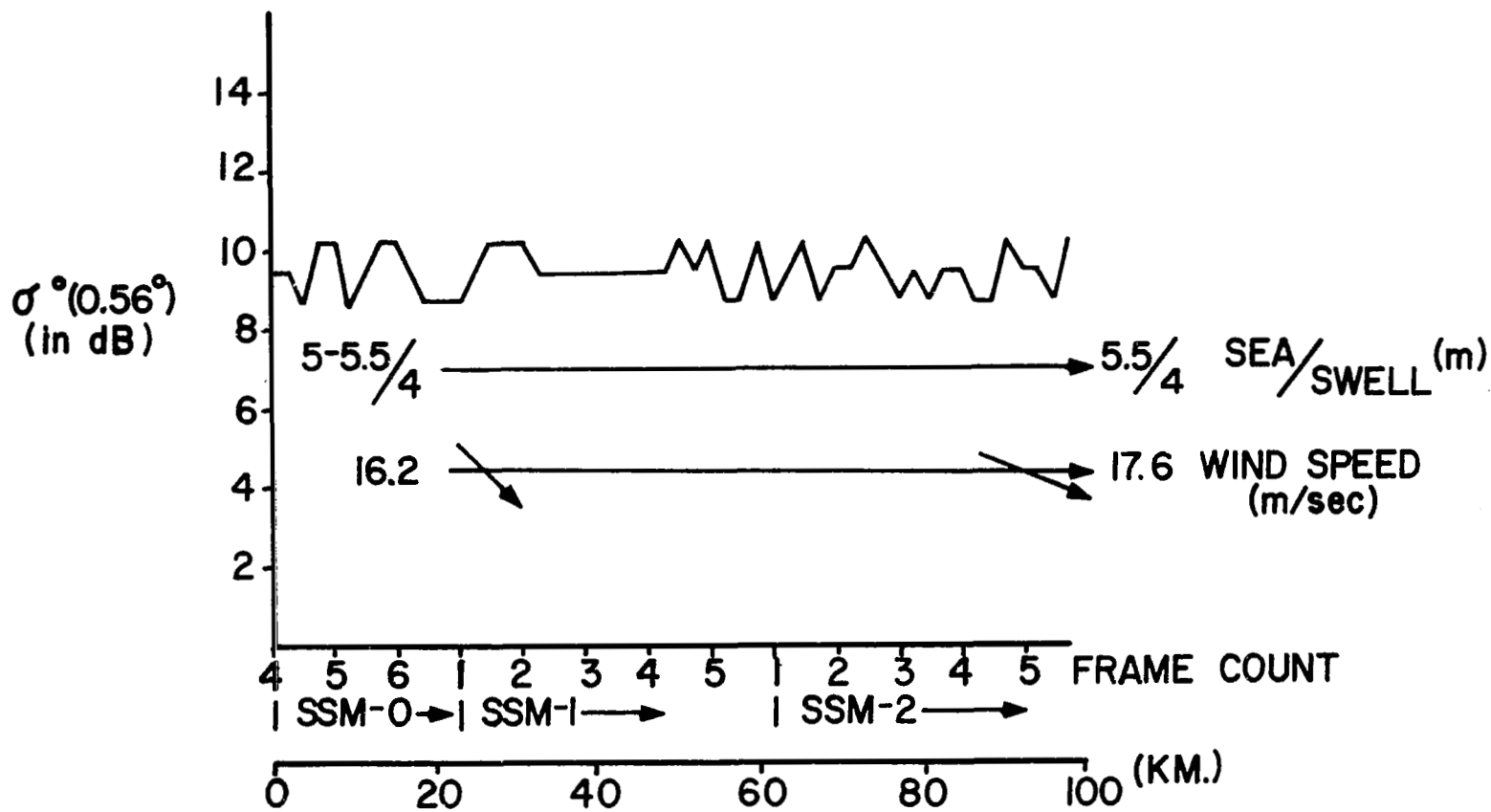


Figure 8. Measured σ^0 and corresponding surface conditions for SL-4 EREP Pass 83, Mode V (1 of 4), submode 0. (Add 0.1 dB for 0.6° pointing error in roll.)

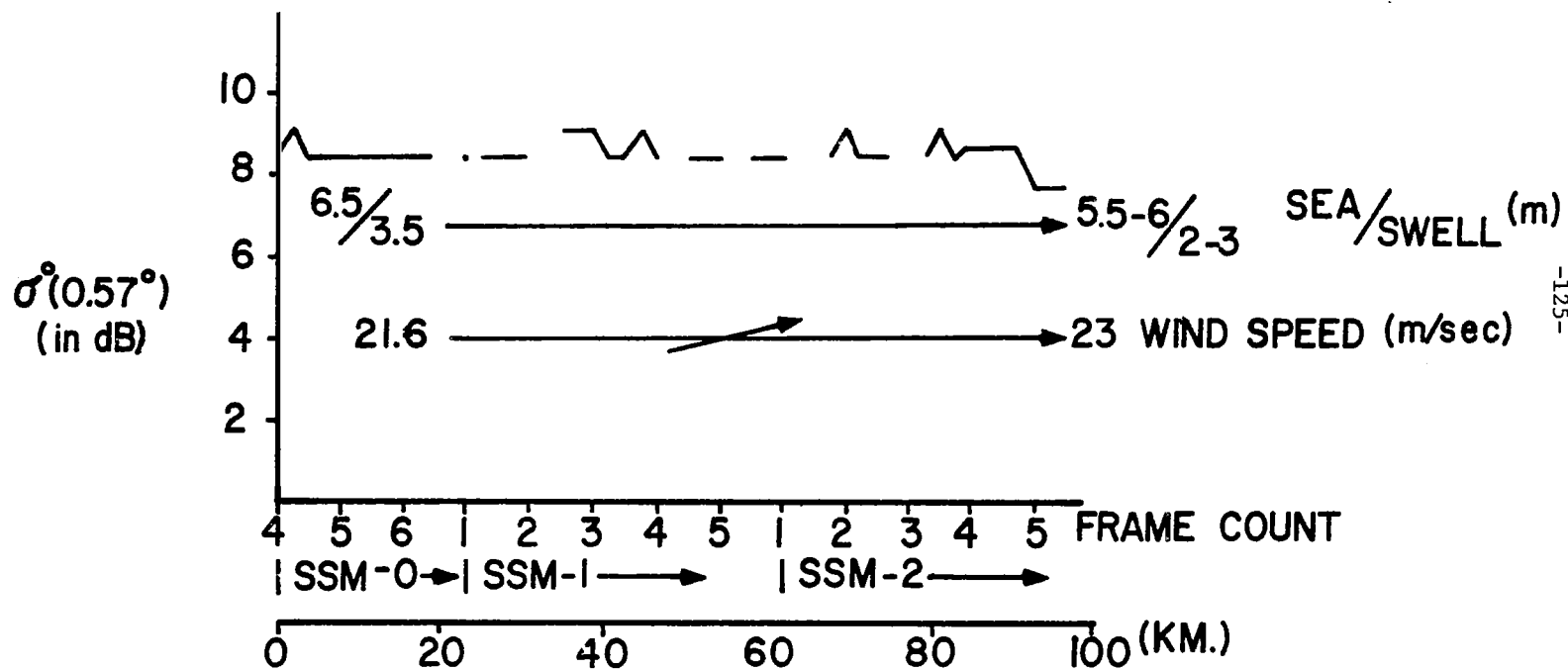


Figure 9. Measured σ^0 and corresponding surface conditions for SL-4 EREP Pass 83,
 Mode V (2 of 4), submode 0. (Add 0.1 dB for 0.6° pointing error in roll.)

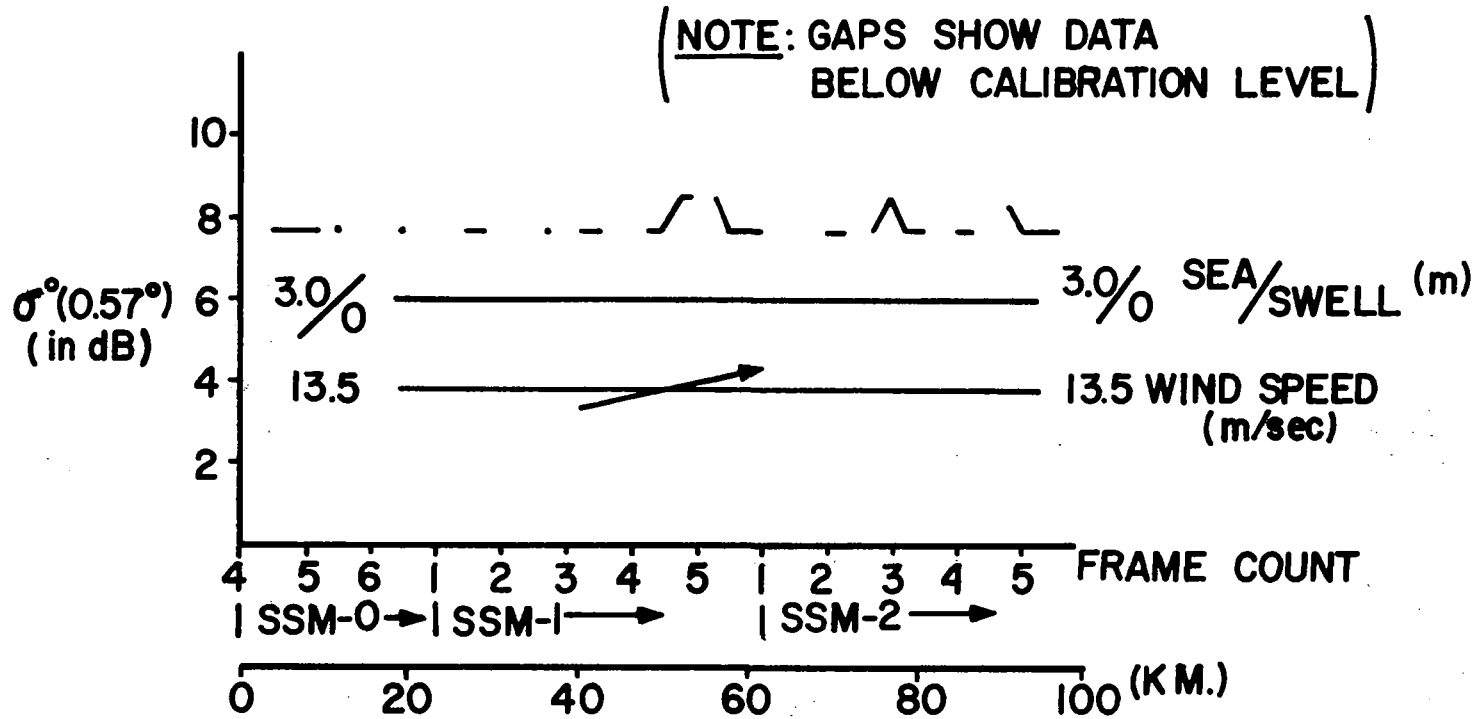


Figure 10. Measured σ^0 and corresponding surface conditions for SL-4 EREP Pass 83, Mode V (3 of 4), submode 0. (Add 0.1 dB for 0.55° pointing error in roll.)

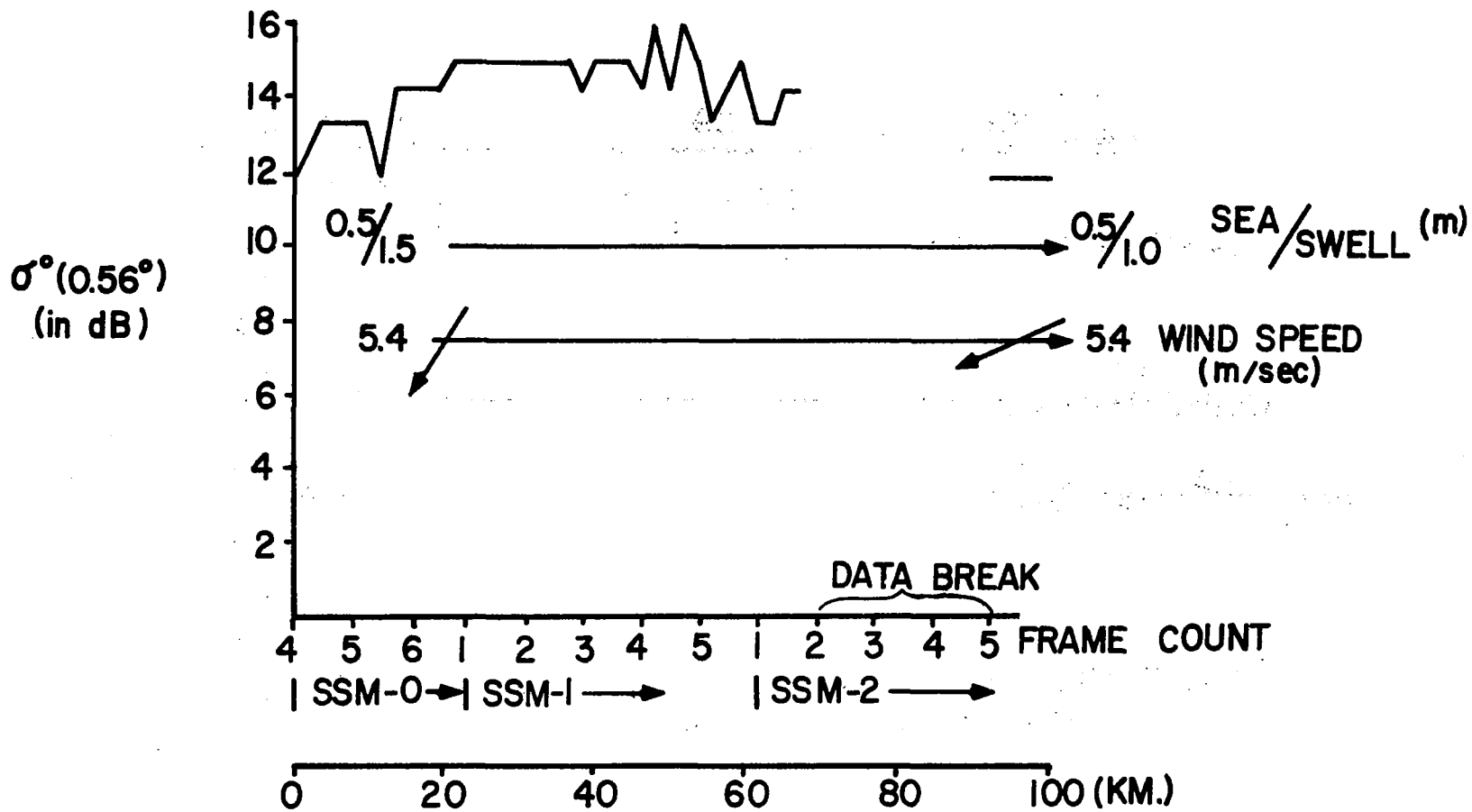


Figure 11. Measured σ^0 and corresponding surface conditions for SL-4 EREP Pass 86, Mode V (1 of 1), submode 0. (Add 0.1 dB for 0.6° pointing error in roll.)

trends in the data are clearly obvious and no real purpose would be served in smoothing the data. It should be noted that we have plotted the lower bound of σ° (pointing error in the pitch direction) with an indication of the correction to be used to obtain the upper bound. The choice in this case was totally arbitrary.

With the exception of the results in Figures 7 and 11, σ° is either nearly constant or exhibits a very small linear change. The sharp decrease shown in Figure 7 is interesting because the surface data does not indicate any significant departure from small waveheight and low wind speed conditions. The 15 to 16dB value at the start of the data span is considered to be about normal for the indicated surface conditions. There was no appreciable change in any of the radar "housekeeping" data during this interval and the calibration data did not show a system malfunction. In analyzing these data we have concluded that the indicated decrease in σ° is due to a change in spacecraft attitude, i.e. the pointing angle increased. We base this conclusion on the following facts: simultaneous with the decrease in σ° is an increase in altitude and an apparent change in the shape of the average return waveform. From the waveform data, we estimate that the pointing angle increased from $\xi_p \approx 0.6^\circ$ to $\xi_p \approx 1.0^\circ$; this would account for about 4dB of the indicated change. Thus, the last half of the data span in Figure 7 is in error and should be ignored.

Apart from the erroneous σ° data in Figure 7, we note that the variation in σ° values over the data span is in general agreement with the variation in surface truth. That is, neither data set show a large change over the ground track. Figure 11 does show about a 2dB rise in σ° which is not accompanied by a change in surface data. Figure 3 shows a 2dB decrease in σ° . In neither of these cases do we attribute the variation to changes in the radar system. Without more detailed surface data, it is not possible to identify the source of these variations.

3.1 Average σ° Variation with Surface Conditions

The σ° data presented in Figures 2 through 11 illustrate the degree of variation along the radar ground track. However, these measurements are on a much finer scale than the surface truth data. In order to reduce the two measurement sets to a common scale, we averaged the cross section data. In performing the averaging, we omitted certain data which were either known or suspected to be erroneous. For example, we did not include the last half of

the data in Figure 7 since there was an obvious pointing angle error. The data in Figure 10 were also ignored since the altimeter was very near unlock (as evidenced by the obvious data gaps) and the system calibration at this return power level was suspect.

For the data shown in Figures 12 through 14, we have split the data spans (shown in Figures 2 through 11) in half and computed an average value for σ° for both halves. The first half average is associated with the first noted surface data while the second half average is associated with the second indicated surface data. The resultant σ° averages were then plotted against individual surface parameters and selected combinations.

Figures 12 and 13 illustrate how the averaged σ° data varied with the wind driven significant waveheight and the swell significant waveheight, respectively. In constructing each of these plots we have ignored the existence of the other component of significant waveheight. As expected, these results are not particularly illuminating except to show that there is a trend toward an inverse relation between σ° and the wind driven significant waveheight. Based upon spectral analysis, a more realistic measure of significant waveheight would be the root-sum-square of the wind driven and swell components. A plot of the averaged σ° data versus this combination is shown in Figure 14. This figure clearly shows a reduced σ° resulting from larger waveheights. Also, it is particularly interesting to note the cluster of values for the root-sum-square greater than 6 meters. This result would tend to indicate that for large waveheights, there is not much variability in the resultant values of surface cross section for near normal incidence, as theory [5] predicts. We also note that the minimum average value is about 8.5dB which is considerably higher than previously reported aircraft-based measurements [2].

In constructing a plot of σ° versus surface wind speed we were more selective in forming the averaged values of σ° . That is, we chose to use only those frames of σ° data in the immediate vicinity of a point on the ground track where wind speed was indicated. Table II illustrates what frames were selected and the resultant values of averaged σ° along with the indicated wind speed. Figure 15 is a plot of the data in Table II. As noted in the case of Figure 14, we see that there is very little variability in the high wind speed values of σ° . It is obvious from this figure that we need more low wind speed data; we have σ° data for estimated low wind speed conditions, however, we need more hindcast surface data for these cases.

$\sigma^\circ(\psi)$
 $0.5^\circ \leq \psi < 1.0^\circ$
(in dB)

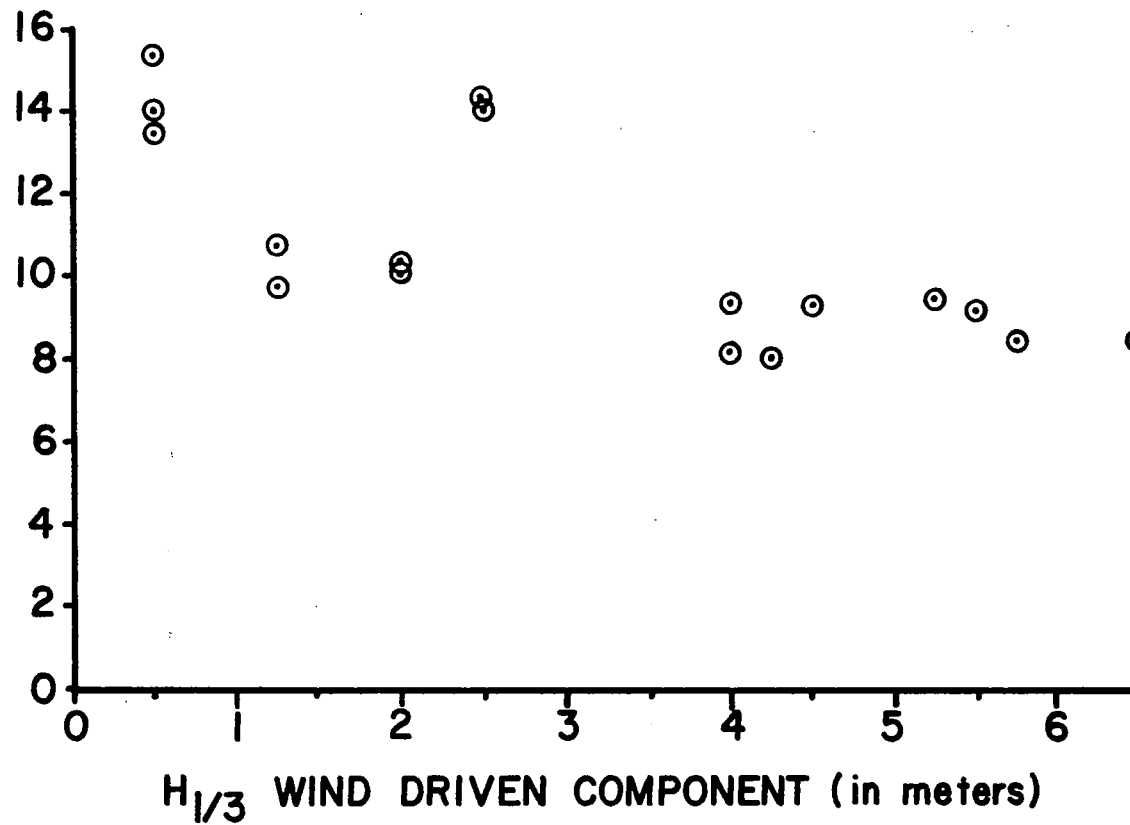


Figure 12. Variation of averaged σ° results as a function of wind driven significant waveheight.

$\sigma^\circ(\psi)$
 $0.5^\circ \leq \psi < 1.0^\circ$
(in dB)

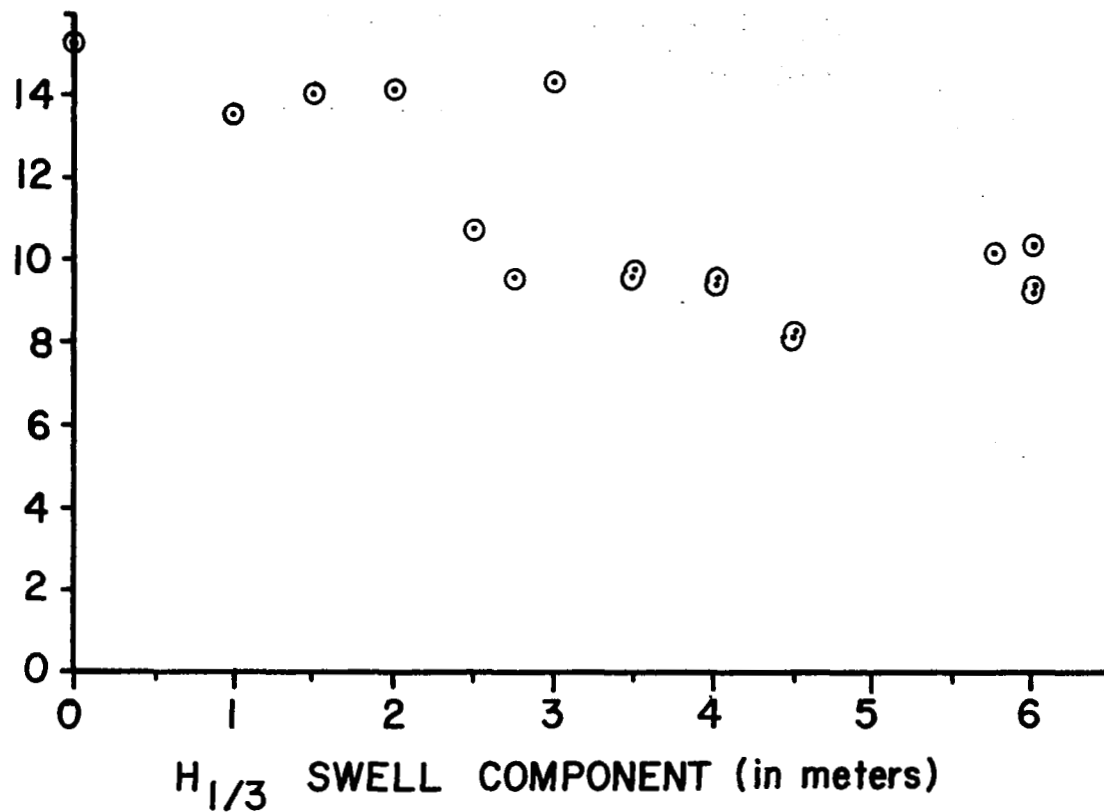


Figure 13. Variation of averaged σ° results as a function of swell significant waveheight.

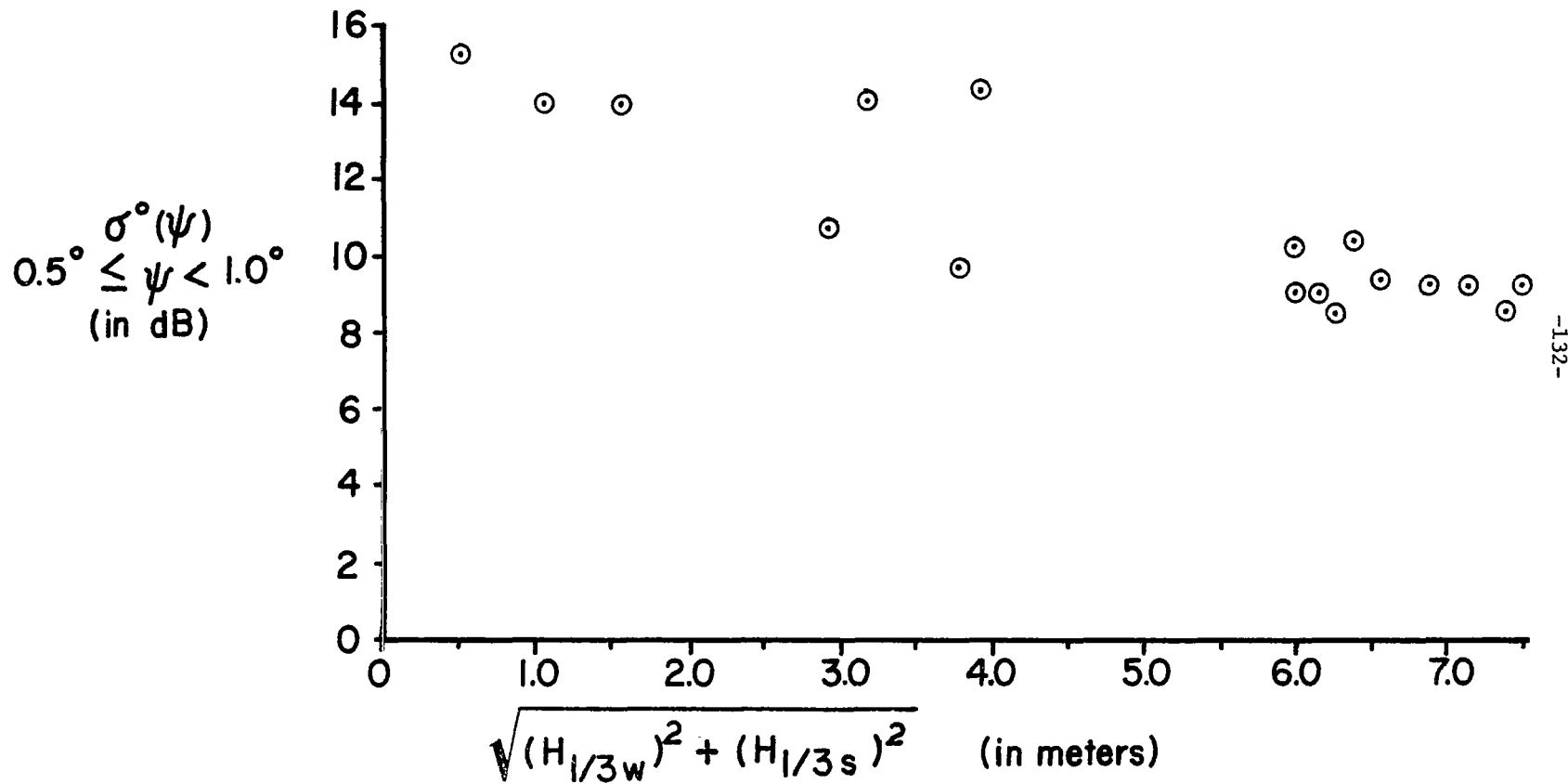


Figure 14. Variation of averaged σ° results as a function of the root-sum-square of the wind driven and swell significant waveheights.

TABLE II

Data Used to Construct Figure 15

EREP Pass and Mode V Designation	Averaging Interval (SSM & Frames)	Average σ° (ψ) (dB)	Average Wind Speed (m/sec)
76 (3 of 5)	SSM-0, 4-6	9.4	12.4
	SSM-1, 1-3	9.2	13.5
	SSM-2, 3-5	9.4	16.2
78 (2 of 2)	All of SM-0	10.4	10.8
79 (4 of 4)	SSM-0, 4-6	8.5	13.5
	SSM-2, 2-5	8.3	12.2
82 (1 of 4)	SSM-0, 4-6	14.6	6.5
83 (1 of 4)	All of SM-0	9.5	17.8
83 (2 of 4)	SSM-0, 4-6	8.5	21.6
	SSM-2, 2-5	8.6	18.9
83 (3 of 4)	All of SM-0	7.8	13.5
83 (4 of 4)	All of SM-0	8.6	~16.2
86 (1 of 1)	All of SM-0	13.9	5.4

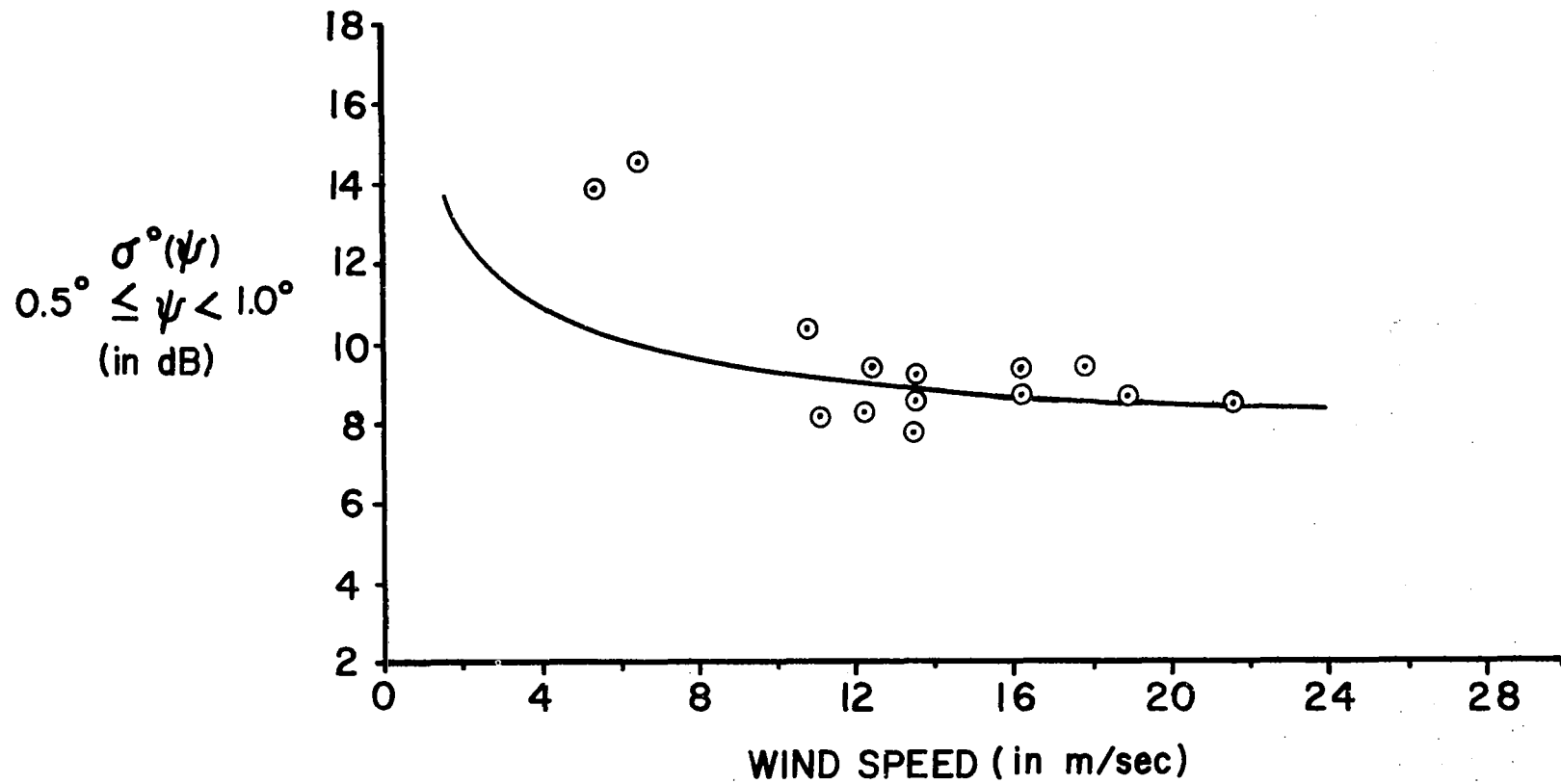


Figure 15. Variation of selected average values of σ° with wind speed.

Also, shown in Figure 15 is a theoretical curve [5] of σ° at normal incidence for a Fresnel reflection coefficient, $|R(0)|^2$, equal to -6dB. We see that the curve provides a very good fit to the high wind speed data. However, the nominal X-band reflection coefficient is about -2.1dB, corresponding to a dielectric constant equal to $55 + j 30.3$. The source of the 4dB difference is unknown at this time. It could be due to three distinctly different effects; (1) an inadequate theory, (2) a significantly different chemical content of the ocean in the North Atlantic, or (3) propagation loss*. Small wind speed data in the North Atlantic should greatly aid in resolving this question. Our present thoughts are that the 4dB discrepancy is probably due to propagation loss.

4.0 Summary

In this report, we have presented an initial comparison of near normal incidence σ° measurements from the S-193 radar altimeter with NOAA hindcast surface data. The available surface data corresponded, in general, to extremely rough conditions in the North Atlantic. We find a definite saturation effect (for high wind speeds) in the dependence of σ° upon wind speed; the smallest recorded value of σ° is about 8.5dB. We note a discrepancy of about 4dB between theoretical predictions and measurements at high wind speeds. The source of this disparity is unknown at the present time although it is expected to be due to propagation loss.

*Although we have ignored the effect, the actual tabulated data [4] for σ° does not account for propagation losses.

REFERENCES

1. Grant, C. R. and B. S. Yapple, "Backscattering from Water and Land at Centimeter and Millimeter Wavelengths," Proc. of I.R.E., vol. 45, pp. 976-982, 1957.
2. Guinard, N. W., "The Variation of the RCS of the Sea with Increasing Roughness," Microwave Observations of the Sea, Proceedings of the Spacecraft Oceanographic Project, pp. 175-203, NASA HQ, Washington, D. C., 1969.
3. Skolnik, M. I. (editor), Radar Handbook, Chapter 25, McGraw-Hill, New York, 1970.
4. Brown, G. S., "Reduced Backscattering Cross Section (σ^0) Data from the Skylab S-193 Radar Altimeter," NASA CR-141401, Applied Science Associates, Inc., Apex, North Carolina, October, 1975.
5. Miller, L. S., G. S. Brown and G. S. Hayne, "Analysis of Satellite Altimeter Signal Characteristics and Investigation of Sea-Truth Data Requirements," NASA-CR 137465, Research Triangle Institute, Durham, North Carolina, April, 1972.

CHAPTER 8

Measurements Of σ° As A Function Of Incidence Angle

by

G. S. Brown

1.0 Introduction

Mode II of the S-193 radar altimeter was designed for the purpose of measuring the variation of the surface scattering cross section with angle of incidence. To accomplish this purpose, the altimeter antenna was discretely stepped through the following nominal off-nadir angles; 0° , 0.4° , 1.3° , 2.6° , 7.6° and 15.6° . Apart from the nadir pointing case, data were acquired for about 29 seconds at each of the other angles of incidence. The ground track coverage resulting from the Mode II pointing angle sequencing and the elapsed data acquisition time is shown in Figure 1. The horizontal bars indicate the segment of ground track covered by each submode or pointing angle. The gap between submode 1 and 2 results from a stepping of the antenna from 0.4° to 15.6° in the forward along-track direction; over this ground track gap, no cross section data was acquired by the altimeter. Of particular significance in this figure is the fact that a complete sequencing through all of Mode II encompasses a ground track coverage of nearly 1300 km. Since it is highly unlikely that identical surface conditions existed over the full 1300 km, we must be very careful in comparing the data from the different submodes or angles of incidence. For example, the shaded areas in Figure 1 correspond to those portions of the ground track which were covered by two submodes or pointing angles. Thus, within these common portions of ground track, we are justified in comparing the cross section data obtained by the two appropriate submodes. That is, we can compare the data as follows;

$\sigma^\circ(15.5^\circ)$ with $\sigma^\circ(7.6^\circ)$
 $\sigma^\circ(7.6^\circ)$ with $\sigma^\circ(2.6^\circ)$
 $\sigma^\circ(2.6^\circ)$ with $\sigma^\circ(1.3^\circ)$
 $\sigma^\circ(1.3^\circ)$ with $\sigma^\circ(0^\circ)$

However, in comparing 0° data with 15.5° data we would be comparing data sets which are roughly 690 km apart and it is certainly conceivable that the surface

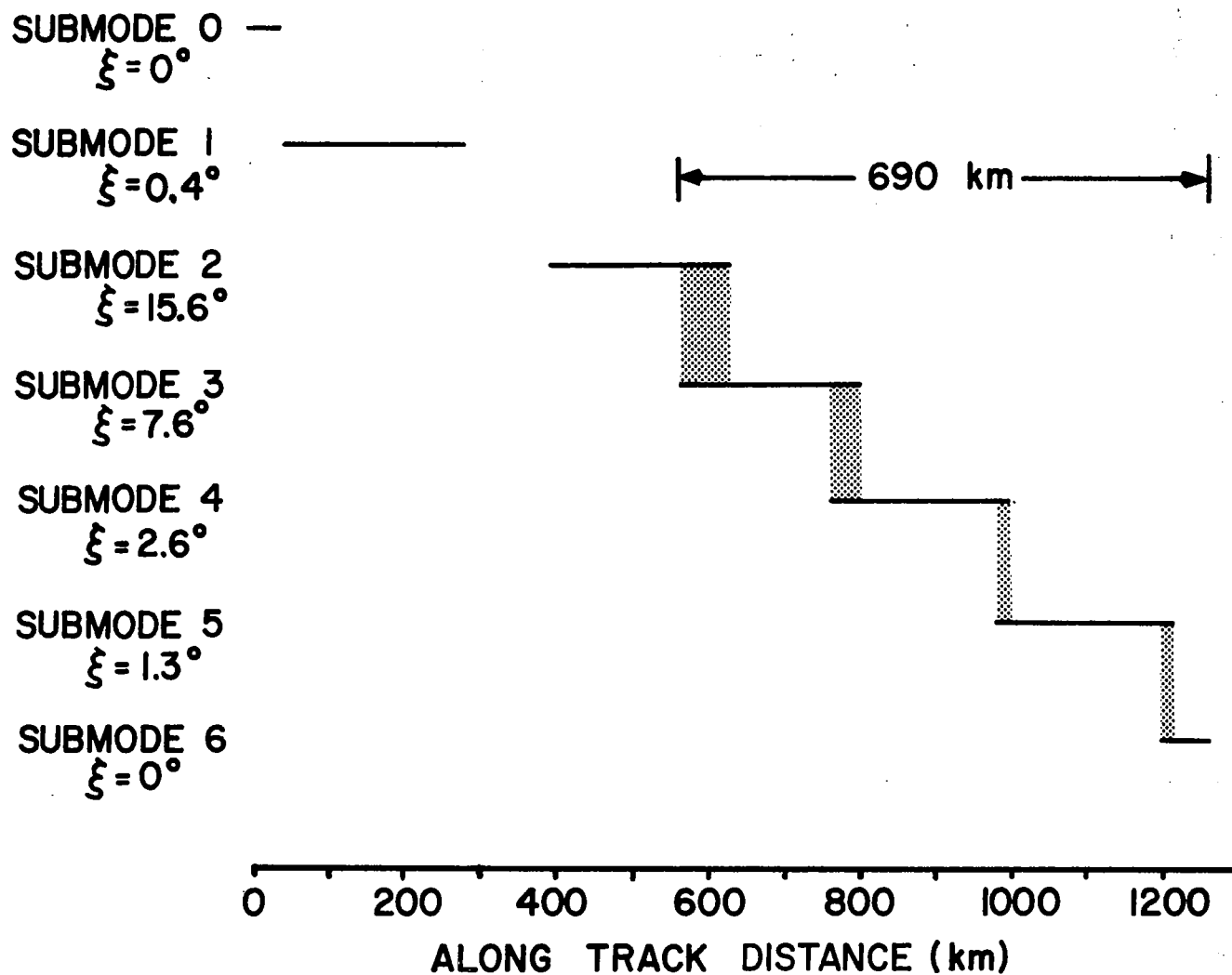


Figure 1. Mode II ground track coverage as a function of submode and pointing angle. The shaded regions correspond to distance intervals where overlapping data were acquired.

conditions are not constant over this distance. As was the case with most S-193 altimeter measurement results, we see that the data should not be interpreted without due regard to how they were acquired.

Since the altimeter was time-shared with the radiometer and the scatterometer, only a limited number of data passes were available for its operation. The original usage plan for Mode II was to employ it sparingly during SL-2 and SL-3 and then to increase its operation during SL-4. This plan was predicated on the desire to obtain Mode II data during high sea state conditions which, in turn were most probable during SL-4. Unfortunately, the loss of antenna scan capability near the end of mission SL-3 defeated the plan since the antenna was fixed at nadir during all of SL-4. Consequently, only a very small quantity of off-nadir σ° data were acquired. Of the two over-water Mode II data passes during SL-2, only one produced reducible data. For SL-3 the total number of over water Mode II passes was four, however we were only able to reduce the data from one pass. The SL-2 data resulted from EREP pass 9 (12 June 1973) while the SL-3 data came from EREP pass 17 (9 August 1973). A strip map showing the approximate location of the passes is contained in Figure 2; the direction of travel of the spacecraft was from north to south.

2.0 Analysis

Typical data segments from [1] are shown in Figures 3 and 4 as a function of elapsed time and distance. As expected, there is some variation in the average value of σ° , apart from the quantization, as a function of along-track distance. Unfortunately, this variation could be due to either a change in surface conditions or a drift in the spacecraft attitude control system, i.e. a change in pointing. As noted in the pointing angle summary in [1], there was a long term drift in the pointing for both pass 9 and 17, i.e. about one degree over the entire portion of the pass during which time the altimeter was operated. However, the sensitivity of the altimeter's AGC to one or two degrees angle change when the nominal pointing angle is 15° is very small [1]. Thus, the one decibel change in σ° for $\psi=15.5^\circ$, as shown in Figure 4, is most probably due to spatially varying conditions. In general, we estimate that the change in σ° as a function of distance is a direct result of changing surface conditions and not attitude drift.

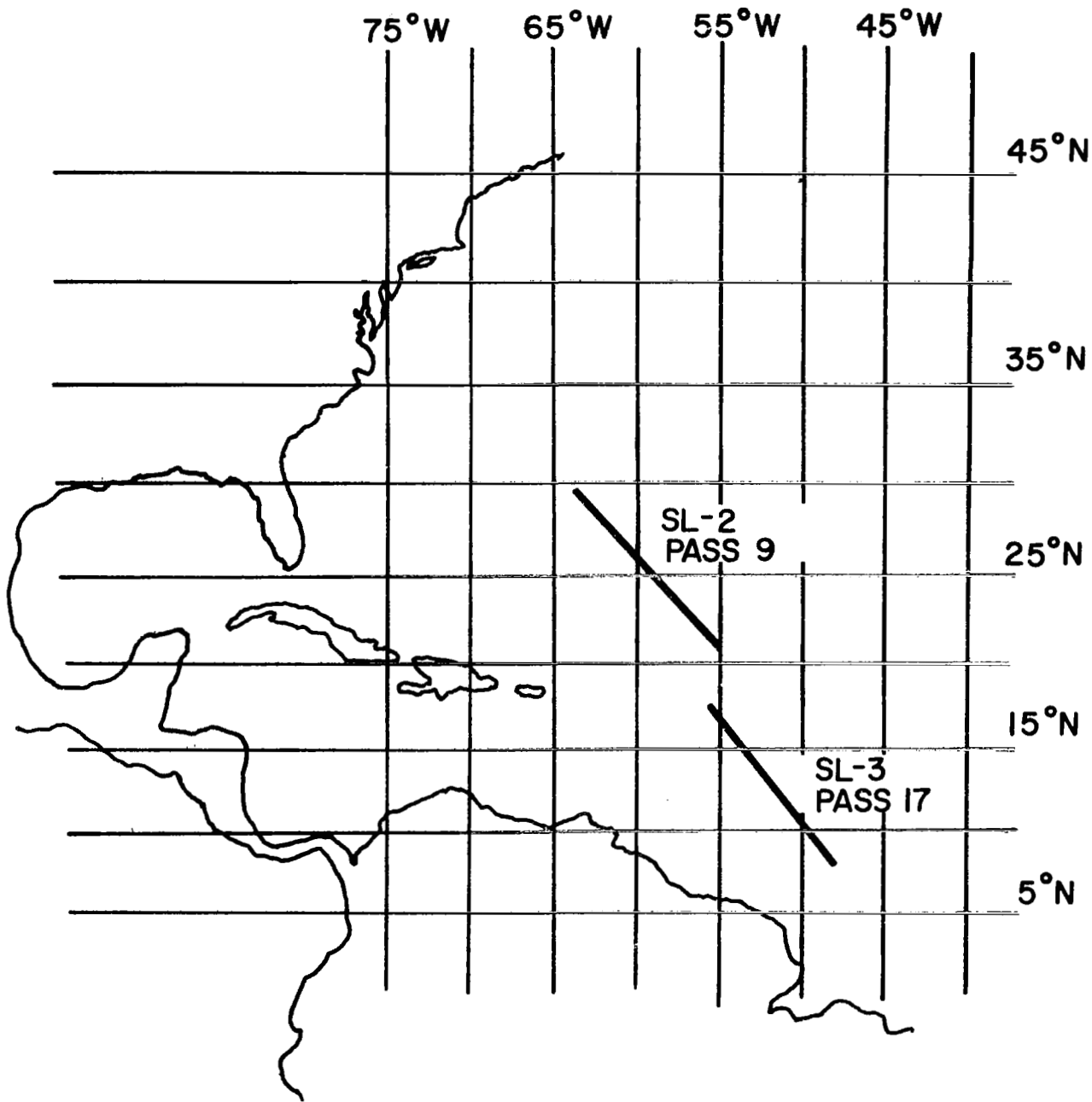


Figure 2. Relative location of the two Mode II passes for which the data could be reduced.

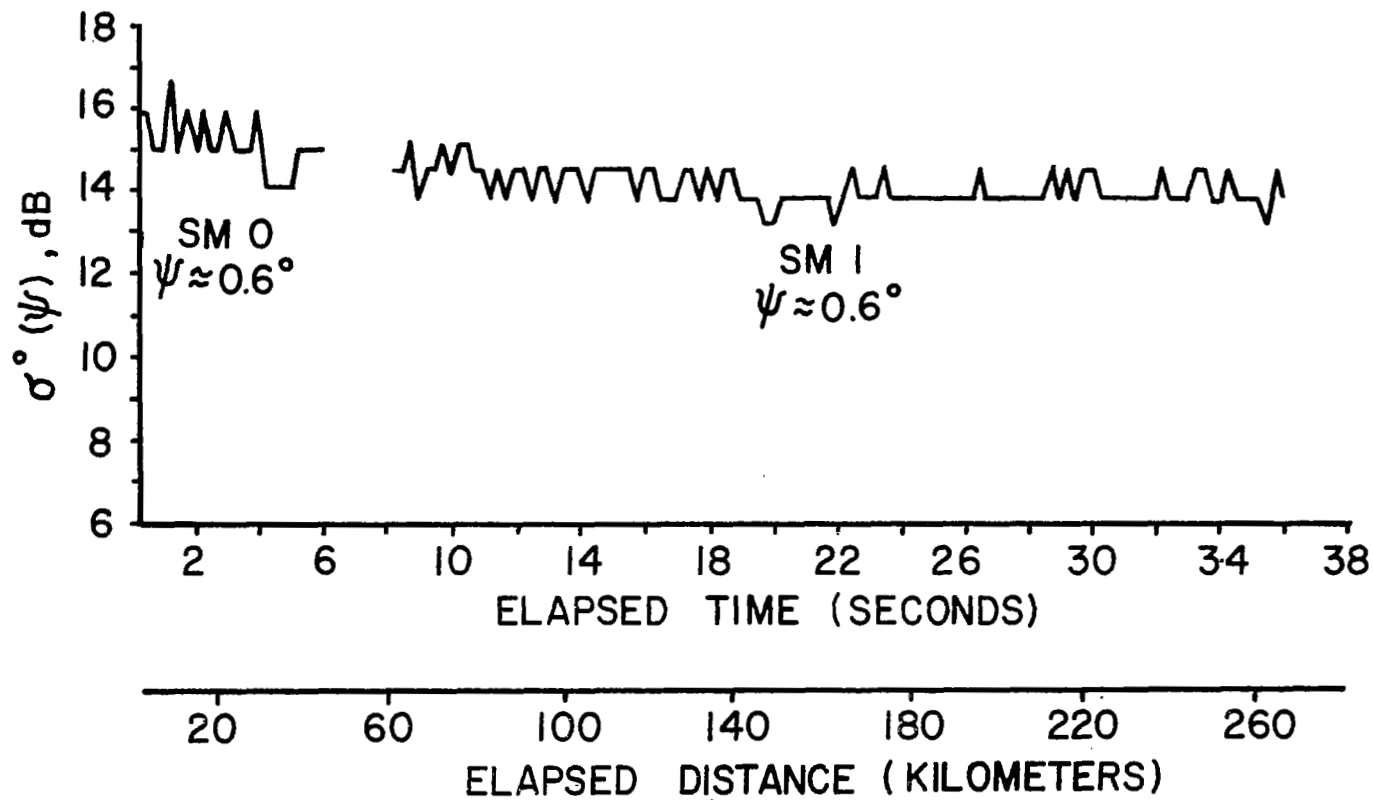


Figure 3. Variation of σ^0 as a function of elapsed time and distance for SL-2 EREP Pass 9, submodes 0 and 1.

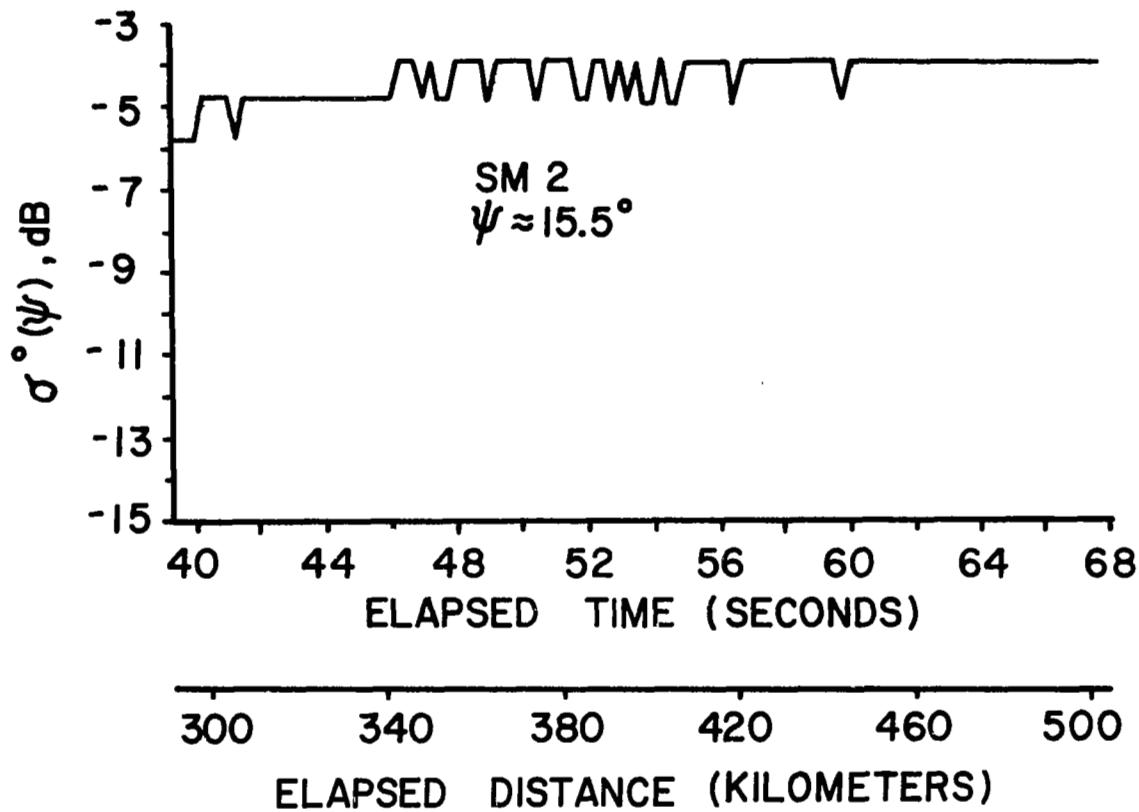


Figure 4. Variation of σ^0 as a function of elapsed time and distance for SL-2 EREP Pass 9, submode 2.

The reduced average values of σ° for EREP passes 9 and 17 are shown in Table I. Since there was some variation in the measured values over the 29 seconds data acquisition period, the average values at both the start and end of the period are presented. The data from submode 0 is not shown since the submode 6 data were more representative of the surface conditions for the majority of the other submodes; both submode 0 and 6 correspond to the (nominal) 0° incidence angle. Since the data set for each pass comprises about a 1000 km ground track, it is highly unlikely that the surface statistics were constant over this spatial extent. This fact is probably a significant contributor to the change in measured σ° values between start and end of the data acquisition periods. Plots of the data in Table I are shown in Figures 5 and 6. The horizontal bar indicates the average value at the start of the submode while the circled point corresponds to the average value at the end of the submode.

Unlike the extensive ground truth compilation accomplished for the near coastal portions of the ground tracks for these two passes (see Chapter 5), no surface truth data were obtained for these ground tracks. However, it is interesting to speculate on the surface conditions implied by these measurements. First, the rather rapid decrease in σ° with angle of incidence would seem to imply a relatively calm surface. For surface wind speeds on the order of 7 m/sec, the S-193 Scatterometer measured $\sigma^\circ \approx 1$ dB for an angle of incidence of about 17° [2]; the data in Figures 5 and 6 is $\sigma^\circ \approx -4.5$ dB for an incidence angle of 15.5° .

In a previous analytical work [3], expressions were obtained for the surface height autocorrelation coefficient for a slightly modified Pierson-Moskowitz spectrum, i.e.

$$\rho_n(r) = \left[1 + .125/(ar)^2 \right] (ar)K_1(ar) - (ar)^2 K_0(ar) \quad (1)$$

where the wind speed dependence is contained in the constant a as follows;

$$a^2 = \frac{\alpha g^2}{3W^4}$$

and $\alpha = 0.74$, $g =$ acceleration of gravity (980 m/sec^2), and W is the 10-meter height wind speed. The functions $K_1(\cdot)$ and $K_0(\cdot)$ are Bessel functions of

TABLE I

Tabulation Of Measured σ° Values As A Function Of
Angle Of Incidence For EREP Passes 9 And 17

SL-2 EREP PASS 9

ESTIMATED ANGLE OF INCIDENCE	σ°	
	START OF DATA ACQUISITION	END OF DATA ACQUISITION
15.5°	-4.8 dB	-3.9 dB
7.6°	6.4 dB	6.4 dB
3.2°	12.7 dB	11.4 dB
1.9°	12.2 dB	11.8 dB
0.6°	12.6 dB	12.5 dB

SL-3 EREP PASS 17

ESTIMATED ANGLE OF INCIDENCE	σ°	
	START OF DATA ACQUISITION	END OF DATA ACQUISITION
15.5°	-5.2 dB	-4.6 dB
7.1°	4.5 dB	3.7 dB
2.2°	9.7 dB	9.7 dB
1.6°	11.3 dB	11.9 dB
0.6°	12.8 dB	12.4 dB

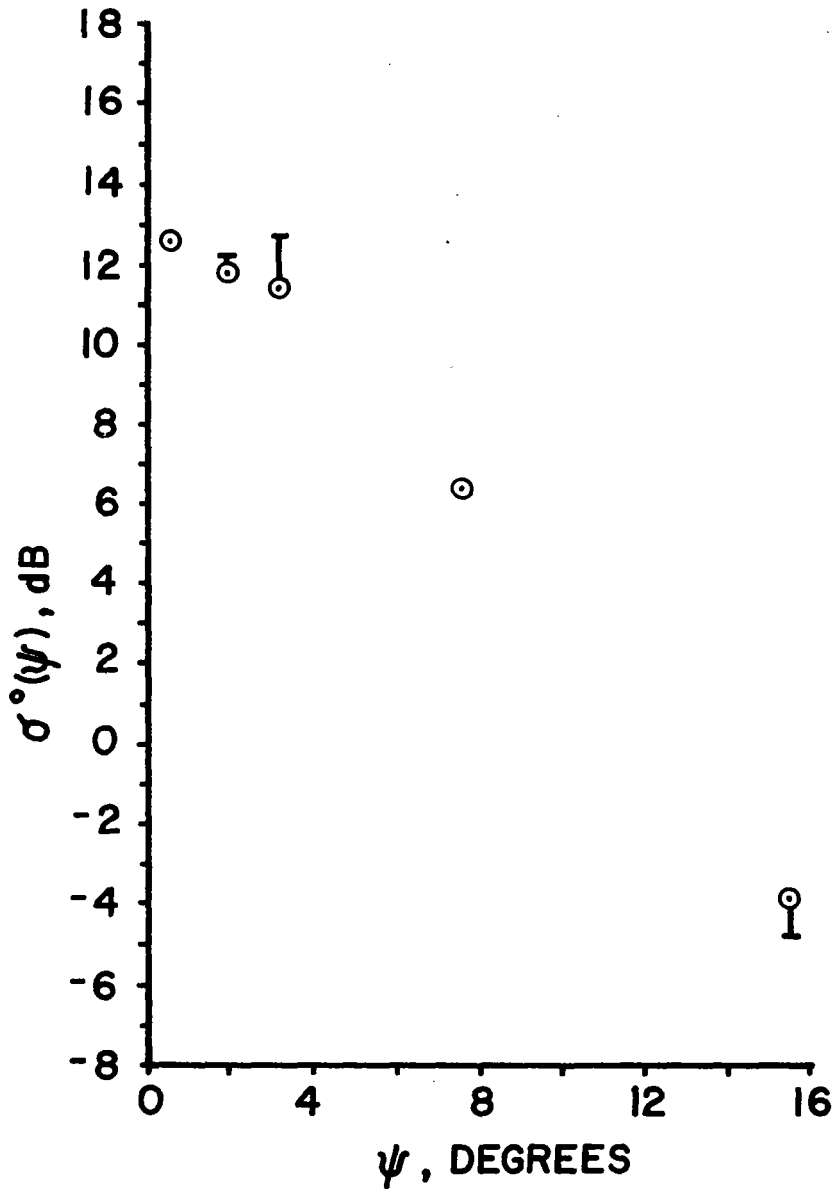


Figure 5. σ^o data from SL-2 EREP Pass 9 as a function of angle of incidence (see text for an explanation of the vertical bars).

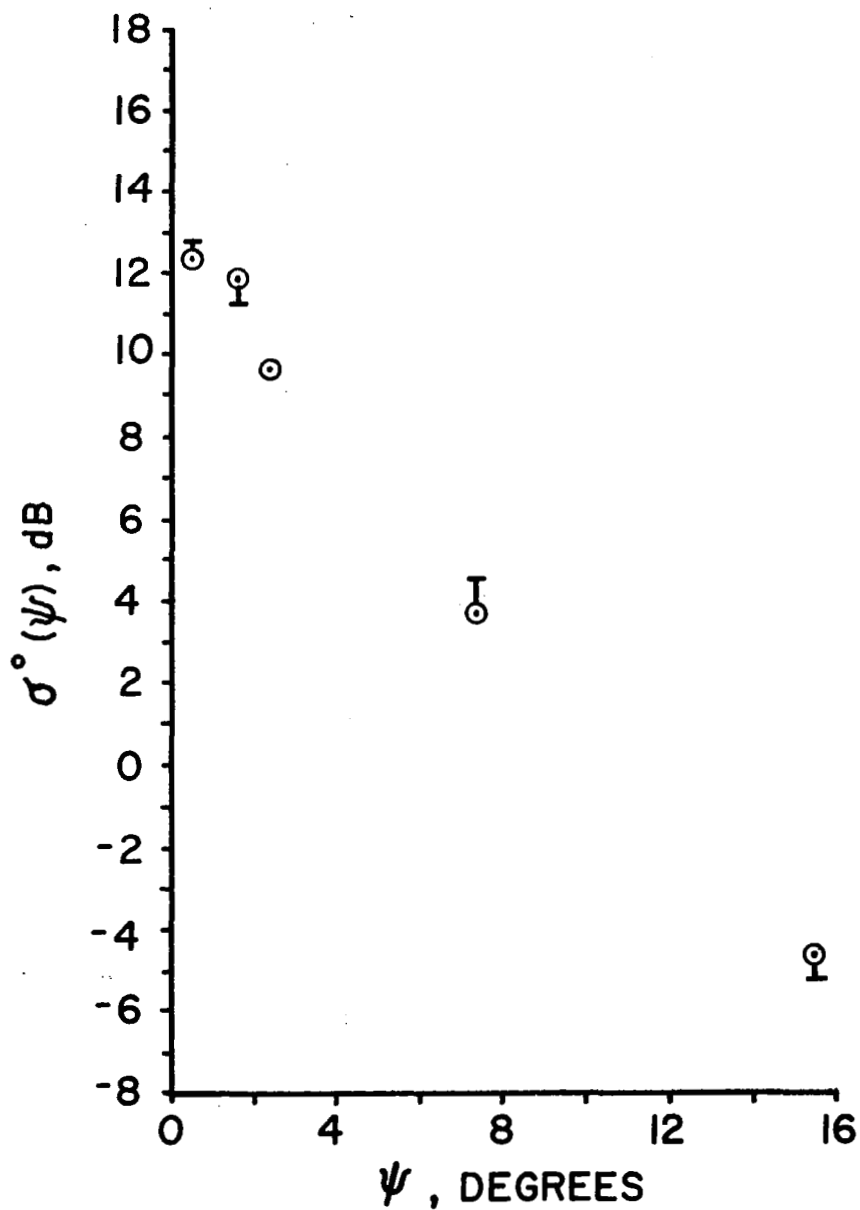


Figure 6. σ° data from SL-3 EREP Pass 17 as a function of angle of incidence (see text for an explanation of the vertical bars).

the second kind. If (1) is substituted in the appropriate equation for $\sigma^\circ(\psi)$, i.e.

$$\sigma^\circ(\psi) = \frac{k_o^2 |R(0^\circ)|^2}{\cos^2 \psi} \int_0^\infty J_o(2k_o r \sin \psi) e^{-4k_o^2 \bar{\zeta}^2 \cos^2 \psi [1 - \rho_n(r)]} r dr, \quad (2)$$

where $k_o = 2\pi/\lambda_o$ ($\lambda_o = 0.0216$ m.), $|R(0^\circ)|^2$ is the Fresnel power reflection coefficient at normal incidence, ψ is the angle of incidence, and $\bar{\zeta}^2$ is the mean square surface height, a reasonable fit to the data for EREP Pass 9 is obtained for $2.2 \text{ m/sec} \leq W \leq 2.7 \text{ m/sec}$ and $|R(0)|^2 = -5.5 \text{ dB}$ as shown in Figure 7. It should be noted that the theoretical curves in Figure 7 were obtained by numerical integration of (2) using the complete expression for $\rho_n(r)$ as given by (1). If it is assumed that the autocorrelation coefficient can be numerically approximated by a two-term quadratic expression, we obtain the standard mean square slope approximation for $\sigma^\circ(\psi)$, i.e.

$$\sigma^\circ(\psi) \approx \frac{|R(0)|^2}{\bar{\zeta}_t^2 \cos^4 \psi} \exp\left(-\frac{\tan^2 \psi}{\bar{\zeta}_t^2}\right), \quad (3)$$

where $\bar{\zeta}_t^2$ is the mean square slope of the two dimensional surface. Using the results from [4] to infer a mean square surface slope for the above wind speeds, i.e.

$$\begin{aligned} W = 2.2 \text{ m/sec} &\rightarrow \bar{\zeta}_t^2 = 0.0206 \\ W = 2.7 \text{ m/sec} &\rightarrow \bar{\zeta}_t^2 = 0.0222, \end{aligned}$$

and substituting in (3), we find for $|R(0)|^2 = -4.2 \text{ dB}$ the theoretical results shown in Figure 8. The fact that (3) does not provide a good fit to the data is not a matter of an incorrect value of $\bar{\zeta}_t^2$; it is, instead, due to the fact that the approximations used in going from (2) to (3) breakdown for small wind speeds, as previously shown [3]. That is, for large wind speeds ($W \gtrsim 10 \text{ m/sec}$) the mean square slope approximation is justifiable; however, for small wind speeds, such as in this case, the autocorrelation coefficient cannot be adequately approximated by a two term series. Thus, for the data from EREP Pass 9, it would appear that the surface is not highly disturbed and the surface wind speed is on the order of 2 to 3 m/sec.

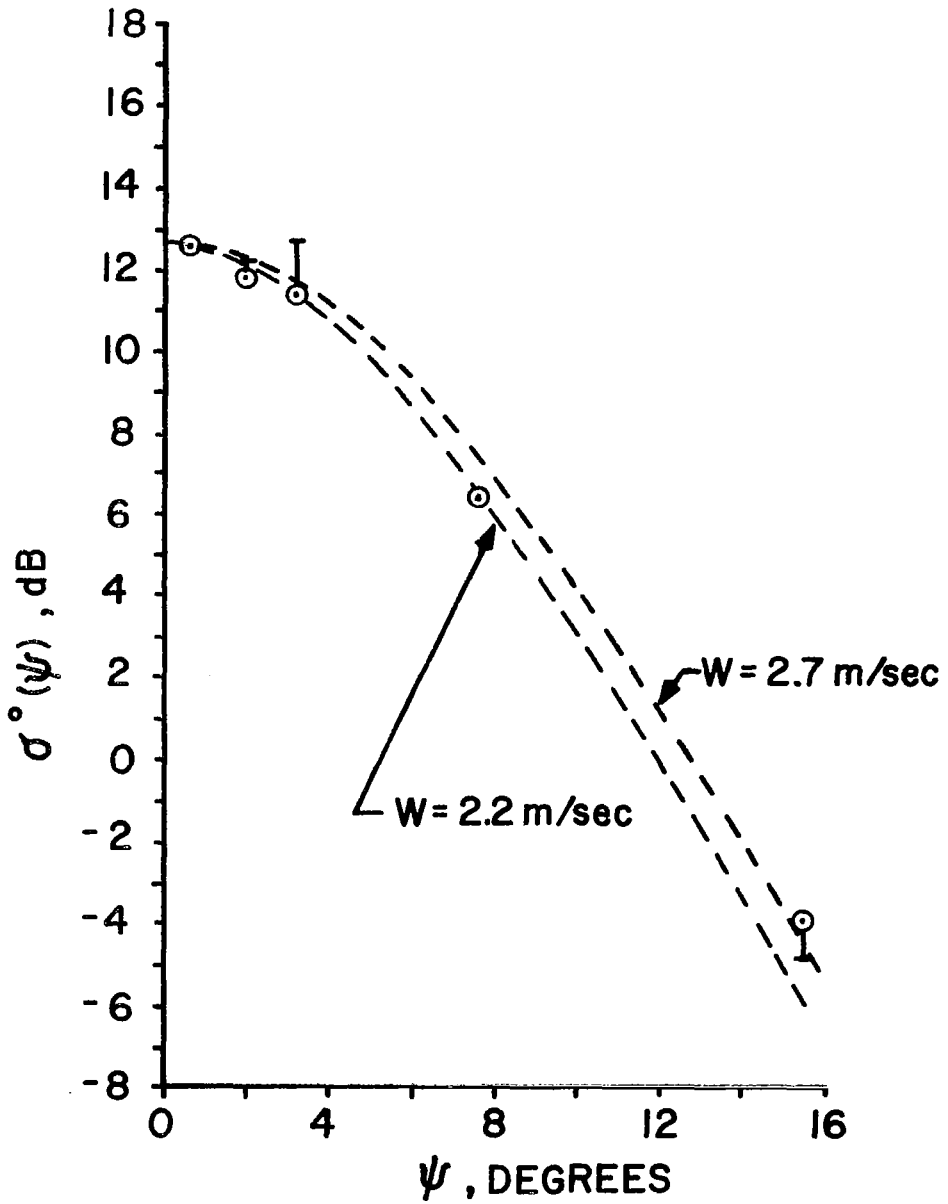


Figure 7. Comparison of EREP Pass 9 data with numerical integration results using the autocorrelation coefficient in equation (1).

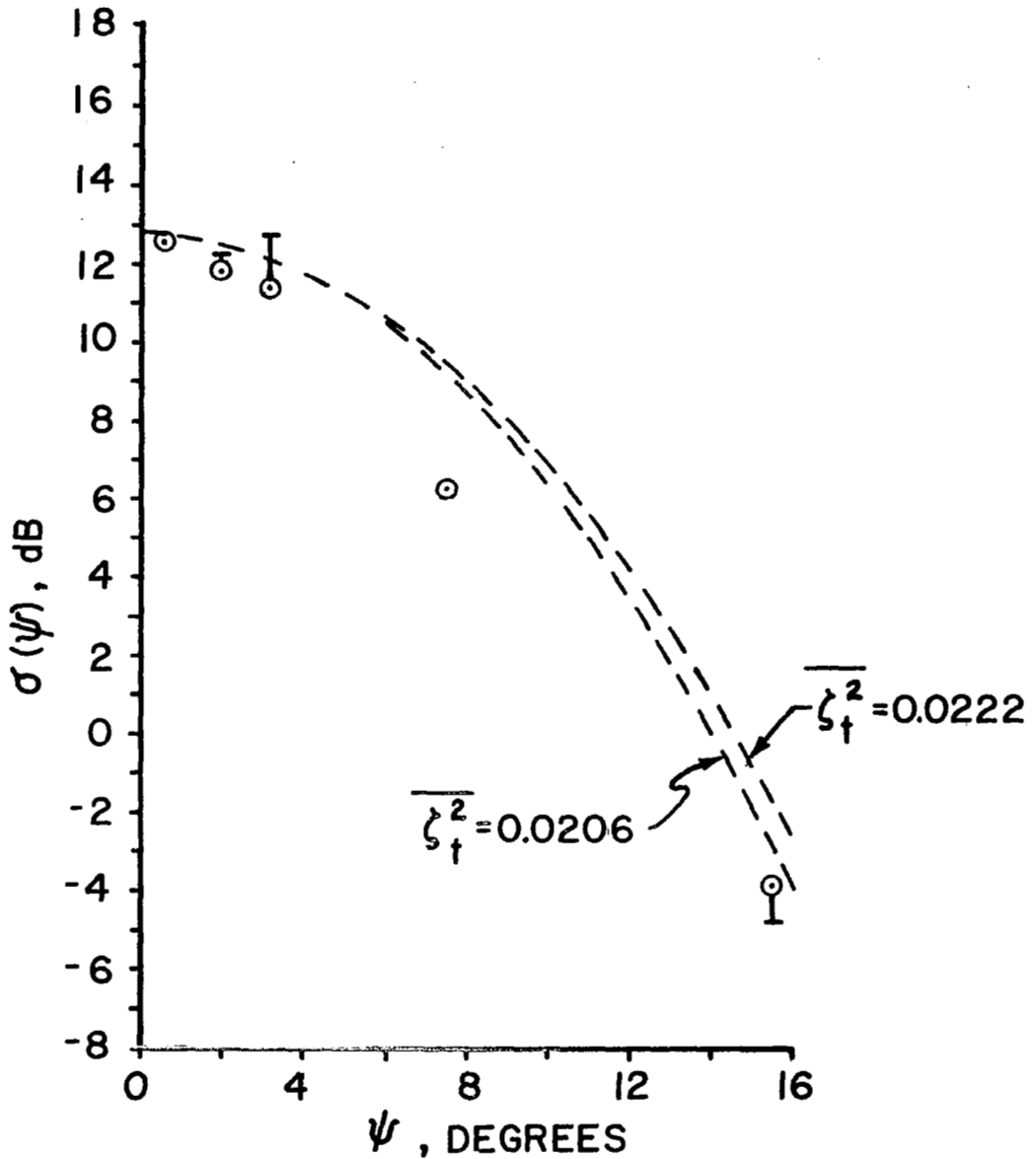


Figure 8. Comparison of EREP Pass 9 data with the mean squared slope approximation results (wind speed = 2.2 and 2.7 m/sec).

For the data obtained during EREP Pass 17, the agreement between measurements and theoretical computations is not good. For example, Figure 9 is a comparison of the measurements and the results from equation (2) for a wind speed of 1.6 m/sec. Below this value of wind speed, there are numerical convergence problems with (2) and the computations are not reliable. Figure 9 does show that the measurements are not adequately explained by the theory. Assuming that surface homogeneity is not a significant problem, there are still a number of approximations and assumptions inherent in equations (1) and (2). Certainly the most questionable are the spectral approximation of an equilibrium range and the jointly Gaussian distribution of surface height and slope assumption. Particularly disturbing in the data of Figure 9 are the σ° values at 2.2 and 7.1 degrees; these measurements indicate a significant departure from the expected behavior. In the absence of any ground truth, it would be pure folly to attempt to determine the source of the disparity between the theory and the measurements.

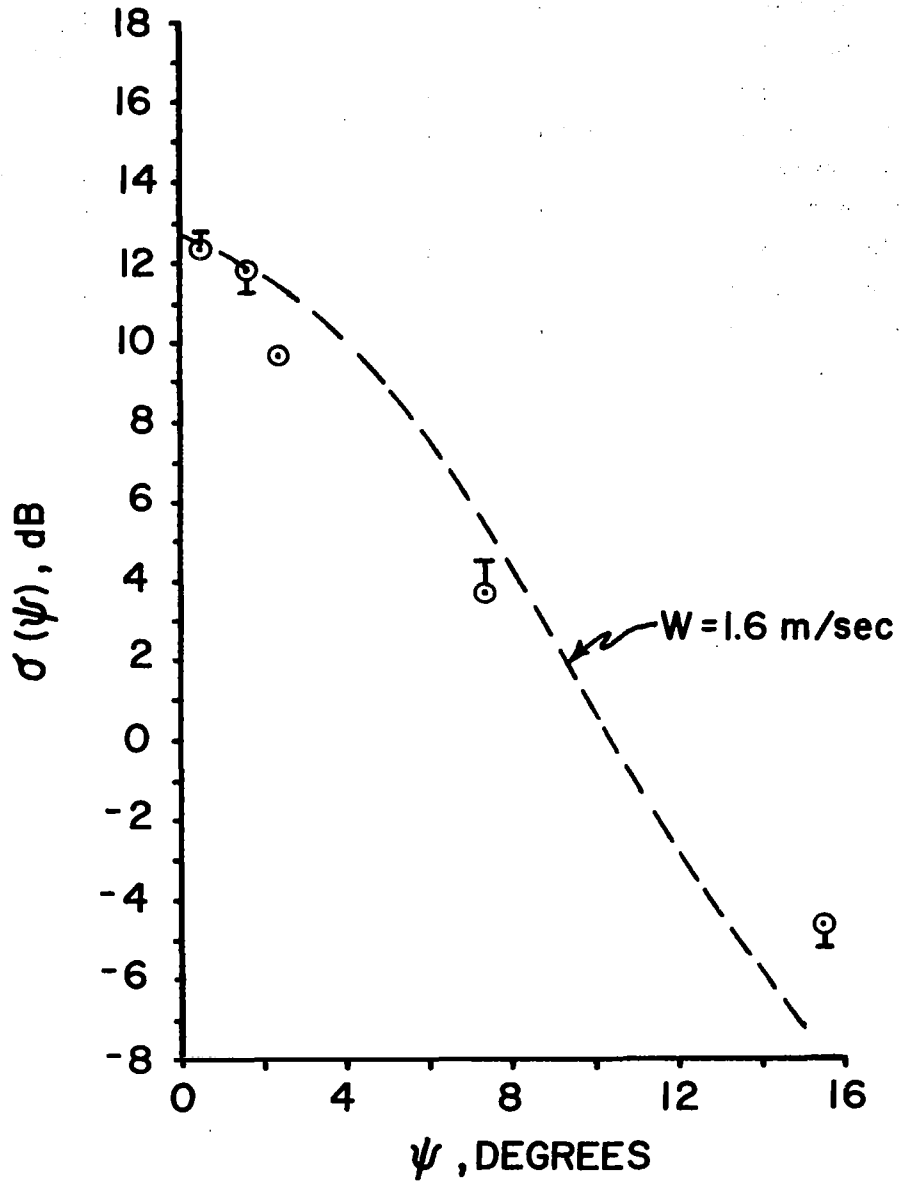


Figure 9. Comparison of EREP Pass 17 data with numerical integration results using the autocorrelation coefficient in equation (1).

REFERENCES

1. Brown, G. S., "Reduced Backscattering Cross Section (σ°) Data From The Skylab S-193 Radar Altimeter," NASA CR-141401, Applied Science Associates, Inc., Apex, N. C., October, 1975.
2. Krishen, K. and D. J. Pounds, "S-193 Scatterometer Backscattering Cross Section Precision/Accuracy For Skylab 2 and 3 Missions," Report No. LEC-6119, Lockheed Electronics Co., Aerospace Systems Div., Houston, Texas, June, 1975.
3. Miller, L. S., G. S. Brown and G. S. Hayne, "Analysis Of Satellite Altimeter Signal Characteristics and Investigation of Sea-Truth Data Requirements," NASA CR-137465, Research Triangle Institute, Durham, N. C., April, 1972.
4. Wu, J., "Sea Surface Slope and Equilibrium Wind-Wave Slope," Physics of Fluids, Vol. 15, May 1972.

CHAPTER 9

An Examination of Near Normal Incidence Backscattering
From The Great Salt Lake Desert Area of Utah

by

G. S. Brown

1.0 Introduction

The Skylab radar altimeter provided experimenters with very high angular resolution scattering measurements at near normal angles of incidence. These measurements were obtained through the use of a peak averaging AGC system along with high speed Sample and Hold (S&H) circuitry which acquired samples of the return power as a function of delay time on a near pulse-by-pulse basis. Along with the altitude measurements, these data provided the capability of measuring σ° as a function of angle of incidence for very near normal incidence and, in addition, identifying and classifying surface scattering regimes.

This latter capability proved to be most beneficial in view of some of the data obtained from the Skylab radar altimeter. McGoogan, et al. [1] first reported the existence of over land average return waveform data which did not appear to be characteristic of random rough surface scattering. Shapiro and Yaplee [2], through analysis of the interpulse correlation, concluded that these types of land returns were due to a specular scattering surface.

In this chapter, we conduct a somewhat more in-depth study of one particular terrain scattering case. We first review the various types of surface scattering as originally classified by Moore and Williams [3]. We then investigate the data obtained from the Skylab altimeter while over the Great Salt Lake Desert area west of Salt Lake City. Particular attention is given to surface statistical homogeneity and the resultant limitations imposed upon the number of pulses that can be averaged. In addition, we find that interpulse correlation is not a sufficient measure of surface specularity since it does not eliminate the possibility of a fluctuating but non fading return.

For this particular case, although the average received power is comparable to that reflected by a specular surface, the fluctuating nature of the return does not support the hypothesis of a purely specular reflecting

surface. We show that this case can be explained as one for which the mean squared surface height is large compared to the rf wavelength but the surface height correlation length is so large that the effective mean squared surface slope is very small. It is also demonstrated that such surfaces can backscatter power the average of which is comparable to the return from a specular reflecting surface and that σ° for these cases approaches a delta function in angular dependence. Aircraft-based laser profilometer data from the same general area also support this interpretation of the behavior of σ° while refuting the specular hypothesis.

1.1 Classification of Extended Target Scattering Surfaces

Based upon airborne pulsed altimeter results, Moore and Williams [3] classified and developed analytical models for the average return power from three distinctly different types of surfaces. These types were called random, specular and large body.

The random surface is characterized by a surface roughness which is large relative to the carrier wavelength of the radar and a correlation length that is small relative to the illuminated area. When the rms roughness of the surface height (relative to a mean flat surface) is small in relation to the pulse width of the radar and doppler effects can be ignored, the average return power as a function of two-way delay time is a convolution of the system point target response, $P_{PT}(\tau)$, with the flat surface impulse response, $\bar{P}_{IR}(\tau)$;

$$\bar{P}_r(\tau) = \begin{cases} \int_{-\infty}^{\tau} P_{PT}(\hat{\tau}) \bar{P}_{IR}(\tau - \hat{\tau}) d\hat{\tau} & \tau \geq 0 \\ 0 & \tau < 0 \end{cases} \quad (1)$$

where τ is the total two-way delay time between time of transmission and time of receipt of the return minus $2h/c$, h is the height of the radar above the mean flat surface and c is the speed of light. When the boresight of the radar antenna is normal to the mean surface and the antenna pattern is azimuthally symmetric, the flat surface impulse response is given by

$$\bar{P}_{IR}(\tau) = \begin{cases} \frac{P_T c \lambda^2}{4(4\pi)^2 L_p} \frac{G^2(\theta) \sigma^0(\theta)}{h^3 \left(1 + \frac{c\tau}{2h}\right)^3} & \tau \geq 0 \\ 0 & \tau < 0 \end{cases} \quad (2)$$

where we have also assumed that σ^0 is dependent only on the magnitude of the angle of incidence relative to the normal to the surface and not on the direction of incidence. In (2), L_p is the two-way path loss and $G(\theta)$ is the antenna gain. We have also chosen to include the peak transmitted power, P_T , in (2) in order to use a normalized form for $P_{PT}(\tau)$ in (1). The angle θ is related to τ in the following manner for typical satellite heights [10];

$$\tan \theta \approx \left[\frac{c\tau}{h} \right]^{1/2}$$

We note from equations (1) and (2) that the dependence of $\bar{P}_T(\tau)$ upon delay time is determined by how rapidly σ^0 varies with θ , or, equivalently, τ . Only for the case where σ^0 approaches a delta function will the average return resemble the system point target response. While equation (1) describes the mean return, on a pulse-by-pulse basis the returns will appear to be no different from noise. That is, to the extent that there is pulse-to-pulse independence, the individual returns will not necessarily resemble the average return. Equation (1) represents the mean of a nonstationary process whose probability density function and autocorrelation are a function of the receiver filtering and detection characteristics.

Specular reflection is significantly different from rough surface scattering in that the energy returned by the surface to the radar is determined by the mechanism of reflection. For specular reflection, the surface must be very smooth, flat and large. Exact criteria have not been developed, however an accepted criterion is that the rms surface roughness should be less than $\lambda/10$ [5], where λ is the wavelength of the incident rf energy, and the surface should obey this criterion at least over the first Fresnel zone on the surface. For specular surface reflection, the return power as a function of delay is given by [4]

$$P_r(\tau) = P_T \frac{P_{PT}(\tau) G^2(0) \lambda^2}{L_p (4\pi)^2 (2h)^2} |R(0)|^2 e^{-4k_o^2 \sigma_s^2} \quad (3)$$

where $R(0)$ is Fresnel reflection coefficient of the surface at normal incidence, k_o is the rf-wavenumber, and σ_s is the rms surface height.

In addition to the h^{-2} dependence upon altitude in (3) is the fact that specularly reflected returns will exhibit very little pulse-to-pulse fluctuation*. That is, for a specular surface the return power will be an attenuated version of the system point target response which on a pulse-by-pulse basis will be nearly constant.

The third category of scattering is perhaps the most difficult to understand because it must explain all of the types of scattering which are neither rough surface scatter nor specular reflection. For this type of scattering, it is assumed that there are $N(\leq 3)$ large bodies on the surface which, because of their size and orientation, dominate the scattering. Assuming that there is some small motion of the radar relative to the scatterers and that the averaging time is sufficiently long so as to consider the phases between the scatterers to be random, the average return power is given by

$$\bar{P}_r(\tau) = \frac{P_T \lambda^2}{(4\pi)^3 h^4 L_p} \sum_{i=1}^N \frac{P_{PT}(\tau - \tau_i) \sigma_i(\theta_i) G^2(\theta_i)}{\left(1 + \frac{c\tau_i}{2h}\right)^4} \quad \tau \geq 0 \quad (4)$$

In (4), τ_i represents the two-way time delay to the i^{th} large body scatterer relative to $2h/c$, θ_i is the corresponding angle of incidence, and σ_i is the cross-section of the i^{th} large body. For spacecraft based radars,

$$\frac{c\tau_i}{2h} \ll 1 \quad ,$$

thus,

*Moore and Williams [3] state that the specular return will not fluctuate, however, experiments have shown [5] that there is a small fluctuation associated with this type of return.

$$\bar{P}_r(\tau) \approx \frac{P_T \lambda^2}{L_p (4\pi)^3 h^4} \sum_{i=1}^N P_{PT}(\tau - \tau_i) \sigma_i(\theta_i) G^2(\theta_i) \quad (5)$$

for $\tau \geq 0$. We note that (4) is just the superposition of N point target returns appropriately delayed in time by the two-way time delay to each target. When N is one, (4) is just the conventional single point target radar equation. In contrast to the rough surface scattering case where it is assumed that there are always a large number of scatterers (≥ 5) per unit time delay, the large body scatter occurs due to a finite number of dominant scatterers which may be, individually, located at distinctly different or the same time delay.

The intrapulse behavior of a single return, i.e. the fading characteristics of the return, is dependent not only upon the number of large body scatterers located at a given time delay but also upon the response time of the receiver. That is, it is possible to have a number of scatterers occurring at the same time delay and also causing a rapidly fading return due to their phasor addition (on an individual pulse basis). However, if the receiver bandwidth is small relative to the bandwidth of the fading, the fading nature of the return will not be observed.

By the same token, the pulse-to-pulse fluctuation of the return may not yield much information on the number or effective size of the large body scatterers. That is, a single large body scatterer whose size changes on a pulse-to-pulse basis* may exhibit the same fluctuation statistics as a number of large body scatterers whose sizes do not change but which cause fluctuation due to pulse-by-pulse changes in their relative positions.*

It should be noted that if large body scatter is present, it might be very difficult to differentiate between it and random scatter. However, because of the along-track velocity of spacecraft-based radars, it is not expected that dominant large body scatterers would lie within the antenna beamwidth for more than a few pulses.

*Due to the motion of the radar.

1.2 Backscattering Cross Section (σ°) Behavior For Various Scales of Roughness

The purpose of this section is to review the dependence of σ° , the surface backscattering cross section per unit scattering area, upon various surface parameters. All theoretical models [6] for σ° require small surface slopes in order to avoid the potential problem of sharp edge diffraction. Generally the models are divided into two categories, namely, the slightly rough surface ($k_o \sigma_s \ll 1$) and very rough surfaces ($k_o \sigma_s \gg 1$). Recent attempts have been made to incoherently combine the two results (the composite surface model) to provide a more realistic model of natural surface scattering for all angles of incidence. For present purposes, it will be necessary to only consider the behavior of σ° near normal incidence.

For an isotropic surface, i.e. no directionality to the roughness*, and a Gaussian surface height autocorrelation function, the small roughness model predicts the following behavior for σ° [4]

$$\sigma^\circ(\theta) = 4k_o^4 \sigma_s^2 \ell^2 \cos^4 \theta |R(\theta)|^2 e^{-k_o^2 \ell^2 \sin^2 \theta} \quad (6)$$

where ℓ is the surface height correlation length and θ is the angle of incidence with respect to the mean surface. An interesting altimetry application of this model occurs if we consider the case of $k_o \sigma_s \ll 1$ and $k_o \ell \gg 1$; this represents a very gently undulating surface with a small roughness relative to a wavelength. Since we are interested in the near normal incidence behavior of $\sigma^\circ(\theta)$, we use the following approximate form

$$\sigma^\circ(\theta) \approx 4k_o^4 \sigma_s^2 \ell^2 |R(0)|^2 e^{-k_o^2 \ell^2 \tan^2 \theta} \quad (7)$$

Neglecting the antenna pattern variation with θ and assuming a rectangular point target response, the average return power is given by

*As used here, the term roughness refers to the surface height and not the slope.

$$\Gamma_s \int_0^T e^{-\frac{k_o^2 \ell^2 c}{h} \hat{\tau}} d\hat{\tau} \quad 0 \leq \tau \leq T$$

$$\bar{P}_r(\tau) \approx$$

$$-\Gamma_s \int_{\tau}^{\tau-T} e^{-\frac{k_o^2 \ell^2 c}{h} \hat{\tau}} d\hat{\tau} \quad \tau > T$$

where T is the point target pulse length,

$$\Gamma_s = \frac{P_T G^2 \lambda^2 c}{4(4\pi)^2 h^3 L_p} 4k_o^4 \sigma^2 \ell^2 |R(0)|^2,$$

and we have used the fact that $\tan^2 \theta \approx c\tau/h$. The above integrals reduce to the following form

$$\bar{\Gamma}_s \left[1 - e^{-\frac{k_o^2 \ell^2 c}{h} \tau} \right] \quad 0 \leq \tau \leq T$$

$$\bar{P}_r(\tau) =$$

(8)

$$\bar{\Gamma}_s e^{-\frac{k_o^2 \ell^2 c}{h} c\tau} \left[-1 + e^{+\frac{k_o^2 \ell^2 c}{h} T} \right] \quad \tau > T$$

with

$$\bar{\Gamma}_s = \frac{P_T G^2 \lambda^2}{4(4\pi)^2 h^2 L_p} |R(0)|^2 (2k_o \sigma_s)^2$$

If the correlation length is long enough so that

$$\frac{k_o^2 \ell^2 c}{h} > 1,$$

the average return power waveform will be nearly equal to the point target response (in shape), i.e.

$$\bar{P}_r(\tau) \approx \begin{cases} \frac{P_T G_o^2 \lambda^2}{4(4\pi)^2 h^2 L_p} |R(0)|^2 (2k_o \sigma_s)^2 & 0 \leq \tau \leq T \\ 0 & \tau > T \end{cases} \quad (9)$$

We note from (9) that for a large correlation length, the average return power is proportional to $(k_o \sigma_s)^2$. The ratio of diffuse or average random power to specular power is given by ratioing the results in (9) and (3), i.e.

$$\frac{\bar{P}_r(\text{random})}{\bar{P}_r(\text{specular})} = \frac{(2k_o \sigma_s)^2}{e - (2k_o \sigma_s)^2} \approx (2k_o \sigma_s)^2 \ll 1 \quad (10)$$

since $k_o \sigma_s \ll 1$ by assumption. Thus, for the case of a slightly rough surface we see that in order to obtain the point target response for the average return power we require a large surface autocorrelation length. However, even under this condition we note that the total return power is dominated by the slightly fluctuating spectral return rather than the random component.

When the surface roughness becomes comparable or large relative to the rf-wavelength, the specular or slightly fluctuating component of the return power rapidly approaches zero for near normal incidence due to the exponential decay factor in (3). Furthermore, the slightly rough model for the random return becomes invalid. For this case, the techniques of "physical optics" are used to model the scattering process. The results are applicable under the conditions of; large roughness ($k_o \sigma_s \gg 1$), isotropic roughness and a large illuminated area relative to the correlation length. If we further assume that the surface height probability density function is Gaussian and that the surface height autocorrelation function is parabolic for small spatial separations, it can be shown [7] that $\sigma^o(\theta)$ becomes

$$\sigma^{\circ}(\theta) = \frac{|R(0)|^2 \ell^2}{4\sigma_s^2 \cos^4 \theta} e^{-\frac{\ell^2}{4\sigma_s^2} \tan^2 \theta} \quad (11)$$

Proceeding as in the case of the slightly rough surface, we find that the average return power for a rectangular system point target response is given by

$$\begin{aligned} \bar{P}_r(\tau) = & \bar{\Gamma}_R \left[1 - e^{-\frac{\ell^2 c}{4\sigma_s^2 h} \tau} \right] & 0 \leq \tau \leq T \\ & \bar{\Gamma}_R e^{-\frac{\ell^2 c}{4\sigma_s^2 h} \tau} \left[1 + e^{+\frac{\ell^2 c}{4\sigma_s^2 h} T} \right] & \tau \geq T \end{aligned} \quad (12)$$

where

$$\bar{\Gamma}_R = \frac{P_T G_o^2 \lambda^2}{4(4\pi)^2 h^2 L_p} |R(0)|^2$$

We now assume that the correlation length is sufficiently large so that

$$\frac{\ell^2}{4\sigma_s^2 h} > 1 \quad ,$$

then

$$\begin{aligned} \bar{P}_r(\tau) = & \frac{P_T G_o^2 \lambda^2}{4(4\pi)^2 h^2 L_p} |R(0)|^2 & 0 \leq \tau \leq T \\ & 0 & \tau > T \end{aligned} \quad (13)$$

Equation (13) is a most interesting result in that it predicts that the amplitude of the average return power from a gently undulating random surface will have the same value as a perfectly flat specular surface and that the average shape will be identical to the system point target response. Thus, given the average return power (in amplitude and shape) from a gently undulating surface, it would not be possible to distinguish it from the return due to a pure flat specular surface. However, the pulse-by-pulse return from a gently undulating surface must necessarily fluctuate for the convolutional model to be valid. This fluctuation will, in general, be due to the variation in the number and location of the specular points illuminated by the radar. It should be noted, however, that all the specular points must lie inside the pulsewidth limited circle or else the average return will not be identical to the system point target response. Thus, unless the receiver filter bandwidth is much greater than the matched filter bandwidth, intrapulse fading will not be observed in the pulse-by-pulse returns. That is, the receiver bandwidth will not be sufficiently large enough to pass the intrapulse fading due to the specular points within the pulsewidth limited circle.

It should be noted that if we let the roughness go to zero ($\sigma_s \rightarrow 0$), the "physical optics" model predicts the correct behavior for the specular return power. The fact that we can "violate" the large roughness approximation of the physical optics theory and obtain the proper result is a consequence of the stipulation of a large surface height correlation length. Mathematically speaking, a large correlation length and small roughness imply that all spatial derivatives of the surface height are small and that their magnitudes decrease very rapidly with increasing order of the derivative. This decrease in magnitude of surface height derivatives with increasing order implies that the stationary phase approximation to the diffraction integral for the scattered field (used in the "physical optics" approximation) accurately represents the true integral. More importantly, however, is the fact that the accuracy of the stationary phase approximation does not require large roughness for the case of rapidly decreasing surface derivatives (with increasing order). Thus, for the case of a gently undulating rough surface, the stationary phase evaluation of the diffraction integral is accurate because it adequately represents the surface height as having a parabolic dependence upon the transverse spatial coordinates (in the neighborhood of a specular point) independent of the surface roughness.

We note from equation (11) that as the surface roughness goes to zero and the correlation length necessarily becomes infinite, $\sigma^\circ(\theta)$ becomes a delta function. Loosely interpreted, this would imply that the cross section per unit scattering area is infinite at normal incidence and zero for all other angles. However, it must be remembered that the delta function only has meaning when it is the kernel of an integral such as the convolutional integral in equation (1). Thus, it is reassuring to note that when we take the appropriate small roughness limiting form (i.e., large correlation length) for the physical optics rough surface scattering theory, it correctly predicts the proper near-specular behavior of the scattering surface. To the author's knowledge, this result has not been previously demonstrated in the literature.

For the case where $(\lambda/2\sigma_s)$ is large but not infinite, equation (12) describes the average return power. One of the most important points of this entire discussion is that the specular model, i.e. equation (3), predicts a dependence upon only the mean square surface height (σ_s^2). The random scattering model, however, indicates that the return power is sensitive to the ratio $(\lambda/2\sigma_s)$ or the inverse of the rms surface slope. For remote sensing applications, the distinction is most significant, i.e. the difference between a purely flat surface and one which is gently undulating. For an altitude of 435.5 km and a wavelength of 0.0216 m, the diameter of the first Fresnel zone is 137 m. In order for equation (3), i.e. specular reflection, to describe the scattering process we require that

$$4k_o^2 \sigma_s^2 \lesssim 1$$

or

$$\sigma_s \lesssim \frac{1}{2k_o}$$

For the S-193 wavelength, it would be necessary to have $\sigma_s \lesssim 1.7 \times 10^{-3}$ m over at least the first Fresnel zone (a circular area of diameter of 137 m). Common sense alone would certainly indicate that such smooth surfaces do not occur in nature!

2.0 Measurement Results From The Great Salt Lake Desert Area

In examining the data obtained by the Skylab radar altimeter, a number of cases were noted for which the AGC output indicated an abnormally high backscattered power level and the altitude data exhibited a very low noise character. The majority of these data spans occurred over land although some were noted during passes over water. Unfortunately, the time duration of these unusual data sets was generally very short indicating that the spatial extent of the dominant surface condition was relatively small. However, over a long period of time, say 60 seconds or more, a number of these types of scattering regions might be included in the radar data. Thus, when the radar return waveform data were averaged, non-typical shapes [1,2] resulted. The only relevant information contained in these average waveforms was the indication of a statistically non-homogeneous scattering surface over the equivalent spatial extent of the averaging time.

In order to investigate these particular scattering cases, it was necessary to find a data span for which the condition persisted long enough to obtain valid statistical estimates of the effect. The set of data satisfying the above criteria was found to have resulted from scattering from the Great Salt Lake Desert area west of Salt Lake City. These particular data were obtained on EREP Pass 39 of mission SL-3 during operation of Mode I Submode 0. A combined plot of raw AGC (Automatic Gain Control) and altitude data are shown in Figure 1. The data are raw to the extent that the AGC output is in terms of PCM counts and the altitude has only been corrected for a constant receiver time delay. The raw AGC data* have been plotted in this way because once the level drops below 20 counts, we do not have a valid calibration curve to convert PCM counts to altimeter input power. It should be noted, however, that although the telemetry channel saturated at the zero count level, this does not imply that the altimeter's AGC system saturated.

The significant points to note about these data are the very high level of return power and the very low noise character of the altitude data and, furthermore, the near time-coincident occurrence of both. A small map of the Great Salt Lake Desert Area is shown in Figure 2. On the map, major

*Very crudely speaking, the lower the AGC PCM count, the higher the return power level.

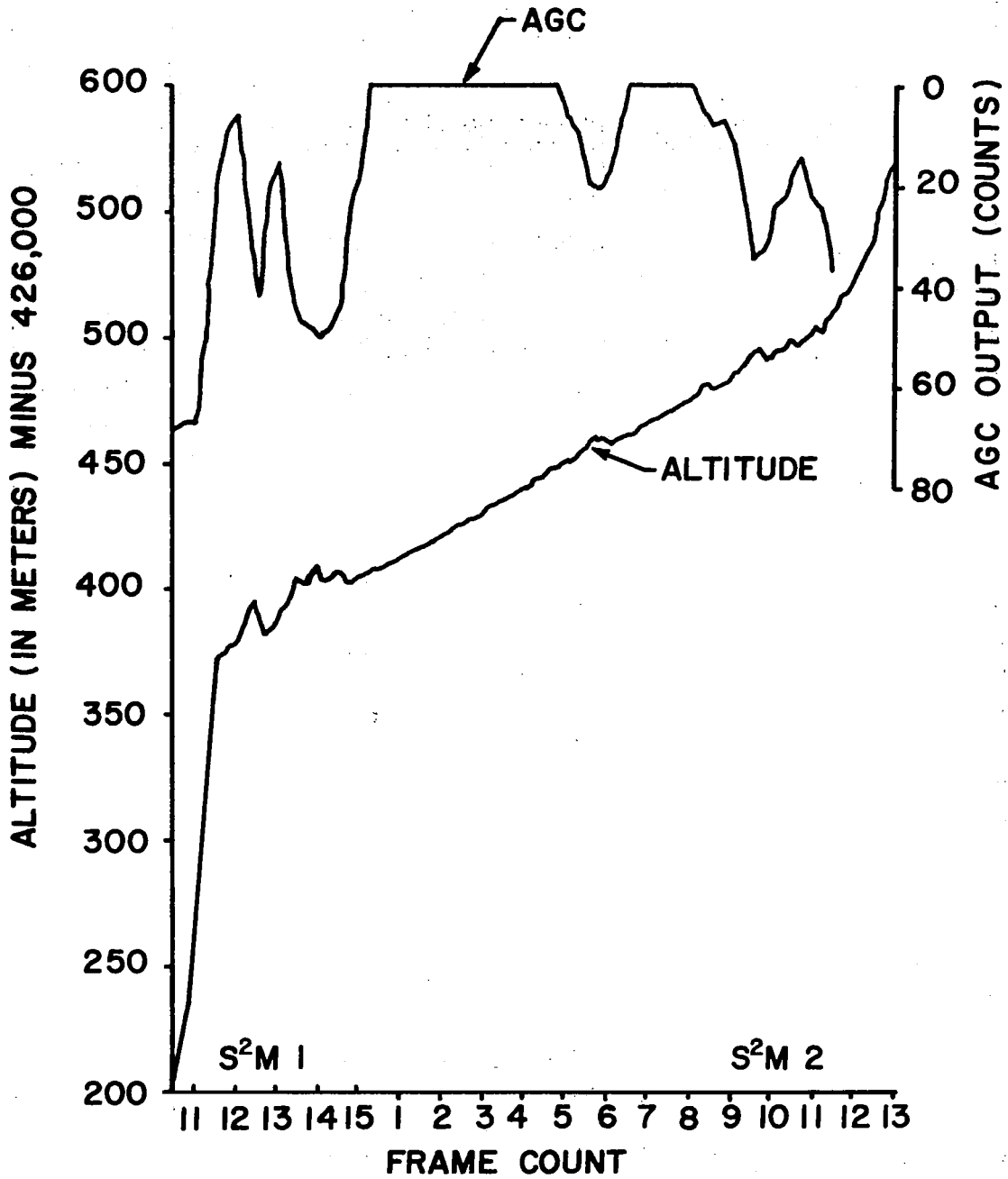
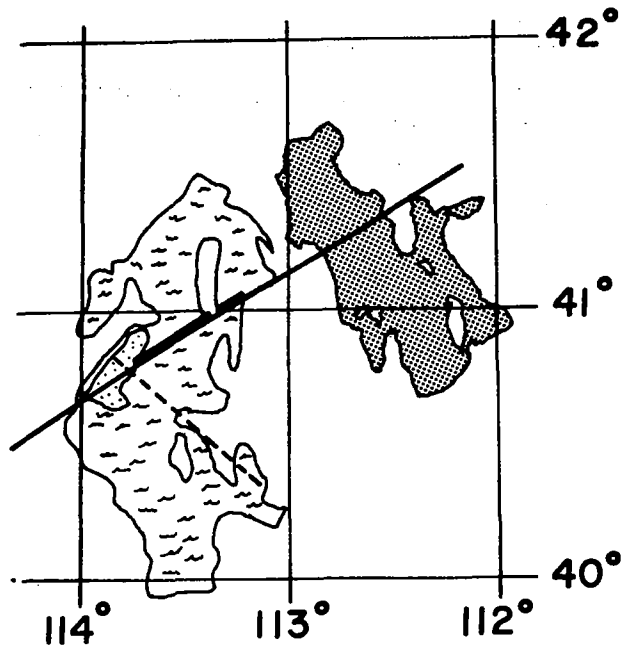


Figure 1. Altitude and AGC data for a portion of the ground track for Mission SL-2, EREP Pass 39, Mode I, Submode 0.



LEGEND


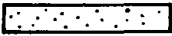

- SKYLAB GROUND TRACK ERP PASS 39 (13 SEPT. 1973)
- AIRCRAFT (WITH LASER PROFILER) TRACK (5 JUNE 1973)
- PERIODS OF HIGH RETURN POWER AND LOW ALTITUDE DATA NOISE LEVEL
-  GREAT SALT LAKE DESERT
-  BONNEVILLE SALT FLATS
-  GREAT SALT LAKE

Figure 2. A map of the Great Salt Lake Desert area showing the ground tracks for both the spacecraft and the surface truth aircraft.

geological areas such as the Bonneville Salt Flats, the Desert and the Salt Lake have been identified along with the location of the spacecraft ground track. The heavily lined portions of the ground track correspond to the times when the AGC indicated an abnormally high return power (see Figure 1). Also shown is the ground track of an aircraft flight which obtained laser profilometer data on the surface roughness. The aircraft flight occurred about three months earlier than the spacecraft pass and its purpose was to support an S-193 Scatterometer pass. The laser profilometer was the only ground truth data available for this area. An interesting observation is the correspondence between the over-desert and high return power portions of the ground track.

From the available calibration data [8], we estimate the power at the altimeter input port (corresponding to an AGC reading of zero counts) to be between 0 and -15 dBm. For a perfectly flat specular surface having a relative dielectric constant of $\epsilon = 55(1 + j0.55)^*$, the equivalent power at the altimeter input port is given by

$$P_{r_spec} = G_{IR} \frac{P_T G_o^2 \lambda^2}{(4\pi)^2 (2h)^2} |R(0)|^2$$

where G_{IR} is the gain of the tunnel diode preamplifier in the front end of the receiver. Using the following values for the various parameters;

$$G_{IR} \approx 31 \text{ dB}$$

$$P_T \approx 2 \text{ kW}$$

$$G_o = 41.3 \text{ dB}$$

$$\lambda = 0.02158 \text{ m}$$

$$h = 435.5 \text{ km}$$

$$|R(0)|^2 = -2.1 \text{ dB} \quad ,$$

we find that the flat surface specular return power is equal to 0.4 dBm.

When the rms roughness of the surface is on the order of 0.3 cm., the specular

*This value of dielectric constant is typical of salt water such as in the Great Salt Lake.

return power as given by equation (3) will be -15 dBm. Thus, we see that the average backscattered power level recorded by the altimeter over this particular area is comparable to the specular return from a surface having a very small roughness. However, the average return power is also comparable to the average return from a gently undulating surface for which the correlation length is large (see equation (13)). To resolve this question of whether the return is random or specular, we must examine the shape of the pulse-by-pulse returns and their fluctuation characteristics.

2.1 Return Waveform Statistical Characteristics and Their Implications

If, as the return power tends to indicate, the surface is truly specular, the shape of the average return waveform should be nearly identical to the system point target response. In-flight measurements of the system point target response are shown in Figure 3 for a 100 ns transmitted pulse-width and a 10 MHz (two-sided) IF bandwidth. The two sets of data correspond to two different ways of positioning the Sample and Hold (S&H) gates on the point target response. The circled data points were obtained by activating the S&H gates at a fixed time delay after start of transmission, while the triangular points resulted when the altimeter actually tracked the point target response (self-tracking). Figure 3 further illustrates that a Gaussian function provides a reasonably good fit to the measured point target response. In Figure 4, we show the self-tracking waveform data along with the position of the S&H gates which obtained the data. It is important to note that if the surface is specular, the average return must be positioned exactly as shown in Figure 4 relative to the S&H gates. That is to say, the tracking loop will locate the S&H gates at the same position on the waveforms for the self-tracking measurement and the specular return since the waveforms are the same in both cases.

In selecting the data to be analyzed, we require that the AGC reading be zero counts since this would imply maximum backscattered power. From Figure 1, we use only the data from the last three-eighths of frame 15 (S^2M_1) and from frames one through four of S^2M_2 . The nomenclature S^2M_{-} refers to where the array of the eight S&H gates is positioned: S^2M_1 corresponds to the earlier time position of the array (see Figure 4) while S^2M_2 refers to the next contiguous location of the array.

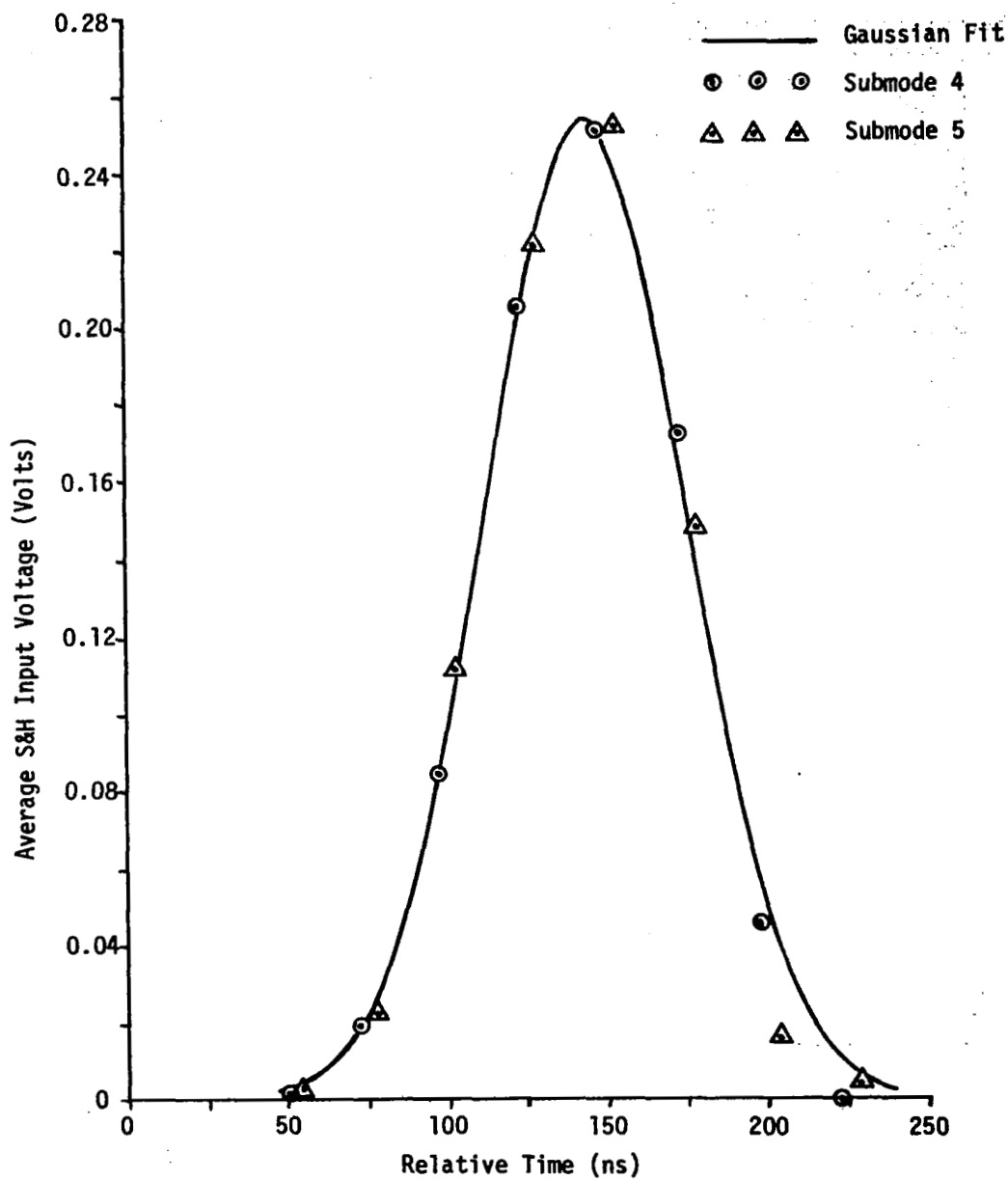


Figure 3. Mode I 100 ns/10 MHz point target response as recorded using a fixed delay trigger to S&H gates (Submode 4) and during self-tracking (Submode 5).

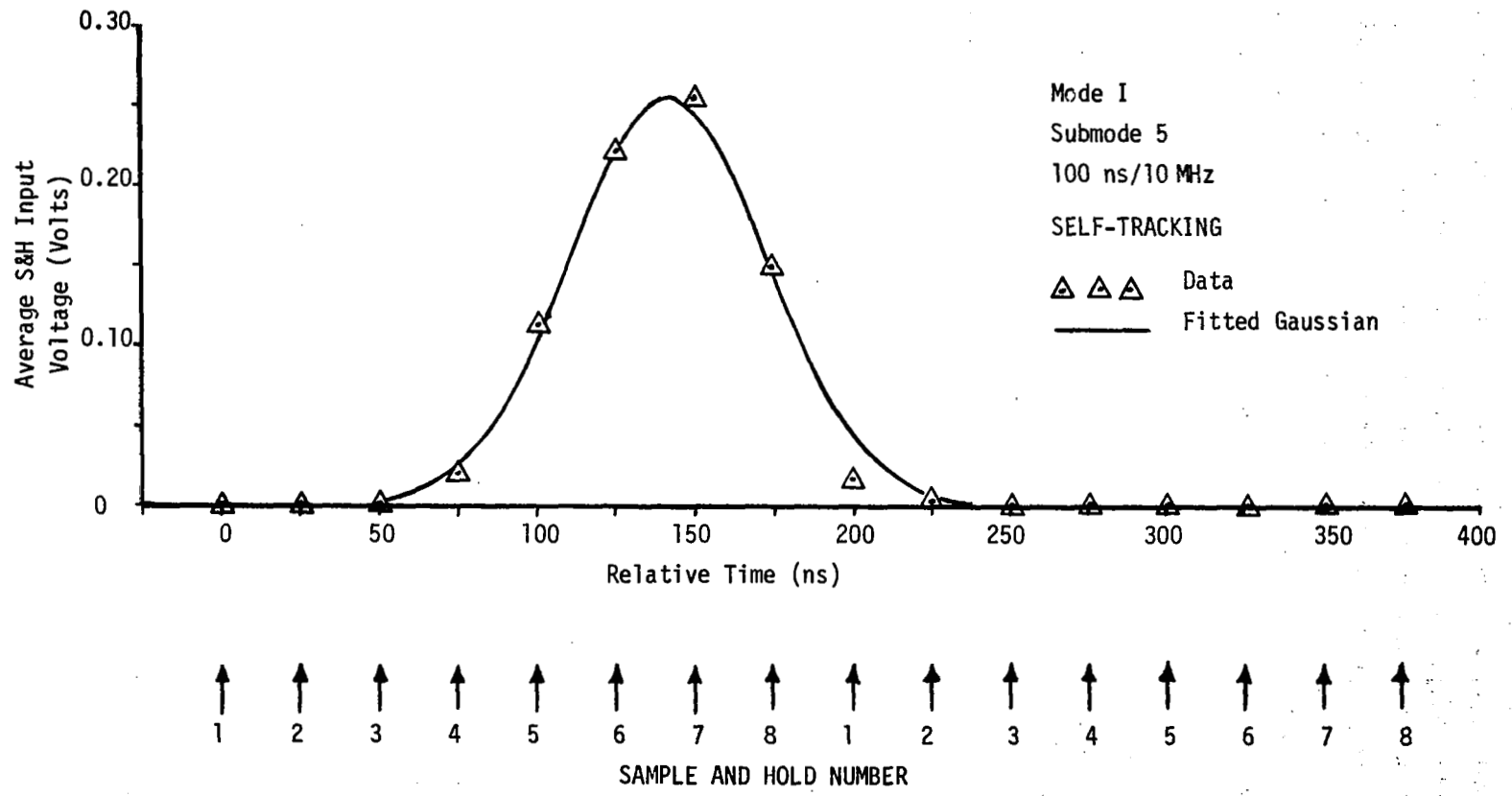


Figure 4. Measured point target response during self-tracking showing the location of the S&H gates.

Figure 5 is a histogram of the S&H voltages recorded during the last 66 returns in frame 15 of S²M 1 (the first S&H array position). Quite obviously, we are hindered by the small number of samples, however, some conclusions can be made based upon the data in Figure 5. The histograms for S&H gates 1 through 3 indicate the presence of noise only. If we had constructed the histogram using smaller bin sizes, the distribution would have appeared nearly exponential. The source of the noise is unknown although it is probably due to some component in the video portion of the receiver since the average single pulse IF signal-to-noise ratio is greater than 50 dB. The histogram for S&H gate 4 shows the presence of an exponentially distributed signal whose mean is significantly larger than the noise. S&H gates 5 through 8 exhibit a less clear resemblance to the exponential distribution: this is the result of a number of effects. First of all, the number of samples is probably too small to obtain a very accurate histogram. Secondly, when the histograms are converted to probability density functions and compared to an exponential density (based upon the mean of the sample), the correspondence becomes significantly more apparent. This is illustrated in Figure 6 for S&H gates 4 and 5. A third reason for the form of the histograms is saturation of either the video amplifier or the S&H gates: this is evident from the histograms for S&H gates 6, 7 and, to a lesser degree, 8. That is we see an obviously large number of samples in the voltage range of from 0.34 to 0.38 volts. The last reason for the particular form of the histograms appears to be linked to the saturation effect. In this and other S-193 altimeter waveform data, we have noted that whenever saturation occurs there is also an attendant change in the resulting histogram. Specifically, the histogram appears to be more closely approximated by a gamma distribution than an exponential one. We might hypothesize that this effect is due to an increase in the high frequency content of the signal due to limiting and a subsequent filtering of these frequency components by the equivalent low-pass filter nature of the S&H gate. Such a situation could give rise to the gamma distribution [9], although we have no measurements to firmly establish this hypothesis. Chapter 13 addresses some of these problems in more depth.

With these points (relative to the histograms in Figure 5) in mind, we can make a very important observation. The histograms appear to be nearly exponential which means that the average return power and the standard

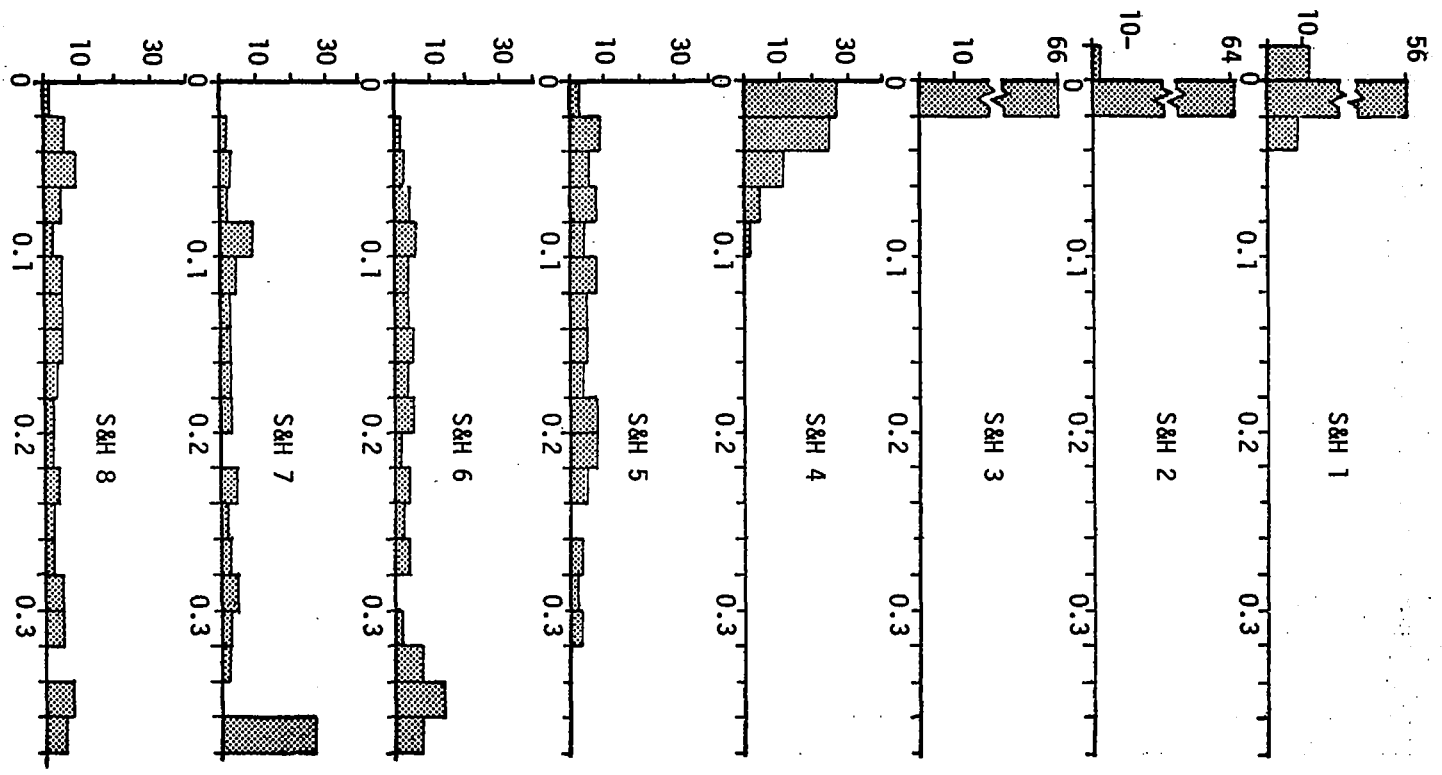


Figure 5. Histograms of S&H voltages corresponding to the last 66 returns recorded in frame 15 of S²M 1 (Vertical axis = frequency of occurrence, Horizontal axis = voltage.)

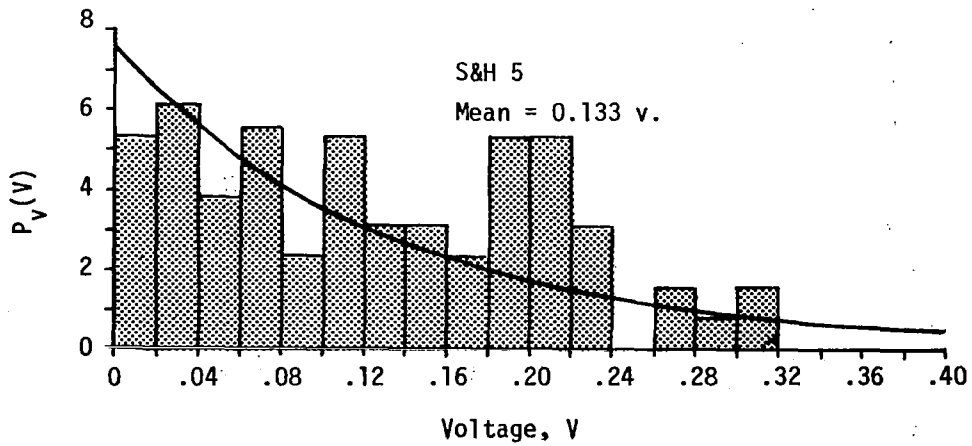
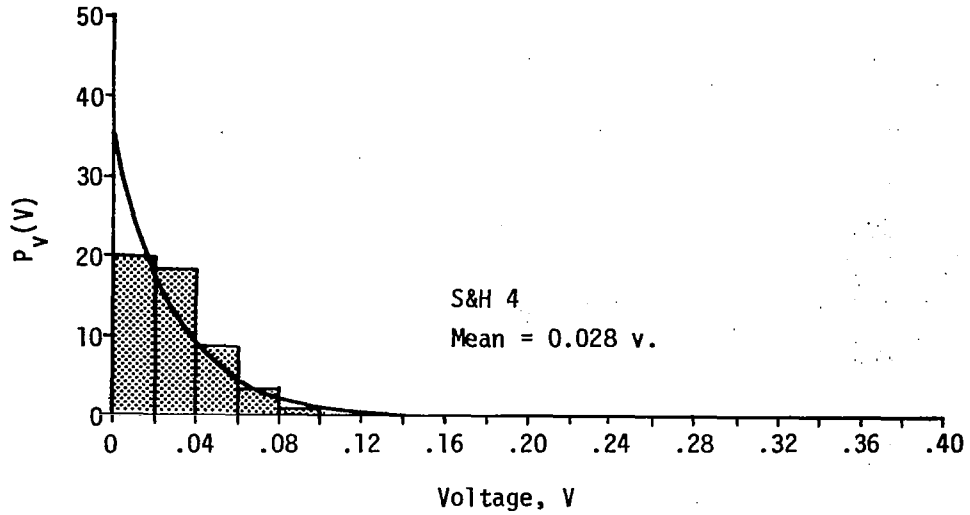


Figure 6. A comparison between exponential pdf's and the pdf's for S&H gates 4 and 5 based upon the histogram data in Figure 4.

deviation of the return power about the mean are equal. A true specular surface will not exhibit this much variation about the mean. An exponential distribution is, however, characteristic of a random scattering surface. Based upon this result, we conclude that the fluctuating nature of the return does not support the hypothesis of a specular scattering surface.

Having rejected the possibility of a true specular surface, the only remaining model which will yield the near-specular return average power is that of a gently undulating surface with a large surface height correlation length (see equation (13)). However, as shown in equation (13), the average return waveform from such a surface must necessarily be a replica of the system point target response. Thus, we must show, for this case, that the average waveform was, indeed, essentially equivalent to the point target response. Unfortunately, this is not an easy task because the true average value for S&H gates 6, 7 and 8 has been lost due to the saturation effect and the small sample statistics.* We can, however, determine how well the non-saturated waveform averages fit the system point target response. That is, we can examine the degree of correspondence between the measured point target response (Figure 3) and average voltage from S&H 3,4 and 5 of S^2M 1 and 1 and 2 of S^2M 2. Such a comparison is shown in Figure 7, where we have plotted the average values and a Gaussian curve with the same variance as in Figure 3. The amplitude of the Gaussian curve has been increased to match the averages from S&H 4 of S^2M 1 and 1 of S^2M 2. Apart from the expected difference in match for S&H's 6, 7 and 8 of S^2M 1, we see that the other data is in excellent agreement with the system point target response. We further note that the S&H gates in Figure 7 occur at almost exactly the same place on the waveform as they did for the point target measurement as shown in Figure 4. This means that the tracking gates are operating on essentially the same waveform in both cases. Therefore, we can state that, apart from an increase in amplitude, the average return power waveform for this case was nearly identical to the system point target response.

Based upon this analysis, we can draw the following conclusions;

*If we had a large number of samples to work with we could analytically reconstruct the average and this has been done with other Skylab waveform data [10].

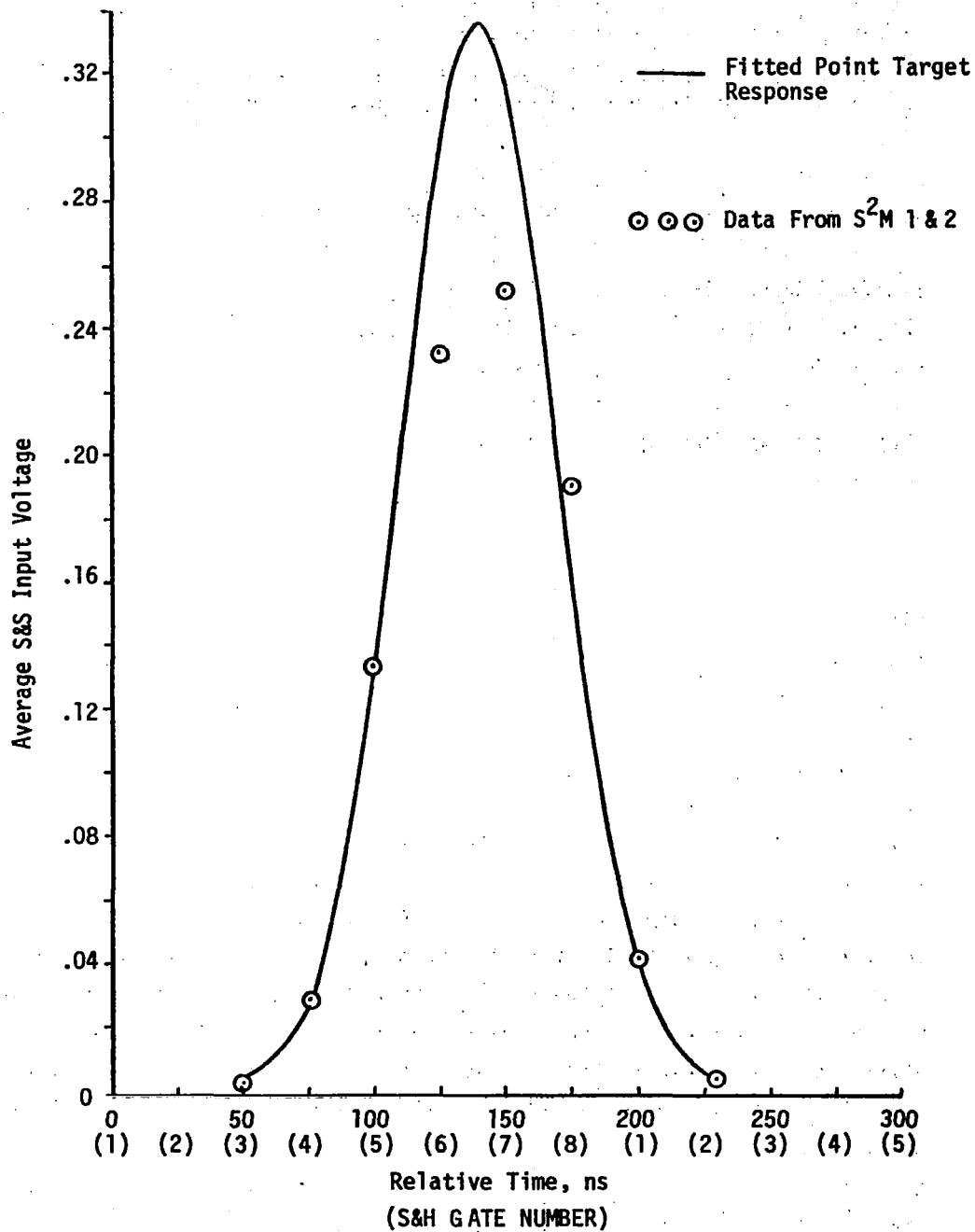


Figure 7. Reconstructed return and fitted point target response. Note that S&H gates 6, 7 and 8 show saturated values.

- (1) the surface is not truly specular because the fluctuation of the return power is too large to support a specular hypothesis,
- (2) the surface most probably is characterized as a gently undulating surface with a relatively small surface roughness and a large correlation length because*,
 - (a) the average return power is nearly equal to that returned by a specular surface,
 - (b) the fluctuation of the return is characteristic of a random scattering surface,
 - (c) the shape of the average return power waveform is identical to the system point target response.

Futhermore, we reiterate the fact that the resulting $\sigma^\circ(\theta)$ is nearly a delta function and measurements of σ° for this case are therefore meaningless.

2.2 Other Consequences Of This Type Of Scattering

In the previous sections of this chapter, we have demonstrated that scattering from the Great Salt Lake area cannot be explained in terms of a specular surface but, rather, is a special limiting form of rough surface scatter. Although this proof is our main intent, there are a number of other consequences of this result which should be noted.

2.2.1 Comments On Previous Analyses

First, we will comment on the analysis used by Shapiro and Yaplee [2] to classify this type of scattering process as purely specular. Their first justification for assuming the surface to be specular was based on the observation that the trailing edge of the average return waveform decayed much more rapidly than the trailing edge of a pure random return. This fact is, by itself, insufficient evidence to classify the surface as specular and, as McGoogan, et al. [1] noted, is merely an indication of a non-typical scattering situation. The correct implication of a rapidly decreasing trailing edge is that either $\sigma^\circ(\theta)$ is decaying much more rapidly

*See the latter part of Section 1.2 for a rigorous justification of these conditions.

with incidence angle than for a random surface (such as the ocean) or the surface is specular.

The second implied measure of surface specularity employed by Shapiro and Yaplee was the so-called waveform autocorrelation. In further private discussions with Shapiro, it was determined that what was actually calculated was something akin to a pulse-to-pulse correlation coefficient. That is, using S&H 4 in S^2_{M1} (see Figure 7), he computed the normalized correlation between a first and second return (jump index = 1), a first and third return (jump index = 2), and so forth until reaching the point where he was comparing S&H 4 for a first and fifth return (jump index = 4). In more precise terms, the function in question is given by the following form;

$$C_j(t_4) = \frac{E\{P_r(t_4;0)P_r(t_4;j)\} - \bar{P}_r^2(t_4)}{[\text{Var}\{P_r(t_4;0)\}\text{Var}\{P_r(t_4;j)\}]^{1/2}} \quad (14)$$

where t_4 is the delay time corresponding to S&H 4 in S^2_{M1} and j is the jump index which indicates how many returns were skipped before computing (14). It should be noted that (14) is very similar to the formula for one point on the nonstationary pulse-to-pulse autocorrelation coefficient (see Chapter 10) except that the spacing between returns is an integer multiple of the interpulse period.* In essence, (14) describes the degree of correlation at S&H 4 in S^2_{M1} between selectively spaced returns.

For a specular return there is little or no pulse-to-pulse fluctuation; thus, taking the proper limit, we find that

$$C_j(t_4) \Big|_{\text{specular}} \approx 1 \quad j = 0, 1, \dots, 4 \quad . \quad (15)$$

In other words, there is nearly complete correlation between successive returns. For a completely random or diffuse return, the pulse-by-pulse returns are independent and

*The actual interpulse period between recorded returns alternately varied between 8 and 12 ms due to the recording of only 100 returns per second rather than 250.

$$C_j(t_4) \Big|_{\text{random}} = \begin{matrix} 1 & j = 0 \\ 0 & j \neq 0 \end{matrix} \quad (16)$$

For the periods in this data set corresponding to a very high return power and low noise character of the altitude data, the return power will exhibit pulse-to-pulse fluctuation (interpulse variation) but little or no fading (intrapulse variation). Thus, the return power assumes the following form;

$$P_r(t;j) \approx P_o(j)f(t),$$

where $P_o(j)$ is an exponentially distributed random amplitude variable and $f(t)$ is the non random point target response (normalized to a peak value of one). In other words, for this special type of extended target scattering the "shape", i.e. $f(t)$, of the return power is not random but the pulse-to-pulse amplitude variation is still random. For this case, (14) assumes the following form;

$$C_j(t_4) \Big|_{\text{special}} = \frac{E\{P_o(0)P_o(j)\}}{P_o^2} - 1 \quad j = 0, 1, \dots, 4 \quad (17)$$

In (17), we note that when $j=0$, $C_0(t_4) = 1$ since P_o has been shown to be and exponentially distributed random variable. For $0 < j \leq 4$, $0 < C_j(t_4) < 1$ (depending upon the degree of pulse-to-pulse correlation) as Yapplee and Shapiro have demonstrated. However, the fact that $C_j(t_4) \neq 1$, $j=1, 2, \dots, 4$, definitely shows that this type of scattering is not specular since true specular scattering is characterized by the result in (15).

In view of the above discussion it should be noted that the correlation coefficient, as given by (14), provides no more information on the physics of the scattering process than the shape of the average return power. That is, as the return power waveform approaches the point target response then so must $C_j(t_4)$ approach the limiting form given by (15). In this case, the correlation coefficient and the average return waveform are redundant and it is not necessary to compute both from the data. For the case of pure random surface scattering, the average return and the interpulse correlation are not so simply related (see Chapter 10).

2.2.2 Agreement of Model and Low Noise Altitude Data

The minimum observed standard deviation of the altitude output from the S-193 radar in this mode/submode and over the ocean's surface was about 1.2 meters. Since this occurred for an SNR in excess of 30 dB, the resultant noise on the altitude data was essentially independent of SNR and was a consequence of the fading and fluctuating character of the random return. The 1.2 meters standard deviation is in reasonable agreement with theoretical predictions of the noise level for a random surface for which σ^0 is nearly constant over the antenna beamwidth.

An analysis of the altitude data shown in Figure 1 for frame 15 of S²M 1 and frames 1 through 4 of S²M 2 yielded an altitude noise level of 0.37 m. This value for the standard deviation of the altitude noise is considerably below the theoretically predicted minimum for a fading and fluctuating return and, in fact, is very near the instrument quantization noise level of 0.2 m. As will be shown below, the reason for the low altitude noise level is that we are dealing with a non-fading return whose so called "self-noise" is very small.

Hofmeister [11] has shown that the variance of the altitude data resulting from a typical split-gate tracking loop is related to the average value of the conditional covariance of the equivalent additive noise in the tracking loop due to the fluctuating and fading nature of the return, i.e.

$$\sigma_h^2 = \left(\frac{c T K_g}{2R} \right)^2 \overline{K_e^T(0; \tau_f)} \quad (18)$$

In (18),

T = Width of the transmitted pulse,

K_g = Slope of the tracking loop discriminator curve at $\tau_f = 0$,

R² = Variance reduction factor due to averaging in the tracking loop,

and

$$\overline{K_e^T(0; \tau_f)} = \int_{-\infty}^{\infty} K_e^T(0; \tau_f) p(\tau_f) d\tau_f \quad (19)$$

where τ_f is the pulse-by-pulse misalignment between the return pulse and the time discriminator gates and $p(\tau_f)$ is its probability density. The conditional covariance of the equivalent additive noise is given by [11]

$$K_e^T(0; \tau_f) = \iint E \left\{ [v(\alpha) - \bar{v}(\alpha)][v(\beta) - \bar{v}(\beta)] \right\} r(\alpha + \tau_f) r(\beta + \tau_f) d\alpha d\beta$$

where $v(\cdot)$ is the backscattered waveform as seen by the tracking loop time discriminator* and $r(\cdot)$ is the split-gate function. A representative plot of $K_e^T(0; \tau_f)$ is shown in Figure 8 for typical rough surface scattering, i.e. a fading and fluctuating target. For the case studied in this paper, the target is only fluctuating and $v(\alpha) = P_o f(\alpha)$, where P_o is an exponentially distributed random variable and $f(\alpha)$ is the system point target response. Thus, the conditional covariance for the additive loop noise is given by

$$K_e^T(0; \tau_f)_F = \text{Var}(P_o) \left\{ \int f(\alpha) r(\alpha + \tau_f) d\alpha \right\}^2 \quad (20)$$

A typical plot of (20) is shown in Figure 9. It should be noted that when $\tau_f = 0$, corresponding to the case when the output of the time discriminator is zero, the covariance is likewise zero.

If the probability density of τ_f is concentrated about $\tau_f = 0$, which is usually the case, then

$$\overline{K_e^T(0; \tau_f)}_{FF} \approx \overline{K_e^T(0; 0)}_{FF} = A > 0$$

and

$$\overline{K_e^T(0; \tau_f)}_F \approx \overline{K_e^T(0; 0)}_F = 0 \quad ,$$

where $\overline{K_e^T(0; \tau_f)}_{FF}$ is the average covariance** for a fading and fluctuating

target and $\overline{K_e^T(0; \tau_f)}_F$ is the average covariance** for a fluctuating only target.

* $\bar{v}(\cdot)$ is the average backscattered waveform as seen by the tracking loop.

**The average is over the parameter τ_f upon which the covariance is conditioned.

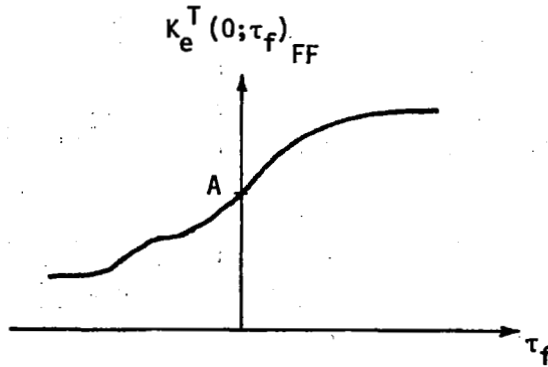


Figure 8. Conditional covariance of the equivalent tracking loop noise for a fading and a fluctuating (FF) target.

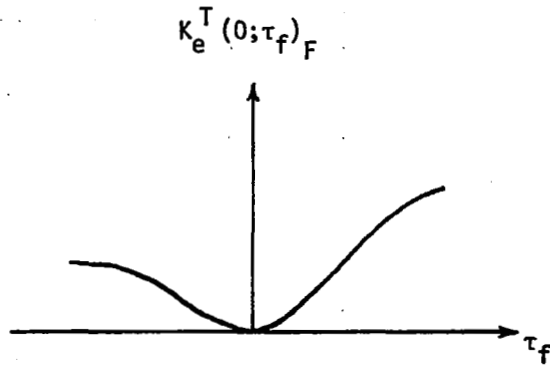


Figure 9. Conditional covariance of the equivalent tracking loop noise for a fluctuating (F) target.

Thus, we see that when the return is only fluctuating in amplitude, the noise in the altitude data is due primarily to quantization since the so-called "self-noise" is essentially zero. This explains why the noise level of the altitude data is below the theoretical minimum for a typical, i.e. fading and fluctuating, rough surface.

2.2.3 Transitions in the Waveform Data as a Function of Surface Conditions

In section 1.2, we posed an interpretation of the large surface roughness "physical optics" scattering model which adequately explains the data presented so far. Both the AGC and altitude data shown in Figure 1 indicate possible transitions from the special case of rough surface scatter where $\sigma^\circ(\theta)$ approaches a delta function to the more conventional situation where $\sigma^\circ(\theta)$ does not vary quite so rapidly with incidence angle. In this section, we present an analysis of this transitional data in order to verify that it also supports the model.

We first investigate the effects of surface height correlation and roughness on the average return power waveform. In Section 2.1 we noted that the system point target response was adequately represented by a Gaussian function, i.e.

$$P_{PT}(\tau) = e^{-\frac{(\tau-\tau_o)^2}{2\sigma_p^2}},$$

where $\sigma_p = 30$ ns and $\tau_o \approx 2\sqrt{2} \sigma_p$ is a time shift introduced to insure that there will be no return before $\tau=0$ (total two-way delay time = $2h/c$). Using equation (11) for $\sigma^\circ(\theta)$, a Gaussian antenna gain of the form

$$G^2(\theta) = G_o^2 e^{-\frac{4}{\gamma} \sin^2 \theta},$$

the small angle approximation, i.e. $\sin \theta \approx \tan \theta$, and equation (3), the flat surface impulse response for a nadir pointed radar may be written as

*The average is over the parameter τ_f upon which the covariance is conditional.

$$\bar{P}_{IR}(\tau) = \begin{cases} \frac{P_T c \lambda^2 G_o^2}{4(4\pi)^2 L_p h^3} \frac{|R(0)|^2 \ell^2}{4\sigma_s^2} e^{-\frac{c}{h} \left(\frac{4}{\gamma} + \frac{\ell^2}{4\sigma_s^2} \right) \tau} & \tau \geq 0 \\ 0 & \tau < 0 \end{cases}$$

Substituting the above expressions for $P_{PT}(\tau)$ and $\bar{P}_{IR}(\tau)$ in equation (1), we find the following result for the average return power as a function of delay;

$$\bar{P}_r(\tau) = \frac{P_T \lambda^2 G_o^2}{4(4\pi)^2 L_p h^3} \frac{c \sigma_p \sqrt{\pi/2}}{4\sigma_s^2} \frac{|R(0)|^2 \ell^2}{4\sigma_s^2} \left\{ 1 + \operatorname{erf} \left[\frac{1}{\sigma_p \sqrt{2}} \left(\tau - \left\{ \tau_o + \sigma_p^2 \beta \right\} \right) \right] \right\} e^{-\beta \left[\tau - \left(\tau_o + \beta \sigma_p^2 / 2 \right) \right]} \quad \tau \geq 0 \quad (21)$$

and $\bar{P}_r(\tau) = 0$ for $\tau < 0$. In equation (21), we have used the following notation;

$$\beta = \frac{c}{h} \left(\frac{4}{\gamma} + \frac{\ell^2}{4\sigma_s^2} \right)$$

Equation (21) illustrates how the amplitude and shape of the average return power vary with surface height correlation length and roughness. Figure 10 is a plot of $\bar{P}_r(\tau)$ (normalized) versus τ for various values of $(\ell/2\sigma_s)$. The curve for $(\ell/2\sigma_s) = 2$ corresponds to the "normal" rough surface case where σ° is essentially constant over the angular extent of the illuminated area ($\approx 0.8^\circ$). As $(\ell/2\sigma_s)$ increases, σ° decreases much more rapidly with angle of incident and this causes the "tail" of the average return to decay more sharply. In addition, the peak in the return occurs earlier in time. Figure 11 compares the system point response with the average return waveform for $(\ell/2\sigma_s) = 400^*$; we note that the two nearly

*The average return for $(\ell/2\sigma_s) = 400$ has been shifted to an earlier delay time by 2.5 ns.

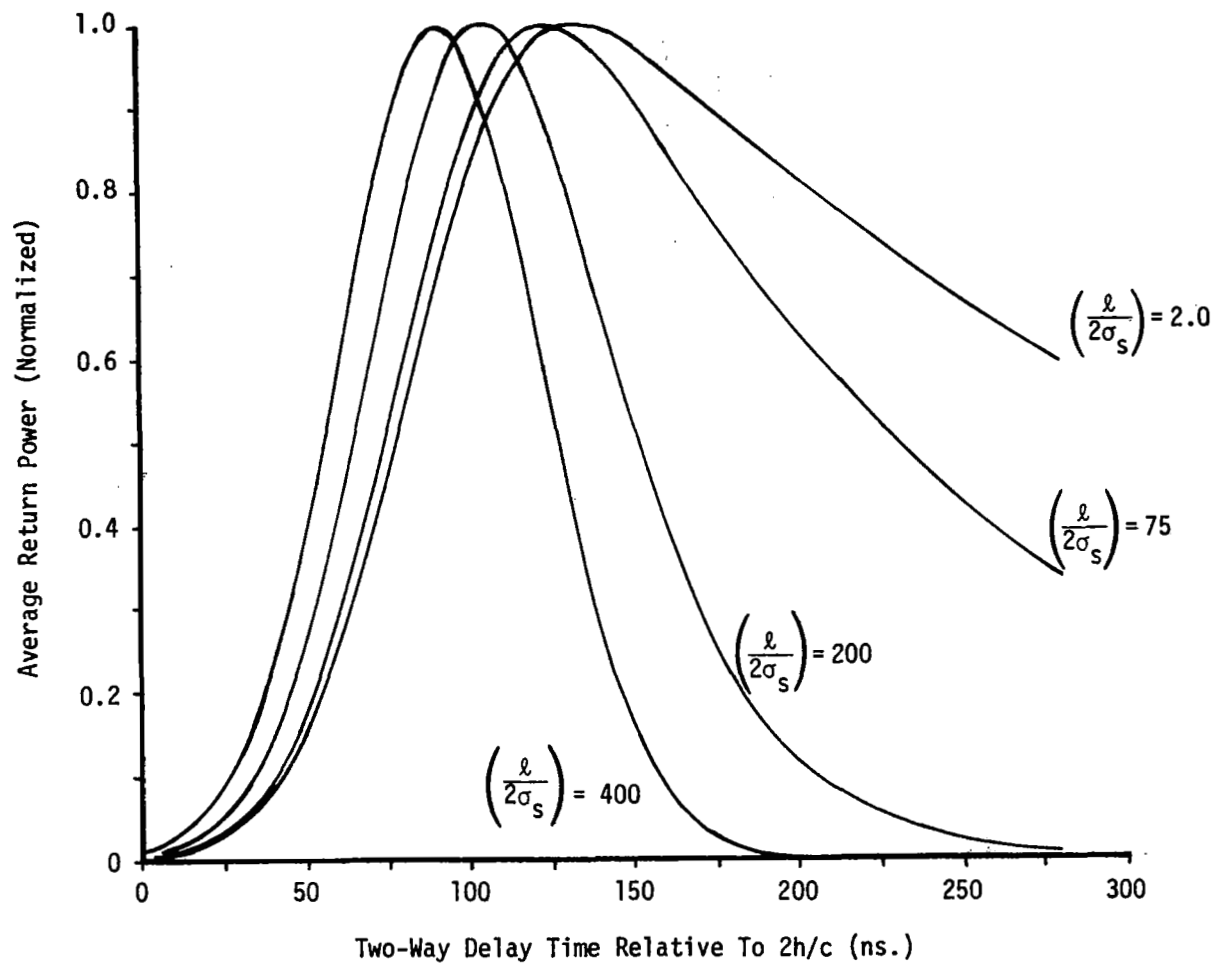


Figure 10. Variation of average return power waveform as a function $(l/2\sigma_s)$.

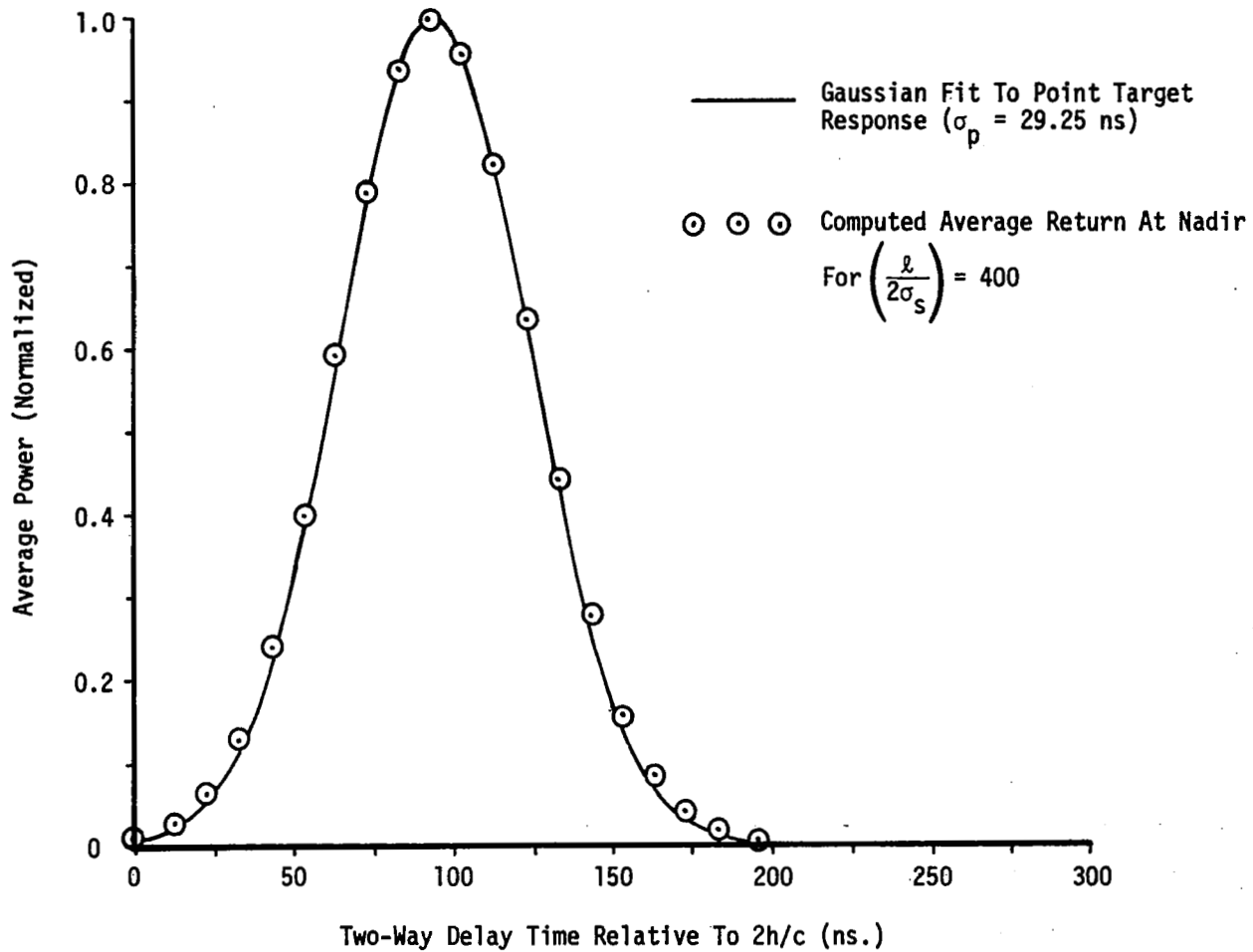


Figure 11. Comparison of system point target response and average return waveform for $(\lambda/2\sigma_s) = 400$.

overlap. Thus, for $(\lambda/2\sigma_s) \geq 400$, the average return waveform is nearly identical to the system point target response

It is also instructive to compare the peak of the average return power, as computed from equation (21), with the peak return from a specular surface, i.e. equation (3) with $\sigma_s = 0$. The ratio of these two quantities is shown in Figure 12 as a function of $(\lambda/2\sigma_s)$. We note that for $(\lambda/2\sigma_s) = 400$, the peak average return power is approximately 0.93 times as large as the specular power, or about 0.3 dB less. The dashed portion of the curve was not computed but rather is an extrapolation. It should be remembered that the curve in Figure 12 corresponds to very large values of σ° at normal incidence. For example, $(\lambda/2\sigma_s) = 40$ yields $\sigma^\circ(0^\circ) = 32$ dB, assuming $|R(0)|^2 = 1$.

Figures 10 and 12 indicate how the theoretical average return power varies with the correlation length to roughness ratio. We now turn our attention to extracting similar information from the recorded data. From Figure 1, we see that there is a significant decrease in return power and an increase in altitude noise during frames 5,6,8,9 and 10 of $S^2M 2$. Unfortunately, during this sub-submode, the S&H gates are positioned on the trailing edge of the point target response. This fact is illustrated in Figure 7 where the second set (later in time) of S&H gates correspond to the $S^2M 2$ position. Thus, for those cases where the average return waveform is nearly equal to the system point target response, only S&H gates 1 and 2 will be measuring signal while the remaining six will be responding to internal system noise. This can be more graphically demonstrated by plotting the single frame averages for S&H gates 1 through 8 such as shown in Figures 13 and 14.

Starting with frame 1, we see that S&H gates 2 through 8 were measuring system noise. However, as we look at succeeding frames, we see that the "tail" of the average return begins to "pull-up" and decrease less rapidly with increasing S&H gate number. Comparing these changes in the "tail" of the average return with the AGC and altitude data in Figure 1, we see that those frames for which the decay rate of the "tail" decreases correspond to the frames exhibiting low return power and higher altitude noise level. We note that these results are in excellent qualitative agreement with the model results. That is, as $(\lambda/2\sigma_s)$ decreases, the "tail" of the average return decreases (see Figure 12), and the altitude measurement noise level increases due to fading of the return. Unfortunately, it is not possible, to any

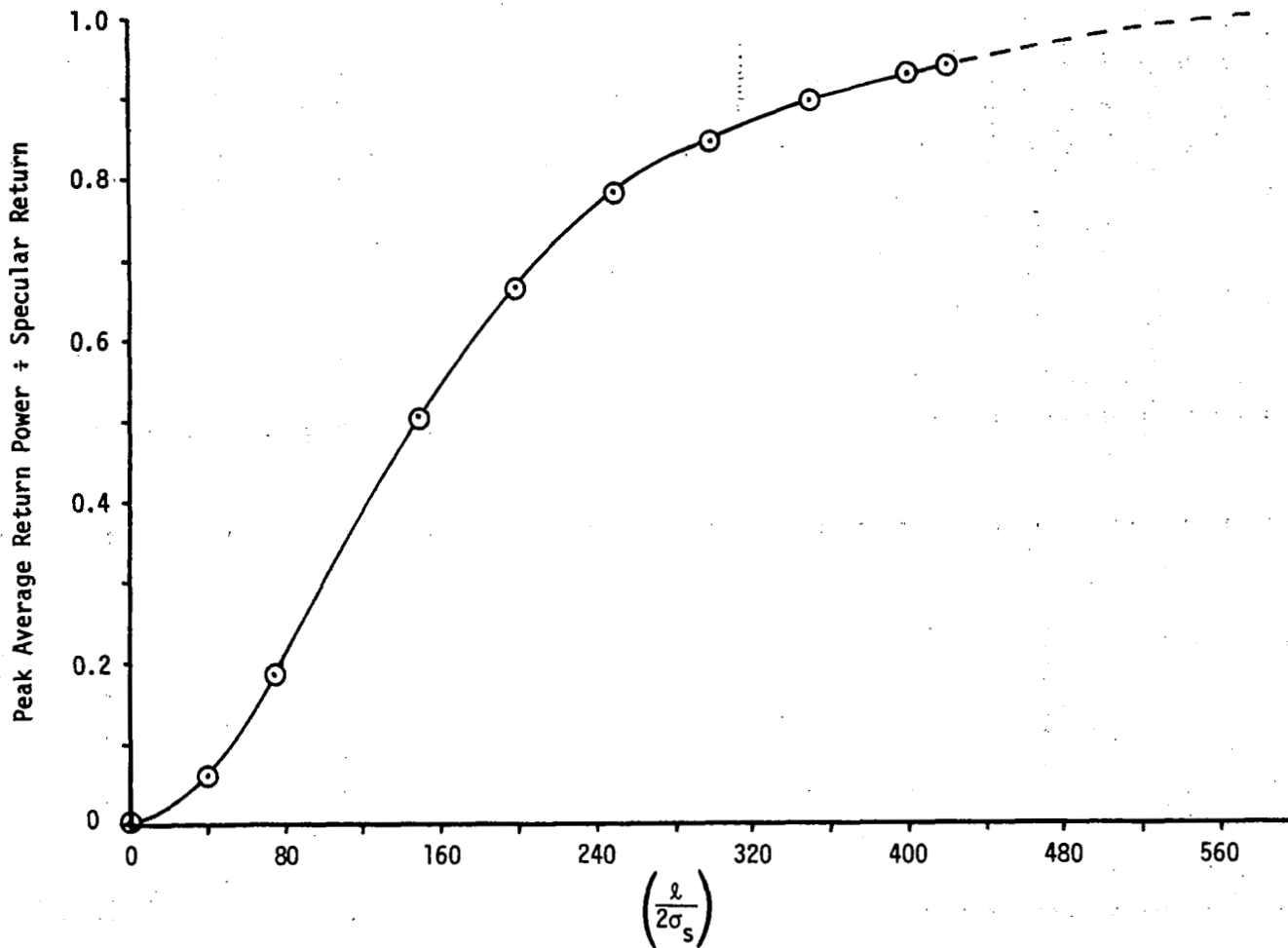


Figure 12. Comparison between the peak specular return power (with $\sigma_s = 0$) and the peak average return power as a function of $(\lambda/2\sigma_s)$.

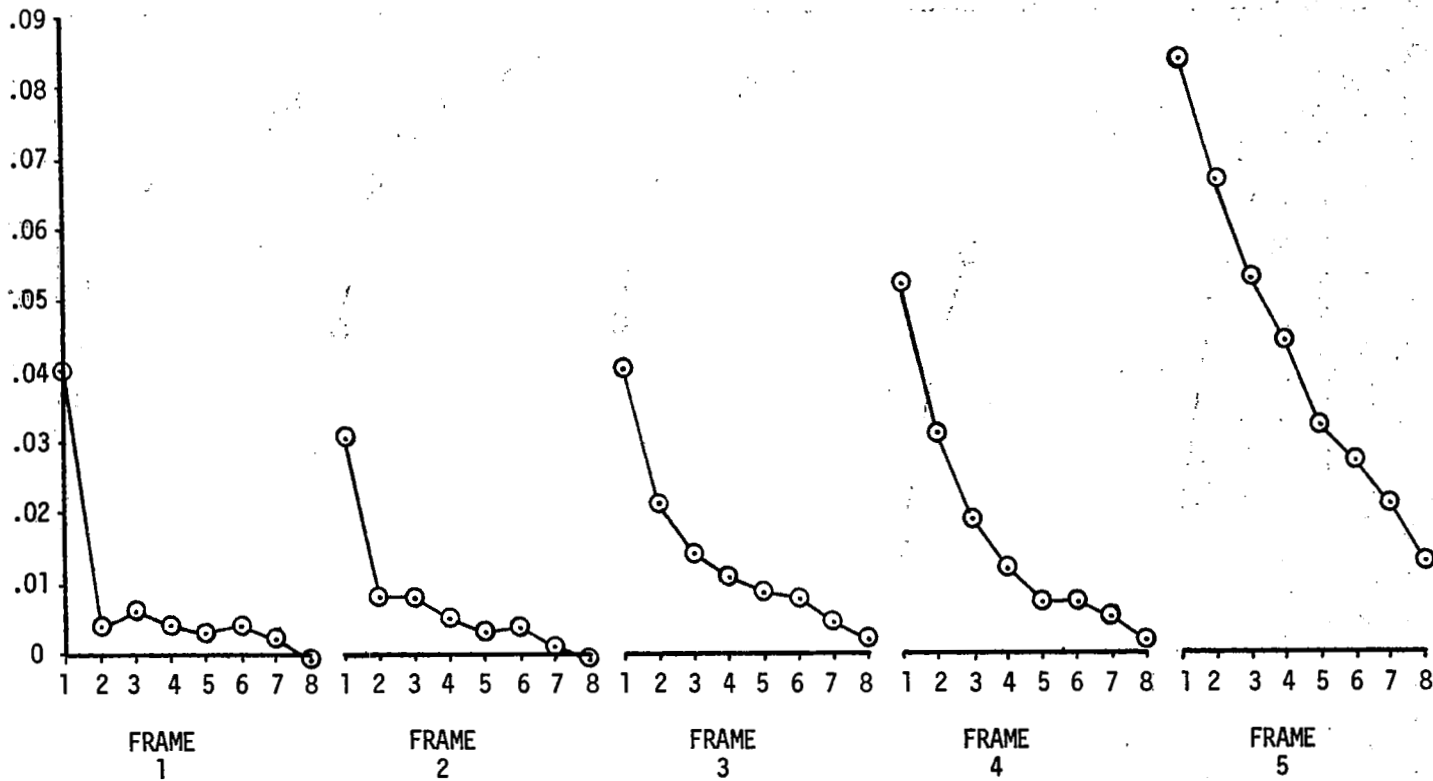


Figure 13. Single frame (104 returns) waveform averages for S^2M 2 and frames 1 through 5. Vertical axes in volts, horizontal axes in S&H gate number.

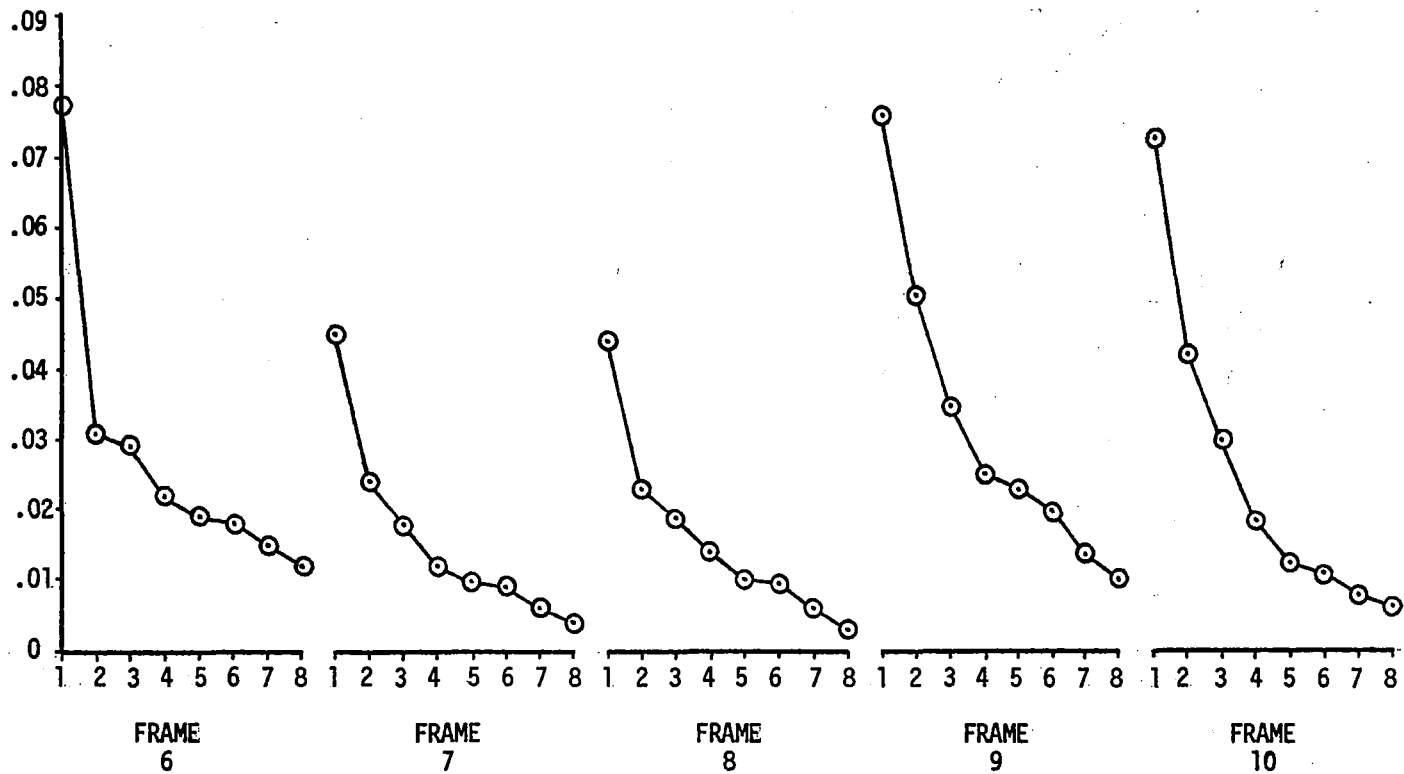


Figure 14. Single frame (104 returns) waveform averages for S²M 2 and frames 6 through 10. Vertical axes in volts, horizontal axes in S&H gate number.

reasonable degree of accuracy, to go beyond this qualitative comparison because (1) the S&H gates only measured a small portion of the return, and (2) we do not know exactly where the tracker positions* the S&H gates. However, we do note that there is good qualitative agreement between the radar data and the model predictions in the transitional region, i.e. from $(\lambda/2\sigma_s)$ very large to $(\lambda/2\sigma_s)$ moderate.

Figures 15 and 16 are histograms of S&H gates 1 and 2 in S^2M^2 for frames 1 through 8. These data further confirm the fact that the fluctuating nature of the return does not change character** as the surface conditions vary. The exponential behavior of the histograms justify our use of the superposition integral for the average return power, i.e. equation (1), and deny the possibility of a truly specular scattering surface.

3.0 Correlation Of The Model With Laser Profilometer Surface Measurements

About three months prior to the occurrence of EREP pass 39, there was an aircraft overflight of the Desert area in support of the S-193 Scatterometer. The aircraft carried a laser profilometer to measure the surface topography and statistics. The ground track of the flight is shown in Figure 2. Although the aircraft's flight was nearly orthogonal to the Pass 39 ground track, the laser data is considered to be representative of the Great Salt Lake Desert area in general. Data corresponding to the "smoothest" surfaces encountered during the aircraft flight were reduced by Krishen and Pounds and summarized in Reference 12. For these particular data the rms surface height was on the order of 0.15 m while the equivalent correlation length was approximately 77.65 m. These results yield a value of 258.9 for the ratio $\lambda/2\sigma_s$.

From the plots in Figure 10, we see that $(\lambda/2\sigma_s) = 258.9$ would produce an average return power waveform which is very close to the system point target response. Furthermore, this value of $(\lambda/2\sigma_s)$ would yield a peak average return power level which is about 0.8 of the maximum ($\sigma_s = 0$) specular

*The average position of the S&H gates on the waveform is determined by the centroid point of the tracker. This centroid point is also a function of the shape of the average return waveform.

**Although the mean and variance change, the basic probability density function is very nearly exponential in all cases.

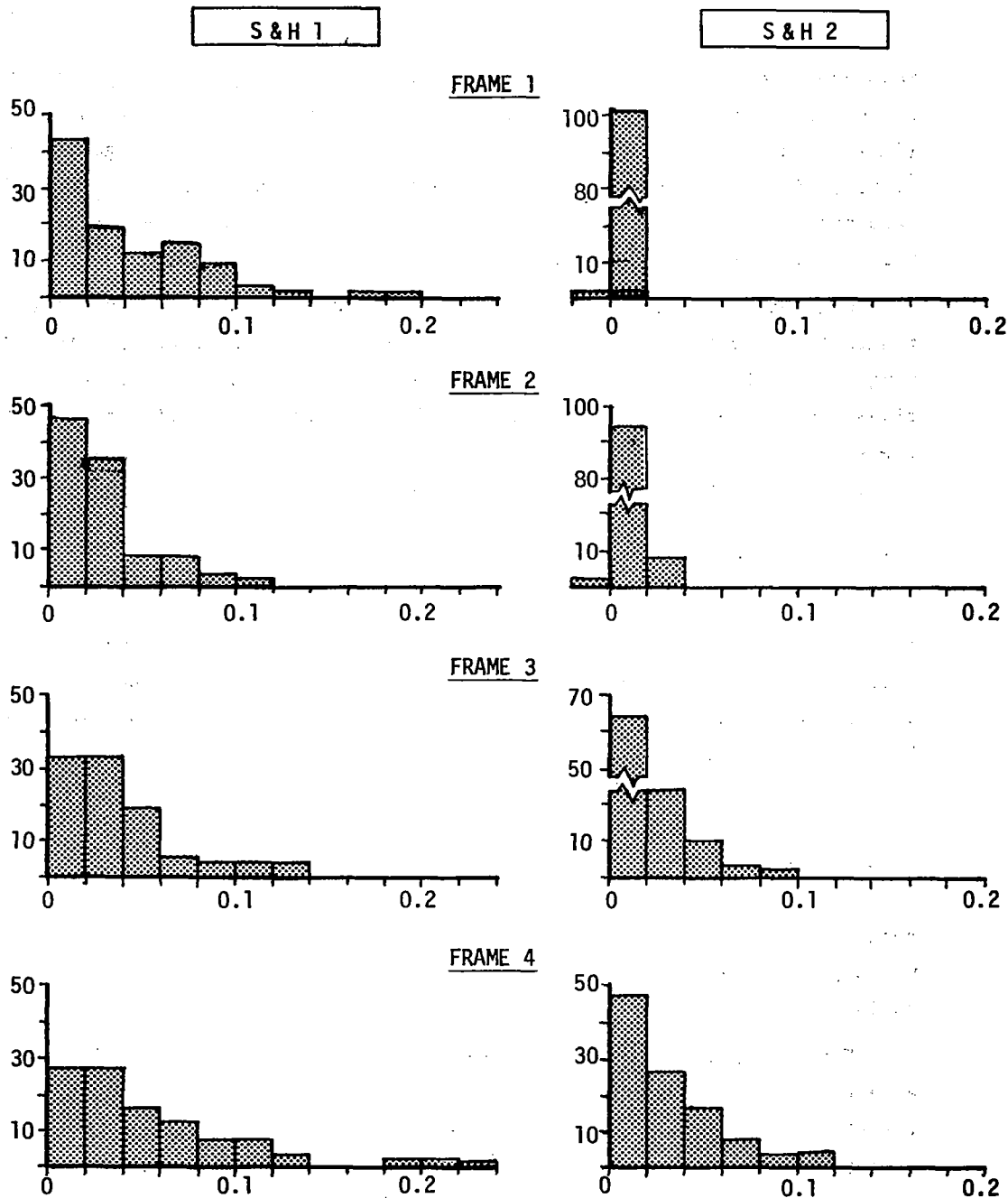


Figure 15. Histograms for S&H gates 1 and 2 in S^2M^2 (frames 1 through 4). Vertical axes in frequency of occurrence, horizontal axes in voltage.

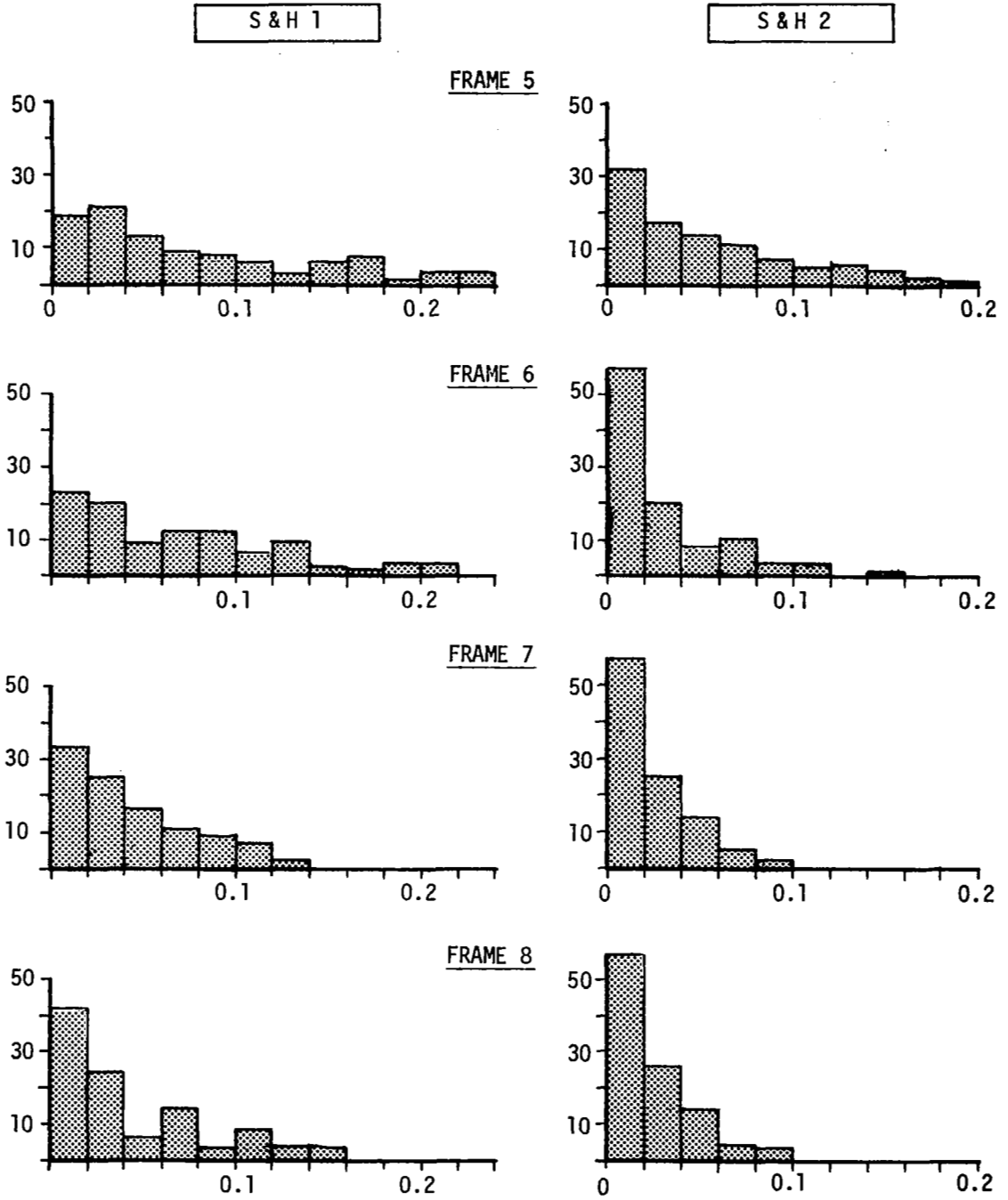


Figure 16. Histograms for S&H gates 1 and 2 in $S^2M 2$ (frames 5 through 8). Vertical axes in frequency of occurrence, horizontal axes in voltage.

return. Thus, we see that the profilometer data supports the scattering model put forth in this chapter. An even more convincing argument against pure specular reflection is the fact that for $\sigma_s = 0.15$ m

$$4k_o^2 \sigma_s^2 = 7.63 \times 10^3$$

and the specular return as given by equation (3) is extremely small. In other words, the pure specular reflection model for the Great Salt Lake Desert scattering data is incorrect because it

- (1) fails to predict the fluctuating nature of the return,
- (2) only predicts a point target return for the average return and does not explain all of the observed waveform data,
- (3) and is, finally, not consistent with the mean square height data obtained by the laser profilometer.

4.0 Conclusions

In this paper we have analyzed radar altimeter measurements obtained over the Great Salt Desert Lake area which, in general, are typical of the kind of data acquired over numerous land targets by the S-193 instrument. These data are characterized by; (1) a very high return power level, (2) a very low altitude measurement noise level and, (3) an average return waveform which is very similar to the system point target response.

We investigate the various models for extended target scattering and conclude that the observed data are best explained by a special case of the so-called large roughness "physical optics" model where the ratio of surface height correlation length to rms roughness is very large (≥ 800). We show that as this ratio becomes infinite, the surface scattering cross section per unit scattering area (σ^o) approaches a delta function. In this limit, the average return power approaches the power reflected from a perfectly flat specular surface. We further demonstrate that in this case, the shape of the average return power as a function of delay time is identical to the system point target response. We also point out that for this model to apply, there must be pulse-to-pulse fluctuation, i.e. even for $(\lambda/2\sigma_s)$ large, the scattering process must still be random.

In analyzing the data obtained over the Great Salt Lake Desert area, we note that, in every respect, it is in agreement with the special limiting form of the large roughness physical optics scattering model. In this sense, we can therefore state that the behavior of the data is explained and the model is verified.

Our analyses of these data lead us to reject a previous hypothesis that these types of surfaces behave as specular targets. Our reason for rejecting this hypothesis is that true specular surfaces produce a return which exhibits relatively small fluctuation whereas the data obtained by the S-193 altimeter exhibited exponential fluctuation, i.e., a characteristic of a random scattering surface. The distinction between true specular surface scatter and the limiting form of the "physical optics" model is important because of their differing dependence upon surface parameters. That is, whereas the specular return power depends only on the mean square height of the surface, the return power predicted by the physical optics model is a function of both the mean square height and the surface height correlation length. For remote sensing applications the distinction can be significant.

REFERENCES

1. McGoogan, J. T., L. S. Miller, G. S. Brown, G. S. Hayne, "The S-193 Radar Altimeter Experiment," Proc. of IEEE, Vol 62, pp. 793-803, June 1974.
2. Shapiro, A. and B. S. Yapple, "Anomalous Radar Backscattering From Terrain at High Altitudes," Proc. of IEEE, Vol 63, pg 717, April 1975.
3. Moore, R. K. and C. S. Williams, Jr., "Radar Terrain Return At Near-Vertical Incidence," Proc. of IRE, Vol. 45, pp. 228-238, February, 1957.
4. Ruck, G., D. Barrick, W. Stuart, and C. Kirchbaum, "Radar Cross Section Handbook", Plenum Press, pp. 700-703, 1968.
5. Beckman, P. and A. Spizzichino, The Scattering of Electromagnetic Waves From Rough Surfaces, Macmillian Co., Chapter 12, 1963.
6. Barrick, D. E. and W. H. Peake, "Scattering From Surfaces With Different Roughness Scales: Analysis and Interpretation," Battelle Memorial Institute Technical Report, Contract DA-49-083 OSA-3176, 1 Nov., 1967.
7. Barrick, D. E., "Rough Surface Scattering Based On The Specular Point Theory," IEEE Trans. Antennas and Propagation, Vol. AP-16, pp. 449-454, July, 1968.
8. _____, "S-193 Microwave Radiometer/Scatterometer Altimeter Calibration Data Report," Vol 1B, General Electric Co., Valley Forge, PA., 22 March, 1973.
9. Steenson, B. and N. Sterling, "The Amplitude Distribution and False Alarm Rate of Filtered Noise," Proc. of IEEE, pp. 42-55, January 1965.
10. Brown, G. S., "Reduced Backscattering Cross Section (σ^0) Data From The Skylab S-193 Radar Altimeter," NASA CR-141401, Applied Science Associates, Inc., Apex, N. C., October 1975.
11. Hofmeister, E. L., "Analysis and Measurement of the Performance of a Signal Tracking Loop for a Satellite Radar Altimeter When Excited by a Random Process," Ph.D. Thesis, Syracuse University, Syracuse, New York, December, 1973.

REFERENCES (Cont'd.)

12. Krishen, K. and D. J. Pounds, "S-193 Scatterometer Backscattering Cross Section Precision/Accuracy For Skylab 2 and 3 Missions," Report No. LEC-6119, Lockheed Electronics Company, Inc., Aerospace Systems Division, Houston, Texas, June, 1975.

CHAPTER 10

Pulse-to-Pulse Correlation Measurements

by

E. J. Walsh

1.0 Background

Mode III of the S-193 radar altimeter was designed to study pulse-to-pulse correlation as a function of pulse spacing, SNR and pulse length. Pulse-pairs of both 100 ns and 10 ns durations were transmitted. A pair of pulses was transmitted every 4 ms with a variable time interval, Δt , between them. Four of the Sample and Hold (S&H) gates sampled the first return pulse while the other four (at the same relative positions) sampled the second return pulse. Pulse-pairs were transmitted at the rate of 250 per second but to reduce the data rate, only the first and third of each group of five were recorded for an effective data rate of 100 returns per second (104 per frame). The mode began with $\Delta t = 819.25 \mu\text{s}$; 104 of the returns were recorded by the S&H gates per frame. Then with the S&H gates sampling the same relative positions on the return pulses the pulse-pair separation was reduced to $409.65 \mu\text{s}$ and another 104 pulse-pair returns were sampled per frame. The procedure was repeated four more times with Δt being reduced successively to 153.65, 76.85, 19.25 and $1.05 \mu\text{s}$. Then the S&H gates were shifted to sample later portions of the return pulses and the six pulse-pair separations were stepped through again with 104 pulse-pairs recorded at each separation interval.

When the 100 ns pulses were transmitted, the S&H gates were spaced 25 ns apart and shifted through four sets of positions so that the first and second pulses were eventually sampled at the same 16 points spaced uniformly at intervals of 25 ns. The first Mode III of EREP Pass 24 will be used for an example since the pointing angle (0.15°) was the closest to nadir of any of the Mode III data sets. Figure 1 shows the averages of the 104 pulse returns for the first pulse (solid line) and the second pulse (dashed line) for each of the six pulse-pair separations. It took 25 seconds to record the data and because data were acquired for all pulse-pair separations before the S&H gates were shifted to new relative locations on the pulses, the data in the 300, 325, 350 and 375 ns ranges were acquired 18.7 seconds after the data in the 0, 25, 50 and 75 ns ranges. If the pointing

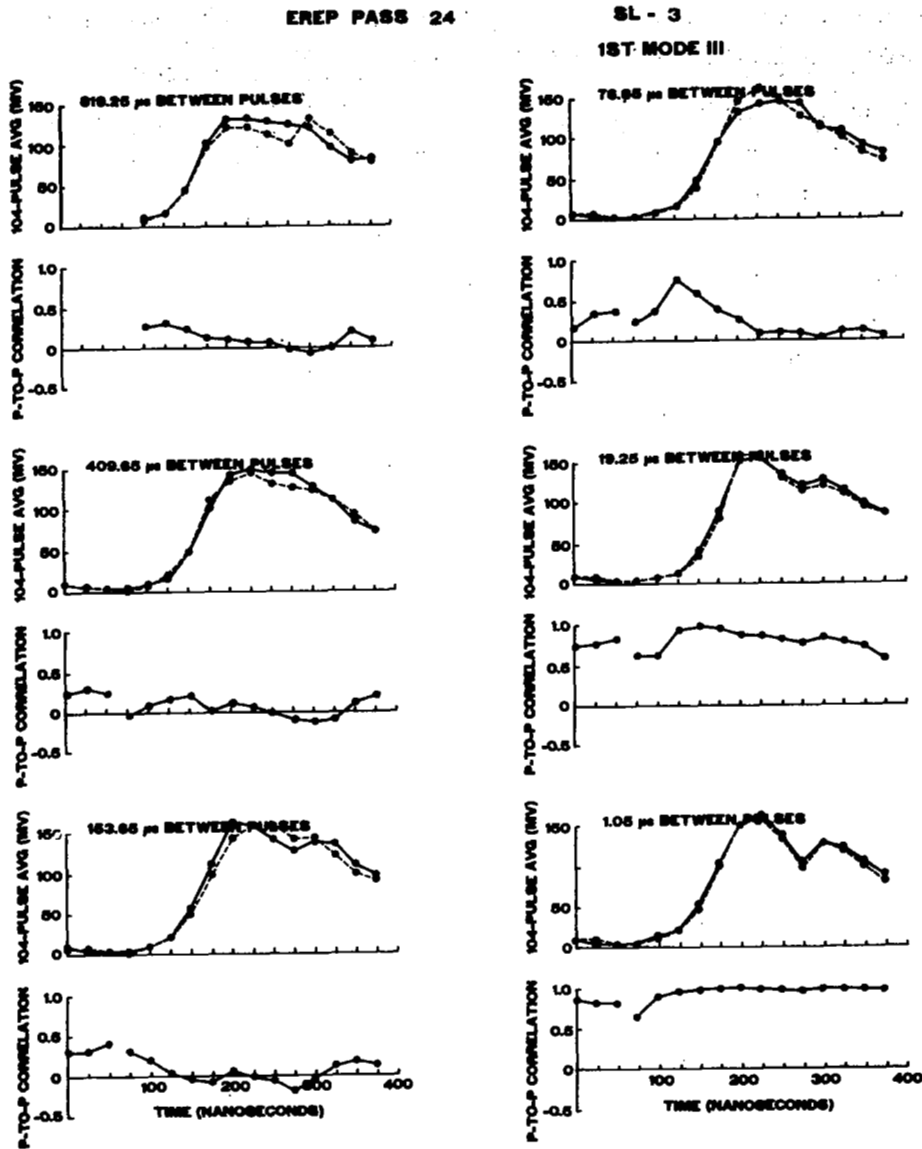


Figure 1. Mean return shapes for the first and second (dashed curves) transmitted pulses and pulse-to-pulse correlation for the six interpulse time intervals in Mode III of the Skylab S-193 radar altimeter. The plateau decay indicates that the antenna boresight was somewhere on an ellipse whose semiminor axis was 0.15° along-track and whose semimajor axis was 0.2° cross-track.

angle were changing with time then each of the four portions of the composite pulse returns would correspond to a somewhat different pointing angle.

Below each set of mean returns is a plot of the variation in the pulse-to-pulse correlation. A brief discussion of autocorrelation, cross correlation and the computational technique used in computing the correlation coefficients will be undertaken before the data are examined in detail. Figure 2a represents the output, x , from some continuous process which is sampled at n discrete, evenly spaced intervals. The autocorrelation coefficient with lag j could be obtained for the process from the expression

$$C_j = \frac{n}{n-j} \frac{\sum_{i=1}^{n-j} z_i z_{i+j}}{\sum_{i=1}^n z_i^2}, \quad j \neq 0 \quad (1)$$

where

$$z_i = x_i - \mu$$

$$\mu = \frac{1}{n} \sum_{i=1}^n x_i$$

If two separate process, x and y (Figure 2b) are to be compared then it would be appropriate to use the cross correlation coefficient, i.e.

$$C = \frac{\sum_{i=1}^n z_i w_i}{\left\{ \left(\sum_{i=1}^n z_i^2 \right) \left(\sum_{i=1}^n w_i^2 \right) \right\}^{\frac{1}{2}}} \quad (2)$$

where

$$w_i = y_i - v$$

$$v = \frac{1}{n} \sum_{i=1}^n y_i$$

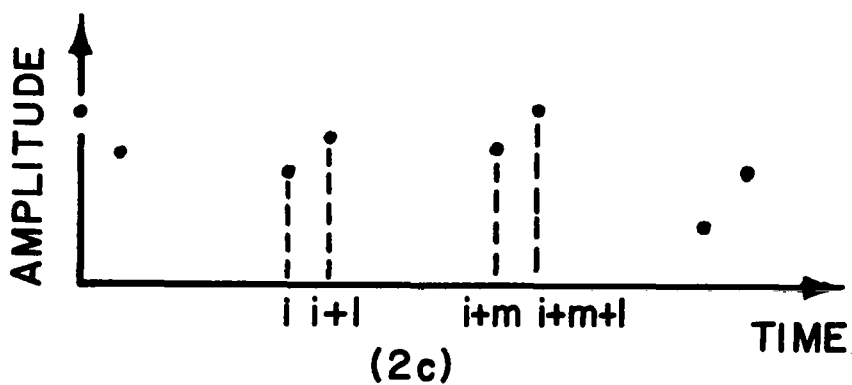
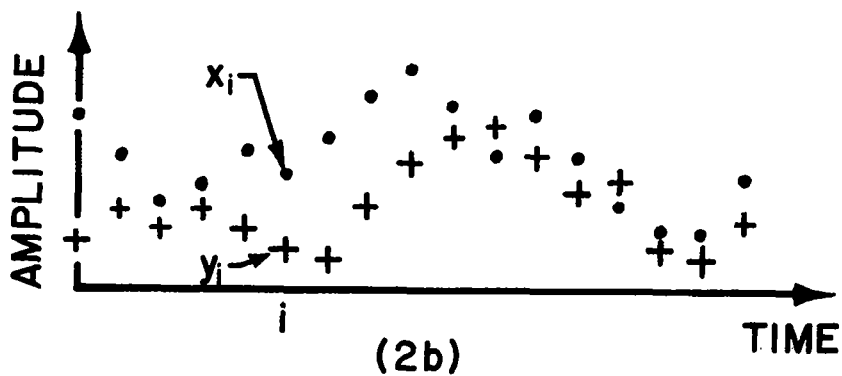
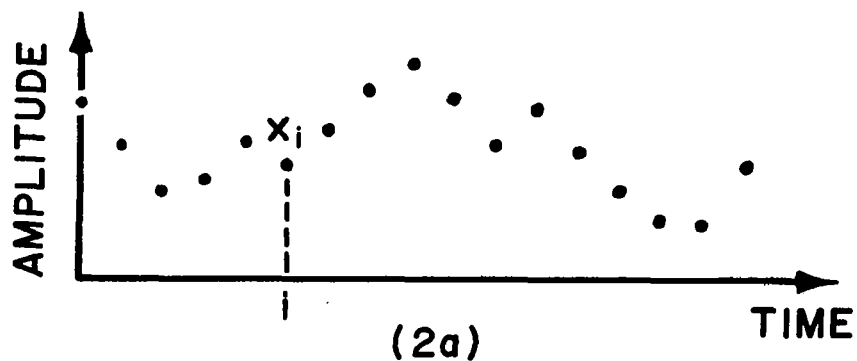


Figure 2. Three situations for computing correlation: (a) autocorrelation with lag j for evenly spaced samples from a single process; (b) cross correlation for two separate processes; (c) auto-correlation for a single lag for widely separated pair of pulses.

Figure 2c indicates the situation which exists in the Skylab data. The pulses are transmitted in pairs separated by Δt . The time interval between the i^{th} pair and the $(i+1)$ pair is so long (≥ 8 ms) that the pairs are completely uncorrelated from each other. In this situation one could only compute the autocorrelation coefficient for one lag, corresponding to the time interval Δt . If there are n pulse pairs then (1) would have to be modified to

$$C_{\Delta t} = \frac{\sum_{i=1}^n z_i z_{i+\Delta t}}{\frac{1}{2} \sum_{i=1}^n (z_i^2 + z_{i+\Delta t}^2)} \quad (3)$$

where

$$z_i = x_i - \mu$$

$$z_{i+\Delta t} = x_{i+\Delta t} - \mu$$

$$\mu = \frac{1}{2n} \sum_{i=1}^n (x_i + x_{i+\Delta t})$$

Equations (3) and (2) are very similar with the main difference being that the cross correlation expression (2) allows for two different mean values whereas the autocorrelation expression (3) has only one mean value since it represents only one process. If the cross correlation expression is evaluated with $y_i = x_{i+\Delta t}$ then (2) becomes

$$C = \frac{\sum_{i=1}^n z_i z_{i+\Delta t}}{\left\{ \left(\sum_{i=1}^n z_i^2 \right) \left(\sum_{i=1}^n z_{i+\Delta t}^2 \right) \right\}^{\frac{1}{2}}} \quad (4)$$

where

$$z_i = x_i - \frac{1}{n} \sum_{i=1}^n x_i$$

$$z_{i+\Delta t} = x_{i+\Delta t} - \frac{1}{n} \sum_{i=1}^n x_{i+\Delta t}$$

When x_i and $x_{i+\Delta t}$ are part of the same process with the same mean and n is large (as in the Skylab case),

$$\frac{1}{n} \sum_{i=1}^n x_i \approx \frac{1}{n} \sum_{i=1}^n x_{i+\Delta t} \approx \frac{1}{2n} \sum_{i=1}^n (x_i + x_{i+\Delta t}) \quad (5)$$

and (3) and (4) would produce nearly identical answers. The Skylab data were analyzed using both (3) and (4), but the correlations presented are those determined by (4) since the trailing edge of the first pulse changed the mean value of the second pulse for the 1.05 μ s pulse separation when the antenna was pointed off nadir. In the cases where the second pulse of the pair was not affected by the first the results were virtually identical.

2.0 Comparison of Measurements and Theory

The first four points on the 819.25 μ s separation returns were missing from the data due to a hardware sequencing malfunction. On the remaining pulse separations the first three S&H gate correlations should have been near zero since they were located in the noise ahead of the returns. However, the correlations are significantly greater than zero. There is apparently some significant correlation in the gates in the absence of a return signal. To emphasize that this is an anomalous, there is no line joining the correlation values for the third and fourth gates as a reminder that the first three values should be ignored. S&H data anomalies are discussed more thoroughly in Chapter 13.

Taking the reciprocal of the doppler bandwidth for a 100 ns pulse-limited circle [1] indicates a 87 μ s decorrelation time. The Van Cittert-Zernike theorem (modified by halving the decorrelation distance in applying

it to a radar system [2]) suggests a decorrelation time of 106 μ s for the beginning of the plateau region. A cursory examination of the data indicates these are reasonable decorrelation times since the 819.25, 409.65 and 153.65 pulse separations are uncorrelated, the 19.25 and 1.05 μ s pulse separations are correlated and the 76.85 μ s separation seems to contain a transition region.

The fluctuations in the correlations observed in the data are lower when the mean correlation is high (1.05 and 19.25 μ s pulse separations) than when the mean correlation is low (819.25, 409.65, 153.65 μ s separations). Dr. R. W. L. Thomas of Wolf Research and Development Corporation (personal communication, 1973) has shown that when (1) is used to compute the correlation of independent random numbers there will be a negative bias in the correlation of $-1/(n-1)$. This bias would be unnoticeably small (-.0097) in this data set. Of more importance in this study is that Dr. Thomas has shown by simulation that the variance in the computed correlation coefficient is approximately $1/(n-1)$ so the standard deviation of the computation on 104 totally independent points would be approximately 0.0985.

To develop predictions of the pulse-to-pulse correlation variation to be plotted for comparison with the observations a Monte Carlo simulation (described in the Appendix) was employed rather than an analytic approach [1]. Two sets of conditions were considered in the simulation: 104 consecutive pulses spaced at the pulse-pair separation (1); and 104 pairs of pulses with large time intervals between pairs (4). When 10 cases were run for each simulation for the 76.85 μ s pulse-pair separation the variation of the mean values were very nearly the same.

The standard deviations of the 10 cases were computed for each 25 ns time interval for each simulation and they were also nearly equal. The average of all the standard deviations for intervals where the mean correlation was less than 0.5 was 0.1043 for (1) and 0.0987 for (4) which is in good agreement with the results of Thomas. The standard deviation of the individual standard deviations from the mean standard deviation was 0.0236 for (1) and 0.0203 for (4) so by any measure either simulation gives a result to the same accuracy. The running time of the simulation using (1) was less than half that using (4) and it produced a smoother variation in correlation than (4) did so the simulation employing (1) was used. The simulation curves indicated are for one case, not an average of 10 cases.

Figure 3 shows the point target response of the radar [3] for the 100 ns pulse. It indicates the zero in the time origin used in plotting the pulse returns and correlations predicted by the simulation. It generally differs by about 75 ns from the origin used in plotting the actual data where zero time was referenced to the first S&H gate. Figure 4 is a comparison of the data from Figure 1 and the simulation predictions for pulse separations of 153.65 and 19.25 μ s. Because of the 75 ns shift in the time origin the first three radar data points (which have erroneously high correlations) do not appear in the figure. Although one would expect the pulses with 19.25 μ s separation to be correlated, the simulation indicates that the correlation should gradually decay as the range into the pulse is increased and that is borne out by the data. Note that the correlation in the plateau region of the 1.05 μ s separation data in Figure 1 appears perfectly flat as it should.

Only a single symbol (diamond) is used to represent the mean return pulse for the 19.25 μ s separation because the differences between the first and second pulse returns were always less than the symbol height. That is the way it should have been because of the high correlation between the pulses. There is good agreement between the data and the simulation mean pulse return. At the 25 ns point the data points are significantly above the simulation curve, indicating that the actual point target response started more abruptly than the Gaussian curve used to represent it.

The fit to the simulation would improve for both the mean return and the correlation if the four data points in the 125 to 200 ns regions were shifted to the right by about 15 ns. Similarly, the 153.65 μ s separation data points in the last four ranges of the mean return pulse show a positive bias and a more rapid decay than the simulation. Those data points would be in better agreement with the simulation if they were shifted to the left in range by about 40 ns. The possibility of a set of gates sampling other than the range interval they were supposed to is discussed in Chapter 13. However, the same relative positions on the first and second pulses generally appear to have been sampled even when there is apparently a shift from the proper delay. This is evidenced by the closeness of the amplitudes for the first and second pulses at the 19.25 μ s separation in Figures 4, 6, 7, 8, 21 even though there are kinks in the mean pulse returns at points where two successive sets of four data points join. The

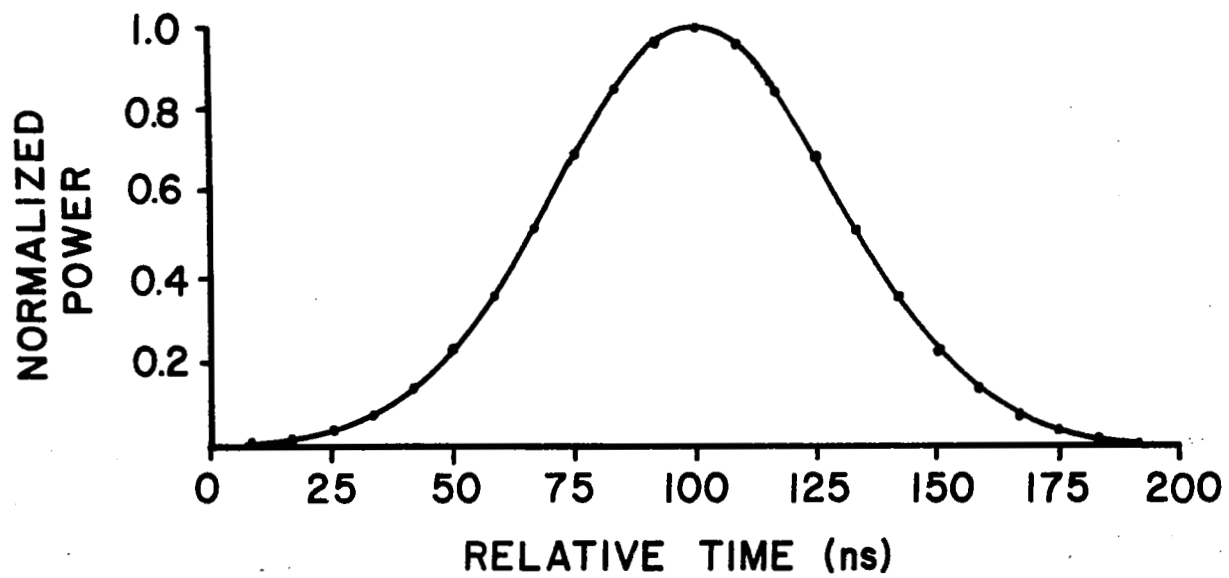


Figure 3. Radar altimeter point target response for the 100 ns transmitted pulse.

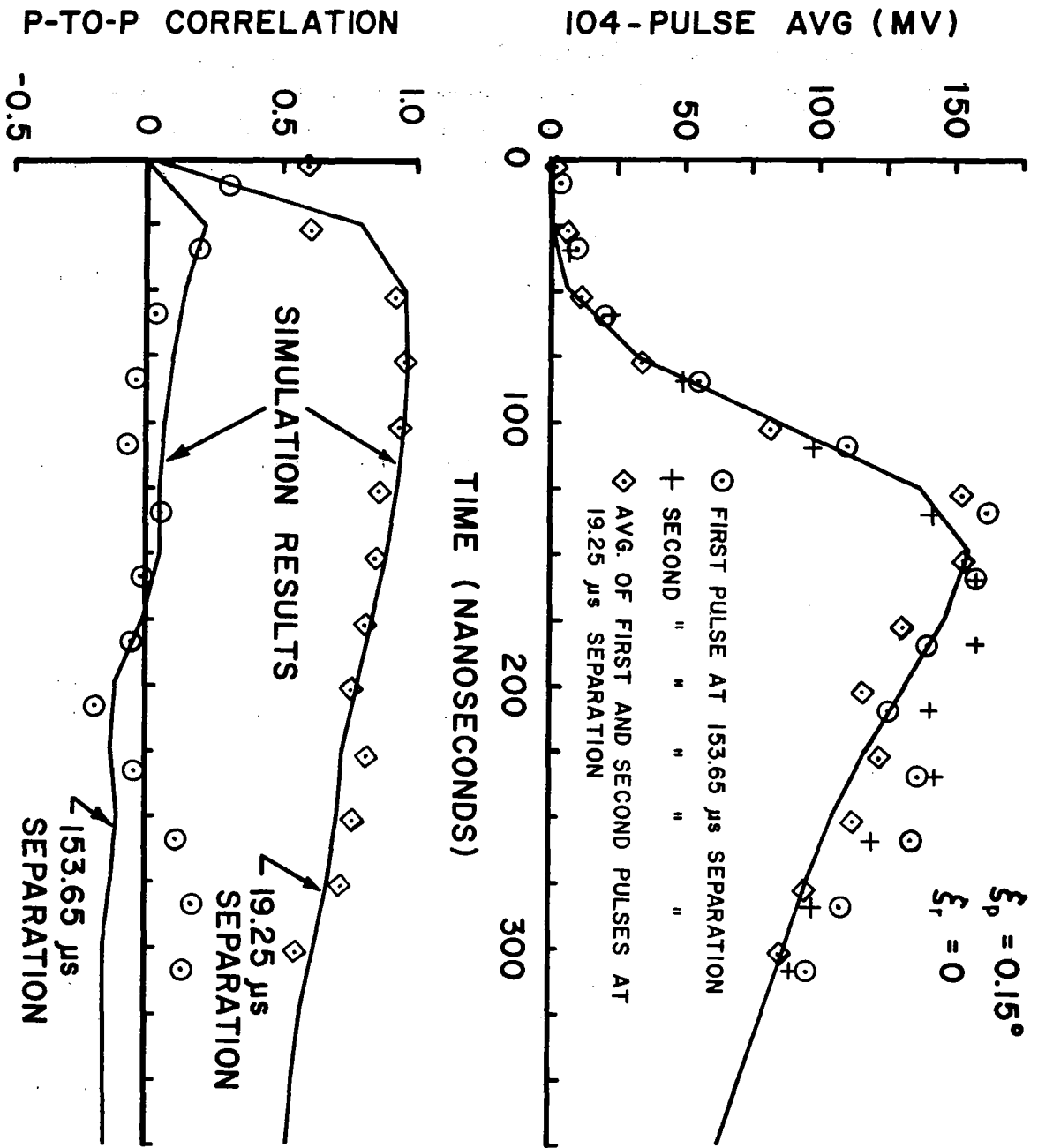


Figure 4. Data points from the 19.25 and 153.65 μ s pulse separations in Figure 1 compared with the Monte Carlo simulation results (solid curves) for an along-track angle of 0.15° .

data correlation points for the 153.65 μ s separation are in agreement with the simulation except for a positive bias in the last three points. The correlation should be zero in that region and the difference occurred because the simulation happened to be low when the observation happened to be high. That is why shifting the data to the left by 40 ns would not help.

2.1 The Effect of Pointing Direction

Since the pulse-pairs are entirely correlated for separations of 19.25 μ s or less and entirely uncorrelated at separations of 153.65 μ s or more, those are not very interesting cases for analysis. The rest of the chapter will be devoted to the 76.85 μ s separation case since the pulse-to-pulse correlation varies significantly within the pulse itself and the effects of pointing angle and SNR are more apparent. Figure 5 is a comparison of the 76.85 μ s separation data in Figure 1 and the Monte Carlo simulation results. The signals returning early in the pulse are highly correlated but the observed correlation is low because of the poor signal-to-noise ratio. As the signal level increases the observed correlation increases. But as the radius of the pulse-limited circle increases, the doppler bandwidth introduced by the satellite velocity increases and the correlation decreases. A detailed discussion of platform induced doppler in pulse-limited altimetry has been made by [2].

Figure 6 shows the doppler spectrum, normalized to their respective peaks, that would exist at various points in the return signal if an omnidirectional antenna were used. The curves correspond to the various times indicated in Figure 3 for the point target response. Curves 1 and 2 correspond to the rising portion of the return where the maximum illumination is at nadir. Curve 3 corresponds roughly to the beginning of the plateau region and the maximum illumination is beginning to shift away from nadir as evidenced by the dip in the doppler spectrum at zero frequency. At later times the illuminated area is an annulus of constant area whose width narrows and radius increases with time. This is apparent in the bimodal distributions of curves 4, 5, and 6. The peaks narrow and shift apart and the minima between the peaks deepen as time increases.

When the actual antenna pattern is considered the situation does not change a great deal if the antenna is pointed at nadir. However, if the

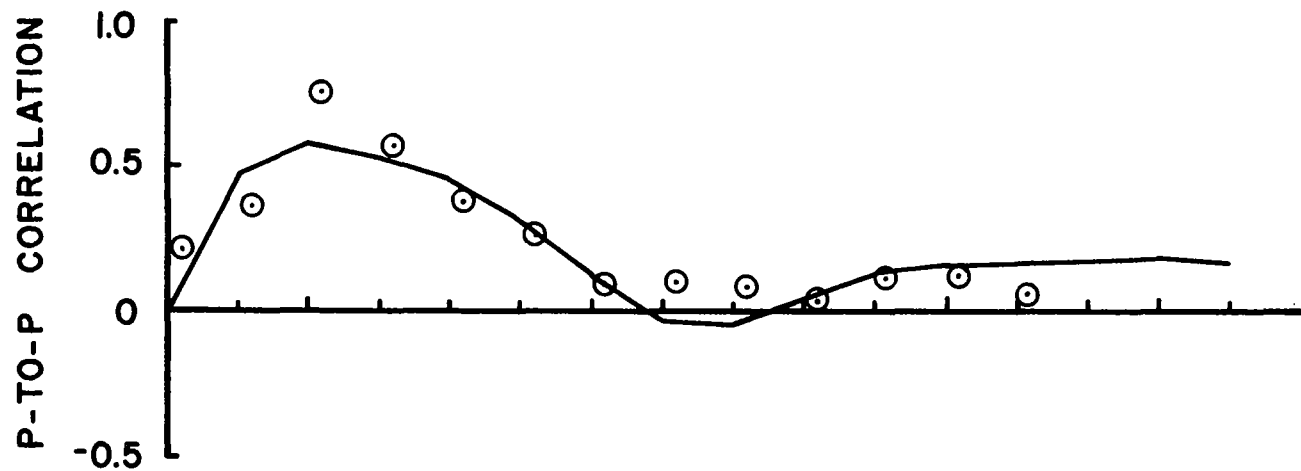
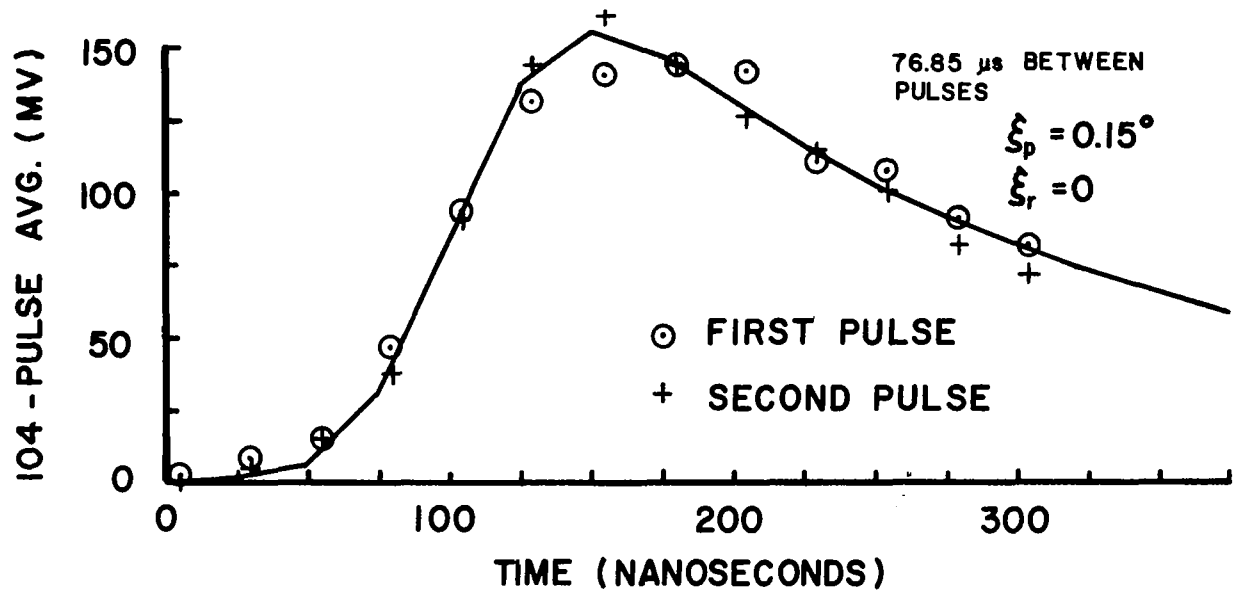


Figure 5. Data points from the 76.85 μ s pulse separation in Figure 1 compared with the Monte Carlo simulation results (solid curves) for an along-track pointing angle of 0.15° .

- 1- 25 ns
- 2- 100 ns
- 3- 150 ns
- 4- 225 ns
- 5- 300 ns
- 6- 375 ns

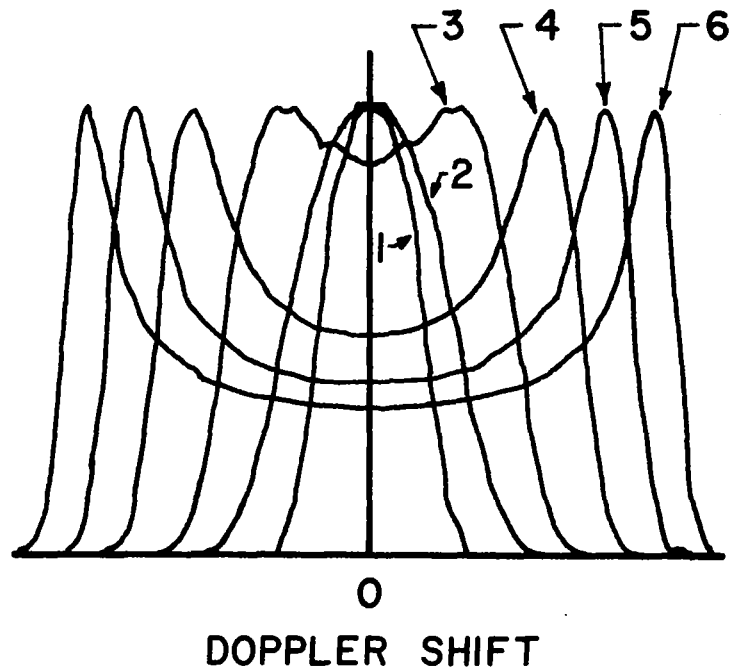


Figure 6. Doppler power spectra which would exist if an omnidirectional antenna were used. The various spectra have been normalized to their respective peaks.

antenna pointing angle is off-nadir the situation can be very different. Figure 7 indicates the manner in which the doppler spectrum for the 100 ns point (Curve 2) is affected by the antenna being directed off-nadir. If the antenna is pointed cross-track, then the lines of constant gain are nearly perpendicular to the lines of constant doppler and the narrowing of the doppler spectrum in going from nadir to 1.5° is approximately equal to the line thickness of the curve. However, when the antenna is pointed along-track the lines of constant gain are nearly parallel to the lines of constant doppler and that causes the spectral peak to shift towards the antenna and to narrow. If the SNR is sufficiently high the narrowing of the doppler spectrum will cause the correlation to be higher than it would have been if the antenna were pointing at nadir. For the region of the return pulse indicated by Curves 4, 5 and 6 in Figure 6 the correlation could show an increase with time for an along track pointing error because one peak in the bimodal spectra would be severely attenuated while the other one would be in the main part of the antenna pattern and would be narrowing with time.

Figures 8 and 9 show the relative variation in the return power as a function of pointing angle and position within the pulse return for the antenna pattern which existed during SL-2 and SL-3. The power is lower for a pointing angle along-track than for the same angle cross-track because the antenna pattern was slightly asymmetrical ($1.33^\circ \times 1.76^\circ$) with the more narrow axis being along-track [3]. The typical value of SNR during SL-2 and SL-3 for a nadir-directed antenna was 35 dB. If the antenna were pointing 1.5° off-nadir along-track the SNR would be above 15 dB for times greater than 200 ns. The SL-4 data were taken with a damaged reflector feed assembly and a resulting antenna pattern which was more symmetrical ($1.62^\circ \times 1.76^\circ$) but whose gain was 12.5 dB lower so the typical maximum SNR was only 10 dB.

Figure 10 shows the simulation predictions for the variation of the mean return and the pulse-to-pulse correlation as a function of pointing angle. The results for the SL-2, 3 antenna pattern are shown on the left where it was assumed that the peak SNR when the antenna was pointed at nadir was 35 dB. On the right side the simulation results are shown for the SL-4 antenna pattern assuming that the peak SNR with the antenna directed to nadir was 10 dB. Those SNR values were typical of the observations (see Chapter 13). Four curves indicating the variation with azimuthal angle are

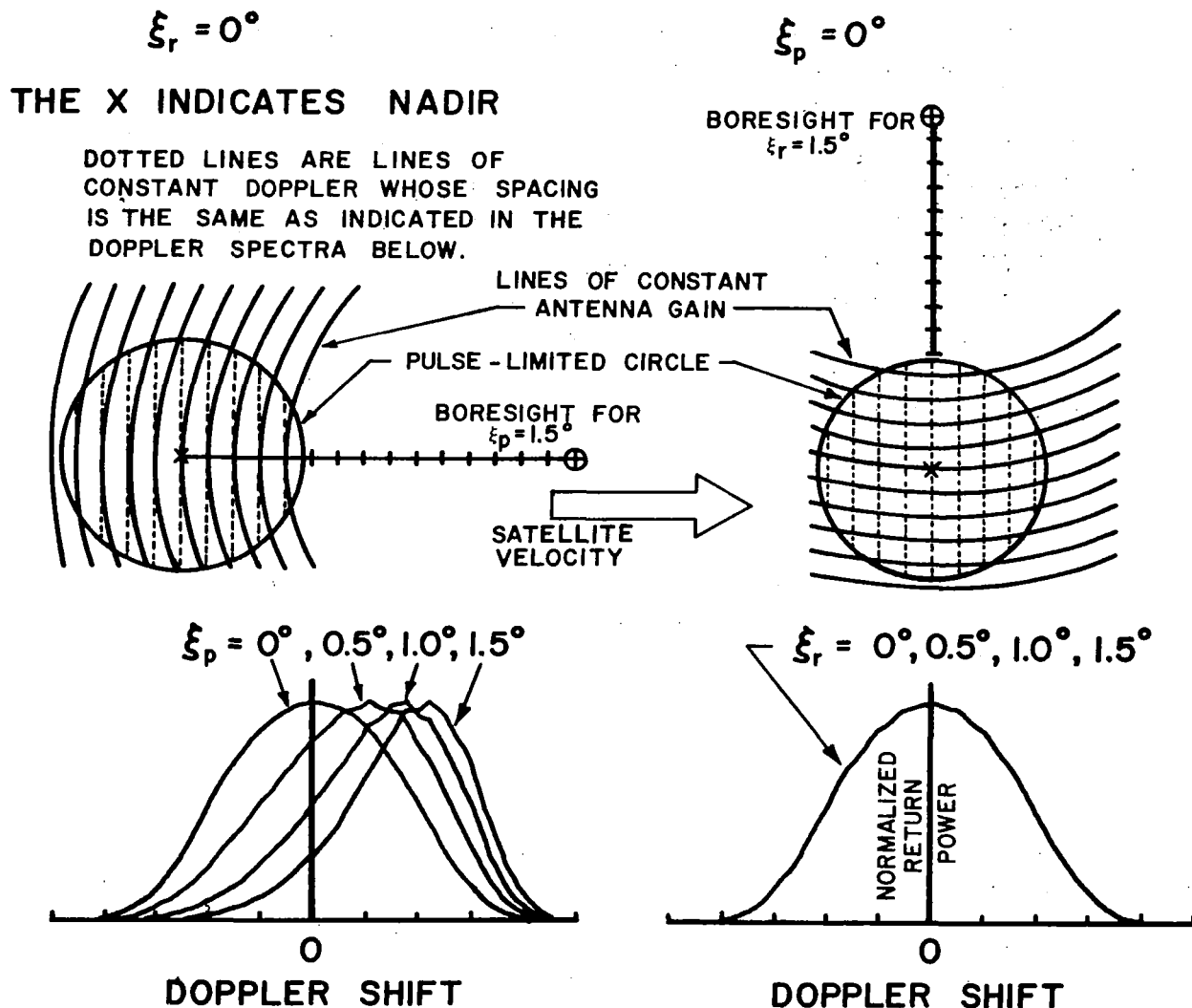


Figure 7. The lines of constant doppler shift and constant antenna gain and indicated for the 100 ns pulse-limited (time reference shown in Figure 3) for boresight angles of 1.5° . The doppler spectra, normalized to their respective peaks, for the 100 ns pulse-limited circle are shown for boresight angles along-track and cross-track of $0^\circ, 0.5^\circ, 1.0^\circ$, and 1.5° off-nadir for the SL-2,3 antenna pattern.

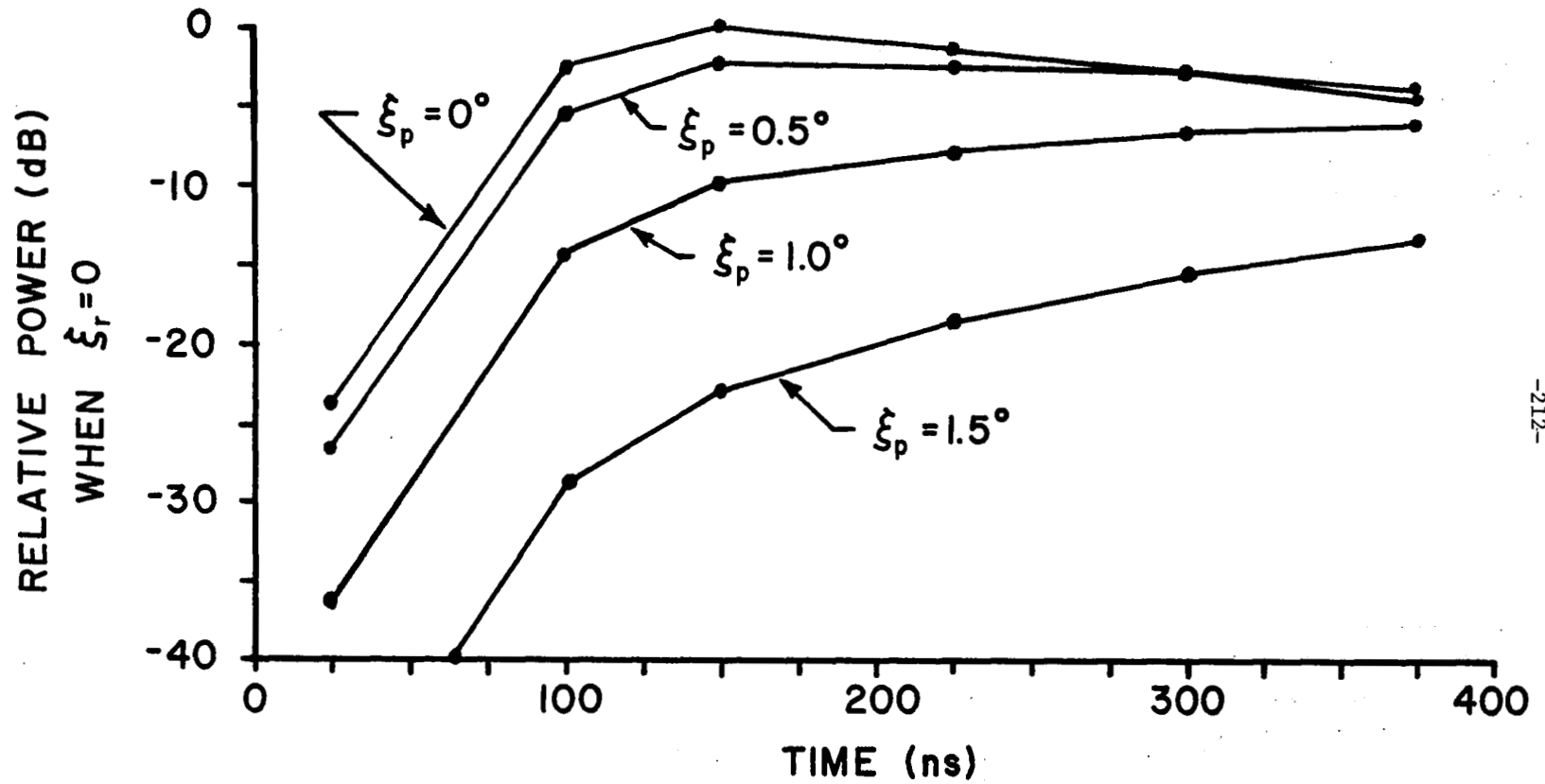


Figure 8. Relative power as a function of position within the pulse return for various along-track pointing angles for the SL-2, 3 antenna pattern.

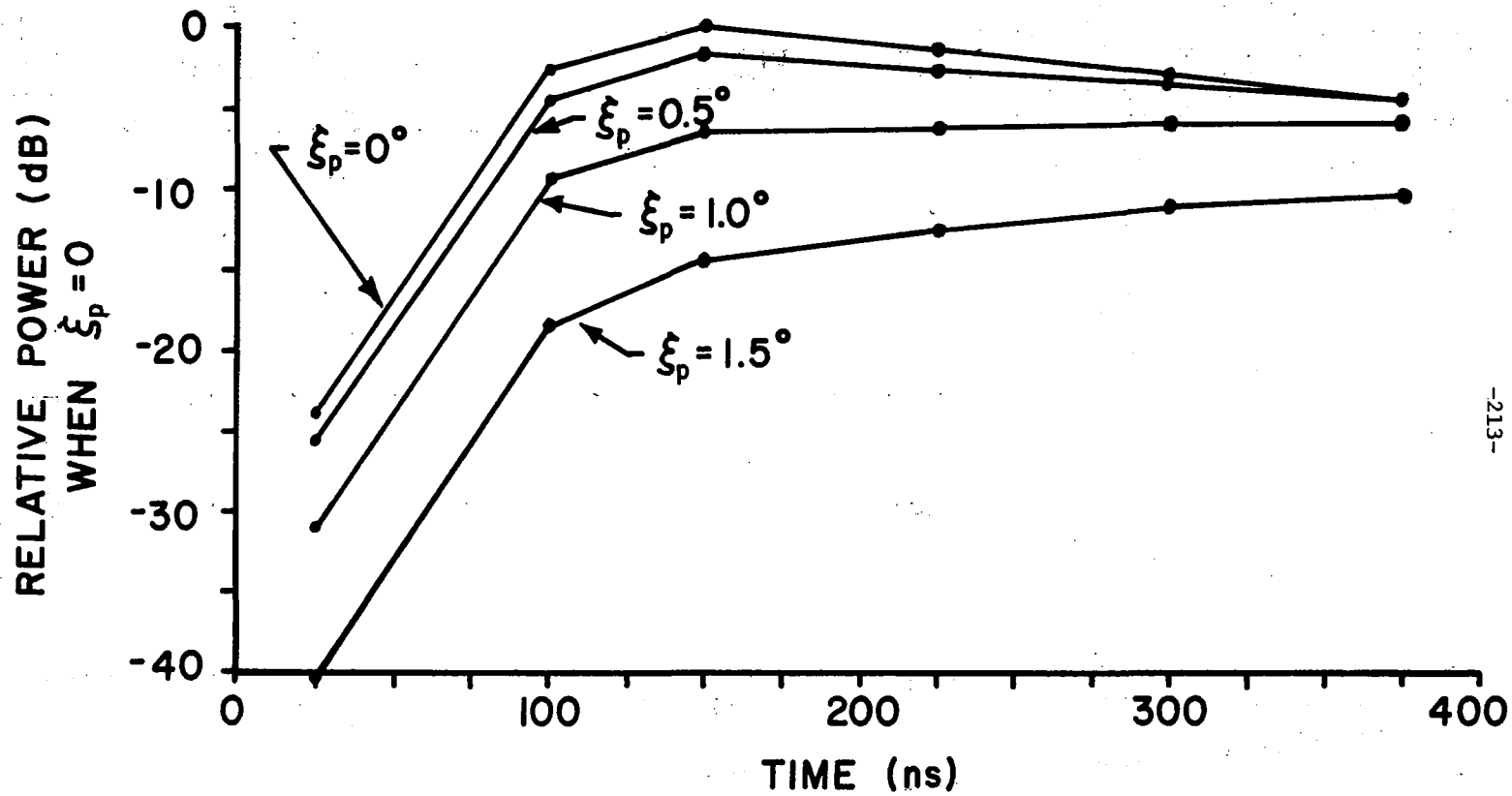


Figure 9. Relative power as a function of position within the pulse return for various cross-track pointing angles for the SL-2, 3 antenna pattern.

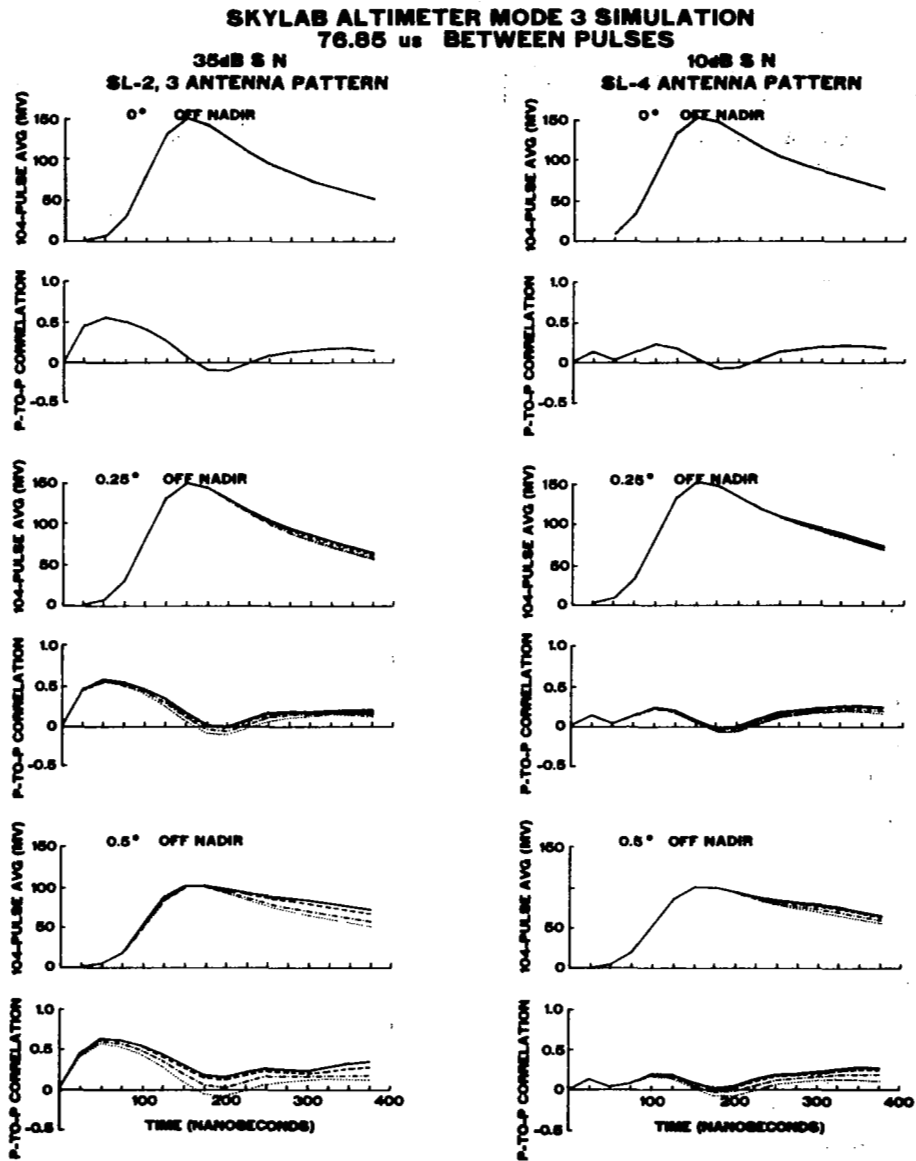


Figure 10a. The curves in the figure correspond to the following azimuthal pointing angles: along-track (solid), 30° from along-track (dash), 60° from along-track (dot-dash), cross-track (dotted).

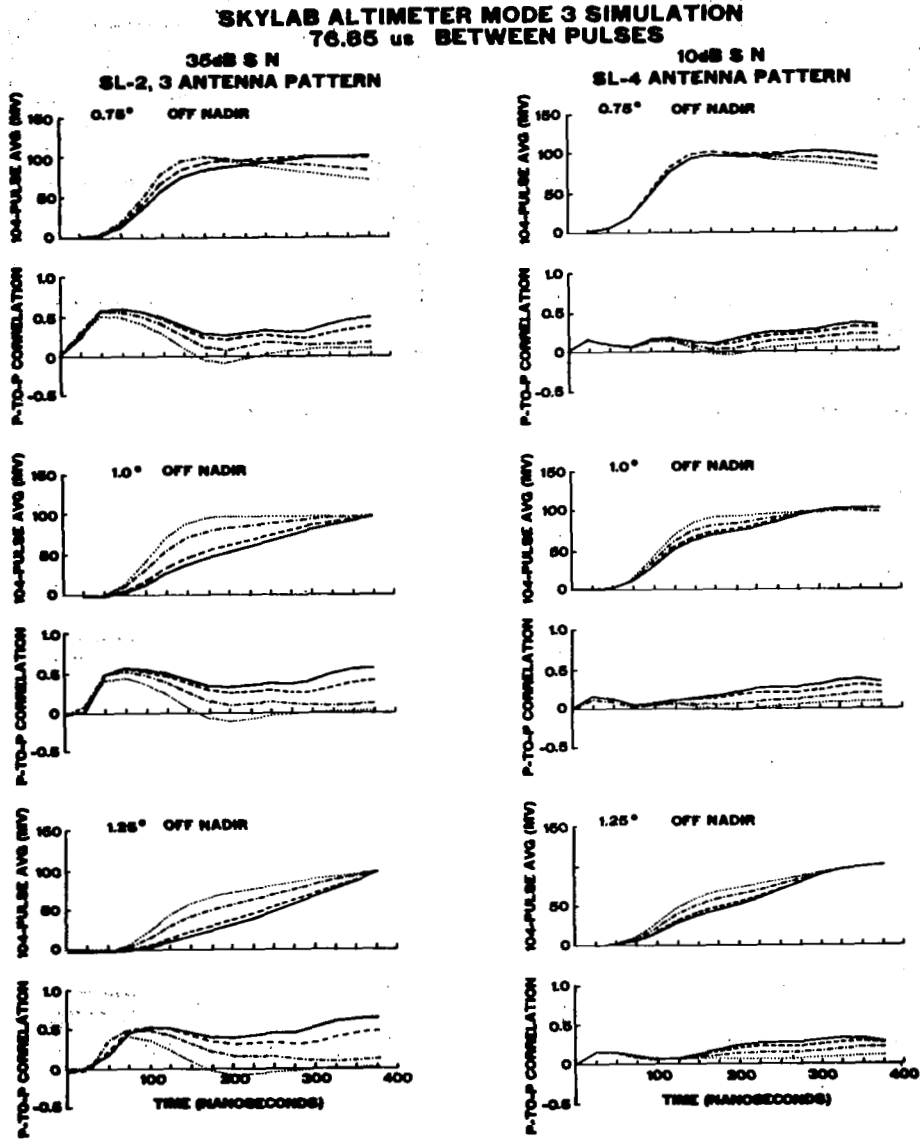


Figure 10b. The curves in the figure correspond to the following azimuthal pointing angles: along-track (solid), 30° from along-track (dash), 60° from along-track (dot-dash), cross-track (dotted).

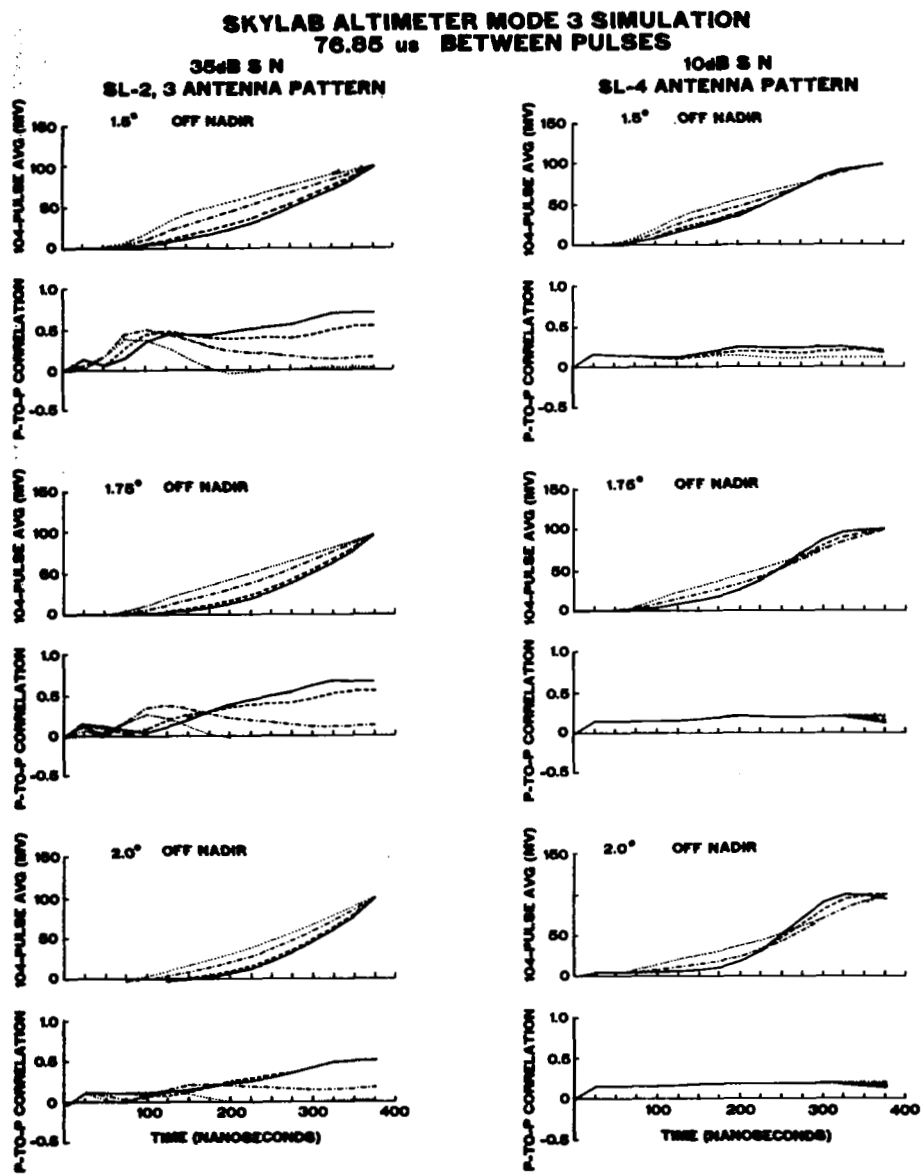


Figure 10c. The curves in the figure correspond to the following azimuthal pointing angles: along-track (solid), 30° from along-track (dash), 60° from along-track (dot-dash), cross-track (dotted).

shown in each plot except when the antenna was pointed at nadir. The solid curve is when the antenna was pointing along-track and the dash, dash-dot and dotted curves correspond to the antenna pointing 30° from along-track, 60° from along-track and cross-track. To facilitate comparison with the Mode III data the mean return pulse curves have been arbitrarily normalized so their peaks are at 150 mv for nadir and 0.25° off-nadir and at 100 mv for the other off-nadir angles. As the pointing angle increases the plateau decay of the mean return flattens out and then changes into a continuous increase. The cross-track curves always lag the along-track curves in the progression because any given pointing angle is a smaller percentage of the cross-track beamwidth. This causes a spread in the curves of the mean return pulse for any given off-nadir angle. The spread is less for the SL-4 antenna pattern because the asymmetry is less. This spreading causes some uncertainty in trying to determine the absolute off-nadir angle from the plateau decay since the same off-nadir angles in pitch and roll do not have the same effects [3]. However, the pulse-to-pulse correlation can aid in resolving this ambiguity. When the antenna is off-nadir by 0.5° or more there is a significant variation of the pulse-to-pulse correlation with the azimuthal angle, especially in the high SNR case.

Figure 11 shows the mean return pulse and pulse-to-pulse correlation data for the third Mode III of EREP Pass 24. It has been determined [3] that the observed plateau decay could have been caused by either an along-track angle of 0.4° or a cross-track angle of 0.55° . The simulation predictions for the correlations corresponding to each of these situations are also plotted. There is not a great difference but the data favors the along-track pointing.

In Figure 12 the x's correspond to a return pulse which could have been caused by either an along-track off-nadir angle of 0.7° or a cross-track angle of 1.0° [3]. The correlation data for the most part lies well above the simulation predictions (solid curves) but it favors the along-track pointing angle. For comparison another set of data from SL-4, EREP Pass 81 (diamonds) is plotted. The antenna pattern was more symmetrical and the candidate pointing angles were 0.75° along-track and 0.80° cross-track [3]. The data in this case favors the cross-track pointing.

Figure 13 indicates the data and simulation results corresponding to

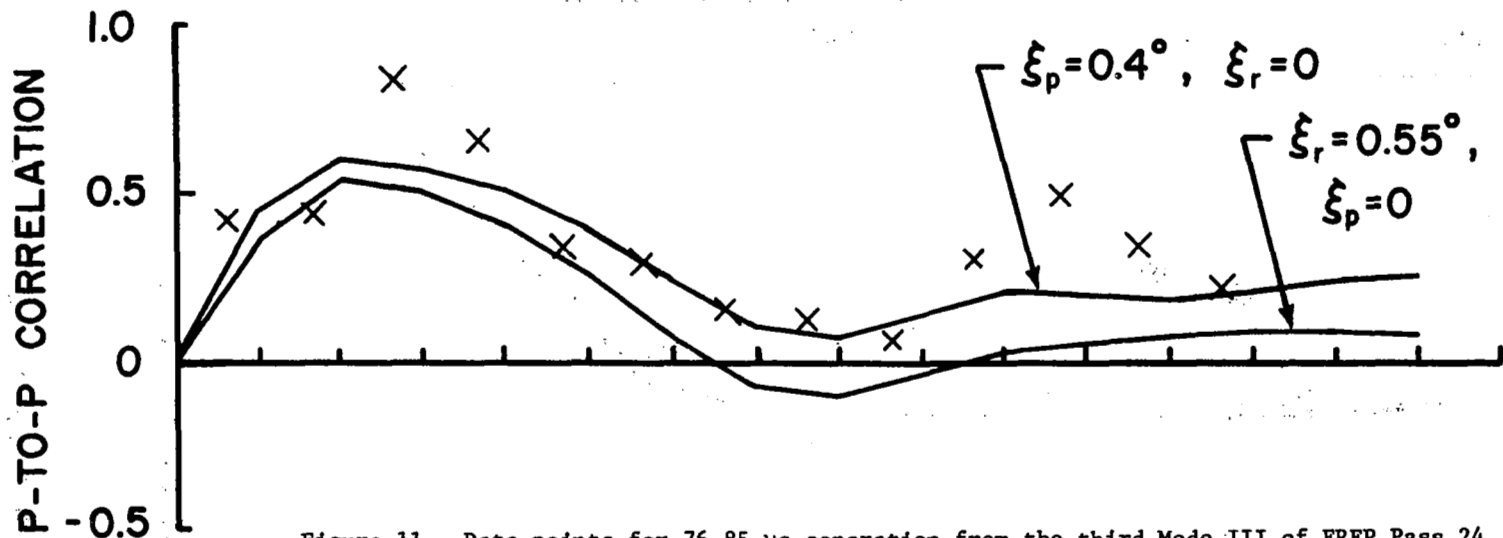
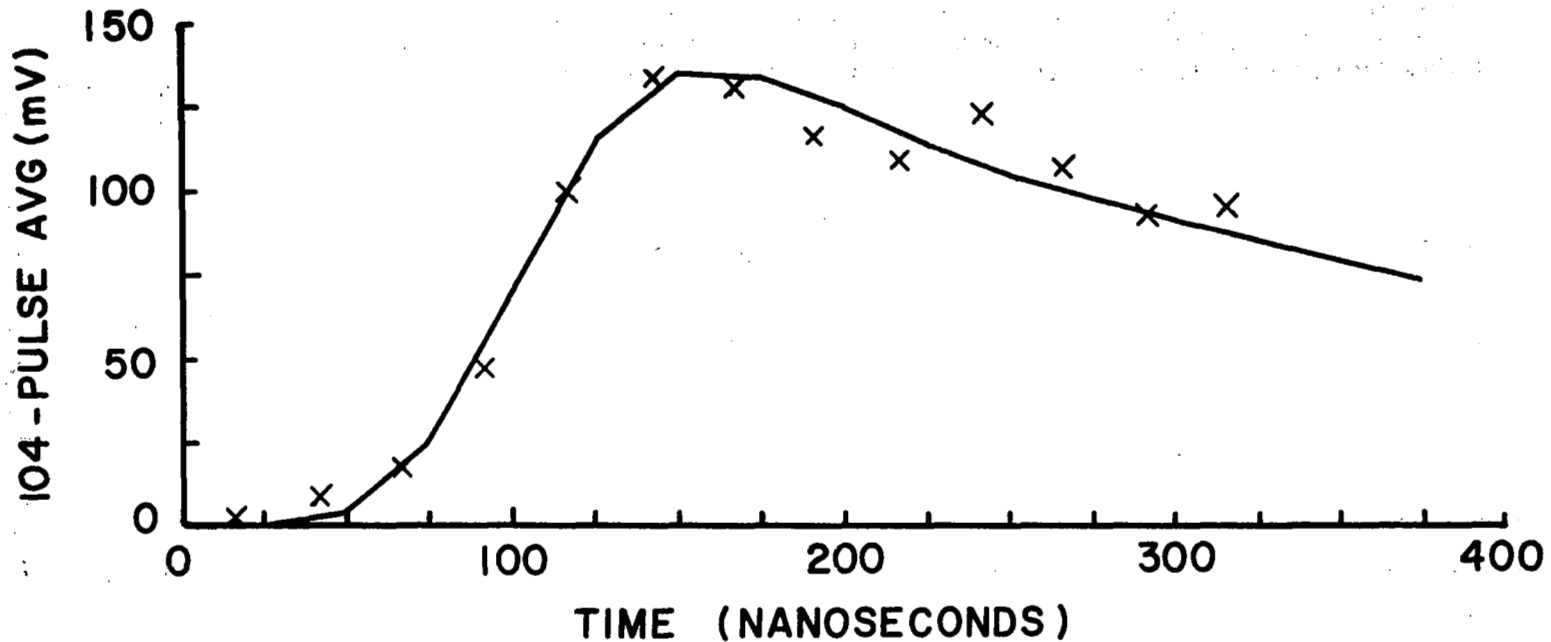


Figure 11. Data points for 76.85 μ s separation from the third Mode III of EREP Pass 24 and simulation results for the along-track and cross-track pointing errors of 0.4° and 0.55° [3].

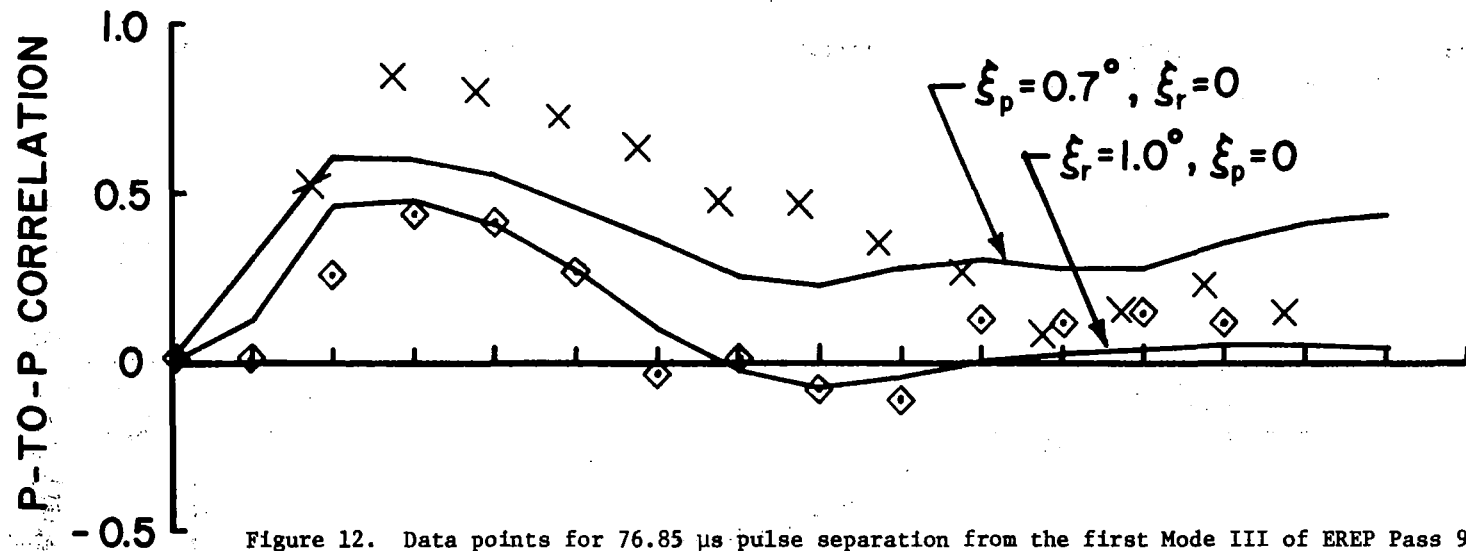
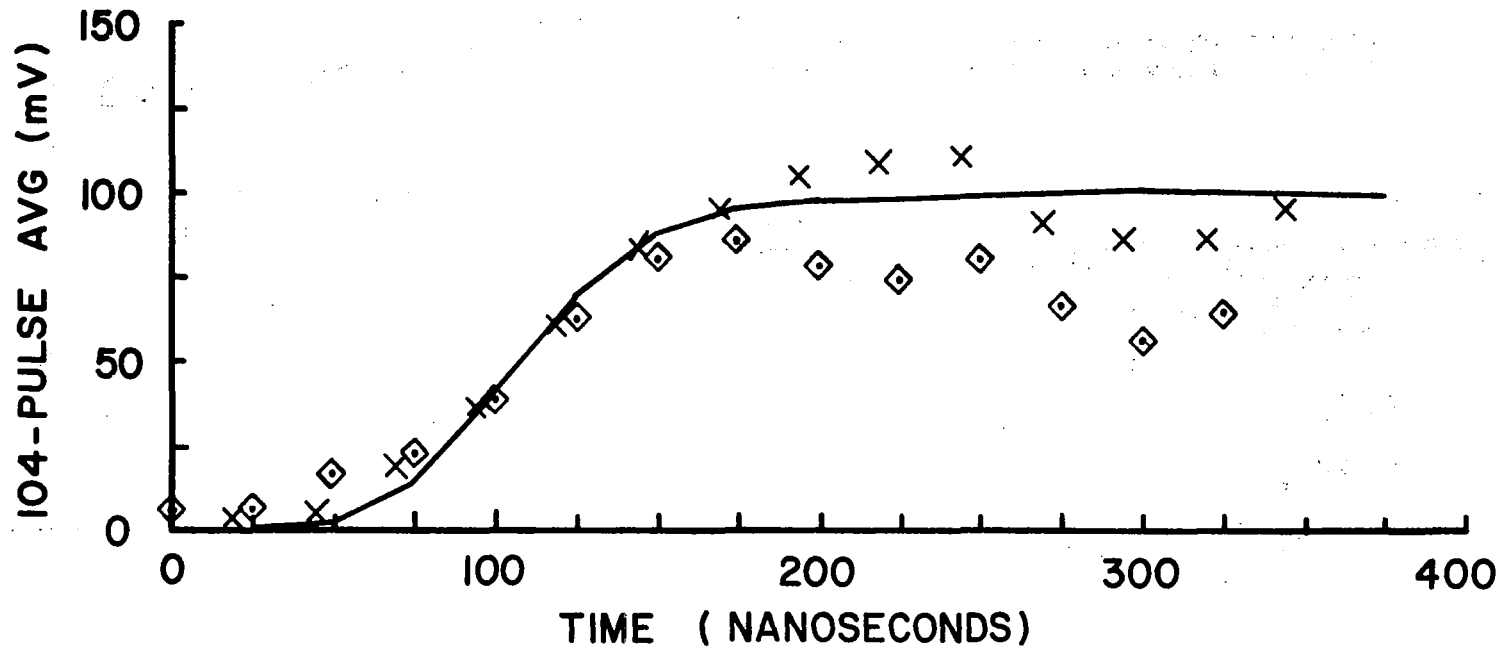


Figure 12. Data points for 76.85 μ s pulse separation from the first Mode III of EREP Pass 9 and simulation results for the along-track and cross-track pointing errors of 0.7° and 1.0° [3]. Also shown is the EREP Pass 81 data for which the pointing errors were 0.75° and 0.8°, respectively [3].

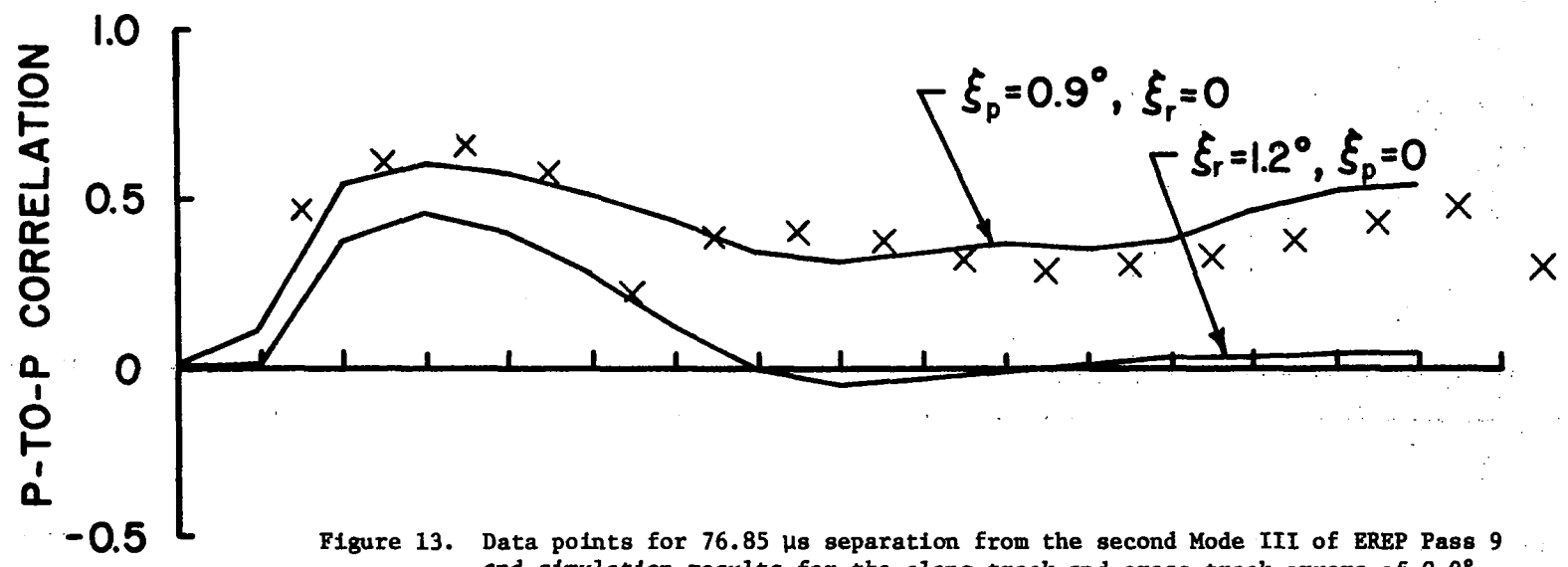
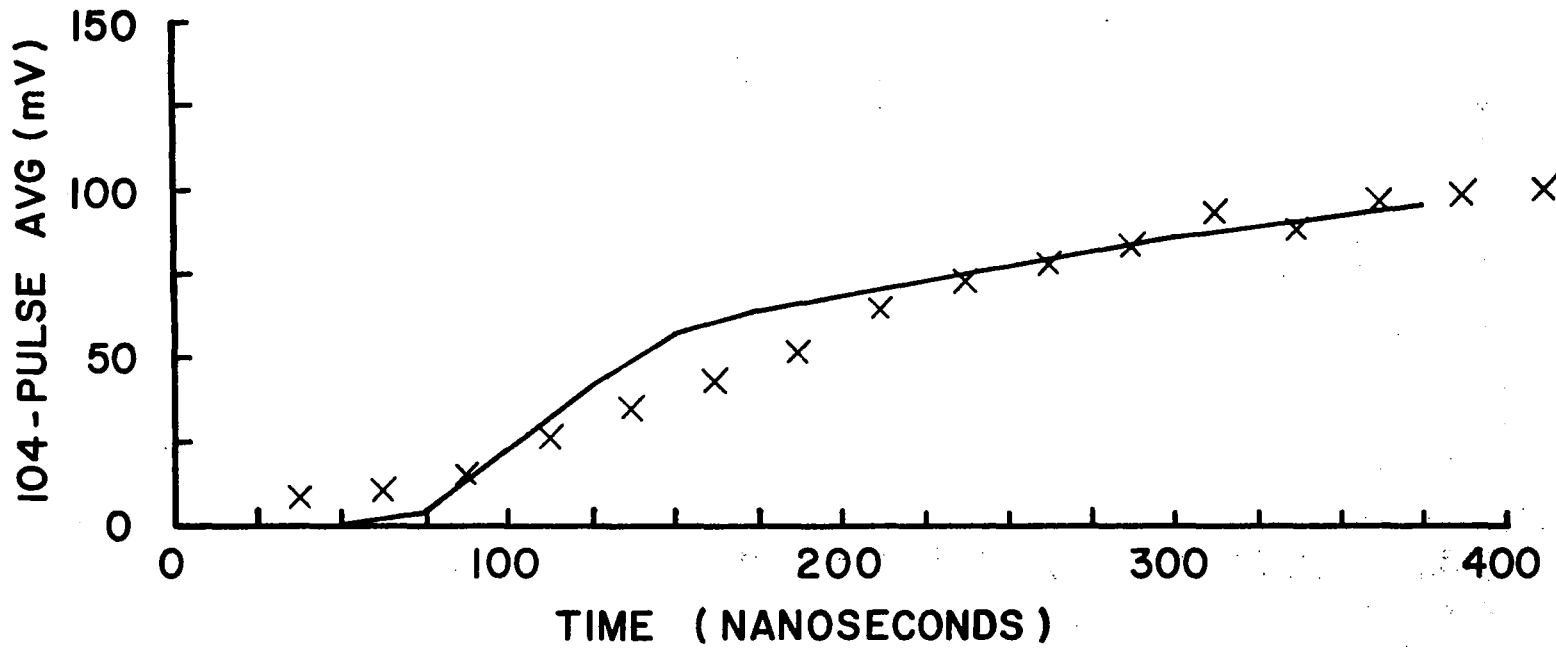


Figure 13. Data points for 76.85 μ s separation from the second Mode III of EREP Pass 9 and simulation results for the along-track and cross-track errors of 0.9° and 1.2° [3].

the second Mode III of SL-2 EREP Pass 9. The correlation data is in excellent agreement with the along-track pointing. Note that there is about a 75 ns shift in the tracking point caused by the return pulse shape. The slight mismatch in the return pulse shape between the data and simulation indicates that the magnitude of the angle probably increased somewhat over the angle presented in [3]. However, the simulation correlation curves do not change significantly in the 1.0° to 1.25° range (Figure 10b) so the correlation comparison would still be valid.

The remaining figures contain all the pulse-to-pulse correlation for all the Skylab EREP missions.

REFERENCES

1. Berger, T., "Satellite Altimetry Using Ocean Backscatter," IEEE Trans. on Antennas and Propagation, Vol AP-20, pp. 295-309, May, 1972.
2. Walsh, E. J., "Analysis of Experimental NRL Radar Altimeter Data," Radio Science, Vol. 9, pp. 711-722, Aug-Sept., 1974.
3. Brown, G. S., "Reduced Backscattering Cross Section (σ°) Data From The Skylab S-193 Radar Altimeter," NASA CR-141401, Applied Science Associates, Inv., Apex, N. C., October 1975.

EREP PASS 7

SL - 2

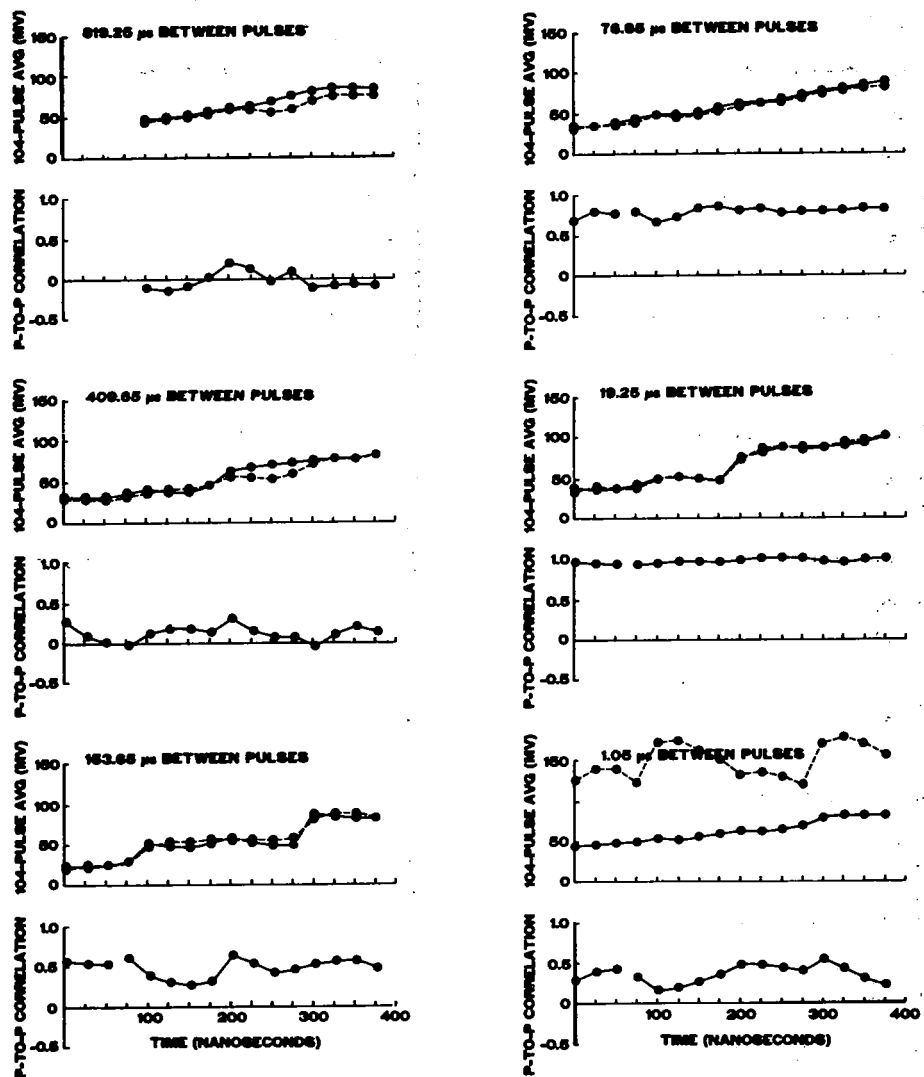


Figure 14. Measured mean returns and interpulse correlations for a pointing error on the ellipse whose semiminor axis was $>0.95^\circ$ along-track and whose semimajor axis was $>1.2^\circ$ cross-track.

IREP PASS 8

SL - 2

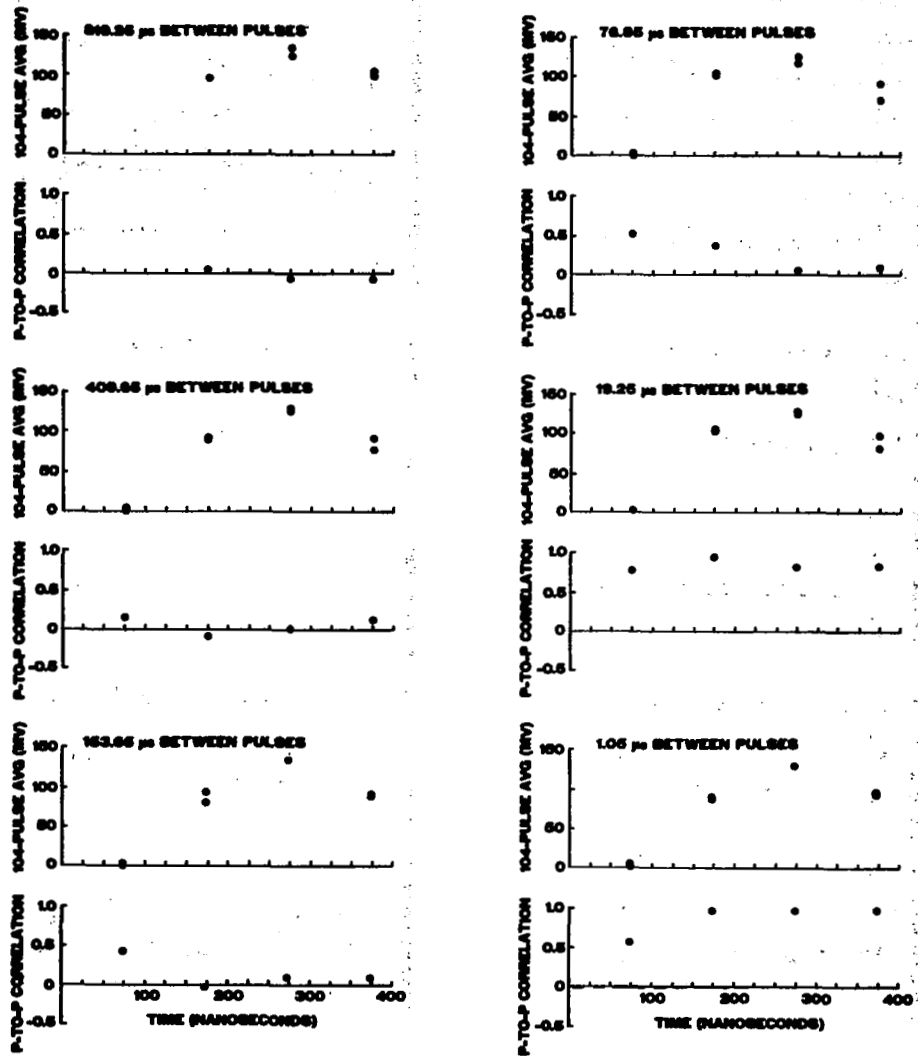


Figure 15. Measured mean returns and interpulse correlations for a pointing error on the ellipse whose semiminor axis was 0.35° along-track and whose semimajor axis was 0.5° cross-track.

EREP PASS 9

SL - 2
1ST MODE III

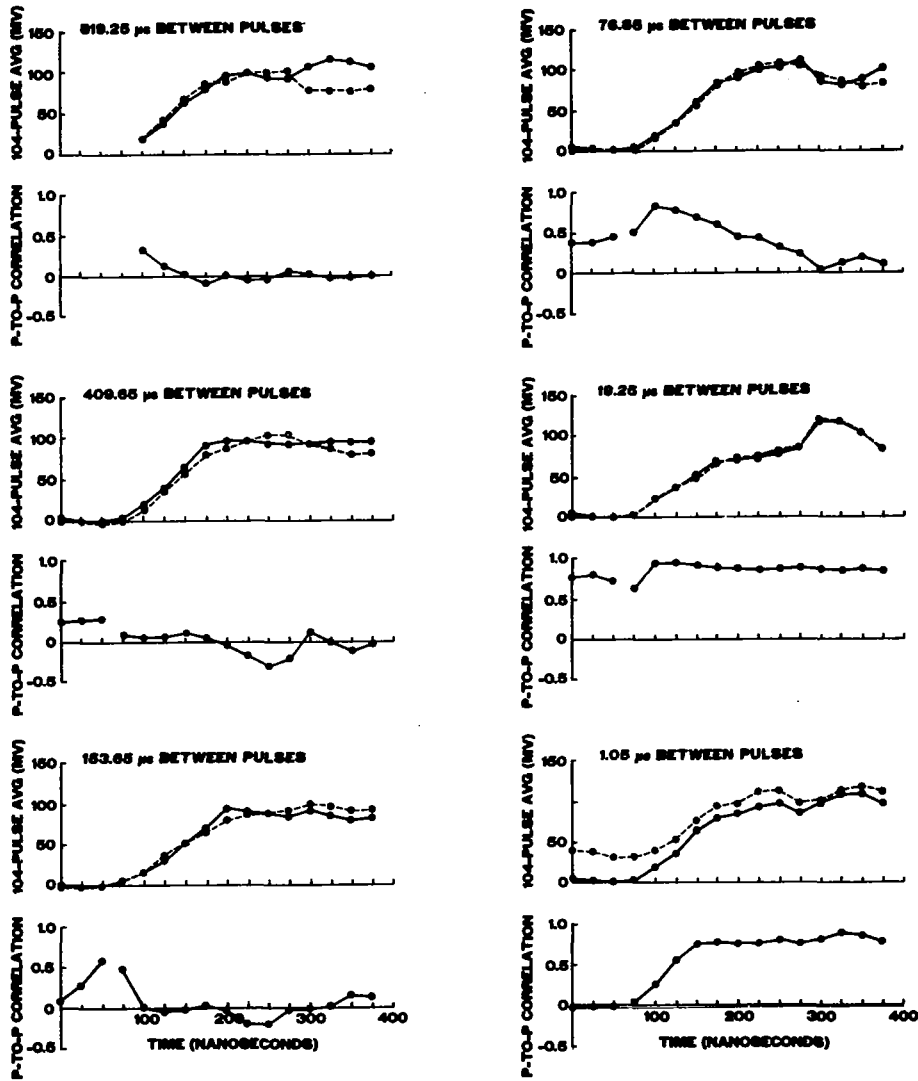


Figure 16. Measured mean returns and interpulse correlations for a pointing error on the ellipse whose semiminor axis was 0.7° along-track and whose semimajor axis was 1.0° cross-track.

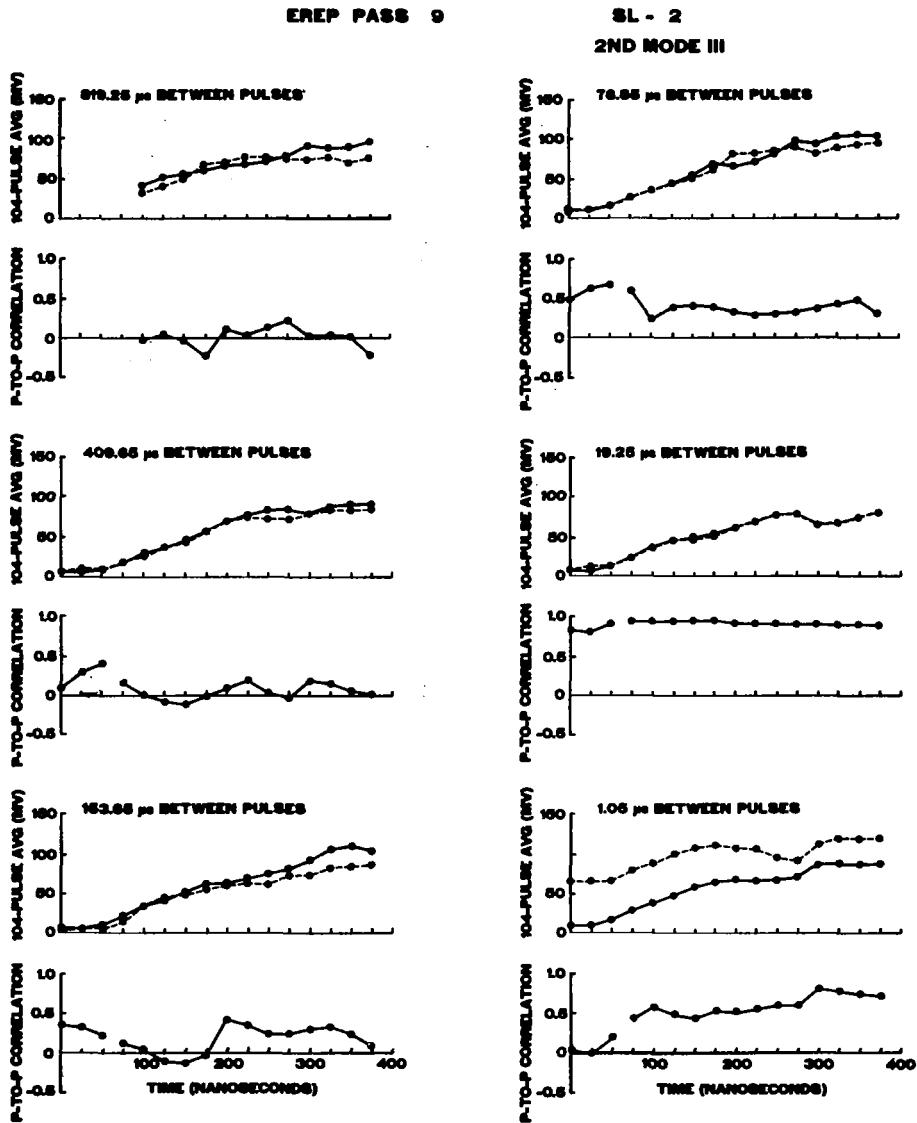


Figure 17. Measured mean returns and interpulse correlations for a pointing error on the ellipse whose semiminor axis was $>0.95^\circ$ along-track and whose semimajor axis was $>1.2^\circ$ cross-track.

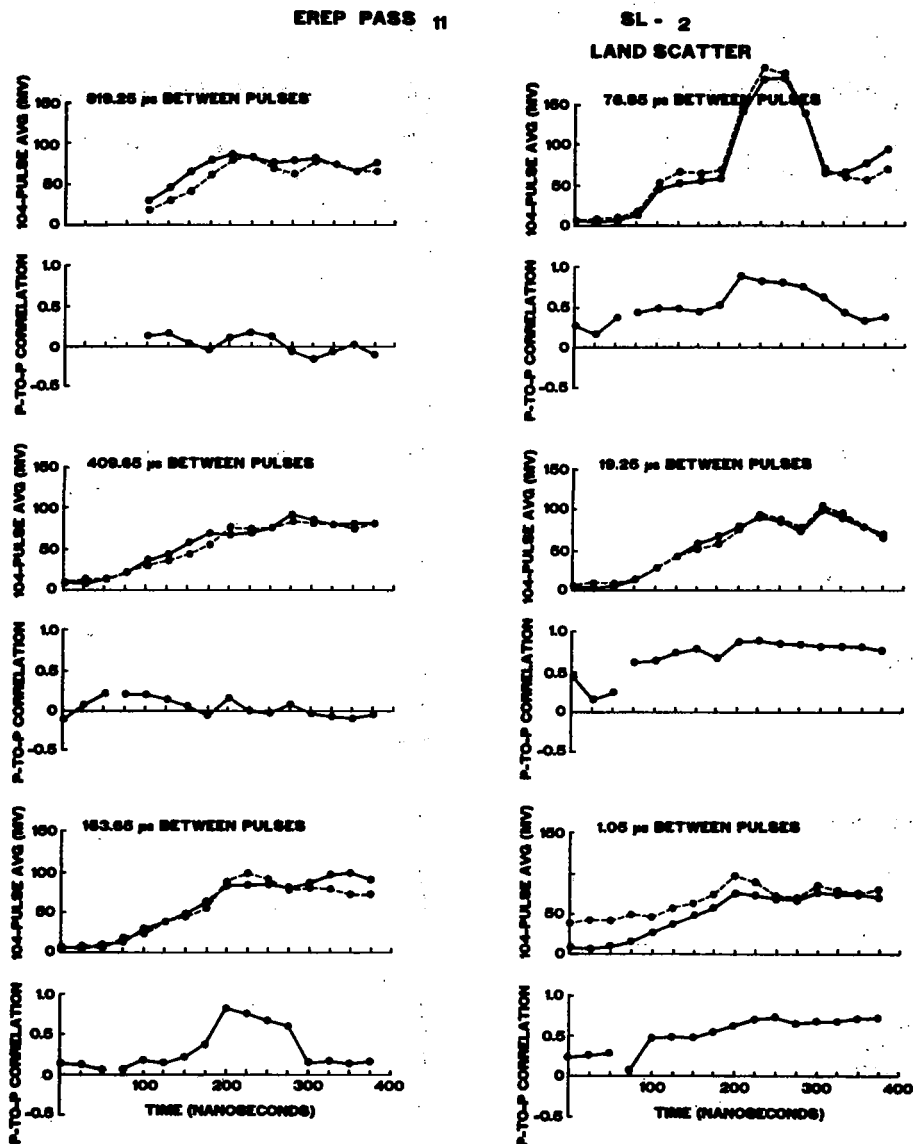


Figure 18. Measured mean returns and interpulse correlations for a pointing error on the ellipse whose semiminor axis was unknown along-track and whose semimajor axis was unknown cross-track.

EREP PASS 17

SL - 3

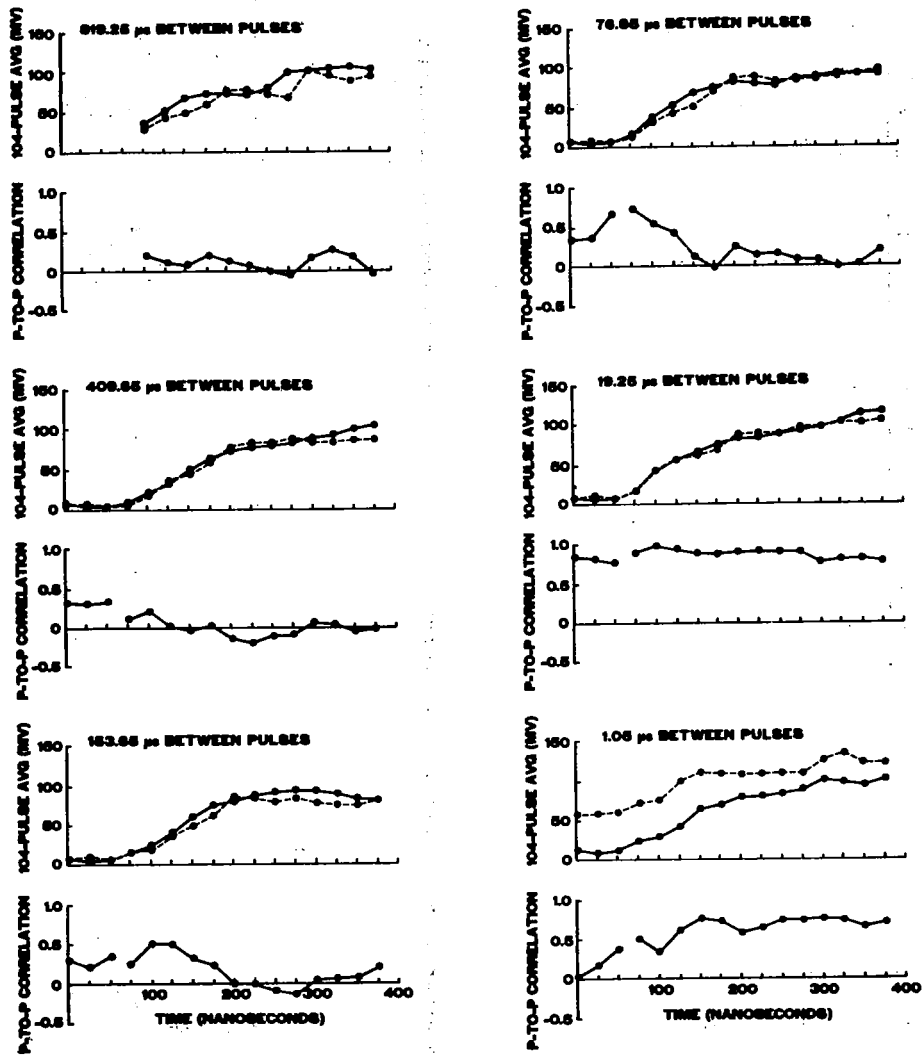


Figure 19. Measured mean returns and interpulse correlations for a pointing error on the ellipse whose semiminor axis was 0.9° along-track and whose semimajor axis was 1.2° cross-track.

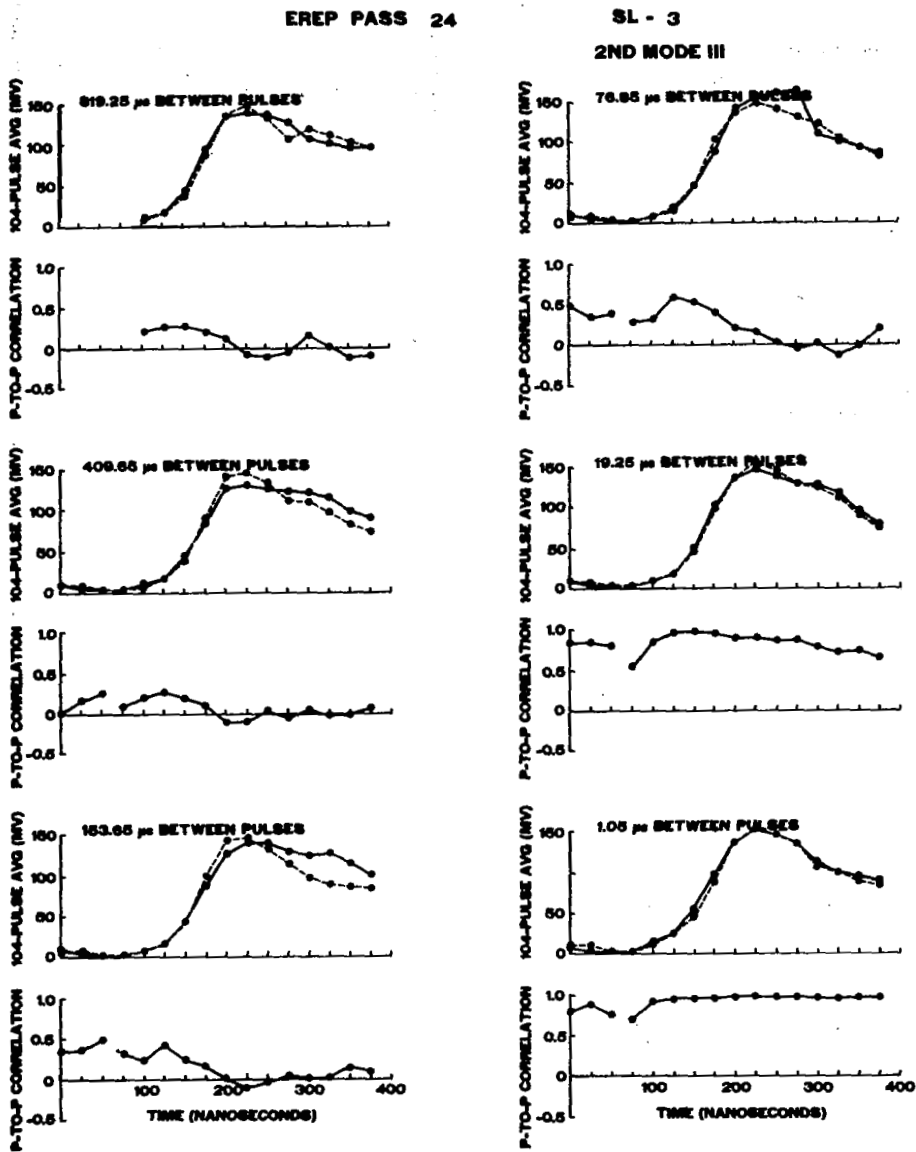


Figure 20. Measured mean returns and interpulse correlations for a pointing error on the ellipse whose semiminor axis was 0.2° along-track and whose semimajor axis was 0.3° cross-track.

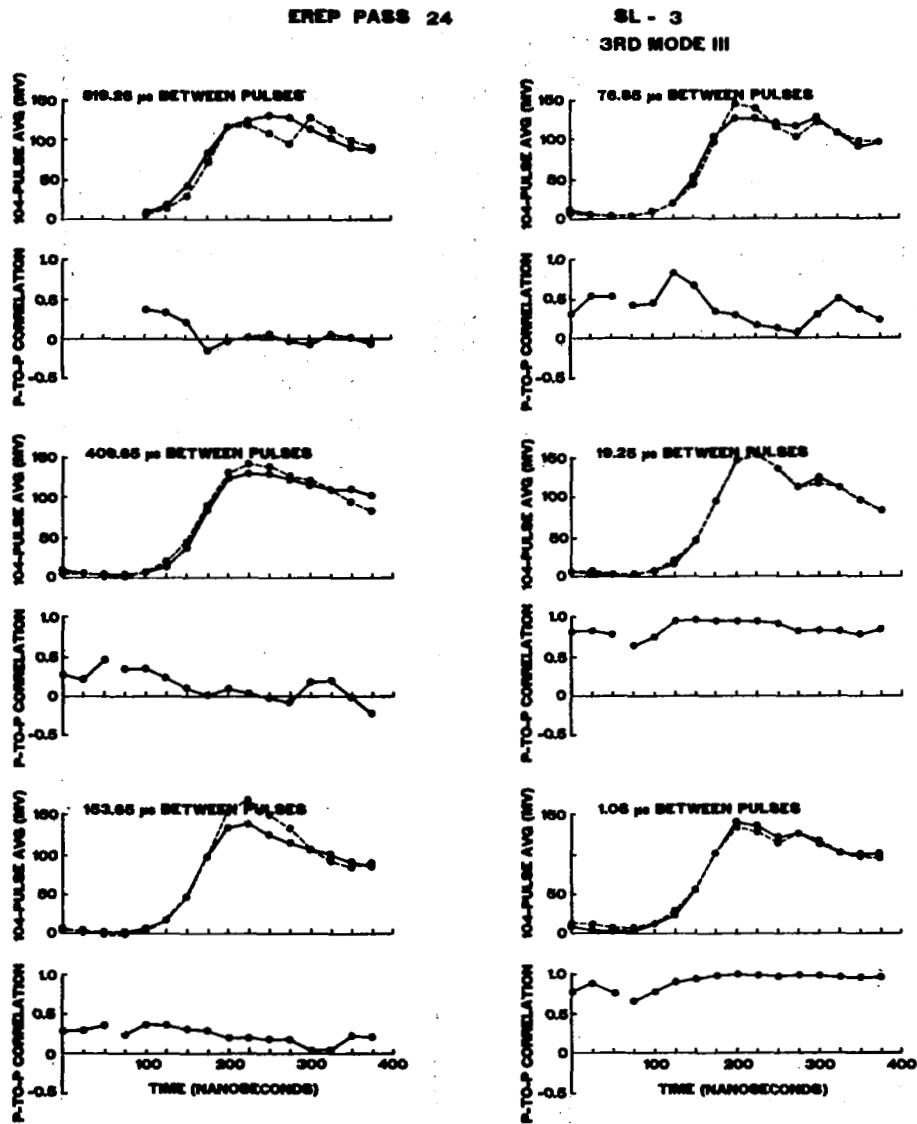


Figure 21. Measured mean returns and interpulse correlations for a pointing error on the ellipse whose semiminor axis was 0.4° along-track and whose semimajor axis was 0.55° cross-track.

EREP PASS 40

SL - 3

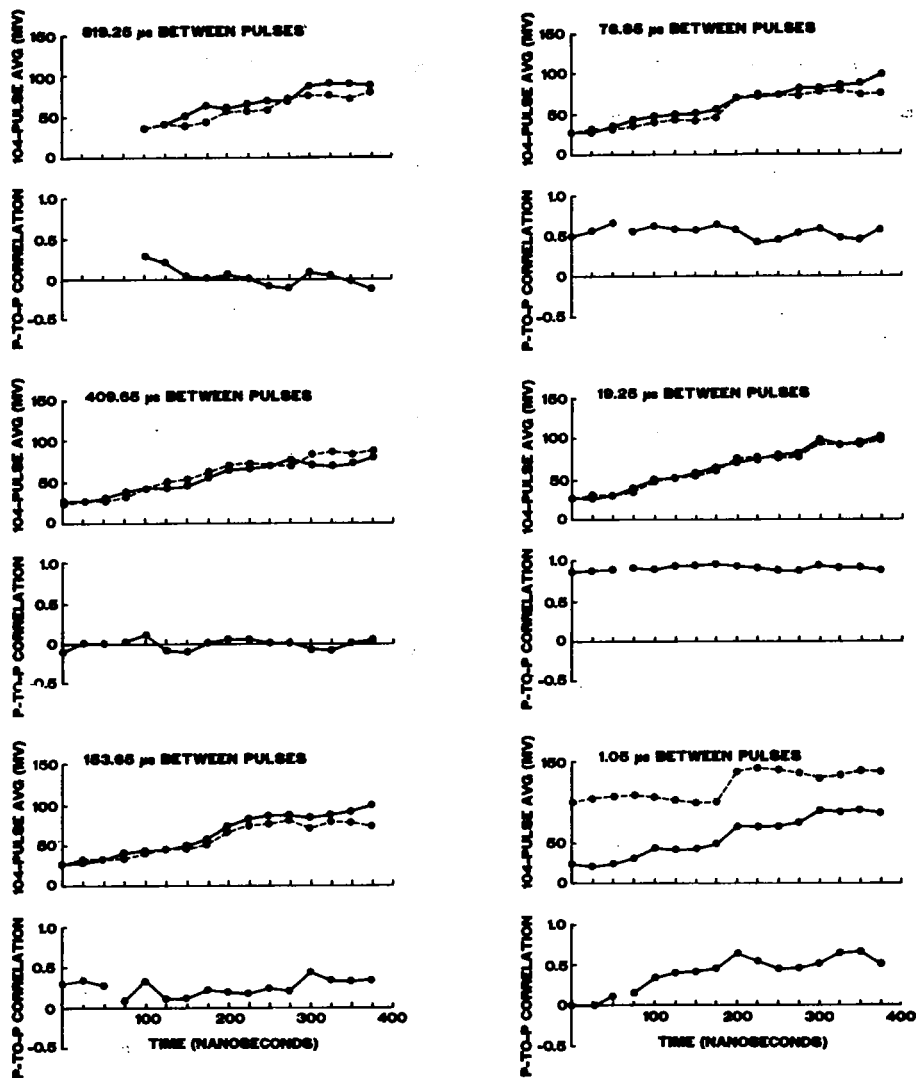


Figure 22. Measured mean returns and interpulse correlations for a pointing error on the ellipse whose semiminor axis was $>0.95^\circ$ along-track and whose semimajor axis was $>1.2^\circ$ cross-track.

EREP PASS 57

SL - 4

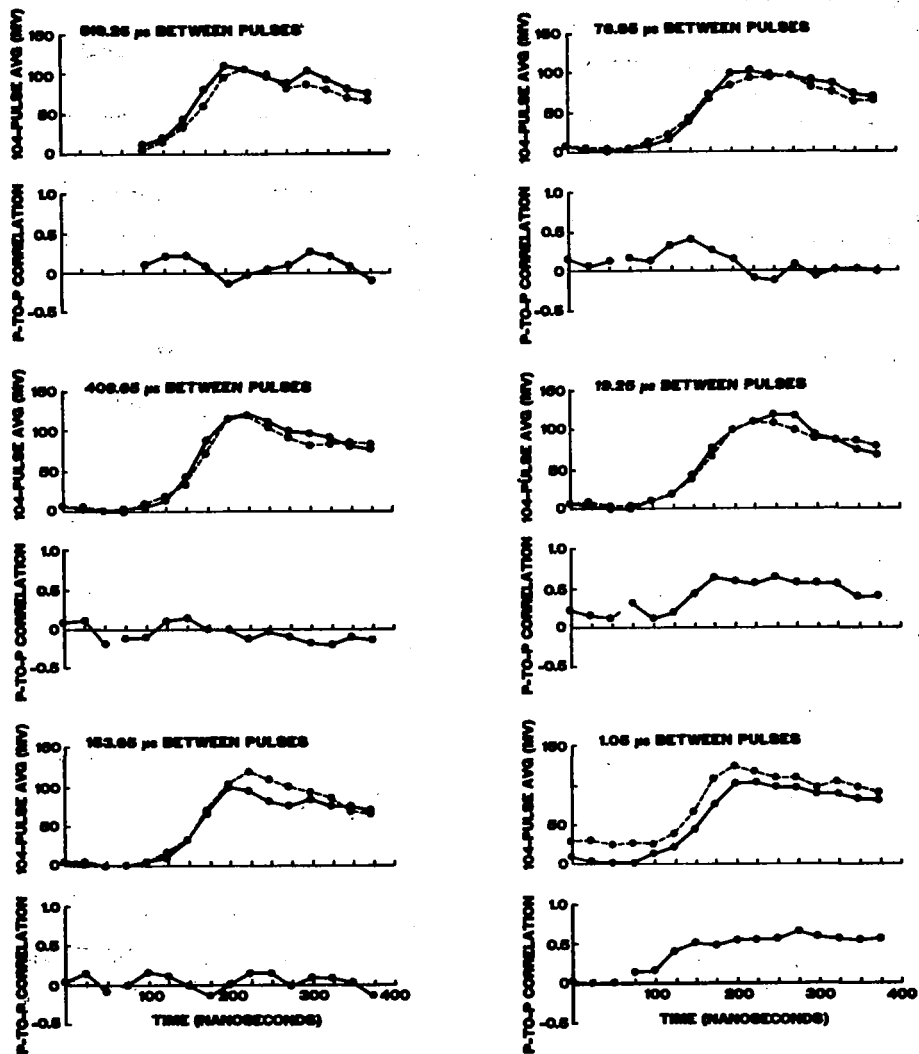


Figure 23. Measured mean returns and interpulse correlations for a pointing error on the ellipse whose semiminor axis was 0.7° along-track and whose semimajor axis was 0.75° cross-track.

EREP PASS 61

SL - 4

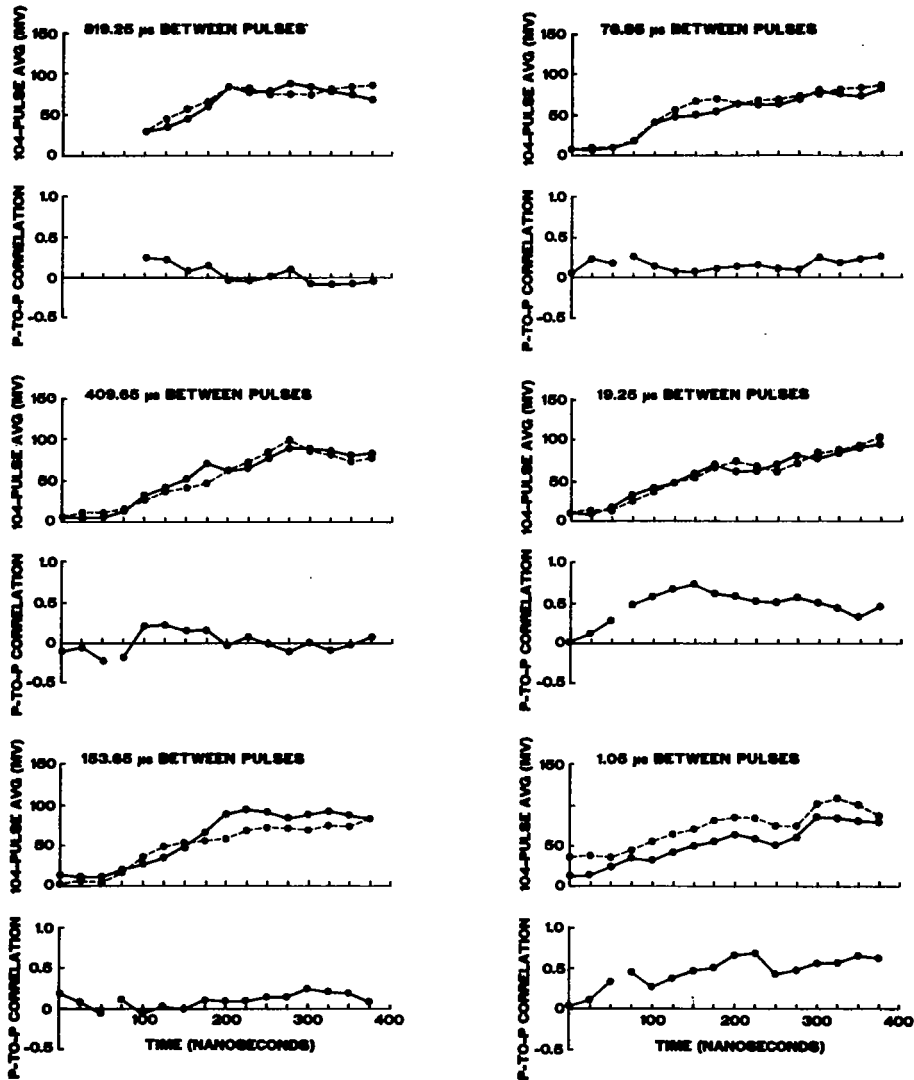


Figure 24. Measured mean returns and interpulse correlations for a pointing error on the ellipse whose semiminor axis was $>1.1^\circ$ along-track and whose semimajor axis was $>1.15^\circ$ cross-track.

EREP PASS 81

SL - 3

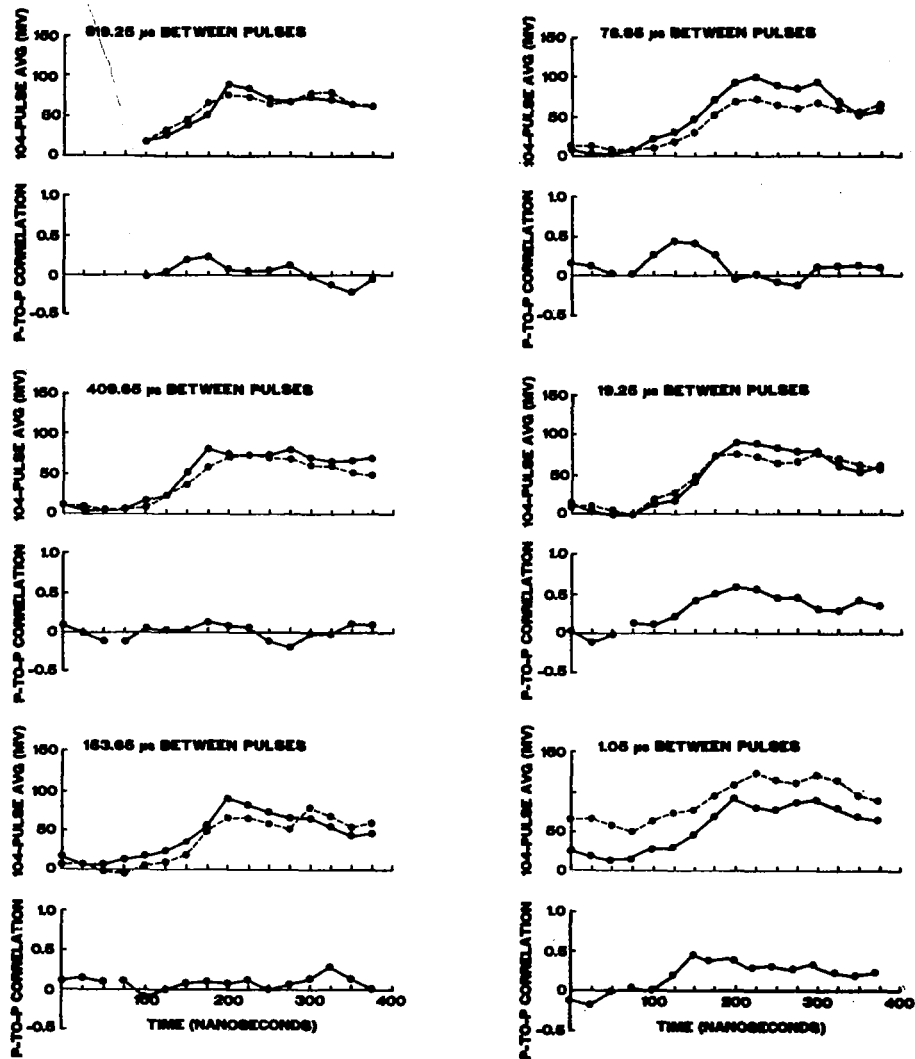


Figure 25. Measured mean returns and interpulse correlations for a pointing error on the ellipse whose semiminor axis was 0.75° along-track and whose semimajor axis was 0.8° cross-track.

APPENDIX

This appendix describes the Monte Carlo simulation used to predict the pulse-to-pulse correlations for the various values of pulse separation, antenna pattern, pointing angle and SNR. The purpose is not to give a detailed listing of the program but rather a general description of the procedures and approximations. The system point target response shown in Figure 3 was represented by its value at 25 points spaced evenly between 0 and 200 ns (8.33 ns intervals) and was assumed to be zero outside that range. The effect of surface height distribution was ignored entirely since the point target response was so broad. The time response was divided into 15 increments of 25 ns each with the time reference that of Figure 3. The radii of 15 pulse-limited circles were computed corresponding to 25, 50, 75, ..., 375 ns. The sea surface was divided into narrow strips perpendicular to the ground track (constant doppler) of thickness equal to one tenth the radius of the 25 ns pulse-limited circle. Twenty such strips just covered the 25 ns pulse-limited circle whereas the 375 ns pulse-limited circle required 78 strips.

Since the largest off-nadir antenna pointing angle considered was 2° and the antenna beamwidth was less than 2° it was possible to simplify the calculations involving the antenna pattern by considering the angle from boresight to be proportional to the distance from the antenna boresight position on the ground. The nice thing about that procedure is that everything can be normalized to the radius of the 25 ns pulse-limited circle. Correcting the actual altitude, 435.5 km, for earth curvature results in an effective altitude of 465.2 km for a flat earth and 0.23° for the effective 25ns pulse-limited angle off-nadir. That means that the normalized distance from nadir on the sea surface corresponding to a 1.0° off-nadir boresight angle would be 4.347.

The boresight position on the sea surface is determined by the off-nadir angle and the azimuthal angle. Then for each of the 15 intervals of time in the return pulse the mean return power from each of the 78 constant doppler strips is computed. This is done by dividing each of the constant doppler strips vertically into 78 squares. The distance of each square from the boresight position is found and the total power for the strip is incremented

by the appropriate value from the point target response (determined by the time interval and the distance from nadir), weighted by the gain of the antenna pattern at that point.

For each interval of time each of the 78 constant doppler strips is assigned an amplitude which is the square root of the mean power determined in the previous calculation. Each of the 78 intervals has an initial phase angle assigned to it for the phase of the signal returning from it. The phase angles are randomly selected from a uniform distribution in the interval $(0, 2\pi)$. The 78 signals are added vectorially to determine the amplitude and phase of the first return pulse. Then the initial phases are incremented by the appropriate amount corresponding to the round trip path length change to each strip caused by the satellite translation in the interpulse interval. Because of the small angles involved the phase change was just

$$\Delta\phi = 2\pi \cdot 2d\theta/\lambda \quad (A1)$$

where d is the satellite displacement in the interpulse interval, θ is the angle along-track to the center of the constant doppler strip under consideration and λ is the radiation wavelength (2.158 cm).

The satellite velocity used was 7.65 km/sec (W. T. Wells, Wolf Research and Development Corp., personal communication, 1975). This is the average of four values obtained from satellite ground tracking data; two from SL-2 EREP Pass 1 (7.659, 7.646 km/sec) and two from the SL-4 EREP round the world pass (7.658, 7.654 km/sec). It is interesting to note that the simple formula $V^2/(a+h) = g$ produces a velocity of 7.649 km/sec where a is the radius of the earth (6378 km), h is the satellite altitude, and g is the gravitational acceleration extrapolated to the satellite altitude, $g = g_0 a^2/(a+h)^2$, from its value at the surface of the earth, $g_0 = 980 \text{ m/sec}^2$.

The 78 signals are then added vectorially with their new phase angles to determine the amplitude and phase of the second return pulse. The phase angles are again incremented by the appropriate amounts and the signals added vectorially. The process is repeated until return amplitudes and phases have been generated for 104 pulse returns spaced uniformly at the interpulse interval. To obtain the total power from signal and noise a noise signal was added vectorially to the 104 return signals and the power calculated. At each of the 104 points the noise signal phase and amplitude

were randomly selected from a uniform distribution in the interval $(0, 2\pi)$ and from a Rayleigh distribution. The mean and the autocorrelation of these 104 return powers were calculated using (1) with $j=1$ and the process was repeated for each of the 15 time intervals in the return pulse.

CHAPTER 11

The Effect Of Tracking Loop Jitter On First
And Second Order Waveform Statistics

by

G. S. Brown

1.0 Introduction

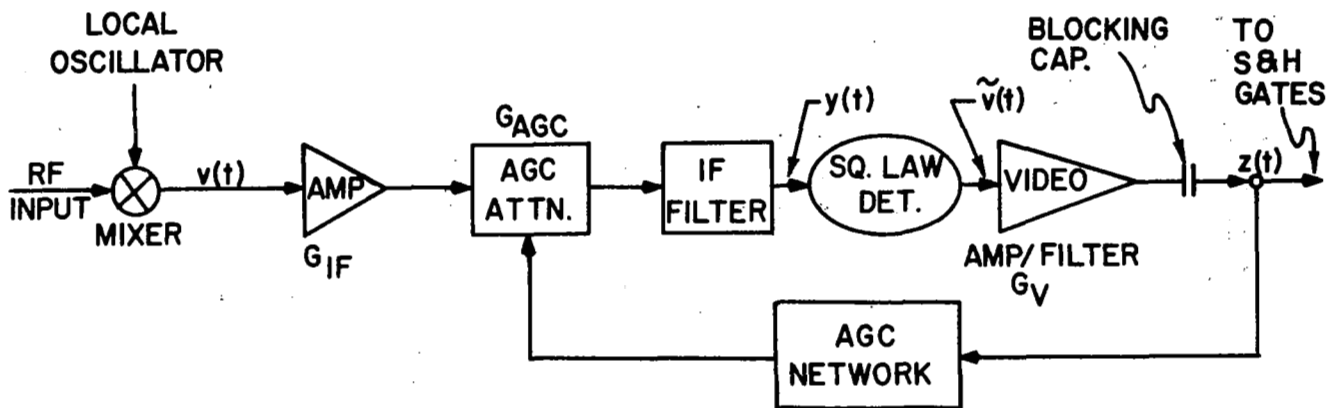
The Sample and Hold (S&H) gates used by the altimeter signal processor to record the AGC normalized return power were positioned by the tracking loop error voltage. Because of the fluctuating nature of the return, the tracking loop error voltage was very similar to a quantized noise-like process. The tracking loop output therefore imparted a noisy positioning signal to the S&H gates which resulted in the so-called S&H gate position jitter. This position jitter can have a significant effect on first and second order moments of the waveform statistics especially in the rise time or ramp portion of the return. More specifically, the jitter can mask or give rise to false inferences of surface roughness effects. For this reason, it is essential that we have a complete understanding of the effects of S&H positional jitter. In this chapter we shall show that the influence of positional jitter on the mean return results in a waveform which is a convolution of the true mean waveform with the probability density function describing the positional jitter. We also obtain results for the effect of jitter on the variance of the waveform; the variance is more significantly influenced by jitter than is the mean. The analysis points out the need to correct 10 ns short pulse return waveform data for tracking loop jitter effects.

2.0 Jitter-Free Analysis

A block diagram of that portion of the altimeter we will be concerned with is shown in Figure 1. The voltage out of the IF-mixer may be expressed as;

$$v(t) = G_{RF} \{ [x_c(t) + n_c(t)] \cos \omega_{IF} t + [x_s(t) + n_s(t)] \sin \omega_{IF} t \}$$

where G_{RF} is the RF-gain of the receiver front end, ω_{IF} is the IF radian frequency and $x_c(t)$, $x_s(t)$, $n_c(t)$ and $n_s(t)$ are zero-mean, independent, Gaussian



G_{IF} = IF AMP VOLTAGE GAIN (MIDBAND)

G_{AGC} = AGC ATTENUATOR VOLTAGE GAIN (MIDBAND)

G_V = VIDEO AMP/FILTER VOLTAGE GAIN (MIDBAND)

Figure 1. Applicable IF and video parts of the altimeter receiver.

distributed, in-phase and quadrature signal and noise voltages, respectively. In particular, the density functions are given by

$$\begin{aligned}
 f_{x_c(t)}(x_c(t)) &= \frac{1}{\sqrt{2\pi SP_r(t)}} \exp\left\{\frac{-x_c^2}{2SP_r(t)}\right\} \\
 f_{x_s(t)}(x_s(t)) &= \frac{1}{\sqrt{2\pi SP_r(t)}} \exp\left\{\frac{-x_s^2}{2SP_r(t)}\right\} \\
 f_{n_s(t)}(n_s(t)) &= \frac{1}{\sqrt{2\pi N}} \exp\left\{\frac{-n_s^2}{2N}\right\} \\
 f_{n_c(t)}(n_c(t)) &= \frac{1}{\sqrt{2\pi N}} \exp\left\{\frac{-n_c^2}{2N}\right\}
 \end{aligned}
 \tag{1}$$

where N is the noise power ($= \sigma_{n_c}^2 = \sigma_{n_s}^2$), S is the peak of the mean "signal" power ($= \sigma_{x_c}^2 = \sigma_{x_s}^2$) and $P_r(t)$ is the mean return waveform normalized such that

$$\max[P_r(t)] = 1$$

The effect of the IF amplifier, AGC attenuator and IF filter is assumed to be equivalent to a multiplication of $v(t)$ by $G_{IF} \cdot G_{AGC}$; thus at the input to the square-law detector

$$y(t) = G_{IF} G_{AGC} v(t)$$

The output of the square-law detector is $[a y^2(t)]$, where a is the detector constant. After video amplification and ideal low-pass filtering, the output is $\tilde{v}(t)$ where

$$\tilde{v}(t) = a G \{ [x_c(t) + n_c(t)]^2 + [x_s(t) + n_s(t)]^2 \}$$

and $G = [G_{RF} G_{IF} G_{AGC}]^2 G_V$. The mean of the video amp output is given as follows;

$$\begin{aligned} E\{\tilde{v}(t)\} &= aG E\{x_c^2(t) + x_s^2(t) + 2[x_c(t)n_c(t) + x_s(t)n_s(t)] \\ &\quad + n_c^2(t) + n_s^2(t)\} \\ &= aG\{SP_r(t) + SP_r(t) + 0 + N + N\} \end{aligned}$$

or

$$E\{\tilde{v}(t)\} = 2aG\{SP_r(t) + N\} \quad (4)$$

When the blocking capacitor, following the video amplifier/filter, is large, it has the equivalent effect of subtracting any constant mean terms in the signal out of the detector. From (4), the only steady term in the mean is $2aGN$, thus

$$z(t) = \tilde{v}(t) - 2aGN$$

or

$$z(t) = aG\{[x_c(t) + n_c(t)]^2 + [x_s(t) + n_s(t)]^2 - 2N\} \quad (5)$$

which is the voltage into the S&H gates and the AGC network.

Assume for the moment that $G_{AGC} = 1$ and the signal is just entering the AGC network to set the proper value of G_{AGC} . The AGC network "picks" local maxima of $z(t)$, i.e. the set $z_1(t_1), z_2(t_2), \dots, z_M(t_M)$ where for ϵ some small positive number

$$\begin{aligned} |z_1(t_1)| &> |z_1(t_1 \pm \epsilon)| \\ |z_2(t_2)| &> |z_2(t_2 \pm \epsilon)| \\ &\vdots \\ |z_M(t_M)| &> |z_M(t_M \pm \epsilon)| \end{aligned}$$

After this "peak-picking" operation, the AGC network performs a time average over the output. Assuming ergodicity, this time averaging is equivalent to a special ensemble average, i.e.

$$\langle z_i(t_i) \rangle = \frac{1}{M} \sum_{i=1}^M z_i(t_i) = \tilde{E}\{z(t)\} \quad (6)$$

where the symbol $\tilde{E}\{ \}$ indicates that we only average over local maxima of the process $z(t)$. We know that (6) yields a value which is proportional to the "mean of the peaks" of the return signal. Thus, we can set

$$\tilde{E}\{z(t)\} = \frac{S}{r} [G_{RF} G_{IF}]^2 G_v a \quad (7)$$

where r is the r -factor relating "mean-of-the-peaks" and "peak-of-the-mean" return power.* To obtain the proper AGC gain, G_{AGC} , we multiply (7) by a scaling factor α to insure that we operate in a linear region of the S&H gate's curves and add a small offset δ to insure that G_{AGC} does not become infinite when $S \rightarrow 0$. Taking G_{AGC} to be the inverse square root of the above yields

$$G_{AGC} = \left\{ \frac{1}{\alpha a G_{RF}^2 G_v (S/r + \delta) G_{IF}^2} \right\}^{1/2}$$

A typical plot of G_{AGC} is shown in Figure 2.

The voltage into the S&H gates is $z(t)$ where

$$z(t) = \frac{1}{\alpha(S/r + \delta)} \left\{ [x_c(t) + n_c(t)]^2 + [x_s(t) + n_s(t)]^2 - 2N \right\} \quad (8)$$

For a given time, say $t=T$, the mean of $z(t)$ is

$$\begin{aligned} E\{z(T)\} &= \frac{1}{\alpha(S/r + \delta)} \{2SP_r(T) + 2N - 2N\} \\ E\{z(T)\} &= \frac{2S}{\alpha(S/r + \delta)} P_r(T) \end{aligned} \quad (9)$$

It should be noted that

*See Chapter 13 for a discussion of the r -factor and its verification from the waveform data.

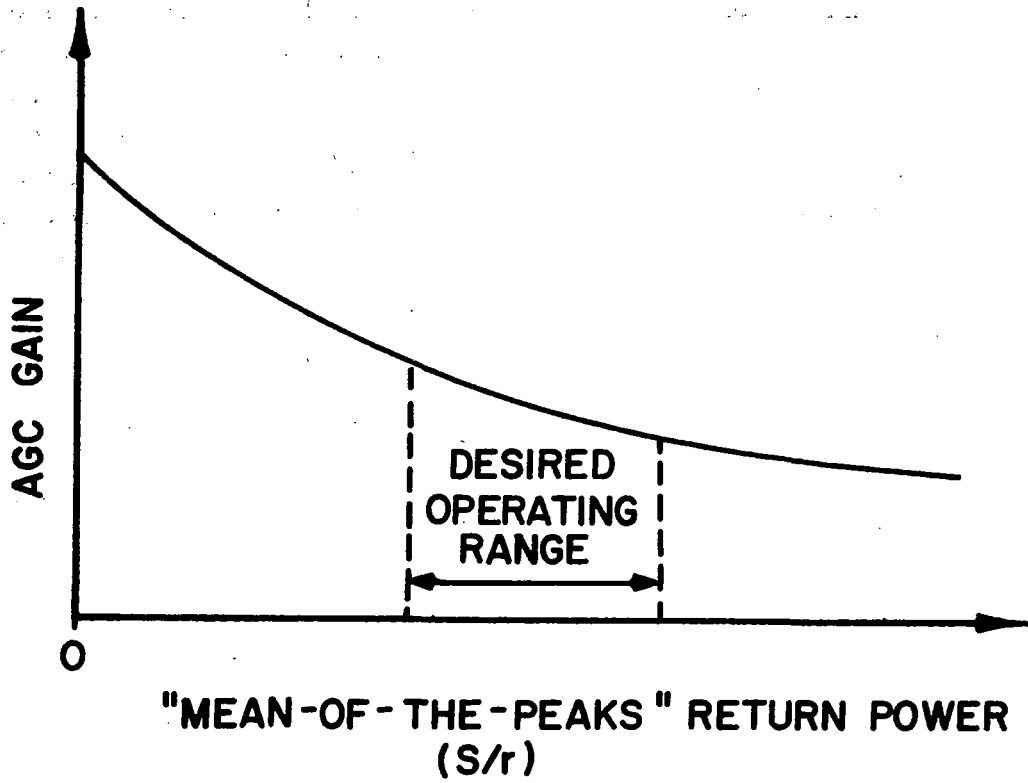


Figure 2. Typical AGC gain versus received signal power plot.

$$\lim_{S \rightarrow 0} E\{z(T)\} = 0$$

and

$$\lim_{S \rightarrow \infty} E\{z(T)\} = \frac{2}{\alpha/r} P_r(T)$$

It is interesting to note that even when the "peak-of-the-mean" return power is large, the amplitude of the mean voltage as recorded by the S&H gates is dependent upon the r-factor. This, of course, occurs because of the manner in which the AGC circuit operates. The above result also poses the interesting possibility that one may be able to determine the ratio of r-factors by noting the ratio of voltages as recorded by the S&H gates. For example, let $S = S_1$ for a given pointing angle of the altimeter antenna, say $\xi = \xi_1$, and let $S_1 \gg 1$. The peak of the mean return waveform is normalized to one at $t = T_1$ so that for $t = T_1$,

$$E\{z(t = T_1)\} \approx \frac{2r(\xi_1)}{\alpha}$$

For $\xi = \xi_2$ and $S = S_2$, where $S_2 \gg 1$, we have

$$E\{z(t = T_2)\} \approx \frac{2r(\xi_2)}{\alpha}$$

where T_2 is the time of the peak in the mean return waveform. Combining the above results yields

$$\frac{E\{z(t = T_1)\}}{E\{z(t = T_2)\}} = \frac{r(\xi_1)}{r(\xi_2)} \quad (10)$$

Equation (10) presents an interesting result which is investigated more thoroughly in Chapter 13.

The variance of $z(t)$ is given by

$$\text{Var}\{z(t)\} = E\{z^2(t)\} - E^2\{z(t)\}$$

and

$$E\{z^2(t)\} = \left[\frac{1}{\alpha(S/r + \delta)} \right]^2 E\left\{ \left[\{x_c(t) + n_c(t)\}^2 + \{x_s(t) + n_s(t)\}^2 \right] \right. \\ \left. - 4N \{ [x_c(t) + n_c(t)]^2 + [x_s(t) + n_s(t)]^2 \} + 4N^2 \right\} \quad (11)$$

After much algebra (11) reduces to

$$E\{z^2(t)\} = \left[\frac{2S}{\alpha(S/r + \delta)} \right]^2 \left[2P_r^2(t) + 2\left(\frac{N}{S}\right) P_r(t) + \left(\frac{N}{S}\right)^2 \right]$$

and using (9) leads to

$$\text{Var}\{z(t)\} = \left[\frac{2S}{\alpha(S/r + \delta)} \right]^2 \left[P_r(t) + \left(\frac{N}{S}\right) \right]^2 \quad (12)$$

When $P_r(t) = 0$, the S&H gates are sampling noise and

$$E\{z(t)\} = 0$$

$$\text{Var}\{z(t)\} = \left[\frac{2S}{\alpha(S/r + \delta)} \right]^2 \left(\frac{N}{S}\right)^2 \quad (13)$$

When the signal power S is large and the S&H gates are sampling noise only,

$$\text{Var}\{z(t)\} \approx \left[\frac{2r}{\alpha} \right] \left(\frac{N}{S}\right)^2 \quad (14)$$

and when S is much less than N ,

$$\text{Var}\{z(t)\} \approx \left[\frac{2}{\alpha\delta} \right]^2 N^2 \quad (15)$$

or the variance is proportional to the square of the noise power. When $P_r(t) = 1$, i.e. the peak of the mean return,

$$\text{Var}\{z(t)\} = \left[\frac{2S}{\alpha(S/r + \delta)} \right]^2 \left[1 + \left(\frac{N}{S}\right) \right]^2$$

and for large S

$$\text{Var}\{z(t)\} \approx \left[\frac{2r}{\alpha} \right]^2$$

while for small S

$$\text{Var}\{z(t)\} \approx \left[\frac{2}{\alpha\delta} \right]^2 N^2 \quad (16)$$

and (15) and (16) yield the same answer (as they should).

3.0 Analysis Including Jitter

When jitter is present, we must take conditional expectations when computing the mean and variance of $z(t)$. That is, for the mean of $z(t)$ we have

$$E\{z(t+\tau)\} = E_{\tau}\{E_z\{z(t+\tau)|\tau\}\} \quad (17)$$

where $E_z\{z(t+\tau)|\tau\}$ is the expected value of $z(t)$ conditioned on the fact that $t = t+\tau$. Since the tracking loop updates the positioning of the S&H gates with a minimum discrete step size of 5 ns, τ is taken to be a zero-mean discrete random variable having a probability density function given by $f(\tau)$ where

$$f(\tau) = \sum_{m=-\infty}^{\infty} p_m \delta(\tau+m5) \quad (18)$$

The $\delta(\cdot)$ are delta functions while the weights p_m are such that

$$\sum_{m=-\infty}^{\infty} p_m = 1$$

Combining the above results, we find that the first and second moments of the waveform recorded in the presence of jitter are given by the following;

$$E\{z(t+\tau)\} = \frac{2S}{\alpha(S/r+\delta)} \sum_{m=-\infty}^{\infty} p_m P_r(t+m5) \quad (19)$$

$$\mathbb{E}\{z^2(t+\tau)\} = \left[\frac{2S}{\alpha(S/r + \delta)} \right]^2 \sum_{m=-\infty}^{\infty} p_m \left\{ \left[P_r(t+m5) + \left(\frac{N}{S} \right) \right]^2 + P_r^2(t+m5) \right\} \quad (20)$$

Equations (19) and (20) are easily recognized as the convolutions of the true first and second moments, respectively, with the density function of the time jitter. Due to the smearing effect of the convolution, it is possible that the variance of $z(t)$ when jitter is present is less than the variance of $z(t)$ with no jitter.

One means of explaining this variance reduction (with jitter) is shown in Figure 3. First consider the case of sampling with no jitter ((A) of Figure 3) and let the sampler be located at the breakpoint on the mean (where the linear rise intersects the plateau). Since the point sampler does not change its location, it is in essence sampling a process with a constant variance as shown in (B) of Figure 3 and the variance of the sampled process will be equal to a^2 . Now consider the case shown in (C) of Figure 3 where the sampler may be located, at say, 5 distinct positions* according to its probabilistic behavior. As shown in (D) of Figure 3, we must now consider the time varying nature of the variance of the process. With the exception of the zero error sampling position, for every sample of the process whose variance is constant (in the plateau region) we have a sample of a process whose variance is less than the plateau value. Thus, the variance of the process as recorded by the jittered sample must be less than the variance of the plateau. Very crudely, we see that the variance of the sampled process will be some weighted average of the variances which the sampler sampled. This is exactly what the convolution in (20) is doing.

When the tracking loop is operating within the linear range of the time discriminator and the spacecraft vertical rate is small, the density function of the tracking loop jitter is approximately Gaussian [1,2]. In this case the density weights are symmetrical, i.e. $p_m = p_{-m}$, and are given by [3]

$$p_m = 0.5 \operatorname{erf} \left(\frac{2.5+m5}{\sigma_j \sqrt{2}} \right) - 0.5 \operatorname{erf} \left(\frac{-2.5+m5}{\sigma_j \sqrt{2}} \right) \quad m = 0, 1, \dots$$

*We assume here that for $|m| \geq 2$, $p_m \approx 0$.

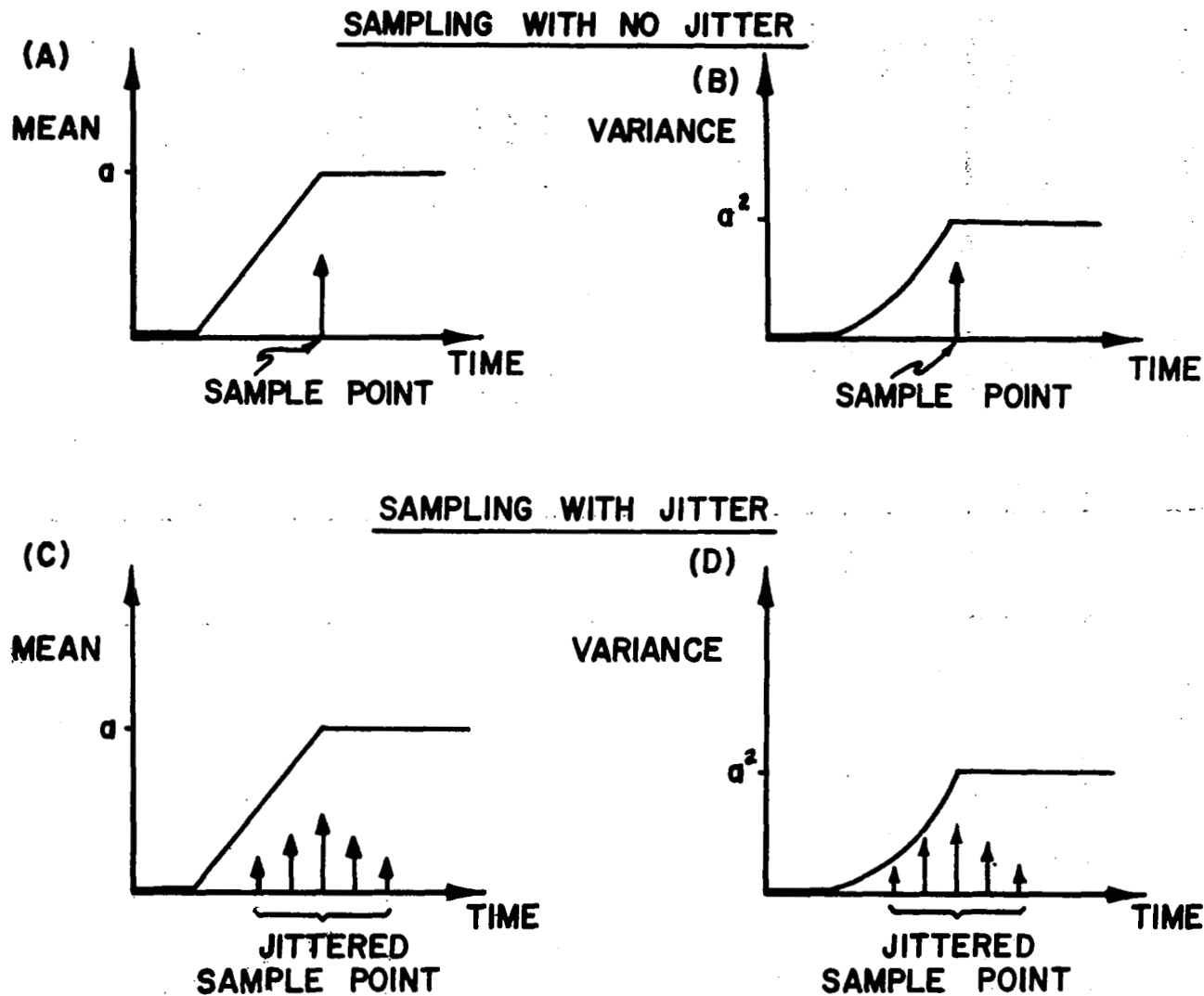


Figure 3. An illustration of the effect of time jitter on the waveform mean and variance.

where erf (\cdot) is the error function and σ_j is the standard deviation of the jitter. For low IF single pulse signal-to-noise ratios (≤ 5 dB) or large pointing errors the density function of the tracking loop jitter may deviate rather markedly from the Gaussian form. Apart from a small correction for quantization, the standard deviation of the tracking jitter (σ_j) is nearly equal to twice the standard deviation of the output altitude noise (σ_h) because of the highly correlated nature of the altitude data on Skylab; that is, for σ_j in nanoseconds and σ_h in meters

$$\sigma_j \approx 6.67 \sigma_h \quad .$$

For the Skylab 100 ns mode, the effects of tracking jitter can generally be ignored for all three missions since it was small relative to the system point target response width. For the 10 ns mode jitter should be properly accounted for since it can be mistaken for surface roughness effects. To illustrate this point, we have selected a situation which is somewhat representative of a high seas short pulse return. In particular, we have assumed an IF signal to noise ratio of 10 dB, a 10 ns tracking jitter (implying an altitude noise level of 1.5 m), a significant waveheight ($H_{1/3}$) of 4.4 m and nadir pointing. The signal-to-noise ratio is very close to that resulting from operation of the non pulse compression mode during high sea state conditions. The effect of jitter and surface roughness upon the mean return is shown in Figure 4. If we ignore the discrete nature of the jitter density function, the leading edge of the mean return is approximately equal to an integrated Gaussian* having a composite σ given by

$$\sigma \approx \sqrt{\sigma_p^2 + \sigma_j^2 + (1.67 H_{1/3})^2} \quad (21)$$

where σ_p is the equivalent one-sigma width of the point target response (≈ 7.6 ns), and $H_{1/3}$ is the significant waveheight in meters. If we measure σ from the jittered mean in Figure 4 and neglect σ_j in the expression for $H_{1/3}$ in (21), we would infer $H_{1/3}$ to be about 7.4 m and therefore incur

*This assumes Gaussian system point target response and waveheight probability density functions.

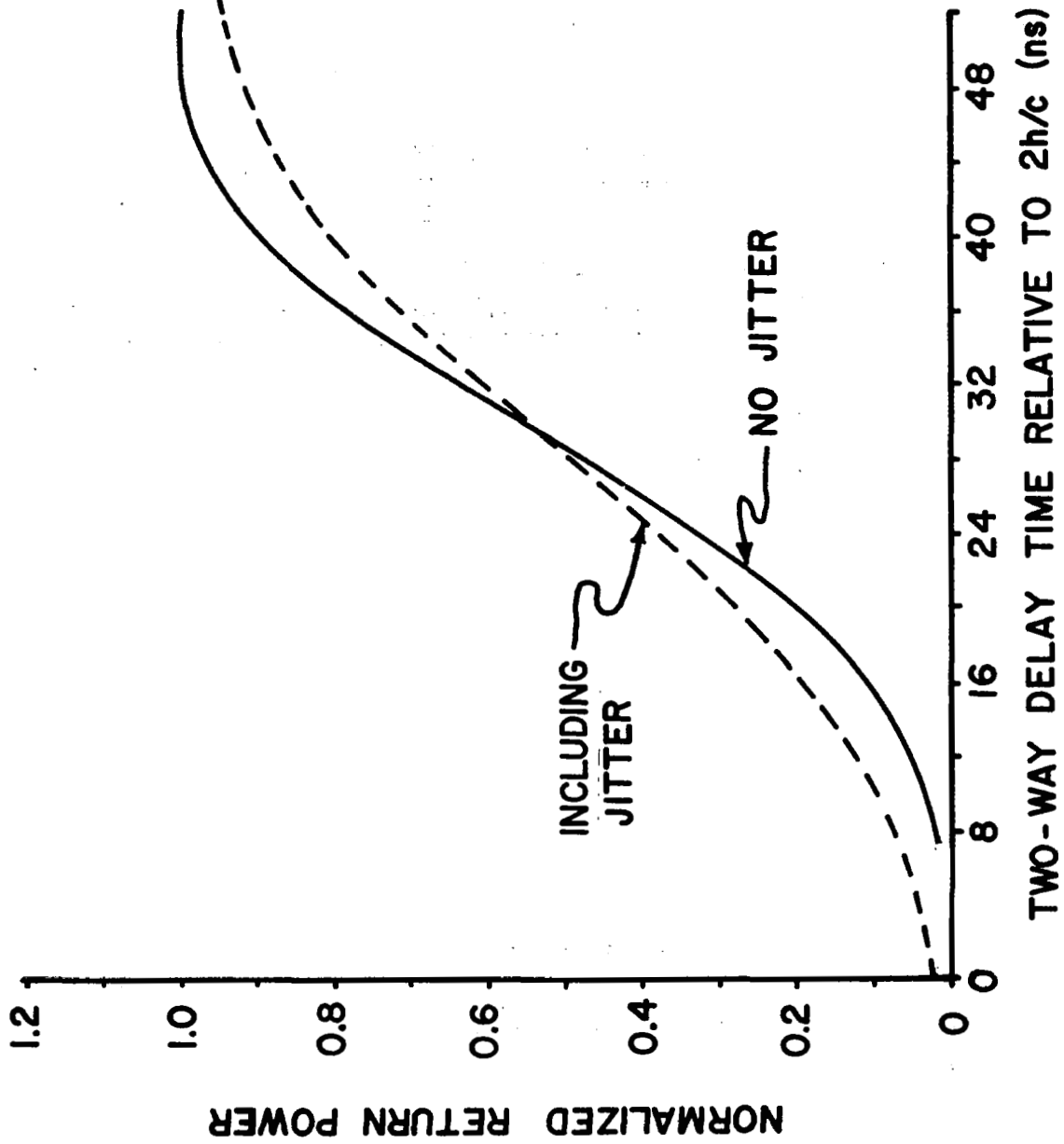


Figure 4. The effects of a 10 ns jitter on the short pulse mean return leading edge for a significant waveheight of 4.4 m.

a 69% error in over estimating $H_{1/3}$. Thus, for the short pulse mode, jitter effects must be properly accounted for. Figure 5 illustrates the effect of jitter on the standard deviation of the leading edge of the return. We note that unlike the effect upon the mean, the jittered standard deviation has no symmetry about the one-half amplitude point. We also note that the inclusion of signal-to-noise effects gives rise to the greatest discrepancy in the early part of the rise time and at the point of greatest curvature. Figure 6 shows the jittered mean and standard deviation together; the purpose of this plot is to illustrate the fact that a mean and standard deviation comparison will not necessarily show the effects of jitter. Stated another way, Figure 6 does not appear too different from a no-jitter case. For correcting waveform data, the jitter must be obtained from the altitude data and accounted for using equation (21) or time realignment (see Chapter 12).

REFERENCES

1. Hofmeister, E. L and B. Keeney, "Radar Altimeter Return Waveform Sampling Study," Final Report, Contract NAS6-1823, General Electric Co., Utica, N. Y., October, 1971.
2. Hofmeister, E. L., "Analysis and Measurement Of The Performance Of A Signal Tracking Loop For A Satellite Radar Altimeter When Excited By A Random Process," Ph.D. Thesis, Syracuse University, December, 1973.
3. Nelson, A. C., Private communication, 1 August, 1973.

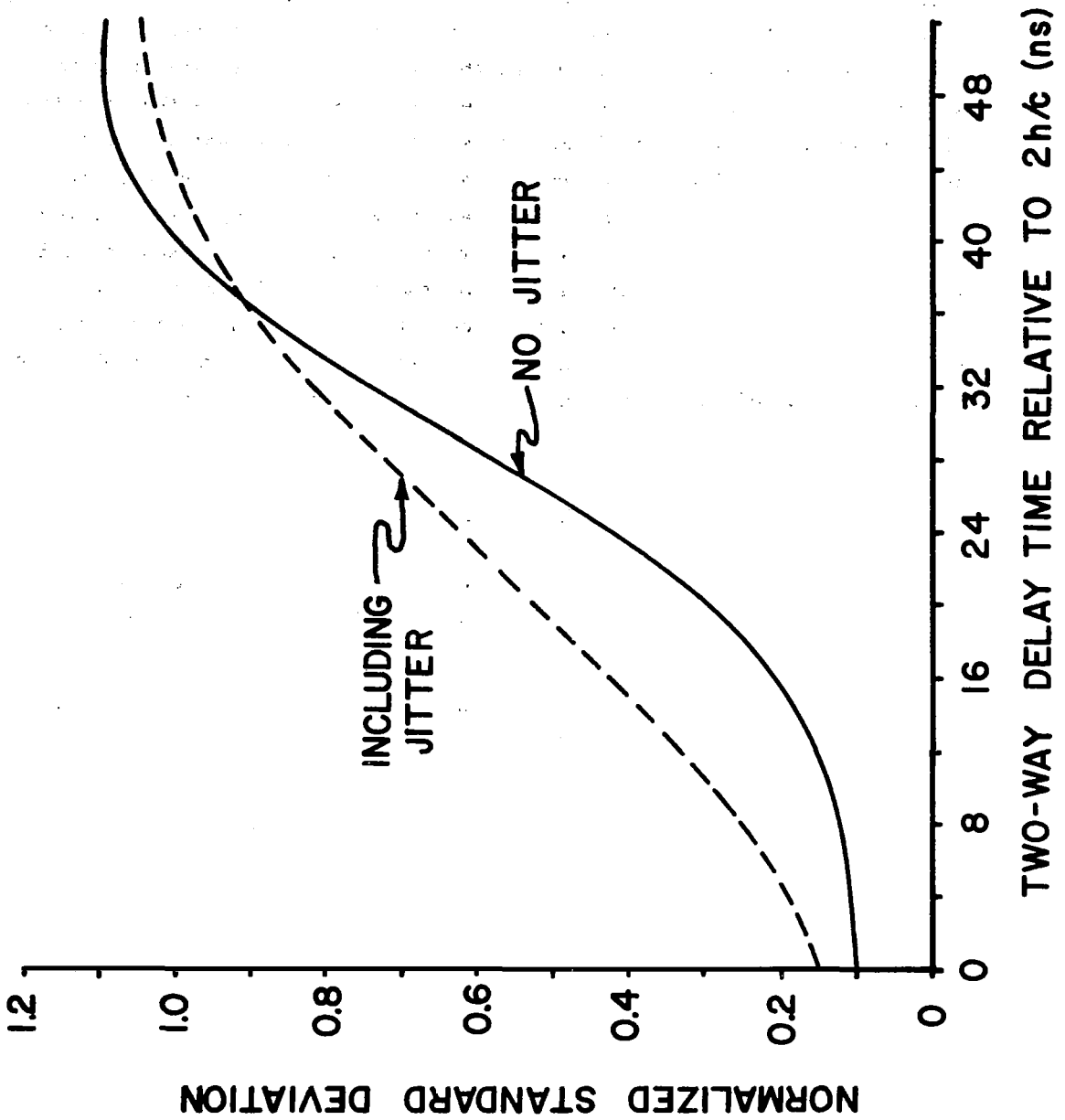


Figure 5. The effect of a 10 ns jitter on the standard deviation of the leading edge of the return for a significant waveheight of 4.4 m and SNR = 10 dB. Normalization is with respect to the jitter-free average return power.

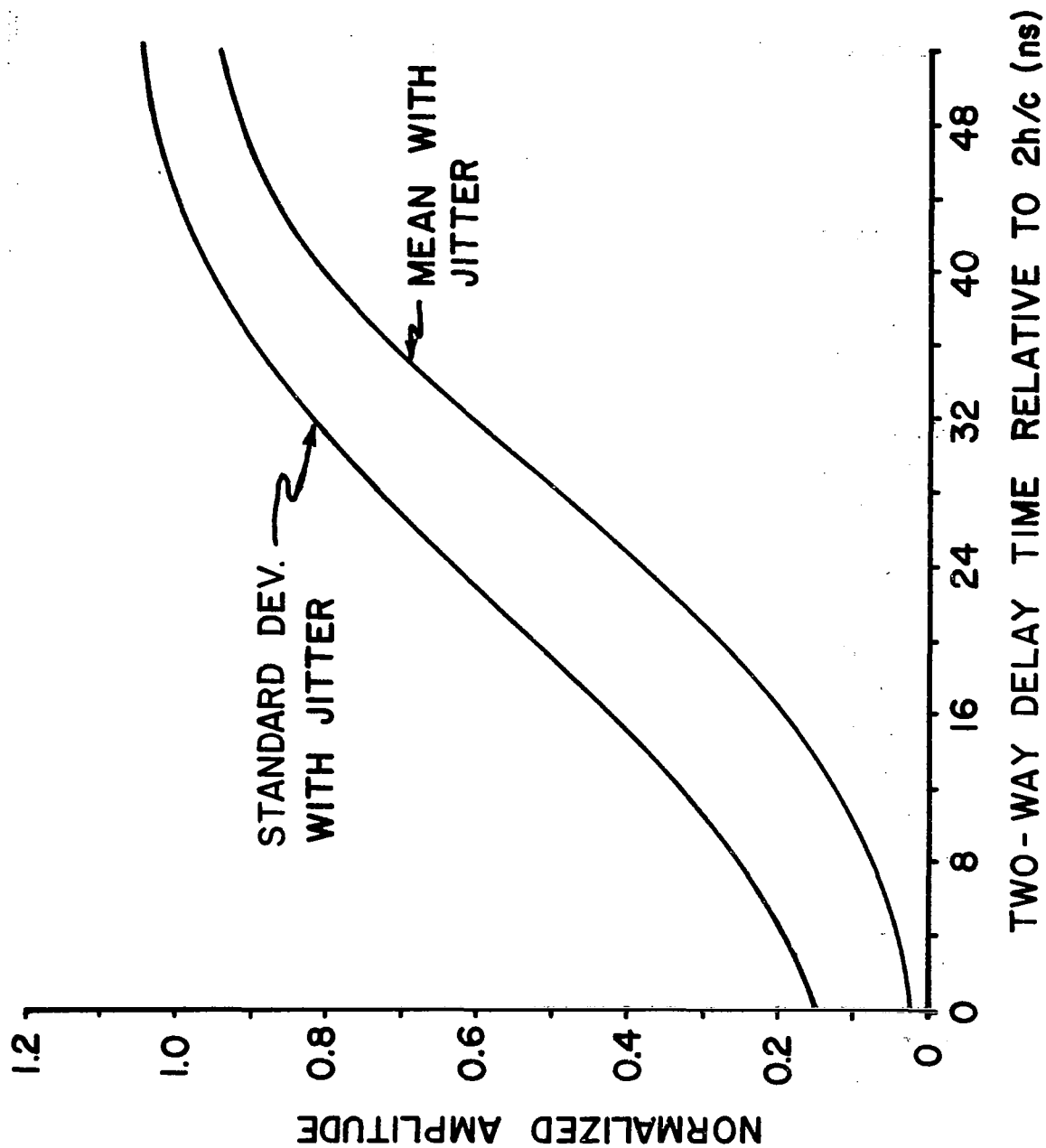


Figure 6. A comparison of the mean and standard deviation of the leading edge of the short pulse return for a 10 ns jitter, a significant waveheight of 4.4 m and SNR = 10 dB.

CHAPTER 12

Correlation Of Waveform Derived Sea State Estimates And Ground Truth

by

L. S. Miller

G. S. Hayne

1.0 Introduction

As discussed in [1]; it is possible to extract information on ocean surface roughness through changes in the rise time of the processed mean return waveforms. Figure 1 shows an example of the average waveform obtained during calm seas (SL-4, EREP Pass 74) and for 6 meter significant waveheight conditions (SL-4, EREP Pass 78). Waveheight surface truth data for the latter of these passes is shown in Figure 1 of Chapter 7 and will not be repeated here. Figure 1 also shows computed waveshapes for the appropriate sea state conditions; these comparisons demonstrate the essential agreement between the observed data and the convolutional theory of surface roughness effects. In Figure 1, the theoretical curves and processed experimental data are in very good agreement except for values in the plateau region of the waveforms. This departure is most probably due to sampling gate saturation effects, which are discussed in Chapter 13.

This chapter discusses the procedures used in processing S-193 waveform data and the general character of the waveform data base obtained from the S-193 altimeter activities. A number of problems were encountered in analyzing S-193 waveform sampled data, and the task of extracting sea state information became an arduous undertaking. The principal difficulty experienced was that of a shift in the location of the waveform samplers relative to the rise time of the received waveshapes. This shift occurred when pulse compression started to function properly (SL-3, EREP Pass 39, first Mode V). SL-4 data constitutes virtually all of the moderate to high sea state data base; consequently, the leading edge portion of the waveshape was largely unrecorded during SL-4 because of the shift in the waveform samplers. Figure 2 illustrates the situation; this figure shows waveform sample values and a fitted curve. The curve fitting method used in Figure 2 is detailed in Appendix A. Examination of Figure 2 shows the first sampled value to be approximately one-third of the way into the rise-time period. However,

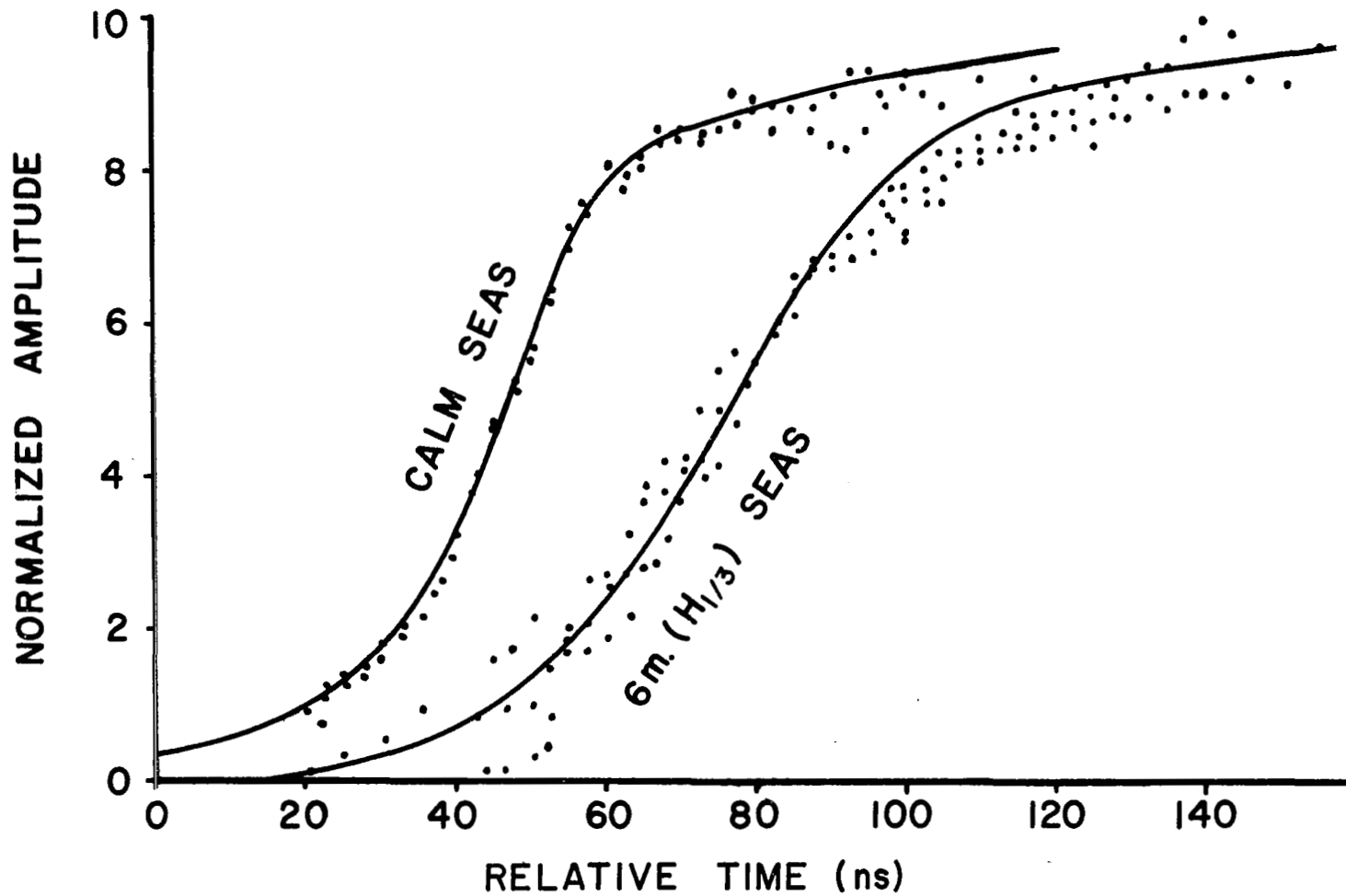


Figure 1. Comparison of time realigned and filtered waveform data with theoretical predictions (including estimation filter residual error); calm sea data from EREP Pass 74, first Mode V, Submode 1; 6 m. sea state data from EREP Pass 78, second Mode V, submode 1. Both data sets were obtained using pulse compression.

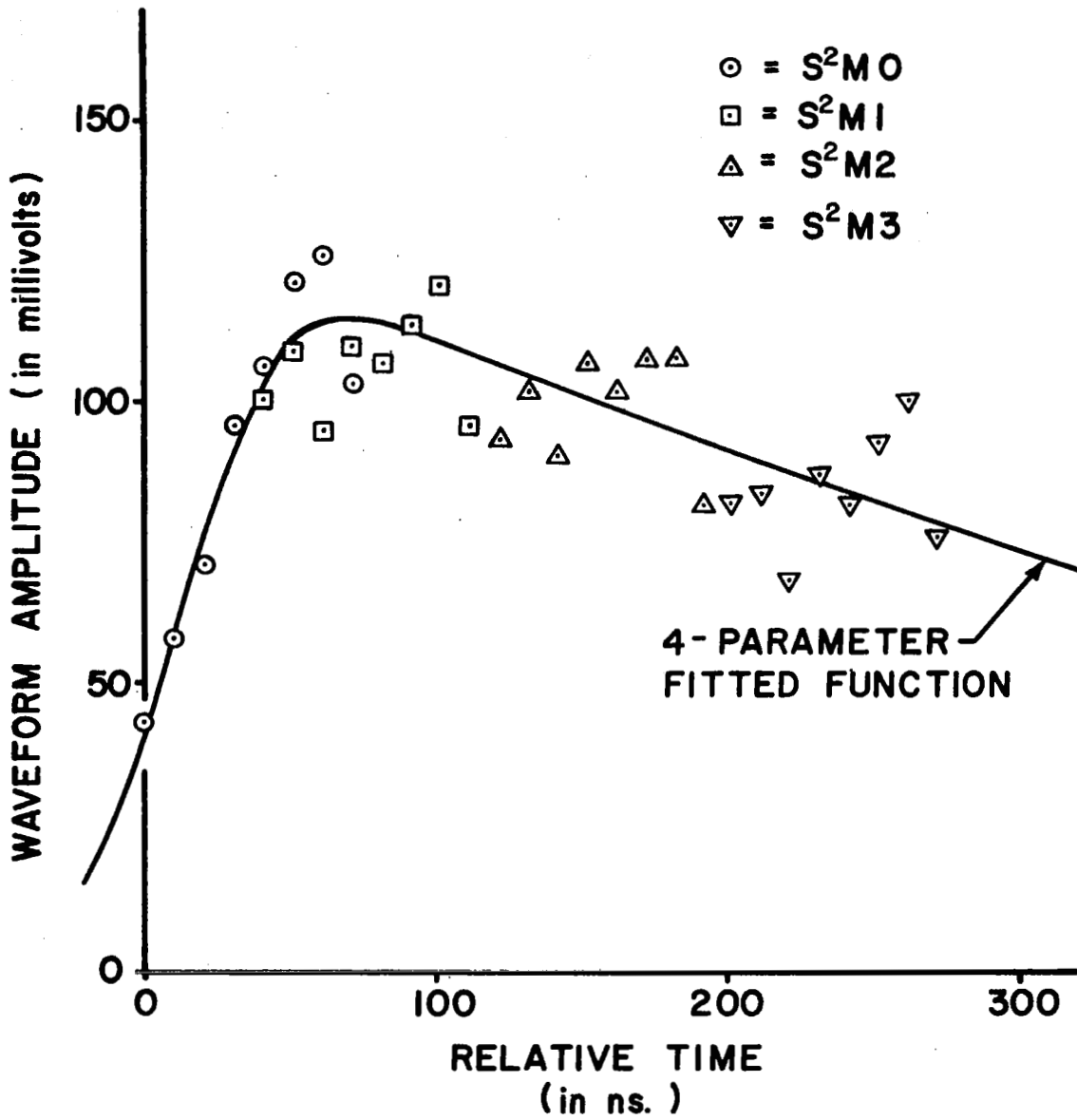


Figure 2. Comparison of non time realigned measured data and fitted function for EREP Pass 74, first Mode V, submode 1.

sensitivity studies of the implemented curve fitting method (see Appendix A), show that the rise time of the fitted curve is heavily influenced by a baseline or offset parameter which must be estimated. That is, the lack of a recorded baseline caused the estimation procedure contained in Appendix A to be marginally reliable.

The technique of compensating for the sampled data time positioning jitter based on use of the altitude tracker time history was found to largely overcome the waveform sampler shift problem. This technique, known as time realignment and described in [2], was first investigated relative to waveform variance reduction (see Section 3.0 of Chapter 11) with inconclusive results. Time realignment was later employed in an attempt to recover waveform baseline values according to the following rationale. The rms time positioning jitter of the waveform samplers for the data in Figure 2 is approximately 10 ns; thus, a three-sigma negative time excursion would provide a sample point about 30ns earlier in time than the earliest value shown in Figure 2. Figure 3 shows the waveform data for EREP Pass 74 (Frames 2-11) obtained using time realignment; it should be noted that the waveform baseline is strongly in evidence. Therefore, this technique was found to be the *sine qua non* of the sea state analysis effort, albeit an involved time consuming computation. Time realignment is an estimation rather than an exact procedure because the altitude tracker time history is not directly observed. Averaging and round-off operations in the system partially obscure the time-history; this effect is discussed in Section 3.0.

A number of other data limitations and problems were experienced. Briefly, these were as follows.

- There was no overlap between operation of the pulse compression and non pulse compression submodes.* The pulse compression system malfunctioned during most of SL-2 and SL-3. The S-193 antenna was damaged before SL-4 altimeter passes began with an attendant gain loss of greater than 20 dB. Since the non pulse compression submode was designed to provide a nominal signal-to-noise ratio of 10-15 dB, the antenna gain loss essentially disabled this submode

*See Appendix C for a discussion of the performance of pulse compression relative to non pulse compression and the 100ns pulsewidth.

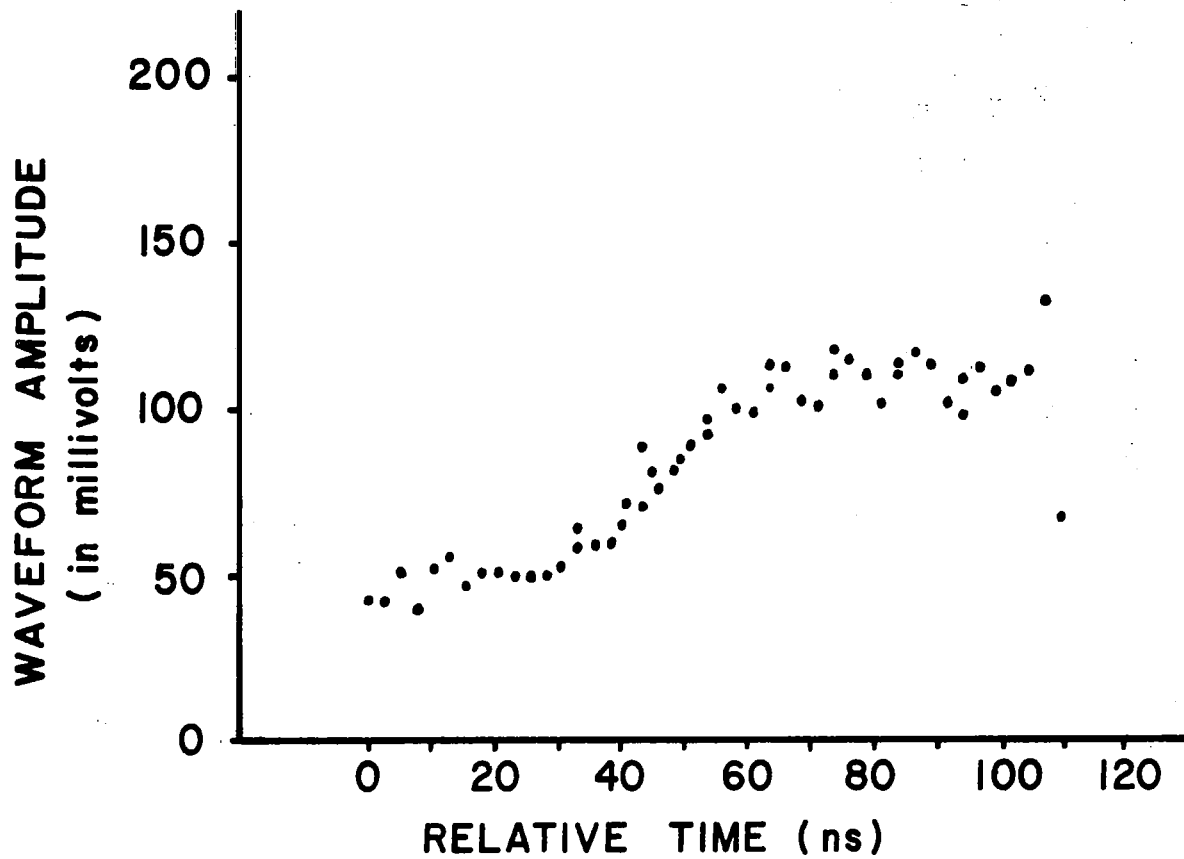


Figure 3. Time realigned waveform data from EREP Pass 74, first Mode V, submode 1, frames 2 through 11. The spacing between the data points is 2.5 ns.

(see Section 6.0 of Chapter 13).

- The sampled waveform data exhibited saturation effects and an apparent time variability to the offset and gain parameters. Although the system was designed to zero mean the receiver thermal noise, the noise baseline, when observed, appeared to be dependent on receiver gain value. Also, the sampled values seemed to contain an unknown noise component or random error superimposed on the signal self-noise.* For short term averaging (≤ 1 Frame) self-noise is dominant; for longer averaging periods, the unidentified measurement noise dominates.

2.0 Waveform Data Processing Operations

The experimental and theoretical waveforms shown in Figure 1 were subjected to a rather involved data processing procedure to place these data on a comparable basis.

Discussing first the theoretical waveforms; the calm sea waveshapes were computed by first integrating the point target response waveform samples (CDS values) recorded during SL-4 and then convolving these values with the effective tracking loop time jitter (based on uncorrected σ_h values from [3] and residual values detailed in Section 3.0). These data were then filtered using the least squares, linear operation described in Appendix B. This recursive filtering operation results in a small time smearing, which must be incorporated into the theoretical waveforms since these effects are present in the processed experimental data. Additionally, the theoretical waveshape for the case of $H_{1/3} = 6$ m. was obtained by convolving the flat sea waveshape with a Gaussian waveheight probability density of $\sigma = H_{1/3} \div 4$ (for this case, Pass 78, the signal-to-noise ratio was near unity and according to [3] tracking jitter variance was 11.42 meters²). Neither the theoretical nor the experimental waveshapes shown in Figure 1 contain corrections for antenna pattern effects, sampler saturation (see Section 5.0 of Chapter 13), and off-nadir pointing angle effects. The major effect which was included in these theoretical waveforms is that of time sidelobes. Since high

*The term self-noise was coined by radar astronomers and denotes the natural signal fluctuations due to random surface scattering. Also, see Section 5.0 of Chapter 13 for a further discussion of this effect.

seas occurred during SL-4 when only pulse compression was functioning, the non pulse compression submode is not of interest. The time sidelobes cause the theoretical waveshapes to significantly depart from an integrated Gaussian form; for example a "constant" plateau value does not result since the time sidelobes continue to contribute to the integration for the time expanse shown and for negligible antenna pattern effects.

Turning to the data processing operation appropriate to the experimental values; these data were obtained from a linear, least squares filtering operation on the time realigned sample values for these passes. Pass 74 contains twenty data frames and Pass 78 contains thirty data frames*; these data were filtered in ten-frame segments. The following points should be noted; (1) time-realignment causes the population of each data point to be different (for example, in Pass 78 the first plotted point comprises 65 samples and typical values for the plateau region are approximately 200 samples per data point), (2) the time-quantization with time realignment used here is 2.5 ns, and (3) with Pass 78 data the experimental values become more sparse below an amplitude level of about 30% of peak value since only values from the time realignment procedure exist in this time zone (c.f. Figure 2). Finally, the calm sea and 6 m. waveheight curves have been displaced from the data by approximately 30 ns at the 50% point for convenience of data presentation.

3.0 Time Realignment Uncertainty

In the S-193 altimeter system the tracking loop signal is averaged over a .128 second interval and these data are recorded on magnetic tape as altitude measurements. Because of the round-off applied following the averaging operation, it is not possible to exactly reconstruct the tracking loop altitude values which are in one-to-one correspondence with the waveform sampling time jitter. These effects are depicted in Figures 4 and 5. Reference 4 considered this problem in detail and derived a technique for estimating the waveform time jitter based on the output altitude data. The purpose of this paragraph is to assess the residual time uncertainty of the waveform sample values after use of the estimator given in [4]. The analysis given below indicates that approximately 58% of the time jitter effects can be

*104 waveforms were "recorded" by the eight S&H gates per frame of data.

Loop Accumulator Update Times (8 Possible)

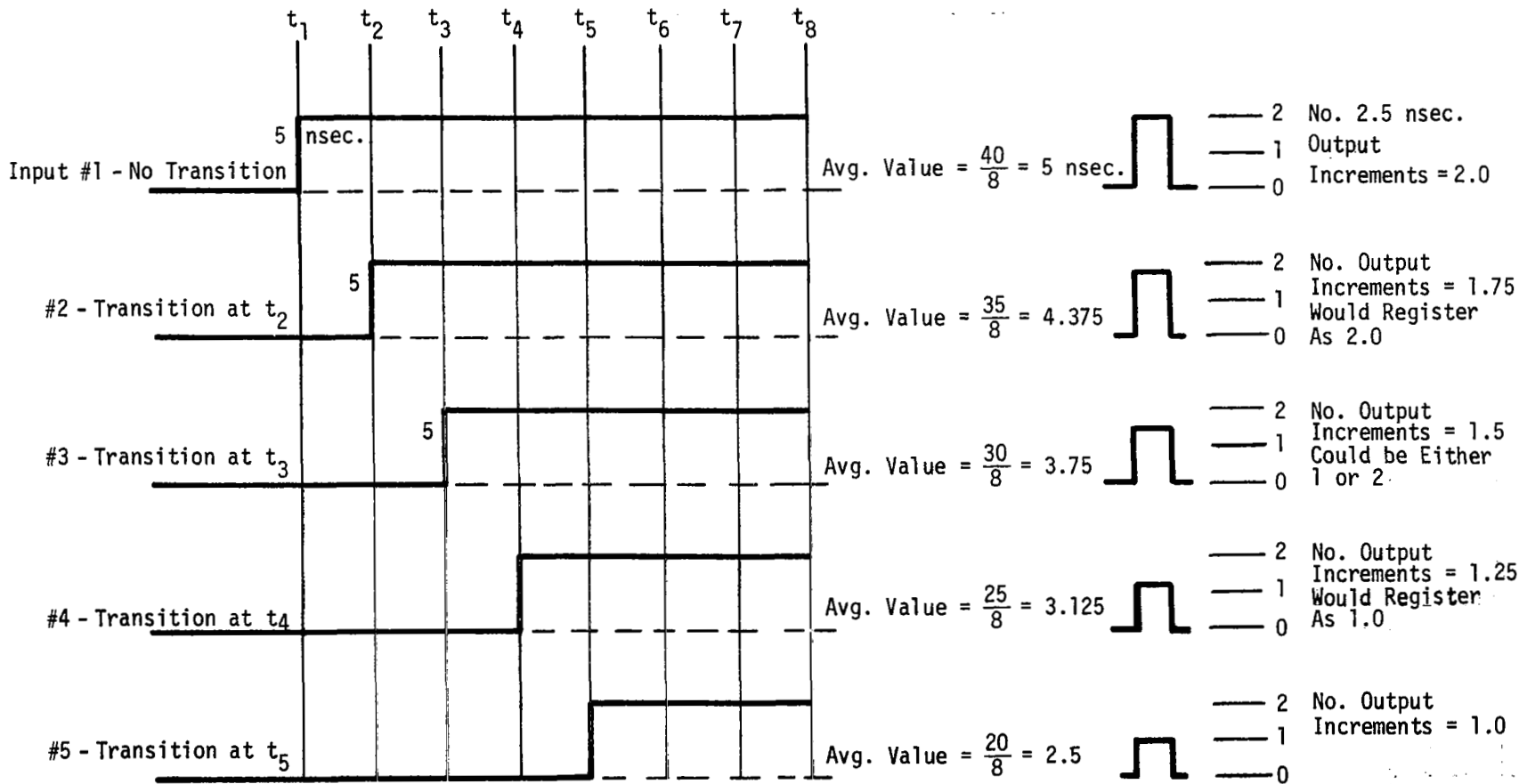


Figure 4. Illustration of output quantization effect on input signal reconstruction accuracy.

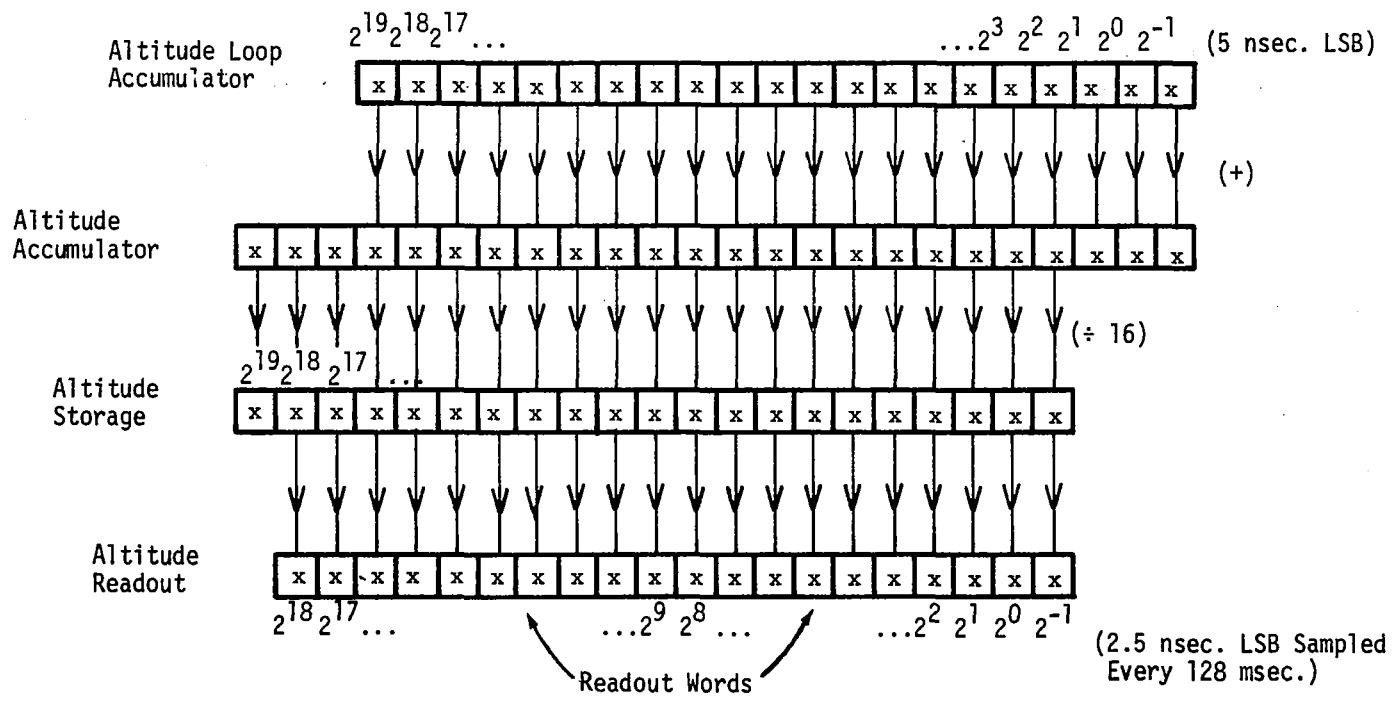


Figure 5. Altitude processing and readout scheme.

removed from the waveform data by the application of the estimation filter.

Following the estimation procedure given in [4], the relative variance reduction as a result of the estimation filter is, c.f. [5], R where

$$R = \frac{\frac{1}{2\pi} \int_{-\infty}^{\infty} [S_T(\omega) |H_a(\omega)|^2 + N(\omega)] |H_o(\omega)|^2 d\omega}{\frac{1}{2\pi} \int_{-\infty}^{\infty} S_T(\omega) d\omega} \quad (1)$$

and

$S_T(\omega)$ = the spectrum of tracking loop signal in terms of the closed loop transfer function $H_T(\omega)$ and

$$S_T(\omega) = |H_T(\omega)|^2 = \left(\frac{35}{4}\right)^2 \left| \frac{4 + j\omega}{-\omega^2 + j\omega 8.875 + 35} \right|^2$$

$H_a(\omega)$ = the transfer function of the altitude averaging operation; its approximate form is

$$H_a(\omega) = \frac{1}{T} \frac{\sin \omega T/2}{\omega T/2} \quad (T = .128 \text{ sec.})$$

$N(\omega)$ = the spectrum of the additive quantization noise which is represented as white noise with density equal to $0.1 \text{ m}^2/\text{rad}$

$H_o(\omega)$ = the transfer function of the estimation filter.

Figure 6 is a plot of $|H_T(f)|^2$ and $|H_T(f)|^2 |H_a(f)|^2$, where $f = \omega/(2\pi)$.

All of these terms are reasonably simple in characterization with the exception of the estimation transfer function, $H_o(\omega)$. A continuous-time transfer function is given in [4] which is inverse transformed and time-truncated and the resulting estimator represented as weighting coefficients in a time convolution. There are two methods for converting the convolution operation into a spectral description. The closed form impulse response function given in [4], $h_o(t)$, can be operated on by a unit square wave in

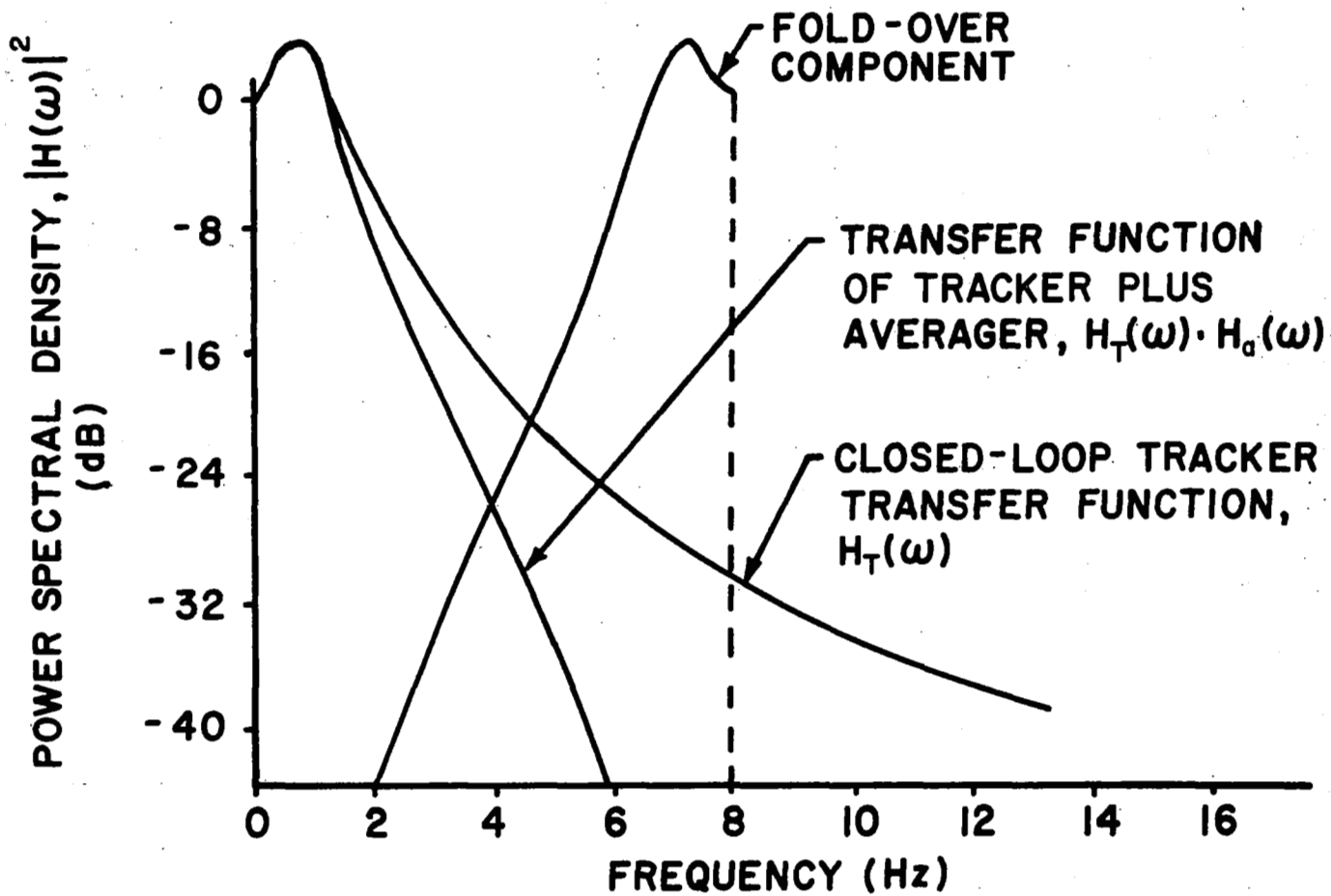


Figure 6. Bandpass characteristics of the altitude data.

a multiplicative form, i.e.

$$h_o(t) \cdot [u(t) - u(t-T)] ,$$

where T is the time truncation parameter. In the frequency domain this becomes a convolution (denoted by *)

$$H_o(\omega) * \frac{\sin \omega T/2}{\omega T/2}$$

In the approach used here, the weighting coefficients were converted into a spectral description through use of a discrete Fourier transform. Using the sine and cosine transforms as follows;

$$S_m = \sum_{n=0}^{N-1} h(n) \sin\left(\frac{2\pi mn}{N}\right) \quad m = 0, 1, 2, \dots, \frac{N-1}{2}$$

and

$$C_m = \sum_{n=0}^{N-1} h(n) \cos\left(\frac{2\pi mn}{N}\right) \quad m = 0, 1, 2, \dots, \frac{N-1}{2}$$

$|H_o(\omega)|^2$ is then represented by the discrete frequency values $C_m^2 + S_m^2$ where the frequency and time increments satisfy

$$\Delta F \Delta T = \frac{1}{N}$$

or

$$\Delta\omega = \frac{2\pi}{N \Delta T}$$

and $\omega_m = m \Delta\omega$. For the computed values of C_m and S_m , $h_o(n)$ was represented by [4]

$$h_o(n) = e^{-4.94(n-k)\Delta T} \left(\cos[3.7(n-k)\Delta T] - .879 \sin[3.7(n-k)\Delta T] \right)$$

for $(n-k)\Delta T = 0$ to 2.048

$$h_o(n) = 0$$

for $(n-k)\Delta T > 2.048$

where k is used for time translation since the $h_o(n)$ values must have fold-over symmetry*. Values were computed for $N = 61$ and ΔT chosen such that $\Delta\omega = 2$; the results are shown in Figure 7.

Because of the mixture of transcendental and polynomial terms in equation 1, closed form integration would be difficult; therefore, numerical integration techniques were used. The results were as follows;

$$\frac{1}{2\pi} \int_{-\infty}^{\infty} S_T(\omega) d\omega = 5.874 \text{ m}^2$$

$$\frac{1}{2\pi} \int_{-\infty}^{\infty} \left\{ S_T(\omega) |H_a(\omega)|^2 + N(\omega) \right\} |H_o(\omega)|^2 d\omega = 3.406 \text{ m}^2$$

or

$$R = 0.58$$

Therefore this analysis indicates that time realignment will produce a variance reduction of 58% in the waveform time jitter. It should be noted that the 42% residual error may still be comparable to the sea state effects.

*This procedure provides a time truncation of two data frames where one frame = 1.024 sec. for the altitude data (see Figures 10 and 11 of Chapter 2).

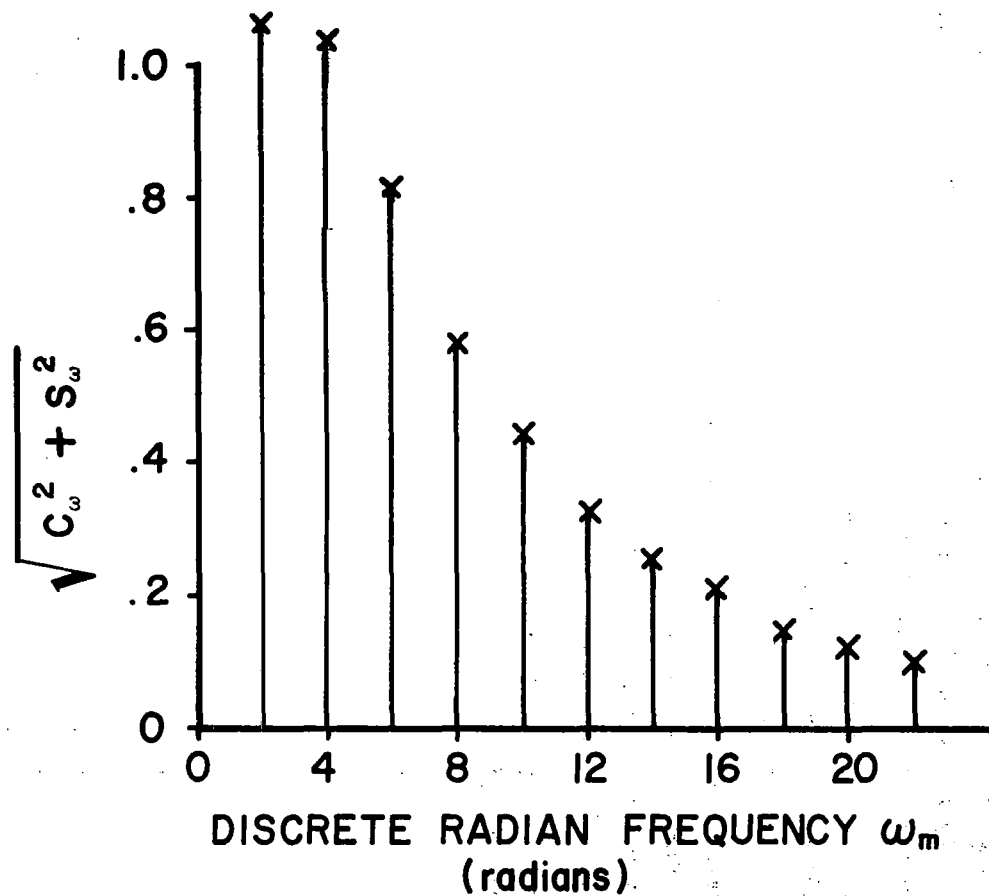


Figure 7. Transfer function (magnitude) of the estimation filter based on the discrete Fourier transform of the time-truncated weighting coefficients.

REFERENCES

1. McGoogan, J. T., L. S. Miller, G. S. Brown and G. S. Hayne, "The S-193 Radar Altimeter Experiment," Proc. of IEEE, vol. 62, pp. 793-803, June, 1974.
2. Hayne, G. S., "Engineering Studies Related To The Skylab Program," Final Report on Task F of Contract No. NAS6-2307 (NASA/WFC), Applied Science Associates, Inc., Apex, N. C., September, 1974.
3. Hatch, W. E., "Noise Characteristics of the Skylab S-193 Altimeter Altitude Measurements," NASA CR-141403, Business and Technological Systems, Inc., Seabrook, MD., November, 1974.
4. Miller, L. S. and G. S. Hayne, "Estimation of Sample and Hold Gate Position Signal Based On Altimeter Output Data," Final Report on Task A of Contract No. NAS6-2307 (NASA/WFC), Applied Science Associates, Inc., Apex, N. C., July, 1973.
5. Davenport, W. B. and W. L. Root, An Introduction to the Theory of Random Signals and Noise, McGraw-Hill Book Co., New York, 1958.

APPENDIX A

Template Fitting Results For Initial Estimates Of The
Average Return Waveform Characteristics

The time realignment scheme for jitter reduction and baseline (waveform sampler offset) definition was a very involved and time consuming operation. For these reasons, it was not considered feasible to time-realign process all of the Mode V short pulse waveform data. To avoid this volume of data processing and effectively narrow the number of passes to those considered to contain resolvable sea state effects, an alternate approach was employed. All of the short pulse waveform data were first processed using a template matching scheme; those passes which indicated significant sea state effects were then subjected to complete time realignment processing. The purpose of this appendix is to briefly discuss the template fitting technique and tabulate appropriate results; time realignment results are presented in the main body of the chapter.

The basic template matching technique has been thoroughly described elsewhere [A1] and only its salient points will be reviewed here. The approach assumes that a functional form for the average return waveform in terms of a number of unknown parameters is available. The technique then basically generates numerical values for the unknown parameters which minimize the weighted squared deviations of the function from a given set of data points. When each data point is inversely weighted by its own variance, the method can be referred to as either a chi-squared minimizing or maximum likelihood routine. Unequal weighting is an important criterion since the variances of the waveform data are a function of the location of the data point on the mean return and the number of returns used to form the average.

A complete description of the functional form for the average return waveform for the Skylab altimeter is given in [A2]. For the purposes of this study, it is possible to simplify the expression for the average return. Because of the asymmetrical antenna pattern, the pointing angle, of the antenna boresight relative to nadir, i.e. ξ , is dependent upon the spacecraft-centered pitch angle, ξ_p , and roll angle, ξ_r . Conversely, however, for a given mean return waveform and angle ξ , it is not possible to uniquely specify both ξ_p and ξ_r . Thus, given the AGC normalized return power waveform, one

can choose the angles (ξ_p, ξ_r) which produce the waveform in question and also simplify the functional form for the average return (AGC normalized). It can be shown that the choice which results in the most simple form for the average return is $\xi_r = 0^\circ$; for this choice, the flat surface impulse response [A2] reduces to two terms involving the Bessel functions $I_0(\cdot)$ and $I_2(\cdot)$. Because the equivalent width of the short pulse system point target response is much smaller than the time span over which the flat surface impulse response exhibits a significant variation, the convolution of these two functions can be approximated by the product of the flat surface impulse response and the integral of the system point target response. Furthermore, numerical studies have shown that the term involving $I_2(\cdot)$ is much less significant than the $I_0(\cdot)$ term, at least for the range of pointing angles encountered in the short pulse data. In summary then, the appropriate form for the average return power is given by;

$$A_o P\left(\frac{\tau - \tau_o}{\sigma} - 2\sqrt{2}\right) \quad \tau < \tau_o$$

$$\bar{P}_r(\tau) \approx \quad \quad \quad (A1)$$

$$A_o \exp\left[-\eta(\tau - \tau_o)\right] I_o(\beta\sqrt{\tau - \tau_o}) P\left(\frac{\tau - \tau_o}{\sigma} - 2\sqrt{2}\right) \quad \tau \geq \tau_o$$

where

$$\eta = \frac{4c}{\gamma h} (1 + \delta) \cos 2\xi$$

$$\beta = \frac{4}{\gamma} (1 + \delta) \sqrt{\frac{c}{h}} \sin 2\xi$$

$$P(\tau) = 0.5 \left[1 + \operatorname{erf}\left(\frac{\tau}{\sqrt{2}}\right) \right]$$

and $\operatorname{erf}(\cdot)$ is the error function. The constants γ and δ are antenna pattern parameters [A2]; for SL-2 and SL-3, $\gamma = .0007$ and $\delta = 0.75$ while for SL-4, $\gamma = .0007$ and $\delta = 0.18$. The constant c is the speed of light and h is the altitude of the radar above the mean surface. It should be remembered that (A1) corresponds to a pointing direction $\xi_r = 0$, $\xi_p = \xi$.

Also implicit in equation (A1) is the assumption of a Gaussian form for the system point response or the pulse shape recorded in the CDS submode, i.e.

$$P_{PT}(\tau) \approx \frac{1}{\sqrt{2\pi} \sigma_p} \exp \left[-\frac{\tau^2}{2\sigma_p^2} \right] \quad (A2)$$

where σ_p is the effective "width" of the point target response. A comparison of the Gaussian fit with actual measured data is shown in Figure A1 for SL-2 and SL-3 (non pulse compression) and in Figure A2 for SL-4 (pulse compression). For Figure A1, $\sigma_p \approx 6.4$ ns while for Figure A2, $\sigma_p \approx 8.3$ ns and it should be noted that the fit to the pulse compression data ignores a rather strong sidelobe occurring at 80 ns.

The four parameters in equation (A1) which are varied in the template matching routine to fit the data are; the amplitude A_o , the time shift τ_o , the effective rise time parameter σ , and the pointing angle ξ or, in this case, ξ_p . These parameters must be considered to be variable since, (1) the AGC normalized amplitude of the mean return waveform can vary as a function of pointing angle (see Section 2.0, Chapter 13), (2) the change in the waveform as a function of pointing angle can cause a shift in the position of the waveform samplers due to a change in the tracker-sensed waveform centroid, and (3) the effective rise time of the return is dependent on σ_p , the range extent of the ocean surface waveheights, and the variance of the tracking loop jitter (see Section 3.0, Chapter 11).

A summary of the short pulse data (both non pulse compression results from SL-2 and SL-3 and pulse compression data from SL-4) is presented in Table A1. The first column in the table identifies the Mission (SL-2,-3 or -4) and the EREP Pass number. The second column provides Mode and Submode information. The mode will always be Mode V in the table, and the numbers in parentheses by the V in the table are identification as to which Mode V is listed, for those passes having more than one. A question mark will indicate uncertainty about which Mode V is listed.

The third column of Table A1 provides date of pass and day of year and (when available) a reference map number. These reference map numbers correspond to a designation originated in Reference A3. Those maps each provide a triad of time(GMT)-latitude-longitude at the beginning of the map

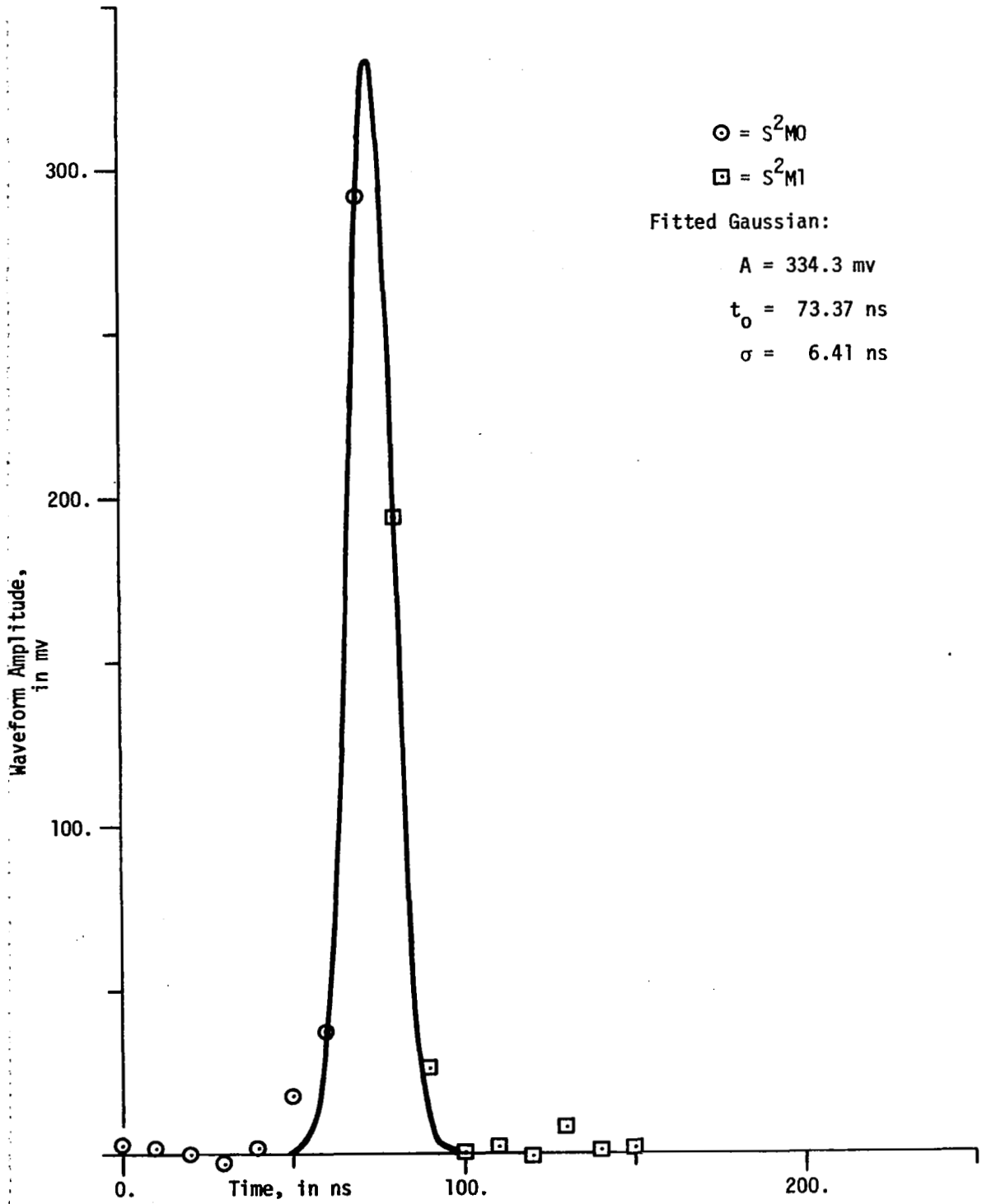


Figure A1. Short-Pulse CDS Data and Fitted Gaussian, SL-2, Pass 9, Mode 5, Submode 4.

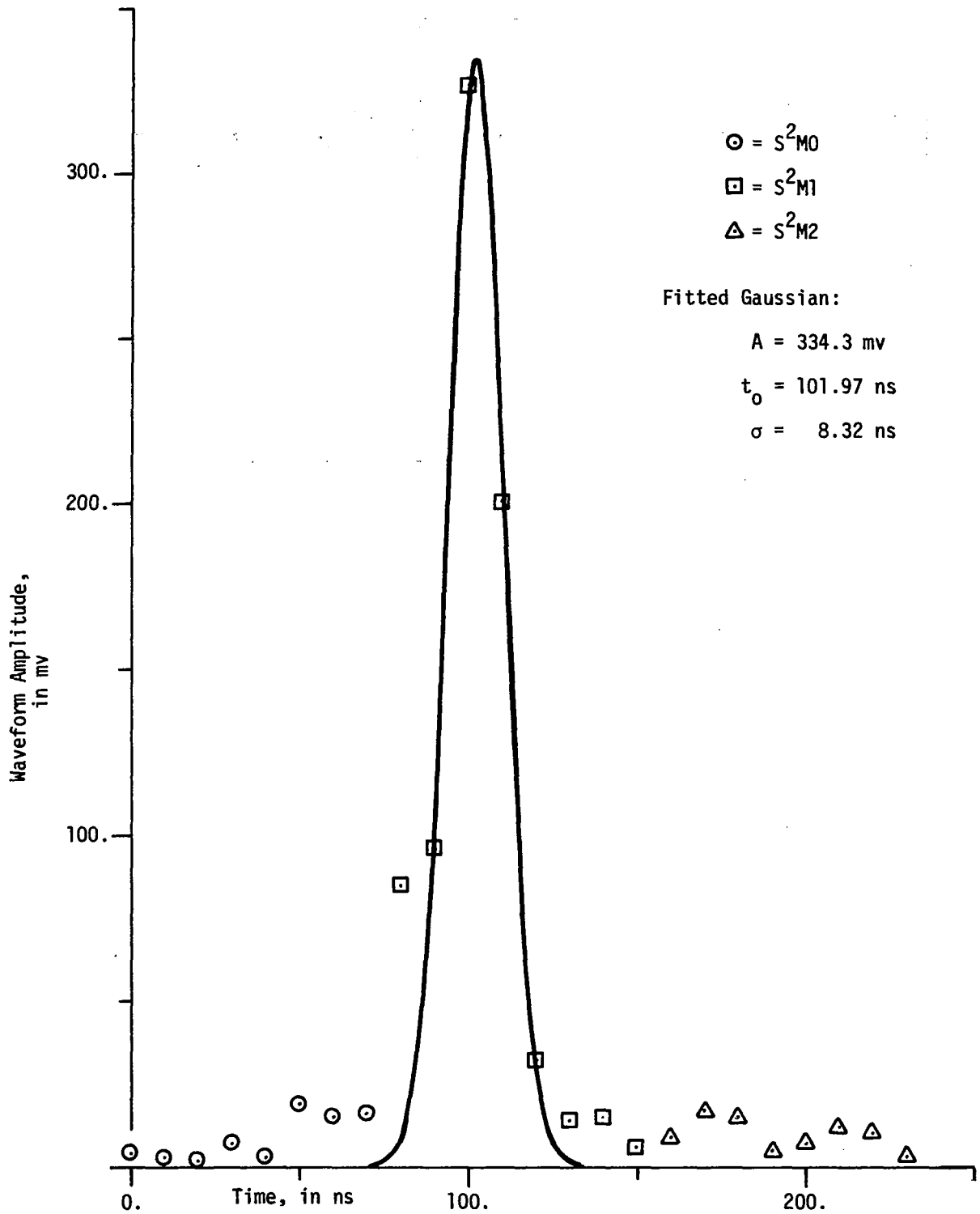


Figure A2. Pulse Compression CDS Data and Fitted Gaussian, SL-4, Pass 79/24, Mode 5 (2nd), Submode 4.

TABLE A1. Summary of Short-Pulse Submodes for Possible Sea-State Estimation by Waveform Analysis

Mission, EREP Pass	Mode, Submode	Date, Day of Year, Reference Map	Start-of-Submode Time, Latitude, Longitude	End-of-Submode Time, Latitude, Longitude	Sub-submodes Present	Altitude Residuals (ESTM)	Pointing Angle	Ratio 1st S&H to Maximum	Comments * = Further Analysis
SL-2 6	V 2	06/09/73 159 Map 5	15-17-32.0 15.7 N 64.6 W	15-18-23.0 13.5 N 62.4 W	all	+ 1 m	medium	0.14	* Caribbean
SL-2 7	V 2	06/10/73 160 Map 7	14-34-01.7 18.1 N 62.4 W	14-34-52.6 15.6 N 60.2 W	all	5	large	0.58	Caribbean to Atlan- tic
SL-2 9	V 2	06/12/73 162 Map 11	13-03-36.8 32.5 N 68.0 W	14-04-27.7 30.4 N 65.1 W	all	1	small	0.04	* SE of U.S., near Bermuda
SL-3 17	V 2	08/09/73 221 Map 30	14-00-28.2 0.3 N 42.5 W	14-01-192 02.3 S 40.5 W	all	2	medium	0.44	Atlantic, off Brazil
SL-3 18	V 2	08/11/73 223 Map 32	15-38-51.8 07.4 N 85.7 W	15-39-42.8 05.1 N 83.9 W	all	1	small	0.02	* Pacific, off Central, South America
SL-3 19	V 2	08/12/73 224 Map 34	02-48-31.7 40.6 S 156.3 E	02-49-22.6 42.2 S 159.3 E	all	3	large	0.57	Tasman Sea, SE off Australia
SL-3 21	V (1st) 2	09/01/73 244 Map 35	15-24-46.0 11.1 S 32.7 W	15-25-37.0 08.8 S 30.9 W	all	1	small	0.02	* Atlantic, E of S. America

TABLE A1. Summary of Short-Pulse Submodes for Possible Sea-State Estimation by Waveform Analysis (Cont'd.)

Mission, EREP Pass	Mode, Submode	Date, Day of Year, Reference Map	Start-of-Submode Time, Latitude, Longitude	End-of-Submode Time, Latitude, Longitude	Sub-submodes Present	Altitude Residuals (ESTM)	Pointing Angle	Ratio 1st S&H to Maximum	Comments * = Further Analysis
SL-3 21	V(2nd) 2	09/01/73 244 Map 36	15-28-37.1 0.2 S 23.9 W	15-29-23.8 01.7 N 22.4 W	all	1	small	0.02	* Atlantic
SL-3 25	V(1st) 2	09/04/73 247 Map 46	14-53-37.6 01.7 N 32.2 W	14-54-28.6 04.1 N 30.4 W	all	1	small	0.02	* Atlantic, off S. America coast
SL-3 25	V(2nd) 2	09/04/73 247 Map 47	14-57-09.2 11.9 N 24.4 W	14-58-00.2 14.6 N 22.3 W	all	1	small	0.02	* Atlantic, approaching Africa
SL-3 27	V 2	09/06/73 249 Map 48	21-21-46.4 25.7 N 120.4 W	21-22-37.4 28.2 N 117.8 W	all	1	small	0.03	* Pacific, off Baja
SL-3 28	V 2	09/07/73 250 Map 50	20-37-15.1 20.8 N 120.7 W	20-38-06.1 23.2 N 118.6 W	all	1-2	small	0.03	* Pacific, off Baja
SL-3 32	V(1st) 2	09/11/73 254 Map 54	13-08-13.6 25.9 N 25.4 W	13-09-04.6 28.2 N 23.1 W	all	7-8	large	0.59	Atlantic, near Canary Islands
SL-3 32	V(2nd) 2	09/11/73 254 Map 55	13-11-43.0 35.2 N 14.0 W	13-12-33.9 37.4 N 11.1 W	all	6	large	0.61	Atlantic, Madeira Islands

TABLE A1. Summary of Short-Pulse Submodes for Possible Sea-State Estimation by Waveform Analysis (Cont'd.)

Mission, EREP Pass	Mode, Submode	Date, Day of Year, Reference Map	Start-of-Submode Time, Latitude, Longitude	End-of-Submode Time, Latitude, Longitude	Sub-submodes Present	Altitude Residuals (ESTM)	Pointing Angle	Ratio 1st S&H to Maximum	Comments
SL-3 35	V 2	09/12/73 255 Map 58	12-27-30.0 30.2 N 15.9 W	14-28-20.5 32.4 N 13.4 W	all	8	large	0.60	Atlantic, Madeira Islands
SL-3 36	V(1st) 2	09/12/73 255 Map 61	16-54-13.7 04.4 S 116.6 W	16-55-04.7 01.9 S 114.6 W	all	4-5	large	0.59	East Pacific, S of Equator
SL-3 36	V(2nd) 2	09/12/73 255 No map ?	16-57-44.6 05.8 N 108.8 W	16-58-35.6 08.3 N 107.0 W	all		large	0.57	
SL-3 36	V(3rd) 2	09/12/73 255 Map 63	17-01-15.2 15.1 N 101.6 W	17-01-30.8 16.4 N 100.5 W	0,1 only		large		
SL-3 36	V(4th) 2	09/12/73 255 Map 65	17-14-25.6 46.8 N 54.6 W	17-15-19.7 48.1 N 50.1 W	all		large		North Atlantic - passes over land at Newfoundland
SL-3 37	V 2	09/12/73 255 Map 66	20-12-34.8 30.3 N 134.1 W	20-13-25.7 32.2 N 131.9 W	all	4	large	0.60	North Pacific
SL-3 38	V(1st) 2	09/13/73 256 Map 70	18-08-33.6 49.8 N 52.8 W	18-09-24.5 50.2 N 48.4 W	all	5-6	large	0.64	E, off Newfoundland in North Atlantic

TABLE A1. Summary of Short-Pulse Submodes for Possible Sea-State Estimation by Waveform Analysis (Cont'd.)

Mission, EREP Pass	Mode, Submode	Date, Day of Year, Reference Map	Start-of-Submode Time, Latitude, Longitude	End-of-Submode Time, Latitude, Longitude	Sub-submodes Present	Altitude Residuals (ESTM)	Pointing Angle	Ratio 1st S&H to Maximum	Comments * = Further Analysis
SL-3 38	V(2nd) 2	09/13/73 256 Map 71	18-11-49.0 49.0 N 34.2 W	18-12-39.9 48.6 N 29.6 W	all	4	large	0.62	North Atlantic
SL-3 39	V(1st) 1	09/13/73 256 Map 73	19-46-05.1 48.2 N 51.4 W	19-47-45.9 46.0 N 43.2 W	all	1	medium- large		Pulse Compression started to work ~ Frame 33 of S ² MO
SL-3 39	V(1st) 2	09/13/73 256 Map 73	19-47-48.0 45.9 N 43.0 W	19-48-39.0 44.8 N 38.9 W	all	1	medium- large	0.36	* North Atlantic, SE of Newfoundland
SL-3 39	V(2nd) 1	09/13/73 256 Map 74	19-49-43.0 42.8 N 34.2 W	19-51-23.9 39.3 N 27.4 W	all	1-2	medium- large	0.48	* North Atlantic, SE of Newfoundland
SL-3 39	V(2nd) 2	09/13/73 256 Map 74	19-51-26.0 39.2 N 27.3 W	19-52-16.9 37.4 N 23.9 W	all	1-2	medium- large	0.50	* North Atlantic, SE of Newfoundland
SL-4 57	V(1st) 1	12/02/73 336 Map 92	18-24-24.1 19.6 N 105.1 W	18-26-05.0 14.7 N 101.0 W	all	1-2			First ~ 10 frames overland, rest in Pacific off Mexico and Central America
SL-4 57	V(2nd) 1	12/02/73 336 Map 93			0(part)only			-	

TABLE A1. Summary of Short-Pulse Submodes for Possible Sea-State Estimation by Waveform Analysis (Cont'd.)

Mission, EREP Pass	Mode, Submode	Date, Day of Year, Reference Map	Start-of-Submode Time, Latitude, Longitude	End-of-Submode Time, Latitude, Longitude	Sub-submodes Present	Altitude Residuals (ESTM)	Pointing Angle	Ratio 1st S&H to Maximum	Comments
SL-4 61	V 1	12/05/73 339 Map 99	16-21-23.6 5.6 N 79.7 W	16-22-41.6 1.6 N 76.5 W	0(part)only			-	
SL-4 64	V 1	12/09/73 342 Map 102	02-37-23.4 10.4 N 101.6 E	02-38-48.6 6.1 N 104.9 E	0,1,2 only	4-5		-	
SL-4 65	V 1	12/15/73 349 Map 105	00-01-15.9 6.7 S 119.2 E	00-02-05.8 9.6 S 121.5 E	0(part)only			-	
SL-4 67	V 1	12/18/73 352 Map 106	02-00-33.3 42.3 N 65.5 W	02-01-46.1 44.6 N 60.3 W	0.1(part) only			-	
SL-4 68	V(1st) 1	12/18/73 352 Map 109	11-45-09.0 14.4 N 96.2 W	11-46-49.9 10.3 N 92.9 W	all	2	medium	0.58	East Pacific, off Central America coast
SL-4 68	V(2nd) 1	12/18/73 352 Map 110	11-48-30.4 .04.8 N 88.4 W	11-50-11.3 00.2 S 84.7 W	all	2-3	medium	0.69	
SL-4 68	V(?) 1	12/18/73 352			0(part) only		medium	-	

TABLE A1. Summary of Short-Pulse Submodes for Possible Sea-State Estimation by Waveform Analysis (Cont'd.)

Mission, EREP Pass	Mode, Submode	Date, Day of Year, Reference Map	Start-of-Submode Time, Latitude, Longitude	End-of-Submode Time, Latitude, Longitude	Sub-submodes Present	Altitude Residuals (ESTM)	Pointing Angle	Ratio 1st S&H to Maximum	Comments * = Further Analysis
SL-4 71	V(1st) 1	01/01/74 01 Map 112?	13-22-15.6 34.8 S 46.5 W	13-23-27.4 31.4 S 43.2 W	all		medium	0.41	* Atlantic, off E coast of S. America
SL-4 71	V(2nd) 1	01/01/74 01 Map 113	13-25-34.5 25.3 S 37.3 W	13-27-15.4 20.5 S 32.7 W	all	2	medium	0.48	Atlantic, off E coast of S America
SL-4 71	V(3rd) 1	01/01/74 01 Map 114	13-29-16.0 14.5 S 27.5 W	13-30-56.9 09.6 S 23.5 W	all	1-2	medium-small	0.39	* Atlantic, off S America
SL-4 71	V(4th) 1	01/01/74 01 Map 115	13-32-54.3 04.1 S 19.3 W	13-34-35.2 00.9 N 15.6 W	all	1-2	small	0.38	* Atlantic, at Equator
SL-4 74	V(1st) 1	01/06/74 06 Map 117	17-55-48.2 23.7 N 91.6 W	17-57-26.0 28.2 N 87.0 W	all	1-2	small	0.37	* Gulf of Mexico
SL-4 74	V(2nd) 1	01/06/74 06 Map 118	18-00-58.0 37.1 N 75.3 W	18-02-38.9 40.8 N 68.9 W	all	1-2	small	0.40	* Off E coast of U. S., just misses land at Norfolk
SL-4 74	V(?) 1	01/06/74 06	18-14-10.0	18-14-37.0	0(part) only		small	-	

TABLE A1. Summary of Short-Pulse Submodes for Possible Sea-State Estimation by Waveform Analysis (Cont'd.)

Mission, EREP Pass	Mode, Submode	Date, Day of Year, Reference Map	Start-of-Submode Time, Latitude, Longitude	End-of-Submode Time, Latitude, Longitude	Sub-submodes Present	Altitude Residuals (ESTM)	Pointing Angle	Ratio 1st S&H to Maximum	Comments * = Further Analysis
SL-4 76	V(1st) 1	01/07/74 07 Map 123	17-18-56.6 38.3 N 68.5 W	17-20-34.4 41.5 N 62.7 W	all	5	large	0.74	Atlantic, E of U.S.
SL-4 78	V(1st) 1	01/08/74 08 Map 128	16-34-19.6 33.3 N 71.3 W	16-36-00.4 37.1 N 65.8 W	all	1-2	medium	0.46	* Atlantic, off SE U.S.
SL-4 78	V(2nd) 1	01/08/74 08 Map 129	16-44-44.1 49.9 N 23.7 W	16-46-25.0 50.1 N 13.6 W	all	1-2	medium	0.58	North Atlantic
SL-4 79	V(1st) 1	01/09/74 09 Map 131	15-46-12.0 18.3 N 82.4 W	15-47-57.0 23.2 N 77.9 W	0,1 only		medium- small	-	
SL-4 79	V(2nd) 1	01/09/74 09 Map 132	15-50-01.6 28.9 N 71.9 W	15-51-42.5 33.4 N 66.5 W	all	2	medium- small	0.41	* Atlantic, E of SE U.S.
SL-4 79	V(3rd) 1	01/09/74 09 Map 134	16-01-00.1 49.3 N 25.7 W	16-02-41.0 50.2 N 15.8 W	all	2	medium- small	0.56	North Atlantic
SL-4 83	V(?) 1	01/14/74 14	15-34-54.5	15-35-29.9	0(part) only		large- medium	-	

TABLE A1. Summary of Short-Pulse Submodes for Possible Sea-State Estimation by Waveform Analysis (Cont'd.)

Mission, FREP Pass	Mode, Submode	Date, Day of Year, Reference Map	Start-of-Submode Time, Latitude, Longitude	End-of-Submode Time, Latitude, Longitude	Sub-submodes Present	Altitude Residuals (RSTM)	Pointing Angle	Ratio 1st S&H to Maximum	Comments * = Further Analysis
SL-4 83	V(?) 1	01/14/74 14	15-36-33.8	15-37-18.5	0(part) only		large- medium	-	
SL-4 83 Part 1	V(1st) 1	01/14/74 14 Map 146	15-38-41.7 49.7 N 26.1 W	15-40-22.6 48.5 N 17.3 W	all	3	large- medium	0.58	North Atlantic
SL-4 83 Part 1	V(?) 1	01/14/74 14	15-41-38.9	15-41-48.3	0(part) only		large- medium	-	
SL-4 86	V 1	01/20/74 20 Map 233	19-18-30.5 34.1 N 73.5 W	19-20-11.4 30.4 N 68.7 W	all	2	medium	0.40	* Atlantic, off SE U.S.
SL-4 88	V(?) 1		19-29-23.3	19-30-00.7	0(part) only			-	
SL-4 88	V(?) 1		19-33-16.1	19-33-27.5	0(part) only			-	
SL-4 89	V(1	01/24/74 24 Map 164	18-09-27.7 12.8 N 56.8 W	18-11-07.6 08.3 N 53.3 W	all	6	large	0.70	Atlantic, E of NE S. America

TABLE A1. Summary of Short-Pulse Submodes for Possible Sea-State Estimation by Waveform Analysis (Cont'd.)

Mission, EREP Pass	Mode, Submode	Date, Day of Year, Reference Map	Start-of-Submode Time, Latitude, Longitude	End-of-Submode Time, Latitude, Longitude	Sub-submodes Present	Altitude Residuals (ESTM)	Pointing Angle	Ratio 1st S&H to Maximum	Comments * = Further Analysis
SL-4 90	V(1st) 1	01/25/74 25 Map 168	17-19-27.5 36.4 N 77.1 W	17-21-08.4 32.4 N 73.3 W	all	4-5	large	0.69	SE, off North Carolina
SL-4 90	V(2nd) 1	01/25/74 25 Map 169	17-22-51.1 24.9 N 62.9 W	17-24-35.1 20.1 N 58.2 W	all	5-6	large	0.77	Atlantic, E of Bahamas
SL-4 93	V 1	01/27/74 27 Map 185	19-09-34.7 09.5 N 87.4 W	19-11-15.6 04.4 N 83.4 W	all	1-2	medium	0.32	* E. Pacific off Central, S. America
SL-4 97 Part 3	V(1st) 1	01/31/74 31 Map 216	15-56-43.6 49.0 N 161.0 W	15-58-24.5 50.0 N 151.5 W	all	1-2	large- medium	0.43	* North Pacific, almost to Bering Sea
SL-4 97 Part 3	V(2nd) 1	01/31/74 31 Map 217	15-59-58.2 50.1 N 142.0 W	16-01-39.0 49.5 N 133.3 W	all	2-3	medium	0.47	North Pacific, near N. America coast (B.C.)
SL-4 97 Part 4	V 1	01/31/74 31 Map 222	16-12-40.9 28.6 N 89.8 W	16-13-51.6 24.8 N 81.6 W	0,1(part) only		medium	-	Gulf of Mexico

and another such triad at the end, and the start- and stop-time latitudes and longitudes in the fourth and fifth columns of Table A1 were obtained from these reference latitudes and longitudes by simple linear interpolation in time; the start- and stop-times of columns four and five are obtained directly from the data tapes.

The sixth column specifies which of subsubmodes (0-3) were present. Although only complete submodes (all four subsubmodes present and with approximately the correct number of frames of data) were used in the analysis presented here, a number of fragments of submodes are included in Table A1 for possible future reference.

The next three columns present, respectively: the approximate rms altitude residuals (in meters) obtained by eyeball estimates from the figures in Reference A3; a qualitative characterization of off-nadir pointing angle, where "small" $\leq 0.65^\circ$ and "large" $\geq 0.75^\circ$; and the ratio of the first S&H value in subsubmode 0 to the maximum S&H value from all four subsubmodes. This ratio of first to maximum S&H is an indicator of whether a template fit is possible at all; when the ratio approaches or exceeds 0.5, the template program cannot decide whether to shift the time origin or to change the rise time in the theoretical function being fitted. Finally, the last column in Table A1 gives a rough geographical description and other relevant comments.

Selection of which data sets should be analyzed was based on the following criteria;

1. all subsubmodes must be present with more or less the correct number of frames of data,
2. the data pass must be entirely over water, with no over-land portions,
3. the rms altitude residuals must be 2 meters or less with no observable large changes over the entire submode,
4. the antenna pointing angle should be medium to small, and
5. the S&H ratio of 1st to maximum should be less than 0.5.

An asterisk in the "Comments" column of Table A1 designates those submodes satisfying these criteria. The measured mean waveform data were corrected for saturation (Section 5.0, Chapter 13) and weighted by the inverse of

the variance of the mean, i.e. $(\text{mean}/\sqrt{N})^2$ where N is the number of returns used to construct the mean, in the template fitting routine.

Figure A3 shows the deviations of the data points from the fitted analytical form as a function of S&H gate and mission. The appearance of a relatively consistent offset for each S&H gate indicated that the fitting process and the resultant estimates for the four parameters (A_o , t_o , σ and ξ) might be improved by assuming an unknown offset for each S&H gate and then let the template routine treat these as free variables. Based on the results in Figure A3 and Section 5.0 of Chapter 13, S&H gate 8 was constrained to zero offset. The four parameter fitting routine was modified to accommodate eleven free parameters (the original four plus seven offsets for S&H gates 1 through 7). Since the number of input data points was 32, this modification presented no problems.

The results obtained for Mode V Submode 2 passes (the non pulse compression short pulse submode) are presented in Table A2 both for the four and eleven parameter fit. The no-offset case is identified in the second column of Table A2 as the case with four parameters fitted. The next four columns give the template match determined A_o , t_o , σ , and ξ (the amplitude, time origin, rise time, and off-nadir angle respectively). The rightmost eight columns in Table A2 present the eight offsets for the 11-parameter case only (notice that offset #8 is always small as it has been constrained in the program to be zero or near zero). The improvement resulting from the eleven-parameter fit is evidenced by the significantly lower value of $\sum \chi^2$ (in column two) relative to the four parameter fit.

Table A3 presents in the same way the Mode V Submode 1 (pulse compression submode) results. In both Table A2 and Table A3 a dagger in column 1 identifies those passes for which the estimated off-nadir angle ξ was greater than 0.65° ; this value was rather arbitrarily chosen as an upper limit for the final data summaries as the fit results are poorer for larger angles. The first column in Tables A2 and A3 assign an index number which is used in the summary figures in this chapter.

Figure A4 presents the S&H offsets from the eleven-parameter fit as a function of ξ for all Mode V Submode 2 entries in Table A2 having $\xi \leq 0.65^\circ$, and Figure A5 presents the same information for Submode 1 entries in Table A3

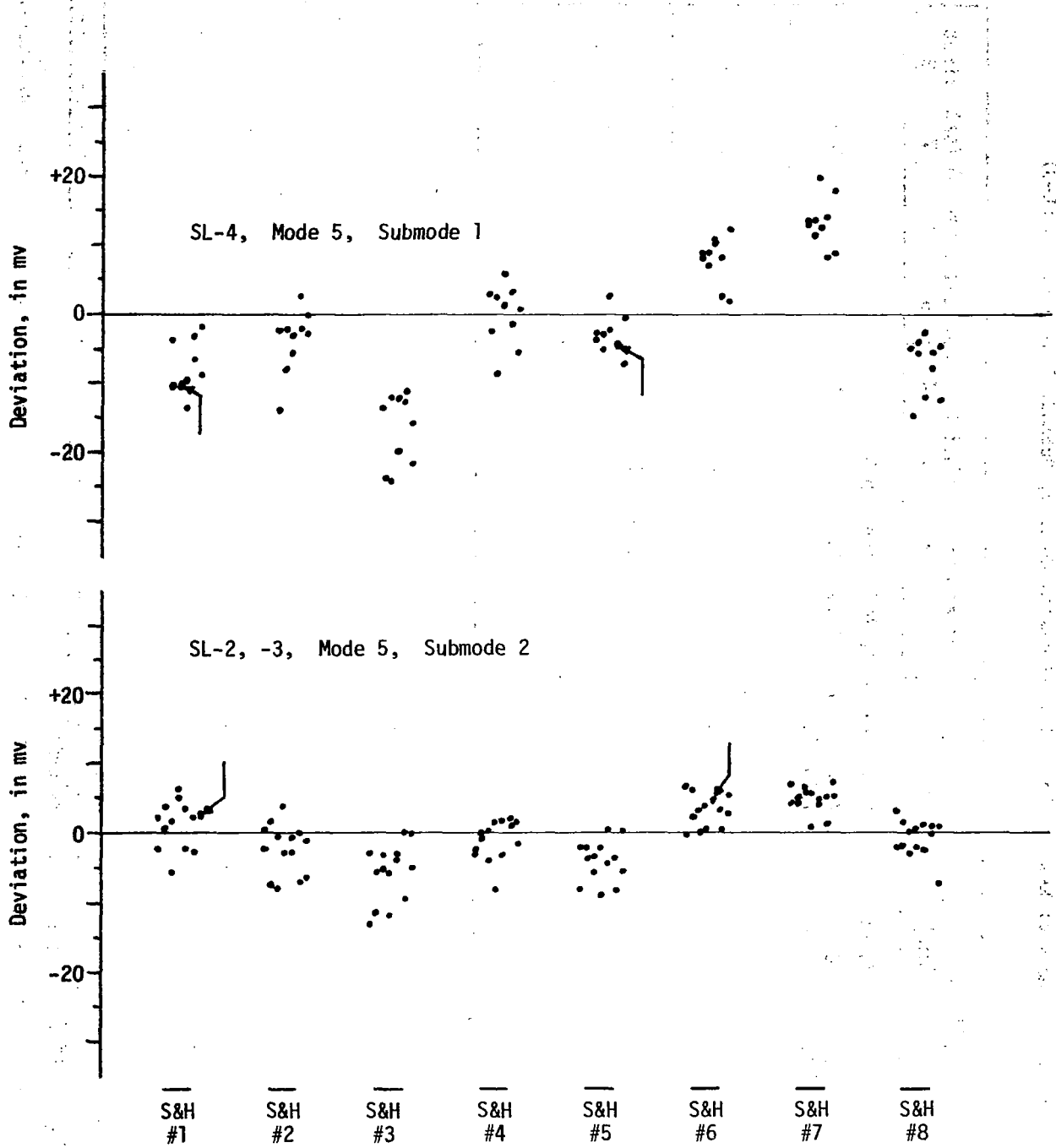


Figure A3. Deviations from 4-Parameter Fit in Subsubmode 2 and 3, Displayed by Sample-and-Hold Gate Number, for Selected Skylab Data Passes , (Arrows Indicate Double Points).

TABLE A2. Summary of Results for Selected Passes (Mode V, Submode 2 of SL-2 and SL-3)

Index No.	Parameters Fitted	$\Sigma\chi^2$	A_0 (mv)	t_0 (ns)	σ (ns)	ξ (deg.)	Offset	Offset	Offset	Offset	Offset	Offset	Offset	Offset	
							1	2	3	4	5	6	7	8	
† 1	11 4	37.0 176.7	SL-2, Pass 6, Mode 5, Submode 2, Reference Map 5				0.686 0.685	+10.4	+6.1	-2.8	+3.0	-1.0	+4.0	+8.4	0.0
			96.7	12.95	7.72	100.3									
2	11 4	43.9 471.6	SL-2, Pass 9, Mode 5, Submode 2, Reference Map 11				0.567 0.555	+ 4.4	+3.8	-4.4	-2.4	-3.3	+3.3	+6.9	+0.1
			133.3	22.92	8.68	138.1									
3	11 4	32.3 427.2	SL-3, Pass 18, Mode 5, Submode 2, Reference Map 32				0.464 0.449	+ 2.4	+1.6	-5.5	-1.9	-4.5	+1.2	+4.1	+0.0
			157.8	28.86	10.76	161.6									
4	11 4	33.8 839.4	SL-3, Pass 21, Mode 5 (1st), Submode 2, Reference Map 35				0.388 0.371	+ 2.9	+3.8	-2.7	+0.6	-1.4	+4.8	+8.0	+0.0
			170.5	33.51	10.49	179.2									
5	11 4	56.6 837.2	SL-3, Pass 21, Mode 5 (2nd), Submode 2, Reference Map 36				0.445 0.427	+ 2.9	+4.3	-3.9	-1.6	-4.4	+3.2	+6.6	-0.0
			163.6	30.86	9.74	170.7									
6	11 4	106.1 2005.0	SL-3, Pass 25, Mode 5 (1st), Submode 2, Reference Map 46				0.369 0.348	+ 3.0	+4.5	-0.3	+0.4	+1.1	+5.8	+8.4	+0.2
			174.6	34.88	8.90	186.2									
7	11 4	51.3 1006.6	SL-3, Pass 25, Mode 5 (2nd), Submode 2, Reference Map 47				0.414 0.390	+ 3.0	+5.8	+1.3	+1.4	-3.7	+3.3	+7.0	+0.1
			167.1	33.18	9.36	178.7									

† = Estimated $\xi > 0.65^\circ$; not used in summary graph.

TABLE A2. Summary of Results for Selected Passes (Mode V, Submode 2 of SL-2 and SL-3) (Cont'd.)

Index No.	Parameters Fitted	$\Sigma\chi^2$	A_0 _(mv)	t_0 _(ns)	σ _(ns)	ξ _(deg.)	Offset	Offset	Offset	Offset	Offset	Offset	Offset	Offset	
							1	2	3	4	5	6	7	8	
8	11 4	60.3 368.1	SL-3, Pass 27, Mode 5, Submode 2, Reference Map 48				0.537 0.528	+2.5	-1.2	-6.9	-.13	-2.9	+1.9	+7.4	-0.1
			140.2	23.77	10.39	143.1									
9	11 4	58.1 753.3	SL-3, Pass 28, Mode 5, Submode 2, Reference Map 50				0.458 0.440	+3.6	+2.9	-4.7	-0.1	-0.1	+4.4	+7.4	+0.1
			157.1	29.64	10.52	165.5									
† 10	11 4	19.0 67.4	SL-3, Pass 39, Mode 5 (1st), Submode 2, Reference Map 73				0.764 0.765	+6.9	+2.4	+0.4	+3.7	-0.1	+3.7	+5.7	+0.0
			73.9	1.77	7.53	75.8									
† 11	11 4	76.0 133.5	SL-3, Pass 39, Mode 5 (2nd), Submode 2, Reference Map 74				0.794 0.794	+4.3	+1.2	+0.1	+4.3	-1.7	+2.1	+5.1	+0.0
			65.1	-1.71	3.29	66.5									

† = Estimated $\xi > 0.65^\circ$; not used in summary graphs.

TABLE A3. Summary of Results for Selected Passes (Mode V, Submode 1 of SL-3 and SL-4)

Index No.	Parameters Fitted	$\Sigma\chi^2$	A_0 (mv)	t_0 (ns)	σ (ns)	ξ (deg.)	Offset	Offset	Offset	Offset	Offset	Offset	Offset	Offset	
							1	2	3	4	5	6	7	8	
† 12	11 4	30.8 97.9	SL-3, Pass 28, Mode 5 (2nd), Submode 1, Reference Map 74				0.791 0.792	+1.0	+0.2	- 0.6	+ 2.5	-3.0	+ 1.4	+ 3.7	+0.0
			64.5	-6.46	12.24										
† 13	11 4	59.7 718.7	SL-4, Pass 71, Mode 5 (1st), Submode 1, Reference Map 112 ?				0.656 0.653	+4.6	+5.1	- 6.0	+10.8	+5.3	+16.9	+22.0	+0.0
			105.8	6.66	22.32										
14	11 4	99.5 1385.4	SL-4, Pass 71, Mode 5 (3rd), Submode 1, Reference Map 114				0.623 0.607	+7.2	+3.8	-11.9	+ 8.5	+6.3	+17.4	+22.3	+0.0
			111.4	10.13	23.40										
15	11 4	83.4 1264.5	SL-4, Pass 71, Mode 5 (4th), Submode 1, Reference Map 115				0.573 0.570	+6.3	+5.9	- 9.2	+10.4	+8.6	+19.0	+22.4	+0.0
			119.2	13.36	26.85										
16	11 4	65.7 1247.2	SL-4, Pass 74, Mode 5 (1st), Submode 1, Reference Map 117				0.618 0.594	+4.4	+2.4	-11.6	+ 8.8	+8.2	+ 8.1	+23.2	+0.0
			111.7	9.75	23.53										
17	11 4	80.2 1116.9	SL-4, Pass 74, Mode 5 (2nd), Submode 1, Reference Map 118				0.627 0.619	+8.7	+6.4	- 8.0	+ 9.3	+6.5	+17.4	+23.1	+0.0
			107.5	9.15	22.15										
† 18	11 4	66.1 1238.3	SL-4, Pass 78, Mode 5 (1st), Submode 1, Reference Map 128				0.661 0.621	-1.0	-0.9	-15.8	+ 4.0	+1.3	+13.6	+19.9	+0.0
			107.5	1.31	26.28										

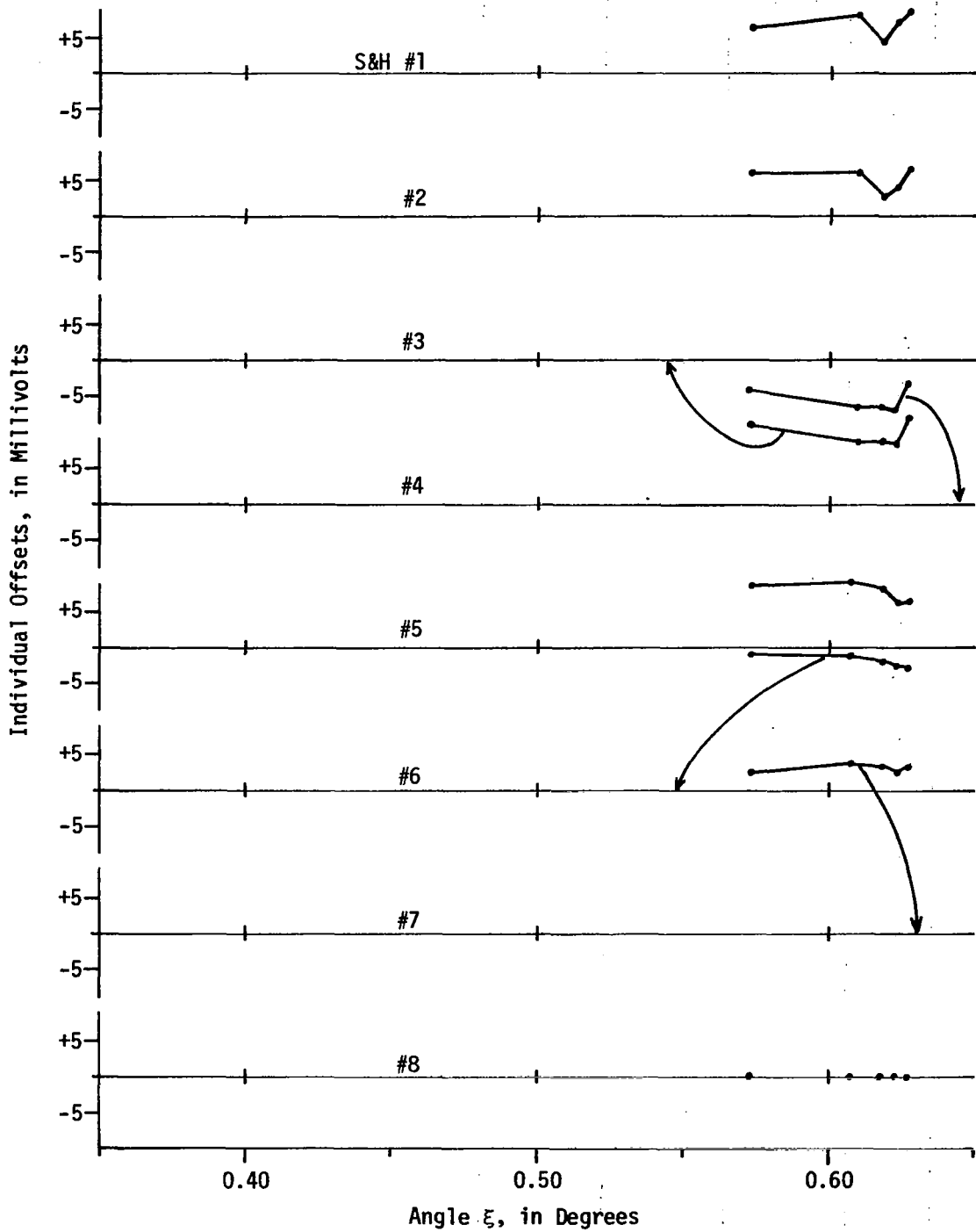
† = Estimated $\xi > 0.65^\circ$; not used in summary graphs.

TABLE A3. Summary of Results for Selected Passes (Mode V, Submode 1 of SL-3 and SL-4) (Cont'd.)

Index No.	Parameters Fitted	$\Sigma\chi^2$	A_0 (mv)	t_0 (ns)	σ (ns)	ξ (deg.)	Offset	Offset	Offset	Offset	Offset	Offset	Offset	Offset	
							1	2	3	4	5	6	7	8	
19	11 4	88.8 1481.4	SL-4, Pass 79, Mode 5 (2nd), Submode 1, Reference Map 132												
			112.6	10.39	26.13	0.607	+8.1	+5.9	-11.7	+8.6	+9.1	+18.9	+23.7	+0.0	
† 20	11 4	32.2 513.6	SL-4, Pass 86, Mode 5, Submode 1, Reference Map 233												
			101.1	7.27	19.23	0.681	+7.3	+6.0	-5.3	+7.9	+6.1	+13.5	+15.0	+0.0	
† 21	11 4	44.7 734.1	SL-4, Pass 93, Mode 5, Submode 1, Reference Map 185												
			97.0	9.24	16.76	0.710	+3.3	-1.3	-10.3	+3.6	+4.9	+14.8	+15.5	+0.0	
† 22	11 4	33.6 1485.5	SL-4, Pass 97, Part 3, Mode 5 (1st), Submode 1, Reference Map 216												
			99.3	4.88	35.21	0.694	+2.2	+5.9	-11.5	+6.2	+4.5	+17.2	+22.7	+0.0	

† = Estimated $\xi > 0.65^\circ$; not used in summary graphs.

Figure A5. Individual S&H Offsets vs. Angle ξ for Selected SL-4 Data Passes. [Offset #8 Constrained to 0.] Arrows Indicate Appropriate Zero-Lines for #3, #4, #6, and #7.



having $\xi \leq 0.65^\circ$. These offsets should show no dependence upon ξ and should be approximately constant and these figures show this to be the case. As always, S&H #3 is low and #7 is high, and the offsets are generally larger in Submode 1 than in Submode 2.

A summary of selected data from Table A2 is shown in Figure A6 (four parameter fit) and Figure A7 (eleven parameter fit). A similar summary from Table A3 is shown in Figure A8 (four parameter fit) and Figure A9 (eleven parameter fit). It should be noted that the time origin, t_0 , and the amplitude, A_0 , are not very sensitive to the number of free parameters in the fitting routine. However, there is a significant reduction in the rise time, σ , with the eleven parameter fit; this is most probably due to a better definition of the baseline for the S&H gates. Reduced signal-to-noise ratio conditions coupled with the shift of the S&H gates during SL-4 contribute to the markedly increased values of σ .

Figures A10 through A31 catalog, in a standardized format, the results of the waveform fitting process as described in the text. It is important to note that what is plotted as "experimental data" is actually the entire subsubmode averaged S&H data as corrected for saturation. In each of the following figures the upper curve's experimental data points have had the offsets subtracted prior to plotting. The fitted waveforms (in both the upper and lower curves) were calculated using the parameters given in Tables A2 and A3.

REFERENCES

- A1. Hayne, G. S., "Engineering Studies Related To The Skylab Program," Final Report on Task F of Contract No. NAS6-2307 (NASA/WFC), Applied Science Associates, Inc., Apex, N. C., September, 1974.
- A2. Brown, G. S., "Reduced Backscattering Cross Section (σ°) Data From The Skylab S-193 Radar Altimeter," NASA CR-141401, Applied Science Associates, Inc., Apex, N. C., October, 1975.
- A3. McGoogan, J. T., C. D. Leitao and W. T. Wells, "Summary of Skylab S-193 Altimeter Altitude Results," NASA TM X-69355, Wallops Flight Center, Wallops Island, VA., February, 1975.

Figure A6. Amplitude, Time Origin, and Risetime Results vs. Angle ξ for Selected SL-2 and SL-3 Data Passes, No Offsets Fitted.

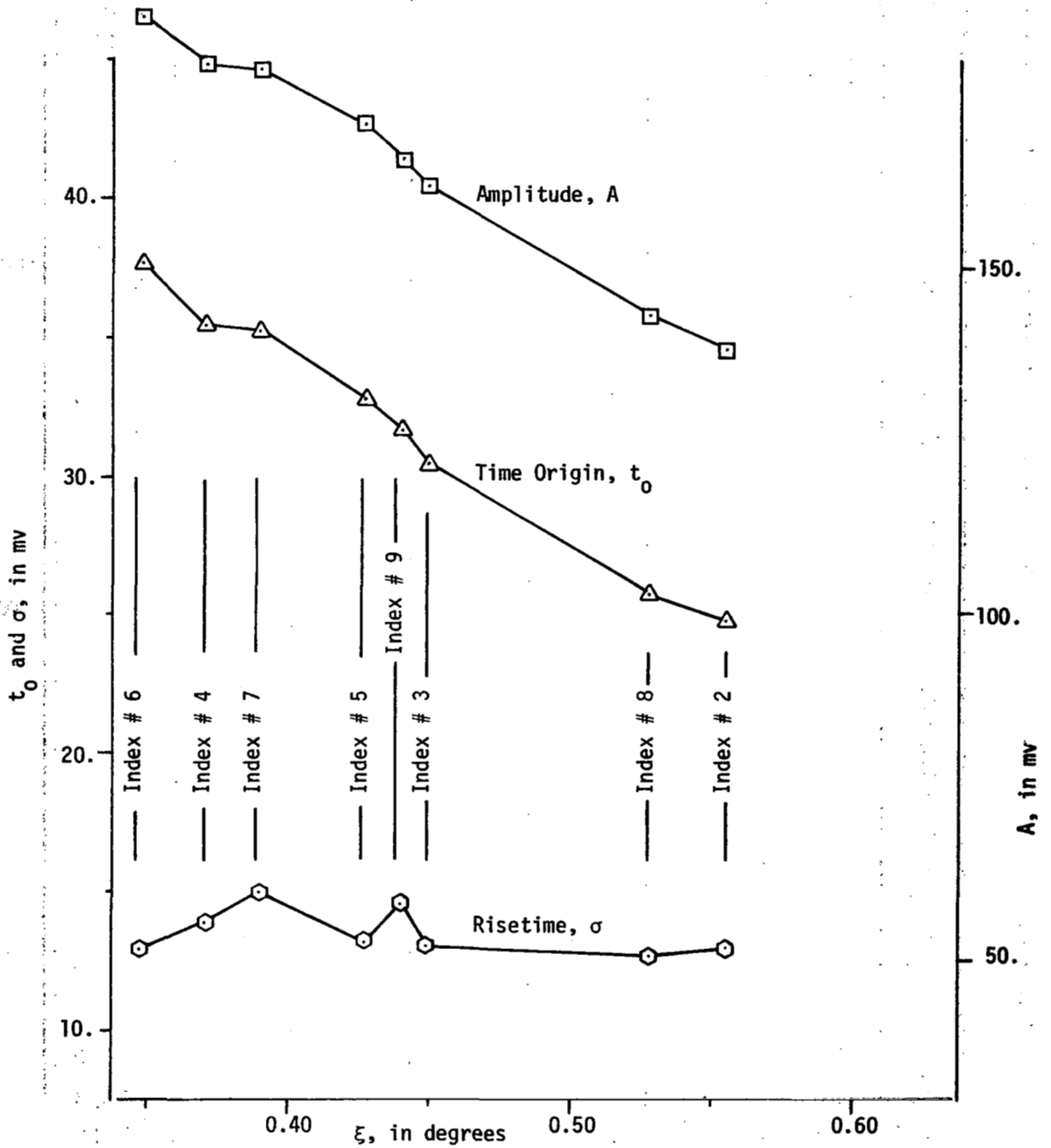


Figure A7. Amplitude, Time Origin, and Risetime Results vs. Angle ξ for Selected SL-2 and SL-3 Data Passes, Offsets Fitted (#8 Constrained to 0.)

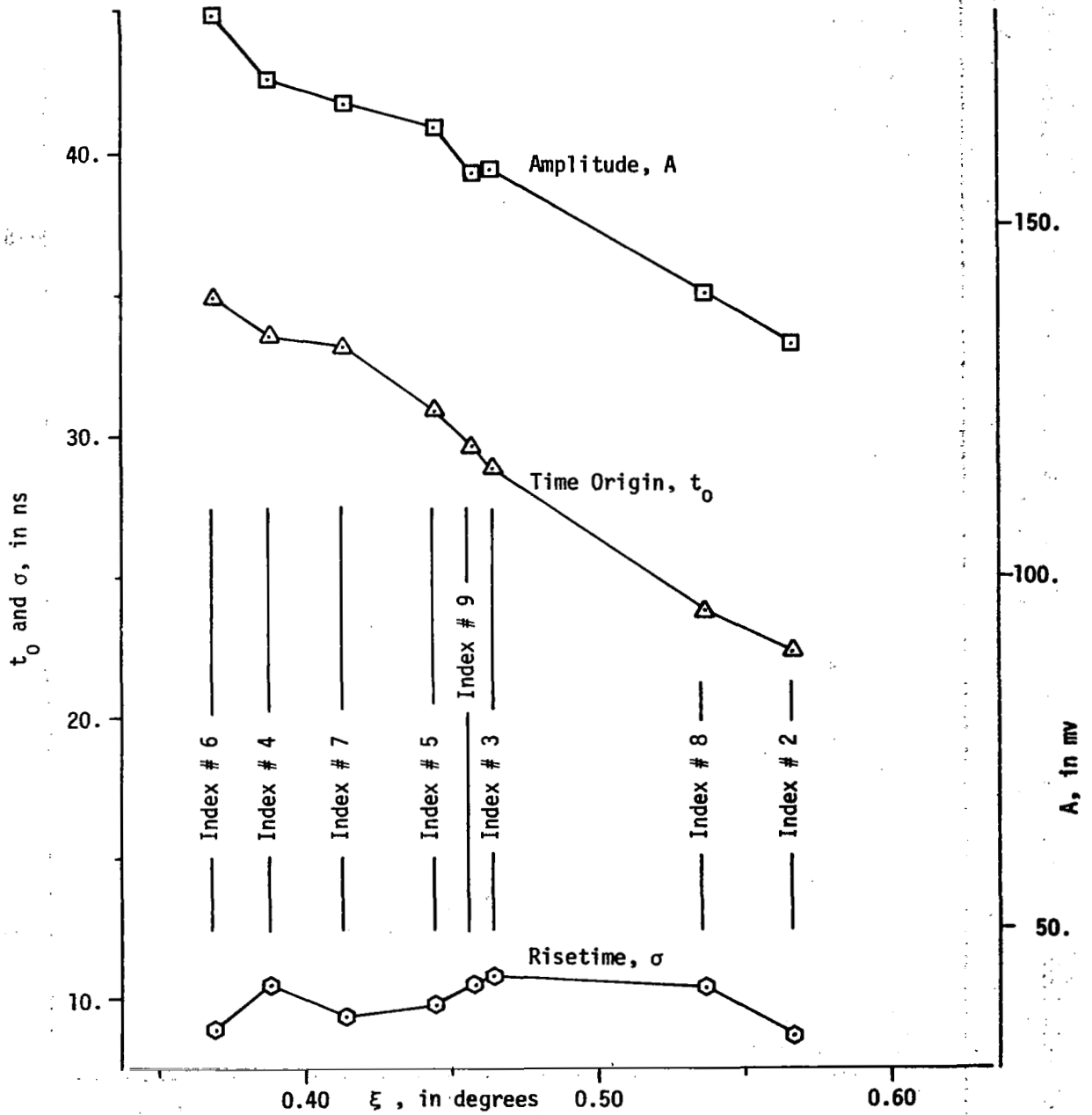


Figure A8. Amplitude, Time Origin, and Risetime Results vs. Angle ξ for Selected SL-4 Data Passes, No Offsets Fitted.

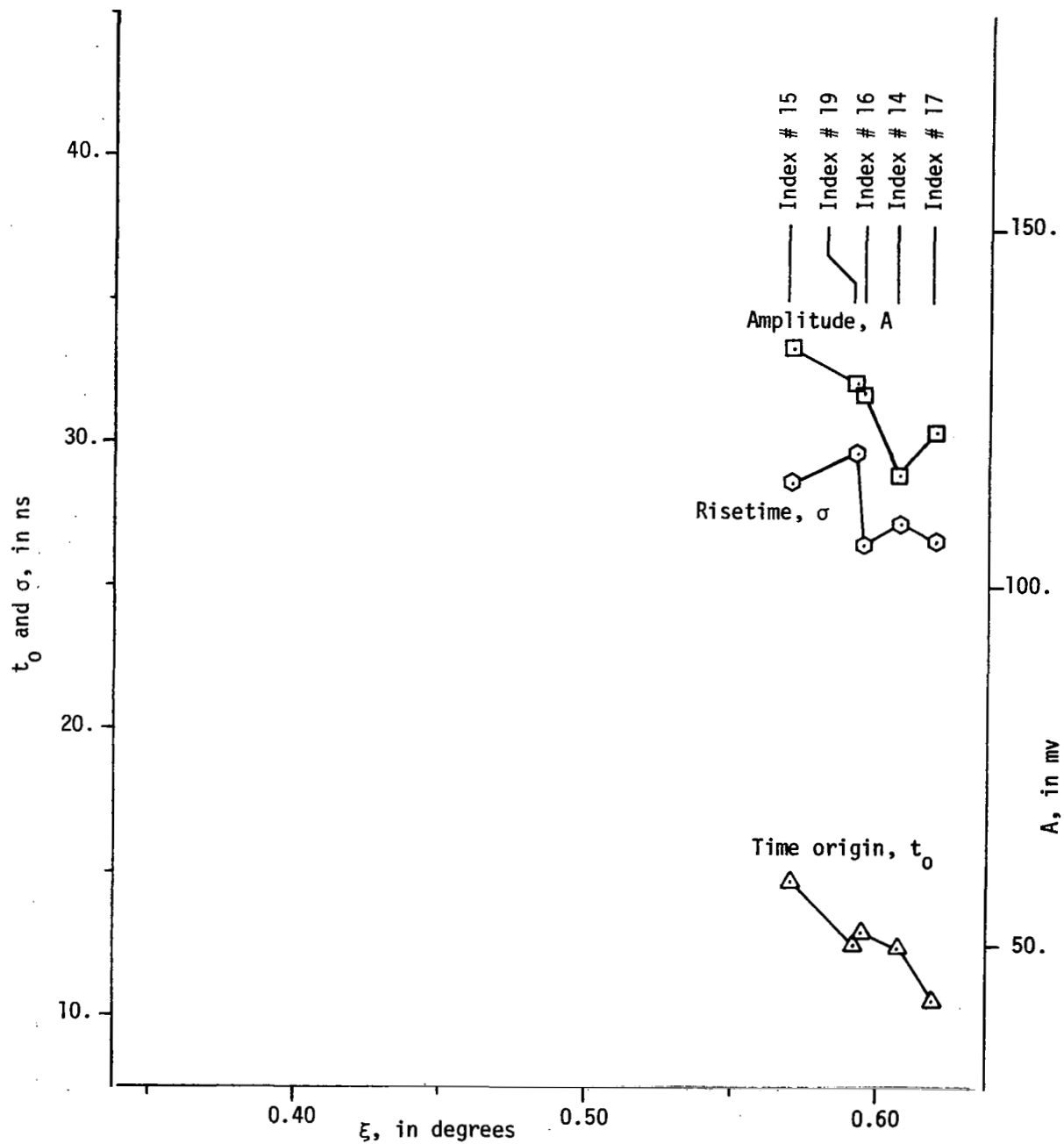


Figure A9. Amplitude, Time Origin, and Risetime Results vs. Angle ξ for Selected SL-4 Data Passes, Offsets Fitted (#8 Constrained to 0.)

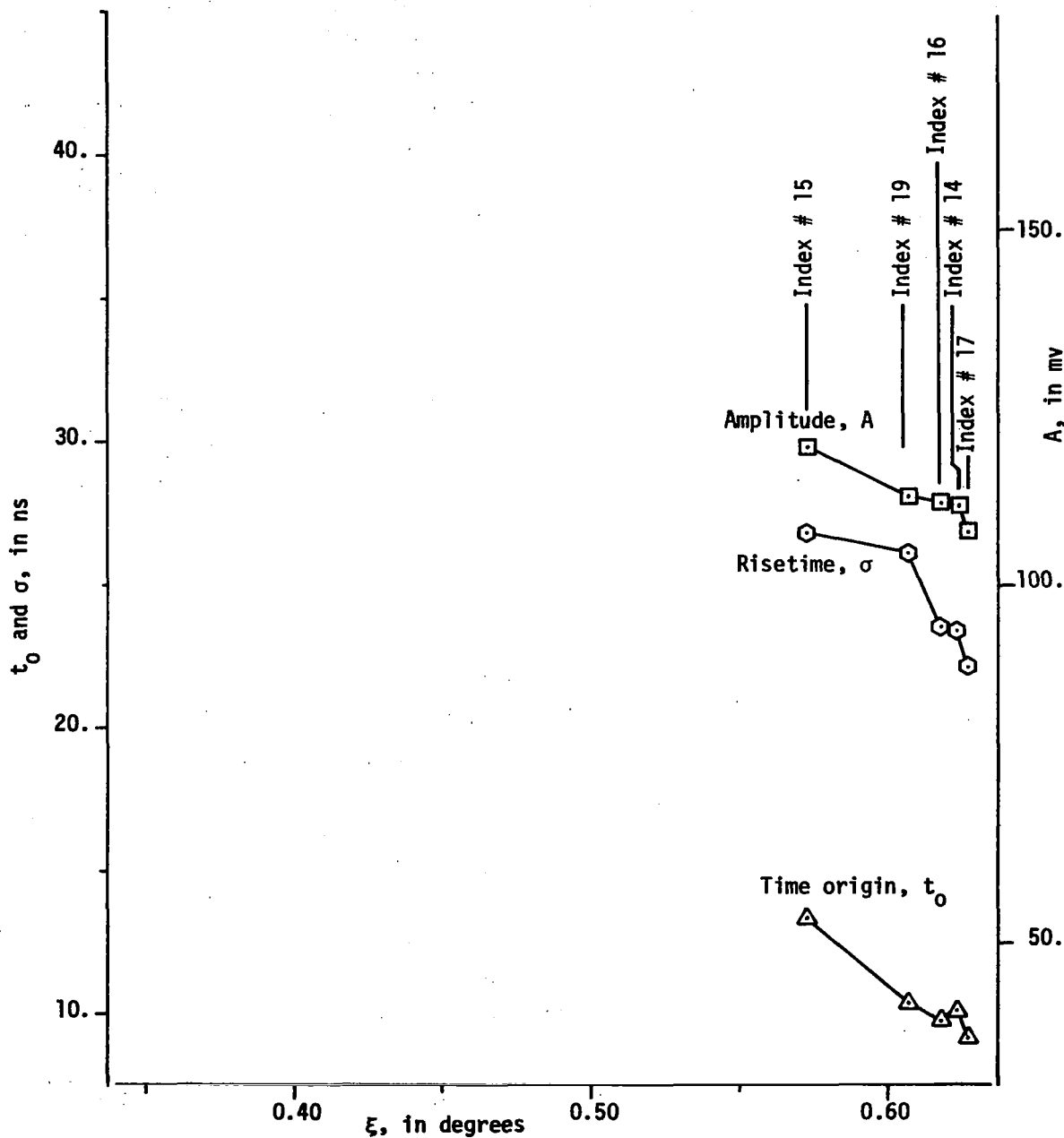


Figure A10. Comparison of Experimental Data and Fitted Functions for SL-2, Pass 6, Mode 5, Submode 2.

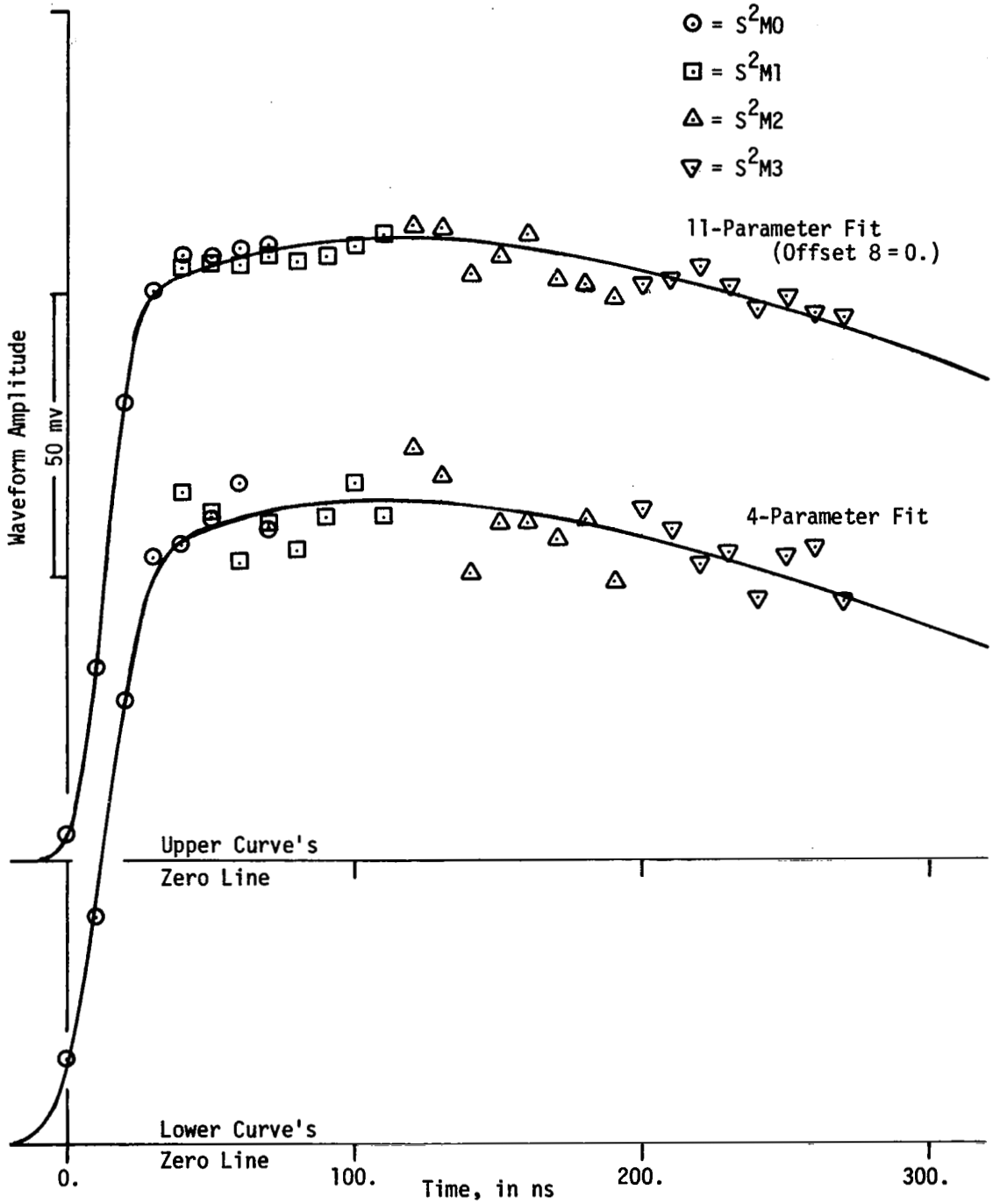


Figure A11. Comparison of Experimental Data and Fitted Functions for SL-2, Pass 9, Mode 5, Submode 2.

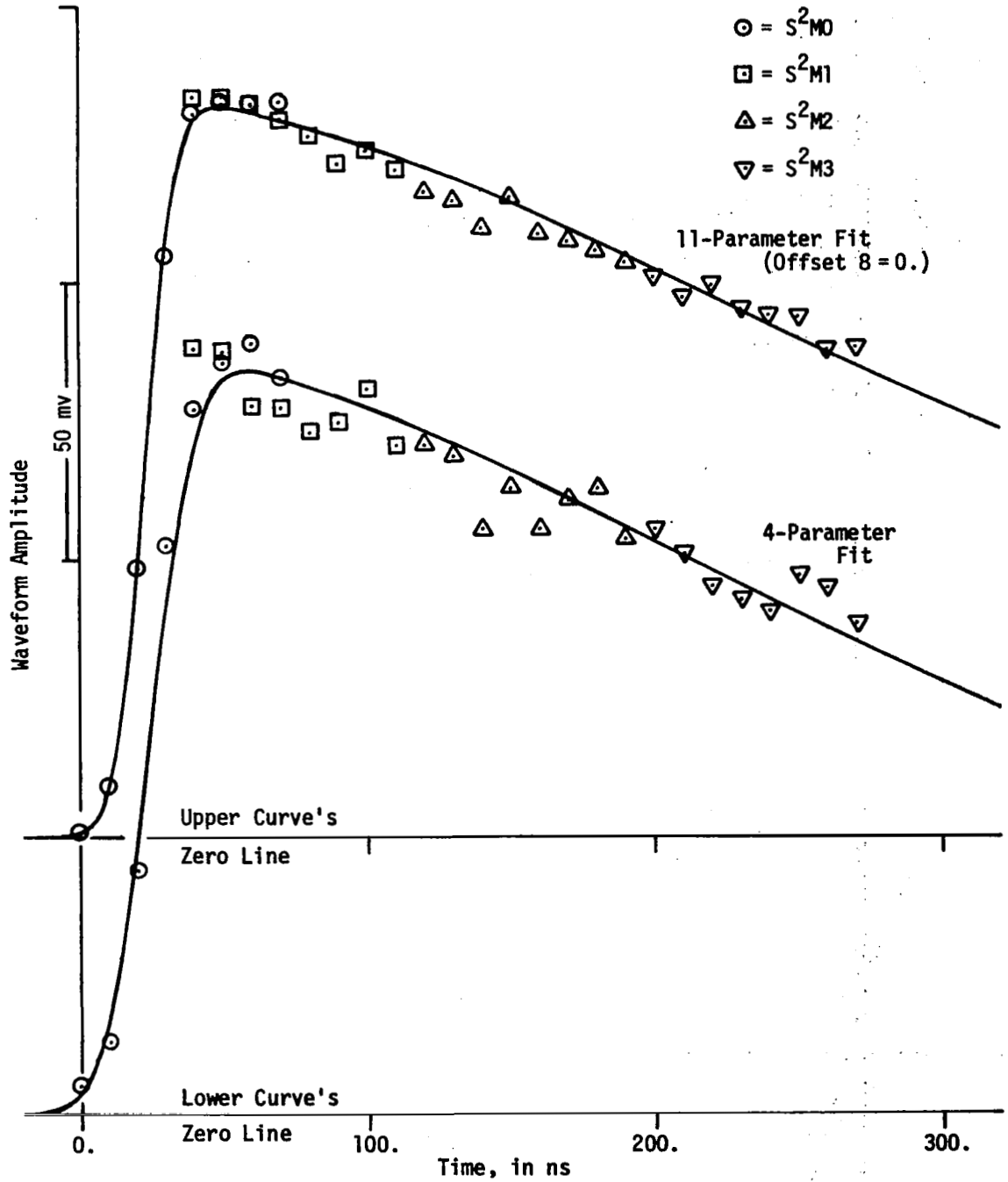


Figure A12. Comparison of Experimental Data and Fitted Functions for SL-3, Pass 7/18, Mode 5, Submode 2.

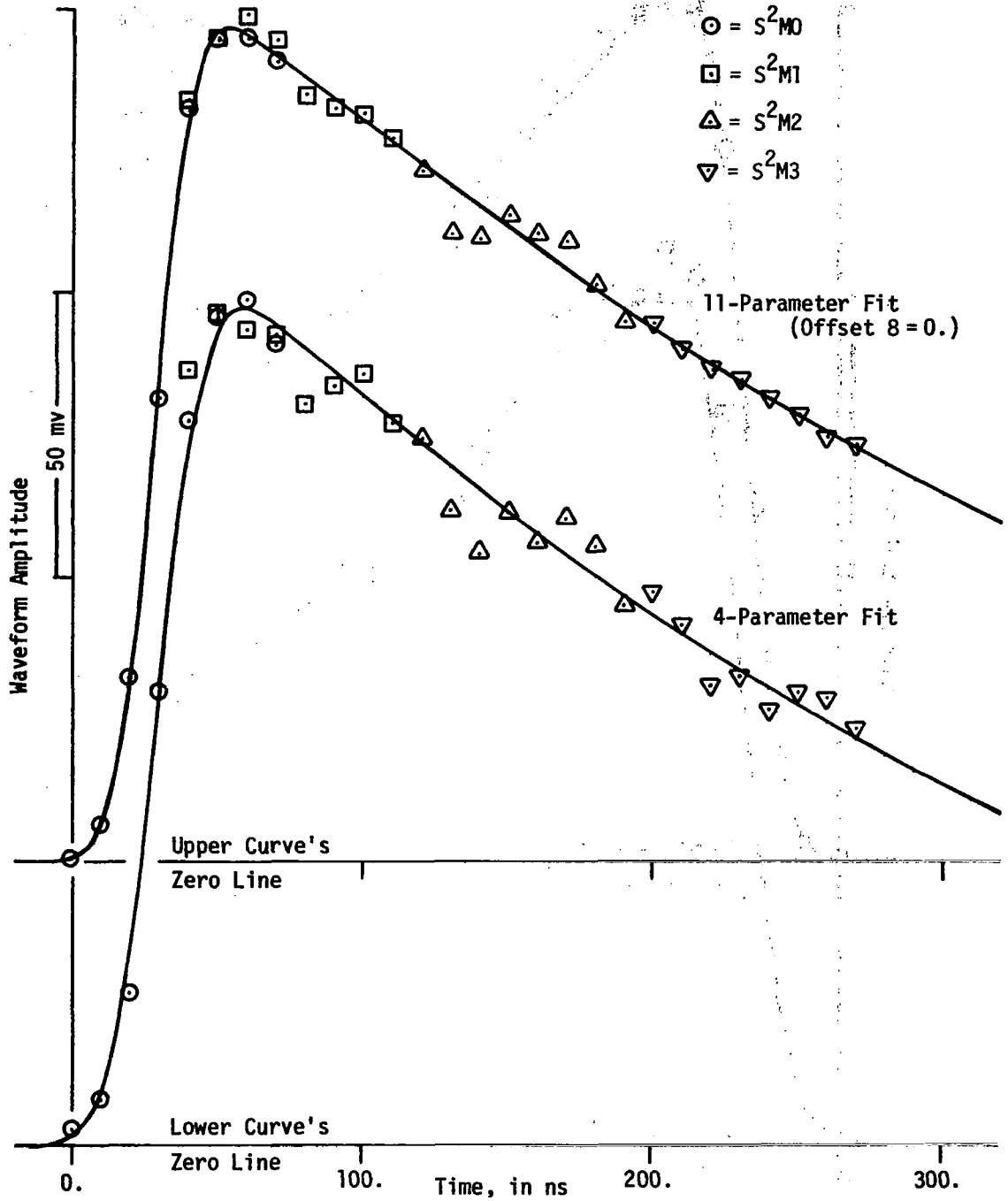


Figure A13. Comparison of Experimental Data and Fitted Functions for SL-3, Pass 10/21, Mode 5 (1st) Submode 2.

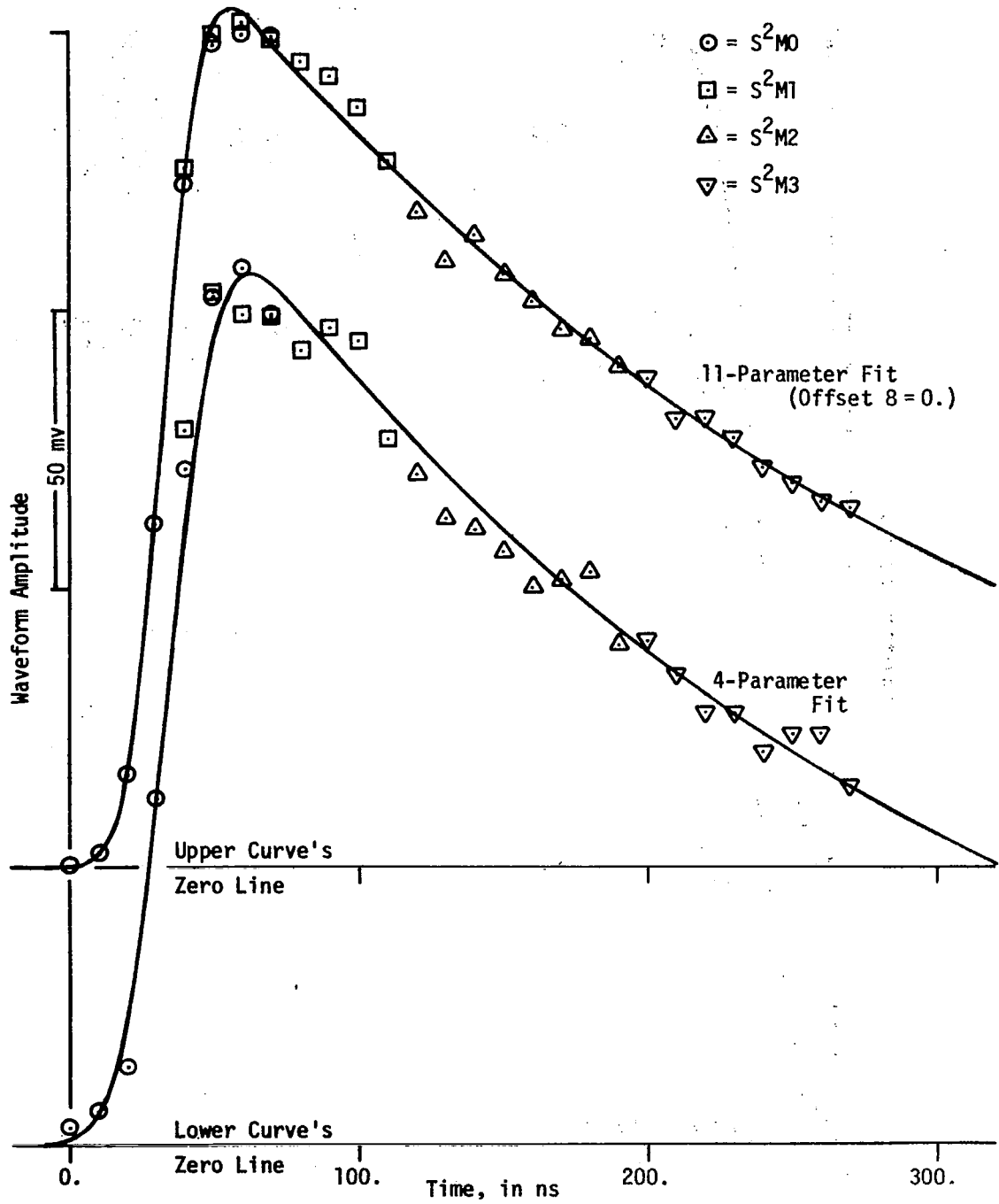


Figure A14. Comparison of Experimental Data and Fitted Functions for SL-3, Pass 10/21, Mode 5 (2nd), Submode 2.

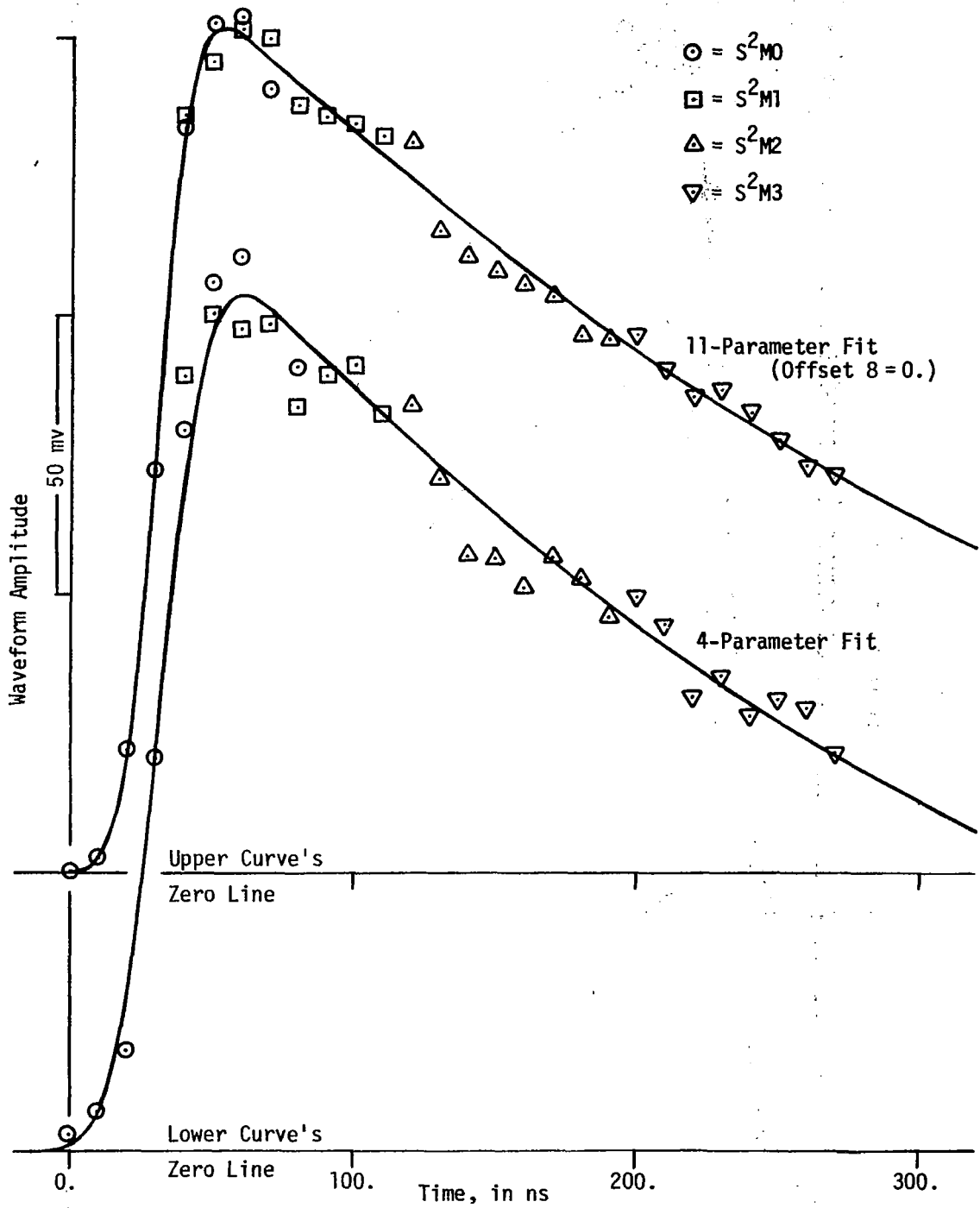


Figure A15. Comparison of Experimental Data and Fitted Functions for SL-3, Pass 14/25, Mode 5 (1st), Submode 2.

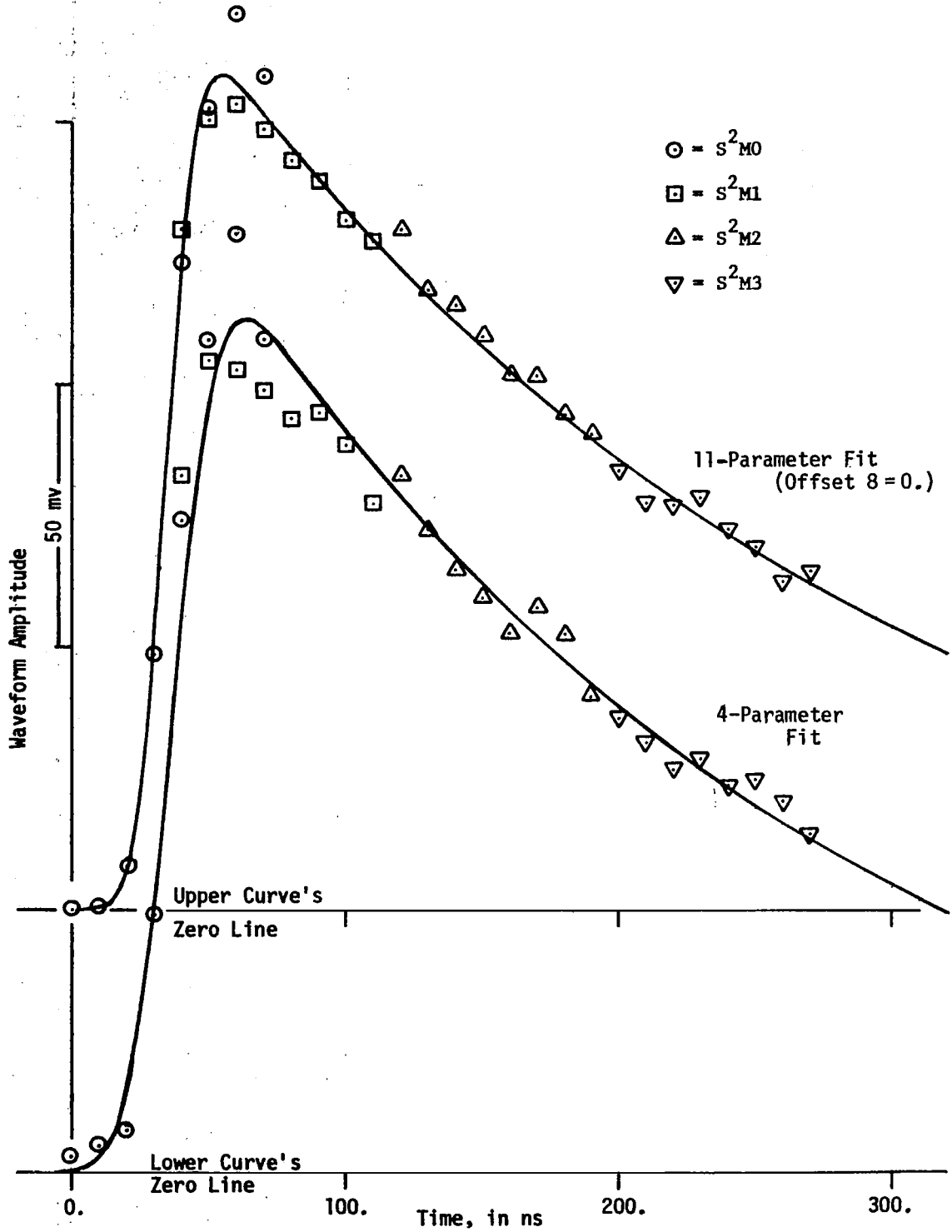


Figure A16. Comparison of Experimental Data and Fitted Functions for SL-3, Pass 14/25, Mode 5 (2nd), Submode 2.

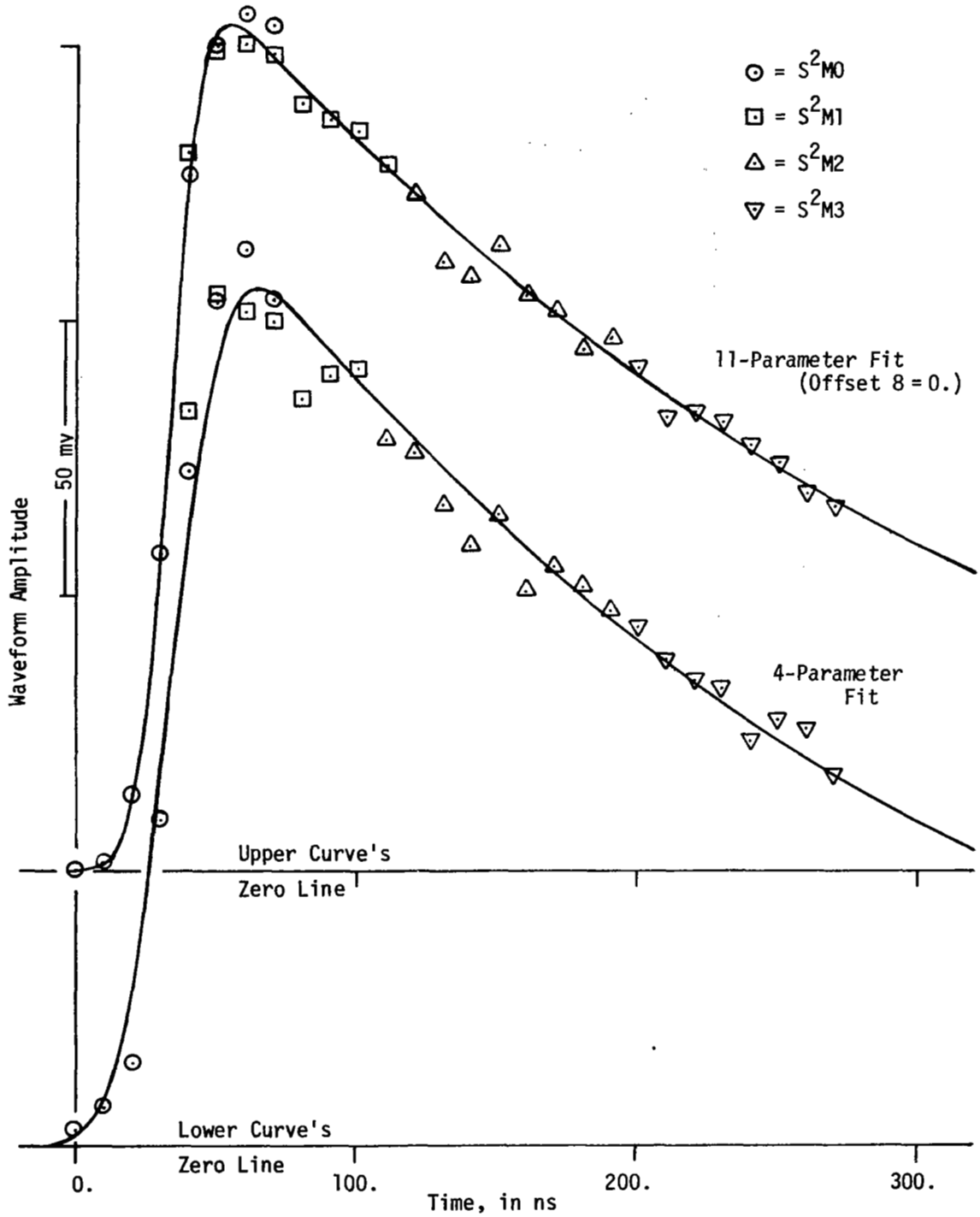


Figure A17. Comparison of Experimental Data and Fitted Functions for SL-3, Pass 16/27, Mode 5, Submode 2.

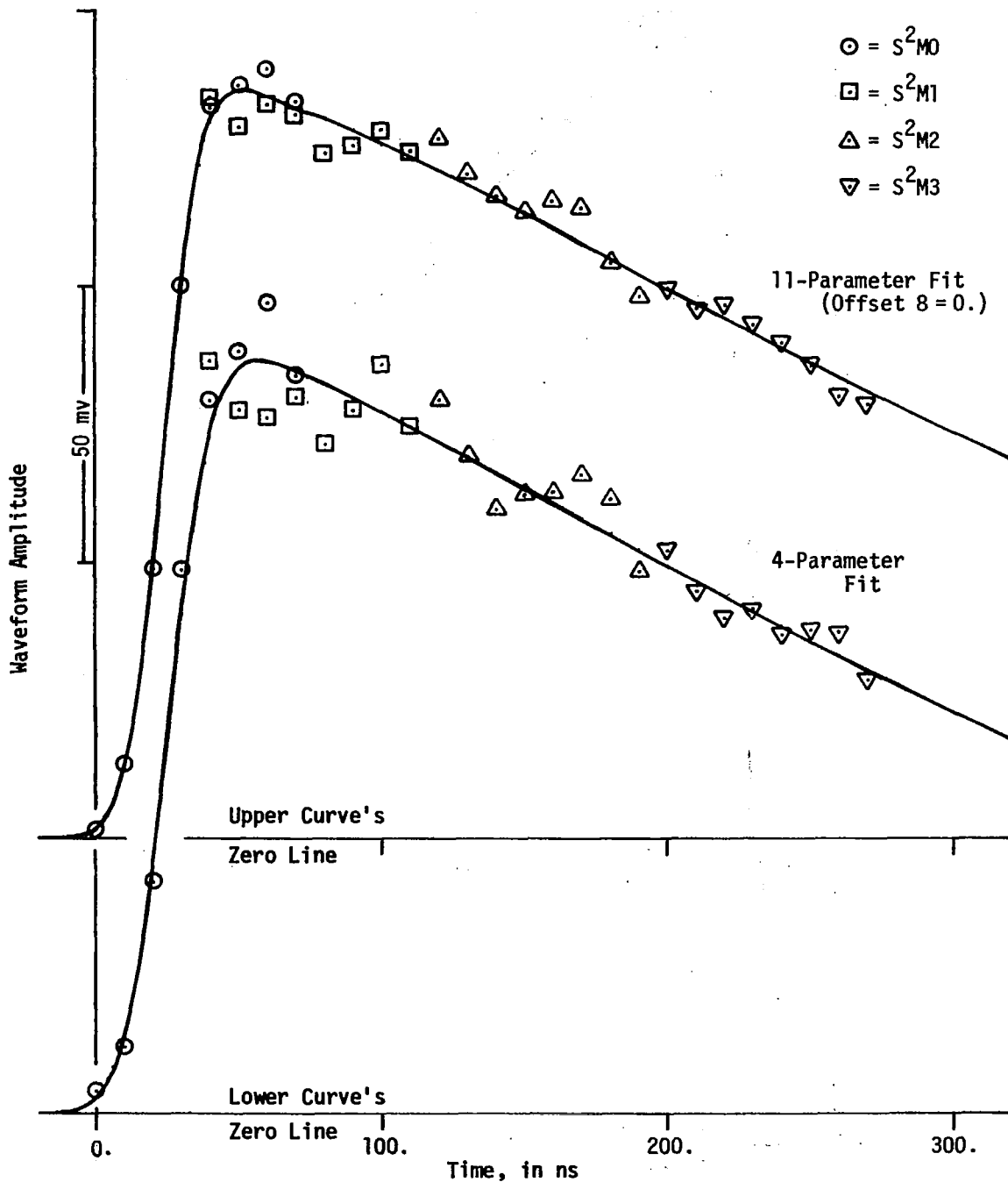


Figure A18. Comparison of Experimental Data and Fitted Functions for SL-3, Pass 17/28, Mode 5, Submode 2.

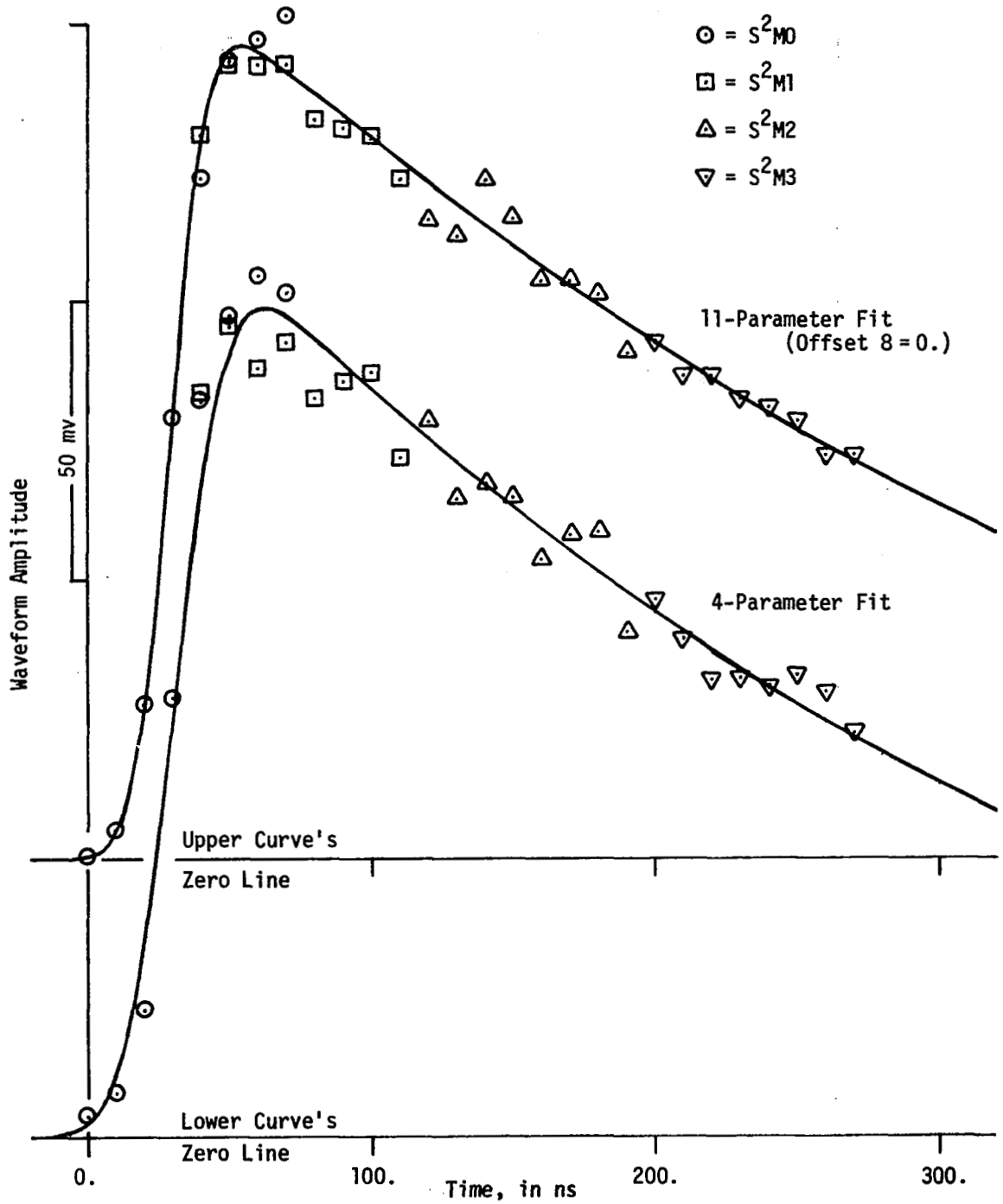


Figure A19. Comparison of Experimental Data and Fitted Functions for SL-3, Pass 28/39, Mode 5 (1st), Submode 2.

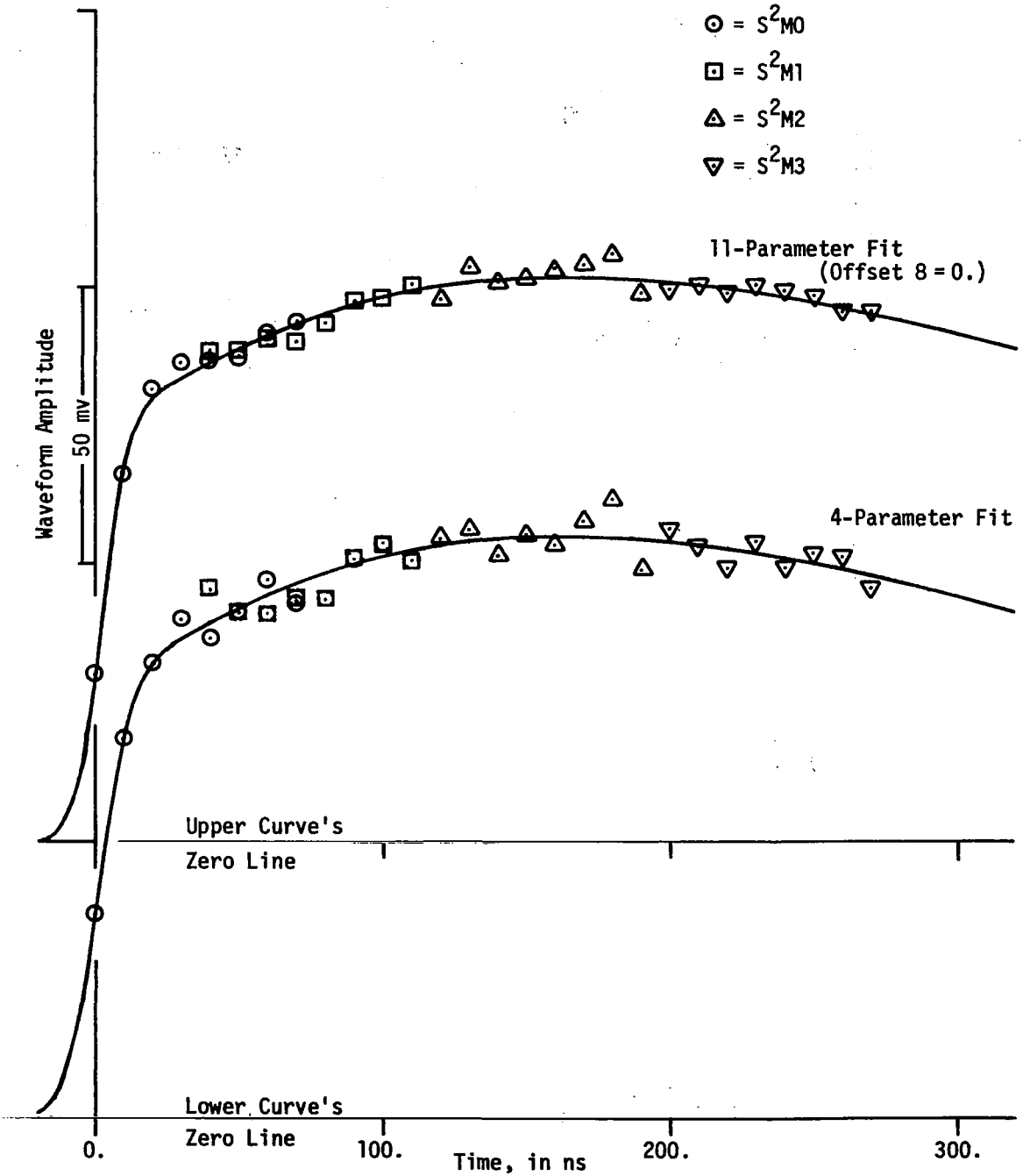


Figure A20. Comparison of Experimental Data and Fitted Functions for SL-3, Pass 28/39, Mode 5 (2nd), Submode 2.

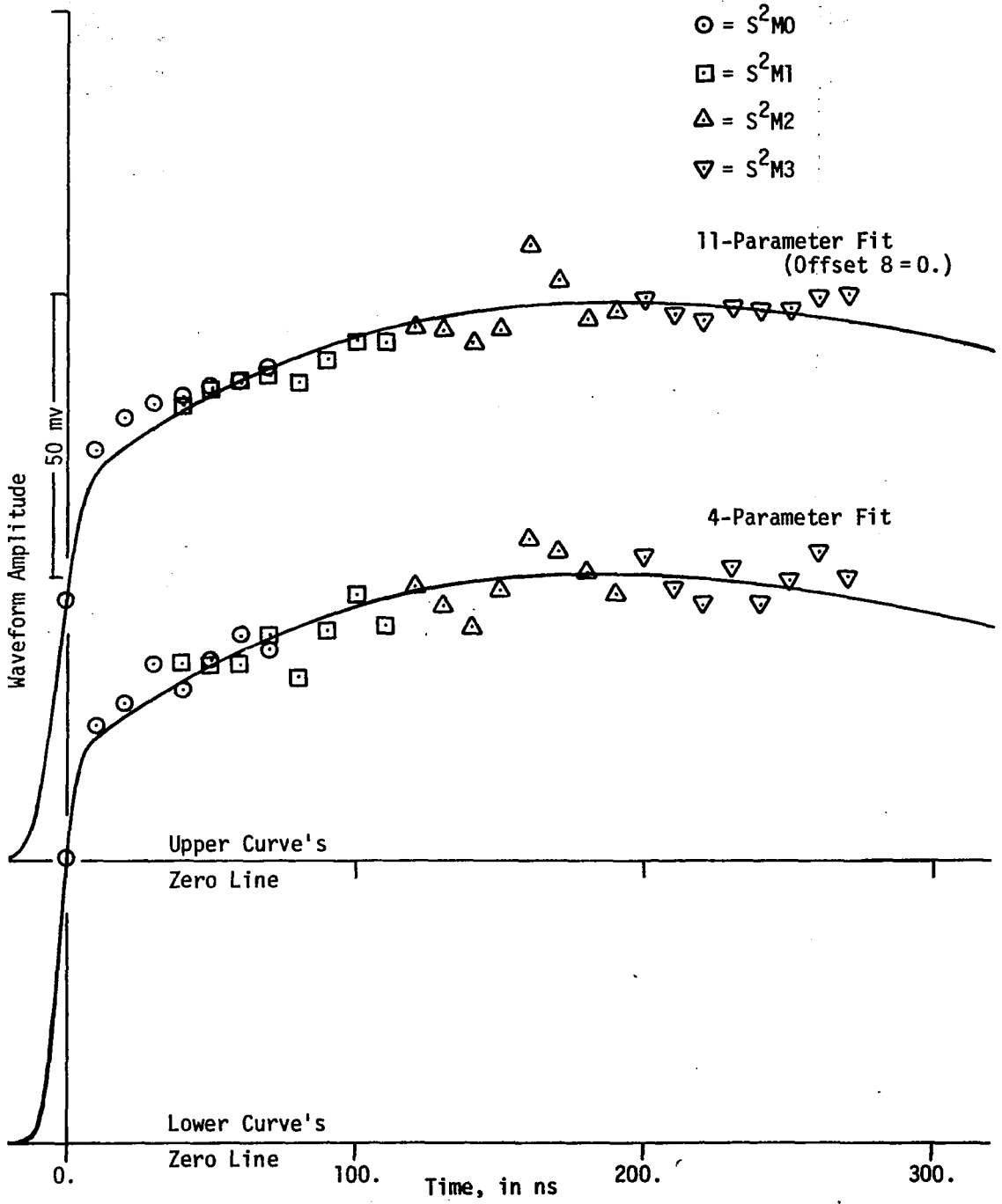


Figure A21. Comparison of Experimental Data and Fitted Functions for SL-3, Pass 28/39, Mode 5 (2nd), Submode 1.

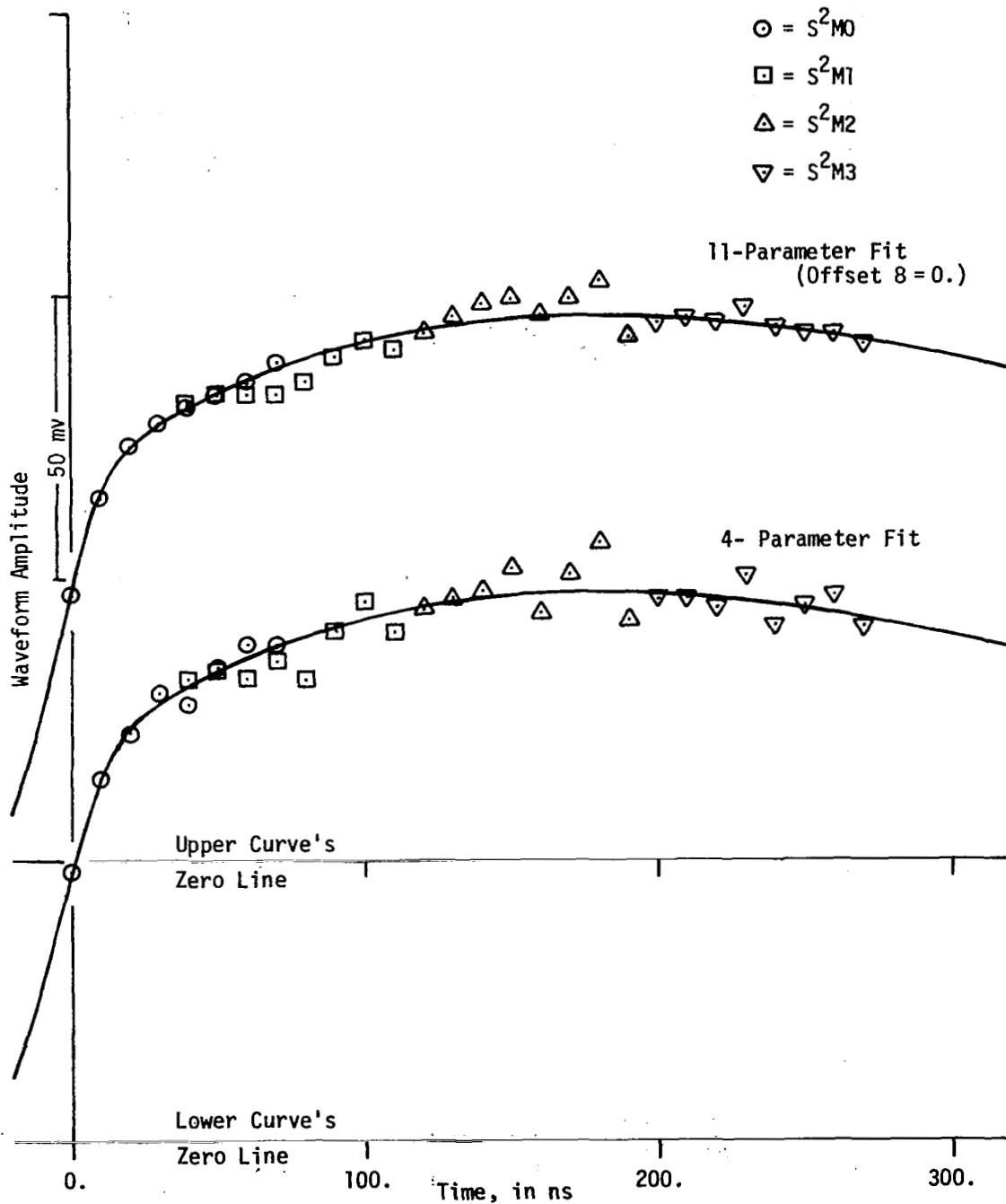


Figure A22. Comparison of Experimental Data and Fitted Functions for SL-4, Pass 71/18, Mode 5 (1st), Submode 1.

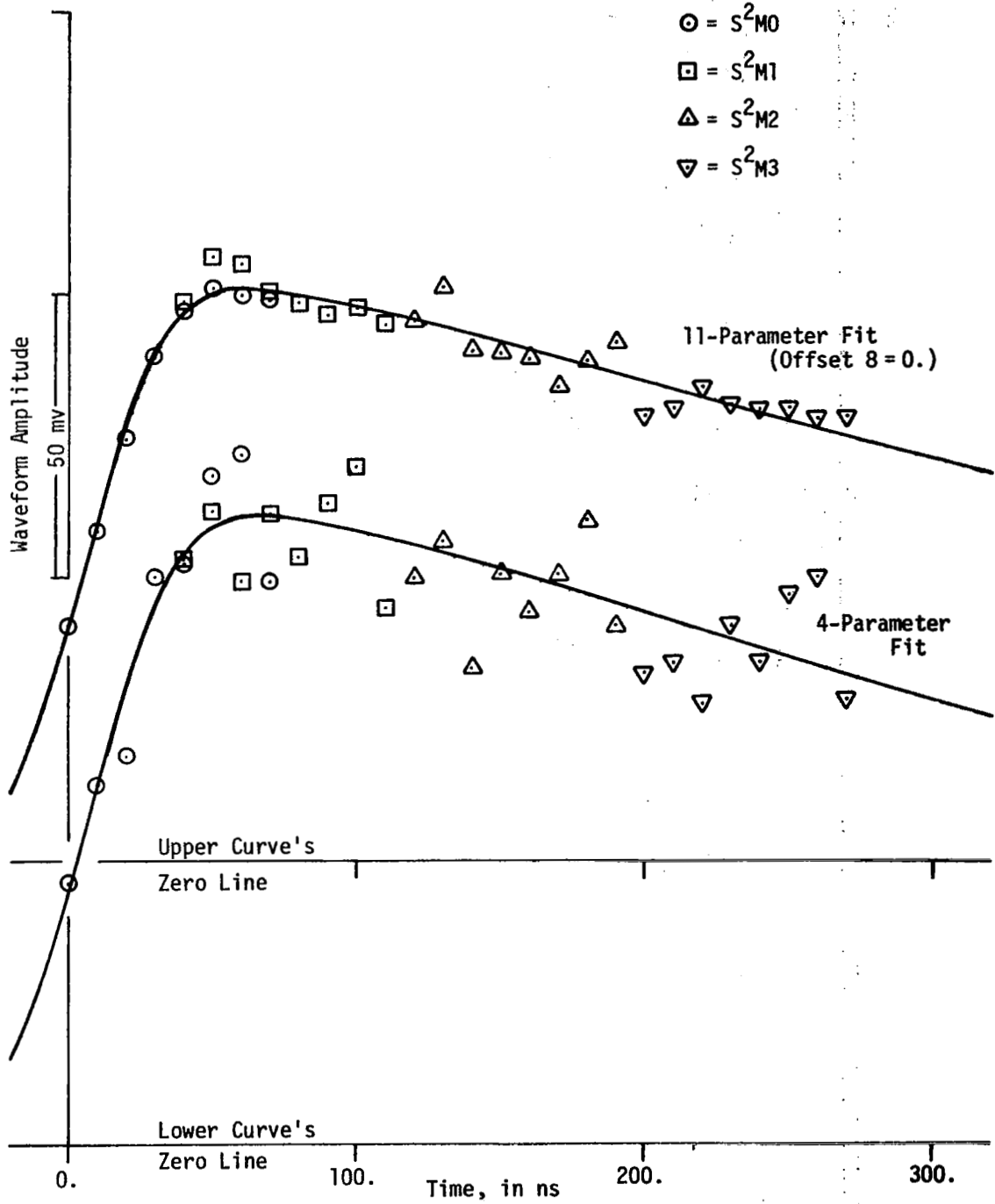


Figure A23. Comparison of Experimental Data and Fitted Functions for SL-4, Pass 71/18, Mode 5 (3rd), Submode 1.

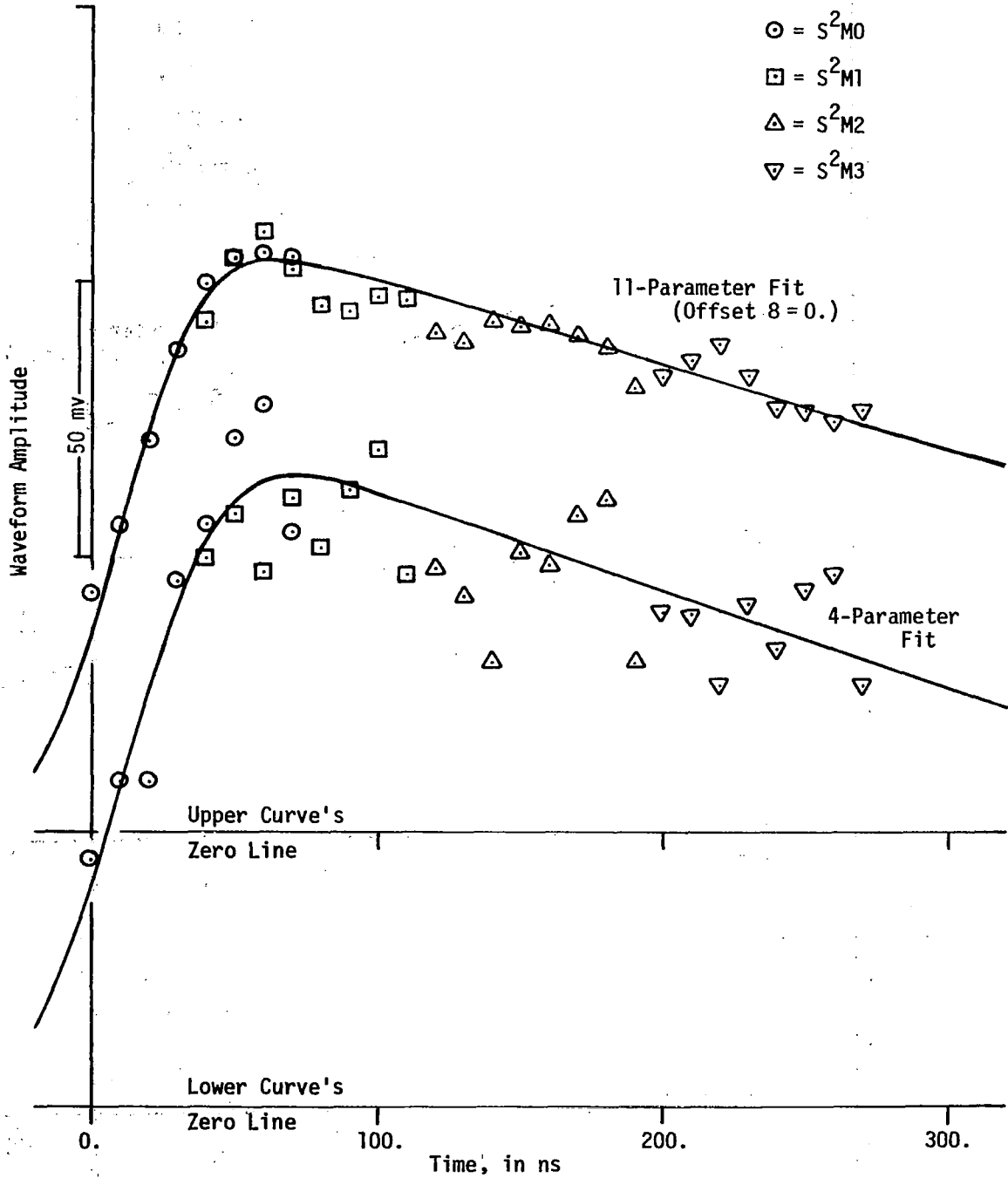


Figure A24. Comparison of Experimental Data and Fitted Functions for SL-4, Pass 71/18, Mode 5 (4th), Submode 1.

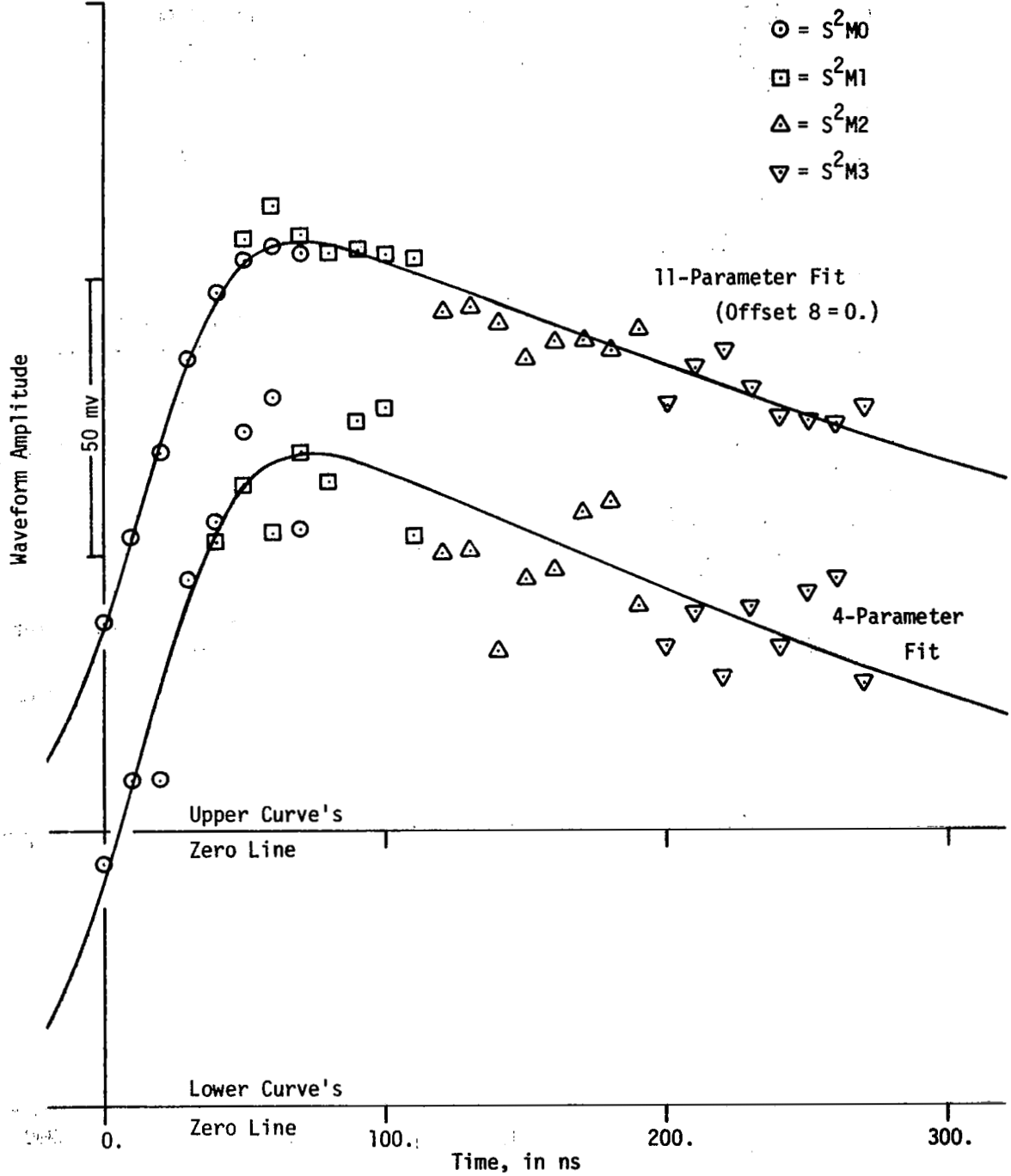


Figure A25. Comparison of Experimental Data and Fitted Functions for SL-4, Pass 74/21, Mode 5 (1st), Submode 1.

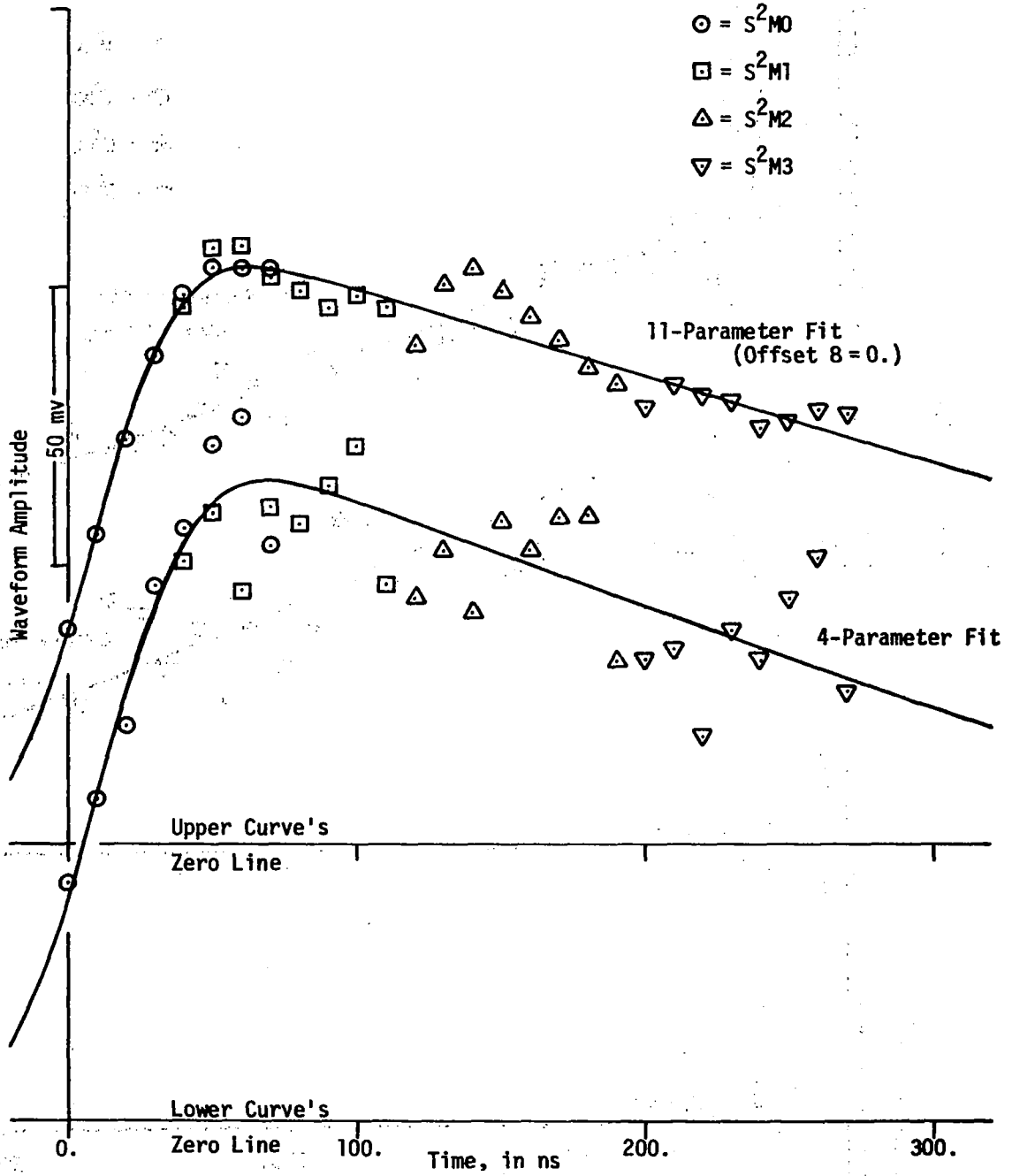


Figure A26. Comparison of Experimental Data and Fitted Functions for SL-4, Pass 74/21, Mode 5 (2nd), Submode 1.

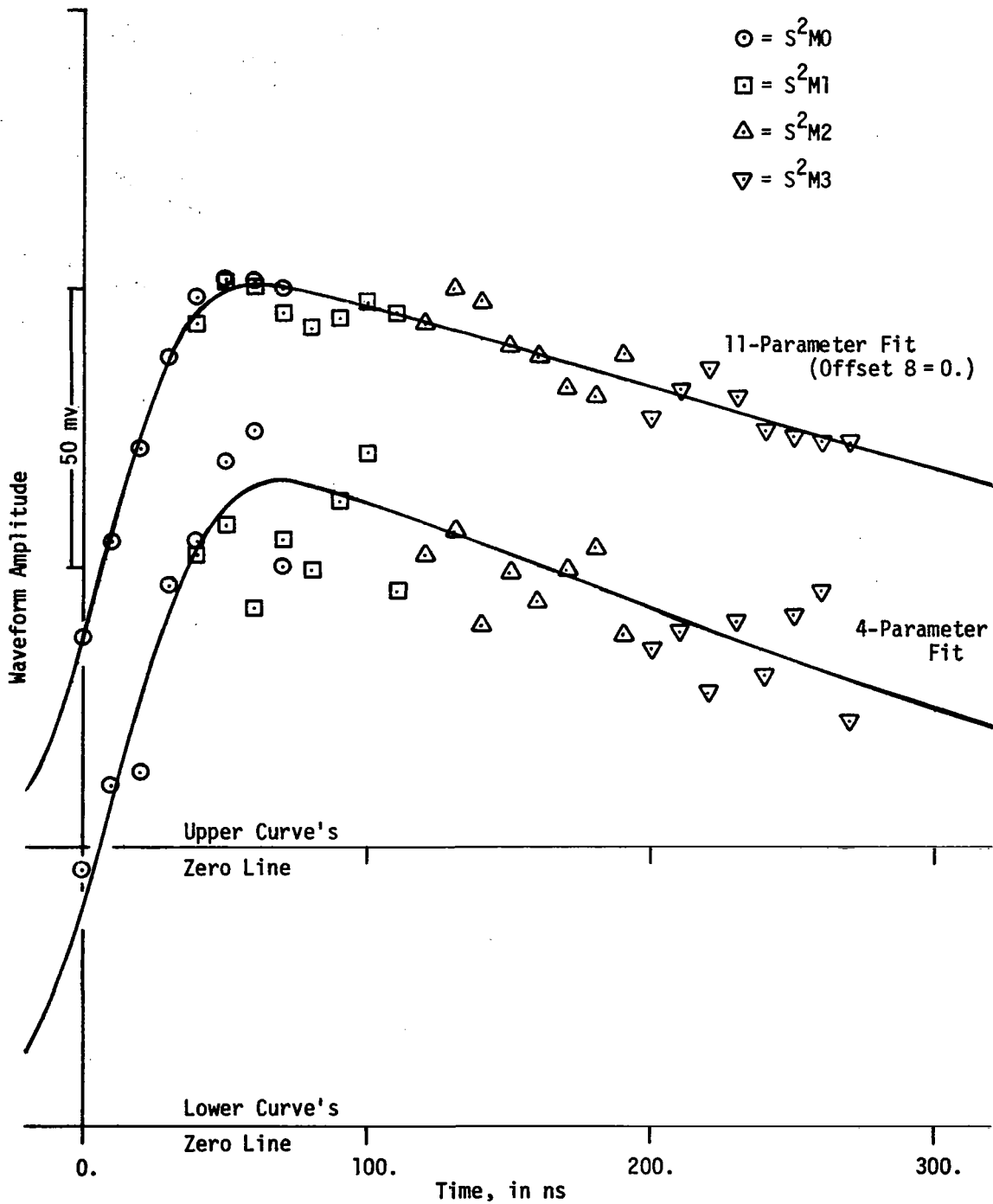


Figure A27. Comparison of Experimental Data and Fitted Functions for SL-4, Pass 78/23, Mode 5 (1st), Submode 1.

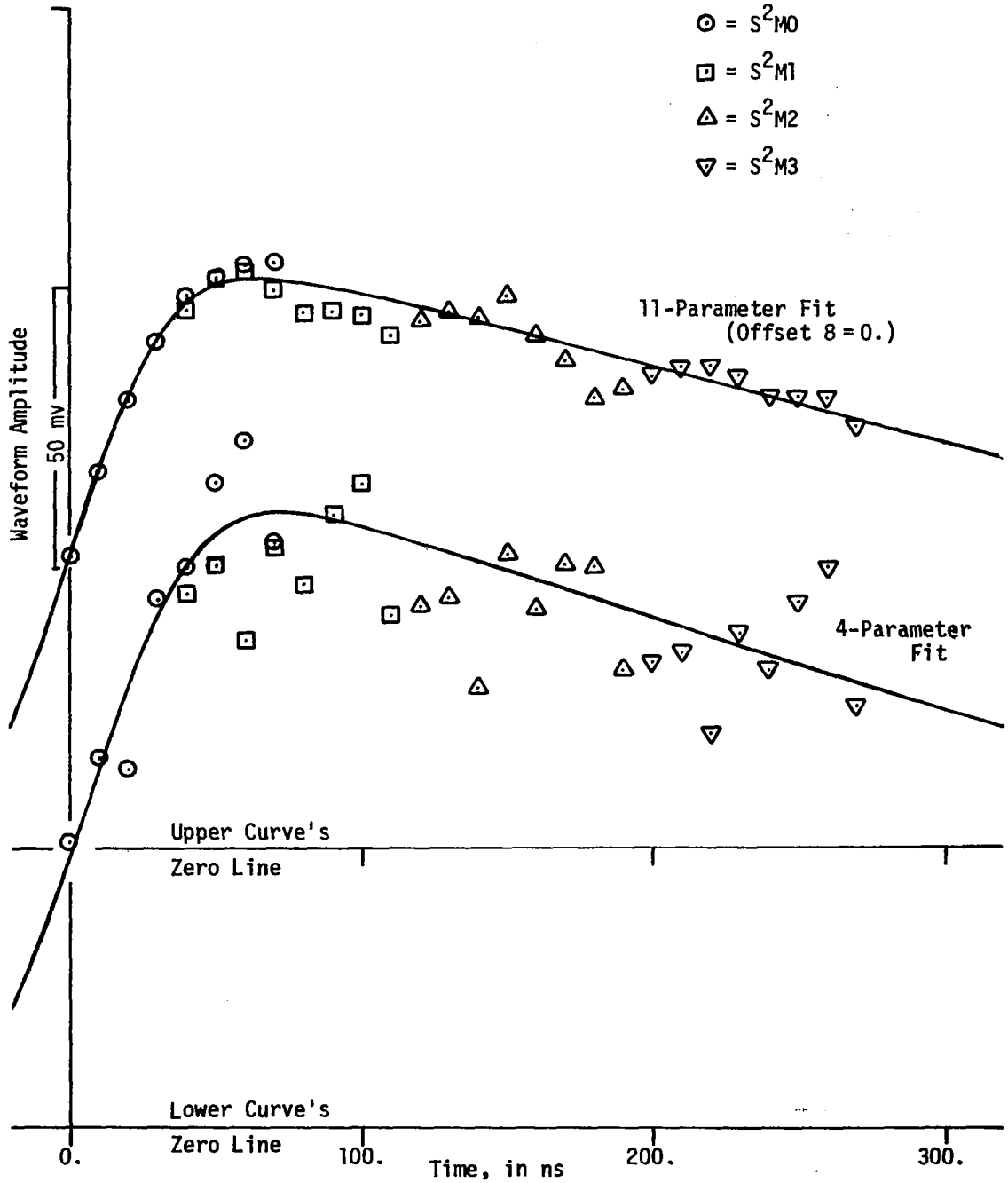


Figure A28. Comparison of Experimental Data and Fitted Functions for SL-4, Pass 79/24, Mode 5 (2nd), Submode 1.

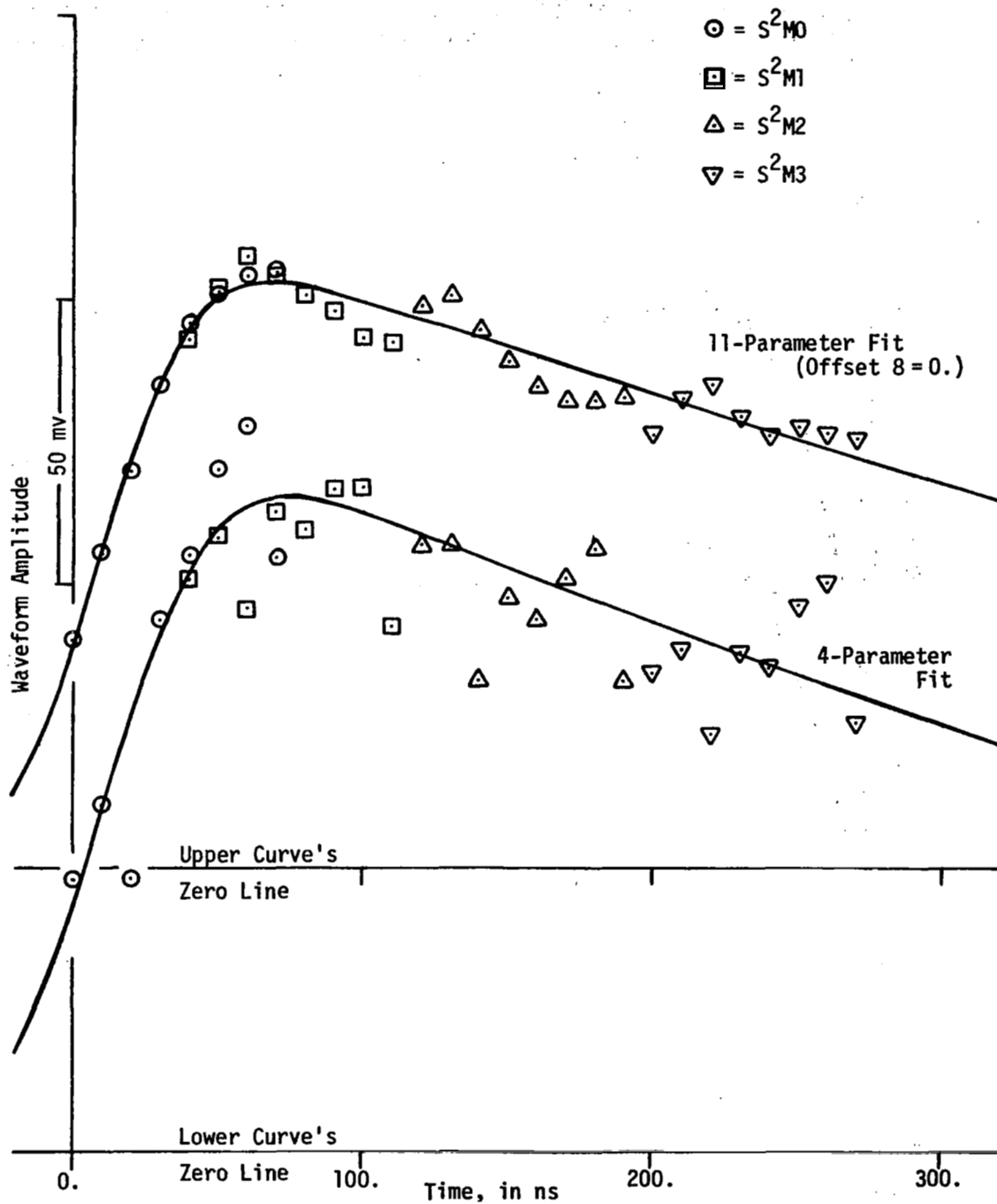


Figure A29. Comparison of Experimental Data and Fitted Functions for SL-4, Pass 86/32, Mode 5, Submode 1.

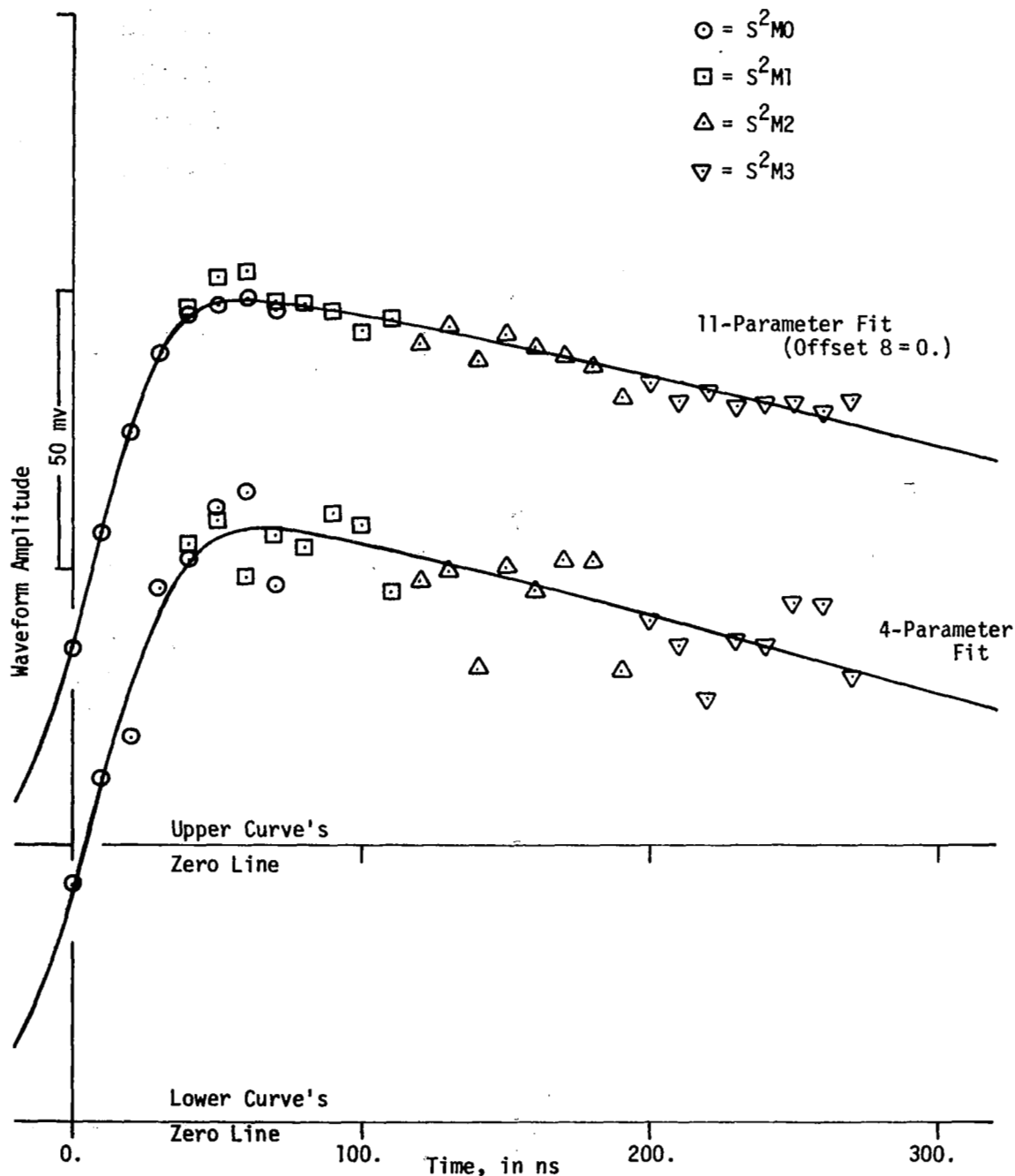


Figure A30. Comparison of Experimental Data and Fitted Functions for SL-4, Pass 93/45, Mode 5, Submode 1.

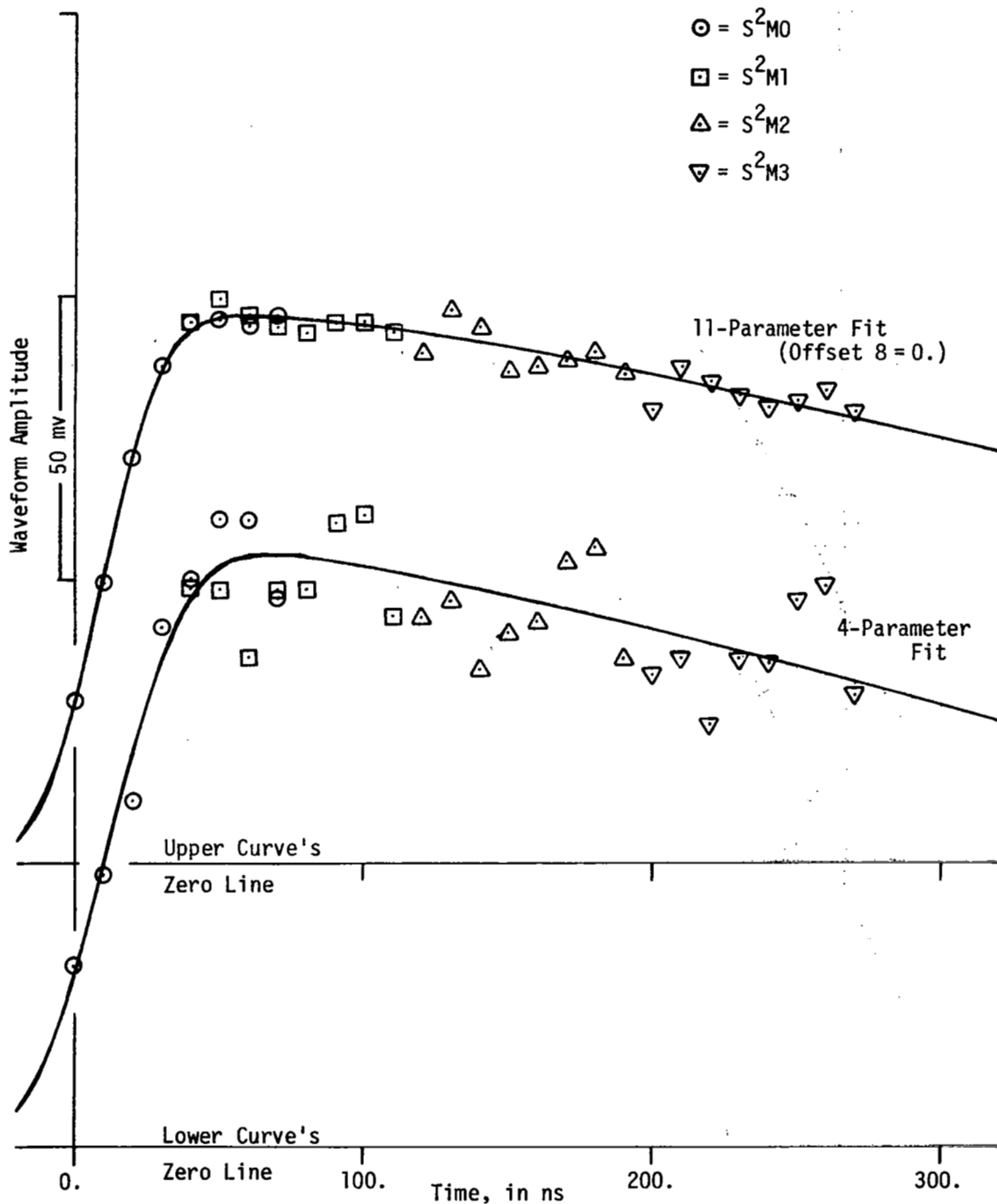
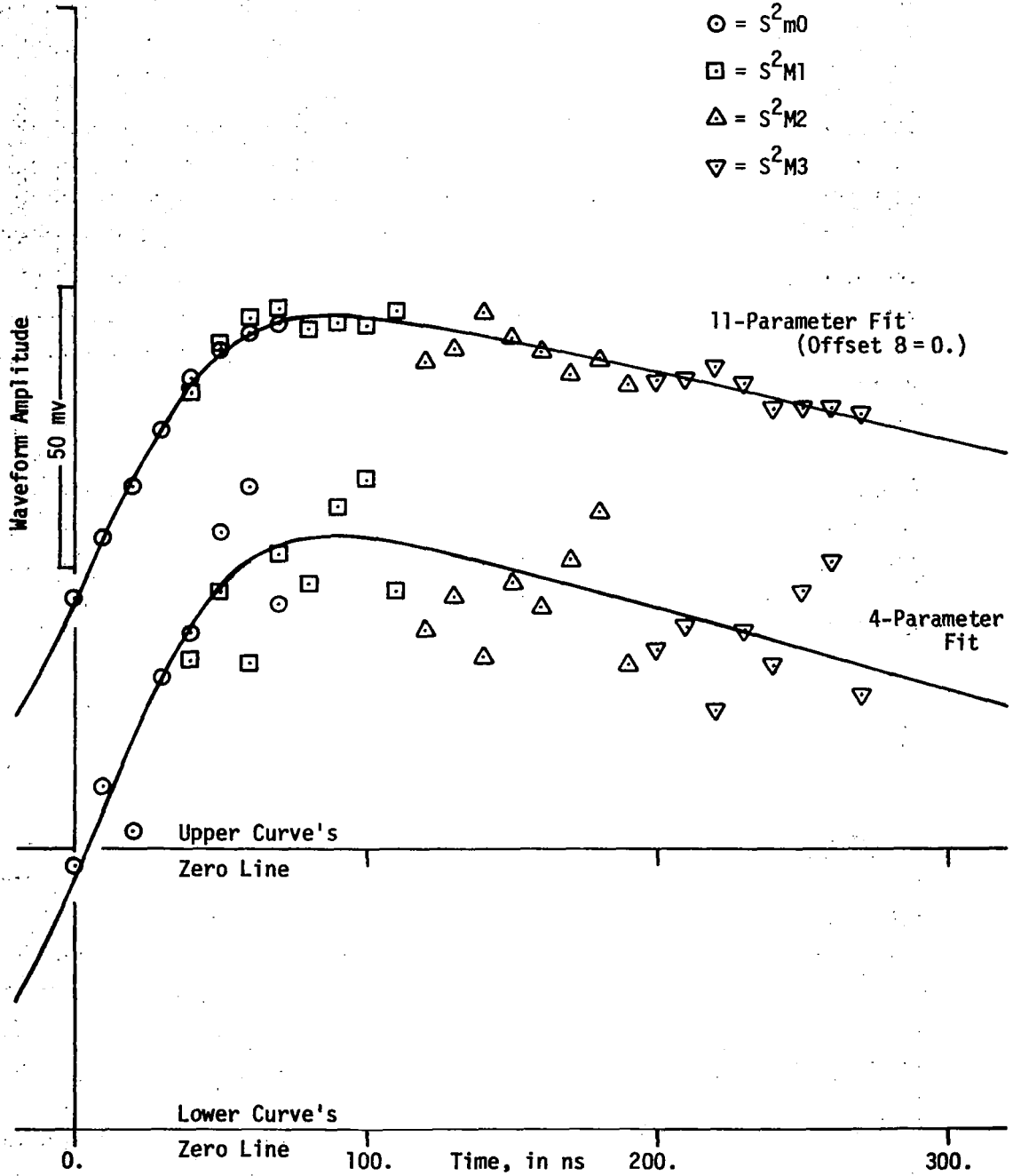


Figure A31. Comparison of Experimental Data and Fitted Functions for SL-4, Pass 97/49 Part 3, Mode 5 (1st), Submode 1.



APPENDIX B

Time Realigned Waveform Smoothing Filter

This appendix describes the smoothing procedure used in processing the time realigned waveform data. The procedure is a simple (linear) minimum mean square error estimator which assumes that the observed values are combined with measurement noise. The measurement noise is modelled only to the extent of assuming stationarity and statistical independence of values. Since only average waveform values were available, the noise, or residuals, should be approximately Gaussian; this observation was used to dictate the choice of linear rather than nonlinear estimators.

The estimator derived below reduces to the convolution of the time realigned waveform sample values with the following (normalized) weighting coefficients;

$$\begin{aligned}w_1 &= .11074 \\w_2 &= .40812 \\w_3 &= .71577 \\w_4 &= 1.0000 \\w_5 &= .71577 \\w_6 &= .40812 \\w_7 &= .11074\end{aligned}$$

other coefficients are taken to be zero in the convolution. Note that these weights are symmetrical and were derived on the basis that the time realigned sample points are separated in time by 2.5 ns.

The basis for design of the smoothing operation is the orthogonality principle in which the error e between the signals s_n and the estimates \hat{s}_n are zero on an expectation measure. That is

$$e_k = \hat{s}_k - s_k$$

and

$$\hat{s}_k = \sum_1^j w_1 x_1$$

and \hat{s}_k is the linear estimate based on the j noisy observations $x_i = s_k + n_i$ ($i=1,2,\dots,j$) where n_i is the noise component. For this problem the orthogonality condition yields

$$E[x_n (\hat{s}_k - s_k)] = 0 \quad n = 1,2,3,\dots,j$$

or

$$E[x_n \hat{s}_k] = E[x_n s_k]$$

$$E[x_n (\sum_1^j w_1 x_1)] = E[x_n s_k]$$

The latter equality leads to the following series of equations for a single point on the waveform, say s_1 ;

$$E[x_1 x_1]w_1 + E[x_1 x_2]w_2 + E[x_1 x_3]w_3 + \dots + E[x_1 x_n]w_n = E[x_1 s_1]$$

$$E[x_2 x_1]w_1 + E[x_2 x_2]w_2 + E[x_2 x_3]w_3 + \dots + E[x_2 x_n]w_n = E[x_2 s_1]$$

⋮

$$E[x_n x_1]w_1 + E[x_n x_2]w_2 + E[x_n x_3]w_3 + \dots + E[x_n x_n]w_n = E[x_n s_1]$$

It should be noted that

$$\begin{aligned} E(x_i s_j) &= E[(s_i + n_i)s_j] \\ &= E[s_i s_j] = R_{ij} \end{aligned}$$

since s and n are uncorrelated and $E[n_i] = 0$. Also,

$$\begin{aligned} E(x_i x_j) &= E[(s_i + n_i)(s_j + n_j)] \\ &= R_{ij} + \sigma^2 \delta_{ij} \end{aligned}$$

since the noise is also assumed to be "white" with variance σ^2 . Using these definitions the previous system of equations becomes

$$\begin{aligned}
 (R_{11} + \sigma^2)w_1 + R_{12}w_2 + R_{13}w_3 + \dots + R_{1n}w_n &= R_{11} \\
 R_{21}w_1 + (R_{22} + \sigma^2)w_2 + R_{23}w_3 + \dots + R_{2n}w_n &= R_{21} \\
 R_{n1}w_1 + R_{n2}w_2 + R_{n3}w_3 + \dots + (R_{nn} + \sigma^2)w_n &= R_{n1}
 \end{aligned}$$

This is readily recognized as the matrix equation

$$\bar{R} \vec{w} = \vec{k}$$

with obvious definitions of the vectors \vec{w} and \vec{k} and the matrix \bar{R} . Therefore, the weights \vec{w} can be found by inversion of \bar{R} .

To proceed, note that the stationarity assumption leads to a matrix which is symmetrical about the diagonal since $R_{ij} = R_{ji}$. The model used for the signal correlation properties is based on an assumed Gaussian shaped system impulse response $h(t)$ of e^{-1} width of 10 ns. For white noise excitation of a linear system the output autocorrelation $R(\tau)$ is the convolution;

$$R(\tau) = h(\tau) * h(-\tau)$$

Therefore, for the system model used

$$R_{ij} \approx e^{-\frac{|i-j|^2}{6^2}}$$

(the 6^2 term arises since $R(\tau) = e^{-1}$ at ≈ 15 ns and 15 ns corresponds to 6 sample periods of the 2.5 ns sampled data). The noise component was estimated to be on the order of $.4 R_{ii}$ based on observed residuals of the time realigned sample values. Use of the numerical values discussed above results in the following reduced form;

$$\bar{R} = \begin{bmatrix} R_{11} + \sigma^2 & R_{12} & R_{13} & R_{14} \\ R_{12} & R_{22} + \sigma^2 & R_{23} & R_{24} \\ R_{13} & R_{23} & R_{33} + \sigma^2 & R_{34} \\ R_{14} & R_{24} & R_{34} & R_{44} + \sigma^2 \end{bmatrix}$$

and

$$\vec{k} = \begin{bmatrix} R_{11} \\ R_{12} \\ R_{13} \\ R_{14} \end{bmatrix}$$

has the "two sided" or smoothing solution previously given, for the rank of R equal to four.

APPENDIX C

Experimental Evaluation of the S-193 Pulse Compression
Performance Under Range Extended Target Conditions

The purpose of this appendix is to present experimental and theoretical waveform data from the Skylab altimeter which demonstrate that the phase reversal pulse compression technique functioned in complete accord with linear scatter theory. The S-193 pulse compression technique is shown to achieve the theoretically predicted range resolution and correctly map range clutter under extended target conditions. In the past, a number of investigators have questioned the extent to which ocean backscatter can be modeled as arising from a collection of frequency independent point scatterers [C1], and if the reflection process is frequency dependent over the signal bandwidth, pulse compression systems may not function according to Woodward's ambiguity function theory [C2]. The results to be presented here show that the compressed waveforms are in close correspondence with the measured waveshapes of non pulse compression operation, and radar cross section analyses show that the expected pulse compression power gain was achieved. It is therefore concluded that the phase reversal systems provide ensemble mean waveshapes equivalent to non pulse compression systems under the ocean scattered, range extended clutter conditions for the operating bandwidth and frequency used.

As discussed in [C3] and [C4], the mean waveform for the near normal incidence, ocean scattered signal comprises a nearly linear rise followed by a constant plateau (for this geometry, antenna pattern and σ° angular effects on the plateau are negligible). Under the physical optics scattering regime and for waveheights much less than the signal range expanse, to first order the waveshape represents the double convolution of the flat sea response, the system point target response, and the measurement time jitter probability density function [C4]. In rare cases, ocean scattered waveforms have been observed for which σ° angular dependency appears to be non-negligible. These cases seem to correspond to very small surface roughness. However, with the exception of these anomalous periods, the waveforms observed were well behaved "ramp like" signals, in full accord with area dependent scatter theory.

Figure C1 shows a comparison of Skylab pulse compression performance. This system comprised a 13-bit, phase reversal Baker Code type of pulse

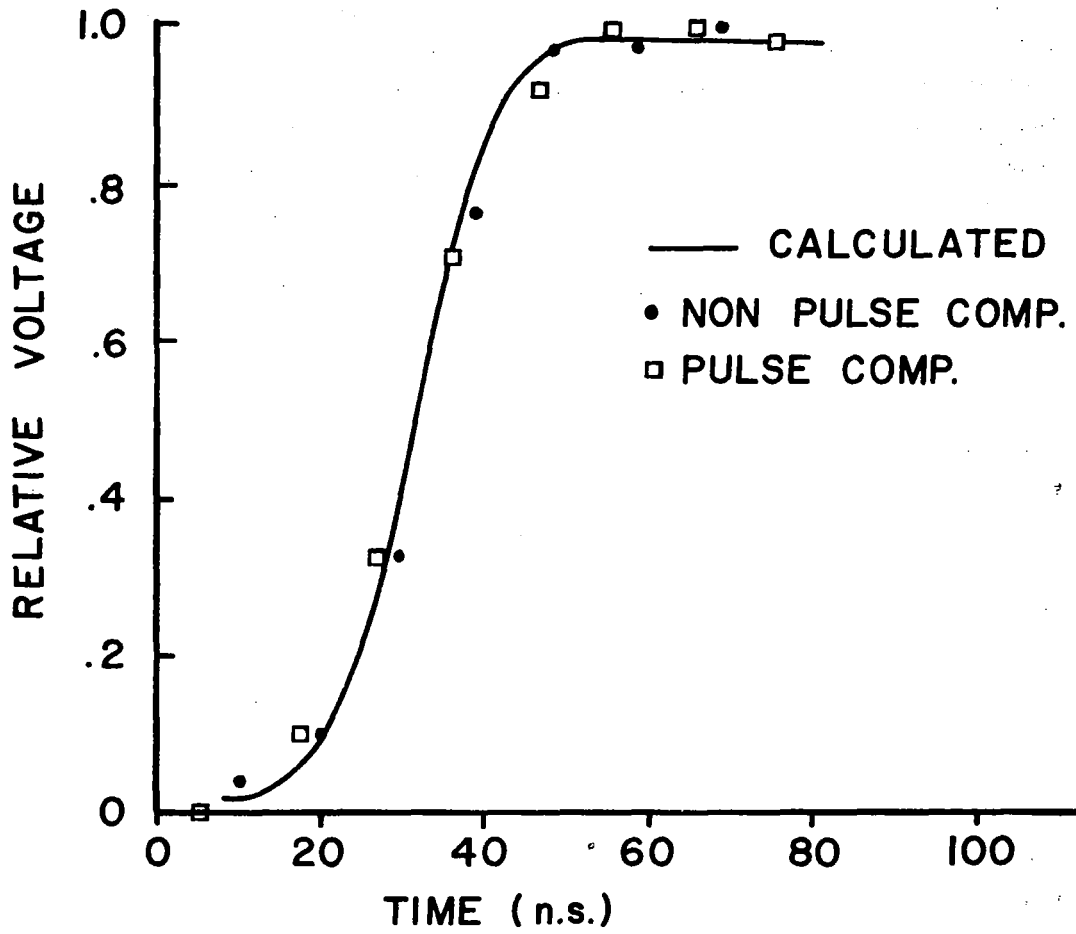


Figure C1. Comparison of measured and theoretical Skylab mean return waveforms.

compression and an uncoded pulse of comparable range resolution [C6], i.e. about 20 ns pulse widths. Figure C1 shows both the theoretically computed and experimental values for the non pulse compression from [C5]; and experimental results of a pulse compression measurement (Mission SL-4 EREP pass 74, frames 2-11). Hardware difficulties prevented acquisition of data in near time coincidence for the two modes of operation. Examination of these results show the experimentally determined ensemble average ocean waveform to be very close to the calculated waveform. Therefore, the range resolution achieved with the pulse compression system is found to be in essential agreement with linear scatter theory.

Preliminary analysis of the signal-to-noise ratio improvement achieved with the Skylab pulse compression systems show values in the neighborhood of 10 dB. Exact values cannot be quoted because of the uncertainty in σ° (estimated to be ± 3 dB) during measurement periods. However, these results indicate that the expected pulse buildup was achieved.

Table C1 shows an interesting comparison of tracking jitter, σ_h , for the 100 ns and 20 ns submodes, during passes in which the pulse compression network did not appear to be functioning (the recorded waveshapes resembled the expanded pulse shape). In Table C1 ξ_p and ξ_r refer to pitch and roll angle estimates from [C4]. Inspection of these data show that the pulse compression and non pulse compression submodes yielded essentially equal σ_h values during the period in which the pulse compression system was not fully functional. It is speculated that the transmitted pulse compression spectrum was normal in this period and that the comparatively low values of tracking jitter display the importance of transmitted signal spectrum relative to waveshape [C7].

REFERENCES

- C1. Hornback, A. G., "Use of pulse compression in mapping type radars," IEEE Southeascon, Louisville, Ky., May 1976.
- C2. Rihazcek, A. W., Principles of High Resolution Radar, Pergamon Press, 1970.
- C3. Moore, R. K., and C. S. Williams, "Radar terrain return at near vertical incidence," Proc. IRE, Vol. 45, pp. 228-238, February 1957.

TABLE C1

Pass No.	ξ_p Deg.	ξ_r Deg.	σ_h Meters
100 ns Pulsewidth			
21(1)	.3	.45	1.22
21(3)	.3	.45	1.47
22(4)	.15	.2	1.95
4	0	0	1.89

Mean tracking jitter = 1.63 meters or 10.9 ns

20 ns Pulse Compression Non Functional*

9	.35	.5	1.3
22(4)	.15	.2	1.2
27	.4	.5	.93
28	.2	.3	.88

Mean tracking jitter = 1.07 meters or 7.1 ns

20 ns Non Pulse Compression

9	.35	.5	.94
22(4)	.15	.2	1.36
27	.4	.5	1.24
28	.2	.3	.88

Mean tracking jitter = 1.05 meters or 7.0 ns

*Based upon observation of the received waveform, it is estimated that the effective received pulsewidth was very near to the transmitted (expanded) width of 130 ns.

- C4. Brown, G. S., "Reduced backscattering cross section data from the Skylab S-193 radar altimeter," NASA CR-141401 (NASA/WFC), Applied Science Associates, Inc., Apex, N. C., Oct. 1975.
- C5. McGoogan, J. T., L. S. Miller, G. S. Brown, and G. S. Hayne, "The S-193 radar altimeter experiment," Proc. IEEE, Vol. 62, pp 793-803, June, 1974.
- C6. Miller, L. S., and D. C. Hammond, "Objectives and capabilities of the Skylab altimeter experiment," IEEE Trans. on Geosci. Elect., Vol. GE-10, pp. 73-79, January, 1972.
- C7. Miller, L. S., G. S. Hayne and G. S. Brown, "Analysis of Satellite Altimeter Signal Characteristics and Investigation of Sea-Truth Data Requirements," NASA CR-137465 (NASA/WFC), Research Triangle Institute, Durham, N. C., Page 2-8, April, 1972.

CHAPTER 13

System Related Observations

by

G. S. Brown

1.0 Introduction

In the preceding chapters, we have primarily discussed operation of the altimeter relative to its impact upon the reduction and interpretation of remote sensing related data. In addition, however, the S-193 radar altimeter acquired data which can also be of benefit to the future design of radar altimeters. Although these latter observations are not of direct interest to the user community, they have a significant bearing on the performance of the instrument and therefore relate directly to the quality of the resulting science data.

In this chapter we will be concerned with those aspects of the altimeter's performance which (1) required verification, (2) indicated a malfunction, or (3) showed anomalous or unusual behavior. We will not deal with previously documented [1] performance related observations such as the failure of pulse compression during SL-2 and SL-3. The items addressed in this chapter are of a more subtle nature and only become apparent after an extensive analysis of the altimeter data base.

2.0 r-Factor Verification Using Waveform Data

Our ability to interpret radar altimetry data depends to a large extent upon a priori knowledge of the average return power as a function of time delay. Thus, if for no other reason than to make the data analysis much simpler, it is most desirable to (1) have the AGC provide measure of the peak of the average return power and (2) provide a linear normalization of the waveform recorded by the S&H gates. Because of design considerations and uncertainties, the S-193 AGC system did not actually respond to the peak of the average return power. Since the nadir average return exhibited a very peaked behavior, the AGC system was designed to respond to the average of the peaks in the return. That is, for each return a predetermined time delay window was searched and the local maximum in the return was sampled and held. The average of a number of these peak detecting operations

was used to generate the AGC voltage.

Unfortunately, the relationship between the peak of the average return and the average of the peaks in the returns is not a simple one and, in fact is a very sensitive function of the shape of the average return and the signal-to-noise ratio. Because of the manner in which the system was calibrated, this dependence was an important factor in extracting cross-section results from the altimeter [2]. That is, we had to generate a set of input power versus AGC voltage curves to properly reflect the sensitivity of the peak detecting AGC system to the shape of the average return power. In order to do this, it was necessary to make use of both computer simulations and pre-flight measurements of the so-called r-factor or the ratio of the peak of the average return to the average of the peaks in the returns. The resultant values for the r-factor could not be verified by pre-flight measurement because the altimeter calibration data base was not extensive enough to do so. Thus, although we used the "hybrid" r-factor numbers in converting AGC voltages to scattering cross section (σ°) values, there was a question as to their accuracy.

There is a way in which the variation of the r-factor with pointing angle can be extracted from the waveform data. As shown in the chapter on tracking jitter effects (Chapter 11) the gain of the AGC system may be expressed as follows;

$$G_{AGC} \approx \left\{ \frac{1}{\alpha a G_{RF}^2 G_{IF}^2 G_V (S/r + \delta)} \right\}^{1/2} \quad (1)$$

where α is an AGC scaling factor, a is constant associated with the square law detector, S is the peak of the average return power, r is the r-factor and δ is an offset to insure finite gain at zero input signal. The factors G_{RF} , G_{IF} and G_V are RF, IF and video system gains. The average return power as recorded by the S&H gates was also shown to be

$$\bar{z}(\tau) = \frac{2S}{\alpha(S/r + \delta)} P_r(\tau) \quad (2)$$

where $P_r(\tau)$ is the true average return power normalized to a maximum value of one. For near nadir operation, $S/r \gg \delta$ and thus

EREP PASS 24

SL - 3
3RD MODE III

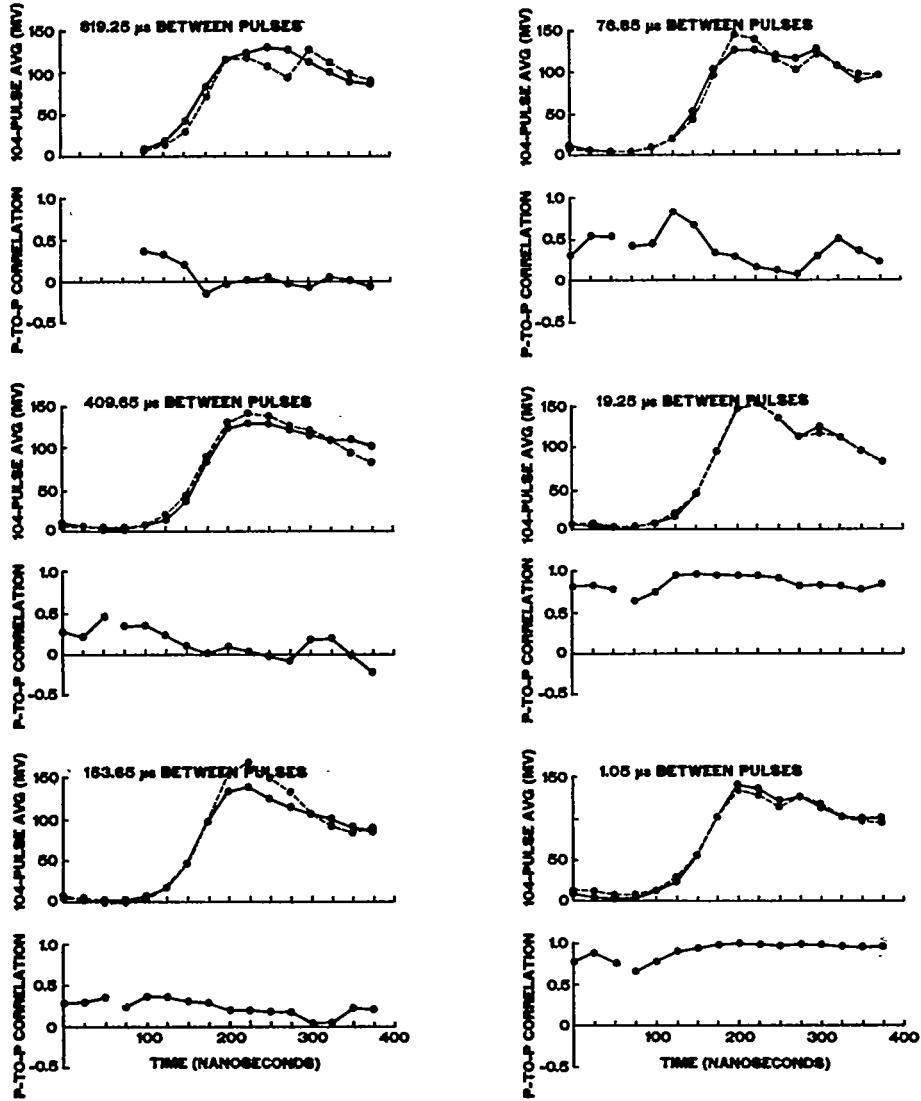


Figure 21. Measured mean returns and interpulse correlations for a pointing error on the ellipse whose semiminor axis was 0.4° along-track and whose semimajor axis was 0.55° cross-track.

EREP PASS 40

SL - 3

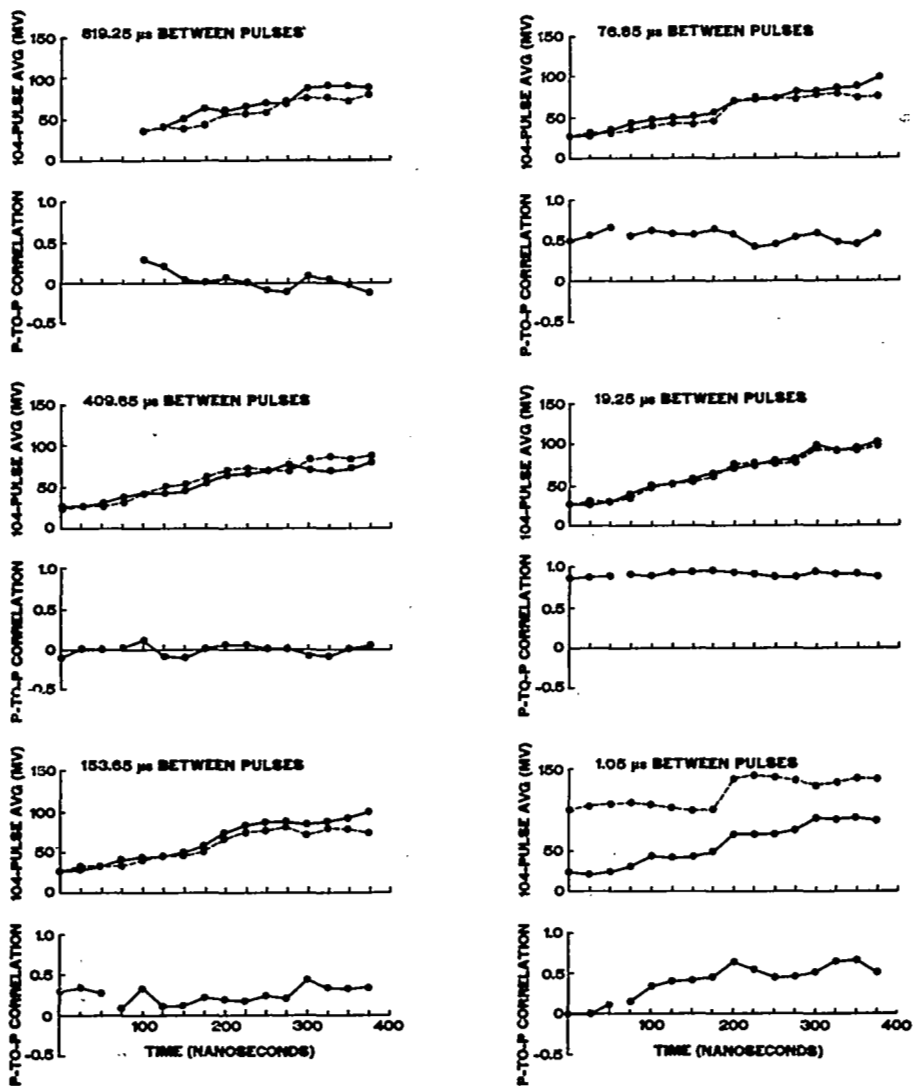


Figure 22. Measured mean returns and interpulse correlations for a pointing error on the ellipse whose semiminor axis was $>0.95^\circ$ along-track and whose semimajor axis was $>1.2^\circ$ cross-track.

EREP PASS 57

SL - 4

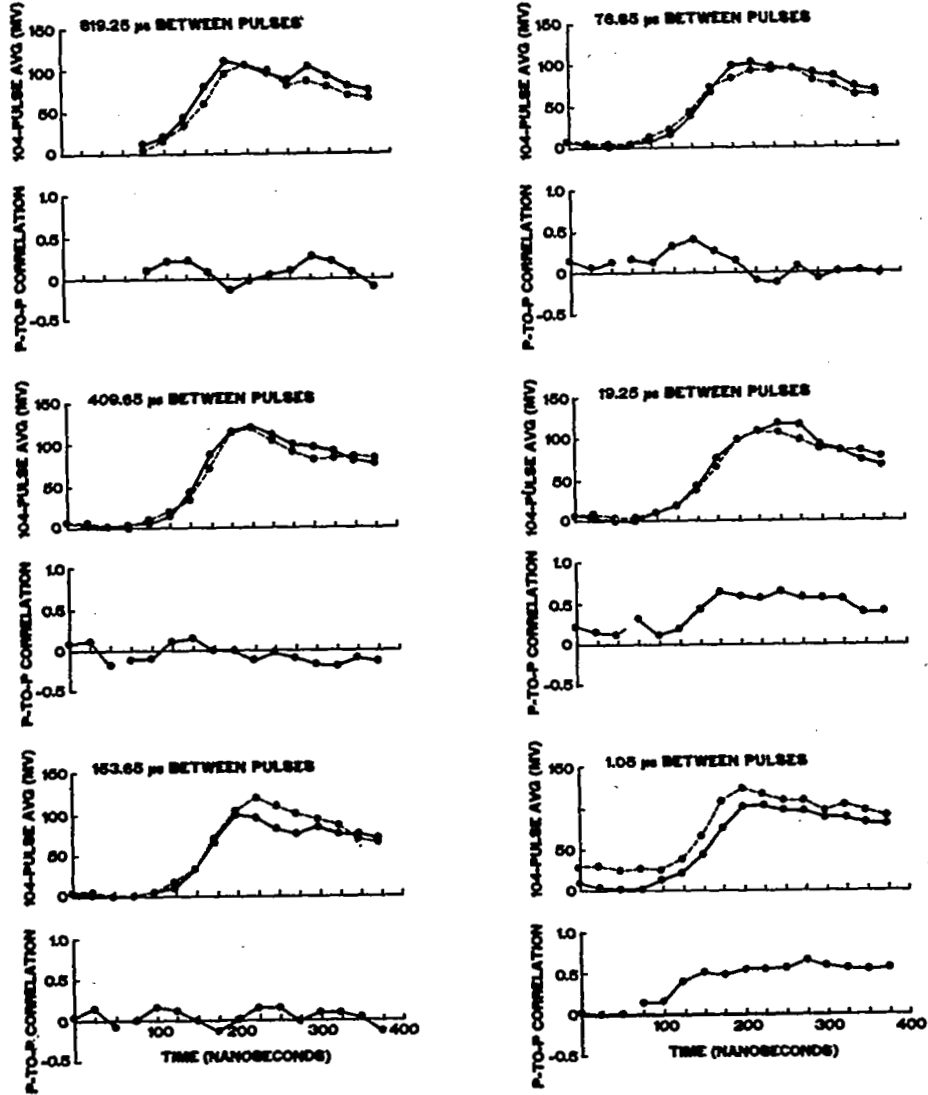


Figure 23. Measured mean returns and interpulse correlations for a pointing error on the ellipse whose semiminor axis was 0.7° along-track and whose semimajor axis was 0.75° cross-track.

EREP PASS 61

SL - 4

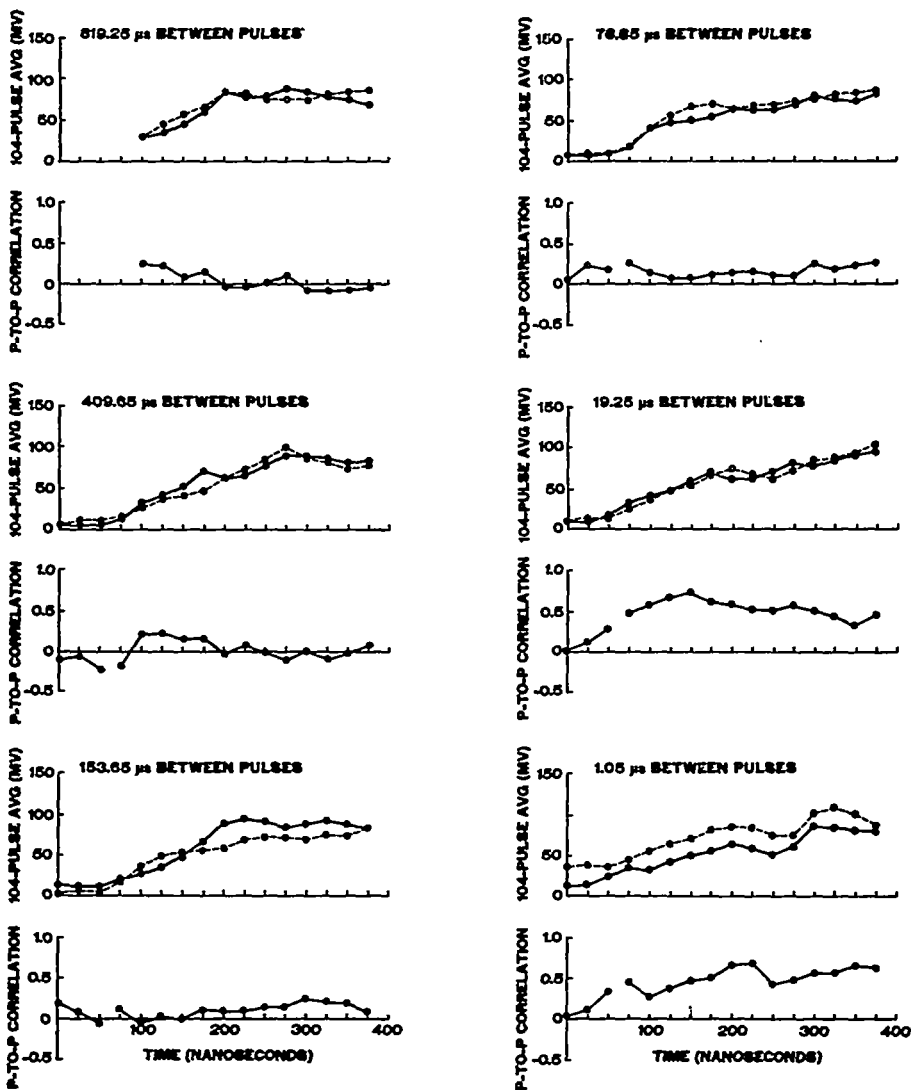


Figure 24. Measured mean returns and interpulse correlations for a pointing error on the ellipse whose semiminor axis was $>1.1^\circ$ along-track and whose semimajor axis was $>1.15^\circ$ cross-track.

to the 100 ns CDS pulse shape. Very crudely speaking, this match then provided the approximate cutoff frequency of the "equivalent" 10 MHz IF filter. Passing a 20 ns pulse through the ideal filter having a cutoff frequency of 8 MHz resulted in the output power waveform also shown in Figure 2. As anticipated, the 20 ns pulse is extremely smeared and, in fact, more closely resembles the 100 ns CDS pulse shape than the input pulse. The time sidelobes have not been shown in Figure 2 since their contribution to the average return power was not considered significant. The 20 ns output waveform in Figure 2 was convolved with the flat surface impulse response corresponding to zero pointing angle and the resultant waveform is shown in Figure 3. Also shown is Mode III, submode 5 data from SL-3 EREP pass 24 (first of three Mode III's).

Considering the degree of approximation involved in estimating the theoretical return for the 20 ns/10 MHz combination, the agreement in the rise time portion is seen to be very good. The rather bad agreement in the trailing edge of the return is thought to be due to improper location of the S&H gates. That is, based upon design and preflight testing, the S&H gates were supposed to be contiguous in each of the eight sub sub submodes. However, it appears that the sample points corresponding to S^3M 3 through 7 should be nonuniformly shifted to the left (earlier in time). The experimental waveform shown in Figure 3 is impossible for a pointing angle near zero (as previously determined from the 100 ns/10 MHz single pulse waveform data by both the template* and angle estimator approach). While it is true that time sidelobes could cause a "raising" of the trailing edge of the return, they would have to be extremely large in amplitude and long in time extent. Inspection of other Mode III short dual pulse data indicated that the suspected shift in the time position of the S&H gates was not always consistent. This variation tends to indicate a digital control logic problem that is almost random in nature. The samples obtained in S^3M 0 and 1 generally appear to be contiguous, however, the other S^3M data is not always in correspondence with the preprogrammed positioning. For this reason, the user is warned that experimental short pulse data on pulse-to-pulse correlation may not correspond to theoretical predictions. For this reason,

*See the pointing angle estimates for this pass as given in [2].

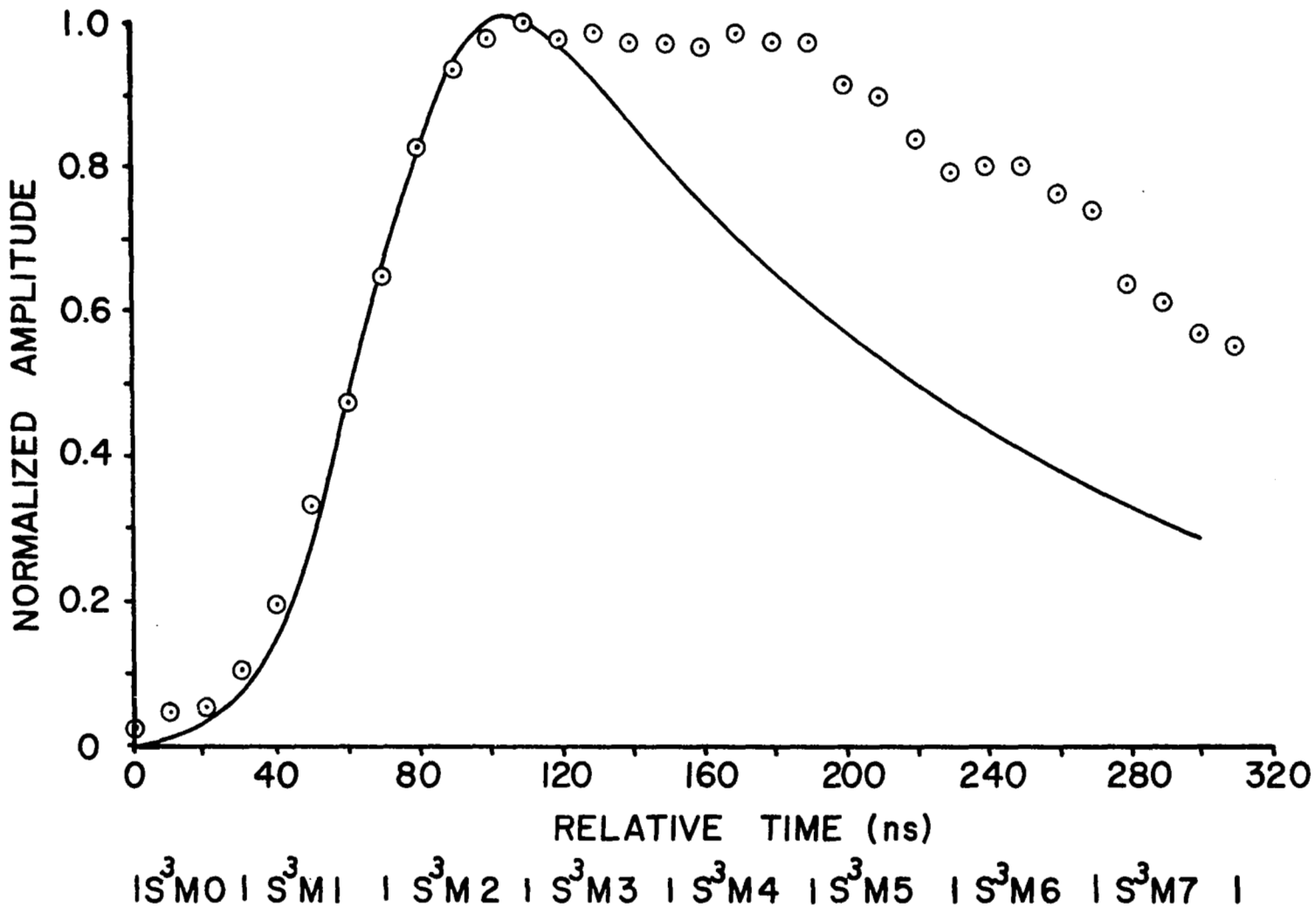


Figure 3. Comparison of the theoretical 10 ns/10 MHz return (no pointing error) with the short pulse data from SL-3 EREP Pass 24 (first of three Mode III's).

analysis of pulse-to-pulse correlation data was restricted to the 100 ns dual pulse case since, apart from the bandwidth reduction, there appeared to be only minor gate positioning problems (see Chapter 10).

4.0 100 ns/10 MHz Intrapulse Autocorrelation Function

Surface roughness and pointing angle effects along with the decay in surface cross section with angle of incidence directly influence the shape of the average return power waveform. When estimating the error involved in extracting such quantities from the mean return, we are nearly always confronted by the requirement to know the intrapulse autocorrelation function. An excellent example of this condition is provided in the Chapter on attitude estimation using 100 ns/10 MHz data wherein the variance of the estimator function was shown to depend directly upon the square of the predetection intrapulse autocorrelation function. Furthermore, study of the intrapulse autocorrelation function can add to our understanding of receiver and S&H effects upon the return signal statistics.

The 100 ns/10 MHz waveform data affords an excellent opportunity to corroborate our analysis with experimental data. That is, since the video bandwidth is nearly ten times as large as the one-sided IF bandwidth, its effects can be ignored and we find that the joint first moment between S&H gate i and j is given by

$$E\{v(\tau_i)v(\tau_j)\} = \bar{P}_r(\tau_i) \bar{P}_r(\tau_j) + R_x^2(\tau_i, \tau_j) \quad (5)$$

where

$$\bar{P}_r(\tau_i) = E\{v(\tau_i)\}$$

and

$$\bar{P}_r(\tau_j) = E\{v(\tau_j)\}$$

are the average return power at relative delay times τ_i and τ_j , and

$$R_x(\tau_i, \tau_j) = E\{x(\tau_i)x(\tau_j)\}$$

where $x(\tau)$ is the in-phase or quadrature component of the predetection signal

envelope. Since $x(\tau)$ is characterized by a time varying mean, $R_x(\tau_i, \tau_j)$ depends not only on the time difference $\tau_i - \tau_j$ but also on the time origin. As previously shown [Chapter 3], in the trailing edge of the return $R_x(\tau_i, \tau_j)$ assumes the somewhat simplified form

$$R_x(\tau_i, \tau_j) \approx \rho(\tau) \bar{P}_r(\tau_i - \frac{\tau}{2})$$

where $\tau = \tau_i - \tau_j$, $\bar{P}_r(\tau_i - \frac{\tau}{2})$ is the AGC normalized average return waveform and $\rho(\tau)$ is the matched filter predetection receiver autocorrelation coefficient. Assuming perfect square law detection and no video filter effects other than rejection of the IF frequency harmonics, $\rho(\tau)$ is proportional to the fourth root of the system point target response, i.e. $\rho(\tau) \sim \exp(-\tau^2/8\sigma_p^2)$ where $\sigma_p = 29.25$ ns [2]. Given the mean waveform and joint first moment data along with extrapolated values of $\bar{P}_r(\tau_i - \tau/2)$, we can compute $\rho(\tau)$ according to the following equation

$$\rho^2(\tau) \approx \left[\frac{E\{v(\tau_i)v(\tau_j)\} - \bar{P}_r(\tau_i)\bar{P}_r(\tau_j)}{\bar{P}_r(\tau_i - \tau/2)} \right]$$

and compare this result with the Gaussian form implied by the system point target response.

A typical comparison is shown in Figure 4 where we have used waveform data from SL-2, Mode I, SM 0, S²M 2. Both the Gaussian function and the experimental data have been normalized to one for zero lag time. The agreement is excellent especially when we realize that the Gaussian form was inferred essentially from $\rho^2(\tau)$ in which case the data points for S&H gates 5 through 8 would only be 1% of the maximum. The agreement is also interesting in that the data was not corrected for saturation effects; this clearly shows that S&H saturation is, at most, a second order effect. We therefore conclude that the model used for the 100 ns/10 MHz intrapulse autocorrelation function is in very good agreement with the experimental waveform data.

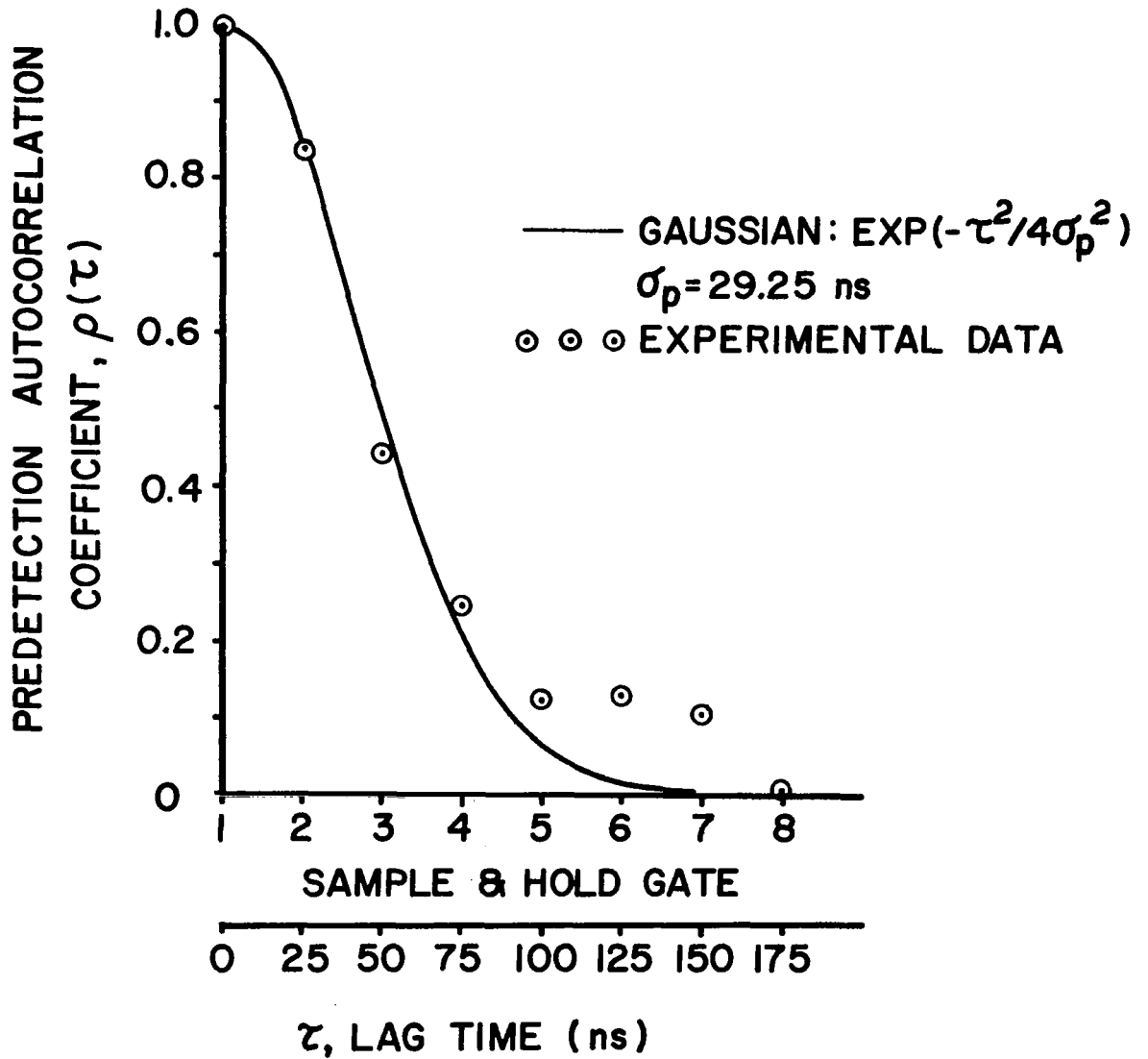


Figure 4. Comparison of theoretical receiver autocorrelation coefficient with reduced data from SL-2 EREP Pass 4, Mode I, Submode 0, Sub Submode 2.

5.0 100 ns/10 MHz Sampled Waveform Considerations

All of the measurements made by the altimeter, including altitude and σ° , are related to the shape of the average return waveform. If the shape of the average return waveform is different from pre-flight expectations, it is possible to correct the data reduction models to account for the difference. A good example of this type of correction is the elimination of biases in the altitude measurements due to changes in the shape of the average return waveform resulting from pointing errors. However, in order to affect such post-flight corrections, we must have an accurate picture of the average return waveform and know how the radar receiver altered its shape. The average waveform available for post-flight analysis is obtained by the Sample and Hold gates; thus, the waveform presented to the tracking loop and the AGC differs from these recorded waveforms only by the S&H induced effects. It is essential then to be able to distinguish between S&H induced effects and those waveform variations which are a result of the scattering process. The purpose of this section is to discuss some of the waveform related results which are consequences of the S&H gate's behavior. Where possible, attempts will be made to explain the observations using pre-flight data.

The S&H circuitry used in the Skylab altimeter was beyond the state-of-the-art relative to commercially available hardware. Each device actually consisted of two series S&H gates, the first being very high speed and the second much slower in terms of acquisition time. The first S&H gate comprised a quad hot carrier diode bridge for switching and a small hold capacitor while the second gate used an FET transistor switch along with a larger hold capacitor. The second unit was used to overcome the rather poor hold capabilities of the first gate. In the conducting or on state, the equivalent resistance of the diode bridge was not constant but depended to some extent upon the charging time [4]. When the S&H gates were operated in the 25 ns acquisition time configuration, this variation was not considered to be a problem since the equivalent RC of the first stage S&H was considerably less than 25 ns. Other than these few details, very little else was published on the design of the S&H devices used in the Skylab altimeter.

A logical starting point for discussing the performance of the S&H gates is to consider how they behaved when sampling ahead (earlier in time) of the

return signal. In this case the gates should only be subjected to zero-mean exponentially distributed receiver thermal noise attenuated or amplified by the AGC. The sampled voltage is proportional to power because of the square law detection and is zero mean because of ac-coupling between the detector and the S&H gates. In the internal calibration submodes (CDS), the transmitted pulse was passed through a calibrated attenuator and subsequently into the radar receiver. Two values of attenuation were provided: 119 and 130 dB. The estimated IF peak signal to rms noise ratio for these two cases was 38 and 28 dB, respectively. With the AGC holding the peak postdetection pulse amplitude to about 0.26 volt, this meant that the rms noise level would be less than 0.26 millivolt. Since the equivalent quantization of the S&H input voltage was 4 millivolts, the standard deviation of the S&H input voltage should be about 1 millivolt ($4/\sqrt{12}$) in the noise only region. Table I shows the average means and standard deviations of the S&H recorded voltages obtained from the 119 dB and 130 dB attenuation internal calibration submodes. Although the standard deviation values are nearly equal to the quantization error, the means show a nonnegligible departure from zero. Since these average values are generally larger than two or three sigma excursions, it would appear that they are true offset values. That is, because of drift, calibration errors or thermal changes the average values shown in Table I correspond to the true zero input signal offset. Assuming that the S&H devices are linear, these offsets should be subtracted from all recorded S&H voltages.

Because the 100 ns/10 MHz Data Acquisition (DAS) submodes yielded an average single pulse IF signal-to-noise ratio in excess of 30 dB for near nadir pointing and $\sigma^{\circ} \geq 10$ dB, the noise-only statistics as recorded by the S&H gates can be compared to the CDS data in Table I. The average mean and standard deviations for such cases is shown in Table II. The means are definitely larger than the means shown in Table I (internal calibration) and the increase is not justifiable by pure statistical error. However, the AGC may be contributing to this increase in offset since the S&H gates respond to AGC normalized noise and the AGC may be time varying due to changing surface conditions. More disturbing however is the gate to gate variation in standard deviation values shown in Table II. Using the same AGC argument as above, it is possible to rationalize a uniform increase in the standard deviations recorded by all gates, but the gate to gate variation shown

TABLE I

Mean and Standard Deviation of Sample and Hold Gate Voltages in Noise-Only During CDS Submodes with 119 and 130 dB Path Attenuation.

119 dB Path Attenuation

		Sample & Hold Gate Number							
		1	2	3	4	5	6	7	8
Mean (mv)		4	3	1	4	2	1	-2	-3
Std. Dev. (mv)		1	1	1	2	2	1	2	2

130 dB Path Attenuation

		Sample & Hold Gate Number							
		1	2	3	4	5	6	7	8
Mean (mv)		3	2	0	5	2	1	-2	-3
Std. Dev. (mv)		1	1	1	2	2	2	2	2

TABLE II

Mean and Standard Deviation of Sample and Hold Voltages in Noise-Only During DAS Submodes For Which the IF Signal To Noise Ratio Exceeded 30 dB.

		Sample & Hold Gate Number							
		1	2	3	4	5	6	7	8
Mean (mv)		6	4	2	5	6	6	2	-1
Std. Dev. (mv)		10	4	4	4	10	8	4	4

in Table II would not seem to be covered by this explanation. Within the realm of linear circuit theory, there is no self-consistent explanation for the differences between the results in Tables I and II short of admitting the possibility of a non-stationary "signal" in the time region ahead of the return. This situation is further complicated by the results shown in Figure 5. Here, the mean voltage has been plotted as a function of the standard deviation for signal-to-noise ratios ranging from 40 dB to less than 10 dB. The data points enclosed by the rectangular boxes represent the data obtained in the internal calibration submode (Table I) whereas the large standard deviation data were obtained from SL-4. After an initial increase in the means (in the transition between internal calibration and data acquisition submodes), the means stay relatively constant until the standard deviations become large and then the means start to increase also. This result is not new; it was previously noted by Godby [3] who explained the observation in terms of differing effective Sample and Hold RC time constants for negative and positive going input voltages. This explanation would appear to be somewhat incomplete since it does not entirely account for the observed relation between the mean and standard deviation. That is, why should the mean be more or less insensitive to the standard deviation and then start to increase with the increasing standard deviation? Unfortunately, no good solid answers have been found to explain the "noise-only" Sample and Hold data.

Since the performance of the S&H gates in the "noise-only" time zone preceding the return is not completely understood, it is not possible to rigorously determine if the "noise only" means should be treated as biases in the signal plus noise time zone. In studying the average waveform data and also histograms of the S&H recorded voltages and comparing the results with theoretical predictions, the evidence tends to indicate that except for S&H gates one and two in the leading edge of the return, the "noise only" mean values should not be subtracted from the "noise plus signal" means. That is, in comparing measured mean values with theoretical predictions, generally, agreement is obtained if the "noise only" mean values are not subtracted from the "signal plus noise" means, except for S&H gates one and two in S^2M 1. Figure 6 presents normalized average waveform data with and without subtraction of the "noise only" means. This particular comparison shows that there is not too much difference in the results except for S&H gates

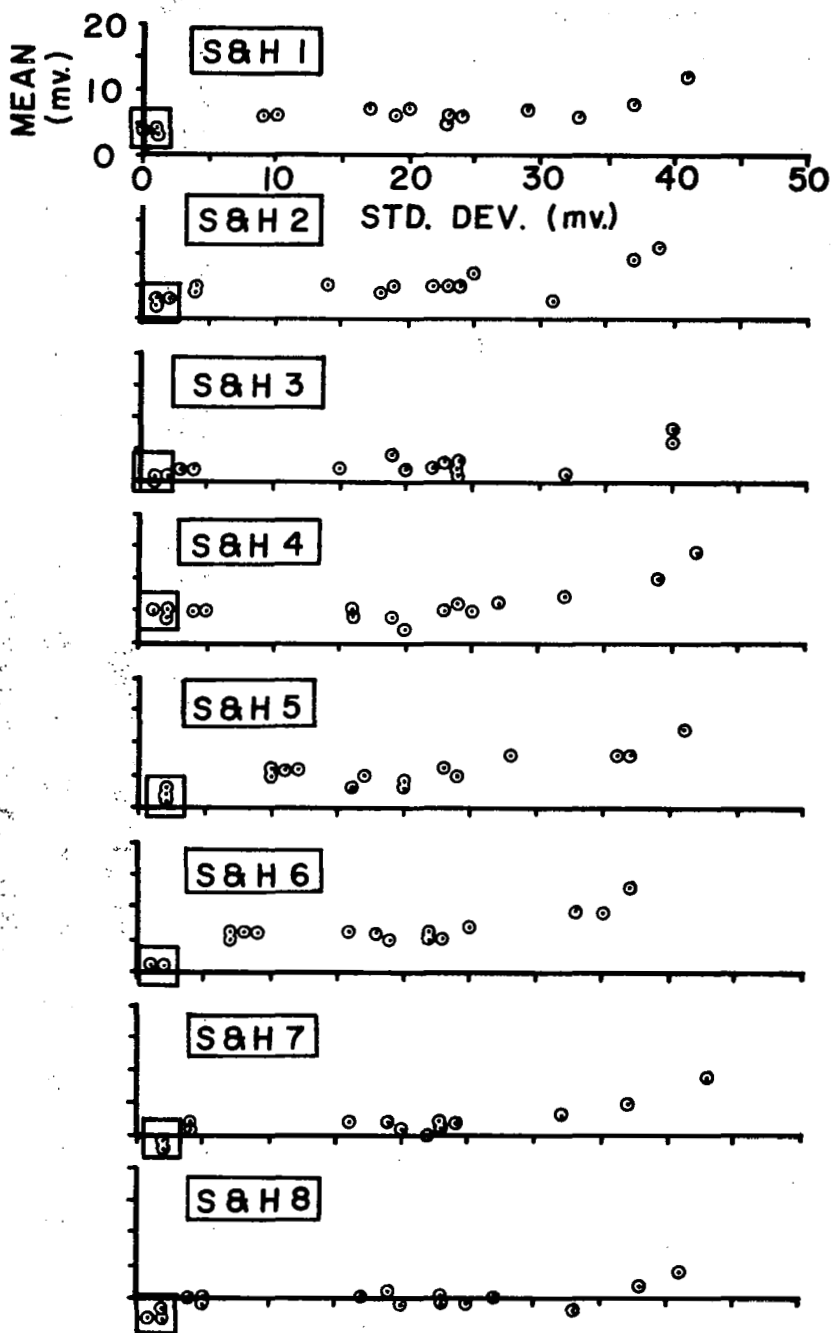


Figure 5. Comparison of "noise only" recorded means and standard deviations of the S&H "input" voltage for all eight gates.

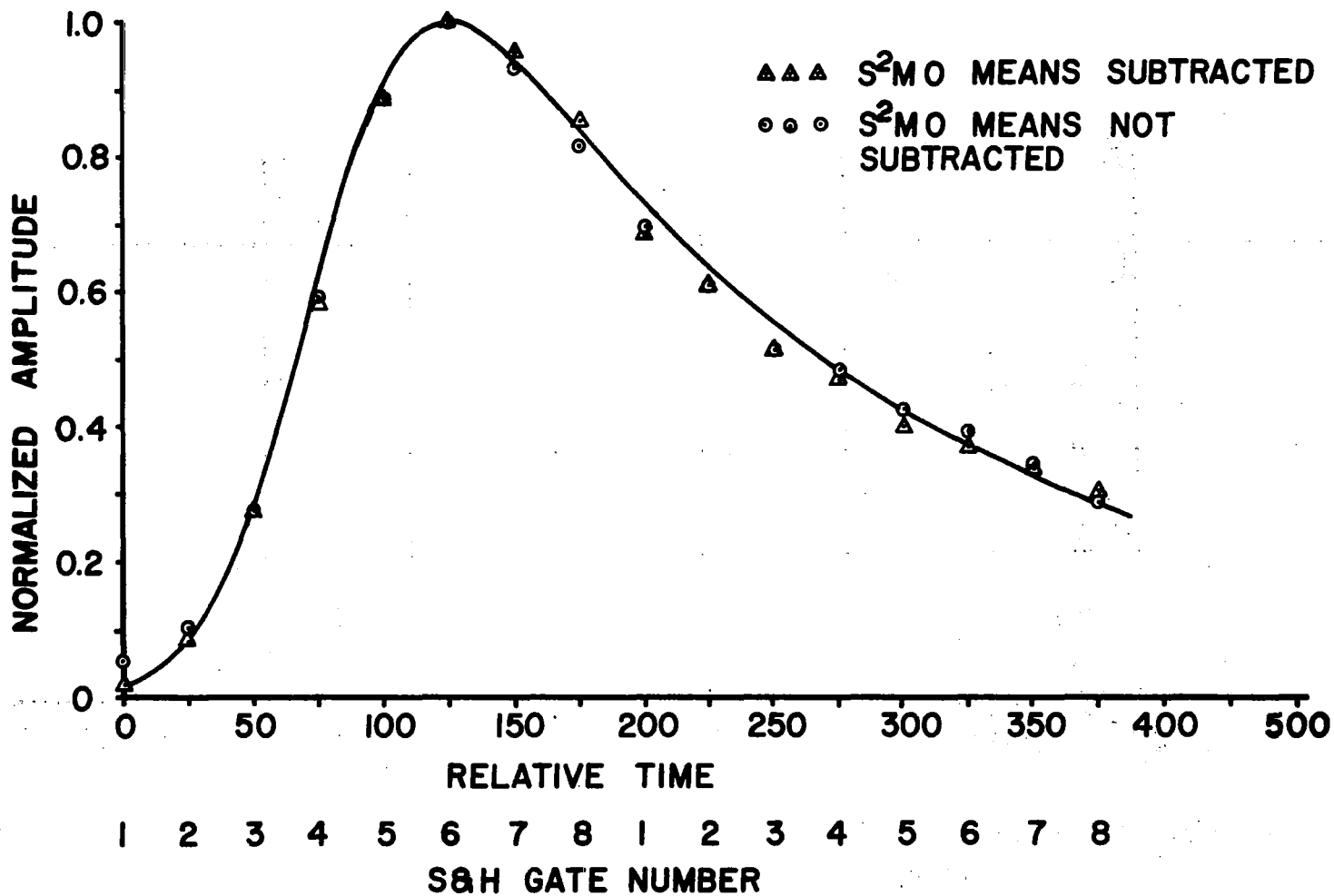


Figure 6. Comparison of average waveform data with (and without) Submode 0 mean subtraction and the theoretical return for $\xi = 0.15^\circ$ (SL-2 EREP Pass 4, Mode I, Submode 0).

one and two in the leading edge of the return. Those cases where the "noise only" corrected data appear to provide a weaker fit to the expected return are typified by a sharp discontinuity between S&H gates 7 and 8 of S²M 1 and S&H gate 1 of S²M 2. Since this discontinuity "smooths out" if the "noise only" correction is ignored and since there is no known reason for the discontinuity, the procedure of subtracting the "noise only" mean values from the signal plus noise means was rejected for all S&H recorded data except S&H one and two in S²M 1.

In the signal plus noise portion of the sampled time delay expanse (S²M 1 and S²M 2), two unexpected factors were observed. The first and most important was saturation of either the video amplifier or the S&H circuitry. This was detected by noting that for mean values greater than about 0.08 volt, the corresponding standard deviation was considerably less than the mean. A histogram of the voltages recorded by the S&H gate in question did indeed show a distinct "pile-up" of values in the range of 0.37 to 0.38 volts, depending on the particular S&H gate. This effect was due to the fact that some part of the post detection portion of the receiver had an insufficient dynamic range to accommodate the exponential statistics. This effect could be approximately corrected based upon knowledge of the statistics resulting from an infinite number of sampled pulses. If $f(v)$ is the exponential density function of the true input process with mean $\bar{v}(\tau)$, the density after saturation is given by $\tilde{f}(v)$ where

$$\tilde{f}(v) = f(v) \left[U(v) - U(v - V_s) \right] + \delta(v - V_s) \\ \cdot \frac{1}{\bar{v}(\tau)} \int_{V_s}^{\infty} e^{-v/\bar{v}(\tau)} dv$$

and $U(\cdot)$ is the unit step function, $\delta(\cdot)$ is the delta function, and V_s is the saturation voltage. Completing the above integral yields, for the saturated process,

$$f(v) = \frac{1}{\bar{v}(\tau)} e^{-v/\bar{v}(\tau)} \left[U(v) - U(v-V_s) \right] + e^{-V_s/\bar{v}(\tau)} \delta(v-V_s)$$

The mean after saturation is given by the following;

$$E_s\{v\} = \bar{v}(\tau) \left[1 - e^{-V_s/\bar{v}(\tau)} \right]$$

With β equal to the ratio of the saturated mean to the true mean, i.e. $E_s\{v\}/\bar{v}(\tau)$, and α equal to $V_s/\bar{v}(\tau)$, the above equation can be rewritten as;

$$\beta = 1 - e^{-\alpha}$$

or

$$\frac{\alpha}{\beta} = \frac{\alpha}{1 - e^{-\alpha}}$$

However, since $\alpha/\beta = V_s/E_s\{v\}$,

$$\frac{V_s}{E_s\{v\}} = \frac{\alpha}{1 - e^{-\alpha}} \quad (6)$$

A graph of equation (6) is shown in Figure 7. Thus, given the saturation voltage V_s and the mean value after saturation, it is possible to obtain α from Figure 7 and thus the true (non saturated) mean value, $\bar{v}(\tau)$. It should be noted from Figure 7 that once the ratio $V_s/E_s\{v\}$ exceeds about five, α is equal to $V_s/E_s\{v\}$ and, thus, $\bar{v}(\tau) = E_s\{v\}$.

Using the above expressions for $f(v)$, it can be shown that the variance of the saturated output is given by the following;

$$\text{Var}_s\{v\} = [\bar{v}(\tau)]^2 \left[1 - 2\alpha e^{-\alpha} - e^{-2\alpha} \right] \quad (7)$$

The true input mean could also be computed from the variance of the saturated

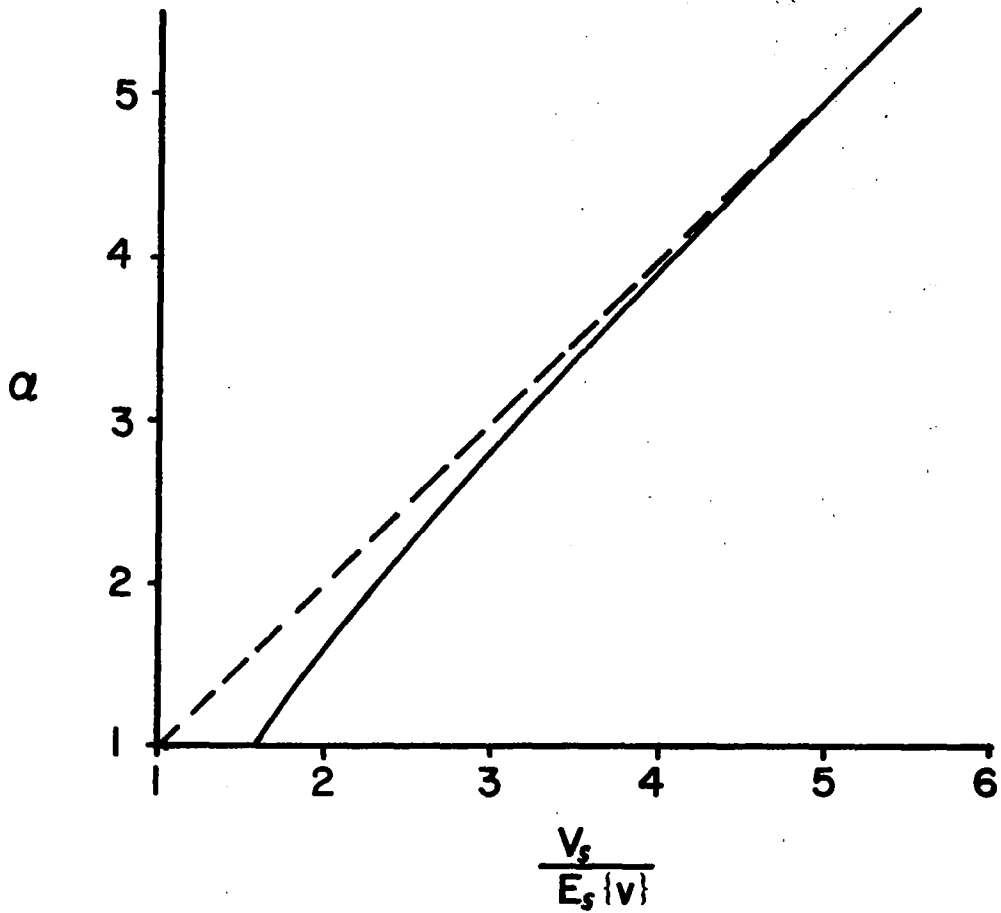


Figure 7. A graph of the relationship between the ratio of the saturation voltage to the true input mean as a function of the ratio of the saturation voltage to the saturated mean value.

process; however, experience has shown that this is not as accurate as obtaining the true mean from the saturated mean data. This occurs because the variance is much more sensitive to the details of the saturation process, i.e. soft versus hard saturation. Also inversion of the variance data is more greatly influenced by the number of recorded saturated voltages.

The saturation correction procedure developed above is approximate in two regards. First of all, the correction logic is based upon infinite sample statistics and not upon the finite number of samples that are actually available for analysis. Thus, for less than 100 or 200 samples, the procedure is certainly prone to error. A second shortcoming of the procedure is the assumption of hard saturation. Analysis of histograms indicated that the saturation did not occur at one particular voltage but was spread over a range of voltages having a width of about 0.01 to 0.015 volts. This soft saturation problem could have been overcome by processing the waveform data with an artificial saturation voltage which was lower than the soft saturation region. This was not done, however, because the error was not considered to be significant. The effect of saturation on the mean return waveform is shown in Figure 8 in which raw S&H average data are compared with the saturation corrected means. One other point should be mentioned in regard to saturation. The calibration curves relating S&H output (in PCM counts) to input (in volts) did not exhibit a saturation until the input voltage reached 0.4 volt. The saturation levels of the in-flight recorded waveform data never exceeded 0.381 volt. Thus, there was a 0.02 volt discrepancy between the preflight measured post detection saturation level and the in-flight data. The cause of this difference could not be explained.

A second phenomenon observed in the signal plus noise portion of the return involved the statistical distribution of the voltages recorded by the S&H gates. As previously noted, the probability density of the fluctuating voltage should, in theory, be exponential with a "pile-up" at the saturation voltage. Figures 9 through 20 compare measured and computed probability density functions for the voltages recorded by various S&H gates in S²M (sub sub mode) 0 through 2 for EREP Pass 4, Mode V, submode 0. The measured densities were obtained from histogram data based upon 520 recorded voltages. The computed densities were found by first correcting the raw

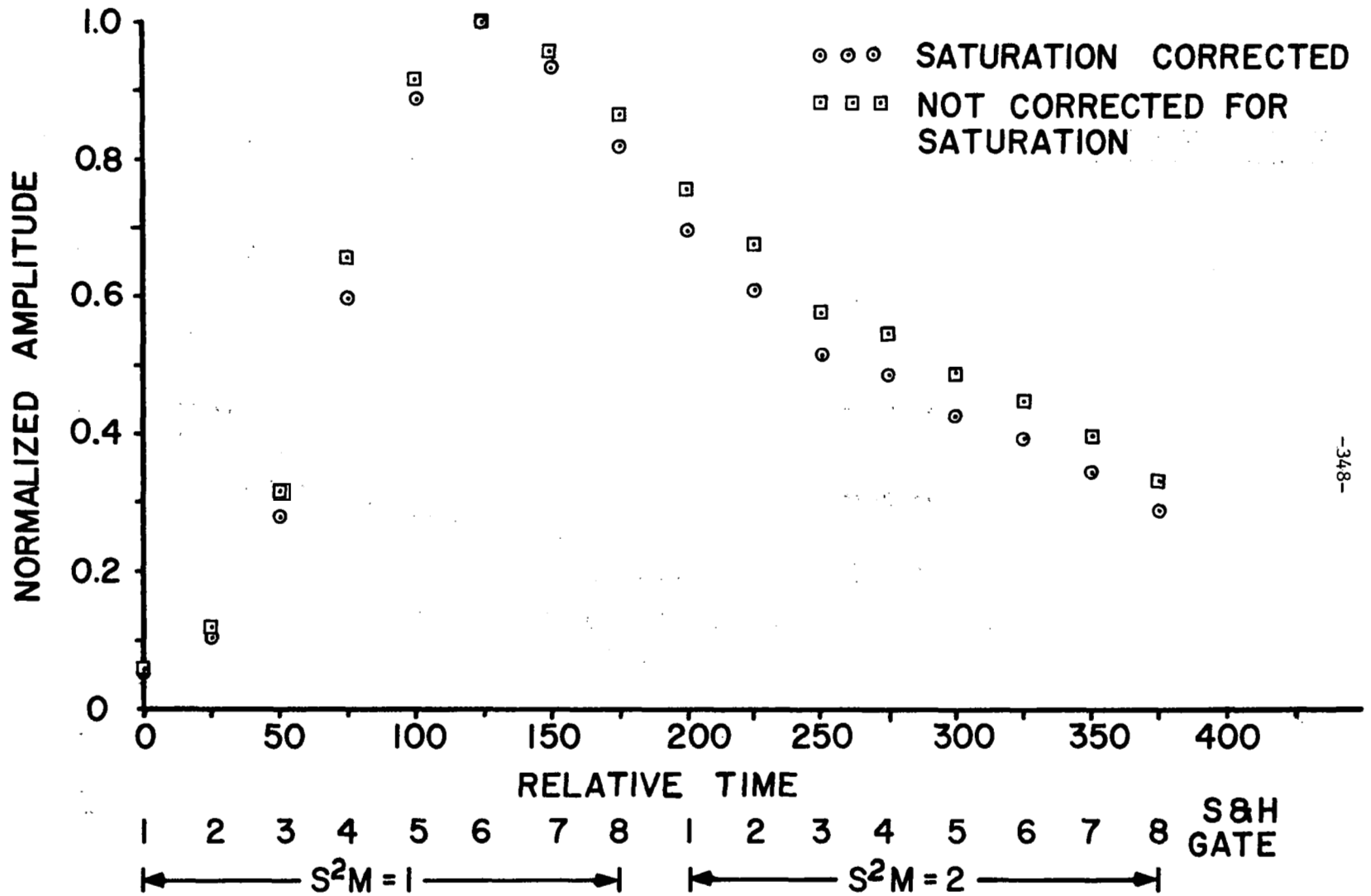


Figure 8. An illustration of the effect of saturation on the average return waveform (SL-2 EREP Pass 4, Mode I, Submode 0).

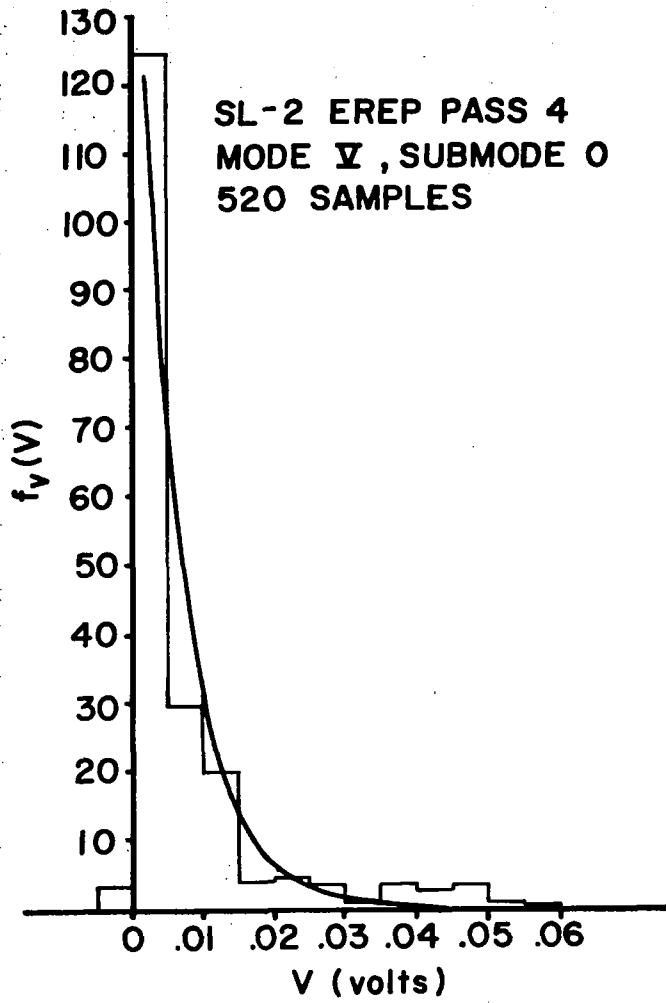


Figure 9. Measured and computed probability densities for S&H ($S^2M 0$).

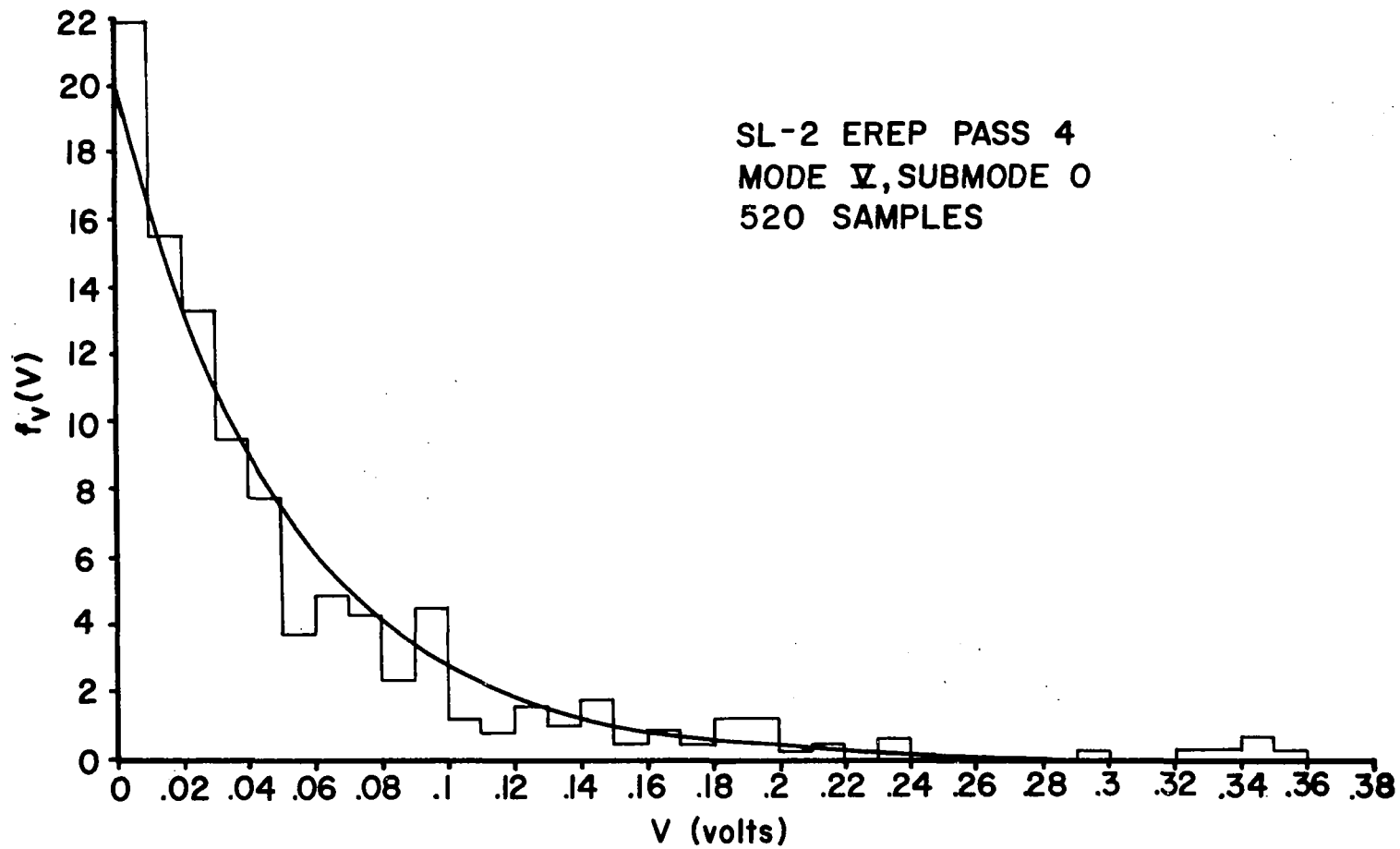


Figure 10. Measured and computed probability densities for S&H 3 ($S^2M 1$).

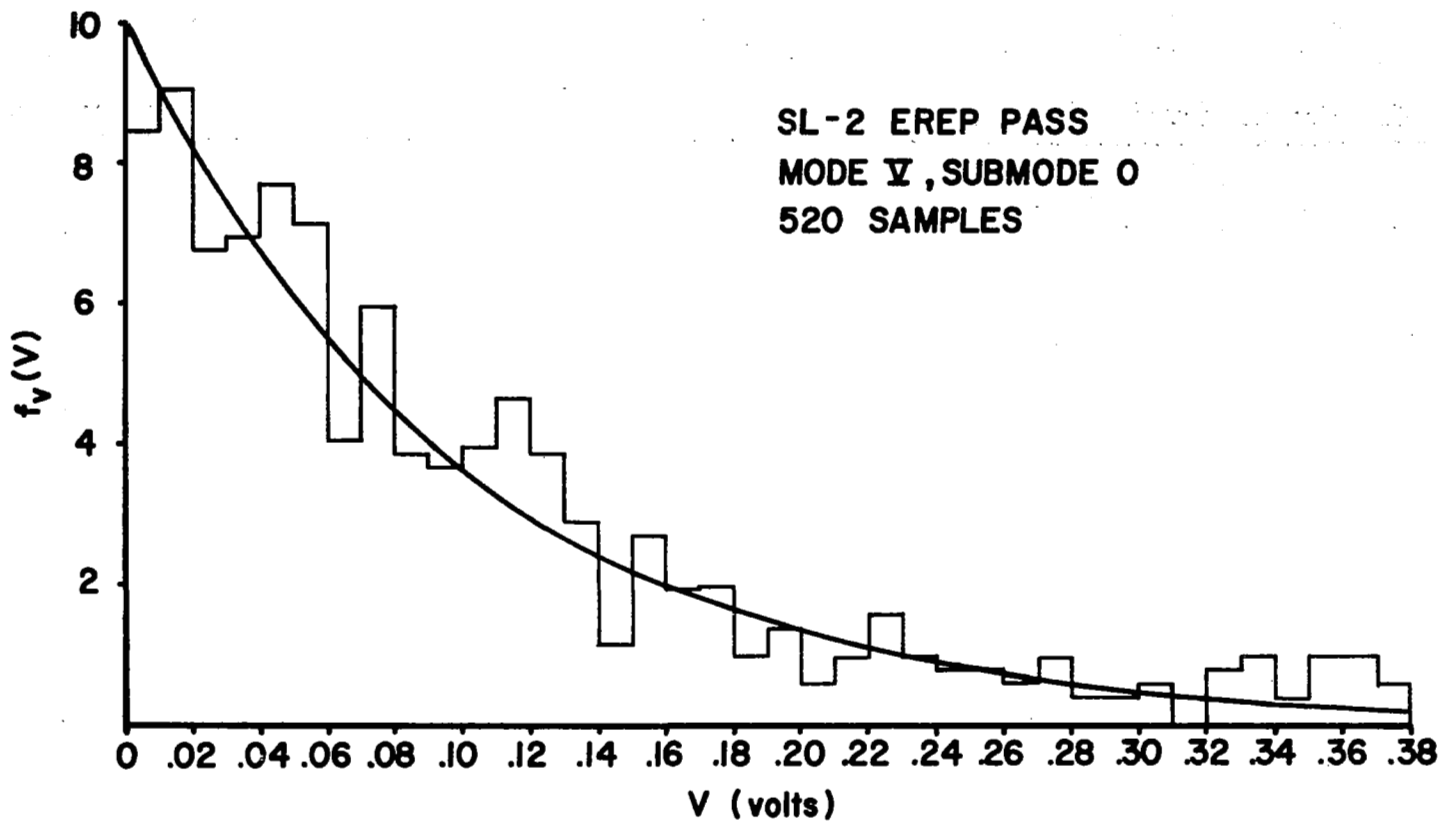


Figure 11. Measured and computed probability densities for S&H 4 ($S^2 M 1$).

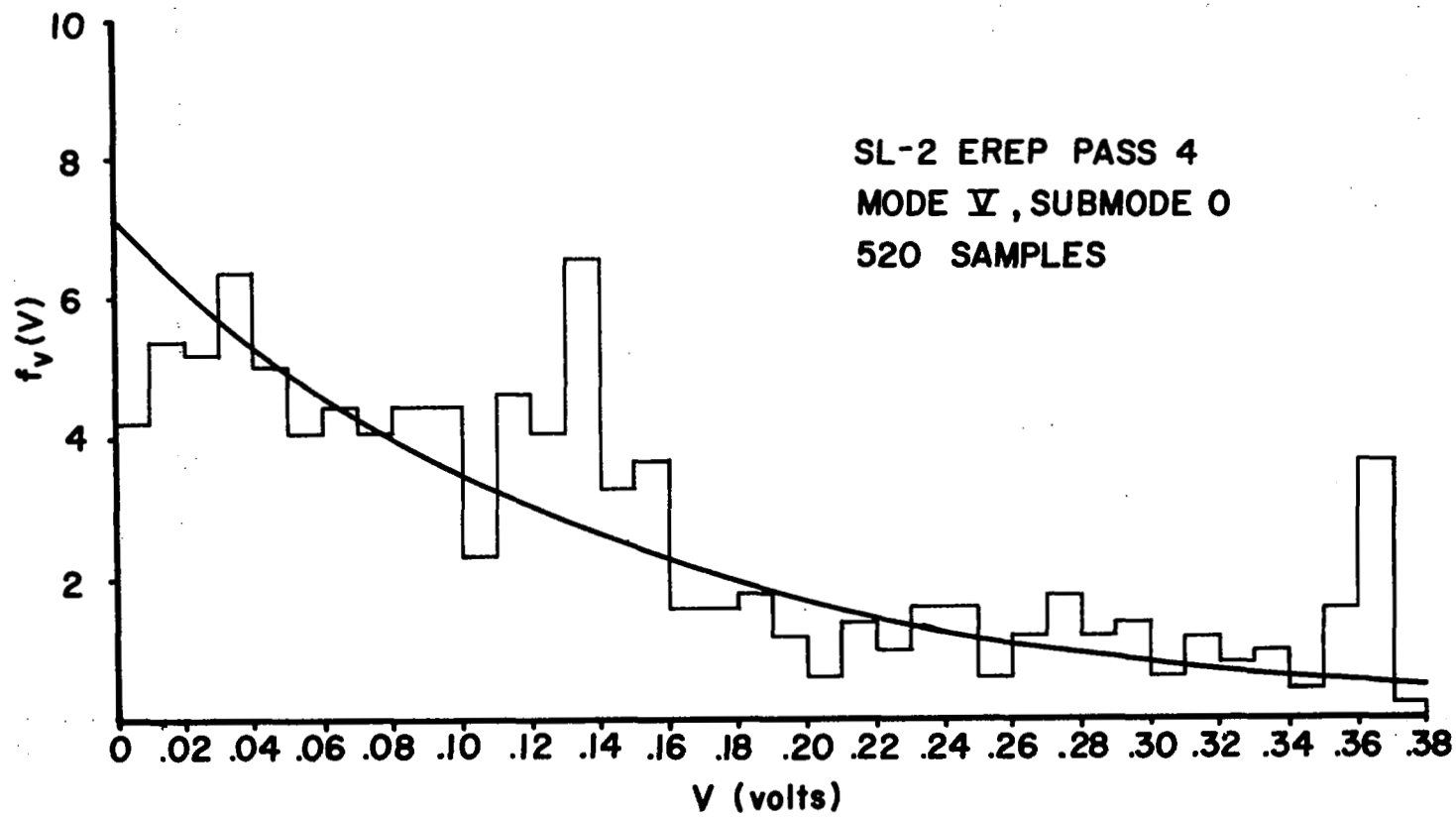


Figure 12. Measured and computed probability densities for S&H 5 ($S^2_M 1$).

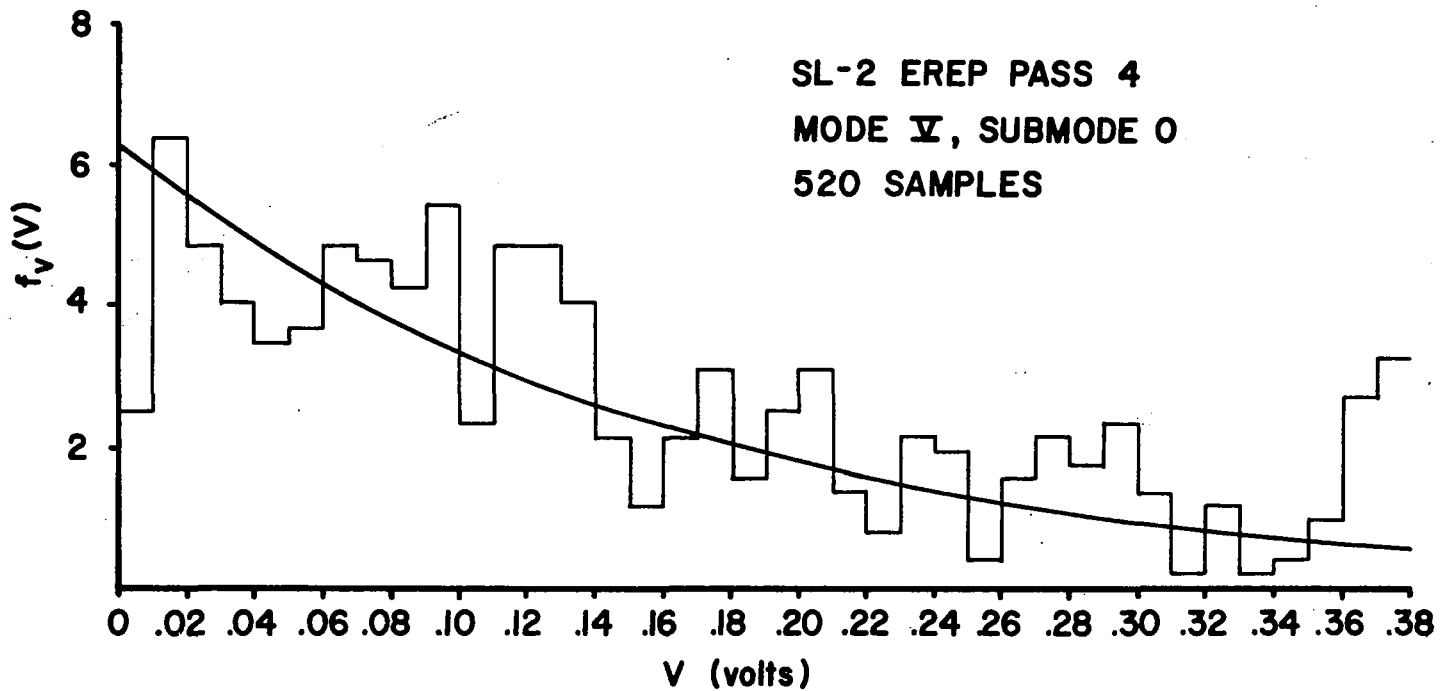


Figure 13. Measured and computed probability densities for S&H 6 ($S^2M 1$).

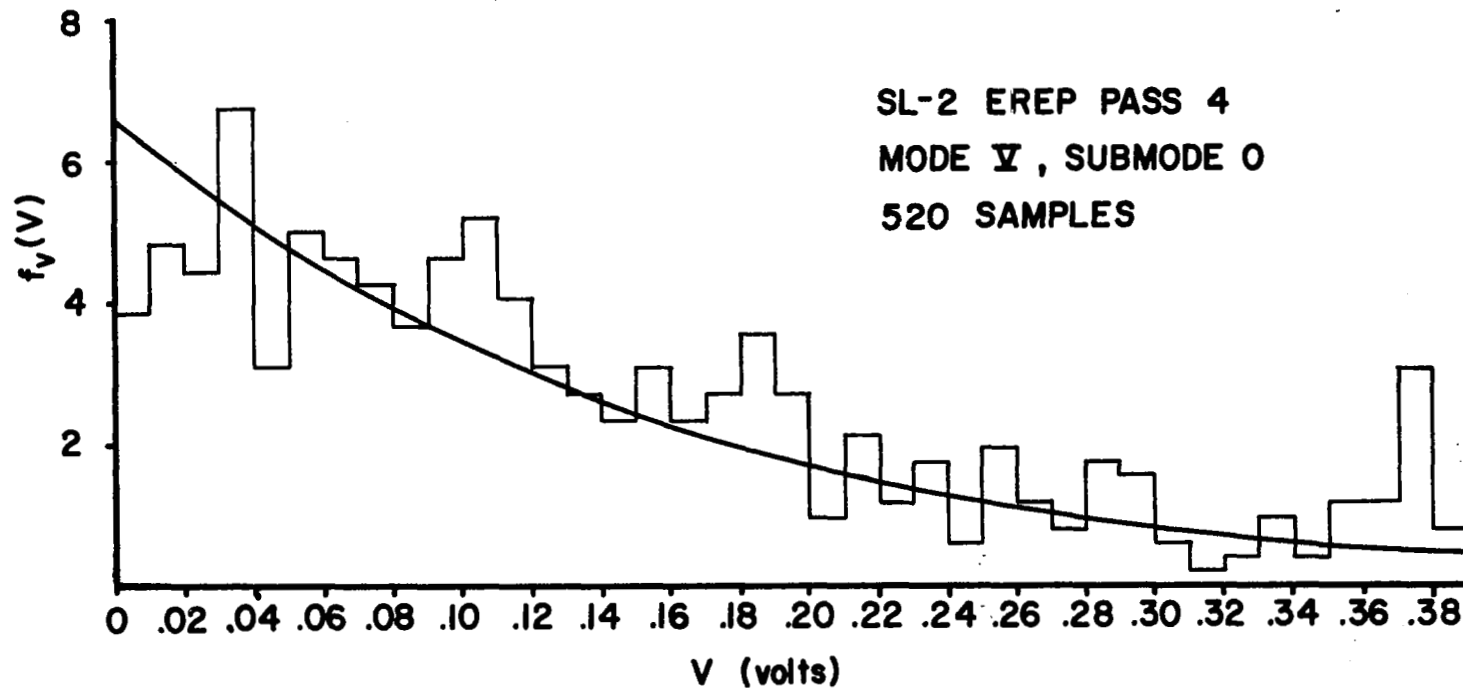


Figure 14. Measured and computed probability densities for S&H 7 ($S^2_M 1$).

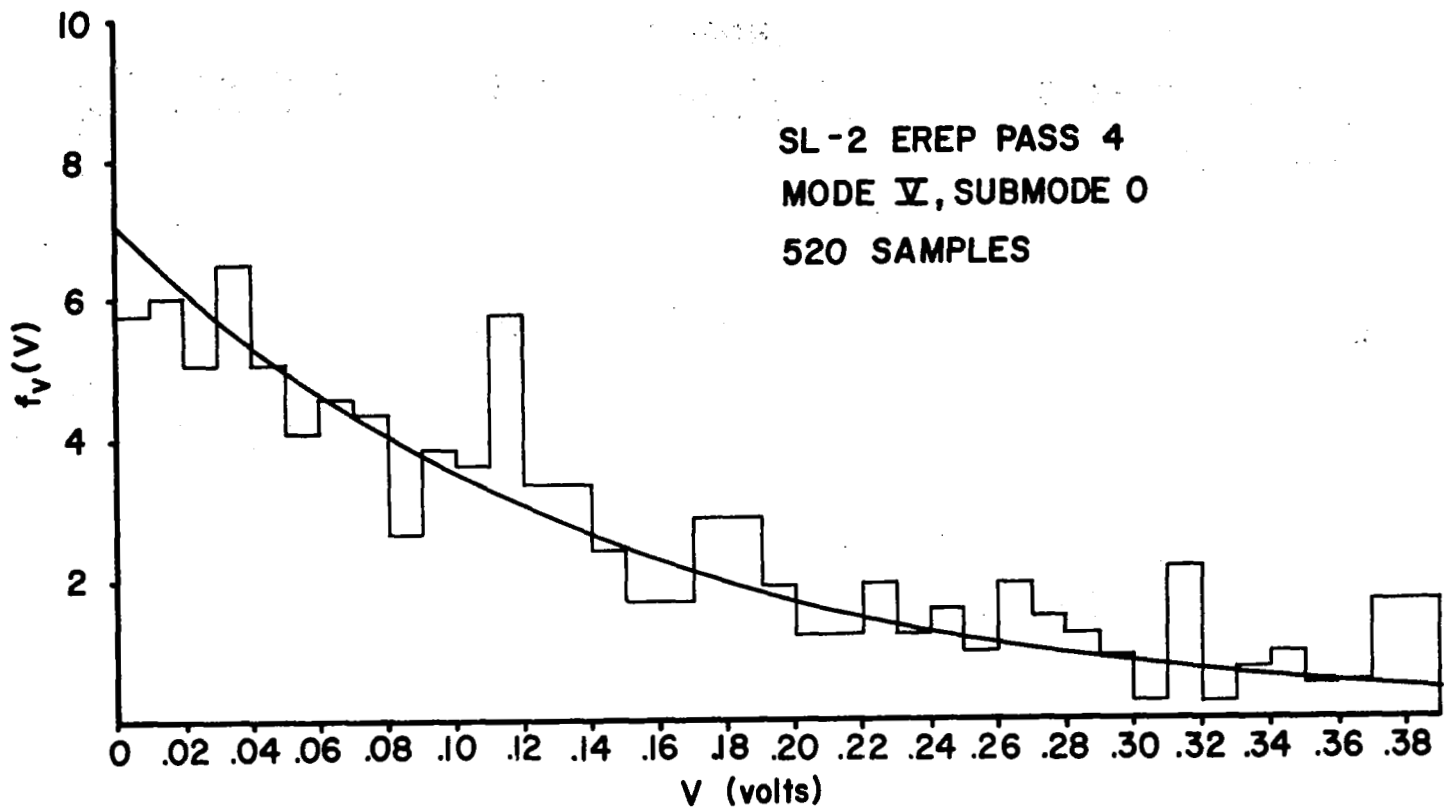


Figure 15. Measured and computed probability densities for S&H 8 ($S^2_M 1$).

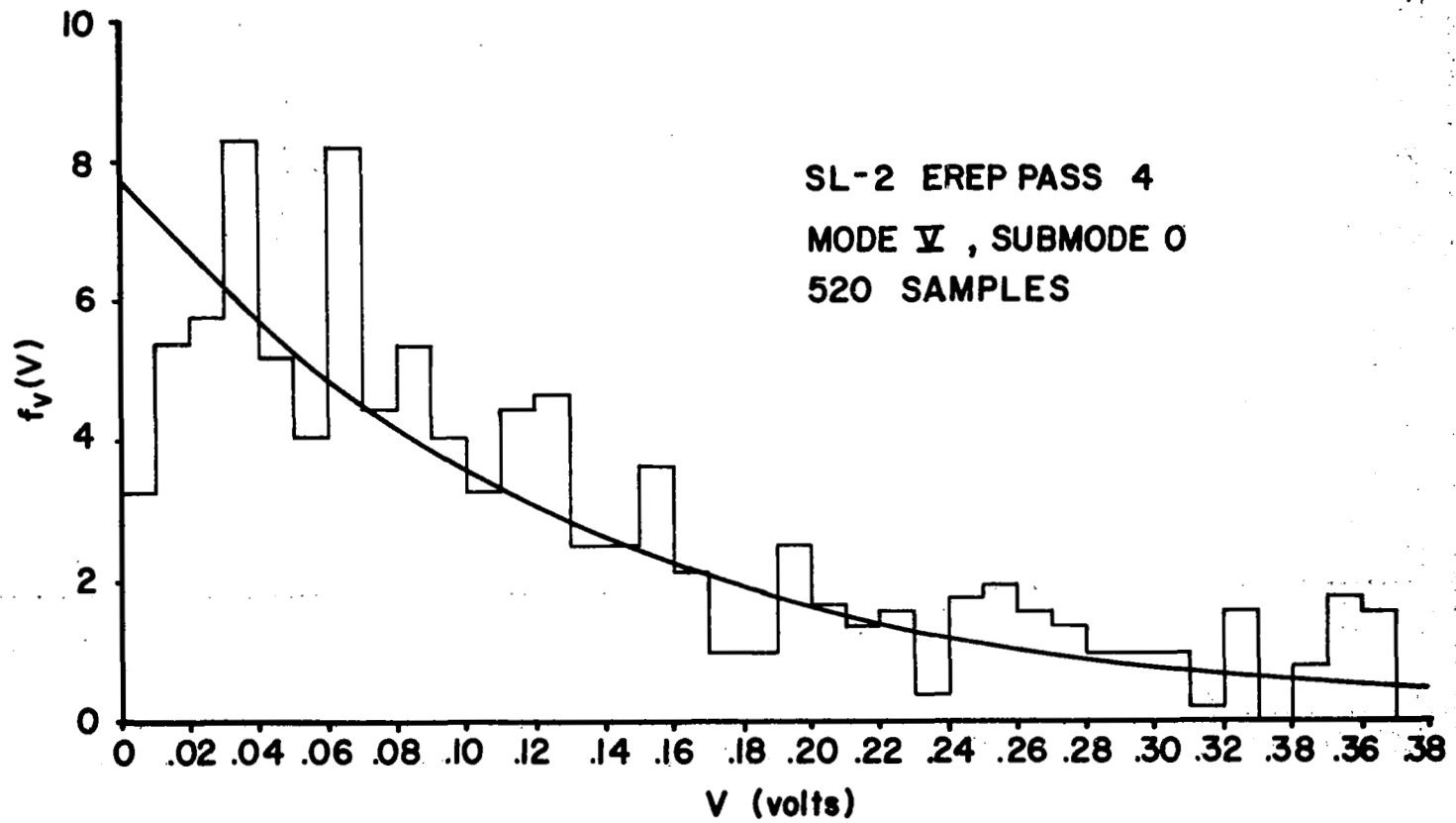


Figure 16. Measured and computed probability densities for S&H 1 ($S^2 M^2$).

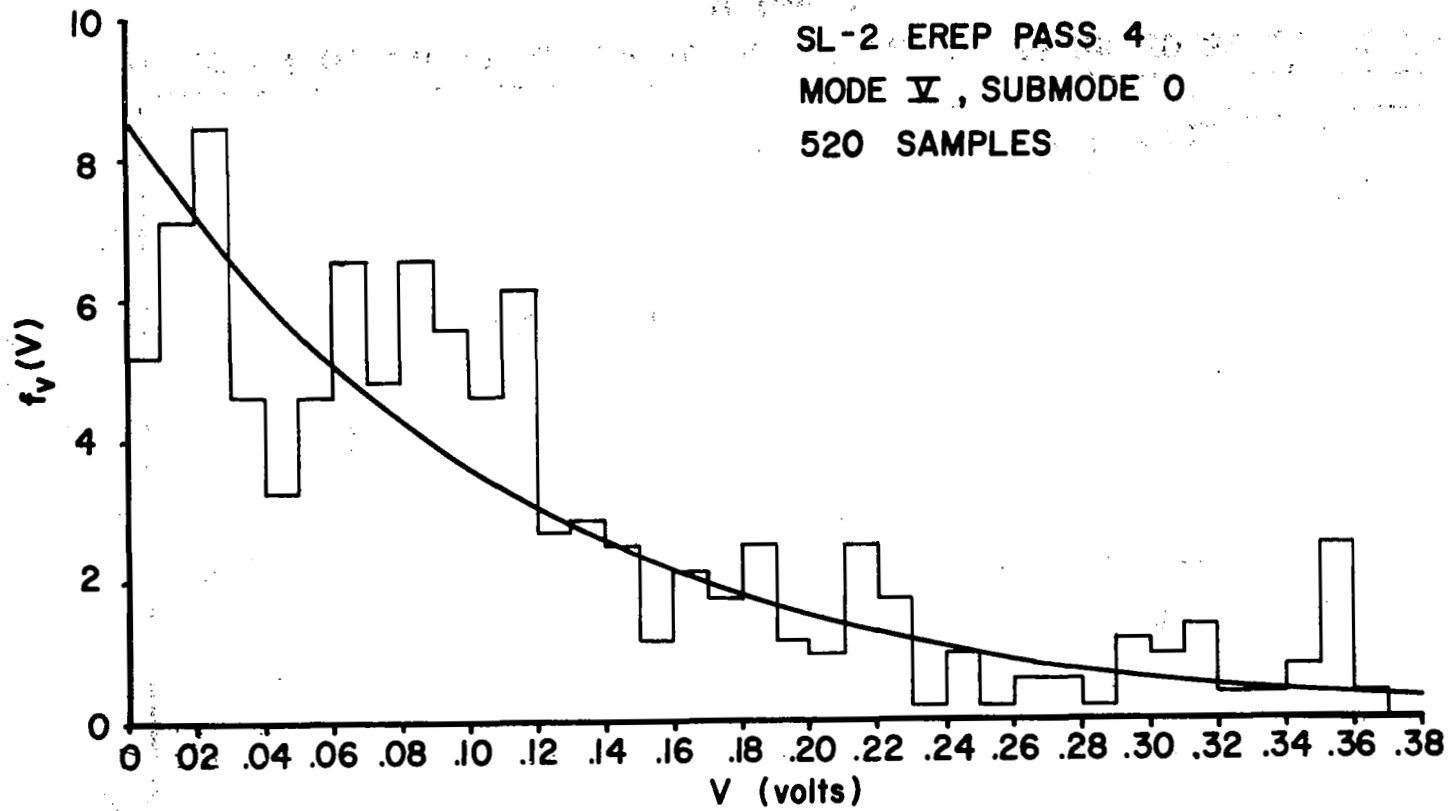


Figure 17. Measured and computed probability densities for S&H 2(S²M 2).

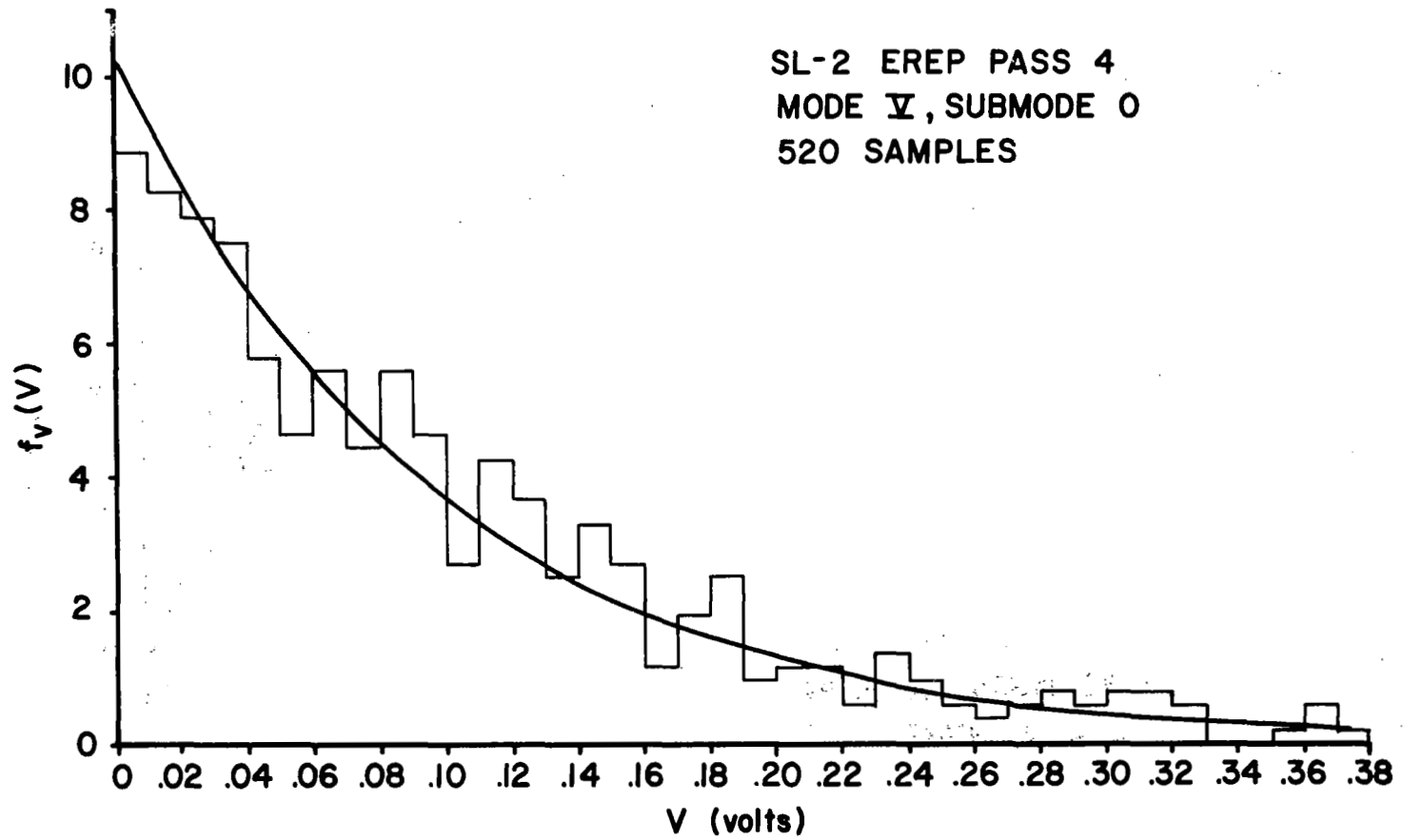


Figure 18. Measured and computed probability densities for S&H 3 ($S^2M 2$).

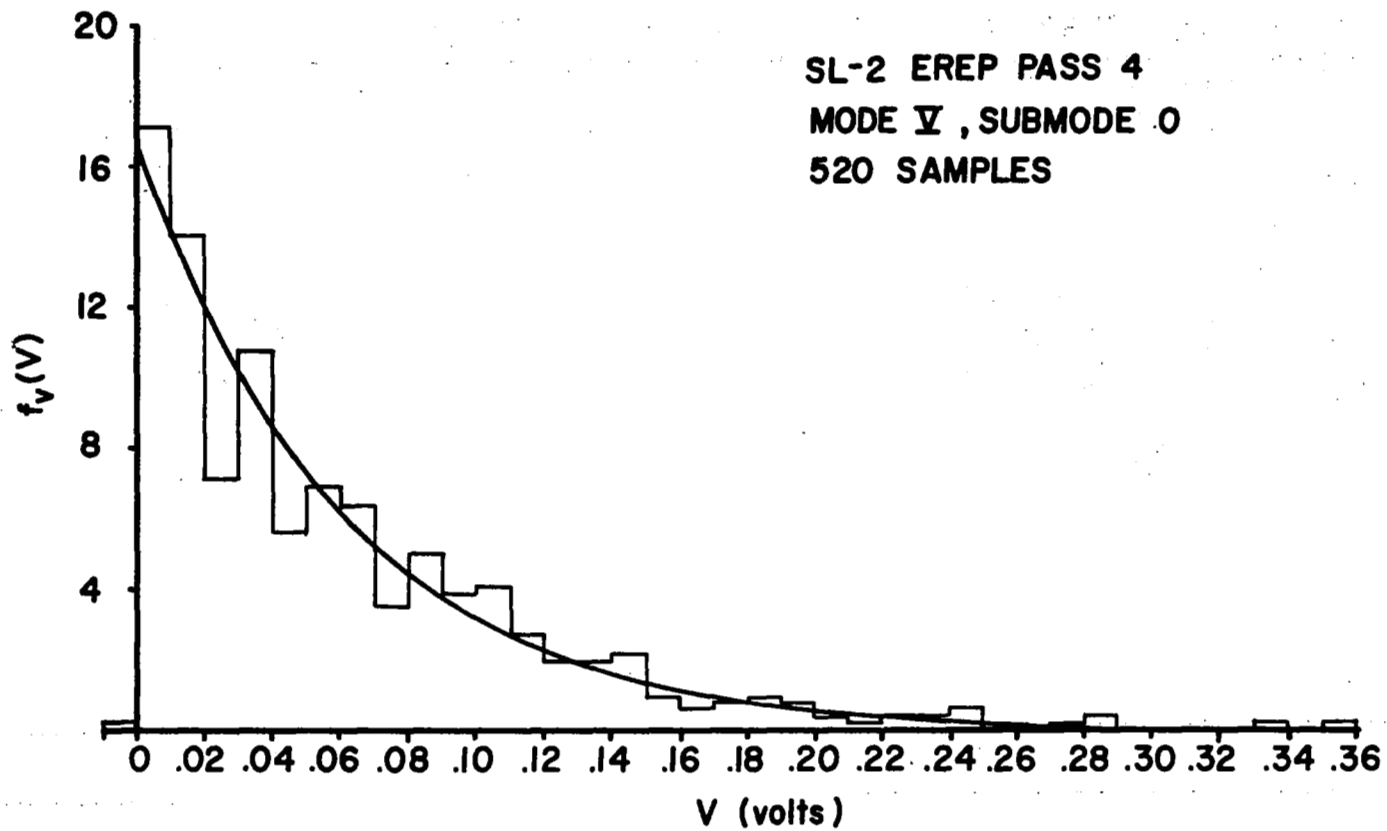


Figure 19. Measured and computed probability densities for S&H 7 ($S^2_M 2$).

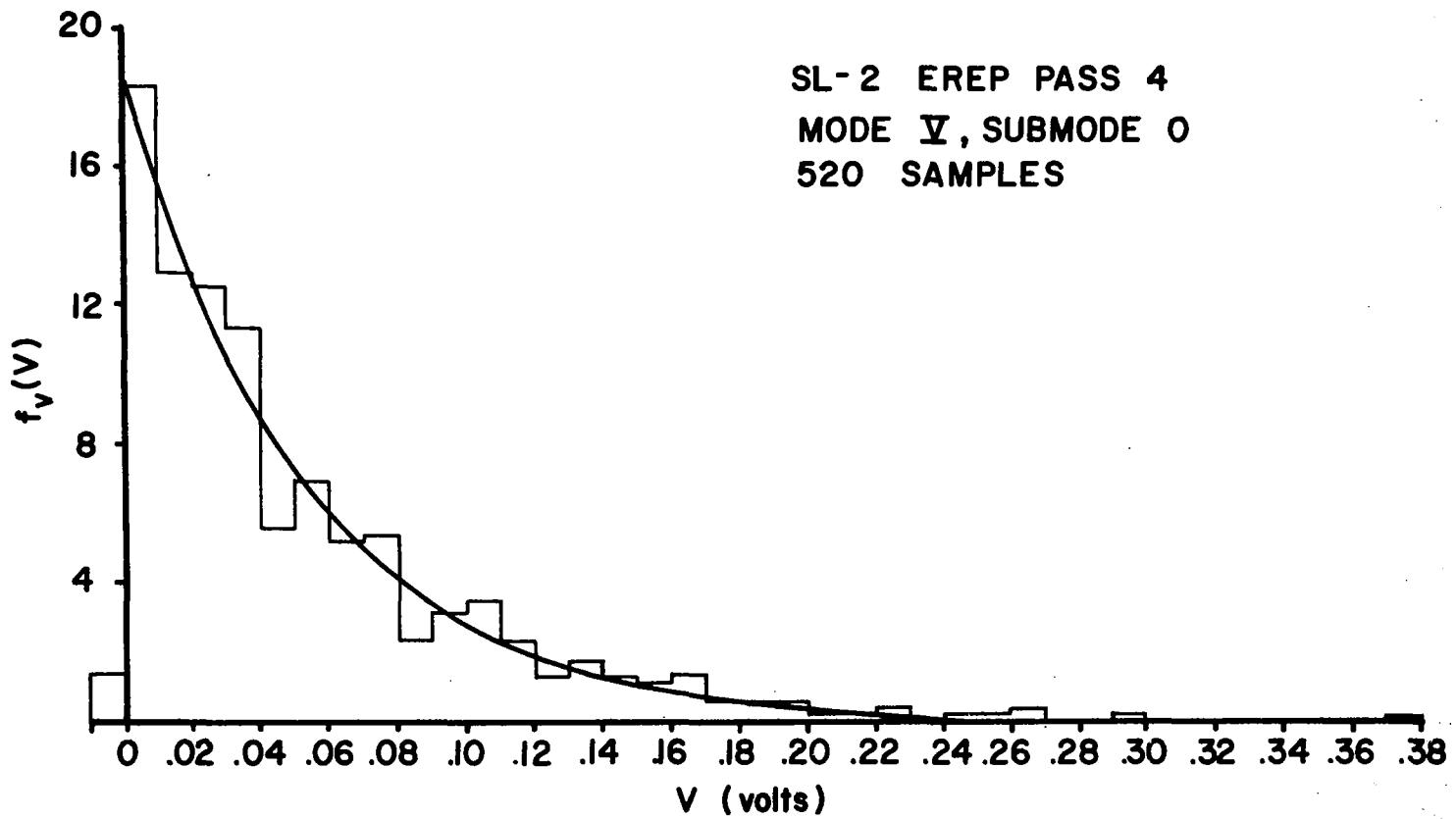


Figure 20. Measured and computed probability densities for S&H 8 ($S^2M 2$).

mean for saturation, if necessary, and then substituting in the following;

$$f_v(v) = \frac{1}{\bar{v}(\tau)} e^{-\frac{v}{\bar{v}(\tau)}} U(v) .$$

The data presented in Figures 9 through 20 is representative of nearly all 100 ns/10 MHz data obtained during SL-2 and SL-3.

Referring to Figure 8 for the location (on the mean return) of each S&H gate in each S^2M , we see that there is generally good agreement between measured and computed densities. In particular, we note the "pile-up" in the neighborhood of $v=0.37$ volts, especially for the S&H gates located in the vicinity of the peak of the mean return. One disturbing fact about these data is the behavior of the measured probability densities near $v=0$. More specifically, as the saturation effect becomes more pronounced, the density near $v=0$ is less abrupt in its rise from zero to some non-zero value. This effect is very well illustrated in Figures 11 through 14 which sequentially represent moving up the leading edge of the mean return, and Figure 16 through 20 which represent moving down the trailing edge of the return. It is tempting to associate this observed distortion in the density function with the saturation since they appear to occur simultaneously. However, other test data have shown that the two effects are not coupled; density distortion has been observed in the absence of saturation [5]. A more detailed examination of the probability density measurements in Figures 9 through 20 tends to indicate that the distortion effect may be a function of the particular S&H gate which recorded the data. For example, of all the S&H gates which indicated saturation, S&H 8 produced the least distortion in the measured density near $v=0$ (see Figure 15). In addition, this same gate appeared to be the "best" reproducer of the noise only data as shown in Figure 5; that is, S&H 8 most nearly produced the zero mean nature of the ac-coupled noise. These two observations might be construed to imply that the noise-only nature of the recorded data and the density distortion were due primarily to the design (or construction) of the individual S&H gates. Without further test data, it is impossible to prove this conjecture; however, the in-flight data certainly seems to indicate such a circumstance. The question of primary concern, namely, what is the impact of the density

distortion upon the saturation corrected mean must, unfortunately, also go unanswered since we do not know the source of the distortion. For the purposes of data analysis and reduction, we have ignored the effect.

The lack of technical data on the design of the S&H gates does not prevent us from theorizing as to the source of the density distortion. A number of different probability density functions were fitted to the data to determine the best fit. These functional forms included Rayleigh, Rice (sine wave plus noise), log normal, contaminated log normal and the gamma density [6]. The best fit appeared to be provided by the gamma density; the other functional forms reached their peak at too large a voltage to represent the measurement data in Figures 11 through 18. The gamma density has the following form [6];

$$f_v(v) = \frac{N^N v^{N-1}}{\{\bar{v}(\tau)\}^N \Gamma(N)} \exp \left\{ -\frac{N}{\bar{v}(\tau)} v \right\} U(v)$$

where $N \geq 1$ but is not necessarily an integer and $\Gamma(\cdot)$ is the gamma function. The average of v is $\bar{v}(\tau)$ and the standard deviation is $\bar{v}(\tau)/\sqrt{N}$. For $N=1$, the density becomes exponential; as N increases, the mean remains constant, the standard deviation decreases, and the slope of the density at $v=0$ decreases. Thus, with only slight variations in N it is possible to produce a very good fit to the type of measured data shown in Figures 11 through 18.

It is interesting to note that the gamma density is an approximate form for expressing the effects of post-detection filtering on white noise in a heterodyne receiver [6]. It is also tempting to say that the S&H gates are therefore acting as post-detection filters whose equivalent time constant is greater than the inverse noise bandwidth of the IF filter. However, this statement alone can not explain why the measured densities appear to be exponential for small mean values (such as in Figure 19 for S&H 7) and gamma for large means (such as in Figure 14 for S&H 7). To explain such an effect would require the parameter N to be a function of the mean $\bar{v}(\tau)$, i.e. a nonlinear behavior. In other words, we arrive at the same conclusion that was previously conjectured; namely, we are most probably dealing with a nonlinear effect such as, possibly, hysteresis in the design of the S&H gates.

The purpose of this section has been to review some of the anomalous

characteristics of the 25 ns Sample and Hold gates which were observed in the waveform data. Because of a lack of detailed design information on the devices, it was not always possible to identify the source of the behavior. It was therefore necessary, for the most part, to rely upon engineering judgement in evaluating the effect upon the data. It is important, however, to note that the observed effects were relatable to the S&H gates and not the data, per se. This section clearly demonstrates that not all the problems of high speed Sample and Hold design and construction are completely understood at least in regard to altimetry.

6.0 Estimated Average IF Single Pulse Signal-To-Noise Ratio

One of the most important measures of a conventional radar's ability to detect and track a finite size target is the IF signal-to-noise ratio (SNR). Although the situation is further complicated in the case of a radar altimeter due to the random nature of the surface, the IF signal-to-noise ratio remains an important indicator of system capability. As demonstrated in earlier chapters of this report, the precision of altitude, surface roughness and pointing angle measurements are directly affected by SNR. Because of AGC nonlinearities, estimation of σ^0 from altimeter data is also degraded by low SNR conditions [2]. For these reasons it is important that estimates of IF SNR be presented in this report.

Figure 21 is a block diagram of those parts of the S-193 system which are important to a discussion of SNR. The antenna and the tunnel diode amplifier/mixer* are common to the three systems comprising the S-193 instrument - the altimeter, radiometer and scatterometer, while the remaining parts are components in the altimeter transmitter or receiver. Of particular interest are the various combinations of transmitted pulsewidths (nominal) and IF bandwidths possible in the altimeter. These combinations, along with the video bandwidths, are summarized in Table III; the designation "PC" refers to the 13-bit Barker code pulse compression implementation. Referring to Figure 21, the peak of the average received power at the output of the IF filters is determined from the following equation;

*In S-193 nomenclature, the tunnel diode amplifier/mixer is referred to as the integrated receiver.

MODULATION

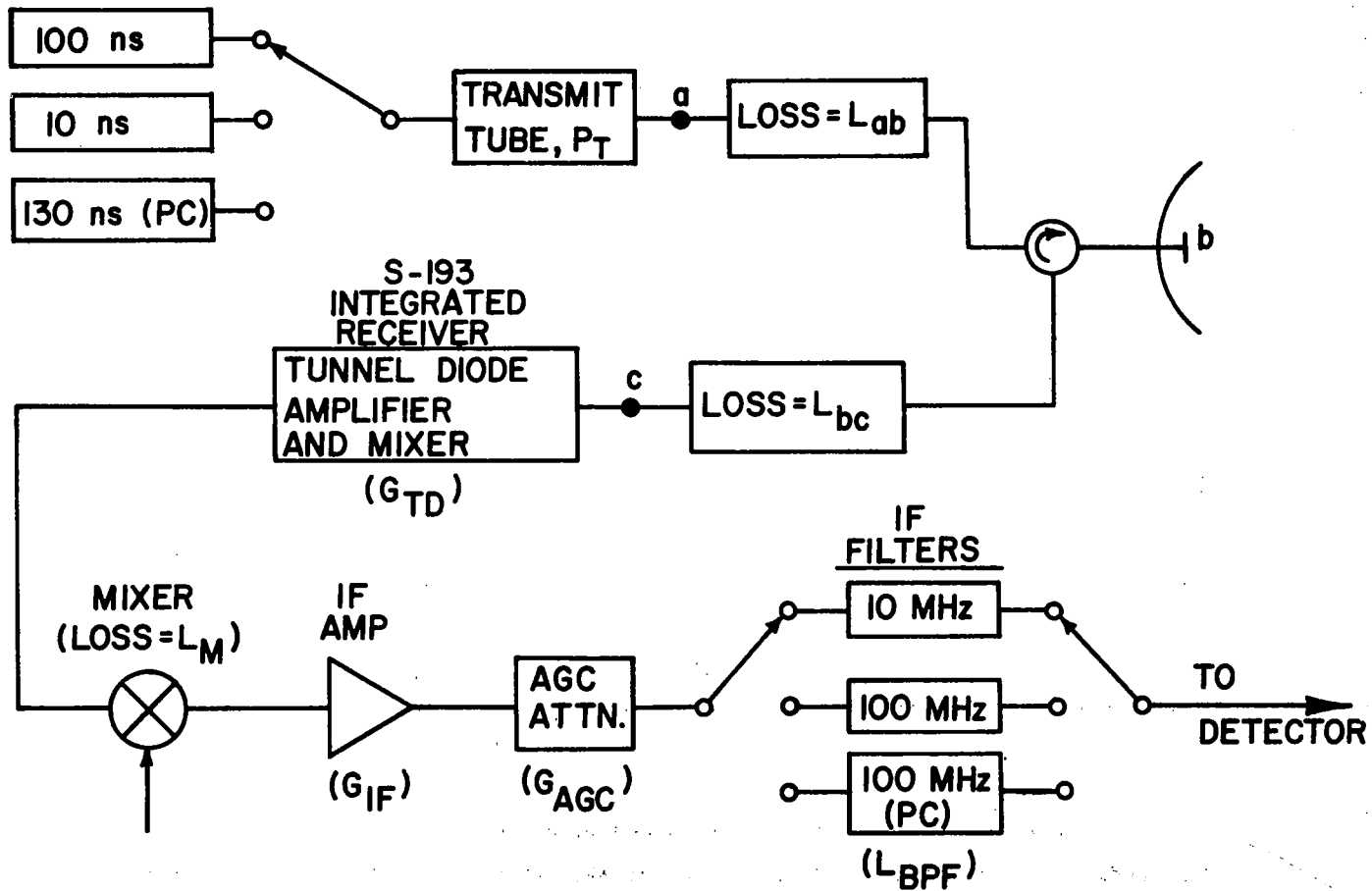


Figure 21. Appropriate S-193 block diagram for estimating the average IF single pulse signal-to-noise (SNR).

TABLE III

Measured Values And Nomenclature For The Radar Altimeter Pulsewidth, IF Bandwidth (two-sided), and Video Bandwidth (one-sided) Possible Combinations From [3].

PREDETECTION PULSEWIDTH (ns)		3 dB IF BANDWIDTH (MHz)		3 dB VIDEO BANDWIDTH* (MHz)	
Nomenclature	Measured	Nomenclature	Measured	Nomenclature	Measured
100	~ 72	10	12.8	50	60
100	~ 100	100	115.3	50	60
10	~ 20	100	115.3	50	60
10(PC)	~ 10	100	115.3	50	60

*This is the video bandwidth as seen by the waveform samplers and the AGC. The video bandwidth as seen by the tracking loop was 5 MHz due to the presence of a 5 MHz low pass filter ahead of the tracking loop. This filter was added to make the 10 ns average return appear (to the tracker) as a 100 ns return and therefore avoid a separate tracking loop for the short pulse mode.

$$\left(\frac{\hat{P}_r}{P_T}\right)_{IF} = \left(\frac{P_T}{L_{ab}}\right) \hat{F} \left(\frac{\eta G_{TD} G_{IF} G_{AGC}}{L_{bc} L_M L_{BPF}}\right) \quad (8)$$

Apart from \hat{F} , the various system gains and losses in (8) are defined in Figure 21. The factor \hat{F} is essentially the peak of the average received power per unit transmitted power at the output of the antenna [2]; it depends upon the altitude (h), pointing angle with respect to nadir (ξ), antenna gain, surface scattering cross section (σ^0) and the effective IF pulse-width. The η in equation (8) is the pulse compression gain ($\eta=1$ for no pulse compression). Of course, it has been assumed in (8) that the bandwidths of the components in Figure 21 are sufficiently wide to pass (without frequency dependent attenuation) the fading nature of the return power. In a similar fashion, the average IF noise power is given by

$$(\bar{N})_{IF} = (kT_e) \left[\frac{G_{TD} G_{IF} G_{AGC}}{L_M L_{BPF}}\right] (B_{IF})_n \quad (9)$$

where k is Boltzmann's constant, T_e is the equivalent noise temperature of the receiver front end and $(B_{IF})_n$ is the noise bandwidth of the appropriate IF bandpass filter. For altimetry, the signal-to-noise ratio will be defined as the average IF single pulse peak return power to average IF noise power, i.e.

$$SNR = \frac{\left(\frac{\hat{P}_r}{P_T}\right)_{IF}}{(\bar{N})_{IF}} = \frac{P_T \hat{F}}{L_{ab} L_{bc} k T_e (B_{IF})_n} \quad (10)$$

From [3] and [7], the values of the quantities in (10) are as follows;

$$\begin{aligned} P_T &= 2 \text{ KW} \\ L_{ab} &\approx 1.02 \text{ dB} \\ L_{bc} &\approx 0.72 \text{ dB} \\ T_e &\approx 1230^\circ \text{ K} \\ (B_{IF})_n &\approx 1.11 (B_{IF})_{3dB} \end{aligned}$$

where $(B)_{3dB}$ is the IF 3 dB (two-sided) bandwidth. The factor \hat{F} has been

previously computed for the 100 ns pulsewidth case [2] and is a function of the direction of pointing error due to the asymmetry in the antenna pattern. That is, for a fixed pointing error, \hat{F} depends upon whether the error is in the pitch direction (ξ_p) or the roll direction (ξ_r). For zero yaw angle, the pitch and roll spacecraft-centered coordinates correspond to the along-track and cross-track directions, respectively.

For the purposes of these approximate computations, the \hat{F} factor for the other pulsewidth/bandwidth combinations can be obtained from the 100 ns/-10 MHz results by multiplying by $PW_{IF}/72$, where PW_{IF} is the effective pre-detection pulsewidth in nanoseconds. For 100 ns/100 MHz, $PW_{IF} \approx 100$ ns; for 10 ns/100 MHz, $PW_{IF} \approx 20$ ns; for 10 ns(PC)/100 MHz, $PW_{IF} \approx 10$ ns. These numbers are taken from Table III. Figure 22 illustrates how the SNR normalized by the surface scattering cross section to path loss attenuation (σ°/L_p) ratio varied as a function of; (1) pulsewidth and bandwidth, (2) pointing angle, and (3) pointing direction for missions SL-2 and SL-3. A curve for pulse compression is not shown in this figure since it only began to function properly at the end of SL-3. The effect of pointing direction is seen to cause a maximum change in SNR of about 1.5 dB and thus will be ignored; the optimistic case of no pitch error ($\xi_p = 0^\circ$) is used. In order to determine the unnormalized SNR for a particular pass, it would be necessary to go to [2] to determine the appropriate value of (σ°/L_p) for the given pass. To give some idea of the resulting values of SNR, Figure 23 shows SNR as a function of (σ°/L_p) for $\xi_r = 0.5^\circ$. The minimum observed value of (σ°/L_p) during SL-2 and SL-3 was approximately 10 dB*. Thus, for all three pulsewidth/-bandwidth combinations the IF SNR was relatively high during SL-2 and SL-3, i.e.

100 ns/10 MHz : SNR \geq 31 dB,
100 ns/100 MHz : SNR \geq 23 dB,
10 ns/100 MHz : SNR \geq 15 dB.

The maximum observed value of (σ°/L_p) was very near 20 dB and thus

100 ns/10 MHz : SNR \leq 41 dB,
100 ns/100 MHz : SNR \leq 33 dB,
10 ns/100 MHz : SNR \leq 25 dB.

*This result applies to over ocean passes only.

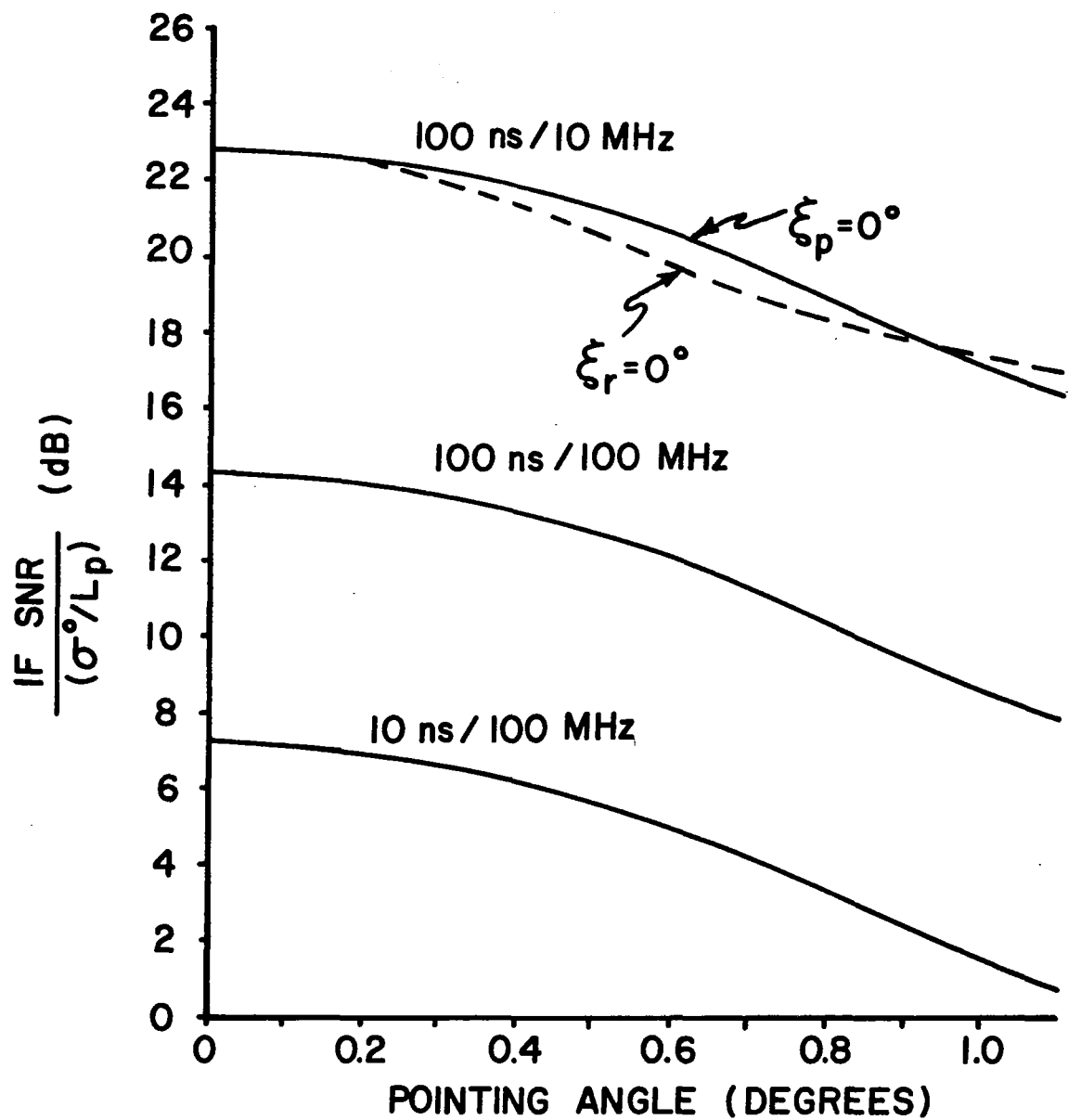


Figure 22. Average IF single pulse signal-to-noise ratio per unit scattering cross section as a function of pulsewidth/bandwidth and pointing angle for SL-2 and SL-3.

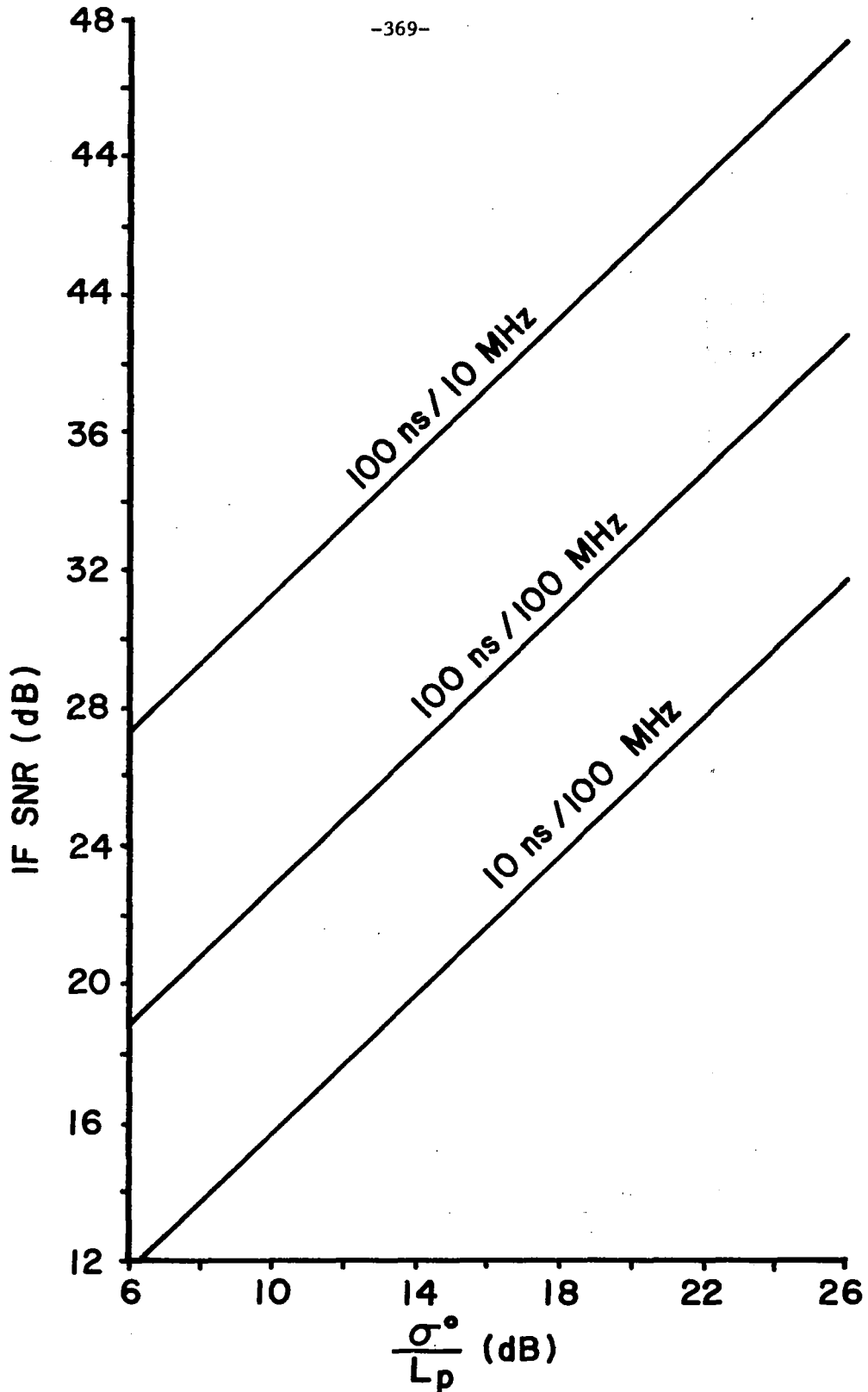


Figure 23. Average IF single pulse signal-to-noise ratio as a function of pulsewidth/bandwidth and σ^0 for $\xi_p = 0^\circ$, $\xi_r = 0.5^\circ$ and SL-2, SL-3.

In summary, for SL-2 and SL-3 passes where the pointing angle was less than about 0.8° , the over ocean SNR values were generally sufficiently high to permit the neglect of thermal noise effects.

For mission SL-4, the situation was somewhat different in that damage to the S-193 antenna resulted in a (one-way) antenna gain reduction of about 12.6 dB [2]. The resulting curves of normalized SNR as a function of pointing angle ξ_r and pulsewidth/bandwidth combinations are shown in Figure 24. It should be noted that because of the effective compression gain of 13, the 10 ns pulse compression case exhibited a higher SNR than did the 100 ns/100 MHz combination. The variation of SNR with (σ°/L_p) for an assumed pointing error of 0.5° is shown in Figure 25. It is rather obvious in Figure 25 why the 10 ns/100 MHz combination generally failed to acquire and maintain tracking; that is, (σ°/L_p) would have to exceed 19 dB for the SNR to go above 0 dB. The lowest measured value of (σ°/L_p) was about 8 dB which implies that the 10 ns(PC) and the 100 ns/100 MHz modes maintain lock below the thermal noise level, i.e. SNR \approx -3 and -4 dB, respectively. The reason for this was the 5 MHz low pass filter ahead of the tracking loop (see the footnote in Table III). Including the effects of this filter, the effective signal-to-noise ratio at the input to the tracking loop was about +2 to +3 dB for $\sigma^\circ = 8$ dB. Thus, it is not surprising that the altimeter maintained lock for an IF SNR below 0 dB. The curves in Figure 25 certainly show that generally all combinations of pulsewidth and bandwidth were operating at a very low IF SNR level.

7.0 Data Problems

Since the S-193 radar altimeter was the first known instrument of its kind and since there were numerous design dependent calibration/corrections required of the raw data, not all of data on the tapes provided the investigators were correct. Also, since these data may be of future interest, this section will document some of the known data problems that were encountered during our investigations. These problems typically cover the complete spectrum, i.e. from inadequate processing to relatively simple errors such as nondeletion of settling frames of data. The comments in this section are not intended, by any means, to reflect on the capabilities of the processing designers; rather, they clearly illustrate the fact that the altimeter was

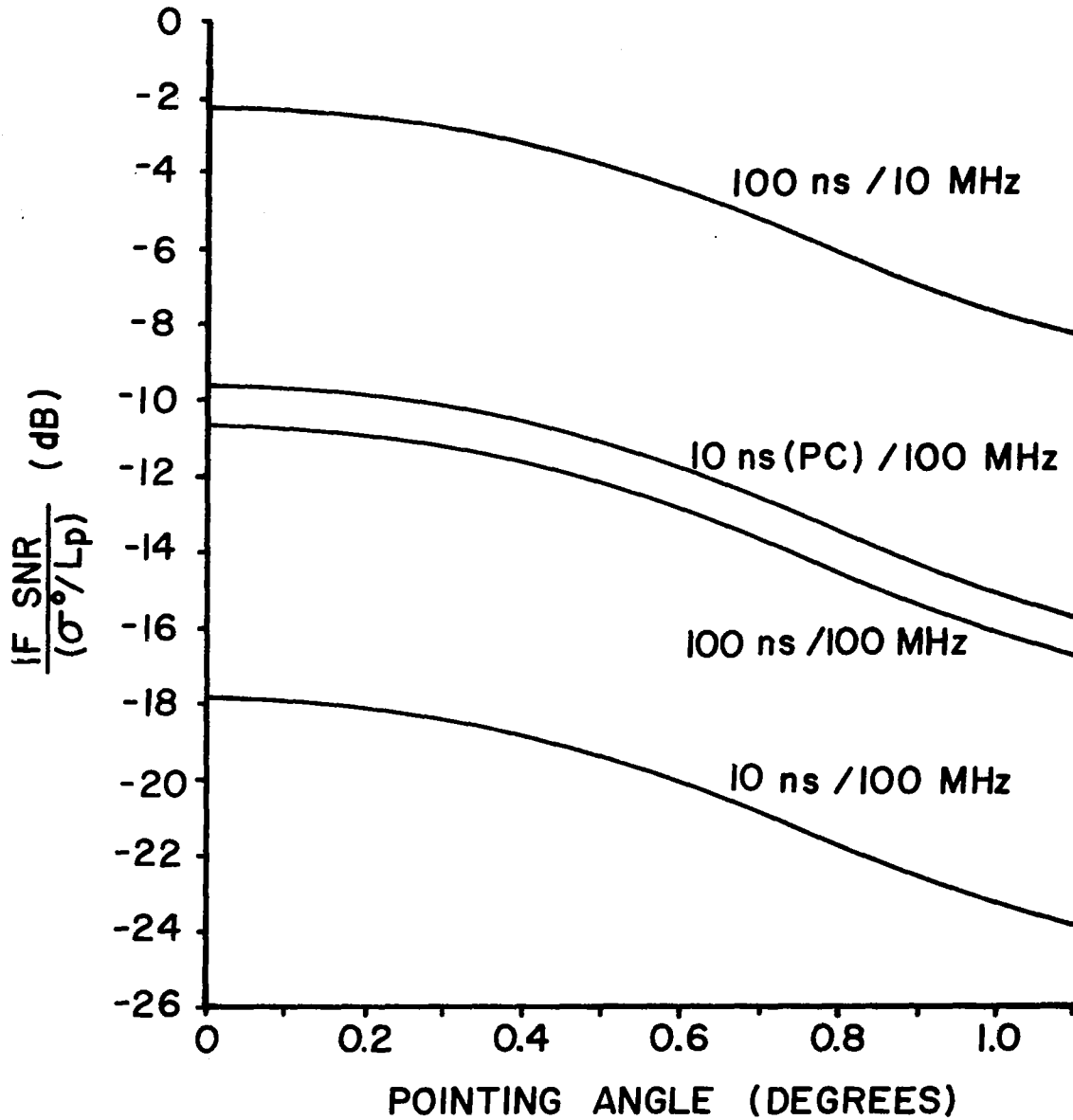


Figure 24. Average IF single pulse signal-to-noise ratio per unit scattering cross section as a function of pulsewidth/bandwidth and pointing angle ($\xi_p = 0^\circ$) for SL-4.

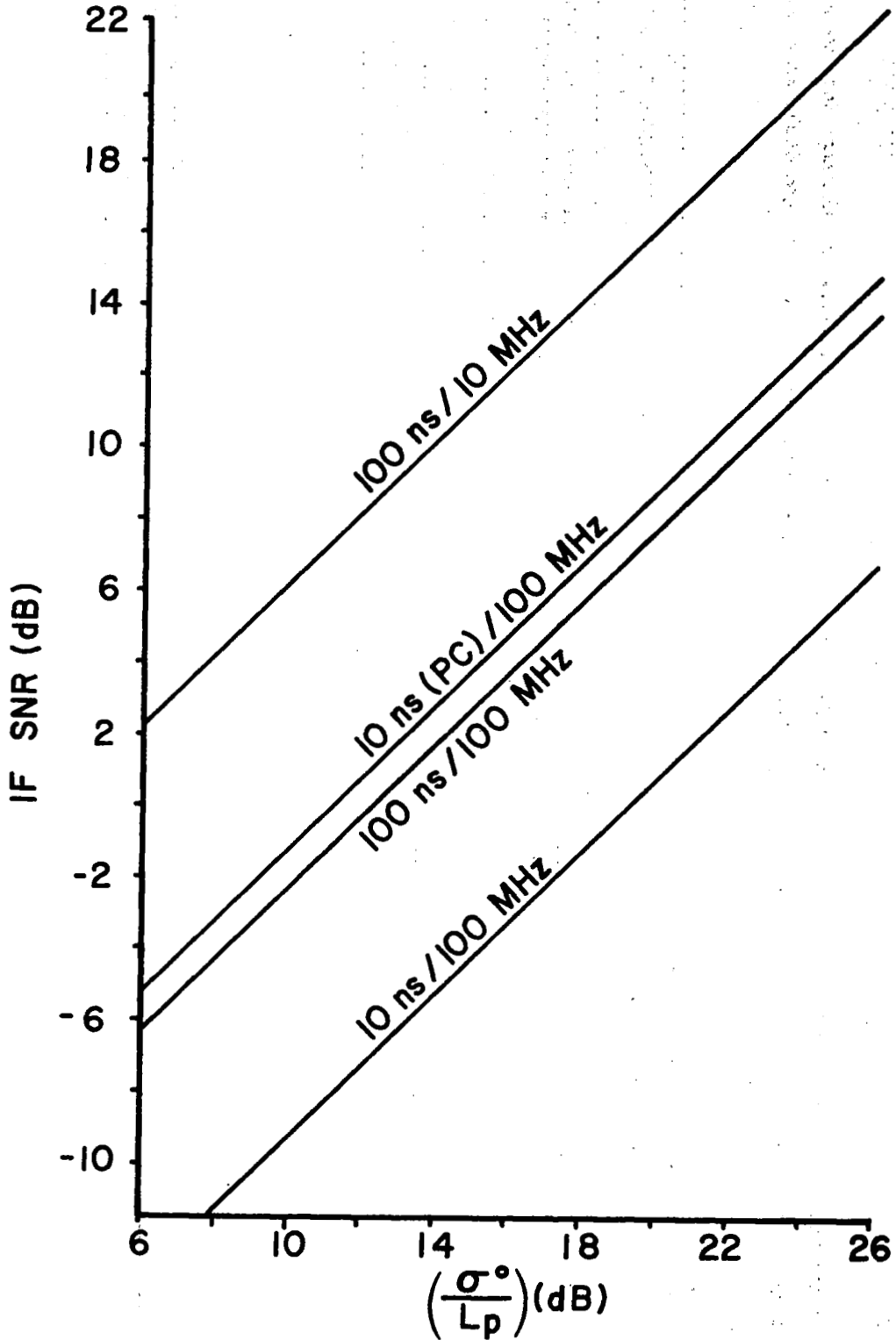


Figure 25. Average IF single pulse signal-to-noise ratio as a function of pulsewidth/bandwidth and σ^0 for $\xi_p = 0^\circ$, $\xi_r = 0.5^\circ$ and SL-4.

operational before the correct and complete processing was ready for implementation. This point is further amplified by the fact that this report is being published nearly three years after the initiation of the first Skylab flight, and a great majority of this time was spent understanding and implementing the necessary data processing.

Probably the most significant problem with the data was that the values of received power were incorrect. The difficulties stem primarily from the following; no accounting for the waveform dependent nature of the AGC system was made, the contribution of the tunnel diode amplifier noise was ignored and the temperature interpolation between different calibration curves was incorrect. Reference [2] discusses these problems in depth and presents the correct (and extremely lengthy) processing procedures required. The net effect of the erroneous processing destroys any absolute determination of received power from the magnetic tape data. One can, however, use the data to give an indication of the relative changes in received power such as was done in Chapters 5 and 6. If an absolute level is essential, one should probably use the estimates of (σ^0/L_p) from [2] and the estimated SNR curves of the previous section (along with the computed noise power) to compute the received power.

A number of other facts should be realized about the basic altimeter data on the magnetic tapes. The altitude data was corrected by a fixed delay, dependent upon the operating mode, to account for the time delay through the receiver. There was a marked change in this delay in the pulse compression mode between when it was malfunctioning and when it operated properly. In addition, none of the altitude data was corrected for pointing angle induced biases or atmospheric refraction. The Sample and Hold waveform data contain a significant number of values which are physically impossible, i.e. wild points, and these values should be deleted prior to any processing. In addition, the data should also be saturation corrected as per the scheme in Section 5. The pitch and roll gimbal angles are not particularly significant since their accuracy is questionable (and in some cases erroneous) and they are somewhat erratic. For pointing angle estimates, one should refer to [2]. The SKYBET (Skylab Best Estimate of Trajectory) values for the longitude and latitude of the sub-nadir (ground track) point may also be in error because of poor tracking station coverage. In addition,

the so-called "sensor field of view" data should be ignored since the true pointing direction of the altimeter antenna is generally unknown. There are certain instances in the data (Mode I Submode 2) where the antenna was supposed to step forward in the positive pitch direction by 0.43° (nominal) but the waveform data did not indicate such a movement. Another important data problem resulted from premature termination of the altimeter sequencing by the Astronauts; as a result, some self-calibration data (CDS) was lost. The tracking lock quality indicator recorded on the altimeter data tapes is subject to some interpretation and the reader should refer to [3] for a more detailed discussion of the meaning of this flag.

In addition to the above problems, there were a few minor data tape difficulties which were more of an annoyance than a true problem. For example, it was determined that some valid data were omitted on the data tapes for no good reason. The proper number of settling frames (frames of data during which the altimeter was undergoing some transient condition) were not deleted from the data tapes. Data dropouts occurred which were due either to a loss of synch between the processing computer and the altimeter (raw) data tape or a change in tape speed of the on-board tape recorder. In some isolated instances there appeared to be some disparity between the exact GMT time tag on the data tapes and earlier processed data; the source of this problem was never found. There was no indication on the tapes when the altimeter experienced a momentary loss of lock and switched to the so-called "fine scan" mode of operation. In general this condition was evidenced by a constant altitude output.

The purpose of the above discussion is to alert the altimeter data user to some of the problems that were encountered during this investigation. The list is certainly not inclusive, but it should serve as a guide.

REFERENCES

1. _____, "Earth Resources Experiment Package Sensor Performance Report (S193 Altimeter)", Vol. V, Document No. MSC-05528 (NASA-JSC), prepared by Martin Marietta Corp., Denver, Colo., 6 September, 1974.
2. Brown, G. S., "Reduced Backscattering Cross Section (σ^0) Data From The Skylab S-193 Radar Altimeter," NASA CR-141401, Applied Science Associates, Inc., Apex, N. C., October, 1975.
3. _____, "S-193 Microwave Radiometer/Scatterometer Altimeter," Calibration Data Report, Vol. 1B, NASA Contract No. NAS9-11195, General Electric Co., Valley Forge, Pa., 22 March, 1972.
4. Hofmeister, E. L. & B. N. Keeney, "Radar Altimeter Return Waveform Sampling Study," NASA Contract No. NAS6-1823, General Electric Co., Utica, N.Y., October, 1971.
5. Hofmeister, E. L., "Analysis and Measurement of the Performance of a Signal Tracking Loop for a Satellite Radar Altimeter When Excited by a Random Process," Ph.D. Thesis, Syracuse University, Syracuse, New York, December, 1973.
6. Steenson, V. & N. Sterling, "The Amplitude Distribution and False Alarm Rate of Filtered Noise," Proc. of IEEE, pp. 42-55, January, 1965.
7. Hofmeister, E. L., "Skylab Altimeter," Section on Signal-to-Noise Ratio, Unpublished Document, Aerospace Electronics Systems Division, General Electric Co., Utica, N. Y., 19 March, 1971.